

Solid Freeform Fabrication Proceedings

September, 1993

ADA 277718

The breadth of Solid Freeform Fabrication as an important and totally integrated approach to design, materials processing and manufacturing is contained in this proceedings of the SFF Symposium held in Austin, Texas on August 9-11, 1993

SFF Topics covered in the Symposium include:

Accession For	
NTIS CRA&I	<input checked="" type="checkbox"/>
DTIC TAB	<input type="checkbox"/>
Unannounced	<input type="checkbox"/>
Justification	
By <i>per S. Fishman</i>	
Distributed <i>ONR 4/5/94</i>	
Availability Codes	
Dist	Avail and/or Special
<i>A-1</i>	

Computer Sectioning
Machine Design
Materials Processing:
Metals
Ceramics
Polymers
Waxes
Composites
Applications

Harris L. Marcus, Joseph J. Beaman,
Joel W. Barlow, David L. Bourell,
and Richard H. Crawford, Editors

© 1993 The University of Texas at Austin

All rights of reproduction in any form are protected by U.S. Copyright Laws.

Permission to copy all or portions of the proceedings contents must be obtained
from the authors and The University of Texas at Austin.

Library of Congress ISSN 1053-2153

94-10192



DTIC QUALITY INSPECTED 3

0444106

**Best
Available
Copy**

BUREAU OF ENGINEERING RESEARCH
THE UNIVERSITY OF TEXAS AT AUSTIN

*Center for Materials Science and Engineering • ETC 9.104 • Austin, Texas 78712-1063
(512) 471-1504 • FAX (512) 471-7681 • Telex 405 705 UT GRAD AUSUD*

March 31, 1994

Scientific Office Code: 1131N
Steven G. Fishman
Office of Naval Research
800 North Quincy Street
Arlington VA 22217-5000

696-0285

REF: Grant no.: N00014-93-1-0371

Dear Steve:

Enclosed are three copies of the **Solid Freeform Fabrication Symposium Proceedings 1993** submitted to fulfill the final report requirement of the referenced grant. Copies of the Proceedings were originally distributed in fall of 1993. A full list of attendees is included in the Proceedings. Please call me at 512-471-3188 if you have any questions.

Sincerely,


Harris L. Marcus
Cullen Trust for Higher Education
Endowed Professorship in Engineering #1

HLM/vl

cc: Office of Sponsored Projects, UT

Table of Contents

Preface.....	v
Material Issues in Layered Forming	1
Christina Amon, Jack Beuth, Helmut Kirchner, Robert Merz, Fritz Prinz, Kevin Schmaltz and Lee Weiss; <i>Carnegie Mellon University</i>	
StereoLithography Epoxy Resin Development: Accuracy and Dimensional Stability	11
Thomas H. Pang; <i>3D Systems, Inc.</i>	
Vibratory Finishing of StereoLithography Parts.....	27
John D. Spencer, Richard C. Cobb, and Phillip M. Dickens; <i>The University of Nottingham</i>	
Structural Ceramic Components by 3D Printing.....	40
J. Yoo, Michael J. Cima, S. Khanuja, and E. M. Sachs; <i>Massachusetts Institute of Technology</i>	
Direct Laser Sintering of Metals.....	51
William T. Carter, Jr., and Marshall G. Jones; <i>GE Corporate Research & Development</i>	
Solid Freebody Forming of Ceramics From Polymerizable Slurry	60
K. Stuffle, and A. Mulligan; <i>Advanced Ceramics Research Company</i> Paul Calvert, and John Lombardi; <i>Arizona Materials Laboratories</i>	
Development of Nanocomposites for Solid Freeform Fabrication	64
Arumugam Manthiram, F. Chi, L. F. Johnson, B. R. Birmingham, and H. L. Marcus; <i>The University of Texas at Austin</i>	
Part Fabrication Using Laser Machining and Welding	74
M. S. Pridham, and G. Thomson; <i>University of Dundee</i>	
Picoliter Solder Droplet Dispensing.....	81
Ronald E. Marusak; <i>MicroFab Technologies, Inc.</i>	
Control Parameters and Material Selection Criteria for Rapid Prototyping Systems.....	86
James W. Comb, and William R. Priedeman; <i>Stratasys, Inc.</i>	
Reducing or Eliminating Curl on Wax Parts Produced in the Sinterstation™ 2000 System	94
Paul Forderhase, and Richard Corden; <i>DTM Corporation</i>	
Computer Aspects of Solid Freeform Fabrication: Geometry, Process Control, and Design.....	102
Richard H. Crawford; <i>The University of Texas at Austin</i>	
Virtual Reality and Rapid Prototyping: Conflicting or Complementary?	113
Ian Gibson, D. Brown, S. Cobb and R. Eastgate; <i>The University of Nottingham</i>	

Optimization of 2D CT Data Sets for Three-Dimensional Craniofacial Imaging and Modeling	121
Richard A. Levy; <i>The University of Michigan Hospitals</i>	
Some Efficient Procedures for Correcting Triangulated Models	126
Ismo Mäkelä, and A. Dolenc; <i>Helsinki University of Technology</i>	
Robust Prototyping	135
Jana K. Chari, and J. L. Hall; <i>Iowa State University</i>	
Simulation of Solid Freeform Fabrication	143
Stuart B. Brown; <i>Massachusetts Institute of Technology</i>	
Automated 4 Axis Adaptive Scanning With the Digibotics Laser Digitizer	150
Stephen Koch; <i>Digibotics, Inc.</i>	
StereoLithography 1993: QuickCast™	158
Thomas H. Pang, and Paul F. Jacobs; <i>3D Systems, Inc.</i>	
FFF at Ford Motor Company	168
Sean O'Reilly; <i>Ford Motor Company</i>	
An Experimental Study of the Parameters Affecting Curl in Parts Created Using Stereolithography	178
Leslie Horton, and Michael Keefe; <i>University of Delaware</i> ; E. P. Gargiulo; <i>E. I. duPont de Nemours & Co., Inc.</i>	
Homogenization Design and Layered Manufacturing of a Lower Control Arm in Project MAXWELL	186
Roy Johanson, N. Kikuchi, and P. Papalambros; <i>University of Michigan</i> ; Fritz Prinz, and Lee Weiss; <i>Carnegie Mellon University</i>	
An Evaluation of the Mechanical Behavior of Bronze-NI Composites Produced by Selective Laser Sintering	193
Mukesh Agarwala, D. L. Bourell, B. Wu, and J. J. Beaman; <i>The University of Texas at Austin</i>	
Silicon Carbide Preforms for Metal Infiltration by Selective Laser Sintering™ of Polymer Encapsulated Powders	204
N. K. Vail, J. W. Barlow, and H. L. Marcus; <i>The University of Texas at Austin</i>	
Fabrication of Ceramic and Metal Matrix Composites From Selective Laser Sintered Ceramic Preforms	215
Lucy Deckard, and T. Dennis Claar; <i>Lanxide Corporation</i>	
Powder Layer Position Accuracy in Powder-Based Rapid Prototyping	223
Sang-Joon John Lee, E. Sachs, and M. Cima; <i>Massachusetts Institute of Technology</i>	
The Physics of Digital Microfabrication with Molten Microdrops	237
Fuquan Gao, and A. A. Sonin; <i>Massachusetts Institute of Technology</i>	

Material and Process Parameters That Affect Accuracy in Stereolithography	245
Richard P. Chartoff, Lawrence Flach and Peter Weissman; <i>University of Dayton</i>	
Thermal Analysis and Modeling of Steady-State Rod Growth During Gas-Phase Solid Freeform Fabrication	253
James L. Maxwell, Joseph Pegna, and Alexander Ostrogorsky; <i>Rensselaer Polytechnic Institute</i>	
Potential Application of Solid Freeform Fabrication (SFF) Process in Ceracon P/M Forging	271
Ramas V. Raman, S. V. Rele, and R. L. Anderson; <i>Ceracon, Inc.</i>	
Machine Vision for Rapid Geometric Modeling	275
Visa Koivunen, and R. Bajcsy; <i>University of Pennsylvania</i>	
Strategy for Composite Development in Rapid Prototyping	283
R. Charan, A. Bagchi, T. Renault, and A. A. Ogale; <i>Clemson University</i>	
Direct Generation of Contour Files from Constructive Solid Geometry Representations	291
Sashidhar Guduri, R. H. Crawford, and J. J. Beaman; <i>The University of Texas at Austin</i>	
Indirect Metal Composite Part Manufacture Using the SLS Process	303
James R. Tobin, B. Badrinarayan, J. W. Barlow, J. J. Beaman, and D. L. Bourell; <i>The University of Texas at Austin</i>	
Solid Freeform Fabrication of Silicon Carbide Shapes by Selective Laser Reaction Sintering (SLRS)	308
Britton R. Birmingham, and H. L. Marcus; <i>The University of Texas at Austin</i>	
Supersolidus Liquid Phase Selective Laser Sintering of Prealloyed Bronze Powder	317
Gopalakrishna Prabhu, and D. L. Bourell; <i>The University of Texas at Austin</i>	
Selective Area Laser Deposition of Silicon Carbide	325
James V. Tompkins, and H. L. Marcus; <i>The University of Texas at Austin</i>	
Drying of Colloidal Binder Infiltrated Ceramic Green Parts Produced by Selective Laser Sintering™	333
M. Glazer, N. K. Vail, and J. W. Barlow; <i>The University of Texas at Austin</i>	
Synthesis, Selective Laser Sintering and Infiltration of High T_c Dual Phase Ag-YBa₂Cu₃O_{7-x} Superconductor Composites	339
Mukesh Agarwala, D. L. Bourell, A. Manthiram, B. R. Birmingham, and H. L. Marcus; <i>The University of Texas at Austin</i>	

Selective Laser Sintering of Al₂O₃	350
P. K. Subramanian, G. Zong, N. Vail, J W. Barlow, and H. L. Marcus; <i>The University of Texas at Austin</i>	
Laser Sintering Model for Composite Materials	360
James C. Nelson, N. K. Vail, and J. W. Barlow; <i>The University of Texas at Austin</i>	
Measurement of the Thermal Conductivity of Powders by Two Different Methods	370
Samuel Sumin Sih, and J. W. Barlow; <i>The University of Texas at Austin</i>	
Selective Laser Sintering of Bioceramic Materials for Implants	376
Goonhee Lee, and J. W. Barlow; <i>The University of Texas at Austin</i>	
Key Word Index	381
Author/Attendee List	383

PREFACE

This Proceedings of the Fourth Solid Freeform Fabrication Symposium, held at The University of Texas in Austin on August 9-11, 1993, reaffirms the dynamic nature of the research area. The interest shown by researchers over the wide range of disciplines and sub-disciplines that make up Solid Freeform Fabrication (SFF) highlights this technical Symposium. The speakers addressed problems in computer software, in machine design, materials synthesis and processing, and SFF in integrated manufacturing. The exponential growth in the research, application and development of SFF approaches was readily apparent from the attendees from industrial users, SFF machine manufacturers, universities, and government. This Symposium is the first where real progress toward structurally sound samples and parts was demonstrated as SFF moves from "feelie" to "non-structural" to "structural" real parts over a range of materials. This advancement in the state-of-the-art of SFF will continue to drive the exponential growth of the area. The excitement amongst the Symposium participants will continue to serve as the catalyst for the continued growth and the availability of Solid Freeform Fabrication. The Symposium organizers look forward to its being a continued source of technical exchange among the growing body of researchers involved in SFF.

The Symposium was organized in a manner to allow the multi-disciplinary nature of the SFF research to be presented coherently, with various sessions emphasizing computer aspects, machine topics, and the variety of materials aspects of SFF. Application-related efforts were scattered throughout the Symposium. To avoid parallel sessions a poster session was organized, and the panel session on SFF was held in the evening, after a visit with Texas barbecue. The dynamic panel discussion on Future Directions in SFF was led by Marshall Burns, Michael J. Cima, Tom Latham, Greg Sanders and Joel W. Barlow. The written versions of the presented papers are incorporated into these Proceedings. The editors would like to thank the speakers for their timely delivery of the manuscripts that expedited the publication of these Proceedings. The constantly changing state of the SFF art as represented by these Proceedings will serve both the people presently involved in this fruitful area as well as new researchers and users coming into Solid Freeform Fabrication.

The editors would also like to extend a warm thank you to Renee Loyless-May for her extensive efforts in the detailed handling of the logistics of the meeting and the Proceedings. We would also like to thank the organizing committee, the speakers, the session chairmen, panel members, and the attendees for their enthusiastic contributions. We look forward to the continued close cooperation of the SFF community in organizing the Symposium. We also want to thank ONR through Grant No. N00014-93-1-0371, ARPA, and The Minerals, Metals and Materials Society for co-sponsoring the Symposium as well as DTM Corporation for hosting the reception.

The editors

Organizing Committee:

Dick Aubin, United Technologies
Joel W. Barlow, The University of Texas at Austin
Joseph J. Beaman, The University of Texas at Austin
David L. Bourell, The University of Texas at Austin
Robert L. Brown, The Gillette Company
William Coblenz, ARPA
Richard Crawford, The University of Texas at Austin
Samuel Drake, University of Utah
Steven Fishman, Office of Naval Research
Harris L. Marcus, The University of Texas at Austin
Fritz Prinz, Carnegie Mellon University
Emanuel Sachs, Massachusetts Institute of Technology
Greg Sanders, General Motors Corporation
Sean O'Reilly, Ford Motor Company
Ralph Wachter, Office of Naval Research
Michael Wozny, Rennselaer Polytechnic Institute

Material Issues in Layered Forming

Christina Amon, Jack Beuth, Helmut Kirchner,
Robert Merz, Fritz Prinz, Kevin Schmaltz, Lee Weiss

Carnegie Mellon University
Pittsburgh, PA

Abstract

A brief overview of key issues in layered thermal processing is given. Incremental sintering and layered fusion of powder and molten droplets are discussed. The criteria for remelting the solid substrate are derived from a one dimensional heat transfer model. Temperature gradients which occur during solidification and subsequent cooling are responsible for the build up of internal stresses which can be estimated through establishing an elastic beam model. The difficulties as well as opportunities regarding the generation of multi-layer multi-material structures are also described in this article.

Key Words

Layered manufacturing, sintering, melting, thermal modeling, residual stress, multi material structures, stress cracking.

Introduction

Solid freeform fabrication through layered material deposition appears to be an attractive method for 3D object generation[1,2,3]. This method offers the possibility of expanding the design space with respect to geometric complexity, material diversity, and traditional cost/time constraints. However, building up materials in layers poses significant challenges from material science, heat transfer and applied mechanics viewpoint.

Depositing materials onto a solid substrate can typically be accomplished through sintering, local melting, chemical synthesis (e.g. photo polymerization), or otherwise gluing, brazing, and soldering. The issues associated with each of these processes can be summarized as follows:

- Local melting requires significant energy input to the semi-finished part which may result in the buildup of internal stresses and consequently distortions.
- Sintering requires less energy to establish bonding of the added layers but local voids may be left unless external forces are applied
- The practical applicability of chemical synthesis is limited to certain derivatives of organic substances
- Gluing, brazing, and soldering have the disadvantage of adding bonding materials to the part which are not necessarily desirable for its function or performance.

Some of these difficulties can be overcome by adopting post processing steps such as annealing, sintering, and material infusion. Building parts through layered forming is further complicated if one attempts to deposit dissimilar materials on to the substrate. In particular, differences in the coefficient of thermal expansion (CTE), and misfit dislocations (due to differences in atomic radii) can lead to even greater distortions of the atomic lattice in comparison with layered material structures of the same kind. This paper discusses some of these underlying issues in layered forming rather than attempting to offer specific solutions to these problems.

Process Classification

Common to all layered forming techniques is the incremental nature of the material build up process. Stepwise material build up requires bonding between layers. Obviously, the material

quality of a part is determined by the quality of each deposited layer as well as the quality of the bond between the layers. The following classification for material deposition processing in layered manufacturing is chosen. Processes are listed with respect to the temperature regimes in which they operate at and issues of concern regarding the resulting articles. This list is by no means exhaustive with important problems like speed, surface quality and accuracy not being addressed.

<u>Process</u>	<u>Temperature</u>	<u>Issues</u>
Sintering	$T < T_M$	Density Postprocessing
Melt On	$T > T_M$	Residual Stress Warping Debonding Postprocessing
Glueing Powder Sheet	$T \sim T_R$	Strength Postprocessing
Photocuring	$T \sim T_R$	Limited Material Range Residual Stress

In the following, we limit our discussion mostly to thermal processing issues (e.g. sintering, melting) some of which are also relevant for processes occurring at room temperature.

Sintering

Layered powder deposition followed by laser sintering has become an established prototyping process; for more details see [1]. The physics of any sintering process is based on particle fusion at temperatures below the material melting point. During sintering necks form between adjacent powder particles thus reducing the surface area and increasing the density of the powder aggregate. The driving force for this process is the reduction of the particle surface free energy. The densification rate is proportional to that reduction.

In order to change the shape of the powder particles, matter or vacancies need to flow. (Vacancy flow can be considered as the counterflow of matter, both concepts are equivalent). The densification rate depends further on the combination of the transport path of the matter as well as the source of the matter. Ashby [4] distinguishes six different path/source combinations e.g.: surface diffusion from surface, boundary diffusion from boundary, or volume diffusion from boundary. At different temperatures different path/source combinations dominate the flow of matter.

During pressureless sintering (i.e., no external force applied) the densification rate decreases as the aggregate density increases due to a decreasing rate of surface reduction. A quick inspection of the theoretically established sintering maps by Ashby such as the example of copper in Figure 1 indicate that close to full density (i.e. when the neck radius is comparable to the particle radius) can only be reached asymptotically. Also, the times required to achieve high densities are significantly higher than the mean time that a selective heat source (e.g. laser) will for practical reasons dwell in a certain location. Hence, selectively sintered powder aggregates need to be subjected to further postprocessing procedures such as hot isostatic pressing to achieve full density.

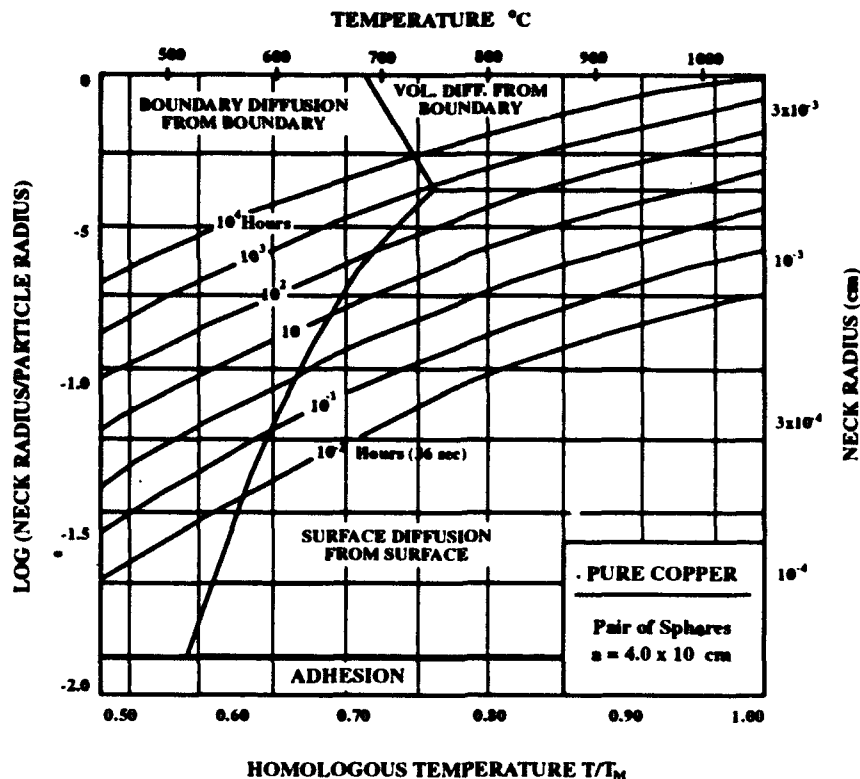


Figure 1: Sintering map of copper particles [4].

Melting On

To further enhance and accelerate the bonding of a layer to the substrate one can locally melt already deposited powder particles or deposit molten droplets as done for example in thermal spraying [2]. Two scenarios can be envisioned: In the first one the molten droplet adapts to the shape of the underlying substrate. In the second the particle has sufficient energy to remelt the substrate and form a solid bond. In the first case two possibilities for bonding exist. The molten droplets simply form a mechanical interlock as commonly observed in thermal spraying [4]. Alternatively, the droplets may also bond to the substrate through a sinter mechanism in which necking occurs by shape adaptation of the molten droplet and diffusion within or on the surface of the substrate. The rate of bond formation will obviously be higher compared to the pure sinter case as described earlier.

In addition to the structure of the bond, the microstructure resulting from the solidification of the droplets is key to the strength of the layered article. Therefore an understanding of the entire temperature history is important for planing layered manufacturing processes. Also, higher temperature gradients involved in melting compared to pure sintering tends to lead to the formation of higher residual stresses.

In the following sections we address the issue of predicting the thermal history of the melting process as well as the build up of residual stresses after solidification.

Thermal Modeling

This section presents a numerical modeling of the thermal history of a molten metal particle on a solidified substrate. The particle can be melted by a laser or plasma alternatively, molten droplets can be sprayed on a solidified substrate as depicted in Figures 2a and 2b. This model is useful for investigating the conditions needed to achieve partial substrate remelting, to create an accurate predictive tool of the particle melt of the thermal spray process, and to investigate the effect of operating conditions such as initial molten particle/droplet and substrate temperatures,

size, surface heat transfer and sprayed material properties on the resulting melting front migration rate and thickness, temperature distribution, and overall cooling rates.

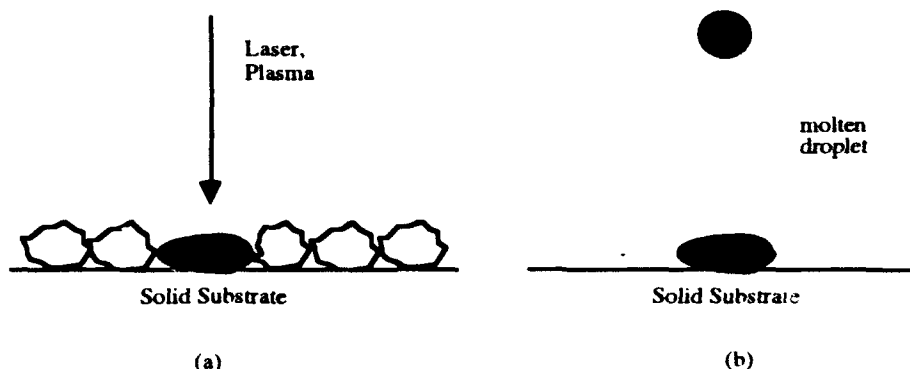


Figure 2 (a) molten powder particle (b) molten droplet deposition.

In the following we refer to molten particles as well as droplets from spraying just as droplets. Application parameters such as laser energy or spray gun power input, and deposition rates may then be modified to optimize the deposited material microstructure.

The numerical model for determining process temperatures and remelting conditions is simplified to a one-dimensional, heat transfer problem by assuming that the impacted droplet width is sufficiently greater than height, and that the droplet flattening time scale is much shorter than the droplet solidification time scale. This phenomena is modeled by the governing equation of the form:

$$\rho c_p \frac{\partial T}{\partial t} = k(T) \left[\frac{\partial^2 T}{\partial x^2} \right] + \frac{\partial k(T)}{\partial T} \left[\frac{\partial T}{\partial x} \right]^2 \quad (1)$$

for temperature T , density ρ , specific heat c_p , and thermal conductivity k . The $\partial k / \partial T$ term is omitted since the thermal conductivity variation is slight for the materials and temperature ranges considered, although temperature dependent thermal properties are used [6]. This equation is valid for both the liquid region as well as the solid region. Above the top liquid surface, combined convective and radiative boundary conditions exist, while the energy balance:

$$\rho L \frac{\partial x}{\partial t} = k_{sol} \frac{\partial T}{\partial t} - k_{liq} \frac{\partial T}{\partial t} \quad (2)$$

is applied at the interface between the liquid and solid regions, balancing the energy flux into and out of the interface with the release of latent heat (L). For the lower boundary of the solid region a constant substrate temperature is assumed at a remote distance from the surface.

The energy equation is discretized using an Eulerian explicit formulation. To track the location of the melting front during the solidification process, a three-point Lagrange interpolation formula is used to approximate the temperature function [7] at the nodes preceding and following the melting point. This assumes a form that can be readily incorporated into the finite difference formulation used, but permits the location of a varying "node" point corresponding to the melting front. The new front location is calculated after each iteration using the discretized interface energy balance equation. To approximate the initial interface temperature when the known liquid droplet first strikes the known solid substrate the analytical Stefan interface solution is used:

$$T_{inter.} = [RATIO * T_{liq} + T_{sol}] / [1 + RATIO] \quad (3)$$

$$\text{RATIO} = \sqrt{(k c_p \rho)_{\text{liq}} / (k c_p \rho)_{\text{sol}}} \quad (4)$$

For the complete duration of the thermal system modeling, the Stefan solution is not an accurate representation of the actual boundary conditions. However, for the initial interface condition the solution above can be used because boundary conditions corresponding to two semi-infinite bodies in contact remain valid until the temperature fluctuation propagates to the liquid surface.

For the first droplet, the initial conditions assumed are uniform droplet and ambient substrate temperatures. When prior molten droplets heat the substrate, the model is then modified to incorporate the two-dimensional effects of substrate preheating arising from the diffusion of energy from previously molten droplets:

$$\rho c_p \frac{\partial T}{\partial t} = k(T) \left[\frac{\partial^2 T}{\partial x^2} + \frac{\partial^2 T}{\partial y^2} \right] \quad (5)$$

This model reflects the process where the laser source or spray gun is moving across the substrate. As with the one-dimensional solidification model, an Eulerian explicit algorithm is used to solve the two-dimensional energy equation. Because remelting does not occur with this lateral case there is no Lagrangian approximation terms required. The substrate temperature profile resulting from this two-dimensional model is then used as the substrate initial condition for the solidification model.

Simulations are made for the model of single droplets of carbon steel, stainless steel and zinc which are residing or have landed on similar substrates, and for a steel droplet on a zinc substrate. This latter case simulates the building up of sprayed materials onto a sacrificial substrate. Parametric studies of remelting sensitivity to surface convection and radiation changes, variations of impacting droplet temperature, droplet size and existing substrate temperature have been performed. The solidification process is completed so rapidly (on the order of milliseconds) that the heat transfer is basically a conductive process, and the surface convective and radiative effects are negligible. Numerical results also indicate that substrate remelting will not occur with realistic droplet temperatures (having less than several hundred degrees centigrade of superheating) on an *unheated* substrate. A remelting condition requires a substrate heated several hundred degrees above ambient temperature. This condition does exist when the preheating effect caused by previous droplets is included with the two-dimensional model.

For the case of a stainless steel droplet landing on a stainless steel substrate, numerical simulations are performed with initial "droplet" thickness of 100 microns and substrate temperature of 1100°C. The time-dependent solidification of this layer is shown in Figure 3 for two cases: a 1550°C and a 1650°C initial droplet temperature. The y-axis of Figure 3. indicates the location of the melting front; 0 represents the interface between the impinging droplet and the substrate, with the droplet extending in the positive direction.

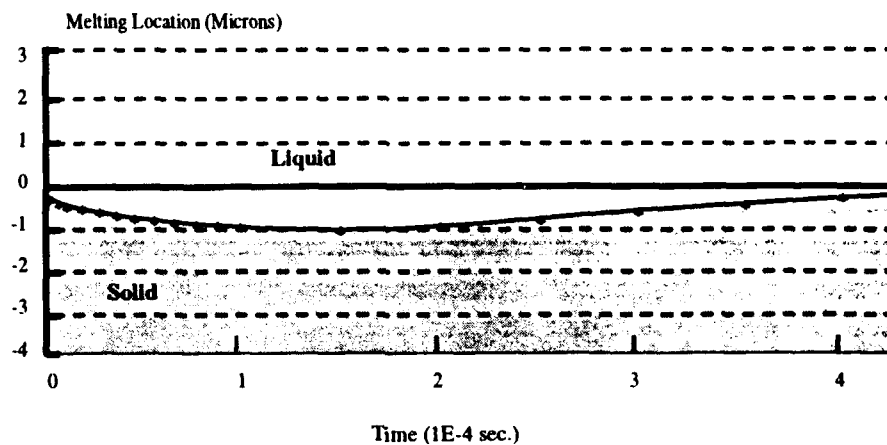
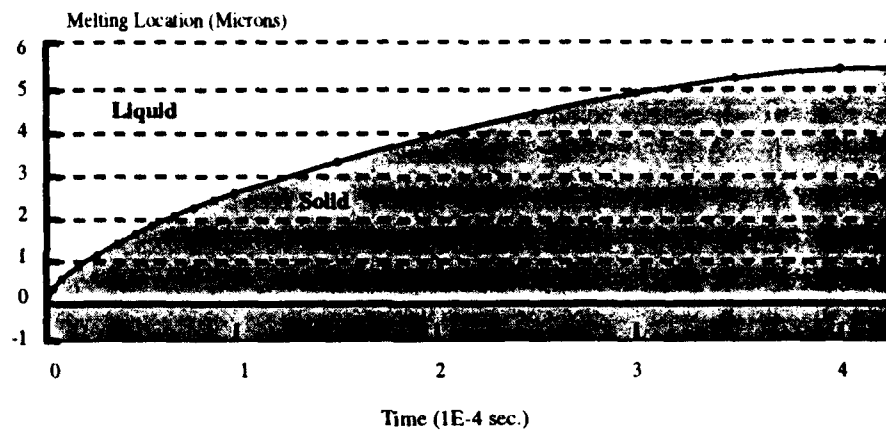


Figure 3: Substrate Remelting
(304 Stainless Steel Preheated substrate, Drop Size 100 Microns)

At the start of the simulation the entire positive y region is liquid and the negative region solid. For the 1550°C temperature no substrate remelting occurs, while for the 1650°C case a small amount of remelting does occur. In Figure 4 the results for a stainless steel droplet on a zinc substrate are shown.

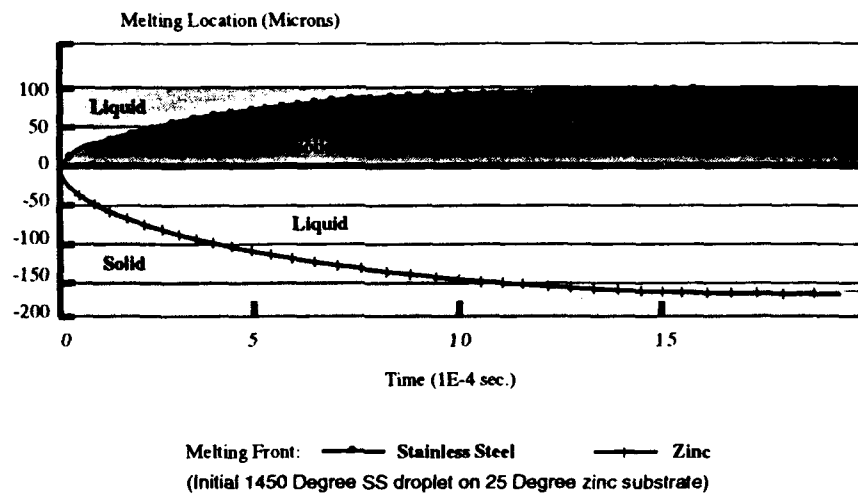


Figure 4: Substrate Remelting (Stainless steel on zinc substrate)

The stainless steel droplet, initially at its melting temperature, solidifies while the lower melting zinc melts and actually vaporizes slightly. This result demonstrates the need to protect sacrificial support material.

Mechanics Issues in Shape Deposition Processes

A current limitation of layered processing is the build-up of residual stresses as artifacts are manufactured. Residual stresses can affect artifact performance (response and life) and are also the root cause of specific deleterious effects including artifact warping, artifact delamination and stress cracking of brittle layers. Understanding the build-up of residual stresses and how to minimize them and their effects are thus the focus of current mechanics research into layered manufacturing.

Residual Stresses and Artifact Warping

In the layered processing, residual stresses are built up as new layers are deposited onto existing layers of the artifact. This build-up is due to the contraction each new layer experiences as it solidifies and cools and occurs even in the successive application of layers of the same material. The process is illustrated in Figure 5 where, for simplicity, a single layer of one material is shown applied to a single existing layer of another material. The layer thicknesses may differ, however, it is assumed that each layer is beam-shaped. It is also assumed that the new layer experiences a uniform contraction as it solidifies on the existing layer and that the contraction can be characterized by a temperature-independent coefficient of thermal expansion, α . Under these assumptions, the elementary analysis of Timoshenko [8] for the stresses in a uniformly heated bimaterial strip can be applied to predict the residual stresses in each layer and the curvature of the two-layered artifact caused by the contraction of the newly applied layer. The predicted curvature, κ , takes the form

$$\kappa \equiv \frac{1}{\rho} = \frac{-\alpha \Delta T}{\frac{(h_1 + h_2)}{2} + \frac{(E_1 h_1^3 + E_2 h_2^3)}{6(h_1 + h_2)} \left(\frac{1}{E_1 h_1} + \frac{1}{E_2 h_2} \right)} \quad (6)$$

where ρ is the radius of curvature of the artifact. In eq (6) α is the coefficient of thermal expansion of the new layer and ΔT is the difference (negative in sign) between the solidification temperature of the new layer and the operating temperature. The layer thickness is designated by h and E is the Young's modulus of the layer.

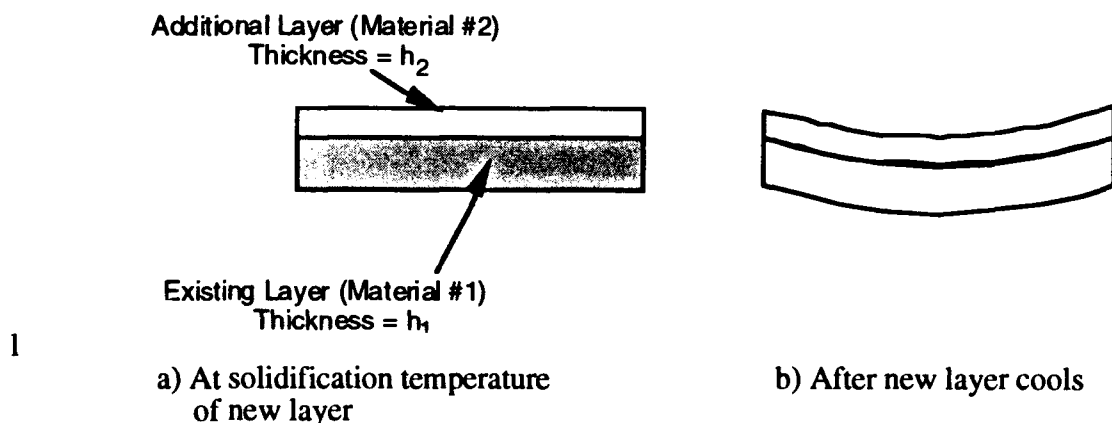


Figure 5 Curvature induced by the thermal contraction of a new layer (material #2) after its application to an existing layer (material #1).

For this simple model the stresses in each layer of the bilayer artifact are composed of axial and bending components and thus vary linearly through the thickness of each layer. In layered manufacturing, this interaction between newly applied and existing layers is repeated for each additional layer applied. The curvature of the artifact and the residual stresses in it are increased with the addition of each new layer.

There is a need in layered manufacturing to experimentally quantify residual stresses created during the process by measuring curvature changes caused by the addition of new layers. Results can be compared to simple models of layer interaction such as the one above. It is expected that enhancements to the model will be necessary, including accounting for the temperature dependency of coefficients of thermal expansion and the modeling of non-uniform thermal contraction of individual layers. In particular, results from thermal modeling of the solidification of layers (see previous section) is expected to yield more precise layer residual stress distributions for use in the solid mechanics model. The goal would be to not only predict residual stress and curvature effects in geometrically complex artifacts, but to also shed light on material combinations and process procedures that minimize them. An example of a layered copper steel tube manufactured by Carnegie Mellon's MD* process [2] is shown in Figure 6

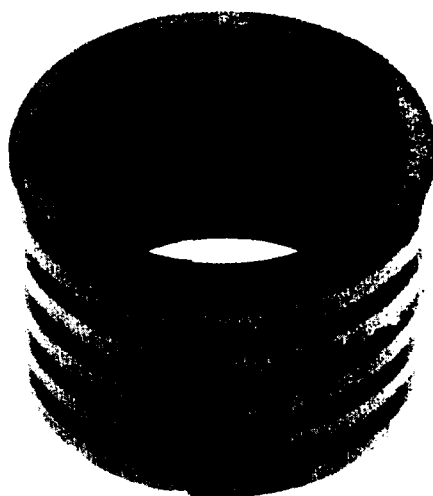
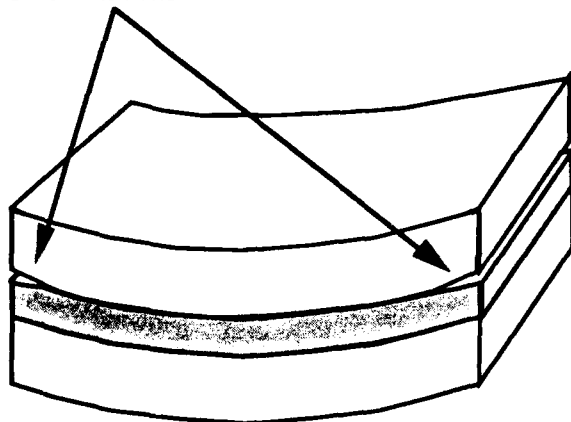


Figure 6. Layered copper steel tube manufactured in MD*

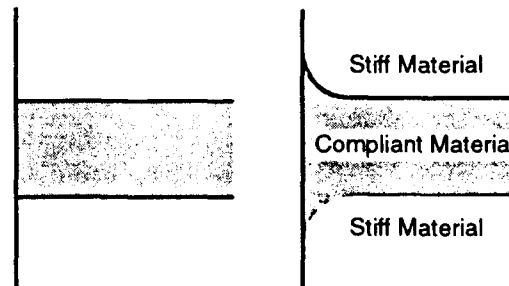
Interfacial Debonding

In addition to warping, residual stresses can cause delaminations between layers by acting as the driving force in the propagation of interfacial cracks from the edges of the artifact toward its center (see Figure 7 a). The delamination may propagate through the entire length of the artifact, separating it into two pieces. This is particularly a problem in the case of artifacts made of layers of different materials, due to the large stress concentrations that exist at the intersection of an uncracked bimaterial interface and a free edge.

Delaminations



(a)



(b)

Figure 7 a) Edge delaminations and b) Untailored and tailored bimaterial interfaces

A fully elastic asymptotic analysis of a bimaterial interface intersecting a free edge (see Bogy [9] or Hein and Erdogan [10]) predicts that stresses are, in general, singular there. Using the notation that the stresses vary as $r^{(\lambda-1)}$ as r approaches zero, where r is measured from the intersection point, λ can take on values from $\lambda=1.0$ (no singularity) to roughly $\lambda=0.60$. The value of λ is a function of the relative mismatch in elastic properties of the two materials and the angle that the interface makes with the free edge. The stress singularities that result from an elastic analysis of the bimaterial problem are important for two reasons. First, they indicate that actual interfaces in manufactured artifacts exhibit very high concentrations of stress at their free edges. Second, from an analysis standpoint, because the strength of the singularity in the elastic stresses is a function of the material combination studied, analytical comparisons of delamination driving force between different material combinations is difficult if an uncracked interface model is used.

We are investigating several approaches to help minimize delaminations. For example, one approach involves attempting to tailor the geometry of the interface to eliminate undesirable elastic stress singularities. This approach was suggested to the authors by G. B. Sinclair and follows the work of Okajima [11] on the bimaterial interface problem and the role of interface geometry in adhesive tensile tests. In Okajima [11] it is shown that the stress singularity at a bimaterial free edge in adhesive specimens can be eliminated if the interface is made to intersect the free edge tangentially, as shown in Figure 2b. In fact, the angle of intersection with the free edge need not be tangential and is a function of the relative elastic mismatch between the layers.

Stress Cracking

Another problem associated with residual stresses layered manufacturing is the cracking of newly applied brittle layers as they cool and contract after being applied to existing layers of the artifact (see Figure 8). A separate but related problem is the cracking of brittle layers after they are embedded between ductile layers within the artifact, typically due to a combination of residual and applied tensile stress. It is important to predict, for a particular brittle material, the maximum allowable thickness of a newly applied layer so that stress cracking will not occur. Similarly, for embedded layers, it is desired to determine the relative thickness of an embedded layer so that no cracking will occur.

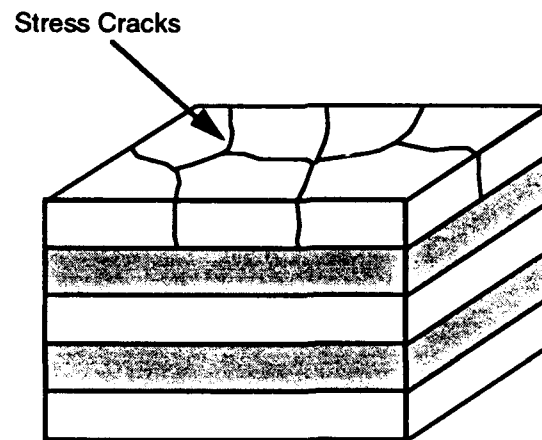


Figure 8. Stress cracking in a newly applied brittle layer.

Summary

Layered manufacturing offers new opportunities for product design. This is true from a geometry and from a materials perspective. Objects of arbitrary geometric complexity can be built from a larger variety of material combinations than with conventional manufacturing methods. However, frequently the quality of the built articles (bond strength between layers and material density) and the rate at which they are created does not meet industrial demands. A better insight into the physics of the underlying bonding processes between layers and the resulting residual stress accumulation due to temperature gradients is expected to lead to improved performance of objects made through layered manufacturing.

Acknowledgements

Financial support of this work by the Advanced Research Project Agency (ARPA/ ESTO) is gratefully acknowledged.

References

1. Bourell, D.L., Beaman, J.J., Marcus, H.L., and Barlow, J. W., (1990) "Solid Freeform Fabrication: An Advanced manufacturing Approach," *Proc. Solid Freeform Fabrication Symposium*, The University of Texas at Austin, Aug. 6-8, 1-7 (1990).
2. Weiss, L. E., Prinz, F. B., Adams, D. A., and Siewiorek, D. P., (1992) "Thermal Spray Shape Deposition", *Journal of Thermal Spray Technology*, Vol. 1, pp. 231-237.
3. Sachs E., Cima, M., Cornie J., (1990) "Three Dimensional Printing: Rapid Tooling and Prototypes Directly from CAD Representation," *Proc. Solid Freeform Fabrication Symposium*, The University of Texas at Austin, Aug. 6-8, 27-33.
4. Ashby M. F., (1974) "A first Report on Sintering Diagrams," *Acta Met*, Vol. 22, pp. 275-286.
5. Herman, H., "Plasma-sprayed Coatings," (1988) *Scientific American*, Sept. 1988, pp. 112-117.
6. Amon, C.H., Prinz, F.B., and Schmaltz, K.S., (1993) Numerical Modeling of Thermal Spray Systems," Technical Report EDRC 24-10693, Carnegie Mellon University, Pittsburgh, PA
7. Y.S. Touloukian, Y.S. (1967) "Thermophysical Properties of High Temperature Solid Materials," Vol. 3, 1967, Macmillan, New York.
8. Timoshenko, S. (1925), "Bending and Buckling of Bimetal Strips," *J. Optical Soc. Am.*, Vol. 11, p. 233-255.
9. Bogy, D.B. (1971), "Two Edge-Bonded Elastic Wedges of Different Materials and Wedge Angles Under Surface Traction," *J. Appl. Mech.*, Vol. 38, pp. 377-386.
10. Hein, V.L. and Erdogan, F. (1971), "Stress Singularities in a Two-Material Wedge," *Int. J. Fract. Mech.*, Vol. 7, pp. 317-330.
11. Okajima, M. (1985), "Analysis of Tensile Testing Configurations for Assessing the Strength of Butt Joints," Ph.D. thesis, Department of Mechanical Engineering, Carnegie Mellon University.

StereoLithography Epoxy Resin Development: Accuracy and Dimensional Stability

Dr. Thomas H. Pang
Research & Development Department
3D Systems, Inc.
26081 Avenue Hall
Valencia, California 91355

Abstract

Recently, a new class of StereoLithography (SL) resins was developed that provide significantly improved overall part accuracy and dimensional stability relative to earlier SL resins. The new resin formulation, XB 5170, is based on epoxy chemistry and has many substantial advantages over conventional acrylate SL resins. In addition to excellent mechanical properties, the epoxy resin has very low shrinkage, resulting in extremely low curl and distortion. A standard UserPart built in XB 5170 achieved the highest level of dimensional accuracy to date from a statistically significant number of measurements taken in the x, y, and z directions. SL parts built in XB 5170 also exhibit superb dimensional stability in the laser-cured state as demonstrated by a new creep test. Dimensional stability in the laser-cured state is critical, especially for parts built in the new QuickCast™ build style. In addition to the epoxy resin, QuickCast is the key to successfully utilizing SL parts for direct shell investment casting applications.

Background

The StereoLithography (SL) process involves building 3-dimensional objects by sequentially generating thin layers of selectively cured liquid resin on top of each other. The current StereoLithography Apparatus (SLA) uses a focused UV laser beam directed by a computer-controlled X-Y scanning mirror system that has an extremely high pointing accuracy. High laser pointing accuracy is undoubtedly a prerequisite to generating an accurate part. However, high pointing accuracy alone does not automatically translate into building accurate parts. Many variables such as resin type, laser spot size and symmetry, and the process used to build a part also affect part accuracy. Therefore, the accuracy of final SLA parts, in addition to inherent machine accuracy, is very important to SL users.

The process parameters required to build accurate SL parts are quite complex in nature. However, insights obtained from fundamental research at 3D Systems in 1990¹ led to a substantial improvement in SL part accuracy. WEAVE™ and STAR-WEAVE™ laser drawing styles developed in 1990 and 1991, respectively, increased the accuracy of acrylate resin by more than 40% based on a statistically significant number of measurements taken on a standard accuracy part called the UserPart.

The SL UserPart was designed, not by 3D Systems, but by the SLA user group in 1990 to determine the overall dimensional accuracy of SL parts.² From a significant number of UserPart measurements accumulated since then, SL has achieved a relatively high level of accuracy even in

the conventional acrylate resins.³ However, it appeared as if the accuracy of SL parts made in acrylate resins and the process optimization techniques were approaching a plateau.

Substantial improvements in part accuracy and resin properties were necessary to apply SL to new markets beyond conventional form, fit, and function prototypes. For instance, a higher level of accuracy is necessary to expand the applications of SLA into the manufacturing arena.

Dimensional stability is also essential for a rapid prototyping part for almost any application. Without sufficient dimensional stability even a part initially built accurately becomes inaccurate over time. A rapid prototyping part would have limited use without high accuracy sustained for a period of time characteristic of the application. For form, fit, and function applications, dimensionally unstable parts may not fit properly. Holes and other intricate features may become misaligned with time.

A high level of dimensional stability becomes especially crucial in an application such as direct shell investment casting. This process requires an efficient conversion of prototype parts from plastic to metal with maximum preservation of accuracy. In shell investment casting, a rapid prototyping part is normally subjected to periods of days up to even weeks before it is shelled. Only rapid prototyping sites with an in-house foundry are capable of initial face-coat shelling within hours after the parts are built. Otherwise, a nontrivial amount of time, typically on the order of days, is required for shipping the part to an appropriate foundry and for the foundry to actually shell the part. Any dimensional instability within this period leads to an inaccurate shell investment casting pattern, rendering the resulting metal cast prototype unacceptable. Clearly, a new type of resin with high accuracy and excellent dimensional stability was needed.

New Epoxy Resin XB 5170

Ciba-Geigy (Switzerland) and the Research and Development Department at 3D Systems have been involved in a program of joint SL photopolymer research and development since 1988. Ciba-Geigy, one of the leading chemical companies in the area of epoxy chemistry, had been looking at SL epoxy resins for sometime.

In July, 1993, Ciba-Geigy released a new resin for the SLA-250 based on epoxy chemistry. The characteristics of this epoxy formulation, XB 5170, are given in table 1. The properties of two conventional SL acrylate resins are also listed for comparison. StereoLithographic properties of the epoxy resin, XB 5170, compare well with those of acrylate resins except that the photospeed is a little slower. The epoxy resin has an excellent set of physical properties that exceed those of acrylate resins in almost every single category. Namely, XB 5170 has:

- 1) very low viscosity
- 2) high laser-cured (green) modulus
- 3) high postcured modulus
- 4) good elongation at break
- 5) good impact strength

However, the high achievements in accuracy and dimensional stability are what makes this new epoxy resin so special. According to the diagnostic accuracy measurements performed, XB 5170 shows:

- 6) substantially reduced thin flat slab distortion
- 7) almost twice the overall UserPart accuracy compared to XB 5081-1 acrylate resin (Note: XB 5081-1 was formerly the most accurate SL resin until XB 5170 was introduced.)
- 8) negligible Cantilever curl during the SL building process.
- 9) superb dimensional stability as measured by the CreepBar diagnostic test.

In addition, the epoxy resin, when built in the new QuickCast™ build style, is especially suited for direct shell investment casting applications.⁴ Many metal parts with high accuracy and smooth surfaces have been cast successfully in the epoxy resin, XB 5170.⁵

Even though the physical properties of XB 5170 are important and definitely deserve discussion of their own, this report will focus on the first three diagnostic tests given in Table 1, that determine the accuracy and dimensional stability of the epoxy resin.

StereoLithography Resin Characteristics			
Resin Type	Acrylate	Urethane Acrylate	Epoxy
Resin Name	XB 5081-1	XB 5149	XB 5170
Dimensional Properties and Accuracy			
UserPart Accuracy* (R.M.S. Error)	5.3 mils	6.1 mils	2.8 mils
Cantilever Curl*	10 %	10 %	1 %
Green Creep Rate*	3.7 mil/log ₁₀ t	11.5 mil/log ₁₀ t	0.5 mil/log ₁₀ t
Linear Shrinkage	0.7 %	0.6 %	0.06 %
Flat Slab Distortion	71 mils	70 mils	20 mils
Physical Properties			
Viscosity @ 30°C	2,400 cps	2,000 cps	180 cps
Green Flexural Modulus**	620 MPa	310 MPa	1700 MPa
Cured Tensile Modulus***	3,000 MPa	1,150 MPa	2,700 MPa
Elongation@Break***	2.5 %	10 %	9 %
Impact Strength***	3 kJ/m ²	23 kJ/m ²	30 kJ/m ²
StereoLithographic Properties			
Critical Exposure, Ec	7 mJ/cm ²	6 mJ/cm ²	9 mJ/cm ²
Penetration Depth, Dp	7 mils	5.5 mils	4.5 mils

* Discussed in Text.

** 2.5 mm Thick strip built on SLA.

*** Specimens cast between glass & UV cured.

Table 1.

UserPart, Cantilever, and CreepBar Accuracy Diagnostic Parts

Diagnostic tests are essential tools used to compare the achievable level of performance for new resin systems or new process techniques. Diagnostic tests allow one to compare new resin or process systems with earlier ones in a quantitative manner. The dimensional properties of the epoxy SL resin, XB 5170, were determined by the following diagnostic tests.

Three diagnostic test parts, UserPart, Cantilever, and CreepBar, shown in figure 1, are representative diagnostic test parts used to determine dimensional properties. The UserPart and the Cantilever parts, discussed in detail elsewhere^{6,7} are a measure of overall dimensional accuracy, and curl distortion during the building process, respectively. The CreepBar test was recently developed specifically to determine the dimensional stability of an SL part over a given period of time.

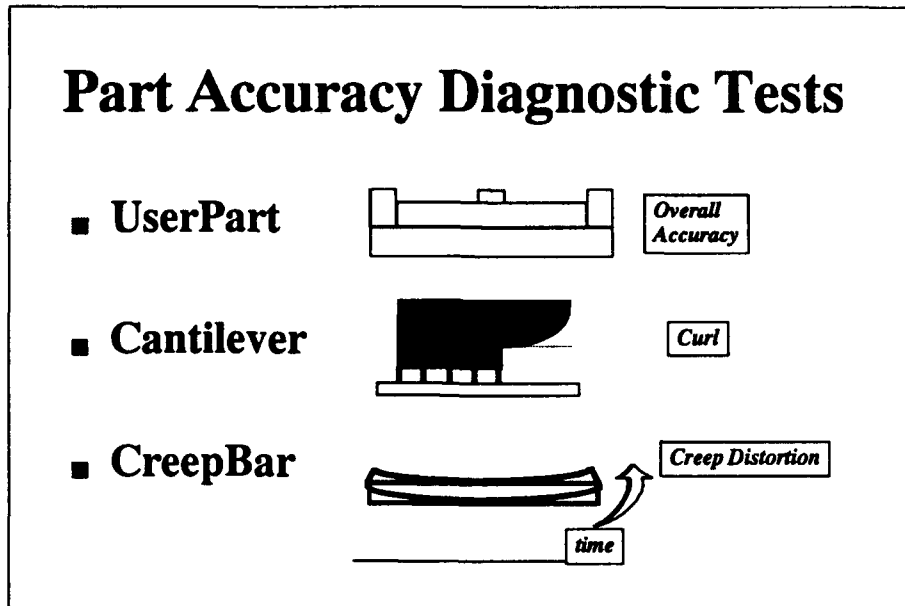


Figure 1. Three accuracy diagnostic parts used to test StereoLithography resins.

UserPart Accuracy

The UserPart is intended as a metric of overall SL part accuracy. It is 9.5 inches long by 9.5 inches wide and about 2 inches high. Many small and large features are included. The accuracy data is obtained by measuring a statistically significant number of dimensions of the features that have varying thicknesses and lengths. From a single UserPart, 78 measurements are taken in the x and y directions and 14 measurements are taken in z. The total number of dimensional measurements per part is 170. These dimensions include thin, medium, and thick walls, short and long dimensions, as well as holes of various sizes. All measurements are taken using a Coordinate Measuring Machine (CMM) that has a repeatability of ± 5 microns, or ± 0.2

mils. The accuracy data obtained from the UserPart includes the normal shrinkage of the resin that takes place in the vat during the SL building process. It also takes into account the dimensional changes that occur during the postcuring process. In other words, the UserPart is subjected to all of those processes incurred when building real SL parts.

To analyze overall part accuracy, the measured UserPart dimensions are compared to the nominal CAD dimensions and dimensional error values are calculated. A histogram called an Error Distribution Function is then constructed from compiling individual error values. The Error Distribution Function for the conventional acrylate SL resin, XB 5081-1, is given in figure 2. The curve is a result of 2550 total data points obtained from 15 UserParts all measured by CMM. The peak occurs at error=0 and the distribution curve is quite symmetrical. The fact that the general shape resembles a Gaussian distribution suggests that the errors on the plot are random events and are not due to systematic errors.

The overall dimensional accuracy of the SL UserPart built in XB 5081-1 can be extracted from the error distribution curve. However, it is usually more convenient to convert the curve into a Cumulative Error Distribution, as shown in figure 3. This is done by simply flipping all the data points in the negative error region to the positive error region and taking a running sum at each specified error window. Using the Cumulative Error Distribution the probability that any dimension will lie within a certain range of error can be immediately interpolated. For example, a commonly quoted characteristic error value is the root-mean-square (R.M.S.) error or equivalently, the standard deviation. The R.M.S. error corresponds to a 68% probability of occurrence.

For XB 5081-1 resin, the R.M.S. dimensional error is ± 135 microns or ± 5.3 mils. This means that 68% of the dimensional measurements taken on the UserPart made in XB 5081-1 are expected to lie within ± 5.3 mils. XB 5081-1 was formerly the most accurate SL resin, until the epoxy resin was recently introduced.

Now, what about the new epoxy resin XB 5170? The Error Distribution Function for a UserPart built in XB 5170 is given in figure 4. Because this resin is just being released, the curve was generated from a single UserPart. Nevertheless, the error distribution curve generated from 170 dimensional measurements already looks quite Gaussian. The peak of the curve is also centered at about error=0. The Cumulative Error Distribution for XB 5170 is plotted in figure 5.

It is clear that the error for the epoxy resin is a lot less than XB 5081-1. The maximum error at 100% probability, is about 500 microns or 20 mils for XB 5081-1, compared to less than 355 microns or 14 mils for the new epoxy resin, XB 5170. The R.M.S. error for XB 5170 is only 71 microns or 2.8 mils. XB 5170 resin provides almost twice the overall accuracy. It should be appreciated that the degree of improvement in the R.M.S. error from 5.3 mils to 2.8 mils, based upon a statistical number of data points, is truly significant.

A history of progress in SL UserPart accuracy is shown in figure 6. In 1989 the R.M.S. error for a UserPart built in the original 50-mil Tri-Hatch build style was about ± 9 mils. With the introduction of WEAVE™ and STAR-WEAVE™ build styles in 1990 and 1991, and subsequent optimization in 1992, the R.M.S. error was reduced by a factor of two to ± 4.5 mils using the same resin. This was comparable to the accuracy achieved by a UserPart machined from an engineering plastic (Perspex) by a CNC milling machine.⁸ This level of accuracy is marked by the horizontal line in figure 6. With the introduction of the epoxy resin, XB 5170, the UserPart R.M.S. error was dramatically reduced to ± 2.8 mils. This improvement brings the accuracy of SL generated UserParts into the same ballpark as an Aluminum UserPart machined by CNC milling⁹, a significant advance in the accuracy of SL parts.

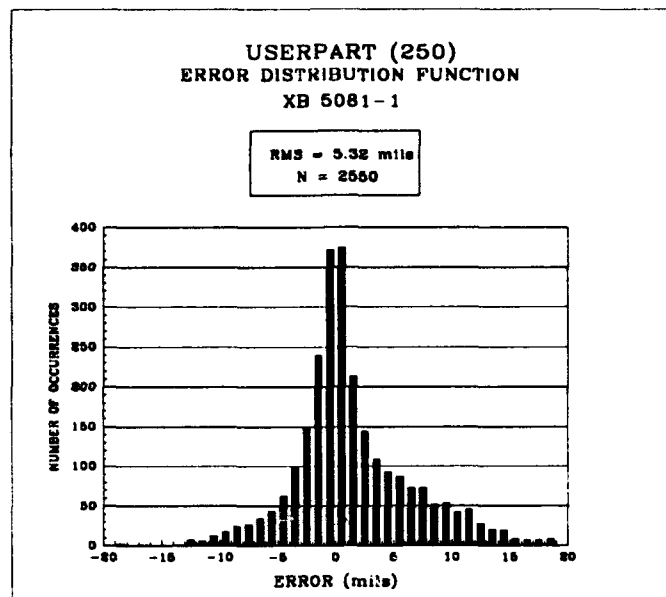


Figure 2. Error Distribution Function for fifteen UserParts made in XB 5081-1 resin.

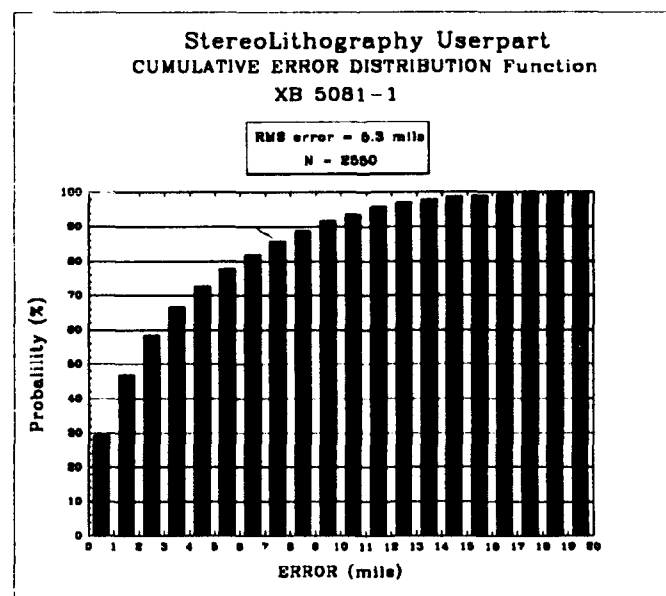


Figure 3. Cumulative Error Distribution for fifteen UserParts made in XB 5081-1 resin.

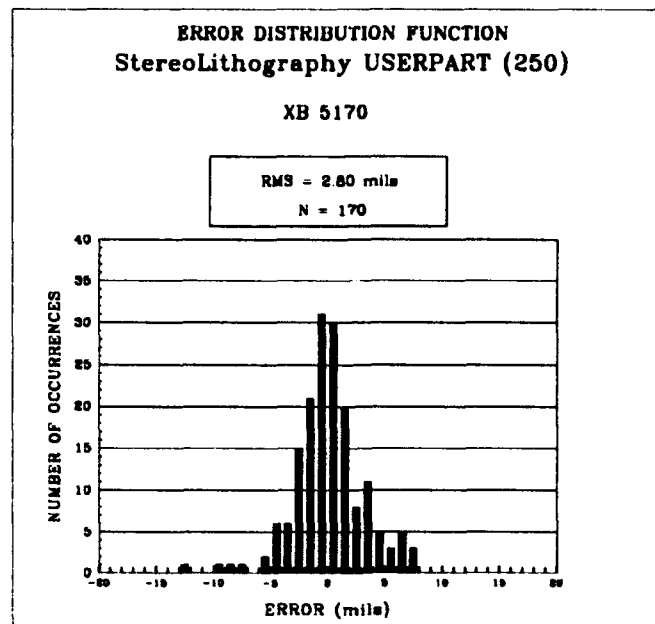


Figure 4. Error Distribution Function for one UserPart built in XB 5170, epoxy resin.

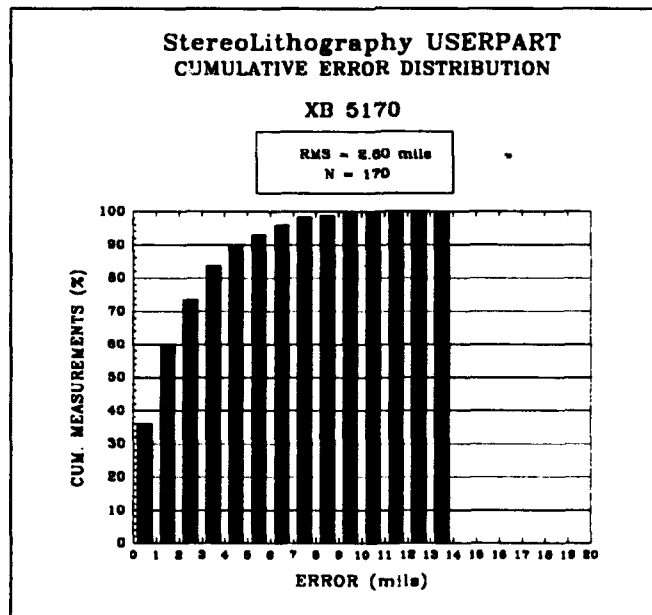


Figure 5. Cumulative Error Distribution for one UserPart made in XB 5170, epoxy resin.

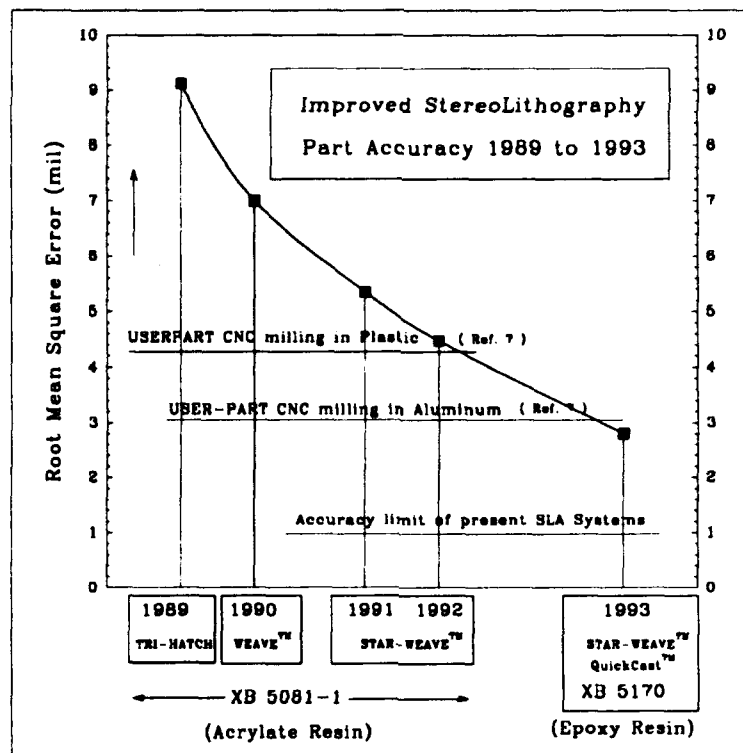


Figure 6. StereoLithography's progress in UserPart Accuracy from 1989 to 1993.

Unsupported Cantilever Curl

The Cantilever diagnostic test, shown in Figure 7, tells us how much the protruding Cantilever areas of a part curl if they are not properly supported. Therefore, cantilever curl is one type of distortion that happens in the vat during the building process. This was a useful measure in the past when feasibility studies were performed to see whether or not parts could be built with minimal supports. Today, cantilever sections of real SL parts are usually supported such that negligible cantilever sections occur. Therefore, while the Cantilever diagnostic part is still very useful in comparing different resin systems, it has some limitations in comparing real parts built with proper supports.

Nonetheless, Cantilever curl is indeed a measure of the inherent tendency for the resin to undergo warpage during the building process. The curl values (rise at 6-mm run) for the conventional acrylate resins manufactured by Ciba-Geigy are typically between 8~13%. As a specific example, for XB 5081-1 it is 10%.

However, the Cantilever curl for the epoxy resin, XB 5170, is extremely small. The curl value for XB 5170 is only 1 %. This result indicates that the epoxy resin has a very small, almost negligible tendency to undergo curl distortion during the building process.

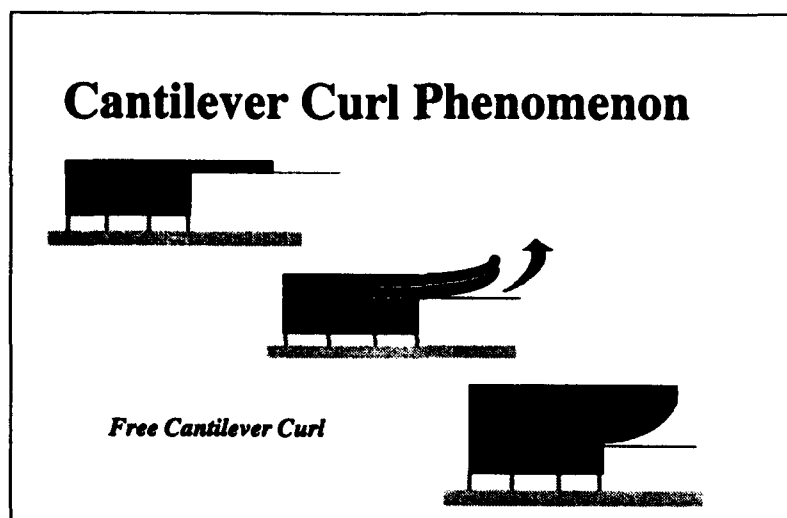


Figure 7. Cantilever free (unsupported) curl phenomenon.

CreepBar Creep Distortion

So what types of accuracy problems do the supported parts typically have? Experience with the conventional acrylate resins has shown that when SL parts are left in the laser-cured or so-called "green" state for a long time without postcuring, their dimensional errors increase. The longer they stay in the laser-cured state, the more inaccurate the parts become. This indicated that SL parts built in acrylate resins are not completely dimensionally stable in the laser-cured state.

For visualization purposes, the degree of dimensional change with time for SL parts is relatively small and causes no problems. However, dimensional instability and its time dependence must be identified and understood in order to build highly accurate and more dimensionally stable parts that meet the requirements for direct shell investment casting applications. Furthermore, resins and specific build processes must be found that can indeed generate parts with high dimensional stability.

While layer-addition fabrication offers many advantages such as the ability to build complex geometries; curl distortion has traditionally been one of the major disadvantages. When additional layers are cured or solidified on top of each other, physical or chemical transformation takes place in the material. For SL, it is a photochemical crosslinking reaction, and for rapid prototyping methods that use solidification of a molten material, it is changes in the density of the materials due to temperature gradients. Both of these changes involve some degree of volumetric shrinkage and lead to the build up of internal stress in the part. This built-in internal stress ultimately manifests itself in a type of warpage known as creep distortion.

Creep distortion may take place quickly or slowly with time. The exact creep behavior depends on many parameters including the part geometry, type of resin and its laser-cured glass transition temperature, ambient temperature, and build parameters. Creep distortion becomes worse for parts having flat geometries and high aspect ratios when the long axis coincides with the building surface. In this report, time dependent creep distortion measurements are presented for a number of SL resins.

The CreepBar is a new diagnostic test that was designed to measure the dimensional stability of an SL part. In the CreepBar diagnostic test, a thin rectangular part, shown in figure 8, having a high aspect ratio, is built fully supported on an SLA. The supports prevent any distortion from occurring in the vat. The CreepBar is then taken off the platform, cleaned, and is allowed to undergo deformation with time. The CreepBar is laid such that the direction of creep distortion is horizontal, to minimize the effect of gravity. An optical creep measurement (OCM) device, shown in figure 9, is used to track the rate of creep distortion with time. The data is recorded on a computer. The resulting creep distortion is a quantitative measure of the dimensional stability of the test part, for a particular resin built in a particular way.

Laser-cured and postcured CreepBar behaviors are expected to be very different. They should be clearly distinguished from each other. For most resin systems, the great majority of the creep distortion occurs in the laser-cured state. Therefore, only laser-cured CreepBar data was considered at this time. The CreepBar, thus, is NOT postcured for the data presented here.

Laser-cured creep distortion arises from built-in stresses generated during the building process on the SLA. Postcured creep distortion is more complex because it involves stresses that are introduced into the part during UV or thermal postcuring in addition to the original laser-induced stresses. Both classes of creep distortion depend strongly on the geometry of the part, on the resin, and the SL build parameters used, as well as temperature. The experimental results for creep distortion should be compared only for the creep tests performed under a controlled environment.

It should be noted that the creep test presented here is distinctively different from the ASTM creep test that involves an externally applied standard weight as a source of stress. In the SL creep test, the internal build stresses serve as the distortion mechanism, and may not be constant throughout the creep phenomena.

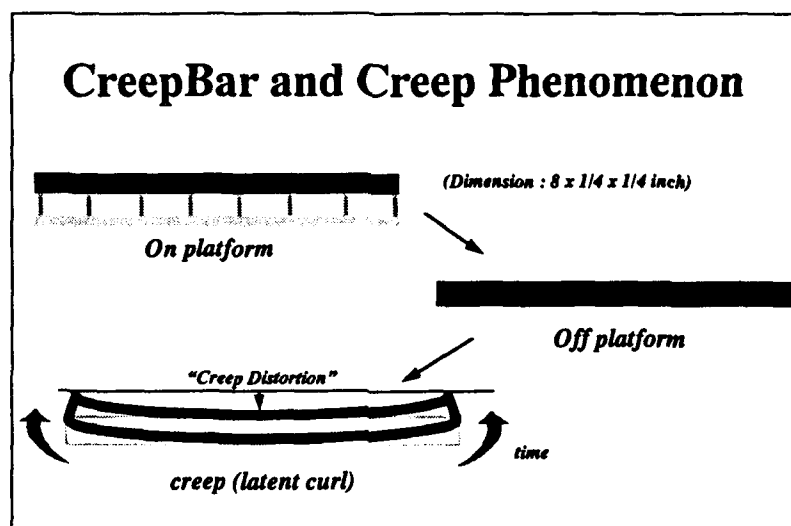


Figure 8. CreepBar diagnostic part dimensions and a schematic of the test sequence and the creep phenomenon.

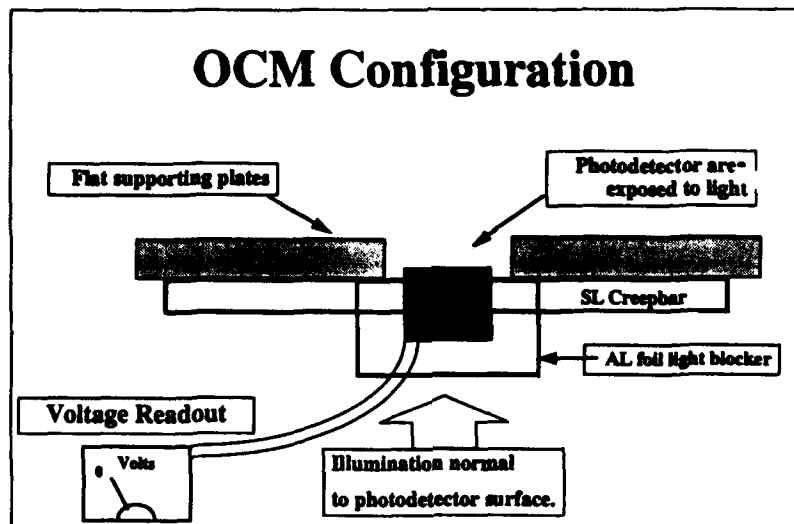


Figure 9. Optical Creep Measurement (OCM) Device configuration. CreepBar at time= 0 after it was removed from the supports.

Creep Experiment

Creep Distortion is a deformation of an SL part that takes place with time. It is the degree of deformation that happens after the SL part is taken off the platform and the supports are removed. The deformation does not begin until this instant because the supports and the platform restrict the SL part from deforming. The built-in stresses begin to affect the dimensional stability of the SL part only after these restrictions are relieved.

In the creep test a high aspect ratio (8 X 1/4 X 1/4 inch) rectangular bar called the CreepBar, is built on an SLA. It is supported completely during the building process in the SLA to prevent it from distorting in the vat. It is then removed from the SLA platform. The degree of out-of-plane curl distortion of the laser-cured bar, marked by the small downward arrow shown at the bottom of figure 8, is measured over a period of 24 hours.

A CreepBar of length = 200mm, width = 6.35mm, and height = 6.35mm is built on an SLA, as shown in figure 8, with supports such that the part does not undergo distortion during the building process. When the CreepBar is complete, it is rinsed in TPM (no solvent cleaning is required for the QuickCast™ build style) and then is taken off the platform with the supports removed as soon as possible. The time that the CreepBar is taken off the platform is taken as time $t = 0$.

As shown in figure 8, the CreepBar begins to undergo creep distortion with time. Because of the way the layers are cured in the SL process, the direction of the stresses force the CreepBar to distort concave upward. This may be thought of as a "latent curl" effect that manifests itself only after the supports are removed.

As soon as the part is cleaned and removed from the supports, it is placed on a custom-built optical device called the OCM (Optical Creep Measurement). An optical approach was

elected because mechanical means of measurement for small displacement distances are both tedious and unreliable. Even a small mechanical force applied to the CreepBar could distort it. A schematic drawing of the OCM device is given in figure 9. The OCM consists of flat supporting plates that are co-linear, a photo detector, a small section of Aluminum foil attached to the CreepBar, and an IR photodiode light source shining down on the photodetector. (The light source is not shown in the schematic drawing.) The IR photodiode does not initiate further photopolymerization.

The principle of OCM operation depends on the variation in total optical power received by the photodetector as the result of displacement by the CreepBar. The voltage reading from the photodetector depends on the total amount of incident light. At time=0, when the CreepBar has not undergone any distortion, the voltage reading is low because most of the IR light is blocked by the CreepBar and the Aluminum foil.

After some elapsed time, the CreepBar distorts and the aluminum foil moves away from the photodetector. A larger area of the photodetector is now exposed to the light source and the voltage reading increases accordingly. From a carefully constructed calibration curve, shown in figure 10, the voltage reading can be directly converted into creep distortion. The creep distortion data is then collected as a function of elapsed time on the computer.

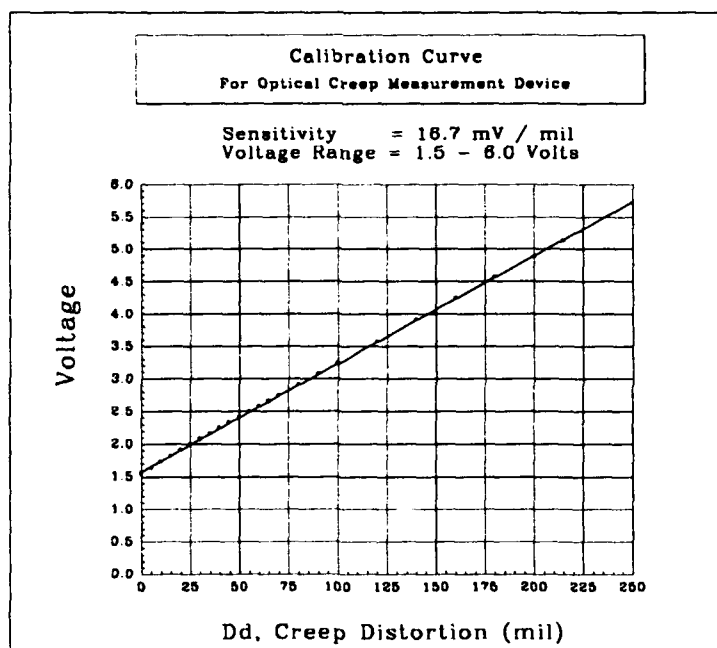


Figure 10. Calibration curve for the Optical Creep Measurement Device relating voltage output to creep distortion.

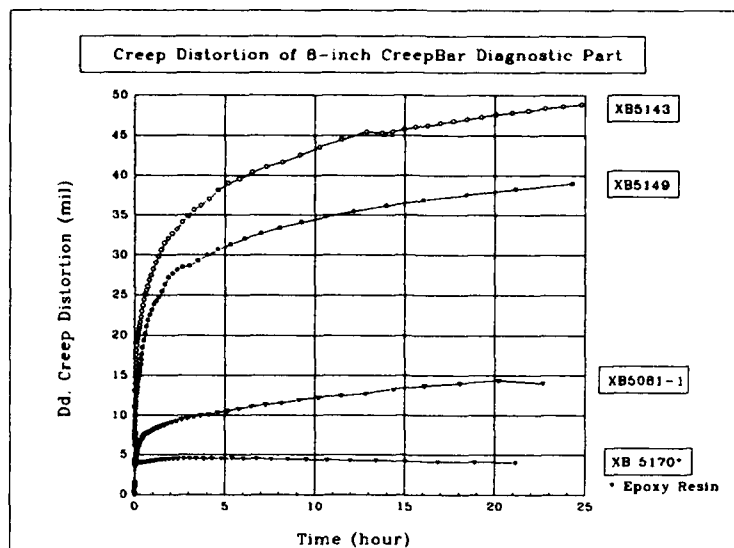


Figure 11. Creep distortion of laser-cured SL resins as a function of time at 21°C.

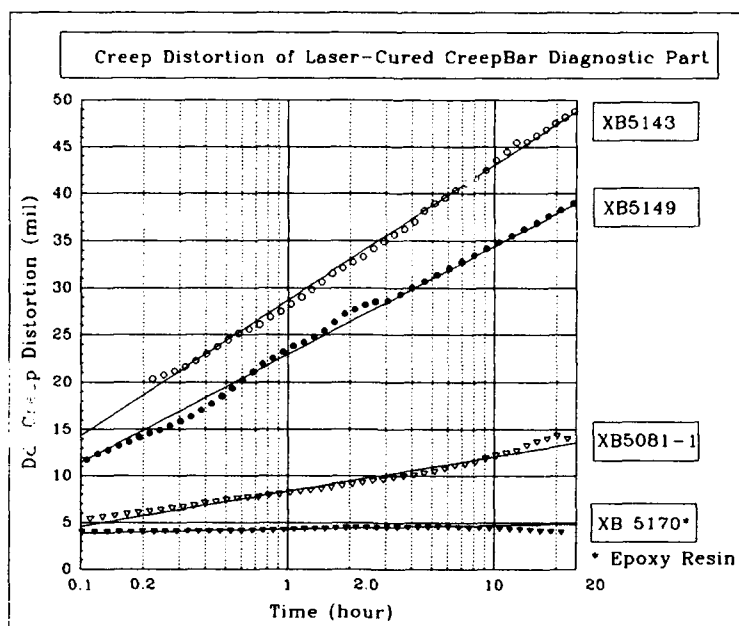


Figure 12. Creep distortion data plotted as a function of the logarithm of time at 21°C. The plot shows every fifth data point and best-fit straight lines.

Creep Data

Green Creep Data for acrylate resins, XB 5143, XB 5149, XB 5081-1, and the new epoxy resin XB 5170 were collected on the OCM. All creep measurements were taken at room temperature ranging from 20 to 22°C, typically at 21°C. The results are presented on figure 11. All creep data show a rapid increase in creep distortion at short times. The creep data appear to reach a plateau at long times. For most of the resins presented here, more than 60% of the 24-hour creep distortion is virtually complete within an initial period of 2 hours.

With respect to absolute magnitude, CreepBars made in XB 5143 have the largest creep distortion. They distort to about 50 mils/ 8-inch length in 24 hours. This suggests that *laser-cured parts should be postcured as soon as possible in order to preserve accuracy*. This precaution is usually taken by most SL users. XB 5143 is then followed by XB 5149, XB 5081-1 and XB 5170. XB 5081-1 shows a dimensional instability of about 15 mils/ 8 inches over 24 hours.

However, the new epoxy resin, XB 5170, has the least creep distortion at every point in time. This creep data shows that the epoxy resin is, by far, the most dimensionally stable resin in the laser-cured state. At every point in time, the creep distortion for XB 5170 is less than 5 mils/ 8-inch length over a period of 24 hours.

Because the rate of creep distortion was found to be rapidly decelerating with time, the creep data was plotted as a function of the logarithm of time in figure 12. Interestingly, all of the creep data was found to be very nearly a log-linear function of time in the 24-hour period. Note the linearity of the data in figure 12. From this observation, a single useful parameter called "creep rate" could be defined for purposes of comparing the creep properties of various SL resins.

Creep rate, defined by the symbol CR, is basically the slope of the creep data when it is plotted as a function of the logarithm of time. Thus, CR is the creep distortion that takes place for every multiple of 10 in time.

For example, consider an SL resin CreepBar that was built in a particular build style and was found to have CR = 15 mils. As the elapsed time increases from 1 hour to 10 hours (one multiple of 10), the creep distortion would increase by 15 mils. As the elapsed time then increases from 10 hours to 100 hours (another multiple of 10), the creep distortion would increase by an additional 15 mils. The total distortion, as time elapses from 1 to 100 hours (two multiples of 10 in time), is twice the CR, or 30 mils. Thus, a single parameter, CR, or creep rate, characterizes the dimensional stability of SL parts.

A summary of CR values for SL resins is presented in table 2.

Creep Rates of StereoLithography Resins

SL Resin	CR (mils / log ₁₀ time)
XB 5170	0.5 mils
XB 5081-1	3.7 mils
XB 5149	11.5 mils
XB 5143	14.4 mils

Table 2.

It is important to remember, though, that SL parts do not continue to creep indefinitely even in the laser-cured state. Internal stress is relieved as the parts undergo creep. When it becomes negligibly small, an equilibrium is reached. Once a distorted equilibrium position is attained the part no longer creeps. The rate at which equilibrium is reached depends on the resin and involves photochemical, process, and viscoelastic parameters, as well as temperature. Also, when SL parts are postcured, their creep rates decrease tremendously.

Nevertheless, it is clear, from the CreepBar data shown above, that the new epoxy resin, XB 5170, shows extremely low creep. Consequently, SL parts made from XB 5170 exhibit superior dimensional stability in the laser-cured state.

Conclusion

A StereoLithography epoxy resin, XB 5170, intended for use in the SLA-250 system was recently released by Ciba-Geigy. This resin has excellent physical properties and outstanding dimensional properties. Namely, it is highly accurate and dimensionally stable.

The dimensional properties of this epoxy resin were presented in comparison to the conventional SL acrylate resins. Accuracy and dimensional stability values were obtained from three diagnostic tests called the UserPart, Cantilever, and CreepBar.

The UserPart showed that *dimensional accuracy for XB 5170 was almost twice as good as the next best acrylate resin*. This SL UserPart was found to have the dimensional accuracy comparable to a UserPart built in aluminum by a CNC milling machine.⁸

The Cantilever curl diagnostic test showed that XB 5170 has a negligible tendency to curl during the SLA building process. For conventional acrylate resin, the best curl value was about 7% curl. *XB 5170 curled only 1%, which is an improvement of a factor of seven*, and indicates that negligible internal stress is introduced into parts when they are made in this epoxy resin.

A new diagnostic test was introduced to demonstrate dimensional stability of SL parts. The test, called CreepBar distortion test, involved the measurement of the out-of-plane creep distortion of an 8-inch long bar built on an SLA. This test also showed that XB 5170 undergoes minimal creep distortion in the laser-cured state. *According to the CreepBar test, XB 5170 is at least 7 times more dimensionally stable than XB 5081-1*, which itself had been historically known as a relatively dimensionally stable SL resin.

An improved level of accuracy and dimensional stability was achieved by the new epoxy resin, XB 5170. The diagnostic tests showed superb overall accuracy, low cantilever curl, and very high dimensional stability. These properties, together with outstanding physical properties such as low viscosity and high green strength, make XB 5170 the resin of choice for StereoLithography, especially when high accuracy is required.

An additional advantage is that SL parts built in the new QuickCast™ build style with XB 5170, have been proven to be effective in direct shell investment casting applications.^{4,5} Therefore, SL users can expect XB 5170 parts to have greatly improved accuracy and dimensional stability as well as direct shell investment casting capability.

References

- 1 Jacobs, P. F., Chapter 4 & 8, "*Rapid Prototyping & Manufacturing: Fundamentals of StereoLithography*", Society of Manufacturing Engineers, Dearborn, Michigan, July 1992.
- 2 Gargiulo, E. P., "*StereoLithography Process Accuracy: User Experience*", Proceedings of the Second International Conference on Rapid Prototyping, Dayton, Ohio, June 23-26, 1991, pp.311-326.
- 3 Gargiulo, E. P., "*StereoLithography Process Accuracy: Further User Experience*", Proceedings of the Third International Conference on Rapid Prototyping, Dayton, Ohio. June 1992.
- 4 Pang, T. H., Jacobs, P. F., "*StereoLithography 1993: QuickCast™*", Proceedings of the Solid Freeform Fabrications Symposium, University of Texas, Austin, August 9-11, 1993.
- 5 Jacobs, P. F., Kennerknecht, S., Smith, J., Hanslits, M., Andre, L. , "*QuickCast™ Foundry Reports*", 3D Systems R & D report, April 1993.
- 6 Jacobs, P. F., Chapter 11, "*Rapid Prototyping & Manufacturing: Fundamentals of StereoLithography*", Society of Manufacturing Engineers, Dearborn, Michigan, July 1992, p. 306.
- 7 *ibid.*, Chapter 10, p.256.
- 8 Gargiulo, E. P., "*StereoLithography Process Accuracy: User Experience*", Proceedings of the First European Conference on Rapid Prototyping, University of Nottingham, England, July 6-7, 1992, pp. 187-201.
- 9 *ibid.*

VIBRATORY FINISHING OF STEREOLITHOGRAPHY PARTS

John D Spencer, Richard C Cobb and Philip M Dickens

**Department of Manufacturing Engineering and Operations Management,
University of Nottingham, UK.**

SUMMARY

Rapid Prototype polymer resin models produced by Stereolithography have, by the nature of the process, a relatively poor surface roughness, particularly on concave and convex surfaces. In many cases this is unacceptable, and slow and tedious manual finishing techniques are often used to improve the surface.

An investigation has been conducted into a range of automated finishing techniques with the aim of producing an acceptable surface roughness. This paper presents the results from two techniques, Vibratory Bowl Abrasion and Ultrasonic Abrasion using components made from Ciba-Geigy XB5081-1 and XB 5143 resins.

Initial results from Scanning Electron Microscopy and surface topography analyses suggest that both techniques are capable of improving the model surfaces.

INTRODUCTION

Since its introduction Stereolithography has become established as the leading commercial Rapid Prototyping (RP) system (Jacobs 1992). A 3D CAD model of the desired component is mathematically 'sliced' into layers which are typically 150 μ m thick. The slice data is then used to control a UV laser which is guided over a vat of liquid photopolymer and is selectively cured as the laser tracks over it. In this way the part is built up layer by layer with the laser curing the required regions of each subsequent photopolymer layer. A post curing operation is then used to fully solidify the part.

Prototype models produced from the process exhibit a relatively poor surface finish, particularly on concave and convex surfaces. For many applications the usual practice is to sandpaper and polish the models by hand which is a tedious and time consuming operation and also presents a potential health hazard from the resin dust. Although prototypes can be rapidly manufactured, parts can end up after finishing with poorly defined features, and the more complex the model the more difficult it becomes to finish.

Where parts are intended for testing, finishing becomes a critical factor. For example, parts tested in say, fluid or gas chambers may not be representative of the final component as the layer steps could disrupt gas flows. Furthermore, in the production of tooling a poor surface on the model will be reproduced on the tool and removal of the model may be difficult if the tool material keys into the surface roughness.

When manufacturing stereolithography parts layers are produced that can form a curved (or angled) surface and it may be either the internal or the external corners that define the required profile. If the external corners define the profile their removal will cause the profile to become undersize. However if the profile is defined by the internal corners then it will be oversize until the steps are removed, see Figure 1. Where material removal takes

place, it is important that the internal corners of the layers are specified as defining the surface, (this is the default setting with 3D Systems machines).

Vertical faces also exhibit a step effect due to the manner in which the laser solidifies the resin. Although the power of the laser spot has a gaussian distribution the resin cures in a parabolic form, thus at the edge of a vertical face it is found that a stack of parabola curves occur, these cause steps on the surface, as seen in Figure 2, (Jacobs, 1992). Even if the model is supplied with a draft angle it is still likely to 'key' into a mating surface as a series of small undercuts will remain.

One of the problems with curved surfaces on SL models is that the size of the steps change as the angle of the curve changes, that is the closer the angle is to the vertical then the smaller the step in the horizontal ('X/Y') plane, as shown in Figure 3. Also, the closer the angle becomes to horizontal, the larger the step in the horizontal 'X/Y' plane. This effect causes problems when using material removal methods as the larger steps, because they require more work to remove them, will still be evident after the smaller ones have been removed, thus effecting the form of the curve.

An experimental programme was therefore constructed with the aim of investigating a range of automated finishing techniques and their potential for smoothing Stereolithography parts without causing any detrimental effect to the 'form' of the part. Although a wide range of options are available to treat the resin surfaces including chemical dissolution and the use of coatings it was decided to concentrate upon the mechanical removal processes and hence test samples were sent to specialist finishing companies.

The first stage of the work detailed three techniques, Abrasive blasting, Barrel tumbling and Centrifugal tumbling (Spencer et al 1993). It was found that abrasive blasting severely eroded models made from two different types of polymer resin, but that centrifugal tumbling was able to smooth the surfaces with improvements in Ra values of up to 81%. However, the process does generate significant damage and the time to process is excessive.

This paper presents the findings from a further two finishing techniques, Vibratory Bowl Abrasion and Ultrasonic Abrasion both of which were applied to the same type of models as in the previous study.

TRIAL COMPONENTS

A standard Stereolithography demonstration component, approximately 50mm diameter, was supplied by Texas Instruments, see Figure 4 and was provided in two different material types :-

Material type 1	Ciba Geigy XB5143	(durable resin)
Material type 2	Ciba Geigy XB5081-1	(general purpose resin)

As indicated below the component provided a range of different design features that any potential finishing technique may have to cope with.

Vertical and horizontal faces	
External corner	(area 1)
Internal corner	(area 2)
Restricted corners	(areas 3 & 4)
The steps on the peripheral radius	(radius)

To assess the ability and limitations of each of the finishing processes, specific areas of the component test piece were identified (areas 1 - 4). Following the surface treatment, each area could be compared with as-cured reference samples of each material.

EXPERIMENTAL PROCEDURE

Experimental Techniques

In order to investigate the effect of each finishing process upon the component, two experimental techniques were adopted. Specific features of the finished models and as-cured reference samples were examined and photographed on a JEOL JSM 6400 WINSEM Scanning Electron Microscope (SEM).

Measurements of the surface roughness (Ra) of all of the samples were made and recorded in the X, Y & Z axis using a Rank Taylor Hobson Taly Surf 4. In all cases the same region of the component photographed on the SEM was measured for surface roughness. The Ra value of the irregularities on a surface is defined as the average value of the departures, both above and below its centre line, for a prescribed sampling length. In the case of both the X and Y plane measurements the section was accurately mounted on a micro X/Y adjustable table.

The surface topography was traced before indexing the sample across 0.07mm and another reading and trace of the surface taken; this was repeated for 5 passes on each section in the X, Y and Z planes. The average of the values measured in each axis was calculated and recorded as was the average of all the readings.

RESULTS

Reference Samples

As-cured reference samples of materials type 1 (XB5143) and 2 (XB5081-1) were mounted and examined on the SEM (see Figures 5-8). By viewing the component in this way the individual slices can be clearly seen, and the surface finish in the 'Z' (vertical height) plane consists of a series of small steps. The size of these steps will depend on the thickness of each layer which can vary between 64-760 μ m. This stepping effect is most noticeable on faces that make an angle to the normal (vertical/horizontal) plane (eg 45° slope).

On further examination it can be seen that in addition to the step formations, the component exhibits a texture on the horizontal surfaces. The surface consists of lines of solidified resin, each \approx 200 μ m in width, running parallel to one another in the 'X' plane, 100 μ m apart with an identical layer, in the 'Y' plane beneath it. The micrograph indicates that approximately 50-75 μ m of the surface material would need to be removed for the horizontal surface to become smoother, Figures 5 & 6.

Comparison of the photographs for each of the materials, Figures 5 - 8, shows that, although the test piece is the same geometry and dimensions, and the layer thicknesses are the same, the two parts are quite different. In contrast to reference material 1, material 2 has much 'smoother' vertical faces with steps of width 130 μ m for the former and 50 μ m for the latter.

Another feature of the component made from material type 1, again on the vertical face, is the two pitch cyclic pattern of 'bumps' which step across a one half pitch each layer, Figure 5. These two pitch cyclic bumps are thought to be a fault of the machine control in

that it would seem that the laser beam used to cure the resin has scanned too far (Galvanometer overshoot).

Vibratory Bowl Abrasion

Finishing is achieved for this process by vibrating, at constant speed, a 'U' shaped bowl containing the abrasive media and the model. As the media recirculates around the bowl the surfaces become abraded. This is a less aggressive process than the tumbling processes which caused damage to the models in the earlier study, (Spencer et al 1993).

Samples of each material were sent to Invicta Super Finishers Ltd, Grantham, UK, who processed them using two different media types, 30mm diameter x 10mm angle cut cylinders and 13mm green plastic cones.

Material type 1 (XB5143) was processed for 1 ¼ hours using 30mm diameter x 10mm angle cut cylinders.

On the exposed vertical walls, 'steps' and 'bumps' have been partially removed, and localised abrasion is clearly evident, see Figure 9. At exposed external edges and corners abrasion is also apparent together with a loss of definition; an approximate radius of 0.5mm is seen. Toward confined regions such as the basal internal corners illustrated in Figure 10, wear is reduced probably as a result of the large size of media used.

With ϕ 13mm Green plastic cones as the processing media and for an equivalent exposure time of 1 ¼ hours, results were not as favourable in smoothing the vertical walls and steps could still be identified. However, the horizontal surfaces did receive a smoothing effect but damage also took place on exposed corners, see Figure 11.

Material type 2 (XB5081 - 1) was processed under the same conditions as for XB5143 but, for both forms of media the process was too aggressive creating extensive damage to the corners of the model.

ULTRASONIC ABRASION

Experiments were conducted at Branson Ultrasonics, Hayes, Middlesex, UK to investigate the use of ultrasonic abrasion as a means of finishing. Carborundum abrasive grit, particle size 250 μ m was used to partially fill a small 100mm diameter containing vessel. The resin model was then laid upturned on the surface of the grit and the ultrasonic horn contacted to the model. A frequency of 20kHz was used at an amplitude of 80 μ m.

Material type 1 (XB5143) was processed under these conditions for 2 seconds.

The main beneficial effect of the process has been on the horizontal surfaces where some smoothing has occurred with localised abrasion evident. Some of the original roughness still remains, as indicated in Figures 12 and 13. There appears to be more erosion at the exposed vertical edge, and as with the models processed by the vibratory bowl method holes have been exposed as a result of the 'skin fill' top surface being removed.

Unfortunately, material type 2 was completely destroyed on the application of 7 seconds exposure with no apparent improvement to the areas under investigation.

Surface roughness results

Table 1 shows the mean Ra values of surface roughness measurement of components in the X, Y and Z directions. The mean of the three mean values has then been calculated to allow direct comparison between the processes. From the overall mean values the overall percentage improvement of each of the processes has been calculated, compared against the original value.

From the table the reference material XB5143 appears rougher than the general purpose resin XB5081 - 1. Furthermore, it can be seen that the Vibratory Bowl abrasion process has achieved a good surface finish in a reasonable amount of time with improvements of around 73% for the XB5143 material. However, there has been a degradation of the form as radiusing of corners and edges has taken place in addition to the exposing of underlying holes in the surface.

The application of Ultrasonics for finishing these models has resulted in a mixed improvement to the surface finish. In the best case an improvement of 66% has been achieved with little degradation to the component form, in a very short space of time (2 seconds). However, from the photographic evidence it can be seen that this has been at the expense of the external corners and edges which were destroyed by the process.

DISCUSSION

Examination of the components with the Scanning Electron Microscope has clearly illustrated the difference in resin types for similar designs of part and for similar build patterns. From the investigation it is evident that, of the materials initially employed, Ciba Geigy XB5143 was the most responsive to surface abrasion with Ciba Geigy XB5081-1 being more resistant and too brittle for both processes.

Both of the processes examined have demonstrated improvements to the surface finish for material XB5143 smoothing the surfaces by up to 73%. Vibratory Bowl Abrasion produced a good finish in a reasonable amount of time and even though the selection of media for this technique was not optimum it provides encouraging results for future work as different medias sizes and types will be examined. The short unmanned processing time is very attractive compared with traditional hand finishing.

Ultrasonic Abrasion removed material very quickly but as the abrasive media was unconstrained wear took place mainly on the horizontal surfaces although vertical edges were badly abraded. Further work will address a range of conditions so that all parts of the models can be accessed. The short processing times were fast and the high energy levels applied had a detrimental effect on the material causing local melting in the area of the component at the centre of the ultrasonic horn.

CONCLUSIONS

- 1) Components manufactured from XB5143 are more responsive to surface finishing techniques than XB5081-1 which appears to be unsuited to most of the abrasive processes due to its brittleness.
- 2) Both Vibratory Bowl Abrasion and Ultrasonic Abrasion have demonstrated that they are potential techniques for deburring polymer Stereolithography parts with encouraging results at short processing times.

- 3) Further investigations need to be undertaken into all of the finishing techniques with regard to the abrasive medias used.

ACKNOWLEDGMENTS

The authors are indebted to Paul Blake and Owen Baumgardner of Texas Instruments for supplying the Stereolithography models used in this work.

REFERENCES

1. Jacobs, P.F., "Rapid Prototyping and Manufacture: Fundamentals of Stereolithography", Society of Manufacturing Engineers, 1992.
2. Spencer, J.D., Cobb, R.C., and Dickens, P.M, "Surface Finishing Techniques for Rapid Prototyping", Proceedings of the SME Rapid Prototyping and Manufacturing Conference, Dearborn, Michigan, 11-13 May 1993.

TABLE 1 SURFACE TEXTURE READINGS (Ra VALUES)

PROCESS	MEDIA	MATERIAL TYPE	Ra VALUE				% IMPROVEMENT
			AREA				
REFERENCE SAMPLE			X	Y	Z	MEAN	
		XB5143	5.35	7.34	7.0	6.56	-
		XB5081 - 1	6.46	7.68	3.0	5.71	-
VIBRATORY BOWL ABRASION	30mm x 10mm angle cut cylinders	XB5143	1.22	2.62	1.2	1.68	74
	13mm diameter plastic cones	XB5143	1.32	2.3	1.9	1.84	72
ULTRASONIC ABRASION	250µm Carborundum grit	XB5143	1.74	3.0	2.0	2.25	66
		XB5143	1.82	3.32	3.0	2.75	58

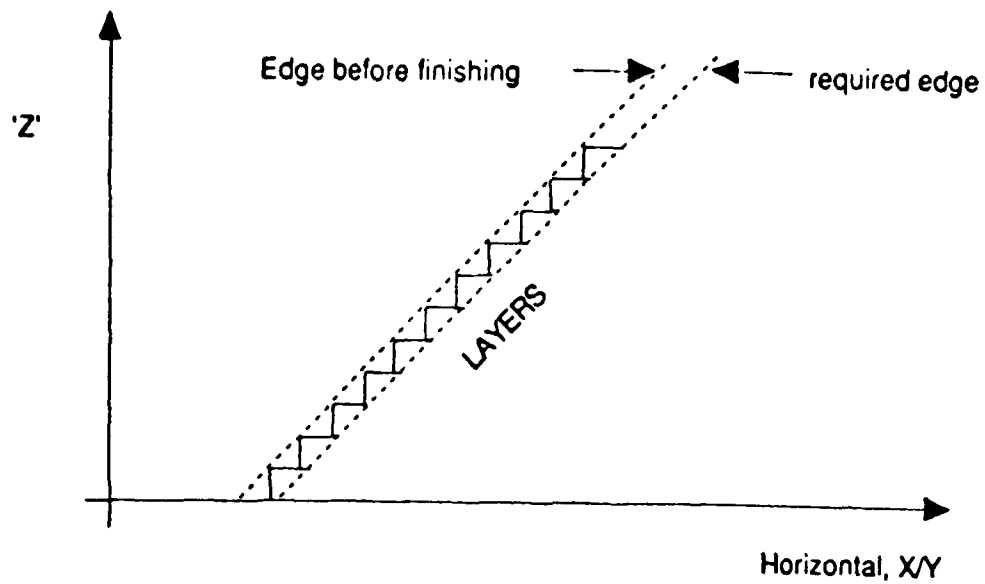


Figure 1 Showing how on removal of steps the component will be the required size when internal corners define the component profile.

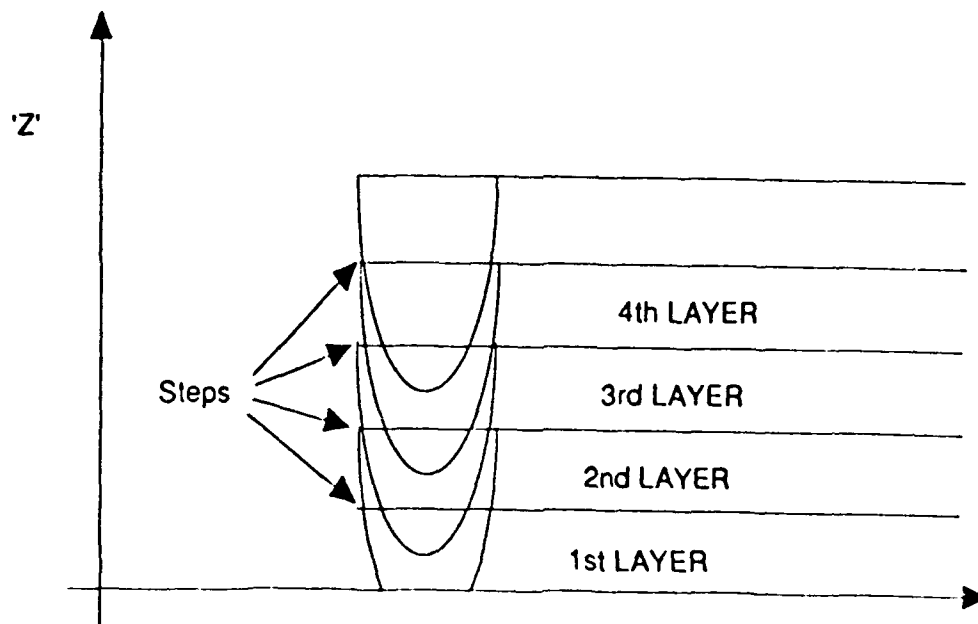


Figure 2 Showing how steps are caused on vertical faces due to the 'parabolic' nature of resin cure (Jacobs 1992)

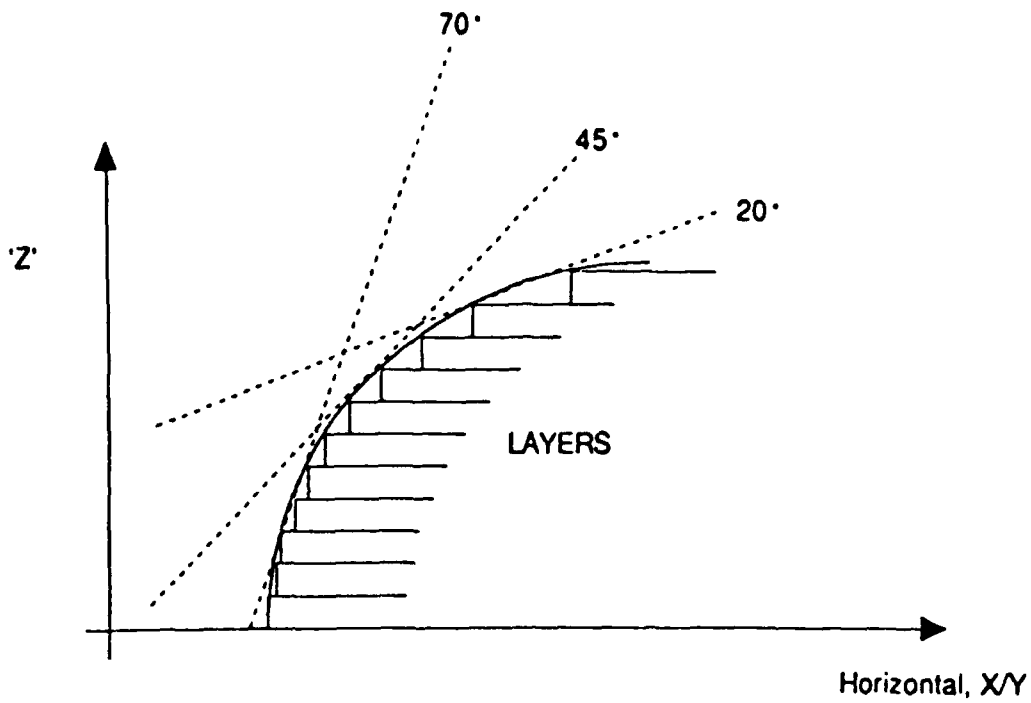


Figure 3 Showing how steps increase in the X/Y plane as arc tends towards horizontal.

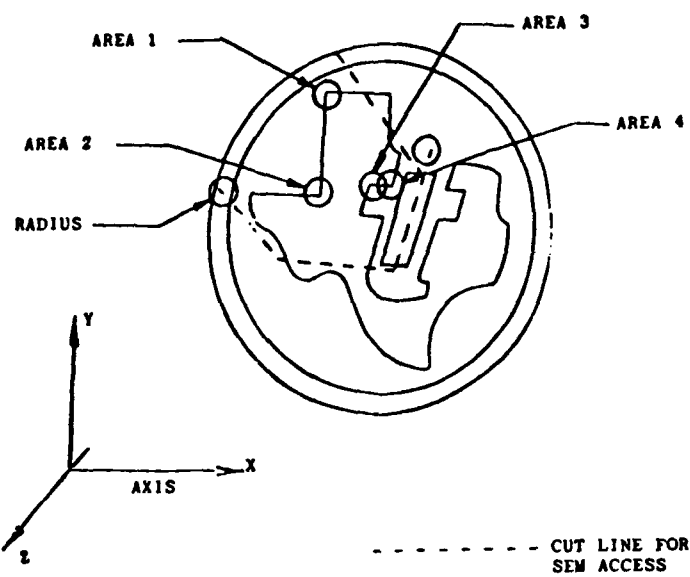


Figure 4 Standard test component supplied by Texas Instruments showing areas of particular interest.

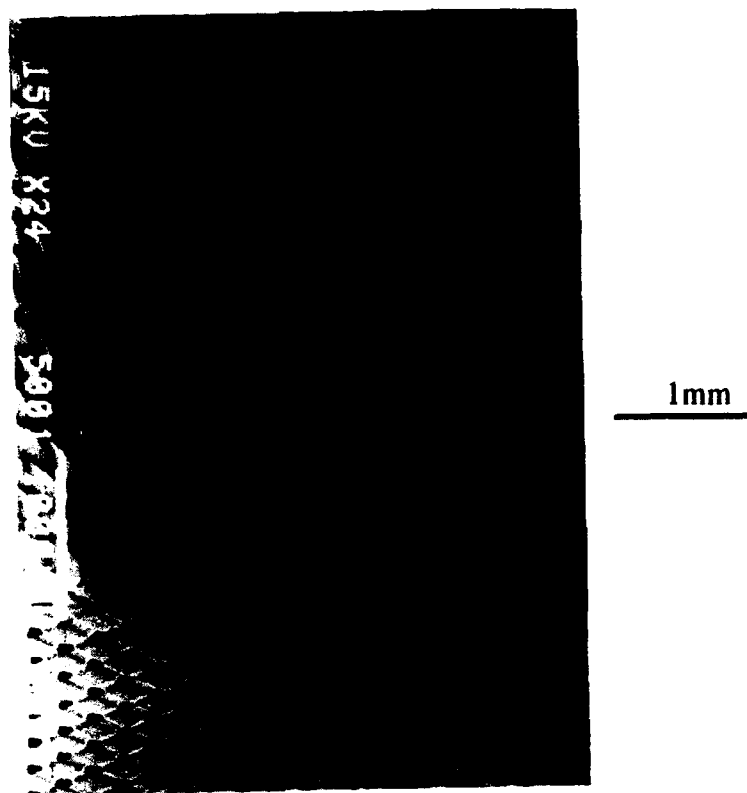


Figure 5 (area 1) Exposed, external corner, showing cyclic 'bumps' and 'steps' on vertical face, as well as a texture on horizontal surfaces. Material XB5143.

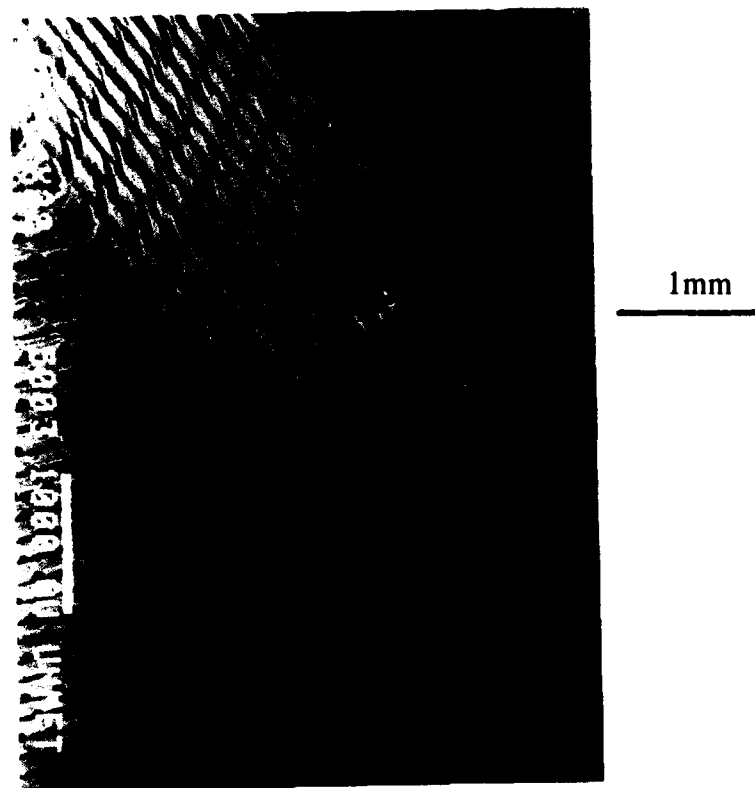


Figure 6 (area 2) Exposed internal corner. Again note the 'steps' and 'bumps' as well as the definition of corners and edges. Material XB5143.

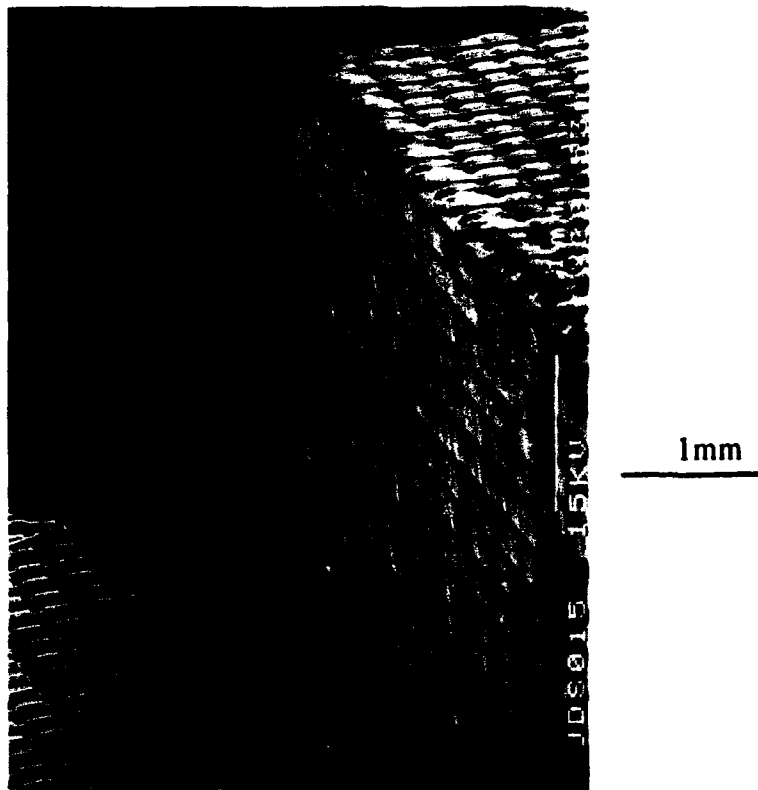


Figure 7 (area 1) Exposed external corner showing 'steps' in vertical 'Z' axis and texture on X,Y surface for material XB5081-1

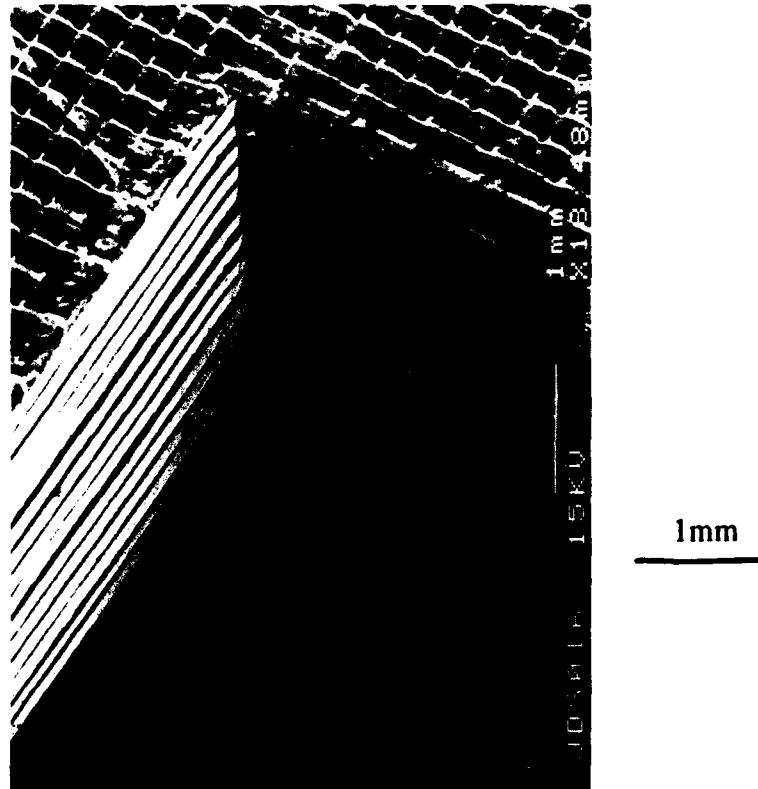
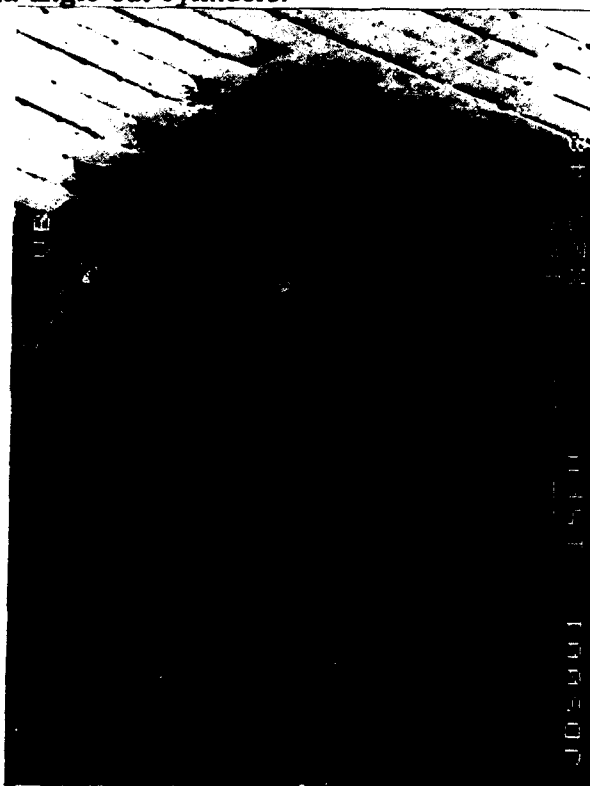


Figure 8 (area 2) View showing exposed internal corner. Of particular note is the definition of the internal edges and corner, also the edge definition into the corner. Material XB5081-1.



1mm

Figure 9 (area 1) Partial removal of steps and rounding to the corner is evident. Material XB5143, media angle cut cylinders.



1mm

Figure 10 (area 2) View of internal corner showing partial removal of steps but little penetration to the basal junction. Material XB5143.

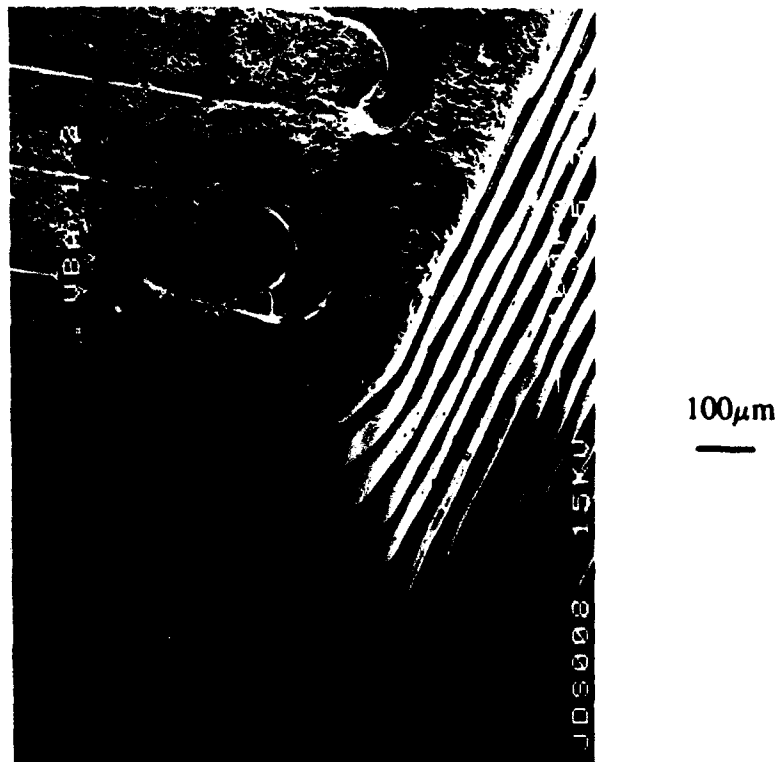


Figure 11 (area 4) Some damage is evident on the corner and little smoothing of the 'steps' is seen. Material XB5143.

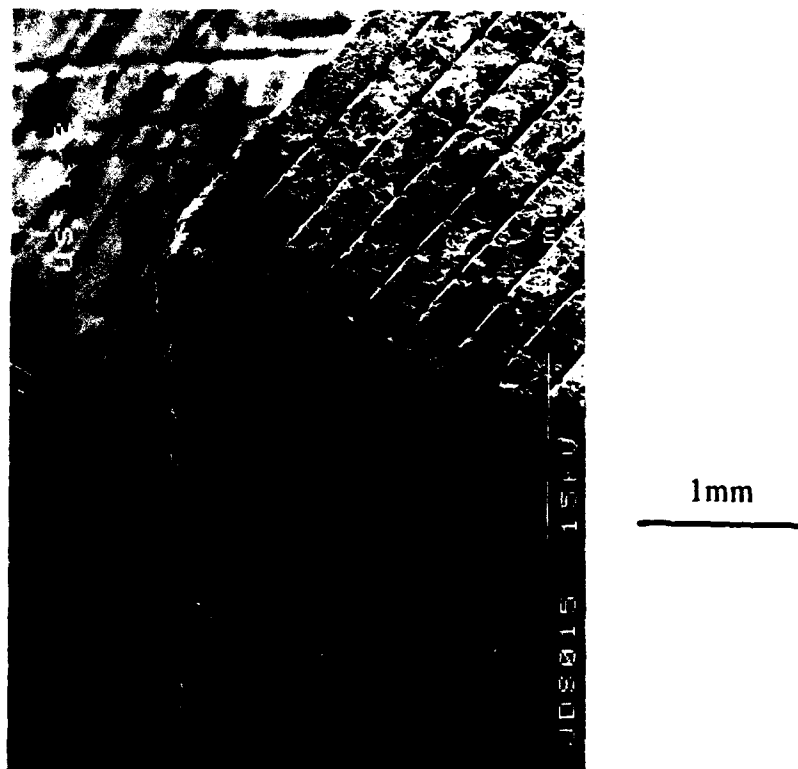


Figure 12 (area 1) Horizontal surfaces have been partially smoothed but some abrasion occurs on the edge. Material XB5143, media Carborundum grit.

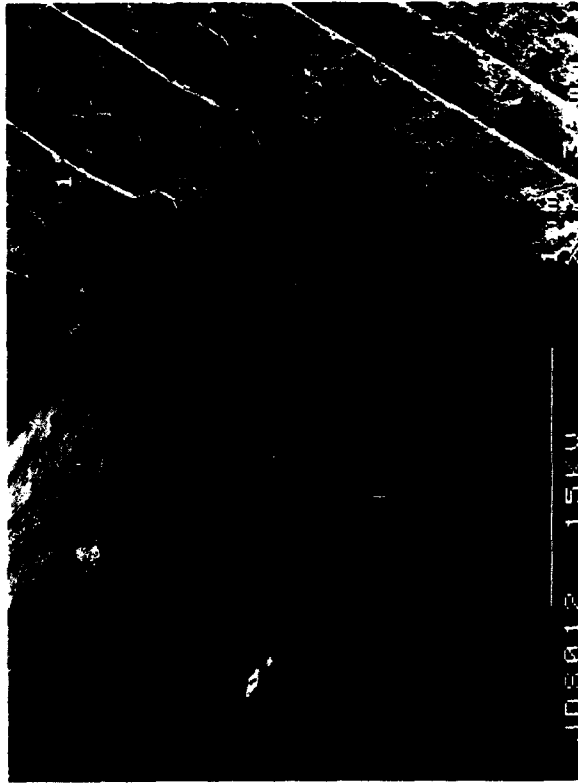


Figure 13 (area 2) Limited abrasion on the internal surfaces. Material XB5143, media Carborundum grit.

STRUCTURAL CERAMIC COMPONENTS BY 3D PRINTING

J. Yoo, M.J. Cima, S. Khanuja, E.M. Sachs

Departments of Materials Science and Engineering and Mechanical Engineering,
Massachusetts Institute of Technology, Cambridge, MA 02139

Abstract

The Three Dimensional Printing (3DP) Process has been adapted for processing of fine ceramic powders to prepare structural ceramic components. Our preliminary study was designed to reveal those aspects of the 3DP process which must be modified for use with fine ceramic powders. The basic elements of the modified process are to spread submicron alumina powder and print latex binder. Several methods were used to spread thin layers of submicron powders. Green parts are isostatically pressed followed by thermal decomposition prior to sintering to remove the polymer. The fired alumina components are greater than 99.2% dense and have average flexural strength of 324 MPa. This is lower than the best conventionally prepared alumina, but we believe that the strength results will improve as we learn more about the relationship between strength limiting flaws and the 3DP build process.

Introduction

3D printing creates solid objects from a CAD representation by selective binding of ceramic or metal powders with "ink-jet" printing of binder droplets. Earlier work has demonstrated the effectiveness of 3DP as a rapid prototyping tool for investment casting tooling[1-4]. 3DP is, however, a flexible process in which any type of material in the form of powder can be used to create complex shapes. The effort involved in processing new materials systems using 3DP is minimal as compared to other SFF processes. 3DP is one of the few rapid prototyping technologies that involves the deposition of matter during the build process. Powder/binder combinations that are used for conventional powder processing can often be used in 3DP since ink-jets can be adapted to print a variety of binders. In principle, simultaneous control of the component microstructure and macrostructure can also be achieved by varying the amount and composition of binder printed into different locations within a layer. Thus, composition and porosity can be varied from point to point by specification in the original CAD file.

This paper reports on the first use of 3DP for fabrication of structural ceramic parts. It also represents the first use of submicron powder in the 3DP process. Submicron ceramic powders are necessary since the 3DP process produces a porous parts which must be fired to attain full density. The relative particle packing density or "green density" of the unfired part must be sufficiently high in order to sinter to full density when fired [5]. Green densities of at least 60% are often required for ceramics which sinter by solid-state diffusion.

Fine powders pose several challenges for direct application in the 3DP process. First, the current generation of 3DP machines spread dry powder across a piston in thin layers.

Fine powders do not generally flow well enough to spread into defect-free layers. Their high surface area causes increased cohesive strength of the unpacked powder and a decreased flowability. Simple modifications were made to the conventional spreading method to overcome the difficulties of fine powder. A press-rolling technique was devised for this purpose and using the initial low packing of the fine agglomerates and the load applied to the powder bed by stream rolling the spreader rod, we were able to spread uniform thin layers of fine powder. Uniformity in the microstructure of green samples is necessary to ensure the elimination of defects upon sintering. Isostatic pressing techniques were used to enhance the density before firing. The effects of this post treatment will be discussed.

Laminated building processes have the potential for producing structural parts that are superior to those prepared by other fabrication methods. Powder molding processes involve deformation of powder masses into dies to form complex shapes. The mass typically includes rather large amounts of organic binder to increase plastic flow into the mold, as is done in powder injection molding. The shear history of each volume element of the component is different because of the complex shape of the mold. This results in nonuniform powder packing in the green part and uncontrolled shrinkage and distortion during sintering. Each volume element of a laminated object is, however, prepared in the same way, regardless of shape or dimension. Secondly, binder removal is often accompanied by the formation of defects and adds considerably to the cycle time for component production [6]. Much less binder is required in the 3DP process, since the binder is used only to hold the green part together rather than plasticize the powder mass.

A process to make complex structural ceramic parts without the need for complex tooling will have a great impact on many applications of ceramics. One of the countless possible applications of this technology is the implementation of an accurate testing method for brittle materials. The theta specimen, first proposed by Durelli, Morse and Parks in 1962 is one such example (Figure 1). The special shape of the specimen allows one to test the tensile strength of brittle materials by diametrical compression. The load is transferred to the central bridge due to the outward motion of the ring on the horizontal axis. The test method eliminates the need for complex gripping schemes often required when testing brittle materials. It is a common practice to use 3 or 4 point bending tests for brittle materials for this reason. Theta specimen testing is not often used, however, because of the difficulty in fabricating the complex shape required. The development of 3DP process for fully dense ceramic parts makes the fabrication of theta specimens a trivial matter and a new standard for mechanical testing of brittle materials can be implemented with the help of 3DP technology.

Experimental Procedure

The powder used for this study was Reynolds RC172-DBM alumina, both undoped and MgO doped, with the mean primary particle size of 0.8 μ m. Through sieving of as-received powder, agglomerates of sizes between 75 and 150 μ m were screened to be used in the experiments. The apparent density and the tap density of the selected agglomerates were measured by using the apparatus and the techniques described by J. Lee [7].

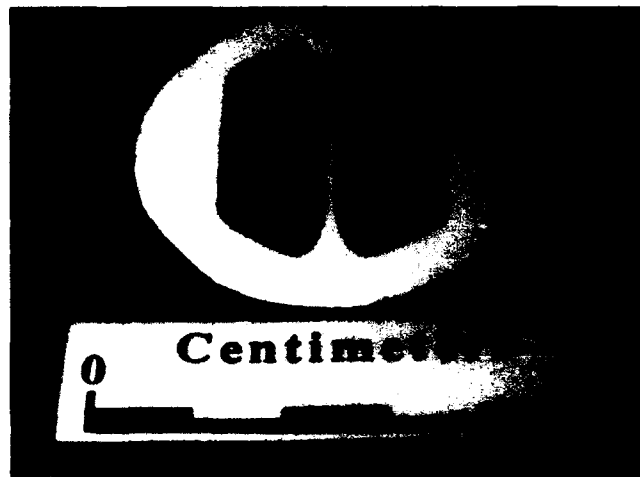


Figure 1. Theta Specimen

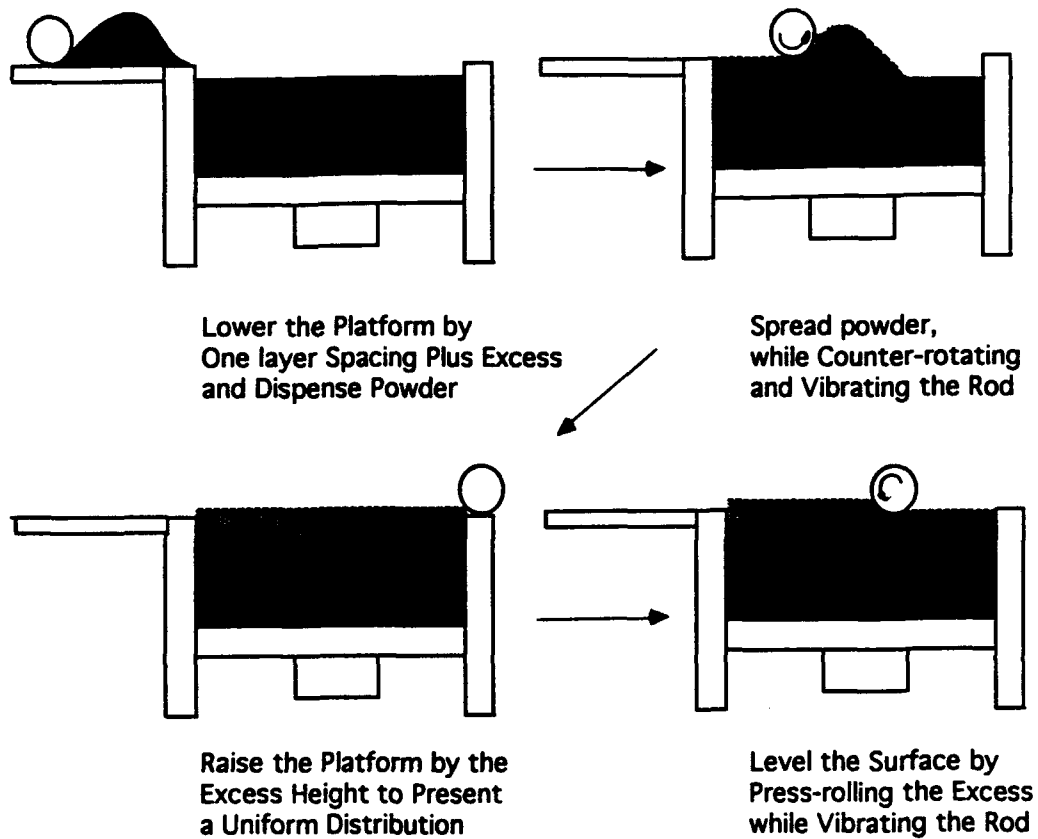


Figure 2. Press-rolling Sequence.

The binder used for this study was the Acrysol WS-24 (Rohm and Haas Company, Philadelphia, PA) which is an acrylic copolymer dispersion resin. Three different concentrations of the binder were used for printing, namely 3, 6, 12 wt%.

The 3D printing machine and the process by which the complex shapes are built is described in earlier publications [1~4]. Spreading of the sieved agglomerates was done by using a press-rolling method which is a modification of our conventional spreading technique. Figure 2 shows the schematic of the process. In the first step, the piston is lowered and a layer of loosely, but fairly uniformly packed agglomerates is produced by traversal of a counter-rotating spreader rod over the piston. On the second pass, the piston is raised to expose part of the loosely packed layer. The spreader rod is then forward rotated across the piston to pack the powder rather than shearing away the excess powder. This procedure results in a well packed uniform layer that is ready for printing.

A continuous jet of Acrysol droplets was made by passing the liquid through a 45 μ m diameter ceramic nozzle vibrated at 60kHz by piezoelectric transducers. The binder flow rate was 1.25cc/min. The printhead was rastered across the piston with a velocity of 1.65m/sec with 178 μ m spacing between the lines. The layer thickness was 127 μ m.

The piston containing the powder bed after the entire build operation was removed and heated at 125°C for one hour to remove water from the bed and cure the binder. The printed parts were then separated from the unprinted region by gently brushing away the matrix powder with soft brushes. The retrieved parts were then isostatically pressed either at room temperature or in heated hydraulic fluid. These processes are called cold isostatic pressing (CIP) and warm isostatic pressing (WIP), respectively. The samples were put in a latex bag, evacuated, and sealed before being placed in the chamber of the isostatic press.

Successfully isopressed samples were then placed in a furnace for binder removal at 450° C and then further fired for densification at 1650° C for 4 hours. The bulk densities of the green, isopressed, and fired samples were measured by using an automated mercury porosimeter.(Micromeritics, Norcross, GA). Shrinkages of rectangular samples were measured with micrometers.

Four point bending tests were conducted to find the flexural strength of the fabricated material. Precision grinding of the surface of bending specimens was performed prior to testing in order to measure the intrinsic strength of the material and eliminate effects due to surface defects. Grinding was performed by Bomas Machine Specialties Inc. (Sommerville, MA). The size and the shape of the specimens, and the testing procedures were in strict compliance with the ASTM standard C1161-90.

Results and Discussion

The fine alumina powder used for this study has considerably lower apparent and tap density than other common powders used for 3DP, as shown in Figure 3. Spreading these agglomerates with the conventional spreading sequence resulted in layers that are inhomogeneous and had low particle packing density. Since the uniformity of packing is

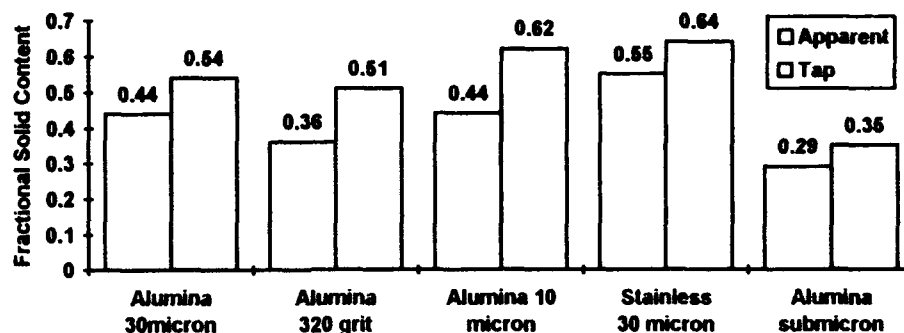


Figure 3. Apparent and tap densities of various powders

crucial for shrinkage control and in preventing the formation of defects in the final component, modifications have been made to the spreading sequence. The press-rolling technique, as described in the previous section has proven to be very effective in creating not only a homogeneous but also well packed layers of dry fine powder. The packing density of the resulting powder bed was 40% which is even higher than the tap density of the material. This phenomena is not observed with any other powders examined in this study. The cohesive strength of the resulting powder bed was quite remarkable and ballistic ejection of particles upon impact of binder droplets was completely eliminated. Ballistic ejection is a common observation for highly flowable powders used in 3DP and must be overcome by increasing the cohesive strength of the powder bed by adding moisture prior to printing [8,9]. The top surface finish was excellent due to the absence of both the ballistic ejection and particle rearrangement caused by capillary force.

The strength of the green parts varied with the concentration of the Acrysol. Samples printed with 3wt% Acrysol were strong enough to hold their shape, but not enough to be handled casually. Samples with 6wt% binder, however, had adequate strength for both loose powder removal and subsequent handling. Excess polymer from the samples with 12wt% Acrysol was found to segregate at the surface of each layer and is detrimental to the lamination of the layers (Figure 4). The excess binder exhibited other adverse effects on the properties of the samples, as will be discussed later.

The green density of the as-printed samples was found to range from 33 to 36% of alumina's theoretical density which is too low to fire to full density by sintering. As described earlier, we have incorporated an isostatic pressing of these 3DP green bodies to effectively increase the green density without sacrificing our ability to make complex shapes. CIP and WIP at 80°C of the parts were effective in increasing the green density of the samples, as shown in Figure 5. Isostatic pressing dramatically increases the final density of the material. The final density also depends on the binder content as can be shown by comparing the samples with 12wt% and 6wt% binder in the green state. Excess binder between the laminates contributes porosity that can not be removed by sintering. A polished cross section of the higher binder content sample in Figure 6 shows huge cracks between fully dense laminates obviously caused by the presence of excess binder.

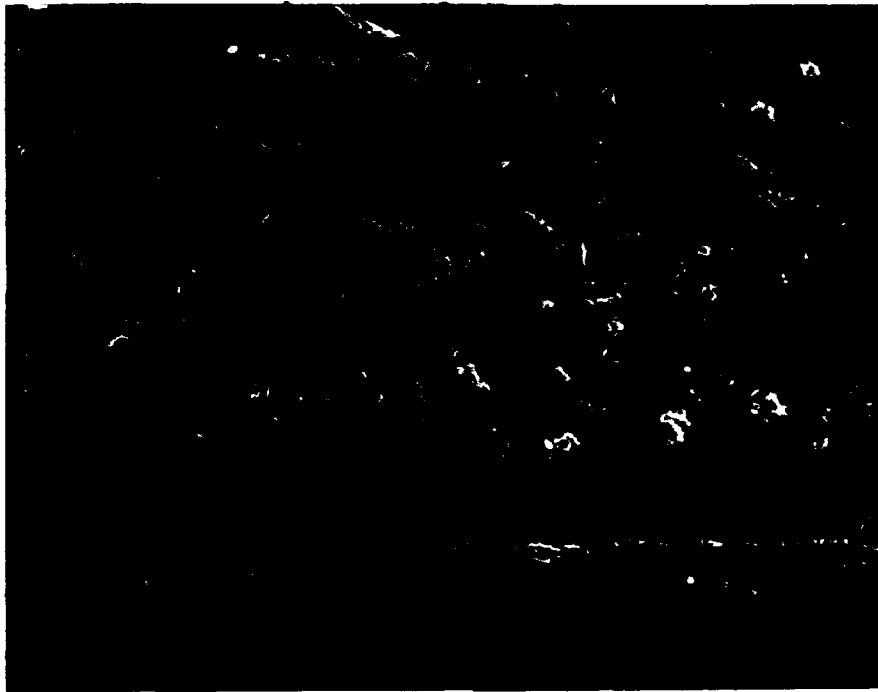


Figure 4. Polished cross section of as-printed part with 12wt% Acrysol.

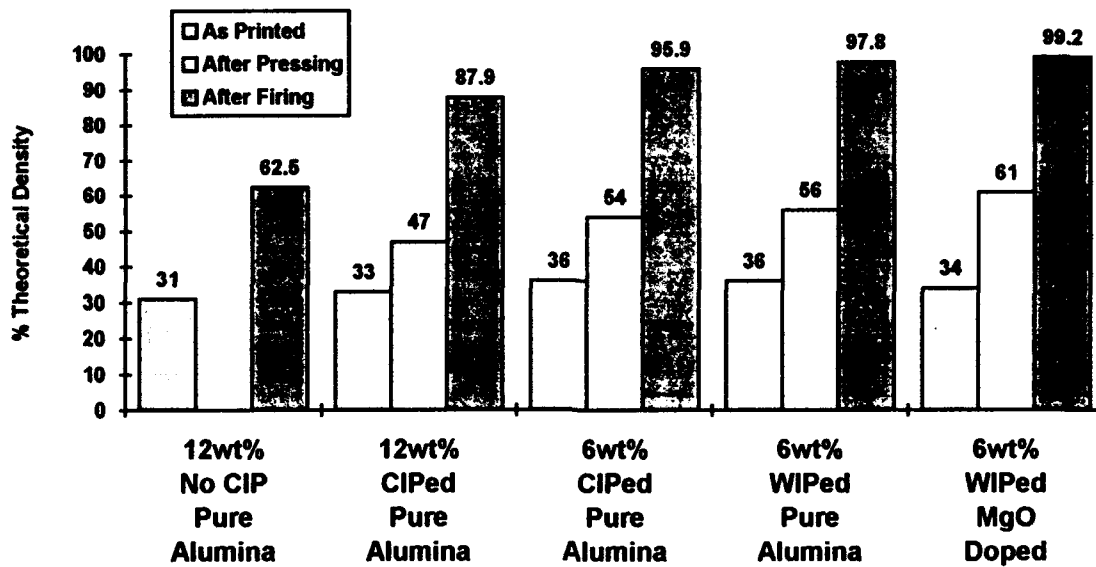


Figure 5. Bulk densities of parts at each stages.

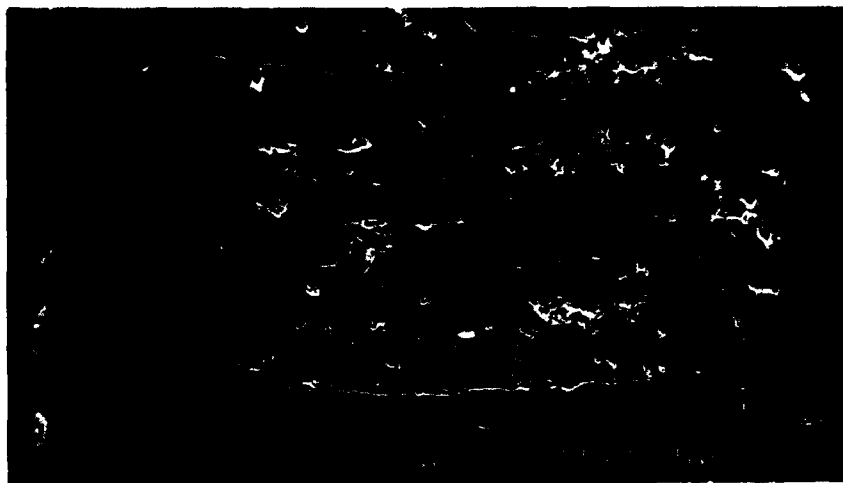


Figure 6. Polished cross section of CIP and fired sample with 12wt% Acrysol (Undoped)

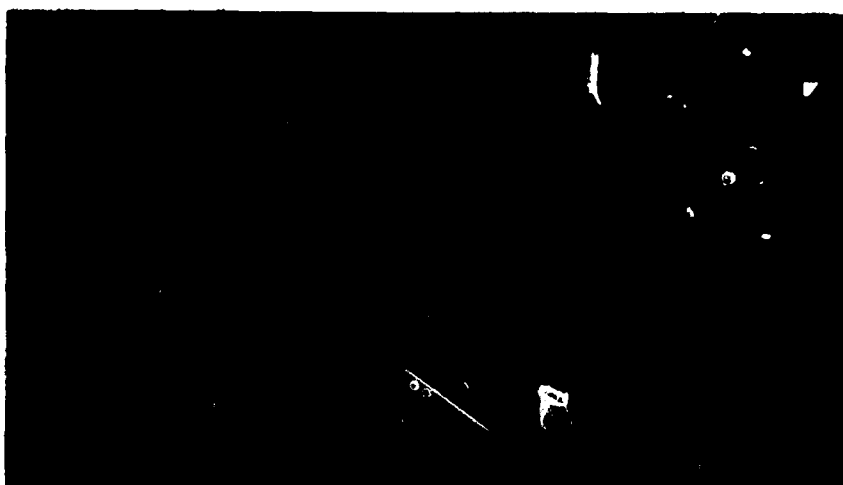


Figure 7. Polished cross section of WIP and fired sample with 6wt% Acrysol (Undoped)

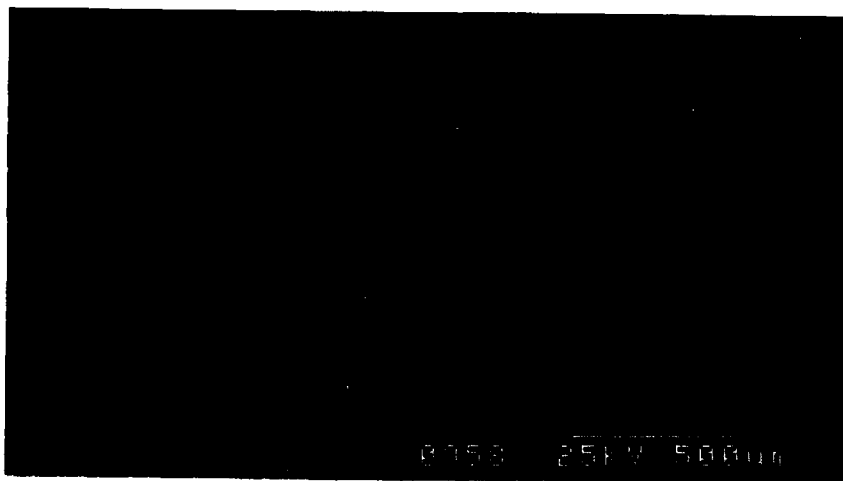


Figure 8. Polished cross section of WIP and fired sample with 6wt% Acrysol(MgO doped)

Density measurements on the samples with same binder content but different isopressing technique also show interesting behavior. Warm isostatic pressing is carried out above the glass transition temperature (46°C) of the Acrysol binder. Thus, the polymer viscosity decreases and results in redistribution of the binder while the pressure induced densification is in progress. The final densities of the subsequently fired parts have shown average value of 98% of the theoretical density of alumina. Figure 7 shows the cross section of a sample produced by WIP and sintering at 1650°C. No defects associated with lamination are apparent in the micrograph.

The results with the MgO doped alumina powder have shown the effectiveness of its role as the grain growth inhibitor and resulted in parts with 99.2% density. Figure 8 shows the MgO doped sample fabricated by the identical conditions as the above mentioned undoped samples.

Sintering shrinkages in different directions were also found to be strongly dependent on process parameters. As shown in Figure 9, the excess polymer present in between the laminates in the case with the 12wt% Acrysol caused more shrinkage in the direction normal to the build plane and thus caused very anisotropic shrinkage. Reduction in the anisotropy was achieved by the elimination of the excess binder content as shown in the case for 6wt% Acrysol. Further improvements and near isotropic shrinkage was obtained by implementing the WIP technique in conjunction with the reduction in binder content.

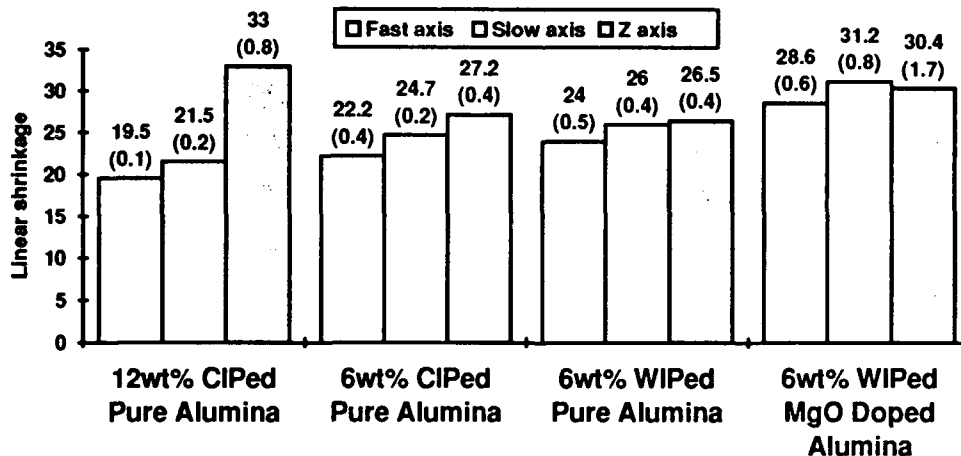


Figure 9. Total linear shrinkage in different directions. (Numbers inside the parentheses indicate the standard deviation of the shrinkage data)

Optimization of the amount of binder and the isopressing technique have allowed us to obtain a near fully dense pure alumina parts with 3DP. Although our current practice of wet-bag isostatic pressing does limit the topologies which can be pressed, alternative procedures are being investigated for isopressing of more complex parts. They include the dipping of the 3DP parts in a latex solution for forming a protective coating, and an *in situ* bagging technique of the samples by printing excess binder only at the edges of the part.

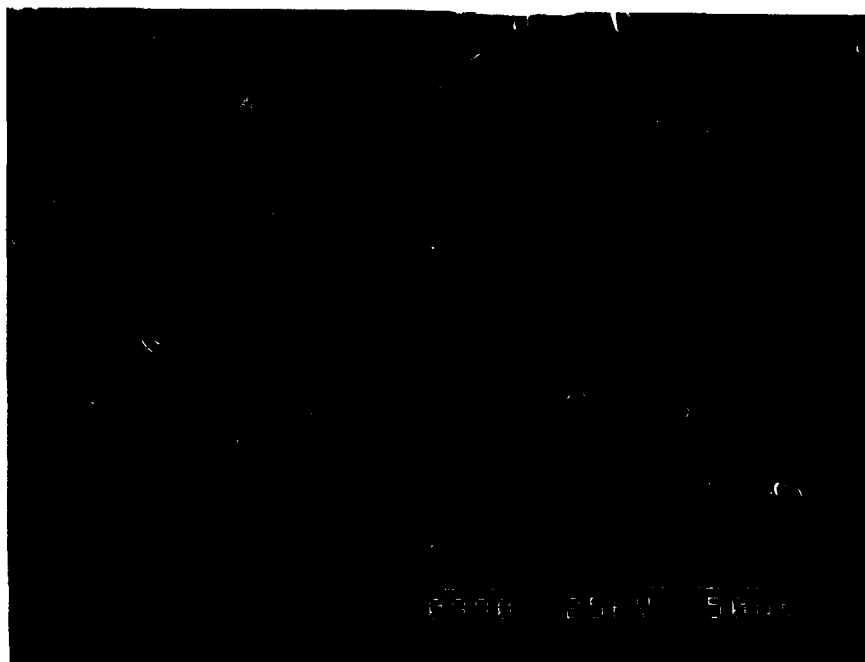


Figure 10. Thermally etched cross section of undoped sample. (6wt% binder, WIPed)

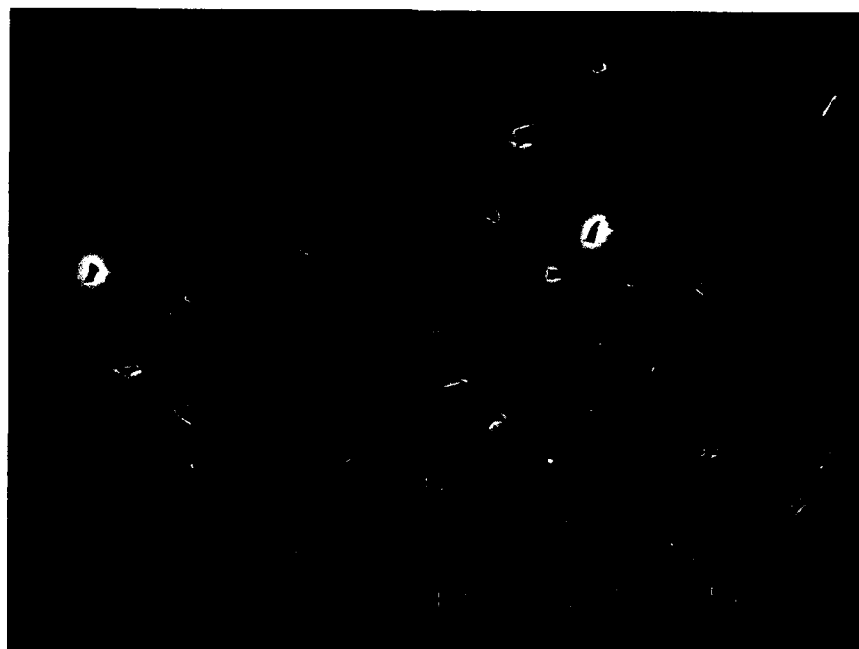


Figure 11. Thermally etched cross section ,MgO doped sample.(6wt% binder, WIPed)

The WIP procedure has also demonstrated effectiveness in improving the green density of other powder systems. In a preliminary experiments, WIPing parts made from printing Acrysol on a powder bed of spray dried alumina have resulted in a fully dense fired part. Further investigation with this system is also being conducted.

The mean flexural strengths of the 3D printed bars upon four point bending was 231.6MPa and 324MPa for undoped and MgO doped samples, respectively. MgO normally is added as an alumina grain growth inhibitor. Absence of MgO caused obvious signs of discontinuous grain growth which accounts for the 1.5% residual porosity and the relatively low strength in the case of undoped samples. (Figure 10) Samples with MgO-doped alumina powders do not exhibit discontinuous grain growth, as shown in Figure 11. Although conventionally prepared alumina has a slightly higher flexural strength of 350 to 450MPa, [10] we view our results as very promising since the microstructure of our samples exhibit signs of slight under-sintering. Optimization of the sintering schedule is under investigation and promises to yield improved properties.

Conclusions

Fine powders coupled with appropriate modifications in the powder spreading mechanism allowed us to fabricate the first near fully dense ceramic parts by 3D printing. The parts also benefited from the absence of particle movement during the printing cycle, thus drastically improving the surface finish of their top surfaces. The amount of binder printed into each layer has been found to play an important role in formation of defects between laminates and shrinkage anisotropy. The WIP method was also effective for enhancing the final density of the parts, as well as, in eliminating the interlaminar defects. Flexural strengths of the bend bars have shown 324MPa and higher upon four point bending tests. MgO-doped alumina powder brought improvements in the strength of the material by inhibiting the abnormal grain growth during firing which increased the final density of the component and decreased the grain size. Sintering schedules are being studied to further improve properties. Successful completion of these investigations will enable us to manufacture complex ceramic parts for structural applications directly by 3D printing.

Acknowledgments

This research was sponsored by the Advanced Research Projects Agency under contract N00014-92-J-1902. The authors also wish to acknowledge the support of the MIT/Industry Consortium for 3D Printing.

References

1. Sachs E., M. J. Cima, J. Cornie, "Three Dimensional Printing: Rapid Tooling and Prototypes Directly from a CAD Model.", *CIRP Annals*, vol. 39/1, p.210-204, 1990
2. Sachs E., et al, "Three Dimensional Printing: Ceramic Tooling and Parts Directly From a CAD Model.", *Nat. Conf. on Rapid Prototyping*, p. 35-37, 1990
3. Sachs E. et al, "Three Dimensional Printing: Ceramic Shells and Cores for Casting and Other Applications.", *2nd Int. Conf. on Rapid Prototyping*, p.39-53, 1991
4. Ashley S., "Rapid Mold-Making For Investment Casting.", *Mechanical Engineering*, 1992, vol. 114, no.11, p.49-51
5. Brunch C. A., *Am. Ceram. Soc. Bull.*, vol. 41, no.12, p.799, 1962
6. Lewis J. A., M. J. Cima, *J. of Am. Ceram. Soc.*, vol. 73, no.9, p.2702-2707, 1990
7. Lee J., "Powder Layer Generation for Three Dimensional Printing" S.M. Thesis, Dept. of Mechanical Engineering, Massachusetts Institute of Technology, June 1992
8. Lauder A. M. J. Cima, E. Sachs, and T. Fan, "Three Dimensional Printing: Surface Finish and Microstructure of Rapid Prototyped Components"; in *Proceedings, Synthesis and Processing of Ceramics: Scientific Issues*, Boston, MA, 1991
9. Fan T., A. Lauder, E. Sachs, M. J. Cima, "The Surface Finish in Three Dimensional Printing," presented at the *3rd Int. Conf. on Rapid Prototyping*, 1992
10. Schwartz M., Ed., "Handbook of Structural Ceramics", McGraw-Hill, 1992

Direct Laser Sintering of Metals

William T. Carter, Jr. and Marshall G. Jones
General Electric
Corporate Research & Development Center

Abstract

The use of a directed laser beam source to selectively sinter multiple layers of binderless metal powder for the purposes of rapid prototyping is described. The work in this paper is restricted to -325 mesh iron powder, which was sintered using a CW 50 W Nd:YAG laser to approximately 35% density. A subsequent post-treatment was performed to achieve a fully dense sample. It is envisioned that such a system can be used to manufacture *functional* metallic prototypes directly from CAD without part-specific tooling.

1 Background

1.1 Rapid Prototyping

The use of rapid prototyping in a concurrent engineering environment results in reduced product development cycle time—a natural consequence of the quick availability of working testable hardware. A functional prototype allows the identification of design deficiencies or areas for design improvement; it allows experimental stress analysis, vibrations testing, and other design performance tests with a very low lead-time. In some cases, experimental analysis of prototypes has proven to be less expensive than computer-based analysis techniques such as finite element analysis [1]. A common characteristic of rapid prototyping methods is that no part-specific tooling, such as a mold or die, is required to make the part. Several reviews of rapid prototyping are available in the literature [2][3][4].

Use of rapid prototyping technology is expected to grow as more materials can be processed using the techniques. Many systems are commercially available; the most popular technique to date is *stereolithography*, which generates a part from a bath of laser-cured photopolymer resin. *Selective laser sintering*, the topic of this paper, is gaining popularity; it generates a part from multiple layers of powder. Commercial systems for SLS are currently limited to ABS plastic, wax, nylon and polycarbonate materials.

To date, no commercial freeform fabrication system is available for metallic materials. The preliminary results of an effort to address this issue are described in this paper.

1.2 Selective Laser Sintering (SLS)

SLS generates a part by selectively bonding multiple layers of powder to build a three-dimensional part in a layer-by-layer manner. The process has been commercially applied to ABS plastic, nylon, polycarbonate, and wax[5][6][7]. The process is very appealing for applications involving metals and ceramics. It is anticipated that SLS of metals will be less expensive and less time-consuming than conventional production methods for metals, such as sand casting or investment casting, when the number of parts required is reasonably small. Therefore, the system will be used by designers and engineers during the prototyping stages of product development. A complete SLS apparatus will allow designers to quickly generate three-dimensional *functional* prototypes of various parts. The process is also attractive to builders of custom tooling, dies and molds since these industries represent one-of-a-kind applications.

Though there are no commercial systems for applying this technique to metals, research is under way at the University of Texas at Austin.¹ One of their techniques is to coat the metal particles with a binder; the binder is selectively cured with a laser, and the part is later fired to burn out the binder and densify the part. Parts of final densities of 48% [8] and higher have been reported. Other work is ongoing to directly sinter metals by using a liquid-phase metallic material to fill the voids in a solid-phase powder, such as copper in nickel. Higher densities (82%) have been reported using this technique [9].

The approach reported here differs in that the metal powder is sintered directly, without the introduction of a binder or a low-melting-temperature liquid phase. A two-step process is proposed: The laser will not be used to generate a fully-dense final part; instead, the laser apparatus will be used to generate a "green" part that requires subsequent processing such as *Hot Isostatic Pressing* (HIPing), oven firing, or infiltration. The goal of this effort is to assess the process by laser sintering a simple cubic sample of iron, performing a HIP densification treatment, and evaluating the density of the resulting material.

2 Experimental Apparatus

A laboratory scale system was constructed for evaluation of the SLS process. The system is capable of making parts up to 1 in. by 1 in. by 3 in. using laser heating.

¹The SLS process is patented by the University of Texas in Austin and has been reduced to practice by DTM, a subsidiary of B.F. Goodrich.

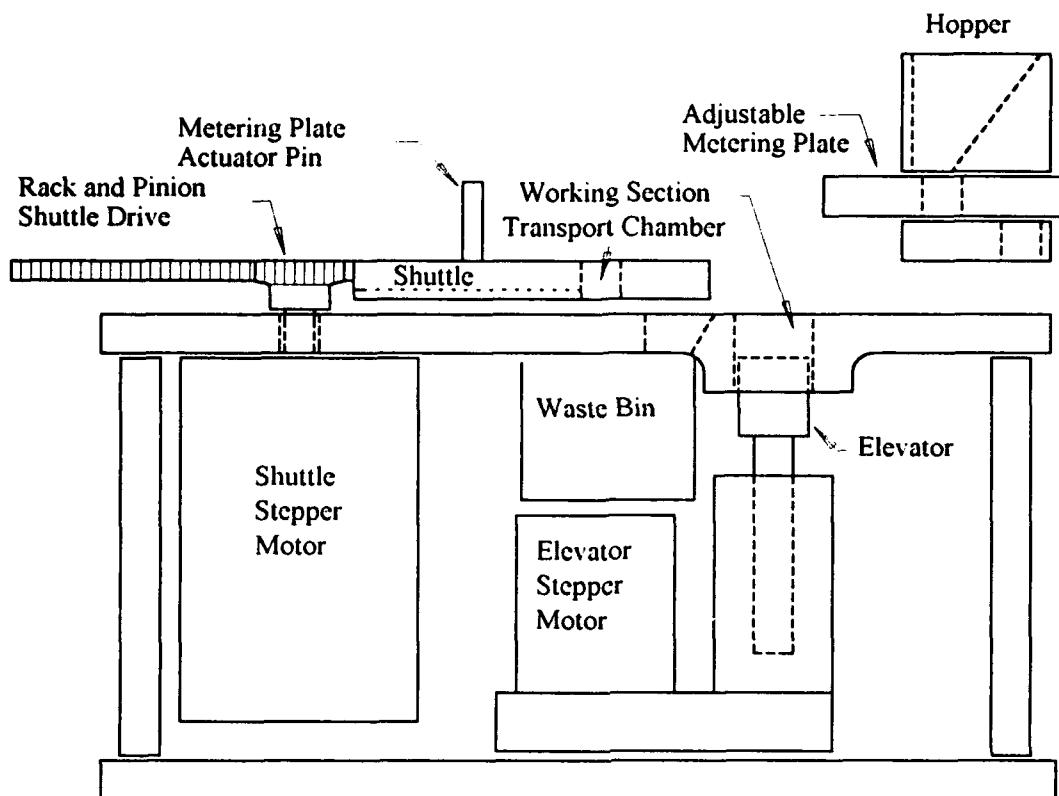


Figure 1: Powder handling system.

2.1 Powder Handling System

The powder handling system is shown schematically in Figure 1. This system includes two stepper motors: one to control the height of an elevator under the working section, another to control the location of a powder shuttle. To add a layer of powder, the elevator is lowered the desired distance, and the shuttle is moved until the actuator opens a powder metering device. A measured amount of powder is dropped through the transfer plate and into the shuttle transport chamber. The shuttle then returns to its home position. As the shuttle returns, a layer of powder is spread over the working section. Excess powder is dumped into the waste bin. The shuttle stops momentarily, completely covering the working section, and the powder is compacted by temporarily raising the elevator.

During a laser sintering experiment, the powder handler is housed in a glove-box with an over-pressure of inert gas or forming gas to avoid oxidation of the metal powder.

Controllable parameters include:

- Powder composition, size and shape.
- Laser power (0 to 50 W)
- Laser spot size (>1 mm dia.)
- Scan speed (<20 in./min.)
- Layer thickness
- Process environment (inert gas, forming gas, etc.)

2.2 Laser System

The laser used in this process is a 50 W continuous wave (CW) neodymium:yttrium-aluminum-garnet (Nd:YAG) laser with a computer-controlled shutter. The 1.06 μm wavelength laser beam is channeled through a 600 μm single core step index quartz fiber optic to the powder handling system. At the terminal end of the fiber optic, an output coupler and a lens focus the beam to approximately 0.5 mm diameter on the metal powder. The Nd:YAG laser is the better laser choice when compared with a CO₂ laser because the 1.06 μm heat source couples with metals more efficiently than a 10.6 μm heat source. See Figure 2. The Nd:YAG laser has the further advantage that, at higher powers, the beam is efficiently transmitted through fiber optics. This allows for more flexible SLS machine design.

The output coupler assembly is mounted on an x-y table, which is translated via two additional stepper motors. The laser's shutter and the four stepper motors (two in the powder handling system and two in the x-y table) are controlled using a single 80386 computer.

2.3 Secondary Processing (HIPing)

The green form generated using the SLS system requires a post-treatment to render a fully dense part. Since the part will, in general, be quite brittle and will possibly contain many small sections, some means of supporting the part during the treatment is required. Furthermore, it is expected that the green structure will contain interconnected porosity that makes conventional gas HIPing impossible. The following technique was successfully implemented to HIP laser-sintered specimens:

1. The specimen was suspended in alumina powder in a Pyrex tube.
2. The tube was evacuated and baked at 300° C for three hours to drive out all moisture and organic material. The tube was then sealed while still under vacuum.

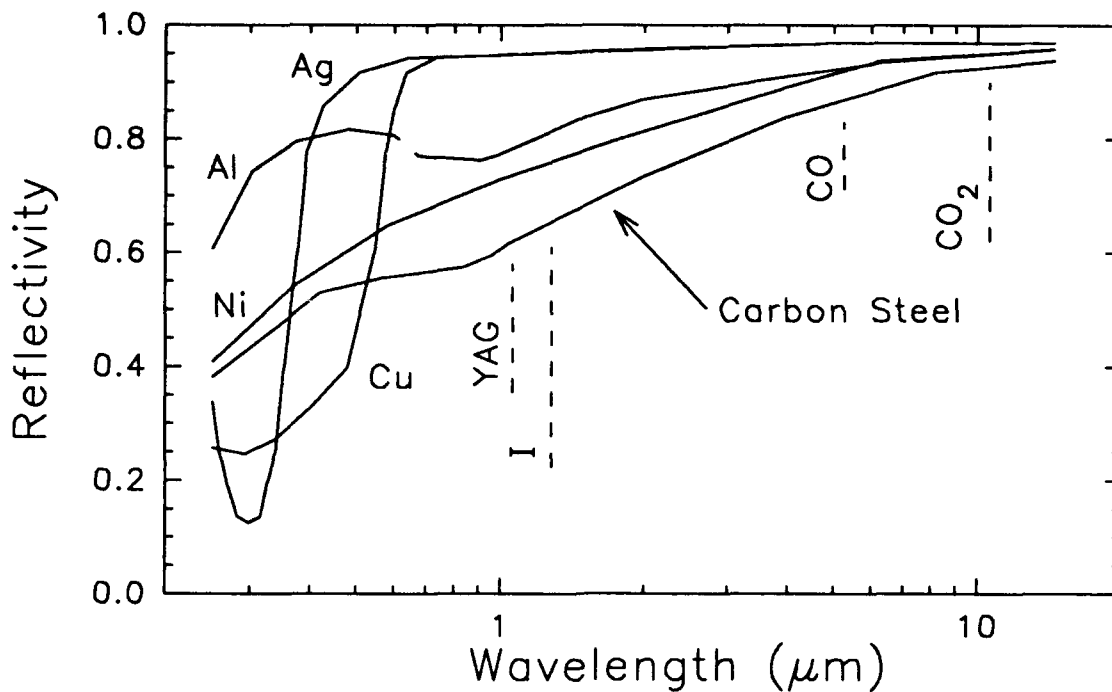


Figure 2: Wavelength dependence of reflectivity for various metals.

3. The sealed tube was HIPed at 15 ksi and 1100° C for 15 minutes. The temperature was linearly increased from room temperature at a rate of 50° C/min. and pressure was kept at 1 atm until a temperature of 900° C was reached.
4. After cooling, the Pyrex tube was broken and the metal part was grit-blasted clean.

3 Findings

3.1 Properties

A laser sintered specimen with a corresponding as-HIPed geometry is shown in Figure 3 along with the cross-sectional metallography of each part. This part was made from 44 μm (-324 mesh) iron powder in an environment of 10% hydrogen and argon using 7.5 W of laser power focused to a 0.5 mm spot. A scan speed of 5 in./min. was used with a scan spacing of 0.020 in. Each powder layer was approximately 0.004 in. thick. The as-sintered part is approximately 35% dense, making it a brittle structure; however, it was able to withstand the small amount of handling necessary to place it

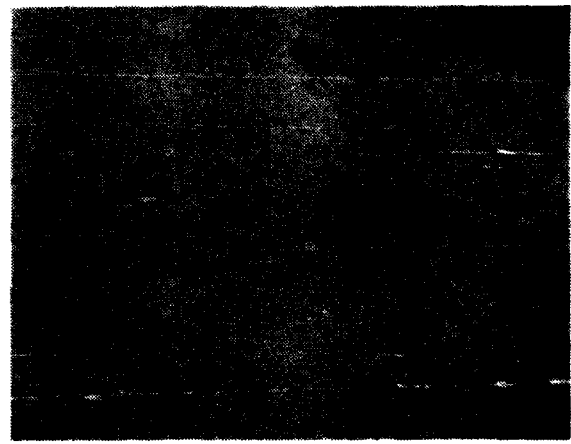
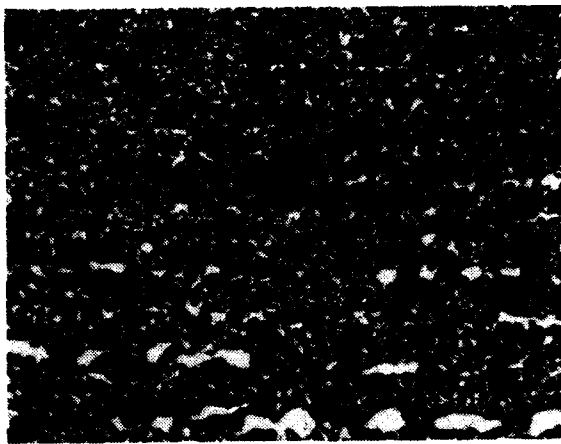
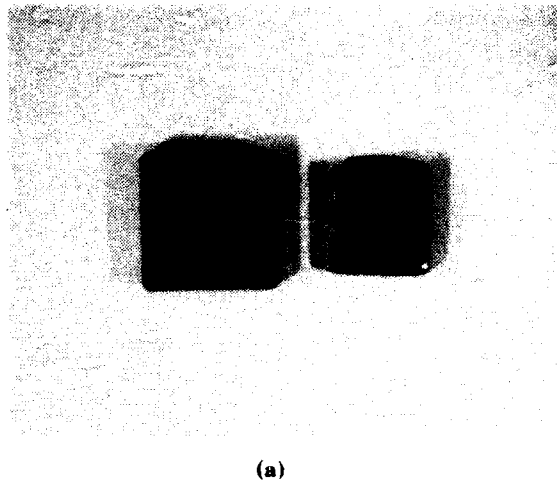


Figure 3: Selective laser-sintered iron sample (a) before and after HIP; (b) and (c) microstructure.

in a HIP vessel. The as-HIPed structure is very dense ($> 99.9\%$) as shown in Figure 3c, with only a small number of remaining voids.

3.2 Environment

The most significant problem associated with SLS of iron encountered in this research effort is the control of the sintering environment and the formation of oxide. For this reason, the powder handling system was placed inside a glovebox and an overpressure of inert or forming gas was applied inside the box. Additionally, the powder was "pre-cleaned" by placing it in a fluidized bed charged with the same inert or forming gas.

3.2.1 Inert Environment

When using -325 mesh iron powder, it was found that a good single layer could be generated in an inert environment of argon. Unfortunately, the bond *between* the layers was generally *inadequate* for the following reasons:

- The free energy of formation for oxide increases with decreasing temperature [10]. Thus, in cooling to room temperature from a high homologous temperature, a period of high oxidation growth can be expected. This oxide is particularly undesirable in the SLS process because it prevents effective sintering or wetting.
- During the sintering of each layer, the temperature of the powder was brought to a value above the melting temperature of the metal. Each laser scan was performed relatively quickly. Thus, adjacent scans occurred before the material cooled and simultaneously oxidized. For this reason, the bonds within the layers (between scans) were acceptable.
- Between layers, the material was allowed to return to room temperature. Thus, each layer ran through a temperature cycle that is very conducive to oxide formation as discussed above. (Oxide was observed in SEM EDAX probing.) Though the atmosphere was free of oxide, enough residual oxygen was present in the powder to form an oxide layer on the upper surface and prevent good bonds between the layers.

3.2.2 Reducing Atmosphere

A common reducing atmosphere for ferrous materials is a mixture of hydrogen and nitrogen; this mixture is often called "forming gas." Laser sintering in this atmosphere proved to be unsatisfactory because of the formation of nitrides between each layer, preventing inter-layer bonds. (Nitriding is a common surface hardening technique for steels.)

When the same iron material was sintered in a reducing atmosphere of 10% hydrogen and argon, excellent bonds between the layers were achieved. It should be noted that all other process parameters (laser power density, scan spacing, layer thickness, etc.) were kept constant between the tests in argon, nitrogen and hydrogen, and those in argon and hydrogen.

3.3 Post-Treatments

From the materials standpoint, HIPing proved to be satisfactory for these preliminary tests—it achieved a dense sample with a predicted reduction in the dimensions of the specimen. From the standpoint of FFF, HIPing is not attractive without a model that gives a "process compensated" geometry for the sintering operation. A model of

the HIPing process is required to define an "as-sintered" part geometry. This model is not straight-forward because, for example, holes and cavities which are temporarily filled with alumina powder will densify at a different rate during HIPing than the adjacent metal.

3.4 Warping

Because the heat is applied at the top surface, the top densifies to a greater extent than does the bottom surface of each layer. Additionally, the upper surface cools from a higher temperature than material below, causing more thermal contraction on the upper surface. For these reasons, each layer of sintered powder tends to warp upward, which is undesirable from a powder-handling standpoint because the thickness of each layer is not uniform. The solution adopted for this work was to build an "anchor" of thin sintered layers onto which the actual structure was constructed. This thin frame gives some stiffness to the overall structure and avoids warping in many situations.

Various other techniques are possible:

- Heating the powder bed. This method has been implemented [11] for laser sintering of metals with good success; it reduces the thermal strain by reducing the temperature excursion. This method has the added benefit that it helps prevent oxide build-up between layers.
- "Knitting" the structure in such a way that the loose powder is allowed to flow to fill the gaps left by the densified material.
- Bonding the prototype to a rigid sample of the same material during the first stages of the sintering process, effectively building an anchor. This may be acceptable for some applications where the anchor can become an integral part of the laser-sintered structure.

4 Conclusions

The proof-of-concept goal that stimulated this work effort was successfully achieved. Binderless iron powder was sintered into a cubic shape of 35% density in a reducing atmosphere using a directed laser beam. The cube was later HIPed to full density with a predicted reduction in overall dimensions. It was demonstrated that the control of the sintering environment is critical for successful laser sintering. In this particular case, an environment of 10% hydrogen and argon yielded the best inter-layer bonds.

5 Acknowledgments

The work and advice of several people is acknowledged: Leon Beha, Jerry Harrison, Jim Resue, Steve Rutkowski, Paul Siemers, Cosimo Montanaro, and Mark Brun.

References

- [1] G.W. Royal, "Application of Stereolithography to Gas Turbine Design," *Proceedings of the National Conference on Rapid Prototyping*, June, 1990.
- [2] S. Ashley, "Rapid Prototyping Systems," *Mechanical Engineering*, April 1991, pp. 36-43.
- [3] B.A. Beckert, "Cutting it in Rapid Prototyping," *Computer-Aided Engineering*, Sept. 1991, pp. 28-40.
- [4] J.P. Kruth, "Material Incess Manufacturing by Rapid Prototyping Techniques," *Annals of the CIRP*, **40-2**, 1991, pp. 603-614.
- [5] H.L. Marcus, et al., "Solid Freeform Fabrication: Powder Processing," *Ceramics Bulletin*, **69-6**, 1990, pp. 1030-1031.
- [6] H.L. Marcus, et al., "From Computer to Component in 15 Minutes: The Integrated Manufacture of Three-Dimensional Objects," *Journal of Metals*, April 1990, pp. 8-10.
- [7] K. Nutt, "The Selective Laser Sintering Process," *Photonics Spectra*, Sept. 1991, pp. 102-104.
- [8] B. Badrinarayan and J.W. Barlow, "Metal Parts from Selective Laser Sintering of Metal-Polymer Powders," *Solid Freeform Fabrication Symposium*, Austin, 1992, pp. 141-146.
- [9] G. Zong, et. al., "Direct Selective Laser Sintering of High Temperature Materials," *Solid Freeform Fabrication Symposium*, Austin, 1992, pp. 72-85.
- [10] F.V. Lenel, *Powder Metallurgy: Principles and Applications*, Metal Powder Industries Federation, Princeton, New Jersey, 1980.
- [11] J. McWilliams, C. Hysinger, J.J. Beaman, "Design of a High Temperature Process Chamber for the Selective Laser Sintering Process," *Solid Freeform Fabrication Symposium*, Austin, 1992, pp. 110-117.

SOLID FREEBODY FORMING OF CERAMICS FROM POLYMERIZABLE SLURRY

Kevin Stuffle, Anthony Mulligan, Paul Calvert* and John Lombardi*
ACR, Tucson, Arizona; *Arizona Materials Laboratories, Tucson Arizona.

INTRODUCTION

In solid free body forming a component is described by a CAD system as a series of slices. The slices are deposited as a sequence of layers which are cured or solidified by a moving head such that a three dimensional part is built up. Systems have been developed based on photocurable polymers, solidifying polymer melts, laser fused powder layers, polymer-bound powders and others.

Difficulties with such systems to date include the low strength of many of the polymer systems and poor resolution. The polymeric components can be used as forms to make molds for later casting of metals or ceramics. The powder components can be sintered to higher density.

In the system described here, the part is built up by deposition of a slurry of ceramic powder in liquid acrylic monomer. As each layer is deposited the monomer is heat-cured. When the whole component is formed, the polymer is burnt-out and the ceramic is sintered.

DELIVERY SYSTEM

The slurry was contained in a 50 ml polypropylene syringe which was connected to an argon pressure line to drive the liquid through a needle of 0.3-1.3 mm diameter. The delivery was started and stopped by a shut-off valve with pressure venting in the air line.

SLURRY

Slurries of Alumina (Al_2O_3 -0.5 wt% MgO, Ceralox Corp.) in liquid acrylic monomers were prepared. The formulations, based on the work of Janney [1], are shown in Table 1. Similar monomer systems have been used for tape casting of ceramic sheets by various workers [2]. Alumina solids loadings up to 53 vol% were used. The acrylate monomers have the advantage of curing very rapidly. Since they are polyfunctional, high degrees of polymerization are not necessary to achieve high molecular weight or gelation. The polymerization rate and brittleness of the resin was controlled by addition of dibasic esters, a mixture of primarily dimethyl glutarate and succinate. Viscosity increases with solids loading as shown in Figure 1. Figure 2 shows

slurry flow rates as a function of applied pressure through a 0.33 mm needle, 1.27 cm long.

Table 1: Composition of Acrylic Monomer Formulations

Alumina, wt%	26.2	34.0	39.5	42.5	45.1	47.7	48.9
Triton X-100, wt%	7.8	10.1	10.3	9.8	9.3	10.8	10.5
TMPTA, wt%	3.4	4.4	4.0	3.8	3.6	3.6	3.2
HODA, wt%	29.6	38.3	34.5	32.8	31.3	28.2	27.9
DBE, wt%	32.9	13.1	39.5	11.2	10.7	9.7	9.5
Mill time, hr	24	24	21	21	41	49	49
Density, g/ml	1.54	1.75	2.01	2.00	2.16	2.19	2.23
Viscosity, P	6	12	29	50	112	127	146

HODA: Hexanedioldiacrylate, TMPTA: Trimethylolpropanetriacrylate, DBE: Dibasic ester, plasticizer.

DEPOSITION AND CURING

Thin layers of slurry were deposited onto a heated platen at about 120°C. The temperature was adjusted to give rapid curing and good shape definition. Oxygen inhibition of the polymerization leaves the surface tacky and improves the degree of bonding between successive layers.

FIBER REINFORCEMENT

Carbon fibers 1 μm in diameter were milled for 30 hours with the slurry, to produce fibers with a length of about 200 μm . With 1% fiber content these slurries flowed readily through the needle and were formed into parts. Fibers tended to align horizontally in each layer. The resulting green parts appeared to be tougher and easier to handle than unreinforced parts.

Figure 1: Viscosity vs volume % ceramic loading

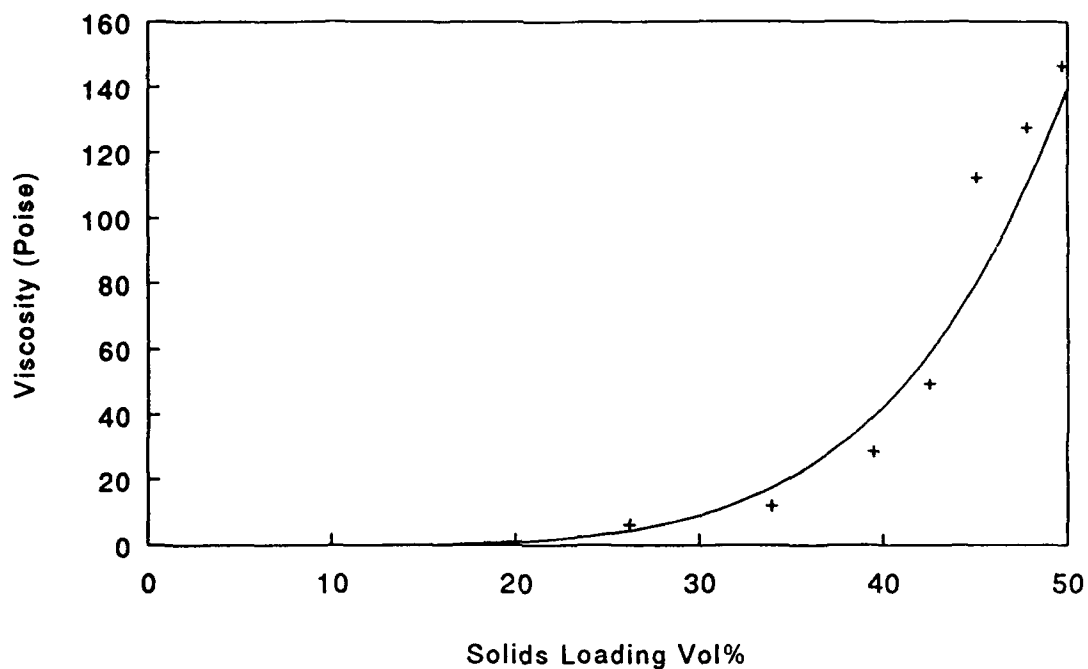
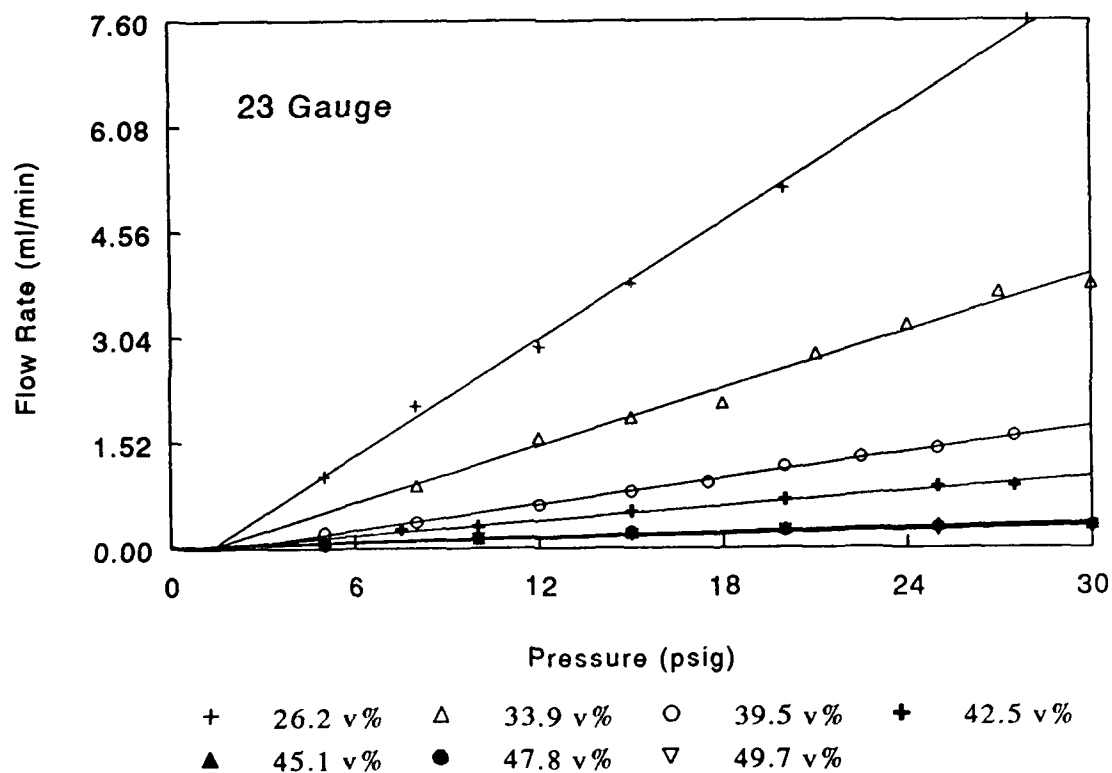


Figure 2: Flow rate vs. pressure profiles for alumina slurries



PART PRODUCTION

Flat plates and thin walled cylinders were produced in monolithic alumina using simple machine instructions to a head mounted on an X-Y table. A nozzle of 0.33 mm was used with a slurry pump pressure of 22 psig and a nozzle linear speed of 100 cm/min.

PART PROPERTIES

Green parts had a density of about 60% of theoretical, based on pure alumina. After firing densities range from 3.64 to 3.94 (90-99% of theoretical). Flexural modulus was measured to be 358 GPa and strengths ranged from 431-606 MPa for 12 samples in three point bend for a sample 2"x1.5"x0.2". This compares favorably with commercial alumina.

REFERENCES

1. M.A.Janney, "Method for molding ceramic powders" U.S. Patent 4,894,194; Jan 16 1990.
2. R.R.Landham, P.Nahass, D.K.Leung, M.Ungereit, W.E.Rhine, H.K.Bowen and P.D.Calvert, "Potential use of polymerizable solvents for tape casting ceramics", Amer. Ceram.Soc. Bull. (1987) 66, 1513.

DEVELOPMENT OF NANOCOMPOSITES FOR SOLID FREEFORM FABRICATION

A. Manthiram, F. Chi, L. F. Johnson, B. R. Birmingham and H. L. Marcus
Center for Materials Science and Engineering, ETC 9.104
The University of Texas at Austin
Austin, TX 78712

ABSTRACT

Nanocomposites in which the constituents are mixed on a nanometer scale can provide important advantages in the Selective Laser Sintering (SLS) and Selective Laser Reactive Sintering (SLRS) processes. The larger surface area and grain boundaries in the nanocomposites compared to that in the conventional microcomposites are expected to enhance the solid state diffusion during laser irradiation as well as during any other subsequent processes. Our strategy is to design and develop nanocomposites in which one nanosize component has a lower melting point than the other nanosize component, either of which can serve as the matrix phase. The nanoscale dispersion of the low melting component can aid the sintering process during SLS or SLRS. Nanocomposite powders of $\text{Al}_2\text{O}_3\text{-CoO}_x$, $\text{Al}_2\text{O}_3\text{-NiO}$, $\text{Al}_2\text{O}_3\text{-Co}$ and $\text{Al}_2\text{O}_3\text{-Ni}$ have been synthesized by sol-gel processing and are evaluated by SLS.

INTRODUCTION

Nanostructured materials are characterized by ultrasmall building blocks whose sizes are of the order of 1-100 nanometers. These materials offer potentially useful and unusual combinations of mechanical, electrical, magnetic and optical properties that are otherwise unachievable in conventional materials [1]. The properties are controlled by a complex interplay among the building blocks and the interfaces between them that are determined primarily by the synthesis and processing conditions. Nanostructured materials promise to advance a range of technologies and there is intensive worldwide activity on these materials both from scientific and technological points of view.

While the terms "nanocrystalline" and "nanophase" materials refer generally to single phase solids of nanometer size, the term "nanocomposite" refers to multiphase solids of nanometer size [2]. The solid phases in a nanocomposite could be of different nature. They could be metals, inorganic ceramics or polymers or combinations thereof but all mixed on a truly nanometer scale. The phases could be amorphous, semicrystalline or crystalline.

Nanocomposites exhibit ultraheterogeneity or nanoheterogeneity, which offer several processing advantages. Because the different phases are mixed on a nanoscale, the diffusion length for solid-solid reaction is much smaller than that in conventional materials. The larger surface and grain boundary energies associated with nanocomposites provide the driving force for enhanced reactions. These factors reduce the reaction temperature as well as time. Nanocomposites have been shown to sinter close to theoretical densities in several systems such as $\text{Al}_2\text{O}_3\text{-SiO}_2$, $\text{Al}_2\text{O}_3\text{-TiO}_2$, $\text{SiO}_2\text{-MgO}$, *etc.* [3]. Nanocomposite gels store much higher metastable energy than homogeneous gels, and this extra energy enhances

densification. In addition, nanocomposites seem to undergo crystallization and densification simultaneously unlike homogeneous gels. Homogeneous gels, due to their atomic scale mixing, often undergo crystallization before densification occurs which either leads to lower densities or necessitates higher temperatures for sintering. It is clear that nanocomposites have the potential to offer lower processing temperatures and flaw-free parts with higher densities.

Our objective is to design and develop nanocomposites that can optimize Selective Laser Sintering (SLS) and selective Laser Reactive sintering (SLRS). Nanocomposites can be synthesized by sol-gel processing or other "soft chemistry" techniques. Although both sol-gel processing and solid freeform fabrication are well known, the idea of utilizing sol-gel derived nanocomposite powders that are specifically designed and synthesized to optimize SLS or SLRS have not been exploited. Our strategy is to select ceramic-ceramic or ceramic-metal nanocomposite systems in such a way that one nanosize component has a lower melting temperature than the other nanophase component, either of which can serve as the matrix phase. The objective is to achieve sintering aid from the low melting phase during SFF processing. Because the low melting component is dispersed on a nanoscale in the matrix phase, it is expected to aid the sintering process, during SFF or any other secondary processing, in a much better way than the mechanically mixed microcomposite powders. By proper selection of composite systems and control of agglomeration during sol-gel processing, the ability to achieve full density SFF parts can be enhanced. We present in this paper our preliminary results with $\text{Al}_2\text{O}_3\text{-CoO}_x$, $\text{Al}_2\text{O}_3\text{-NiO}$, $\text{Al}_2\text{O}_3\text{-Co}$ and $\text{Al}_2\text{O}_3\text{-Ni}$ nanocomposites. CoO, NiO, Co and Ni have melting points of respectively, 1795, 1984, 1495 and 1455 °C, which are lower than that of Al_2O_3 (2050 °C).

EXPERIMENTAL

The ceramic-ceramic nanocomposite powders of $\text{Al}_2\text{O}_3\text{-CoO}_x$, and $\text{Al}_2\text{O}_3\text{-NiO}$ were synthesized by a sol-gel method [4]. The steps involved in the synthesis of $\text{Al}_2\text{O}_3\text{-CoO}_x$ are summarized in Fig. 1. To an aqueous solution of $\text{Co}(\text{NO}_3)_2 \cdot 6\text{H}_2\text{O}$ maintained at about 80 °C, required amount of a solution of aluminum tri-sec-butoxide in iso-propyl alcohol was added under constant stirring. Aluminum-tri-sec-butoxide hydrolyzes during this process to give large suspended particles of $\text{Al}(\text{OH})_3$, which was then dissolved by adding nitric acid to obtain a homogeneous sol of Al^{3+} and Co^{2+} . The sol was heated gently on a hot plate to form a gel, which was then dried rapidly on the hot plate. The dry gel was then heated in a muffle furnace to decompose the nitrate and hydroxide, which resulted in a mixture of $\text{Al}_2\text{O}_3\text{-Co}_3\text{O}_4$. A similar procedure was adopted to obtain $\text{Al}_2\text{O}_3\text{-NiO}$ also. The $\text{Al}_2\text{O}_3\text{-Co}_3\text{O}_4$, and $\text{Al}_2\text{O}_3\text{-NiO}$ powders were also fired at different temperatures ranging from 300-1250 °C to evaluate the reaction process. The ceramic-ceramic nanocomposites so obtained were reduced in a stream of hydrogen at 400-1100 °C to obtain the ceramic-metal nanocomposites $\text{Al}_2\text{O}_3\text{-Co}$, and $\text{Al}_2\text{O}_3\text{-Ni}$.

The composite powders were characterized by x-ray diffraction, electron microscopy and density measurements. Since the large surface area associated with the nanosize powders lead to an adsorption of water, CO_2 etc. on the surface, the powders were baked at about 200 °C for about 24 h before scanning with the laser beam. Single layer tests were performed with various power levels and scan speeds. The specimens obtained were characterized by x-ray diffraction and microscopy.

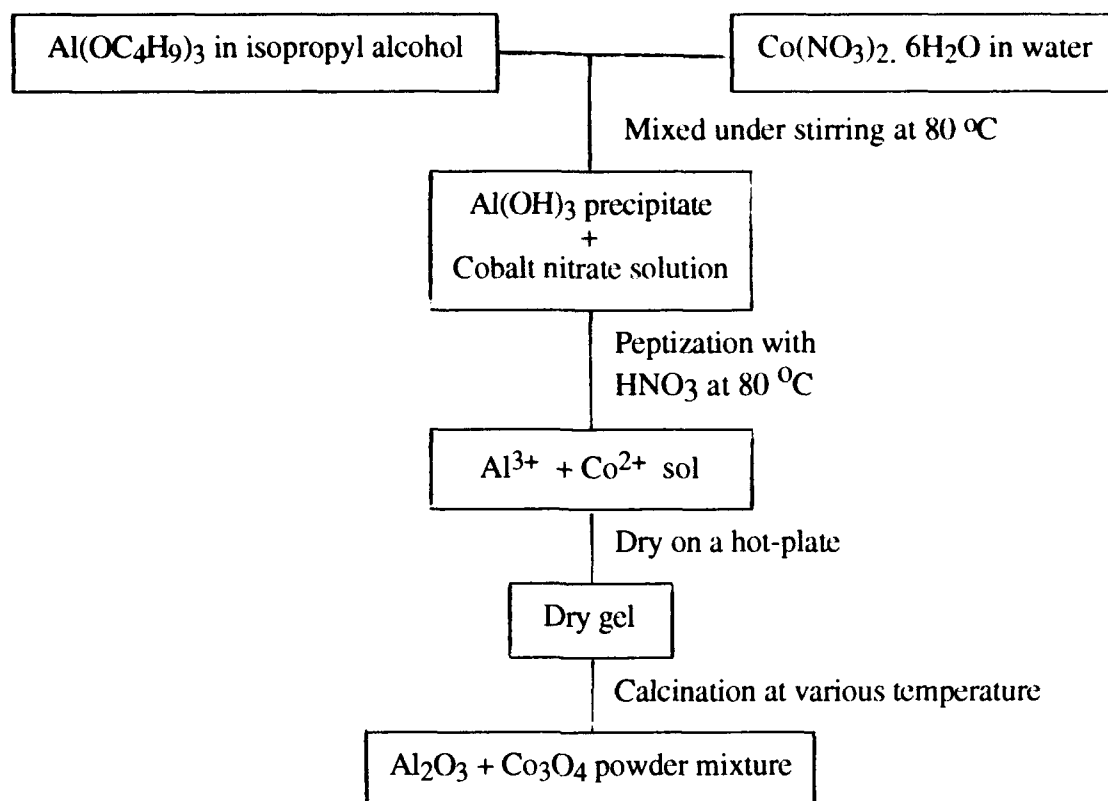


Fig.1 Synthesis scheme for $\text{Al}_2\text{O}_3\text{-Co}_3\text{O}_4$ nanocomposite powder

RESULTS AND DISCUSSION

Powder synthesis and characterization:

The phase identification by x-ray of a nominal composition containing an atom ratio of $\text{Al}:\text{Co} = 2:1$ is summarized in Table 1. It can be seen that Co_3O_4 is formed during the initial stages of drying on the hot plate. Although the exact temperature of hot-plate was not measured, it was presumed that Co_3O_4 formation can occur at temperatures as low as 200°C because firing of pure $\text{Co(NO}_3)_2 \cdot 6\text{H}_2\text{O}$ at 200°C for 20 h gives Co_3O_4 . Up to about 450°C , mostly the reflections of Co_3O_4 are discernible in the x-ray pattern. Aluminum oxide or AlOOH present are very small in particle size and could not be detected by x-ray diffraction. In the region $580\text{-}900^\circ\text{C}$, aluminum oxide was found to exist as $\gamma\text{-Al}_2\text{O}_3$ having a cation-deficient spinel structure. The presence of $\gamma\text{-Al}_2\text{O}_3$ is, for example, seen in the x-ray pattern (Fig. 2) of a powder mixture fired first at 580°C in air and then at 700°C in hydrogen atmosphere. A small reflection corresponding to $\gamma\text{-Al}_2\text{O}_3$ is seen around $2\theta = 67^\circ$ among strong reflections of Co metal. Above 1000°C , any aluminum oxide present is in the form of $\alpha\text{-Al}_2\text{O}_3$ having the corundum structure.

Table 1 Phase identification by x-ray diffraction of the Al_2O_3 - Co_3O_4 nanocomposites after heating at various temperatures for a constant time of 20 h

Temperature (°C)	Phase identification	Color
Dried on a hot-plate	Co_3O_4	Black
300	Co_3O_4	Black
450	Co_3O_4	Black
580	$\text{Co}_3\text{O}_4 + \gamma\text{-Al}_2\text{O}_3$	Black
650	$\text{Co}_3\text{O}_4 + \gamma\text{-Al}_2\text{O}_3$	Black
700	$\text{Co}_3\text{O}_4 + \gamma\text{-Al}_2\text{O}_3$	Black
800	$\text{Co}_3\text{O}_4 + \gamma\text{-Al}_2\text{O}_3 + \text{CoAl}_2\text{O}_4$	Dark blue
900	$\text{Co}_3\text{O}_4 + \gamma\text{-Al}_2\text{O}_3 + \text{CoAl}_2\text{O}_4$	Dark blue
1000	$\text{CoAl}_2\text{O}_4 + \alpha\text{-Al}_2\text{O}_3$	Dark blue
1250	CoAl_2O_4	Blue

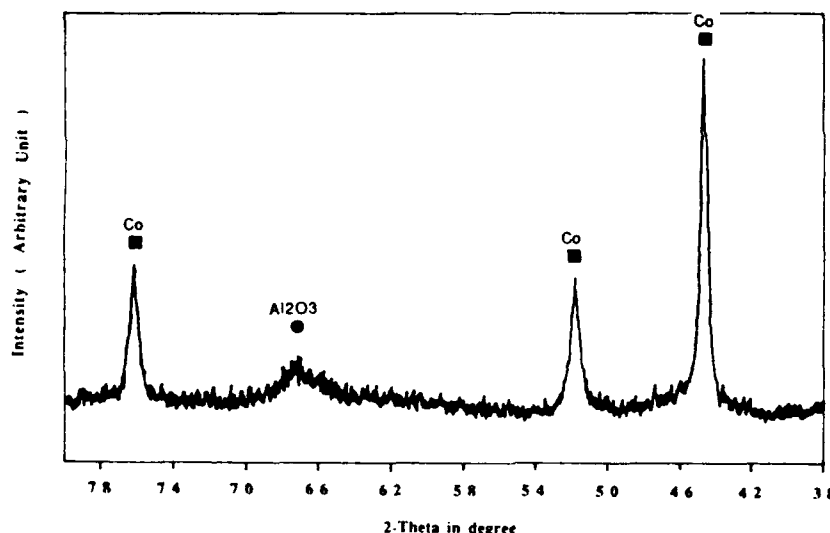


Fig. 2 X-ray diffraction pattern of 75 mole % Al_2O_3 - 25 mole % Co_3O_4 (Al : Co ratio = 2:1) nanocomposite after firing first at 580 °C in air and then at 700 °C in H_2 for 20 h

The oxides of cobalt and aluminum can react to give the spinel oxide CoAl_2O_4 , which is blue in color. The change in color from black to blue around 800 °C (Table 1) seems to suggest that the formation of CoAl_2O_4 occurs around this temperature. However, the formation of CoAl_2O_4 spinel can start much below 800 °C and we cannot rule out its presence below 800 °C from x-ray data since both Co_3O_4 and CoAl_2O_4 have spinel structure with close lattice parameters. The broad nature of the reflections at lower temperatures and their overlap make it extremely difficult to determine the exact temperature

at which CoAl_2O_4 formation begins. Nevertheless, we could clearly see the formation of the spinel NiAl_2O_4 in the analogous system Al_2O_3 - NiO at temperatures as low as 320 °C (Fig. 3). Formation of spinel phases around 300 °C has also been shown in several other systems such as NiMn_2O_4 [5]. Furthermore, formation of CoAl_2O_4 has been suggested to occur around 500 °C from an observation of a decline in the catalytic activity of Co_3O_4 supported on $\gamma\text{-Al}_2\text{O}_3$ [6]. The catalytic activity in this system is due to Co_3O_4 and the degradation of catalytic activity corresponds to a conversion of Co_3O_4 to CoAl_2O_4 . So, it is likely that the formation of the CoAl_2O_4 spinel occurs at temperatures below 500 °C.

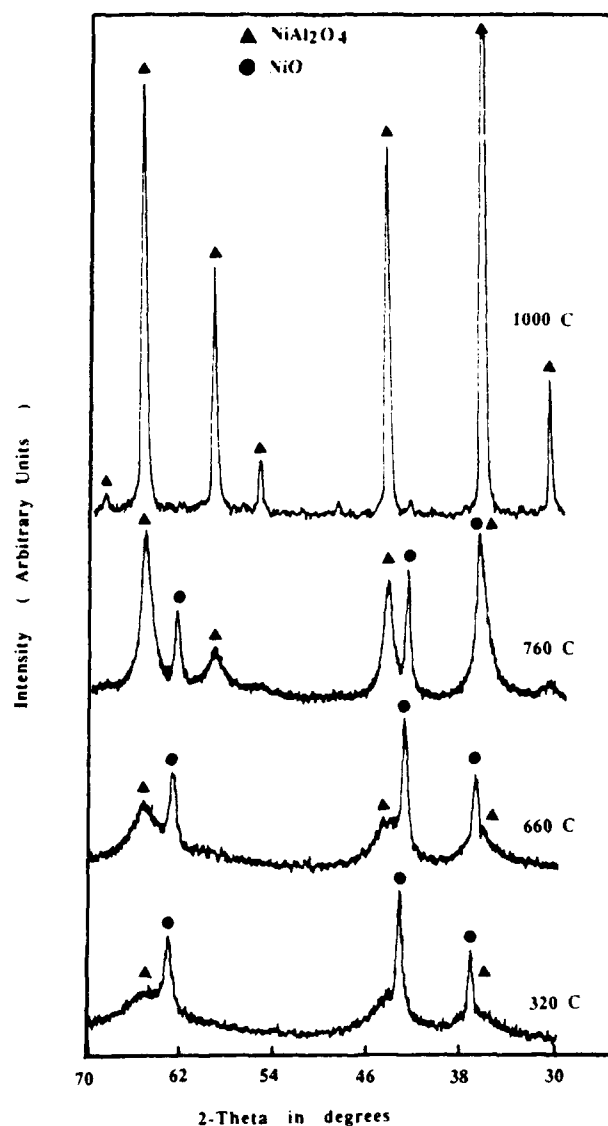


Fig. 3 X-ray diffraction pattern of 50 mole % Al_2O_3 - 50 mole % NiO (Al : Ni ratio = 2:1) nanocomposite after firing at various temperatures for about 20 h



Fig. 4 TEM micrograph of 75 mole % Al_2O_3 - 25 mol % Co_3O_4 (Co : Al ratio = 1:2) nanocomposite after firing at 580 °C in air for 20 h

The TEM micrograph of the Al_2O_3 - Co_3O_4 nanocomposite powder after heating at 580 °C in air for 20 h is shown in Fig. 4. The large particles are about 50 nm in size and were presumed to be Co_3O_4 since they were shown to be rich in Co by EDS analysis. The small particles are less than 10 nm and were shown to be rich in Al by EDS analysis. These observations are consistent with the x-ray results. The TEM image of the nanocomposite powder after heating at 700 °C for 20 h is shown in Fig. 5. The particles have grown significantly to about 150 nm during this process. However, the rise in firing temperature did not have any significant influence on the size and distribution of the agglomerates. An SEM micrograph of the powder heated at 700 °C is shown in Fig. 6, which indicates an agglomerate size of about 100 μm .

Selective laser sintering:

Preliminary SLS experiments with the Al_2O_3 - Co_3O_4 nanocomposites indicated blowing up of the powder under the laser beam. A low powder density of about 20 % together with the adsorbed moisture seem to cause this problem. The powder was then ball-milled for about 30 min and subjected to SLS under an *in situ* baking around 200 °C. This modification allowed use of high enough laser power without the powder being blown. During this process, the color of the powder changed from black to blue indicating the reaction of Al_2O_3 and Co_3O_4 under the laser beam to form the spinel oxide CoAl_2O_4 . A top view after SLS of a 83.2 mole % Al_2O_3 - 16.8 mol % Co_3O_4 nanocomposite is shown in Fig. 7. The corresponding SEM micrograph of the cross section is shown in Fig. 8. Although the powder sinters locally during the SLS process to give relatively higher density, large cracks were found to occur. The low density of the initial powder with large porosity was suspected to cause this problem. Similar results were also obtained with Al_2O_3 -NiO.



Fig. 5 TEM micrograph of 75 mole % Al_2O_3 - 25 mole % Co_3O_4 (Co : Al ratio = 1:2) nanocomposite after firing at 700 °C in air for 20 h

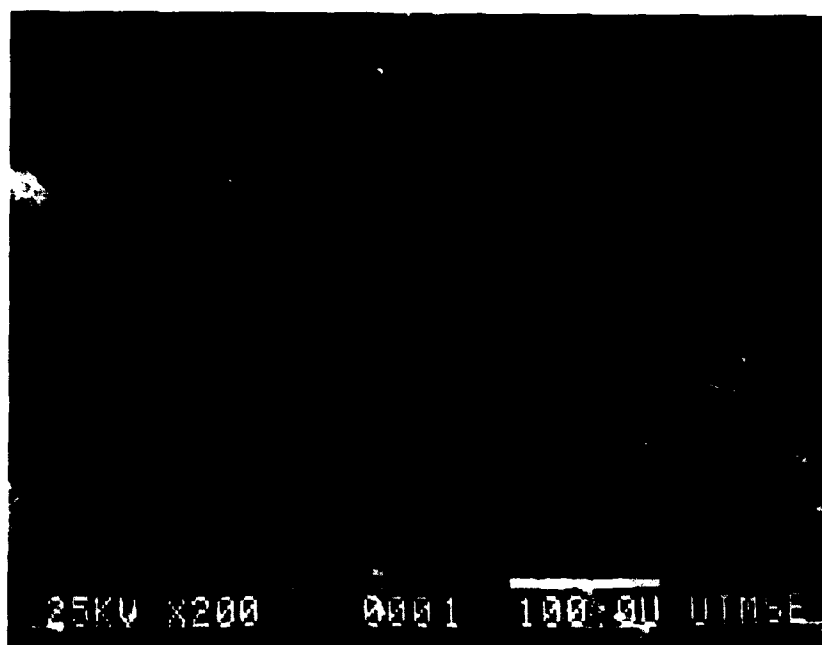


Fig. 6 SEM micrograph of 75 mole % Al_2O_3 - 25 mole % Co_3O_4 (Co : Al ratio = 1:2) nanocomposite after firing at 700 °C in air for 20 h



Fig. 7 Photograph of the top view of 83.2 mole % Al_2O_3 - 16.8 mole % Co_3O_4 nanocomposite after firing at 580 °C in air for 20 h and subjecting to SLS.

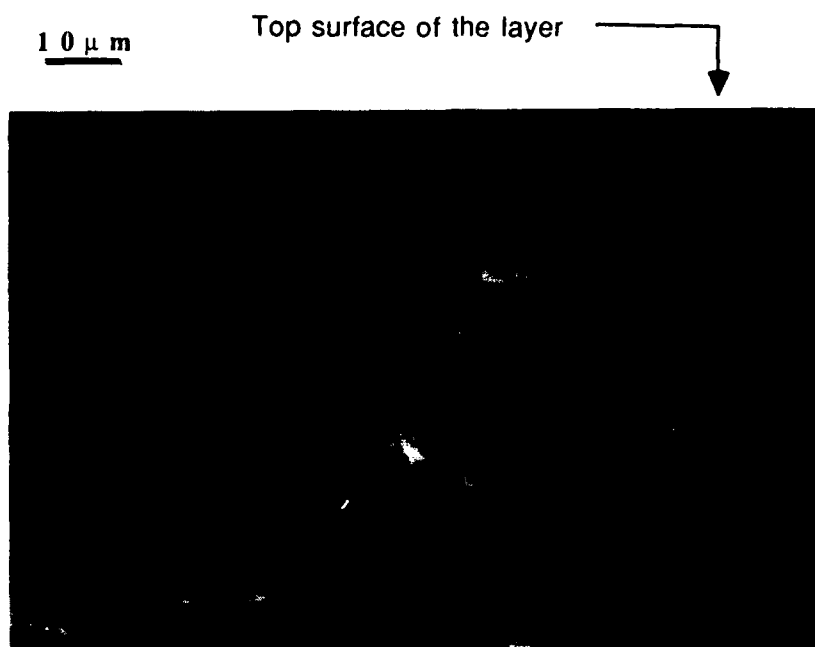


Fig. 8 SEM micrograph of 83.2 mole % Al_2O_3 - 16.8 mole % Co_3O_4 nanocomposite after firing at 580 °C in air for 20 h and subjecting to SLS.

In order to circumvent the above difficulties, strategies to increase the density of the initial powders without sacrificing much of the nanoscale mixing were pursued. One way to achieve higher densities in the powder is to anneal the nanocomposites at relatively higher temperatures (~ 1000 °C). However, such an annealing around 1000 °C of the $\text{Al}_2\text{O}_3\text{-Co}_3\text{O}_4$ nanocomposite will result in the formation of the spinel oxide CoAl_2O_4 , which will in essence consume the low melting component Co_3O_4 and jeopardize our approach to SLS. Therefore, to demonstrate the feasibility of our objective, we decided to pursue the ceramic-metal nanocomposite $\text{Al}_2\text{O}_3\text{-Co}$, which will not undergo any chemical reaction during the preannealing of the powder at higher temperatures. Accordingly, $\text{Al}_2\text{O}_3\text{-Co}$ nanocomposites were first obtained by reducing the $\text{Al}_2\text{O}_3\text{-Co}_3\text{O}_4$ oxide nanocomposite in hydrogen around 1000 °C. The powder was then annealed in N_2 atm at 1350 °C for 8 h to increase the density, and reduced again in hydrogen around 1000 °C to convert back any cobalt oxide that might have formed by reaction with the residual oxygen during N_2 annealing. The resulting $\text{Al}_2\text{O}_3\text{-Co}$ powder was found to have a density of about 42 % and sinter under the laser beam. The single layer test coupons appear to have better structural integrity with much reduced macrocrack formation. An SEM photograph of the powder after SLS is shown in Fig. 9.

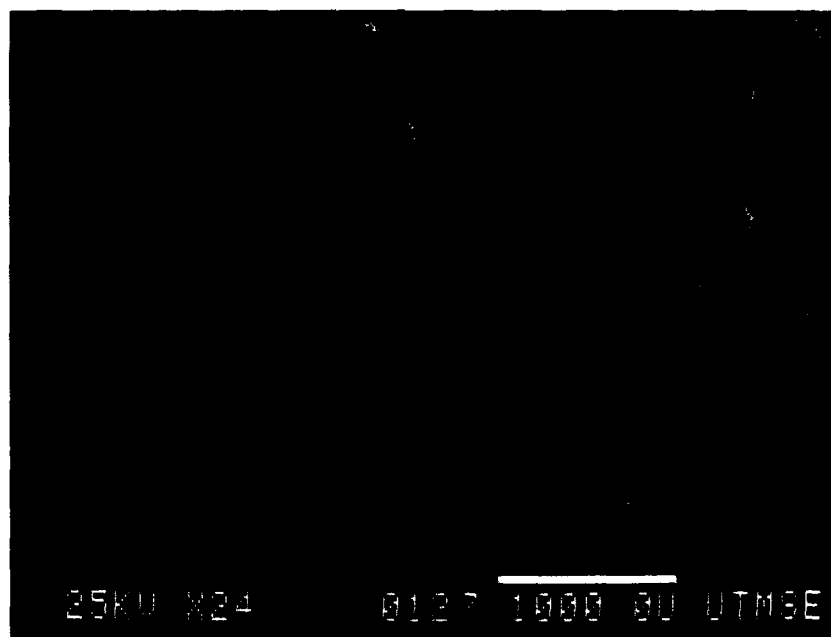


Fig. 9 SEM micrograph of 50 mole % Al_2O_3 - 50 mole % Co nanocomposite after firing at 1350 °C in N_2 for 8 h, 1000 °C in H_2 for 8 h and subjecting to SLS

CONCLUSIONS

Nanocomposite powders of $\text{Al}_2\text{O}_3\text{-CoO}_x$, $\text{Al}_2\text{O}_3\text{-NiO}$, $\text{Al}_2\text{O}_3\text{-Co}$ and $\text{Al}_2\text{O}_3\text{-Ni}$ have been successfully synthesized by sol-gel processing. The powders have been investigated by SLS. Low densities (about 20 %) of the initial powders not only lead to a formation of macrocracks during SLS, but also prevent use of high enough laser power that can cause sintering. Increasing the initial powder densities to about 40 % seems to avoid this difficulty significantly and give structurally sound specimens. Further increase in the densities of the initial powders promises to enhance the success of our strategy, and such experiments are currently being pursued.

ACKNOWLEDGEMENT

Financial support by the DARPA-ONR grant No. N00014-92-J-1394 and ONR grant No. N00014-92-J-1514 is gratefully acknowledged.

REFERENCES

1. R. P. Andres et al, J. Mater. Res. **4**, 704 (1989).
2. S. Komarneni, J. Mater. Chem. **2**, 1219 (1992).
3. A. M. Kazakos, S. Komarneni and R. Roy, J. Mater. Res. **5**, 1095 (1990).
4. E. Breval, Z. Deng, S. Chiou and C. G. Pantano, J. Mater. Sci. **27**, 1464 (1992).
5. X. X. Tang, A. Manthiram and J. B. Goodenough, J. Less-Common Metals **156**, 357 (1989).
6. E. Garbowski *et al*, Appl. Catalysis, **64**, 209 (1990).

PART FABRICATION USING LASER MACHINING AND WELDING

M S Pridham and G Thomson

**Department of Applied Physics and Electronic and Manufacturing Engineering
University of Dundee
Dundee
DD1 4HN
UK**

Abstract

This paper describes the current work on a laser cutting and welding system for the fabrication of prototype parts in mild and stainless steels. The relationship to other rapid prototyping systems and to laminated tool production techniques is discussed, the progress to date is described. Difficulties with current welding procedures are outlined and alternative joining techniques are considered.

Introduction

Despite the tremendous progress made in the whole field of rapid prototyping and the development of processes, the majority of systems remain concentrated on non metals. However work is now being carried out on laser sintering of mild steel and stainless steel powders as well as on 3-D welding processes (1,2). Success in these developments will expand on the current prototype possibilities by enabling the direct production of prototypes in metal, when this is required. This will offer benefits in certain situations, cutting out the need for secondary processing of plastic or wax prototypes, such as in producing investment casting moulds.

Laminate Processes

Work at Dundee has centered on using a laser machining centre to cut and fabricate components in mild and stainless steels, using layer cutting procedures and joining techniques. Work in a similar area is also being undertaken by a European consortium under the BRITE initiative.

There has been considerable work in the field of laminating laser or EDM cut sheet and plate to form tooling such as injection mould cavities (3), drawing dies (4) and blanking tools (5,6). These tools have then been exploited in a number of ways for various applications. The motives for the undertaking of this type of work have been varied, and not all in prototyping, but in all cases reductions in production or development times and costs have been realised.

A recent paper by Glover and Brevick (3) argues that whilst current commercial rapid prototyping systems such as Stereolithography, Selective Laser Sintering Laminated Object Manufacture and Fused Deposition Modelling, have their place in the early stages of design, they rarely provide a full range of pre-production information. For example the prototype material is rarely the same as the required part, production processes, and therefore mechanical and physical properties of the prototype, differ from those intended for production, and prototype tolerances and surface finishes are not usually representative of those obtainable by the eventual production processes.

Many of these points are substantive and undoubtedly there are applications and potential for the further exploitation of laminated tool manufacture in a variety of areas.

The drawback, if it can be called that, is that much as the "conventional" rapid prototyping techniques require secondary processes to produce a metal part, the laminated tool production processes by their very nature do not result in a part until the tool is then used in a production situation. Thus most of the applications of lamination have meant using at least one additional process in the creation of the part.

However the process is very useful when the tool is required for a proven process and product design, perhaps replacing an old or worn tool, but clearly it is not so advantageous at providing a first stage prototype part. A process which could produce parts or tooling as required, directly in metal, would generate considerable interest.

Part Fabrication by Lamination

As previously stated work at Dundee is aiming towards metal prototype part production, in a direct process, in a similar way to the 3-D welding work, but here using lamination and fabrication techniques.

The objective is to produce parts in a layer by layer manner where each layer is cut in turn from plate or sheet by laser machining, and the layers are then joined by laser welding. In respect of the joining technique, the process differs significantly from most laminated tool processes. Laminated tool techniques almost all use mechanical locations and fixtures to hold the assembly together. Clearly when dealing with tooling this is a sensible and straight forward approach. Most tool systems allow for this type of fastening by having a significant "flange" area around the tool or cavity, as indicated in Figure 1, to allow bolts or fastening screws to be used. The fastenings being located such that they do not interfere with the operation of the tool.

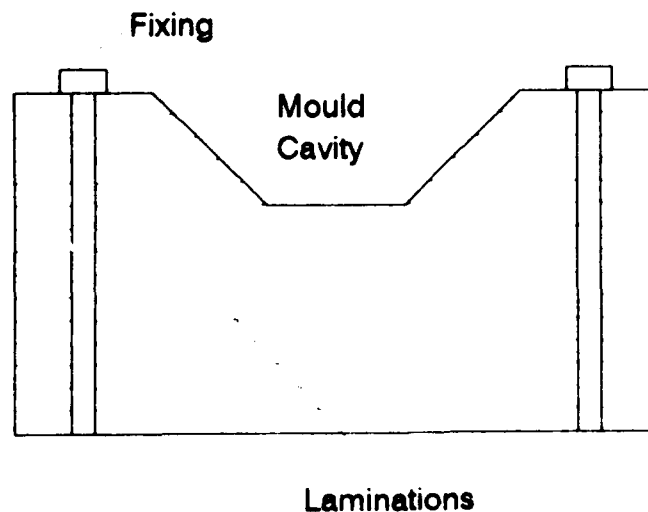


Figure 1. Typical arrangement for holding/fixing laminated tooling.

This approach could also be acceptable in prototyping of large solid parts but it is not suitable for fabricating parts with complex geometries, thin walls or webs or hollow sections.

Laser Cutting

The laser used in the work to date is a "Ferranti MFK 1000" 1000W CO₂ gas laser. Cutting profiles are currently being programmed using an Anorad X-Y control system. The laser machining centre is shown in Figure 2.



Figure 2. Ferranti MFK 1000 CO₂ laser

To date the materials used have been 18% Cr 8% Ni ASI 304 stainless and medium carbon mild steel, in thicknesses of up to 2mm. A full investigation of the limiting values of cutting speeds possible for a variety of sheet thicknesses and material types is yet to be carried out, but cutting speeds are entirely satisfactory without pushing the system to anywhere near its limits. Typically a cutting speed of 1 metre per minute is used with a pulsed beam of 20×10^{-5} s. on and 20×10^{-5} s. off, with oxygen assist gas at a back pressure of 2 bar. Figure 3 shows representative examples of laser cut geometries, in this case in 1mm thick stainless steel.

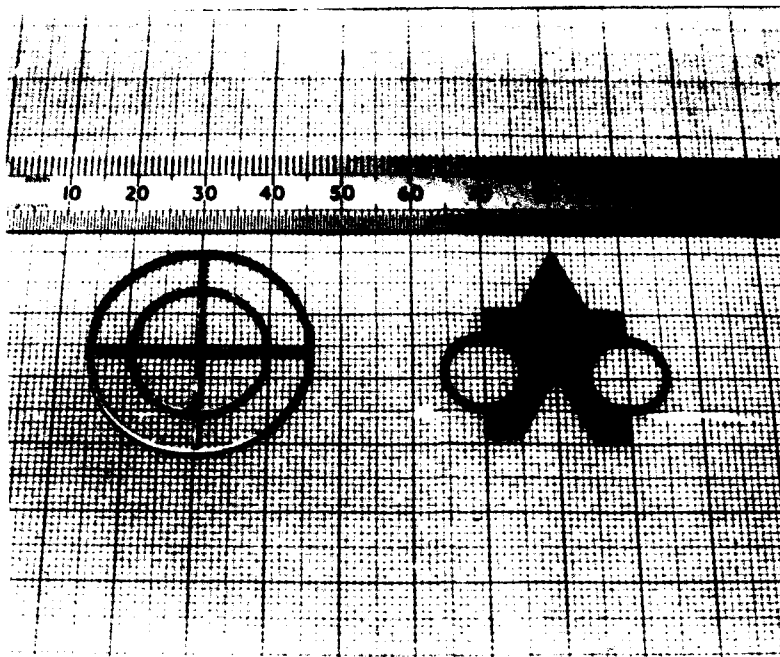


Figure 3. Laser cut parts in stainless steel

Laser Welding

The laser welding aspect of this technique is now the main focus of attention since weld performance and quality are not yet at a level to make the laser cutting and welding route viable as a process. Conventional keyhole laser welding procedures have proved difficult due to the focused beam tending to cut rather than weld. Also the narrow beam means that multiple weld tracks are required to join the layers uniformly. Complete section welding is also desirable to take advantage of obtaining homogeneous or near homogeneous material properties throughout the artifact. Excessive oxidation also resulted in some trials largely due to using compressed air as the assist gas, this should be considerably reduced by using helium gas.

Welding trials were also conducted using a much broader defocused beam, in an attempt to produce a uniform broad conduction weld across the wall section of the parts. This technique shows promise in trials, using a straight weld on large sheet, with the beam focused 50mm off the job, a feed rate of 150mm/minute and 20/20 pulsing it was highly successful. However it was less successful, when using smaller finer laminae, due to problems associated with work holding, heat dissipation and distortion.

Experimentation with welding parameters and development of a system are ongoing and in addition alternative joining methods such as soldering, brazing and structural adhesives are being explored. Figures 4, 5 and 6 illustrate some test pieces which have been laser cut and adhesively bonded together.

Figure 4 shows an approximation of a 60mm diameter sphere fabricated using circular layers of 2mm thick mild steel sheet. This specimen is made up of some thirty layers. The "stepping" observed in the polar regions indicates that for a sphere of this diameter the 2mm thick material is substantially too thick to give a smooth curvature in these zones.

A further stage of development of this system would be to have various thicknesses of sheet available to optimise the build. For example vertical sections

could be cut from relatively thick material thus minimising the number of layers and therefore the number of welding/joining operations necessary, whilst complex geometries and tight radii could be better and more accurately built using thinner layers.

Figure 5 shows a square based hollow pyramid section built from thirty four layers of 1mm thick stainless steel. The sides of each layer are 1mm shorter than the previous layers. The total cutting time for this part was approximately 10 minutes.



Figure 4. Sphere, produced in 2mm mild steel.

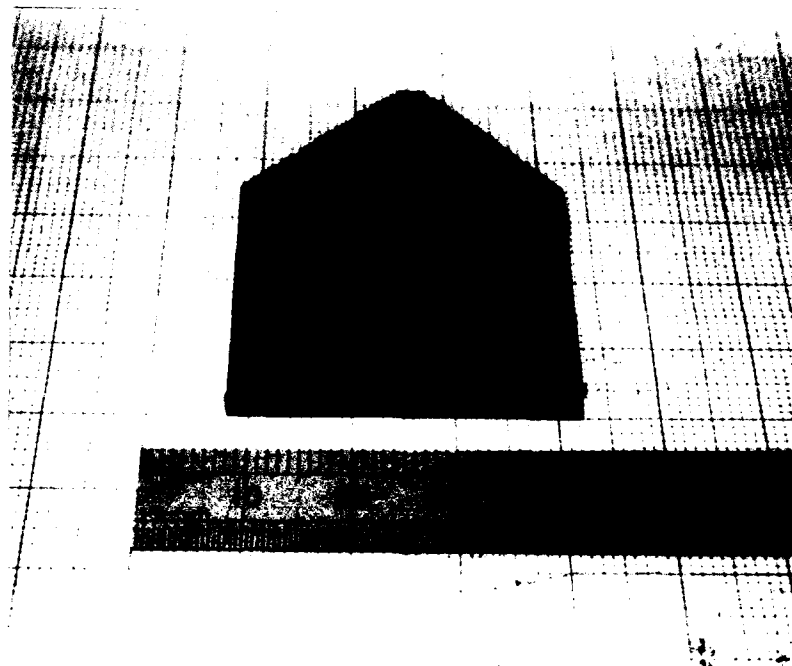


Figure 5. Square based hollow pyramid in 1mm thick stainless steel.

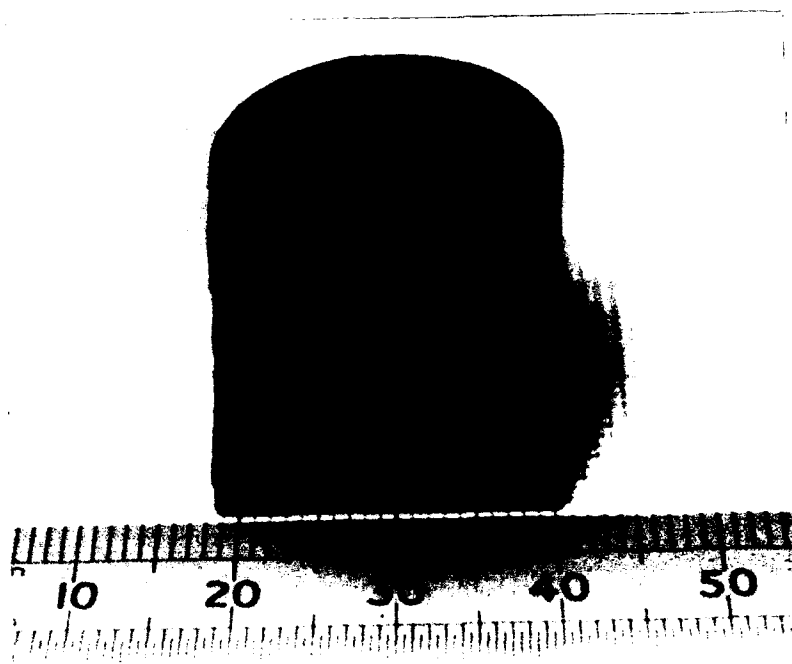


Figure 6. Square to circle transformation in 1mm thick stainless steel.

The section illustrated in Figure 6 is produced in 1mm thick stainless steel and has a wall thickness of 1mm. Over a height of 22mm the section transforms from a 22mm side square to a 22mm diameter circle. This section could, for example have been produced using thick (e.g 5mm) plate for the square base, thin sheet for the transformation region and then reverting to thick section to build on the circular geometry.

Future Developments

Clearly a number of areas in this work require considerable further investigation. They include:

1. Development and understanding of required welding conditions, if this technique is to be pursued as the joining method.
2. Evaluation of alternative joining methods. Suitability in terms of strength, ease of production and versatility will dictate possibilities.
3. Automation of layer feed, selection and alignment; currently each layer is cut individually and when all the layers are prepared they are joined. In a viable system the joining operation would be integrated and synchronized with the cutting operations so that each layer is joined immediately after it is produced.

Conclusion

Laser cutting and welding offers potential as a means of directly fabricating a prototype part in metal. Further development, particularly in the area of laser welding is underway. A fully developed system will help service a requirement for prototypes which may need to display high levels of mechanical properties, high

thermal or electrical conductivity or have the weight and feel of the planned metallic production material.

References

1. *3-D Welding*: P M Dickens, M S Pridham, R C Cobb, I Gibson and G Dixon. Proceedings of the First European conference on Rapid Prototyping pp 81-93, ISBN 0951975900, Nottingham University, UK. 6-7 July 1992.
2. *Rapid Prototyping Using 3-D Welding*: P M Dickens, M S Pridham, R C Cobb, I Gibson and G Dixon. Proceedings of the Solid Freeform Fabrication Symposium 1992, pp 280-290, ISSN 1053-2153 University of Texas, Austin, USA. 3-5 August 1992.
3. *Laminate Tooling for Injection Moulding*: G R Glover and J R Brevick. Proceedings of the Institution of Mechanical Engineers, Vol 207, Part B Journal of Engineering Manufacture, pp 9-14, 1993.
4. *Development of Laminated Drawing Dies by Laser Cutting*: M Kunieda and T Nakagawa Bull, Japan, Soc. of Prec. Engg, Vol 18, No 4, December 1984, pp 353-354.
5. *Laser Cut Blanking Tool*: T Nakagawa, K Suzuki and K Sakaue, Bull, Japan, Soc Prec Engg, Vol 17, No 1, Mar 1983, pp 45-46.
6. *Blanking Tools Manufactured by Laminating Laser Cut Steel Sheet*: K Gotzsche-Larsen. Second European Conference on Rapid Prototyping, University of Nottingham, July 1993.

Picoliter Solder Droplet Dispensing

Ronald E. Marusak, Ph.D.
MicroFab Technologies, Inc.
1104 Summit, Suite 110
Plano, Texas 75074
(214) 578-8076

A device based on ink-jet printing technology was used to produce and place molten solder droplets, approximately 25-125 μ m in diameter, onto substrates. The advantages of an ink-jet based system are direct production of metallic objects, no post-cure, low cost, and the repeatability and resolution for small feature sizes. This paper describes the device, the supporting hardware, and experimental procedures. Results show that bump size can be varied by placing in quick succession, multiple droplets as well as by resizing the device and by altering the signal.

Introduction

The technology that was developed for forming droplets of ink in printing has been applied, over the past several years, in the dispensing of materials during the manufacture of microelectronics (see References). This work has resulted in the development of print heads that can, at elevated temperatures, deliver precise amounts of molten solder with exacting positional control.

This paper presents the results of forming bumps of solder using ink-jet printing technology. Initial applications for solder droplet dispensing include the bumping of chips for flip-chip bonding and tape-automated bonding (TAB), the bumping of substrates for TAB or fine pitch surface mounting, and the repair of solder joints. Potential applications include the formation of metal layers, reinforcement of metal joints, and the freeform fabrication of metal parts.

Description of the Droplet Generator

The device that was used to dispense the liquid solder is based on early ink-jet print heads. A schematic of this droplet generator is shown in Figure 1. The end of the 0.75 mm diameter tube is formed into an orifice of approximately 50 μ m. The other end is attached to a fluid supply. Fluid at essentially ambient pressure fills the glass tube, and surface tension prevents the fluid from leaking out of the orifice. A tube-shaped piezoelectric crystal is adhesively bonded to the outer diameter of the glass. The assembly is mounted in a protective shell.

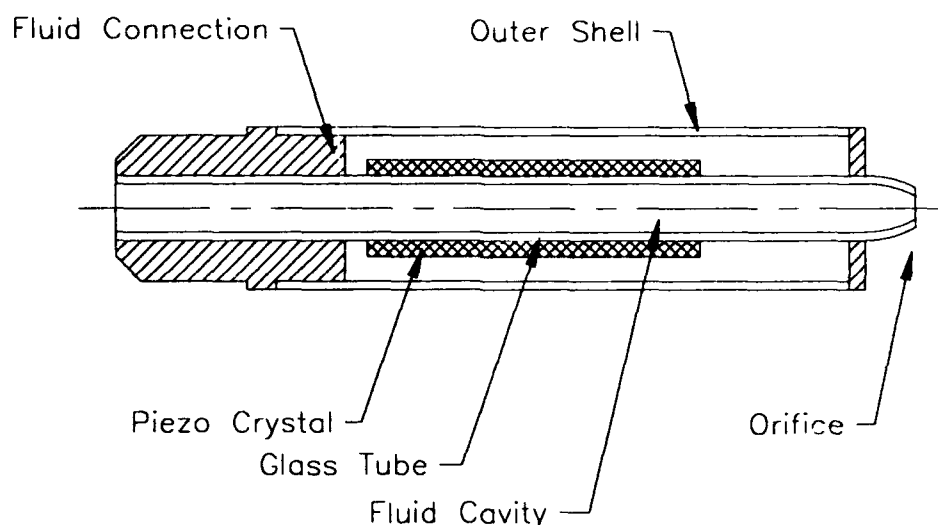


Figure 1 - Schematic of droplet generator.

When a voltage is applied to the piezoelectric crystal, the crystal squeezes the glass tube and entrained fluid. A voltage pulse causes, in the fluid, transient pressure waves which travel toward the orifice. The pressure wave ejects a small drop of fluid from the orifice. The size and velocity of the ejected droplet is determined by the shape and construction of the device, the fluid properties, and the shape and duration of the applied voltage pulse. Typical droplet volumes are ~ 100 picoliters and typical ejection velocities are from 1 to 5 m/s.

This design is called "drop-on-demand" because drops are formed only when a voltage pulse is applied. Other ink-jet designs use a pressurized stream to form droplets continuously. These "continuous" mode devices require hardware to deflect unwanted droplets away from the target and into a gutter for recirculation or disposal. Although the continuous type can form droplets at higher rates than the drop-on-demand type, the deflection and recirculation hardware complicates matters.

Prototype Liquid Metal Printer

The printing system used in this study is shown in Figure 2. The system was designed to provide oxide and contaminant-free molten solder at a controlled temperature to the droplet generator. The solder was melted in the upper-reservoir, where the dross/impurities could rise to the surface while the molten solder was gravity fed to the main reservoir. Teflon coating of the reservoir and the nitrogen environment prevented oxidation/degradation. The ink-jet device was also housed in a controlled heater. Patterns were formed by dispensing droplets raster style onto a copper substrate, which was mounted on an x-y stage.

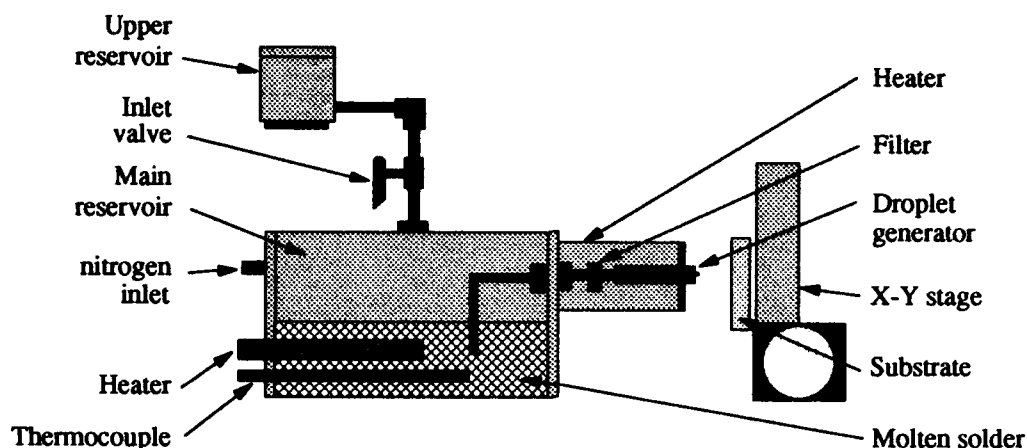


Figure 2 - Schematic of liquid metal printer.

The solder selected for this study was Indalloy-58, a low melting temperature eutectic solder. A eutectic solder composition was selected because it directly transitions from liquid to solid without an intermediate solid/liquid phase. The melting point of Indalloy-158 is 70°C, and the composition is 50 Bi, 26.7 Pb, 13.3 Sn, 10 Cd.

Test Patterns

Using a single drop per location, an array of 60 μm diameter bumps on 200 μm centers was produced and is shown in Figure 3. Multiple droplets (2-10) per location were dispensed at a rate of 500 droplets/second to produce larger bumps, up to 160 μm in diameter, on 200 μm centers (Figure 4).

At the dispensing rate used in these tests, the solder droplets dispensed onto a single site merge into one another before they solidify, forming a single, large bump. If sufficient time for cooling is allowed between consecutive droplets dispensed onto the same location, the individuality of the droplets can be maintained, and a three-dimensional structure created.

Moreover, since solidification is due to phase change, no further cure is needed.

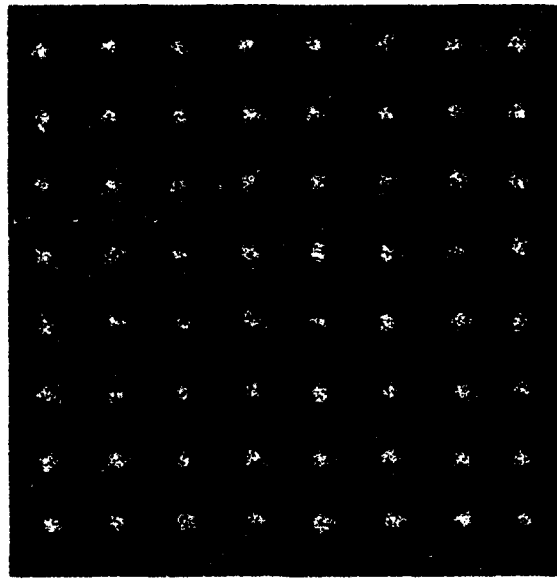


Figure 3 - 60 μm diameter bumps of Indalloy-158 deposited on 200 μm centers on copper using drop-on-demand dispensing.

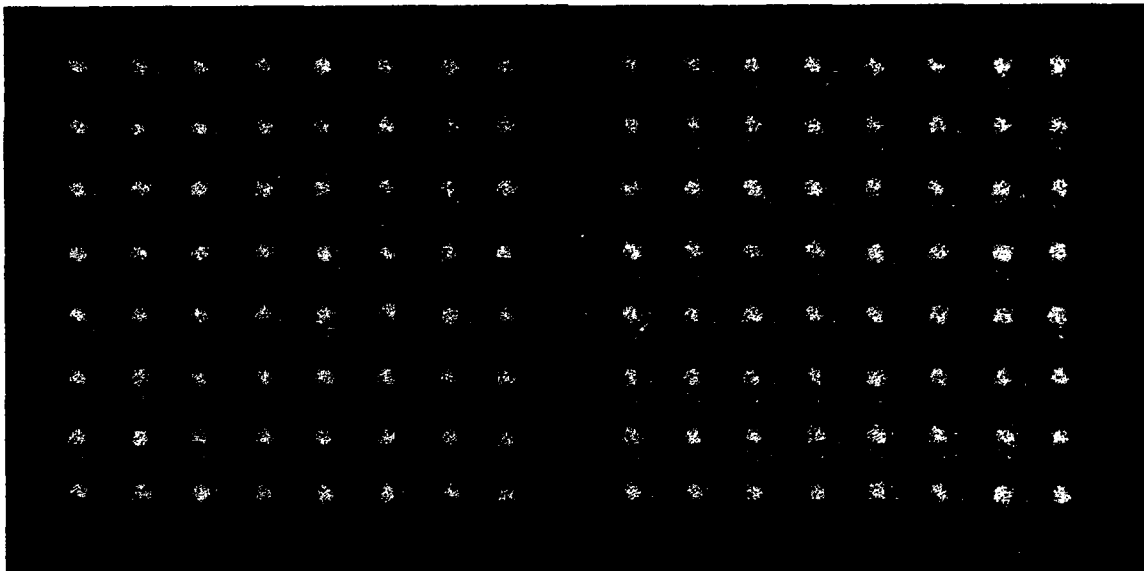


Figure 4 - 90 and 120 μm diameter bumps of Indalloy-158 deposited on 200 μm centers on copper using drop-on-demand dispensing.

The photo of Figure 5 is evidence of the flexibility, control and resolution of the solder bumps.

Conclusion

The ability to dispense molten solder droplets, as small as 60 μm in diameter, in a controlled manner, to create reproducible solder bumps has been demonstrated.

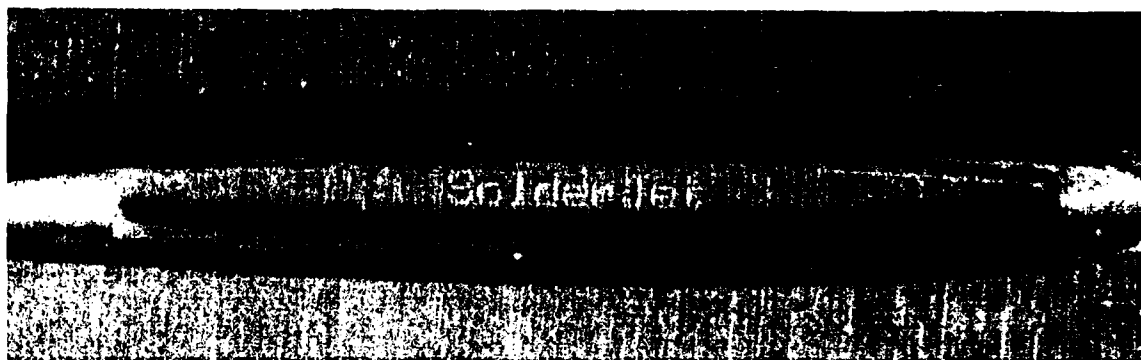


Figure 5 - 60 μ m diameter bumps of Indalloy-158.

References

"Application of Ink-Jet Technology to Dispensing in the Electronics and Semiconductor Industries", D.B. Wallace and D.J. Hayes, *Proceedings, ISHM 1987 Microelectronics Interconnect Conference*, August 1987.

"Application of Ink-Jet Technology to Adhesive Dispensing", D.B. Wallace and D.J. Hayes, *Proceedings, SME Adhesives '87 Conference*, September 1987.

"Automated Electronic Circuit Manufacturing Using Ink Jet Technology," Final Report, National Science Foundation Phase I Small Business Innovation Research Grant ISI-8760091, June 1988.

"Automated Electronic Circuit Manufacturing Using Ink Jet Technology," *Journal of Electronic Packaging*, Vol.36, No.5, 1989.

"Application of Ink-Jet Technology to Microelectronic Packaging," D.J. Hayes and D.B. Wallace, *Proceedings, ISHM '89*, October 1989.

"Overview of Small Holes," D.J. Hayes and D.B. Wallace, invited paper, *Proceedings, SME Nontraditional Machining Conference*, November 1989.

"Picoliter Solder Droplet Dispensing for Electronics Manufacturing," Final Report, National Science Foundation Phase I Small Business Innovation Research Grant ISI-9060945, September, 1991.

"Picoliter Solder Droplet Dispensing," D.J. Hayes, D.B. Wallace, and M.T. Boldman, *Proceedings, ISHM '92*, October 1992, (Best Session Paper award)

"Picoliter Solder Droplet Dispensing," D.J. Hayes, D.B. Wallace, M.T. Boldman, and R.M. Marusak, *Microcircuits and Electronic Packaging*, Vol.16, No.3, 1993.

CONTROL PARAMETERS AND MATERIAL SELECTION CRITERIA FOR RAPID PROTOTYPING SYSTEMS

James W. Comb/William R. Friedeman
Stratasys, Inc.

Abstract

Since the introduction of rapid prototyping technology as a tool for time compression and concurrent engineering in the design and manufacturing process, many enhancements and refinements have been made based on the experience of users and manufacturers of rapid prototyping equipment. These improvements contribute significantly to faster production of quality output from rapid prototyping systems.

There are diverse control and material selection parameters that affect prototype models built using the Fused Deposition Modeling (FDM®) process. This paper reviews the role of several of these parameters in the process. Data will be presented to help the user choose the appropriate material for specific applications including density, tensile stiffness, flexural stiffness, tensile strength, flexural strength, tensile ductility, shock resistance, and hardness.

Introduction

With the commercial Stratasys system now in customer locations for more than two years, we have built a substantial base of real life experience with the equipment. The FDM® process has been an asset to the installed customer base and an acknowledged improvement over previous model building techniques. This experience has prompted design enhancements to better meet the needs of our customers. As is true for all rapid prototyping manufacturers, we are continually seeking improvements which will deliver more accurate models, of superior surface finish, in increasingly attractive materials, for a better price.

Early in 1993, Stratasys released a major enhancement package for the FDM® process which was a direct response to this quest for higher quality models.

The intricacies of the control parameters and the interdependency of the variables which collectively work to produce models were sorted out in a methodical approach in order to deliver improvements to the existing machine. The FDM® process allows user control of the envelope temperature, the liquefier temperature, the modeling speeds and the materials to name just a few variables. Each of these variables can alter the resulting model. The appropriate setting of these parameters by the operator is key to quality model production. Without proper limits being set, negative results will occur. Additionally, several other features of the system were modified to improve overall performance.

The Stratasys FDM® process extrudes material via a simple filament drive system. If the capacity of the filament drive system is exceeded, the filament can break, bulge, or buckle, causing a plug in the lower filament guide when using certain modeling materials. Other materials may not break, but slipping of the drive wheels may cause improper filament feed (Reference Figure 4a). To address these issues, modifications of the drive system were developed to increase the overall drive capacity and extensive testing was performed to determine the operating limits to ensure reliable operation.

Additional testing was performed to determine the temperature set points for the liquefier and modeling environment for each material. This information led to the re-design of the FDM® process liquefier and cabinet. A heater box package and improved seal system were added to the cabinet to improve the uniformity of the modeling air temperature. A longer and more powerful liquefier was added to increase the volumetric flow rate and improve the temperature consistency of the delivered material. Additionally, this liquefier was made to be easily exchanged when changing materials to eliminate cleaning and material "build-up" within the liquefier which contributed to plugging.

An improved hold-down method for the modeling foundation was developed to allow the build of larger, thicker models without foundation warping.

A firmware solution was implemented to eliminate the "oozing" that occurred at the FDM® tip after shut-off of the material flow. Oozing is the overflow of material that produces small irregularities and loss of detail in the resulting model.

Experimental Results

Figure 1 is a diagram showing the relative increase in traction to drive the filament that was achieved with the implementation of the 1/2" elastomeric wheels. The figure shows two curves: the lower curve is a plot of traction force versus filament diameter for the original 1" steel wheels; the upper curve shows the same for the 1/2" elastomeric wheels. As seen in the figure, the available traction force of the 1" steel wheels is significantly lower than the 1/2" elastomeric wheels. The 1" wheels are more sensitive to changes in filament diameter; i.e., normal variations in the filament diameter would produce large variations in the available traction leading to slipping at high material flow rates. The 1/2" wheels, due to their rubber-like behavior, are less sensitive to filament diameter changes and produce more traction in the feed mechanism. This gives the FDM® filament drive system a higher flow rate capacity.

In Figure 2, the pressure flow relationship for various tip sizes and temperatures are shown. The relationship shown is characteristic of each of the modeling materials offered by Stratasys. Curves representing liquefier pressure (P) versus volumetric flow rate (V) are depicted. The liquefier pressure is created by the drive traction force acting on the filament divided by the filament's cross-sectional area. For a given tip diameter (d_i) and liquefier temperature (T_i), the relationship between pressure and flow is roughly linear. As

tip diameter is decreased the pressure required to produce a specific flow rate increases dramatically. As temperature decreases, the pressure required increases due to the increased viscosity of the material. In the Stratasys filament drive system the liquefier pressure attained is limited by: a) the force at which the filament drive slips (F_s); b) the compressive strength of the filament (s_c); and c) the stress at which the filament buckles (s_b). The force levels for each of these limits differ in magnitude and relative order for various materials. Therefore, the system is bounded in pressure by the lowest of these values per material. The system is further bounded by the available liquefier heat exchanger capacity. If operated beyond this maximum flow rate (V_{max}), the material delivered will not attain the desired set point temperature.

To produce a model, tip diameter, process temperature, road width (w), z-slice thickness (z), and speed (s) are selected. The volumetric flow rate is the road width times the z-slice thickness times the speed of the head ($V=w*z*s$). In order to not exceed the operating bounds of the system, the speed must be selected so that pressure and flow rate remain within the operating limits. V_1 and V_2 represent the maximum allowable flow rates for the upper two curves in Figure 2.

The operating parameters discussed above are hard barriers to the modeling process. The system must be operated within these limits to ensure reliable plug-free, slip-free operation.

Figure 3 is a diagram representing the required set points for liquefier temperature and air temperature to achieve good models. In general, there are upper and lower liquefier and air temperature limits for each material. Exceeding these limits do not necessarily mean the model will fail but poor surface quality or low part strength may result. Typically, rippling of the model surface is caused by the air temperature being set too high and, to a lesser degree, by the liquefier temperature being set too high. Conversely, low modeling air temperatures result in poor bonding strength between the layers for some materials and actual delamination of the model in extreme cases. Low liquefier temperatures result in low limits for material flow rates due to the high viscosity of the material and also poor bonding. Therefore, experiments were conducted for each material to define the guidelines to achieve the optimum balance between part strength and surface finish.

System Enhancements

As a result of these experiments several design changes were made to the Stratasys FDM® process to improve its performance. These changes were delivered to all customers during the first quarter of 1993. This enhancement package consisted of the following design modifications:

1. Addition of Seals and Fan Heater Boxes and A New Cabinet Door Design to Improve Air Temperature Uniformity. The combination of these three items improves the

uniformity of the air temperature within the FDM® process during the modeling process. This improved air temperature uniformity eliminates cold spots within the environment that could cause poor bonding or delamination of the model. Additionally, the existing auxiliary heat circuit used to ramp the cabinet up to temperature now operates automatically.

2. **Longer, More Powerful Liquefier to Improve Material Delivery and Set Point Temperature Consistency.** The longer liquefier achieves two things: there is less variation in the temperature for both high and low flow rates and higher flow rates are attainable while maintaining the material set point temperature. This liquefier was also designed to be easily exchanged when changing materials. This attribute allows liquefiers to be dedicated to each material type, thereby eliminating the possibility of residual material coatings from previously used materials. The previous design required cleaning operations to be performed on a regular basis to ensure trouble-free operation. (Reference Figures 4a and 4b.)
3. **Smaller, Elastomeric Wheels and Larger Filament Diameter to Increase the Buckling Strength and Available Drive Traction.** The buckling strength of the filament is a function of its diameter (d) and its compressed length (l). (Reference Figures 4a and 4b.) An increase of the filament diameter and a reduction of the compressed length increases significantly the filament's resistance to buckling. The decrease in the compressed length was achieved by the use of smaller wheels and the elimination of the lower filament guide.

The previous 1" steel wheels were unable to conform to varying filament diameters. Smaller, 1/2" elastomeric wheels are better able to conform to the filament thereby reducing stress concentration and increasing drive traction due to their higher coefficient of friction.

4. **Improved Hold-Down Tray to Prevent Warping.** The Stratasys FDM® process deposits material on a removable foam foundation. Previous methods to retain this foam base were limited in their ability to prevent the foam from warping during the construction of large, thick parts. The new design rigidly holds the foam in an aluminum tray by the use of steel spears. The tray is easily removed from the machine to allow model removal and replacement during pauses in the modeling process. This feature gives the operator the flexibility to perform interim operations on the model not previously possible.
5. **Enhanced Firmware to Eliminate "Ooze."** A roll-back feature was incorporated into the firmware design which rolls back the filament drive wheels at the end of each curve. This feature eliminates the deposition of excess material at the tip, thereby improving the model quality.

Material Selection

Four different materials are currently available for use with the FDM® process: 1) machinable wax; 2) investment casting wax; 3) P200, a polyolefin; and 4) P300, a polyamide. Material selection for a particular model is dependent, in part, upon the end use of the model, part design, part size, and material properties.

Models created on rapid prototyping systems typically are used for concept models for design verification and marketing presentations, prototypes for form, fit, and function testing, or patterns for mold making and investment casting. P200 and P300 are most frequently used for concept models and prototypes while machinable wax and investment casting waxes are used for pattern creation.

Part design and size will determine material selection in the building of a part. Good part design reduces the amount of stress in the part and leads to better model quality; i.e., less warpage and delamination. In the case of designs that require supports for the build process, the lamination strength of materials will vary and affect ease of support removal. Higher strength materials are required where thin wall sections are involved and greater lamination strengths are required for large parts due to the inherent shrinkage factors of the individual materials.

Material properties of interest to model builders include tensile strength, flexural strength, tensile modulus, flexural modulus, notched impact, unnotched impact, elongation, and hardness.

Properties/Material	Machinable Wax	P300 (Polyamide)	P200 (Polyolefin)
Tensile Strength (psi)	1,114	1,765	1,324
Flexural Strength (psi)	1,293	2,113	1,537
Tensile Modulus (psi)	70,000	80,000	90,000
Flexural Modulus (psi)	50,000	60,000	90,000
Notched Impact (ft*lb/in)	0.72	0.24	0.17
Unnotched Impact (ft*lb/in)	12.9	1.46	1.37
Elongation (%)	6.65	3.48	4.68
Hardness (Shore D)	40	70	58

Table 1. Material Specifications (based on ASTM tests)

The selection of the appropriate material for a model must consider all of the above factors.

We are continually researching new materials with improved properties and modeling characteristics. New materials currently under investigation include powdered ceramics, powdered metals, elastomers, and water-soluble materials.

Summary

The nature and properties of each model are affected by a multitude of modeling parameters. The recent design enhancements to the FDM® process better define and control these modeling conditions and relationships. We will continue to incorporate enhancements and materials into the FDM® system as our knowledge base grows.

© 1993 Stratasys, Inc.

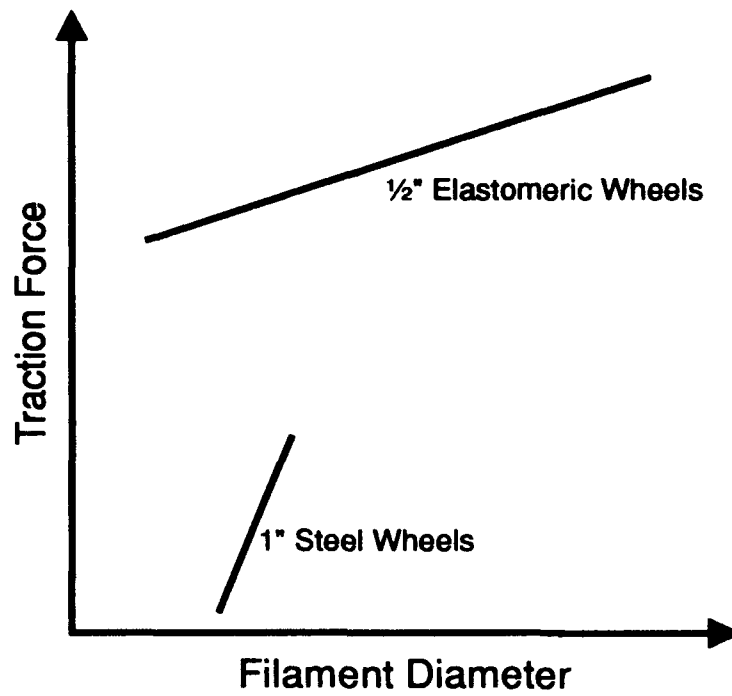


Figure 1.
Drive traction vs. filament dia. for two different pinch roller drives.

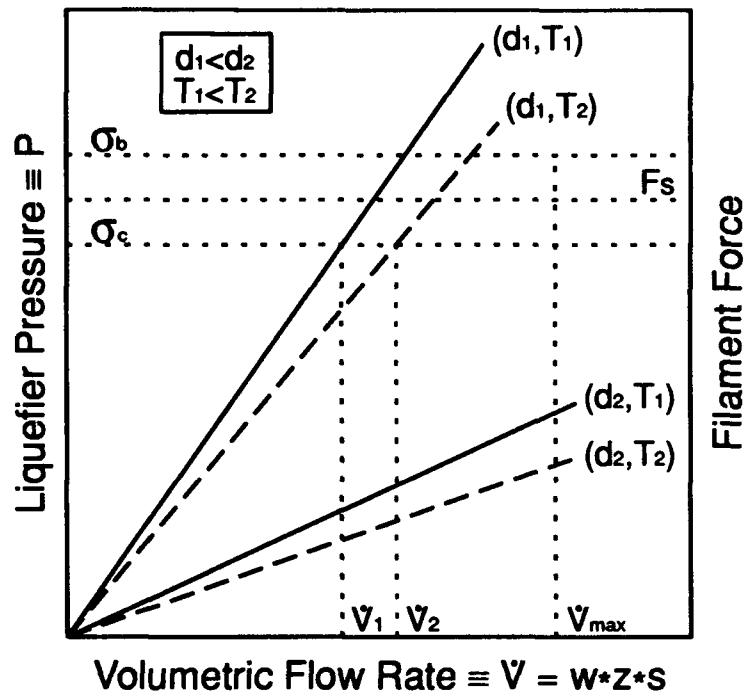


Figure 2.
Pressure vs. flow for various tip sizes and process temperatures.

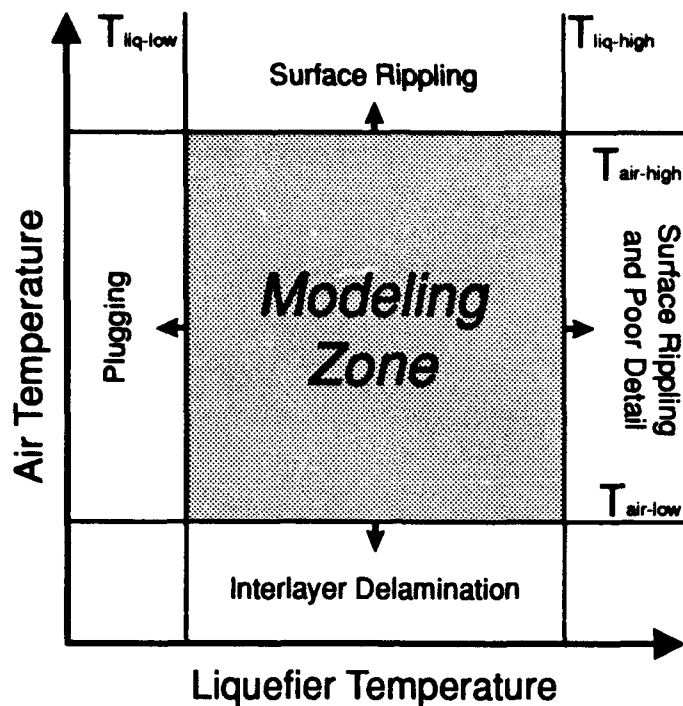


Figure 3. Modeling zone temperature parameters.

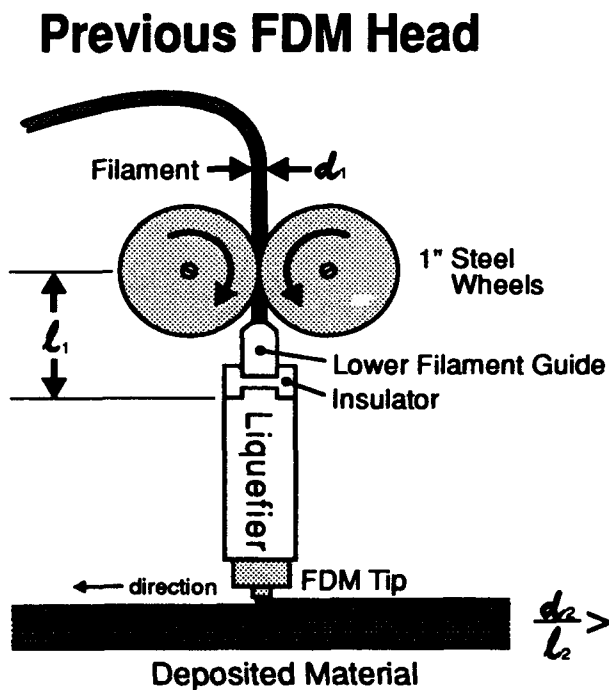


Figure 4a. Schematic diagram of the previous FDM head.

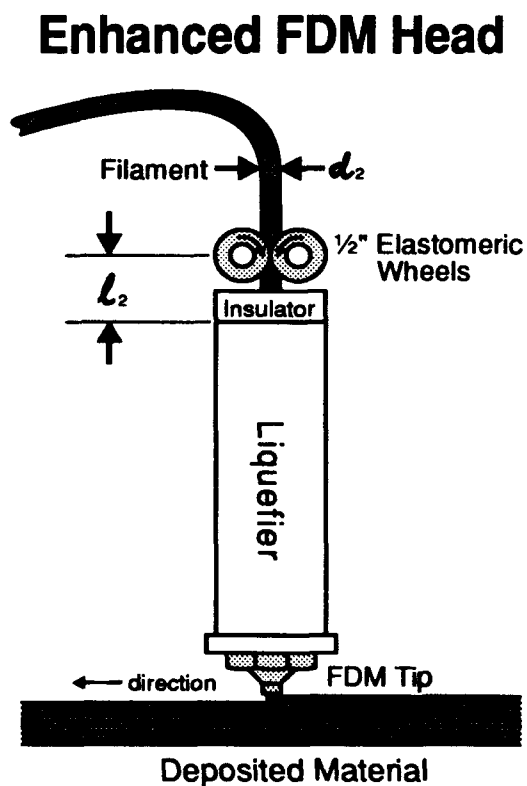


Figure 4b. Schematic diagram of the enhanced FDM head.

Reducing or Eliminating Curl on Wax Parts Produced in the Sinterstation™ 2000 System

by
Paul Forderhase and Richard Corden

Abstract

An experimental program was performed on the beta and production platforms of the Sinterstation 2000 System with the objective of building wax parts without anchors. Changes in operating strategy are described. Following a machine characterization, improvements in part build technique and thermal environment were evaluated to facilitate the processing of wax with reduced or absent anchors. Experimental data is presented showing the effects of the machine and build technique improvements made to date.

Acknowledgments

The authors wish to acknowledge the guidance and support during this project of Dr. Kevin McAlea, Rick Yeager and Mark Henton of DTM Corporation.

Introduction

In the past, wax parts have been built on a "superbase", a 13mm thick piece of beeswax, which is placed on the part cylinder prior to the wax build. Anchors connect the downward facing surfaces of the part to the superbase (figure 1).

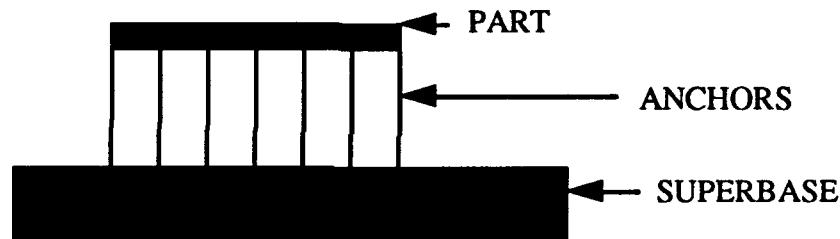


figure 1

This method for producing parts, when executed with sufficient anchors, is capable of eliminating or reducing curl to an acceptable value. The superbase, while serving well as a means to produce flat parts, places constraints on part placement within the build.

If one examines what actually transpires during a wax build, the necessity for anchored supports comes into question. In reviewing the process, however, one must keep in mind that this method for building wax parts was developed on the SLS model 125; an older platform with a different hardware configuration than the Sinterstation 2000 System. When using this procedure on either platform, the process gas is normally kept at a temperature between -5° and 5°C since the wax must cool sufficiently to allow adequate feeding. This need for refrigeration was first identified in work done at the University of Texas and subsequently became a requirement for wax parts built using the selective laser sintering process. Unlike the SLS model 125 platform, however, the process gas in the beta and production platforms must first flow across the part bed before it can be used to cool the feed areas (figure 2). The gas flow over the part bed causes each sintered layer to cool rapidly. This rapid cooling may contribute to curl by differential contraction of the hot layer on top of the cool part inducing a shear force in the plane of the part.¹ The loss of volume in each layer during solidification may also contribute to curl.

¹ . Beaman, J.J. Mechanism for Thermal Distortion in Selective Laser Sintering, unpublished DTM memorandum 7/8/92.

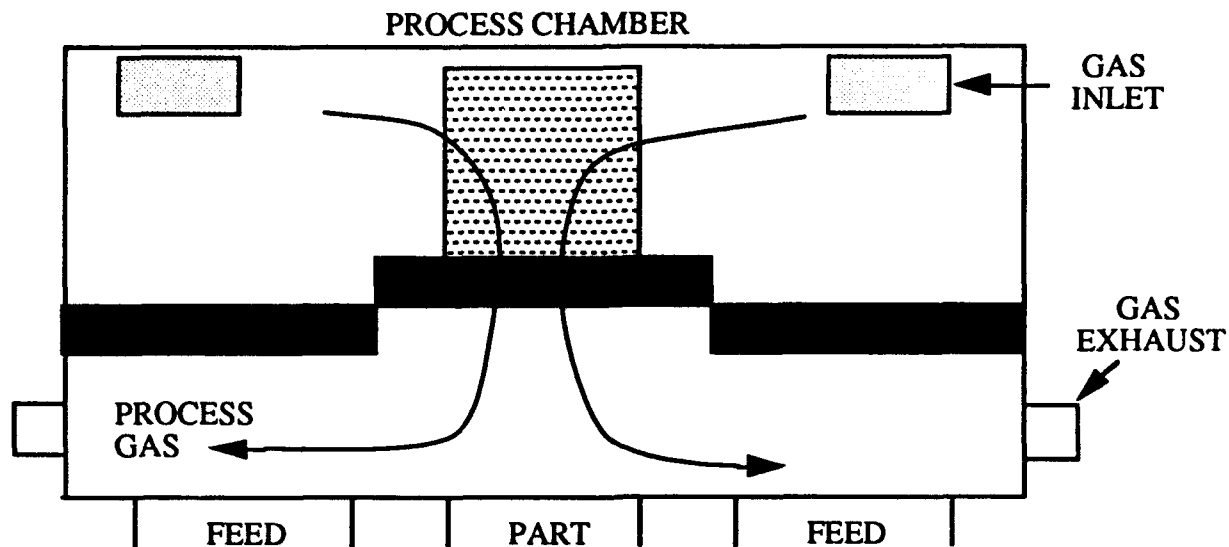


figure 2

Machine Baseline

Using the test platform, a series of SPC (Statistical Process Control) coupons were built without anchors. These builds were not intended to be representative of all parts that can be run on a Sinterstation 2000 System, but they were intended to identify the prominent failure modes encountered when running wax without anchors. Infrared imaging of the part bed under build conditions indicated that a temperature variation of 2°C was maintained over a build area of approximately ten inches. Gas velocity measurements were also taken under build conditions using a hot wire anemometer. Gas velocity over the part bed ranged from 0-20 fpm and could be characterized as being erratic. Flow over the feed cartridges was not detectable under these conditions.

Part Bed Isolation

Part bed isolation, or isolating the part bed from the flow of process gas, was developed to reduce the cooling rate of the part in order to reduce curl. It was discovered however, that when the part build area was completely isolated from the flow of the process gas, the feed material was not cooled sufficiently to allow feeding. To circumvent this problem, "flow bypass boxes" were used to re-direct the process gas flow across the feed beds while avoiding flow across the part bed. The bypass box is a sheet metal box designed to fit in the same space as the feed heater on the beta system and is equipped with a channel to direct the refrigerated process gas over the feed areas without cooling the part build area (figure 4).

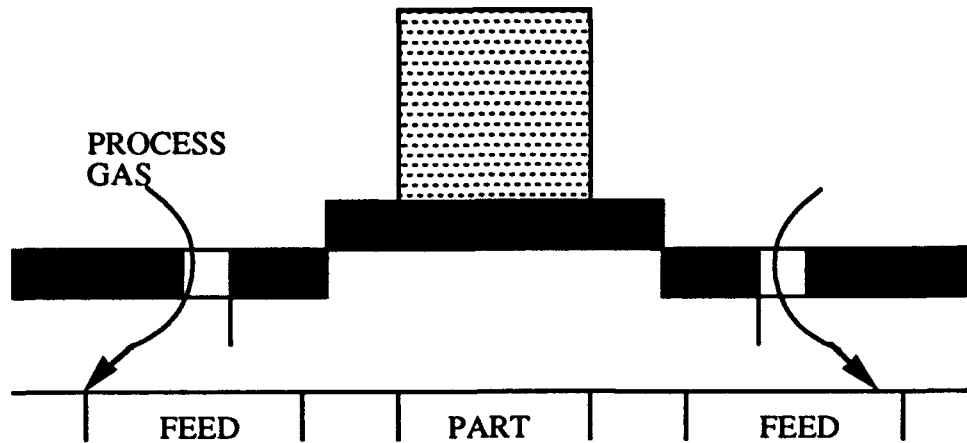


figure 4

Use of the feed bypass boxes had a significant, positive effect on the curvature of the parts. The feed bypass boxes also allowed sufficient refrigerated process gas to pass over the feed areas to facilitate feeding of the wax powder at higher temperatures; the data labelled "std" in table 1 were gleaned from a run which suffered a feed failure. The comparison of baseline runs performed with and without bypass boxes is shown in table 1.

t-Test: Two-Sample Assuming Equal Variances				
Measurement	top dia std	top dia bypass	bot dia std	bot dia bypass
Mean	20.76	36.99	4.38	7.63
Variance	85.48	208.20	1.01	3.77
Observations	8	8	8	8
Pooled Variance	146.84		2.39	
Hypothesized Mean Difference	0		0	
df	14		14	
t	-2.68		-4.20	
P(T<=t) one-tail	0.01		0.00	
t Critical one-tail (90% c.i.)	1.35		1.35	
P(T<=t) two-tail	0.02		0.00	
t Critical two-tail (90% c.i.)	1.76		1.76	

Table 1: feed bypass box comparison

Steady State Optimization

Once the build chamber had been optimized in terms of gas flow and chamber temperature with respect to feed flow quality, it was possible to begin attempts to counter the most significant failure modes present in wax parts built without anchored supports. These failure modes involved part curl and part growth, essentially the opposite extremes of the same process. To map the parameter space between these two failure modes, designed experiments were run on the beta and production platforms.

The Designed Experiments

The variables under study and their high and low values are listed in table 2. Note that the numbers listed for laser power and fan setting are percents of their maximum; the unit for the part temperature is degrees C and the unit for the layer delay is seconds.

For the designed set run on the beta platform.

	Laser Power	Part Temp.	Fan Setting	Layer Delay
Hi	30	38	50	0
Low	20	32	20	10

For the designed set run on the production platform

	Laser Power	Part Temp	Fan Setting	Layer Delay
Hi	16	38	4	0
Low	22	34	12	10

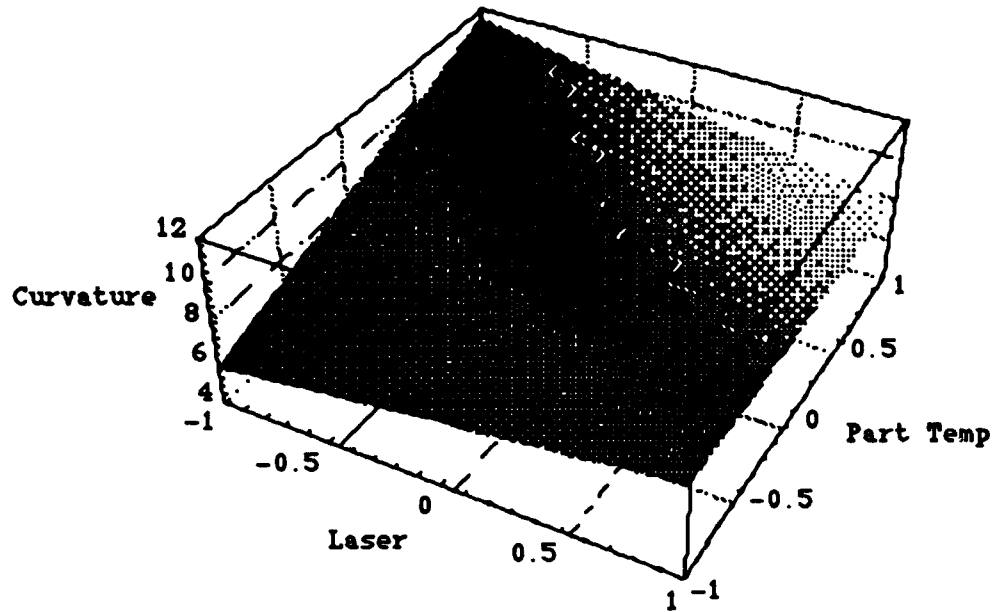
Table 2: designed experiment variable values

The values for laser power and part temperature were established by performing preliminary test runs. The control set points at which catastrophic failures were seen for high and low combinations of variables were used to define the designed set variable window. The values for fan setting were derived by correlating the absolute flow at the build surface on the beta platform to the control flow set points already established as the extremes for build success. This correlation was then applied to the production platform in order to achieve an equivalent absolute flow. These methods were employed for this designed experiment in order to accomplish two things: first, it was necessary to bracket as much of the operating envelope as possible in order to obtain significant results, and second, it was felt that by using part build failure runs and measurements of machine variables, we could compensate for differences in the two platforms. A set of SPC coupons was used as the test build due to its sensitivity to both curl and growth. An eight run resolution IV fractional factorial was used to avoid the aliasing of main effects with each other or with two way interactions.

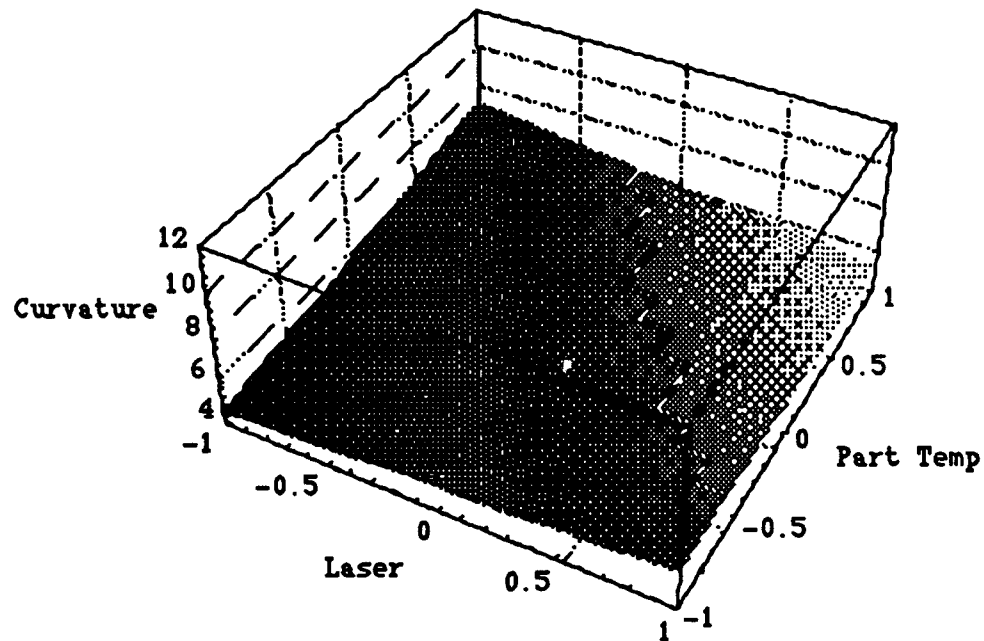
Designed Experiment Results

The response surfaces shown below are a graphical representation of the influence of laser power, part temperature, and their interaction. The height of the response surface represents the curvature diameter of the coupon's lower plane, while the gray scale represents the growth of the part as measured by the mass of the coupon (the white region indicates maximum growth). The response surfaces indicate a high degree of consistency for both platforms, and the equations used to generate the surfaces possess coefficients that are approximately equal with regard to size, sign, and statistical significance. The results indicate that in controlling part curvature, laser power was not significant on either platform; however, there is an indication that part temperature was significant in this respect. Also, in controlling growth, laser power and part temperature had equivalent amounts of influence. The experimental equations along with the probability of the observed difference in the mean being due to chance are shown in tables 3 and 4. None of the variables tested had a significant effect on sample standard deviation.

BETA PLATFORM STEADY STATE RUN OPTIMIZATION



PRODUCTION PLATFORM STEADY STATE RUN OPTIMIZATION



Model	Bottom Curvature			Mass	
Effect	Coefficient	P(2 tail)		Coefficient	P(2 tail)
Constant	8.406	0.000		8.731	0.000
Laser Power	-.210	0.774		1.006	0.000
Part Temperature	1.356	0.072		1.006	0.000
Air Flow	-0.644	0.383		0.218	0.101
Layer Delay	-0.0187	0.979		-0.344	0.019
Laser*Part	-1.594	0.037		0.394	0.010
Laser*Flow	0.848	0.253		-0.047	0.720
Part*Flow	-2.077	0.007		-0.456	0.005

Table 3: Beta Platform Results

Model	Bottom Curvature			Mass	
Effect	Coefficient	P(2 tail)		Coefficient	P(2 tail)
Constant	5.64	0.000		6.290	0.000
Laser Power	-0.181	0.391		0.593	0.000
Part Temperature	0.620	0.006		0.390	0.000
Air Flow	0.144	0.494		-0.318	0.000
Layer Delay	0.325	0.129		-0.256	0.000
Laser*Part	-0.787	0.001		0.157	0.003
Laser*Flow	0.698	0.002		-0.244	0.000
Part*Flow	0.053	0.801		-0.180	0.001

Table 4: Production Platform Results

Note that although the models exhibit acceptable values of significance, the means of the data fall into the range of what is referred to as "poor parts"; i. e. regardless of what was tried, the parts were subject to unacceptable amounts of either curl or growth. The results from the designed experiments led us to conclude that there is no region within the operating envelope in which a unique combination of process variables exist that will allow the manufacture of flat wax parts without anchors. This led to the further conclusion that other methods of suppressing curl or growth must be applied in order to achieve flat anchorless parts.

Laser Power per Unit Area

A simple formula was derived to calculate the amount of power per unit area (P/A) delivered by the laser using the laser power (LP), scan spacing (ScSp.) and step size(SS).

$$P/A = \frac{LP}{(ScSp)(SS)}$$

Preliminary tests indicate that there exists some variation in the results of delivery at constant P/A; i.e. P/A may be maintained by varying both laser power and scan spacing, but a part built with a high laser power and a larger scan spacing will not exhibit the same growth patterns as a part built with a lower laser power and a smaller scan spacing, even though P/A remains constant for both parts. The speed at which the laser power was delivered also had an effect on the amount of curl and growth present.

Table 4 represents a collection of data for test parts built on the beta platform. Note that success, in this case minimizing both curl and growth, is achieved when the correct

"balance" is found between the significant parameters in conjunction with part re-orientation. Note also that curvature decreases as the value increases and that the growth value is derived from an arbitrary comparison scale:

Part #	Curvature	Pt. Temp.	Sc. Sp.	LP	SS	Growth	P/A
1	139.91	25	0.012	20	35	7	47.62
2	388.00	27	0.012	20	35	10	47.62
3	540.30	27	0.010	20	45	1	44.44
4	545.31	30	0.012	20	35	9	47.62
5	620.44	31	0.010	20	45	6	44.44
6	647.64	31	0.010	20	53	5	37.74
7	697.45	30	0.010	20	53	4	37.74
8	753.99	30	0.010	22	45	1	48.89
9	825.57	31	0.012	18	53	0	28.30
10	1343.65	30	0.010	20	53	5	37.74
11	1352.14	31	0.012	20	35	3	47.62
12	1780.15	32	0.010	20	53	6	37.74

Table 4: P/A test results

Angled Parts

Part orientation is perhaps the most significant factor in diminishing the curl experienced by wax parts built without support structures. Rotating the part within its three dimensional build region allows the reduction of the cross sectional surface area of all surfaces that would normally be parallel to the plane of the part bed. The part is subject to less stress, and therefore less likely to curl, when the cross sectional area of these surfaces, referred to as downward facing, is reduced to a minimum since the relative beam strength of that cross section is also reduced. Minimizing cross-sectional area, however, also diminishes the part's stability during the initial stages of the build. With such a small area being scanned at the build's outset, less than 1/8th of an inch for parts tested, it was necessary to raise part temperature to cause partial agglomeration of the surrounding wax bed thus creating a stable base. This "base" allowed the roller to pass across the bed during powder addition without disturbing the part itself.

The partial agglomeration of the surrounding wax may have provided the support needed to establish the part bed, but it also promoted growth and made for a more vigorous breakout. A re-evaluation of the part and its orientation suggested that its geometry could be generalized as being in the form of a cup. If during re-orientation, this "cup" was downward facing, then increasing the part temperature during the build would cause heat to be trapped beneath the part proliferating growth. If, however, the part was oriented so that the "cup" was upward facing, then excess heat could diffuse upward through the bed decreasing growth.

Since growth is affected by the energy introduced into the system during sintering, growth reduction can also be accomplished through laser parameter manipulation. Using information derived from a preliminary portion of this test, laser power, step size and scan spacing were adjusted to minimize growth. Though density, and subsequently strength, suffered as a result of this manipulation; parts built in this fashion had the least amounts of both curl and growth.

Anchor Design or "Surround Support"

Though this test did not follow the "unsupported wax" precept, it does improve upon current methods for building wax parts. The part is "encased" in a box which actually serves as a support structure. The interior of this box is cross-hatched, as opposed to being filled, so that it may be removed from the part after the build has completed. Since it is not required that this box be attached to the bees-wax superbase, parts may be initiated at any point in the cylinder. The initial work indicates that parts which are built without re-orientation still tend to be subject to curl which suggests the need to redesign the box structure.

Conclusion

The ability to build sintered, wax parts without anchored supports to the standards of quality demanded by post build applications is one that can significantly improve the viability and economics of the process. Once the restriction of "superbase attachment" has been removed, the potential for increased productivity becomes obvious. It also appears obvious from the results of various testing included in this paper that simply removing all supports and balancing build parameters accordingly is not sufficient to produce quality parts. Various amendments to the build procedure including: optimized laser parameters, angled builds and "surround support" offer the most promising potential in reducing the constraints currently associated with wax builds.

Computer Aspects of Solid Freeform Fabrication: Geometry, Process Control, and Design

Richard H. Crawford
Department of Mechanical Engineering
The University of Texas at Austin

Abstract

Solid Freeform Fabrication (SFF) is a class of manufacturing technologies aimed at the production of mechanical components without part-specific tooling or process planning. Originally used for creating models for visualization, many industrial users of SFF technologies are realizing the greater potential of SFF as legitimate manufacturing processes for producing patterns and, in some cases, functional parts. Thus, SFF is becoming an important aspect of the product realization process in these industries.

Solid Freeform Fabrication arose from the dream of "push-button" prototyping, in which solid reproductions of three-dimensional geometric models are created automatically under computer control. Perhaps more than any other class of manufacturing technologies, computer software development has been an integral part of the emergence of SFF. As SFF technologies evolve toward the ability to create functional parts, computer issues gain more importance.

This paper discusses three aspects of software design for SFF: processing of geometric data, global and local control of SFF processes, and computer-based analysis and design for SFF manufacturing. The discussion of geometric processing issues focuses on accuracy and completeness of input models, and the algorithms required to process such models. The interplay between the physics of SFF processing and the desired output geometry is discussed in terms of the development of model-based control algorithms for SFF. These two areas, geometric processing and control, are necessary for the practical implementation of any SFF technology. However, for SFF to realize its potential as an alternative for manufacturing functional parts, engineers must be provided with analysis and design tools for predicting mechanical properties, ensuring dimensional accuracy, choosing appropriate materials, selecting process parameter values, etc. For each of these three different but related areas of software design, the state-of-the-art is assessed, contemporary research is summarized, and future needs are outlined.

Introduction

Solid Freeform Fabrication (SFF) is a group of emerging technologies for fabricating physical objects directly from computer-based descriptions (such as solid models) of the geometry of the parts. All SFF technologies are enabled by computer hardware and software, from the input geometric descriptions to control of the fabrication machinery. Clearly, the success of SFF depends on the existence of sophisticated and cost-effective computing equipment and software. As the applications of SFF move beyond visualization models and design verification prototypes into fabrication of functional components, SFF will change from rapid prototyping techniques into legitimate manufacturing technologies. One key to this progress is improvement of the software systems that enable advances in the capabilities of SFF. This paper describes potential opportunities for improvement in SFF software in the areas of geometry processing, process modeling and control, and design tools for SFF.

Geometry Processing

Most Solid Freeform Fabrication processes produce parts on a layer-by-layer basis. The process proceeds by first slicing the geometric description of the part into layers. The slicing operation generates the contours of the part for each layer. The contours are then processed in a manner dependent upon the particular SFF technology. For instance, for Selective Laser Sintering (SLS), the contours are discretized into "toggle points" at which the laser beam must be modulated to produce the desired solid.

Faceted Geometry. The form of the geometric description of mechanical parts to be produced by SLS significantly affects the accuracy of the final part. The current state-of-the-art for most SFF technologies consists of tessellating the surfaces of the geometric model into a mesh of non-overlapping triangular facets. The resulting geometry is transmitted in a standard file format, the so-called "STL" file format, established by 3D Systems, Inc. [1] This format has been adopted by many CAD vendors, is readily available, and is considered adequate for most visualization applications. However, for producing accurate patterns and functional parts, the adequacy of the STL format is unclear. There is a trade-off between the accuracy and the size of the geometric description. Highly non-linear surfaces, such as those that comprise turbine blades, manifolds, etc., must be tessellated into a large number of small facets, resulting in very large data files, and the accuracy of such descriptions is still suspect.

In many cases, the tessellation operation itself introduces errors in the model. Tessellation of surfaces with large curvature can result in errors at the intersections between such surfaces (see Figure 1), leaving gaps or "holes" along edges of the part model [4]. Tessellation of fine features is susceptible to round-off error, which leads to non-manifold models of parts, where more than two facets are adjacent to a single edge, or facets with opposing outer normals meet at a single vertex (see Figure 2). These problems are difficult for slicing algorithms to handle and cause fabrication problems for SFF processes, which require valid solids as input.

Algorithms to overcome these problems with faceted geometric descriptions depend on developing richer data structures that explicitly represent the facet and edge adjacencies that are implicit in the STL format. This information enables the development of efficient slicing algorithms that take advantage of the explicit adjacency information when constructing slice contours [5, 11, 12]. Rock and Wozny [10] have also proposed an alternative to the STL file format that captures the adjacency information in the exchange file. Bøhn and Wozny [4] have developed a method to repair faceted geometric descriptions with problems such as that depicted in Figure 1. Their technique uses the adjacency information to locate gaps between facets. They then use a "shell-closure" algorithm to add missing facets to the close gaps.

Higher Order Geometric Descriptions. The problems with the STL geometry exchange format arise because tessellation is a first-order approximation of more complex geometric entities. An obvious solution to these problems is to exchange higher order geometric entities, preferably the source geometry with which a part is designed. This approach has been adopted at The University of Texas, where an interface based on Constructive Solid Geometry (CSG) has been developed to provide input to SFF processes [7]. With CSG the geometry of a part is modeled as a binary tree whose leaf nodes are scaled and oriented instances of primitive shapes (e.g., spheres, cylinders, parallelepipeds, etc.) and whose non-terminal nodes are the regularized Boolean set operations union (\cup), intersection (\cap), and difference ($-$). Evaluating the CSG tree with a geometric modeler results in an explicit boundary representation of the part's surfaces.

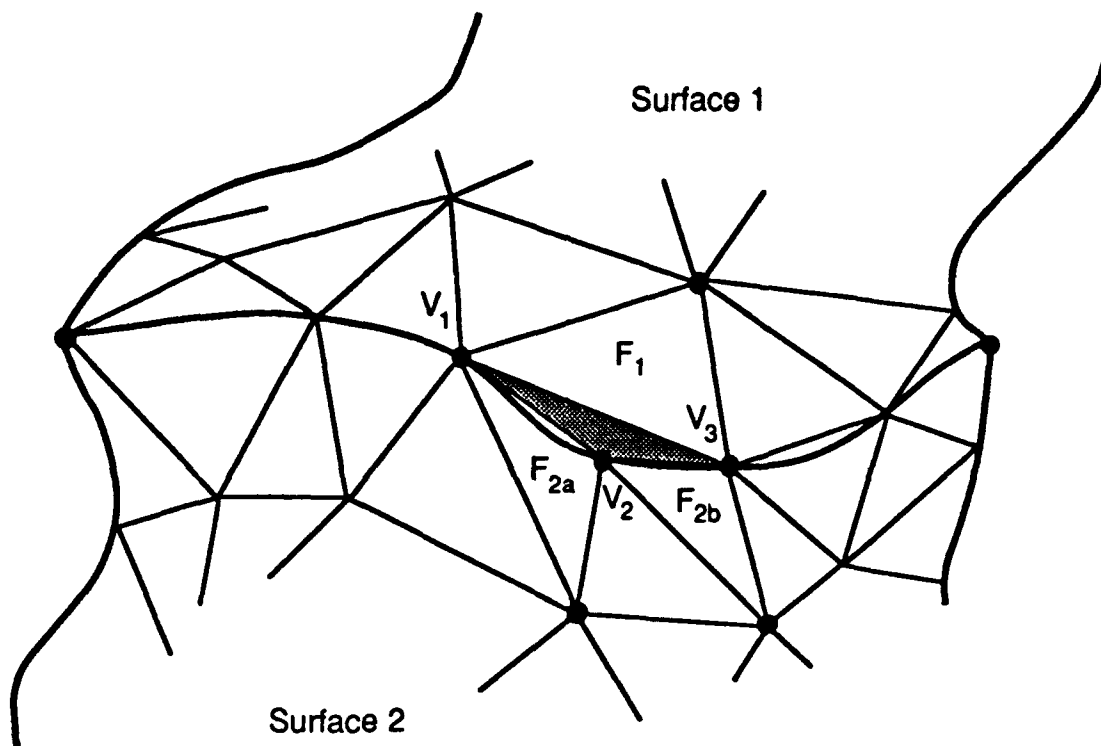


Figure 1. A gap in the seam at the intersection of two surfaces [4].

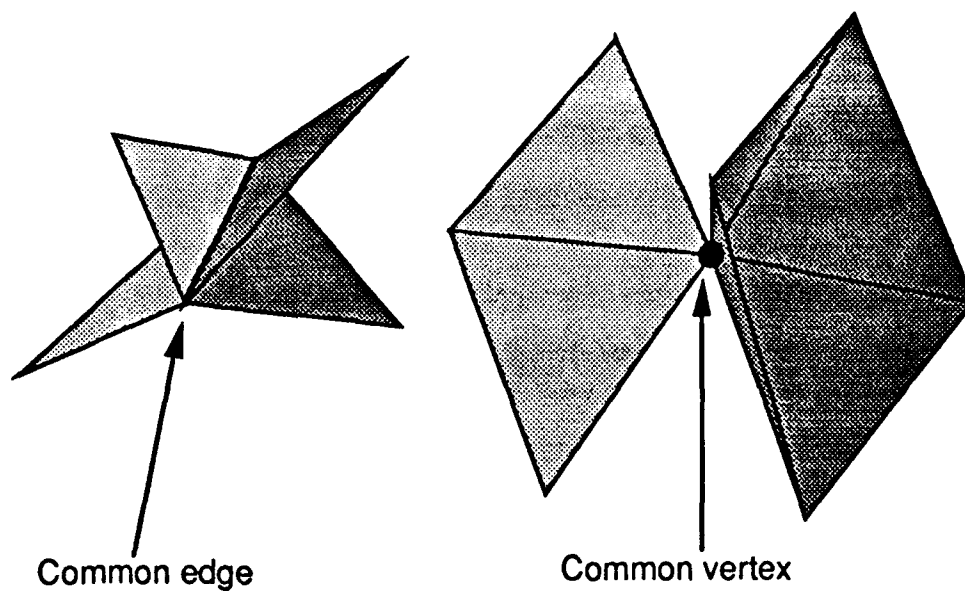


Figure 2. Other examples of non-manifold topology in a faceted SFF model.

Normal evaluation of a CSG tree involves computing the intersection between pairs of primitive or intermediate surfaces and performing set classification in three dimensions. The UT process is based on evaluation of *sliced* primitives rather than 3-D primitives. In this process the primitives in the CSG tree are sliced individually, generating a slice for each primitive. The part contour in the slice plane is then produced by combining the primitive slices based on the Boolean operations at the non-terminal nodes (see Figure 3). The contour of the part in a given slice plane is a collection of piecewise continuous curves. These curves are then scan-converted to produce toggle points.

The net result of this work is a boundary evaluator developed specifically for SFF applications. The approach provides a more accurate, compact part description. Also, all surface-surface intersections are performed in the 2D slice plane, resulting in considerably simpler and more robust algorithms. For the common quadric surfaces (spheres, cones, cylinders, and ellipsoids), the surface-surface intersection calculations are exact (subject to round-off errors). For higher order surfaces, such as the torus, the method requires an approximation of the slice contour of the primitive. Such an approximation is still more accurate and efficient than the linear approximations obtained from a faceted model. In fact, the method provides a rational basis for approximating the geometry, since it is based on error measures in the slice plane. Details of the algorithm are included in [7].

Processing higher order geometry for SFF processes offers several advantages over exchange of faceted geometric descriptions. Generally speaking, files containing higher order information will be smaller and more accurate than comparable faceted geometry files. Also, many of the problems that result in non-manifold geometric information in faceted descriptions can be avoided. For example, because the CSG slicer described above performs the geometric modeling operations, no explicit boundary information is needed in the input file. Instead, it is incumbent upon the SFF geometry processor to ensure that the results are realizable for the particular SFF technology that is used to fabricate the part. Potential problems in the slicing operation can be solved because more information is available about the intended geometry of the part; thus, higher order descriptions are easier to troubleshoot when necessary. Finally, when approximations are necessary for the given input geometry, the approximation process is driven by the particular SFF technology rather than by generic criteria meant to satisfy the requirements of many SFF technologies. This provides a rational basis for approximating the geometry when necessary.

There are disadvantages to higher order geometric data exchange as well. First, there is no single geometry form that is satisfactory for all applications. There are many different geometric descriptions that are used in product design, each with different requirements for a slicing algorithm. Designers of commercial SFF processing software will have to make compromise decisions about which geometric forms to support or risk losing potential customers from lack of geometric coverage. Also, because the geometric input is more complex, algorithms for processing the geometry are more complex as well. Finally, interchange standards must be developed for higher order geometric descriptions. While these standards are under development, they are still subject to change until agreed upon.

Sources of Layered Geometry. Many potential applications of SFF naturally provide data in layer-based formats. For example, Rogers *et al.* [13] report the use of a laser digitizer to provide data for the fabrication of prosthetic devices using Selective Laser Sintering. Levy *et al.* [8] used Computed Tomography (CT) data to produce models of human temporal bones using SLS. Bartels *et al.* [2] used imaging data from a confocal microscope as input to an SLS machine to create models of pollen grains. These are just three examples of the potential applications for SFF in areas other than product engineering. In each of these cases the data was presented to the SFF machine as layers.

sphere1 : center at (0, 0, 0) and unit radius
 sphere2 : center at (1, 0, 0) and unit radius
 sphere3 : center at (0, 1, 0) and unit radius

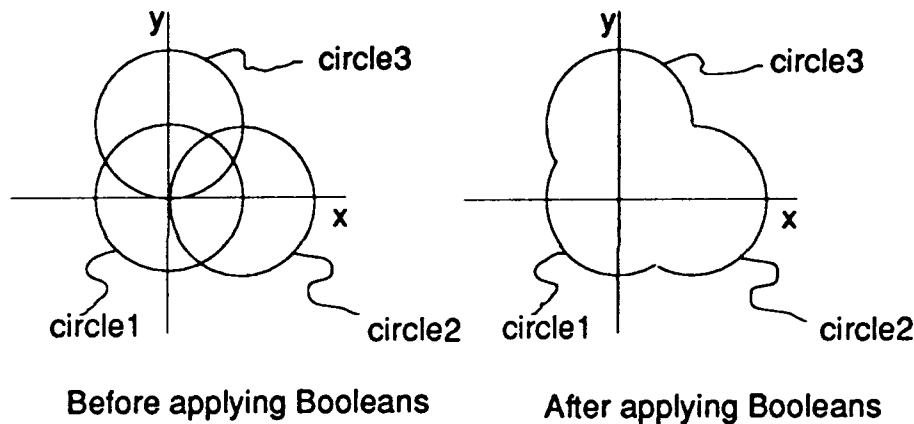
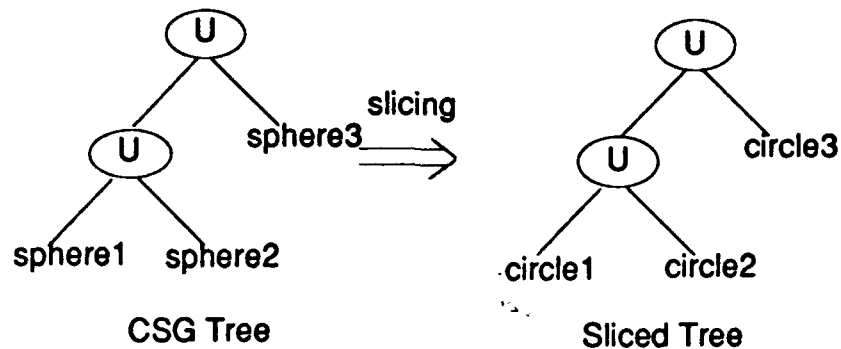


Figure 3. CSG slicing and set operations for SFF [7].

The geometric processing was not particularly sophisticated in any of these cases. For instance, in each of the cases cited above, the thickness of the data slices did not coincide with the thickness required for the SLS process (typically 0.005 to 0.01 in). To compensate for this, the SLS control software either skipped data layers (for thinner layers) or replicated layers (for thicker layers). To achieve higher accuracy, however, more sophisticated strategies must be developed and adopted by the SFF software. The laser digitizer software described in [13] actually interpolates between slices to realize the required resolution for the SLS process. Similar schemes must be developed for processing CT and confocal microscope imaging data.

Both the CT data [8] and the microscope data [2] consist essentially of raster images of the physical objects being imaged. In each case, the data provides a measure of the relative density of the material at each pixel in the imaging plane. However, SFF processes such as SLS require boundary information rather than interior density data. For these studies, then, the raster images were first converted to contour images of the sample slice in each plane by specifying a minimum threshold density below which the data are ignored. For these studies, the threshold value was selected manually and varied from layer to layer. However, to realize the full potential of

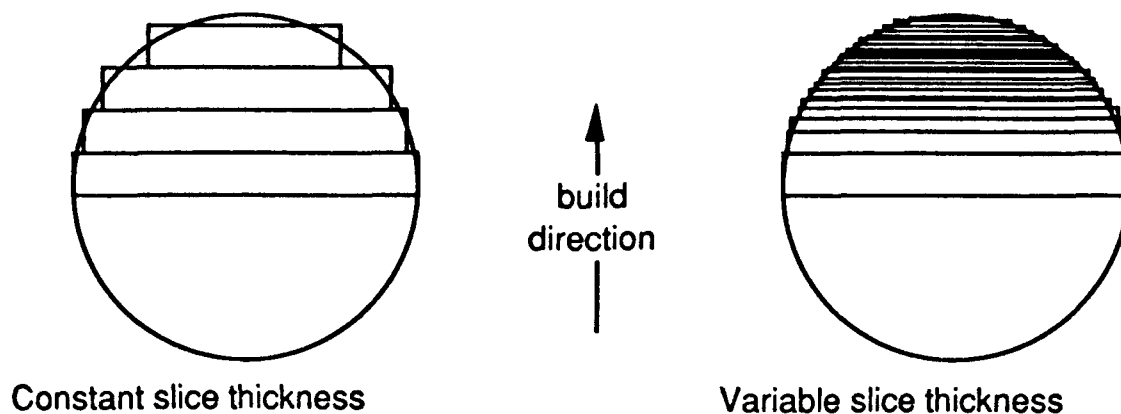


Figure 4. Effect of variable slice thickness on part accuracy.

fabricating such models with SFF, threshold values must be determined automatically. Algorithms for determining optimal threshold values are needed for preprocessing layer-based SFF input.

Before the use of layered data can expand, data interchange standards must be established. Currently there are no standards to specify the form of layer-based geometry for exchange among programs, a necessity for accommodating such data in SFF processing. In the examples cited above, Rogers presented the data to the SLS machine in the form of contours [5]. The other two sources, as described above, present their data as raster bit maps. These examples suggest that two exchange standards should be developed: one for contour data and one for raster data. In any case, the details for processing the input geometry, *i.e.*, interpolation or thresholding as described above, should be left to the particular SFF technology to ensure that maximum part quality can be realized.

Process Modeling and Control

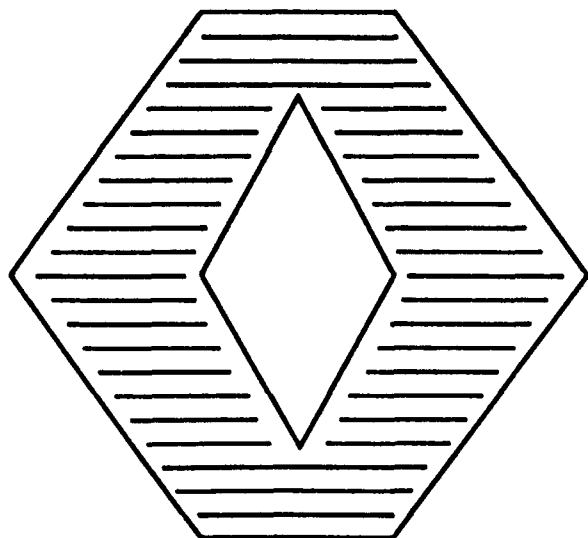
Solid Freeform Fabrication has the potential for producing accurate, structurally sound three-dimensional solid versions of objects. To develop accurate patterns and functional parts with adequate strength, however, requires in-depth basic research to understand the correlation between the mechanical properties and geometric accuracy of the final part with respect to the SFF process parameters [3]. These relationships must be captured in computer models that can be used to control SFF processing. To enable real time control, these models must represent a compromise between accurately modeling the physics of the SFF process and intelligent use of geometric information to approximate optimal processing patterns.

While process planning for SFF is considerably reduced compared to conventional fabrication technologies, there are several considerations which will require reasoning about the geometry of the final part. Scaling and orientation of the part within the work space of the SFF machine have a significant impact on the efficiency of the process. Aside from other factors, the part should be oriented in a manner which minimizes the number of layers. Other factors, however, may override this consideration. For instance, tolerances tend to be directionally dependent. Likewise, the mechanical properties of the final part will depend upon its orientation during the process. These issues require geometric reasoning on both global and local scales. Global reasoning will indicate the best part orientation within the workspace of the SFF machine. Local reasoning refers to considerations of the geometry of each layer to determine scanning and build patterns that maximize geometric accuracy and mechanical properties of the part.

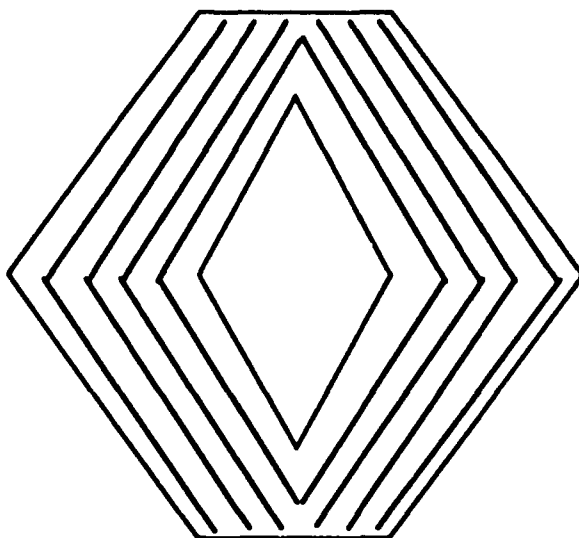
Scanning patterns. Many SFF processes build each layer of a part by raster scanning the powder bed along a single axis, as indicated in Figure 5. For geometries such as this, a unidirectional scanning pattern will result in a large number of very short scanning vectors. A multidirectional scanning pattern, such as that indicated on the right in Figure 5, will result in a smaller number of longer scanning vectors. Longer vectors reduce the errors associated with laser toggling transients and repositioning of the laser beam, resulting in higher part accuracy. The figure implies that preferred scanning patterns are the result of geometry alone; however, other factors may outweigh geometry. For instance, mechanical properties within a layer may be dependent upon the scanning direction; heat transfer considerations and the creation of thermal gradients may indicate preferred scanning patterns; contour scanning of the layer boundaries may reduce aliasing artifacts and result in better surface quality. These considerations must be incorporated into algorithms for determining arbitrary scanning patterns for SFF processes.

Contour Scanning. Recent research at UT Austin has focused on developing an optimal laser control system for scanning along curves [15]. The scanning algorithm and associated hardware maintain constant laser power density by simultaneously controlling laser speed and laser power. The goal is to produce parts with better surface resolution than can be obtained from vector scanning the part contour (see Figure 6). This research emphasizes the need for higher level geometric descriptions for SFF process. The algorithm uses information about the the curvature of the contour to determine appropriate laser parameters to achieve the desired power density. A polygonal approximation of the contour, such as that obtained from slicing a faceted part model, is not accurate enough to support this control scheme.

Process Modeling. Advances in control of SFF processes will depend on developing a better understanding of the physics of each process. For example, the process control program for SLS administers three areas: laser control, control of powder delivery and leveling, and control of the environment within the machine. Input to the module consists of a suitable geometric description of the part layers (at this time, scan lines and laser toggle points) and settings for process parameters, including material properties, bed temperature, gas flow rate, scanning speed, laser power, beam diameter, and scan spacing. The current SLS process control software is built under the assumption that these parameters will be constant for an entire part. However, initial investigations indicate that fabrication of metal parts will require local control of laser beam parameters, allowing these parameters to change from layer to layer or even within different areas in a given layer. Such physically-based scanning is depicted conceptually in Figure 7, where a part layer has been divided into several regions based on part quality predictions from a physical model of the process. A scanning pattern is then generated for each of the simple regions, again based on predictions from a process model. Such a scanning scheme could be precomputed off-line before the part is fabricated, or it may be updated on a layer-by-layer basis, with input about the status of previous layers from sensors. The key to solving this problem is development of physical models of the process. While initial models of the SLS process have been developed [9, 14], they are not structured to support real-time process control of this kind. The solution to this problem will likely require a combination of hardware and software development.

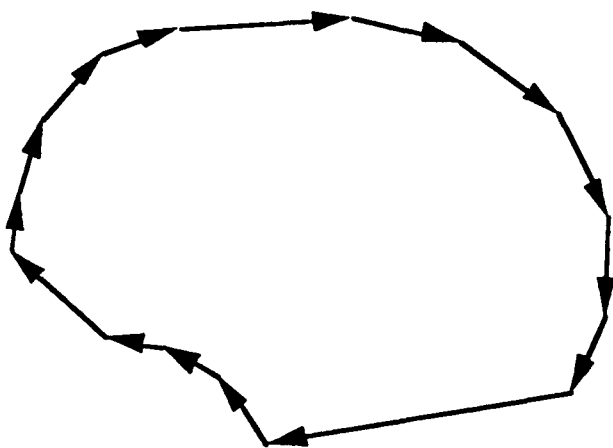


Raster Scanning

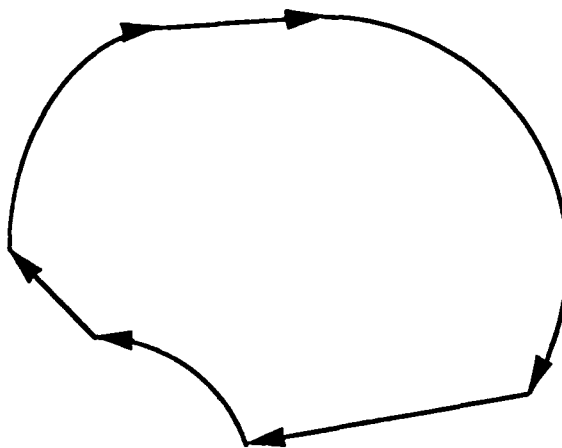


Directional Scanning

Figure 5. Directional scanning versus raster scanning.



Vector Scanning



Contour Scanning

Figure 6. Contour scanning.

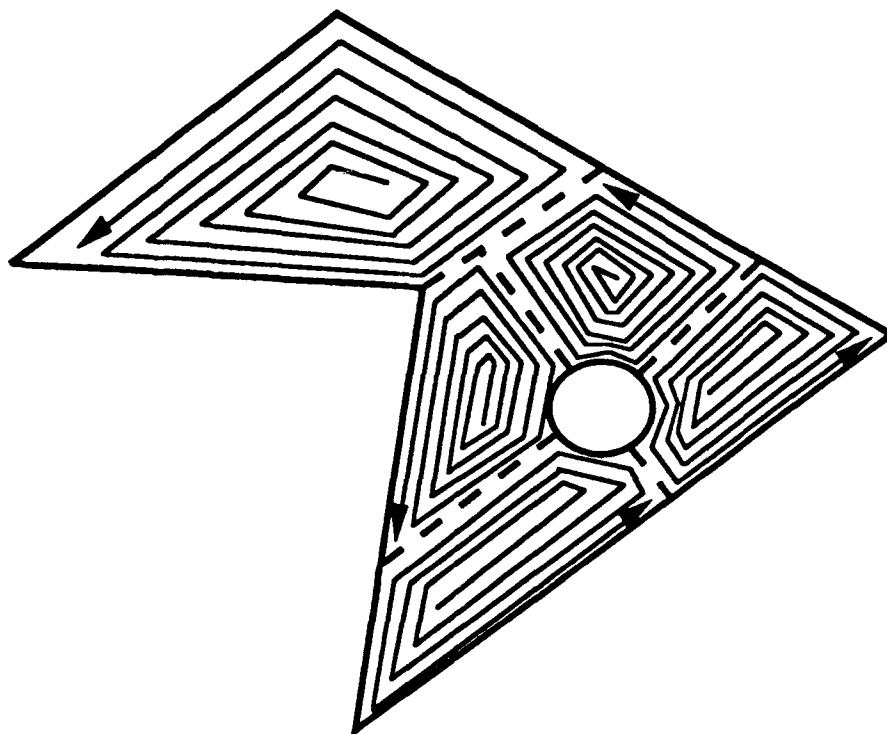


Figure 7. Physically-based scanning.

Design for SFF

Successful design of functional parts produced by SFF will require consideration of the material and mechanical properties in conjunction with their geometry. These properties are directionally dependent due to the layer-by-layer fabrication process. For certain SFF processes, such as SLS, the mechanical behavior of parts is further complicated by the phase change inherent in the process. Therefore, standard techniques for modeling structural behavior of mechanical parts will have to be modified and enhanced to account for these factors. Development of such computer-aided design tools will allow designers to create parts that are optimized for SFF processes.

Physical models of SFF processes provide a starting point for developing these design for SFF tools. However, such models are focused on determining the consequences of choices of process parameters on the properties of the final part. For design, the inverse solution is needed. For desired properties of the final part, the designer must know the appropriate process parameters. Answering such questions will require reformulation of the modeling software.

SFF processes offer the promise of providing manufacturing capabilities that are not realizable by other techniques. One such possibility is selective material property distribution within the part. With conventional material removal processes, the bulk mechanical properties of a part are determined by the stock material chosen, aside from any surface treatment that is applied as a post-process. With SFF technologies the potential exists for the mechanical properties to vary continuously within the part. Again, to realize this possibility, design tools are needed to guide the designer in determining optimal material distribution. Project MAXWELL, a joint effort of the University of Michigan and Carnegie-Mellon University, is developing mathematical techniques for concurrent design of shape and material composition for mechanical components [6]. Tools

such as this will become increasingly important as SFF techniques are employed for manufacturing functional parts rather than prototypes.

Conclusion

One key enabler of Solid Freeform Fabrication technologies is computer software in geometric modeling and process control, without which most SFF processes would be difficult to implement. However, many opportunities exist for improving the performance of SFF processes by improving the software, thereby broadening the application of SFF from producing models and prototypes to functional part manufacturing. This paper provides an outline of some of the issues in software development in the areas of geometric modeling, process modeling and control, and design for SFF. Progress in any one of these areas, however, is dependent upon improvements in the other two areas. These interdependencies are depicted in Figure 8. To realize the potential of SFF, research must continue simultaneously in all of these areas.

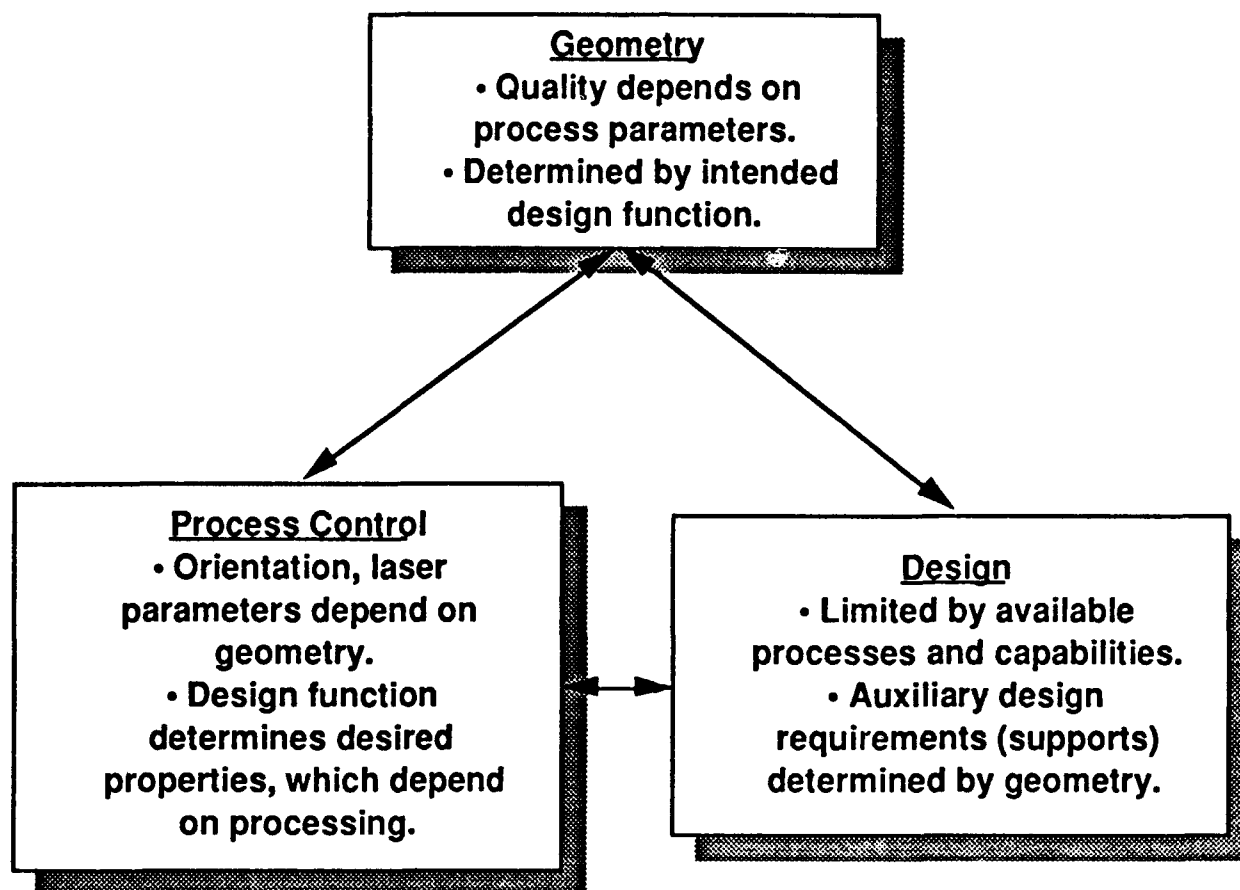


Figure 8. Interdependencies among geometry, process control, and design for SFF.

References

1. 3D Systems, Inc., "Stereolithography Interface Specification", 3D Systems, Inc., Valencia, CA, June 1988.

2. Bartels, K. A., Crawford, R. H., Das, S., Guduri, S., Bovik, A. C., Diller, K. R., and Aggarwal, S. J., "Fabrication of Macroscopic Solid Models of Three-Dimensional Microscopic Data by Selective Laser Sintering", *Journal of Microscopy*, Volume 169, No. 3, pp. 383-389.
3. Beaman, J. J., "Machine Issues Associated with Solid Freeform Fabrication", *Solid Freeform Fabrication Proceedings 1992*, Austin, TX, August 3-5, 1992, pp. 309-330.
4. Bøhn, J. H. and Wozny, M. J., "Automatic CAD-Model Repair: Shell-Closure", *Solid Freeform Fabrication Proceedings 1992*, Austin, TX, August 3-5, 1992, pp. 86-94.
5. Crawford, R. H., Das, S., and Beaman, J. J., "Software Testbed for Selective Laser Sintering", *Solid Freeform Fabrication Proceedings 1991*, Austin, TX, August 12-14, 1991, pp. 21-27.
6. Dutta, D., Kikuchi, N., Papalambros, P., Prinz, F., and Weiss, L., "Project MAXWELL: Towards Rapid Realization of Superior Products", *Solid Freeform Fabrication Proceedings 1992*, Austin, TX, August 3-5, 1992, pp. 54-62.
7. Guduri, S., Crawford, R. H., and Beaman, J. J., "A Method to Generate Exact Contour Files for Solid Freeform Fabrication", *Solid Freeform Fabrication Proceedings 1992*, Austin, TX, August 3-5, 1992, pp. 95-101.
8. Levy, R. A., Guduri, S., and Crawford, R. H., "Preliminary Experience with Selective Laser Sintering (SLS) Models of the Human Temporal Bone", *Solid Freeform Fabrication Proceedings 1992*, Austin, TX, August 3-5, 1992, pp. 161-173.
9. Nelson, J. C. and Barlow, J. W., "Relating Operating Parameters Between SLS Machines Which Have Different Scanner Geometries and Laser Spot Sizes", *Solid Freeform Fabrication Proceedings 1992*, Austin, TX, August 3-5, 1992, pp. 228-236.
10. Rock, S. J. and Wozny, M. J., "A Flexible File Format for Solid Freeform Fabrication", *Solid Freeform Fabrication Proceedings 1991*, Austin, TX, August 12-14, 1991, pp. 1-12.
11. Rock, S. J. and Wozny, M. J., "Utilizing Topological Information to Increase Scan Vector Generation Efficiency", *Solid Freeform Fabrication Proceedings 1991*, Austin, TX, August 12-14, 1991, pp. 28-36.
12. Rock, S. J. and Wozny, M. J., "Generating Topological Information from a 'Bucket of Facets'", *Solid Freeform Fabrication Proceedings 1992*, Austin, TX, August 3-5, 1992, pp. 251-259.
13. Rogers, W. E., Crawford, R. H., Beaman, J. J., and Walsh, N. E., "Fabrication of Prosthetic Sockets by Selective Laser Sintering", *Solid Freeform Fabrication Proceedings 1991*, Austin, TX, August 12-14, 1991, pp. 158-163.
14. Sun, M. M. and Beaman, J. J., "A Three Dimensional Model for Selective Laser Sintering", *Solid Freeform Fabrication Proceedings 1991*, Austin, TX, August 12-14, 1991, pp. 102-109.
15. Wu, Y.-J. E. and Beaman, J. J., "Laser Tracking Control Implementation for SFF Applications", *Solid Freeform Fabrication Proceedings 1992*, Austin, TX, August 3-5, 1992, pp. 161-173.

VIRTUAL REALITY AND RAPID PROTOTYPING: CONFLICTING OR COMPLIMENTARY?

I.Gibson, D.Brown, S.Cobb, R.Eastgate
Dept. Manufacturing Engineering & Operations Management
University of Nottingham
Nottingham, UK

Abstract

It is likely that the uses for virtual reality (VR) will coincide with applications that rapid prototyping systems have already been used for. VR, with the ability to model real life environments, presents an ideal base for the design and development of new manufactured products. As a method of producing physical models directly from 3D CAD systems, rapid prototyping technology has also been used to visualise new product designs. This paper attempts to determine whether the two technologies are a means to the same end or whether they combine to form a more efficient route to product development.

Virtual Reality Systems

A virtual reality system provides a platform for computer generated images to interact with the user. As the user reacts to these images, requiring to change the scene in some way, so the computer complies. The images, along with other possible external stimuli show objects that combine together to form virtual worlds. Perhaps the best definition offered yet on the exact nature of VR comes from Zelter [1]. A virtual reality interface system must offer a degree of 3 key components:-

- **Autonomy:** objects must react to external stimuli, have collision boundaries and exhibit real world effects (e.g., coefficients of restitution, gravity, and friction).
- **Interaction:** one must be able to manipulate the parameters of each object in real time.
- **Presence:** a crude measure of the fidelity of the viewing system.

Whether the system used is desk top or immersive, VR is computer modelling of real life as experienced through sight, sound, and touch.

The above suggests that designers and engineers who wish to address the problem of development and improvement of interactive design tools should consider what benefits VR might offer. The Nottingham University Virtual Reality Applications Research Team, VIRART, was formed specifically to investigate problems of this nature. By building up an expertise in VR systems, VIRART aim to liaise with industry and identify where VR can be used. Current systems are not as easy to use as they should be, and VIRART also set out to influence the development of the technology. With respect to industrial applications, VR appears to be useful in several areas:-

- Where the real world is too inaccessible, dangerous, or expensive to model in real life (e.g., nuclear installations).

- Where the worlds to be modelled are incomplete and require an iterative approach to determine their construction (e.g., control panel design).
- Where the ability to reorder the world requires the manipulation of parts in an unnatural manner (e.g., modelling large, heavy objects to be moved by hand).
- Where some of the required attributes within the world are unreal (e.g., abstract modelling of management systems).

It is considered that when referring to product design in general, the use of VR relates mainly to the 2nd and 3rd of these points.

Rapid Prototyping

Rapid prototyping technology focuses on reducing the lead times and costs associated with new product development [2]. As a new product is introduced, or as products are updated, various aesthetic and functional designs and tests take place. Somewhere during this process, a physical model is evaluated. Using conventional processes and highly skilled artisans, the construction of this single model can take many days.

Rapid prototyping systems are capable of making highly accurate models, or prototypes, in a very short time. The starting point for such systems is a good quality 3D CAD system. Solid models are constructed using the CAD system and then post-processed in a layer format to make them suitable for the prototyping machines. Models made in this way are therefore limited only by the scope of the CAD system and the resolution and dimensions of the prototyping system. Models can therefore exhibit very complex geometries indeed.

At Nottingham, extensive research is being carried out on various aspects of rapid prototyping. The Rapid Prototyping Research Group has had the opportunity to see the development of this emerging technology as it has made its way across the Atlantic to the UK. The group has been able to log the development from only a few machines in 1990 through to the varied and dynamic industrial and research usage of today.

Since Nottingham University has research groups working on both VR and Rapid Prototyping, it was considered appropriate to investigate where a combination of these technologies might lead. An experiment was devised to discover whether one technology falls within the sphere of the other. In this case, it was considered that VR may only provide the same facility that a rapid prototyping system gives when used with an appropriate CAD system. This would then make VR redundant for product development. The emphasis of the experiment therefore changes slightly to a study of whether VR can provide more than CAD, thus relieving the comparatively expensive rapid prototyping systems of some of the product development burden.

Product Development

Some products are purely functional, whilst others require consideration of aesthetic features to achieve an acceptable design. Designers may possess many technical skills, but they may not appreciate, and be conversant, with computer systems. Even if

they can use CAD tools, the technical elements related to what is ostensibly an engineering environment may compromise their artistic ability. Similarly, functional products (e.g., engine components) may require other aspects of design to be considered. These may not relate to the primary function of the product and the designer may therefore be unaware of their effect. For instance, the product may perform perfectly, but is it accessible to easy assembly and maintenance? Only when a part is put in context can it be seen whether it qualifies on all points. To this end, many products go through a physical modelling phase to prove the design fully.

To overcome the above points of conflict between flexibility in design against functionality in the most efficient manner, several solutions can be put forward:-

- **Use conventional modelling techniques (such as clay and card constructions), then digitise them into a CAD system.** This is a compromise between free design and engineering design but it is expensive and may not be time efficient.
- **Train aesthetic designers in CAD.** Some designers are very proficient in the use of CAD software. Many consider that such systems restrict their ability to freely design products. Products with aesthetic properties (e.g., virtually all consumer products) require much consideration to the design media used.
- **Form teams with both aesthetic and engineering designers in close consultation.** This is perhaps the easiest and most common solution. However, inability to communicate between group members is also common, making this a potentially unstable situation subject to the characteristics of individuals.
- **Improve CAD systems to reduce the skill requirement to operate them.** This is the approach adopted by CAD companies. The solution in part is by providing software tools to perform the same function several ways. However, the CAD environment is always likely to exhibit an engineering bias even if VR based devices are used for the interface.
- **Produce a form of 'digital clay' to allow modelling within a computer based system.** This is the VR company approach. The interactive environment and tools for manipulation are there already. What is lacking is the ability to dimension the product effectively to allow for functional design.

It is obvious that the last two points are linked. CAD systems are being developed with VR based interaction. They are however significantly different from existing VR systems (the compromise being generally attributed to the perennial 'lack of processing power' problem). The panacea would be if VR systems could retain their excellent autonomous and interactive properties, whilst adding advanced graphic definition and sculpture tools. The question therefore evolves into one of whether VR systems should be developed to look more like CAD systems? If they should then careful consideration must be given; not to what tools should be provided, but what features of CAD should be left out to allow free expression in design. Since much is already known about CAD tools this experiment concentrated on whether it was possible to create a 'digital clay' approach using a VR system.

Example Worlds

The experiment required the creation of design environments using the desk top VR system, Superscape. Any preference between desk top and immersive systems was not

made at this stage. This system was available to the research team and was seen to provide sufficient features not to restrict the creation of these environments.

The first product chosen was a water thermostat housing for a small automobile. This product was based on a real design and is one that is very familiar to the Rapid Prototyping Group being the subject of many experiments in the past [4]. This is primarily a functional product being a single mechanical structure, constructed from a few primitive component elements. As can be seen, the product looks representative but is far from accurate. The nozzle and base components can be distorted to provide a range of designs for assessment. If put in context with the rest of the engine, say, the product could be assessed for position and ease of maintenance (figure 1). It is unlikely that anyone will be concerned about the aesthetic appearance of products like this one. It could be assessed in terms of suitability, however, a shorter nozzle could be functionally correct, using less material in its construction. It may however produce unacceptable difficulty when connecting the associated hose pipe. A larger nozzle, in contrast, may make it more difficult to access the mounting bolts.

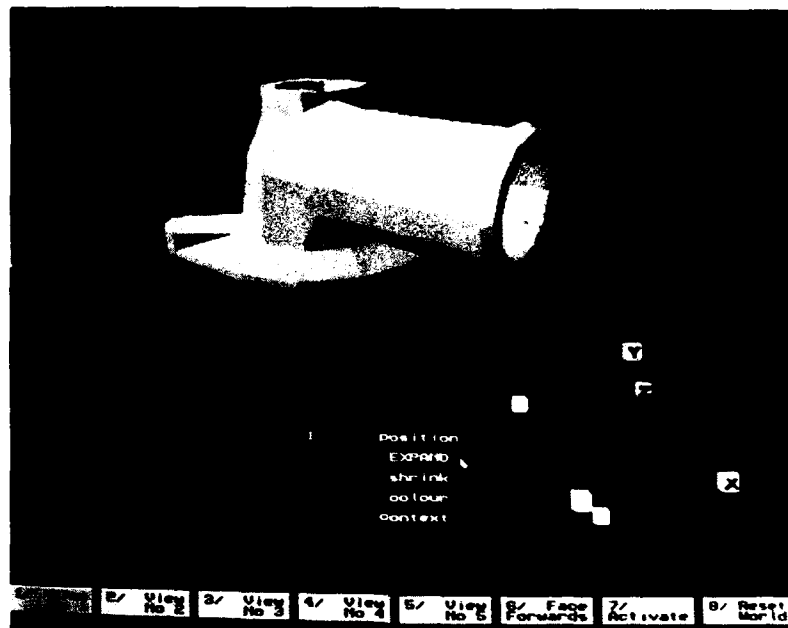


Figure 1 - Complete View of Thermostat Housing

The second example world created was more detailed. This dealt with a product that combines aesthetic attributes with functional elements. The product chosen was the front panel of the 486 computer used to run the VR software. This panel is made up from sub panels that form specialised elements like buttons, disk drives, and LEDs (figure 2). These elements were combined with more general blank features that effectively fill in the gaps. These elements are initially laid out in front of a blank panel that represents the mounting conditions. The designer has the ability to place these components on the mounting panel. It is possible to change the size, shape, position, and colour of each of these elements to assess the effects of different layouts.

This computer panel is a consumer product and therefore must exhibit aesthetic as well as functional features. It is also part of a system that includes the screen, keyboard, and mouse. It must therefore look pleasing within the context of the entire

computer. Views must be acceptable from appropriate angles and each component can be positioned to achieve the best result in many scenarios (figure 3). Assessment of ergonomic features like the clarity of layout and the position and size of control buttons can also be made for different configurations.

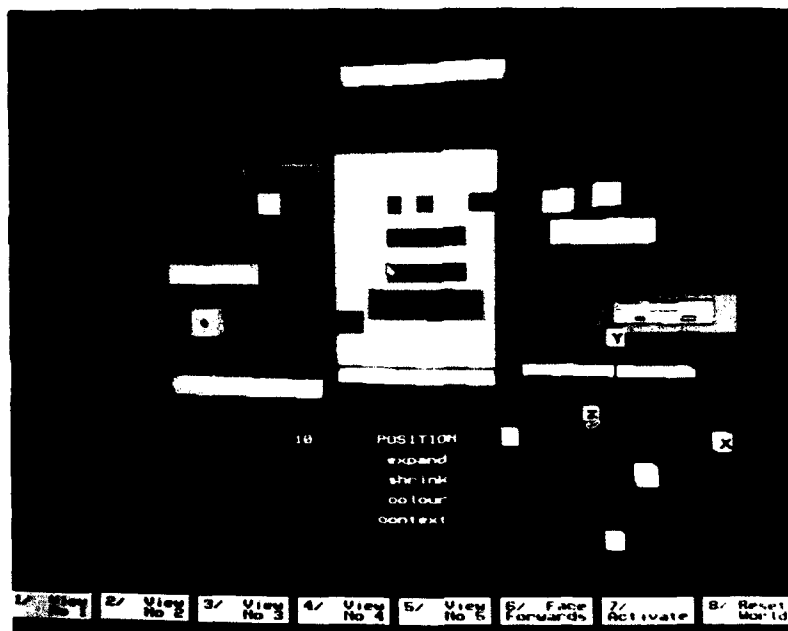


Figure 2 - Base Design System for Computer Panel

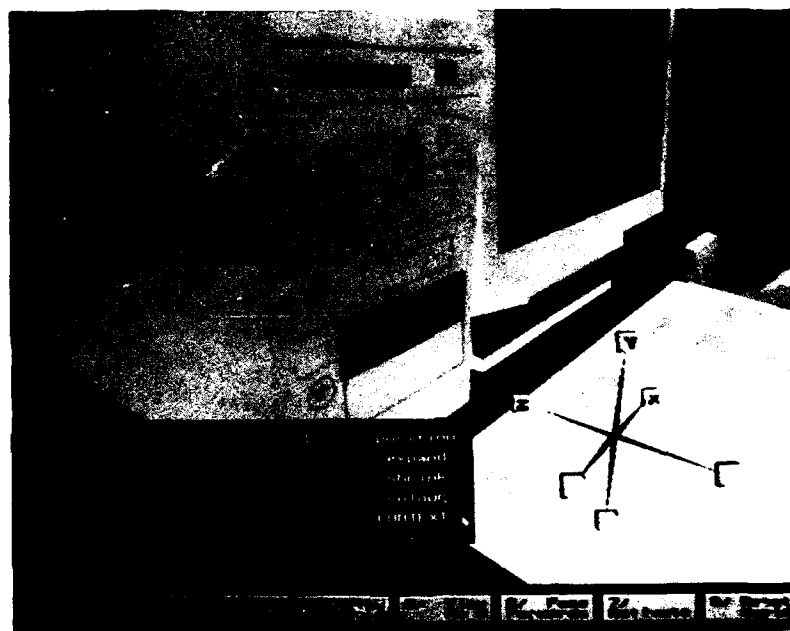


Figure 3 - Completed Computer Panel Placed in Context

The concept of 'digital clay' is more refined in this second case. The elements within the world can be distorted and positioned with ease by merely selecting an item using a mouse driven pointer. The world manipulation controls can then be used to control the attributes of each selected element. The disk drive has greater functionality than the other items and therefore its features are more constrained. Different elements

can therefore be changed with different degrees of freedom, dependent on whether the context of their movement is appropriate.

Experimental Analysis

It was found that the design environments were indeed straightforward to understand, use and manipulate. Rudimentary user trials showed that products could be rearranged with relative ease. Users also adapted to the environment with very little instruction, understanding both the reason for the experiment and the tools provided to change the world. Nobody, however, used the tools to produce products other than the ones designated; a point worth mentioning. These were however initial tests and further more detailed trials are essential to analyze fully its use as well as the necessary requirements for improvement.

In real life, the user performs a more qualitative assessment of the environment by way of comparison between objects within the working context. Quantitative tools were available in the example worlds in the form of readouts of position and size of the components. It was found that people using the worlds did not make use of these tools. The example worlds did appear to form the basis of a useful artistically biased tool for product development. It does not appear that quantitative elements are an essential requirement. What is essential is the ability to interface quickly and efficiently to appropriate CAD systems. These transported object descriptions can then be used by the design engineers and form the basis of an iterative process. Currently, Superscape supports the DXF file format but it is hoped that higher formats will soon be made available.

Further Requirements

There are many features that currently do not exist that a designer would probably prefer in a VR based design tool. Some of these features relate to current limitations in the VR system used whilst others relate more to the example worlds created. The latter are obviously more easy to change under the control of VIRART. Some of these points are more for discussion than specified desired changes.

It is uncertain at this stage whether the example worlds should be context specific. It has already been stated that users did not attempt to design out of context. This may have been because all those who have used the system to date have had an engineering background. An aesthetic designer may have used the system differently but may also consider the example worlds too restrictive. The possible solution could be to present the system at two levels. At the low level is the purely creative environment with no predefined elements. Simple blobs of 'digital clay' can be combined to form more complex structures. At higher levels, objects appropriate to the design context will be provided alongside these simpler elements. The next test will be to provide designers with non context driven tools to see whether they can be used to generate something completely original.

The speed of response and resolution of the system are both inferior to what would ultimately be required. This does not mean however that true, life-like

representations are essential to the working of the system in this context. As the number of facets increases on the screen the speed of response does appear sluggish on what is a comparatively slow machine (PC 486 running at 33MHz). As such for simple objects the speed is probably adequate making it useable in its present form.

So far the examples have not allowed the user to define custom elements. A facility to create new shapes with different shapes, surface features, textures, texts, etc. is desirable. This could constitute a form of digital pen and paper to be used along with the digital clay modelling system. In effect, this becomes CAD meets DTP in 3D.

Continuing on from this point, it is also not possible to manipulate parts as much as would be desired. For example, at present the disk drive cannot be turned on its side. This stands to highlight one of the main differences between desk top and immersive systems. The manipulative ability within an immersive system appears to be more intuitive than a desk top system through its ability to provide more direct contact with the virtual world. With the desk top system, parts are manipulated via the world control tools rather than directly. With an immersive system, the tendency would be to literally grab hold of the object.

Integration with Rapid Prototyping

When the stage is reached where quantitative test data is required then physical prototyping becomes necessary. Rapid prototyping systems shorten this process dramatically making it possible to recoup a significant capital investment in a short period. The operation time of these machines is still significantly long. Generally parts are in a finished, useable state in around 2 days. If all that the part is required for is to assess factors like dimensional fit, accessibility, optimal position, aesthetics, then a system that operates in real time is much more appropriate.

The primary use for rapid prototyping systems is not therefore in qualitative assessment phase of product development. Manufacturers are realising this, and much more use is being made of soft tooling processes (like investment casting) to produce test parts and for short production runs. This is a much more important role for this technology to fill. Competitive marketing policies still dictate that physical models be created for purposes like tendering and user evaluation. VR, with its capacity to model real life provides a practical replacement for rapid prototyping in this sense. VR has the potential to fulfil at least some part of the first 4 uses for rapid prototyping described by Jacobs [2], those of visualization, verification, iteration and optimization. There is no possibility of VR fulfilling the 5th use, that of fabrication. With VR supporting, the more expensive rapid prototyping technology can therefore be considered free to perform the more production related tasks.

The ideal product development environment is therefore a rapid prototyping base supported by CAD systems to supply the engineering detail. VR systems will be linked to the CAD systems that are designated for product development with aesthetic content. A possible layout can be seen in figure 4. This figure also shows the post-processing unit for conversion of CAD solid models into a layer format suitable for the rapid prototyping machine. The ratio of machines is indeterminate but 1 rapid prototyping machine could quite easily support 4 or 5 CAD workstations with perhaps 2 of these working along with

VR software (preferably on the same platform). This ratio of CAD to rapid prototyping machine is likely to be larger where VR is employed.

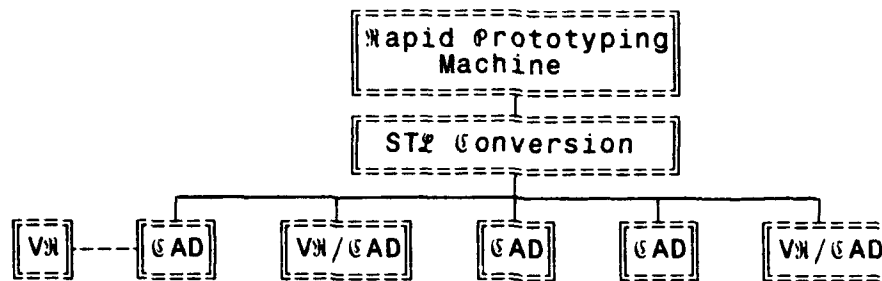


Figure 4 - Proposed Configuration for Optimum use of Rapid Prototyping System

In conclusion, VR is cheaper and less technical to use than rapid prototyping. The turnaround of ideas is much faster with VR and therefore this technology is likely to benefit the aesthetic designer more than the design engineer. VR provides a complimentary technology to rapid prototyping, but the interface is most suitably accommodated through CAD. At some time in the future CAD and VR will merge but not until processing speed has significantly increased to the general user. The potential use of VR does make *some of the intended uses of rapid prototyping* redundant, but it is impossible to use VR beyond the point where testing or production is required. After all, it is only software.

References

- [1] Zelter D., 'Autonomy, Interaction, and Presence', Presence, Vol.1, no.1, 1992.
- [2] Jacobs P.F., 'Rapid Prototyping & Manufacturing', pub. by the Society of Manufacturing Engineers, USA, 1992, ISBN 0-87263-425-6.
- [3] Grimsdale C., 'Virtual Reality: Evolution or Revolution', Proc. 3rd conf, Virtual Reality International 93, VR 93, Olympia, London, April 1993.
- [4] Dickens P.M., Cobb R., Gibson I., Pridham M.S., 'Rapid Prototyping using 3D Welding', Journal of Design and Manufacturing, Vol.3, no.1, March 1993, pp39-44.

Optimization of 2D CT Data Sets for Three-Dimensional Craniofacial Imaging and Modeling

by Richard A. Levy, M.D.¹

Computer-generated anatomic modeling using radiologic data is a well-known entity. Currently, state of the art 3D modeling systems lack the variable thresholding, user interactive, capabilities of 3D imaging software.¹ We investigated clinical parameters - CT scan plane, 2D filter algorithm, surrounding medium - and tested a simple mathematical thresholding algorithm based upon experimentation with a CT phantom, to evaluate a semiautomated approach to 3D craniofacial imaging and model generation. (Figure 1)

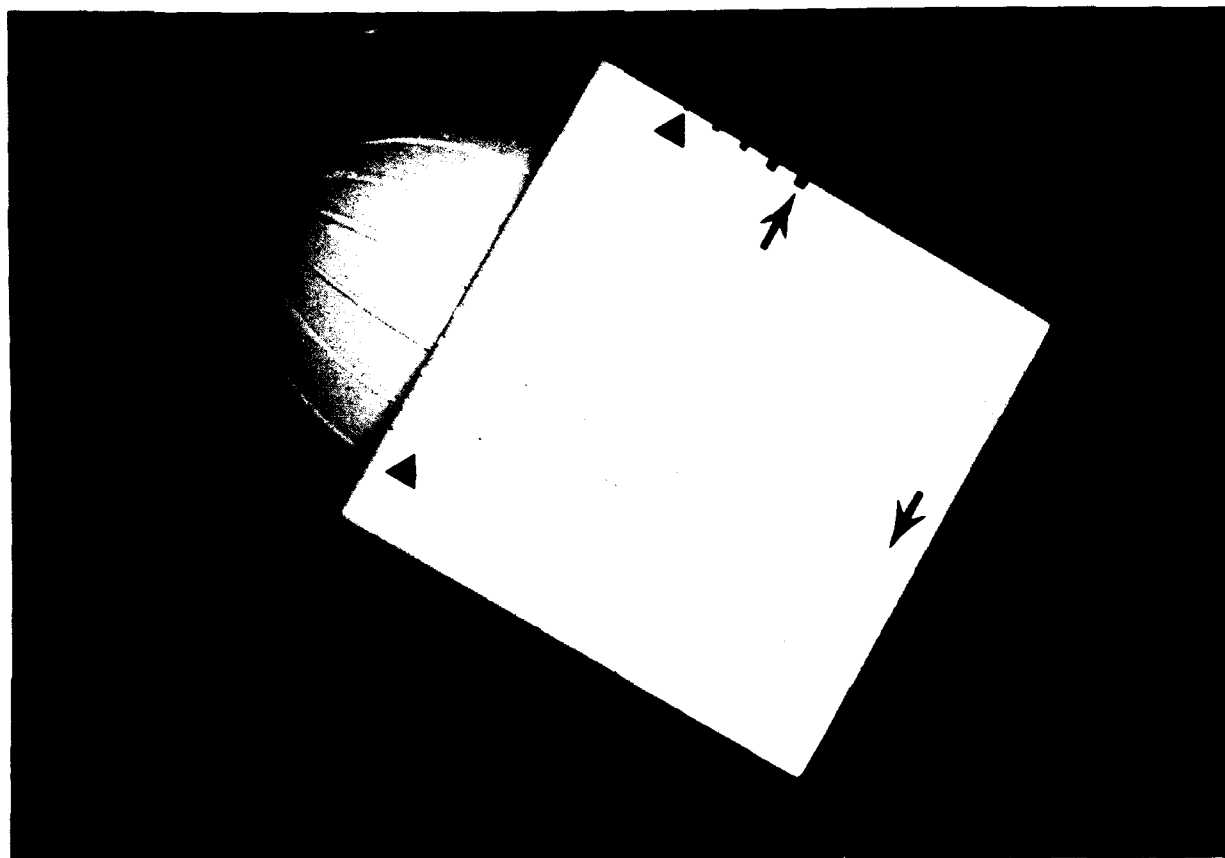
Our investigation indicated that CT scan orientation is a significant determinant of accuracy in 3D image generation. In addition, we propose a simple thresholding algorithm to optimize threshold selection under conditions where only a single threshold value may be utilized - i.e., the generation of anatomic models from craniofacial osseous structures as visualized on CT. This algorithm provides a flexible framework for refining semiautomated thresholding; that is, a coefficient may be modified after further clinical trials (e.g., substituting 0.10 for 0.16 in Appendix I) to better approximate operator-selected thresholds.

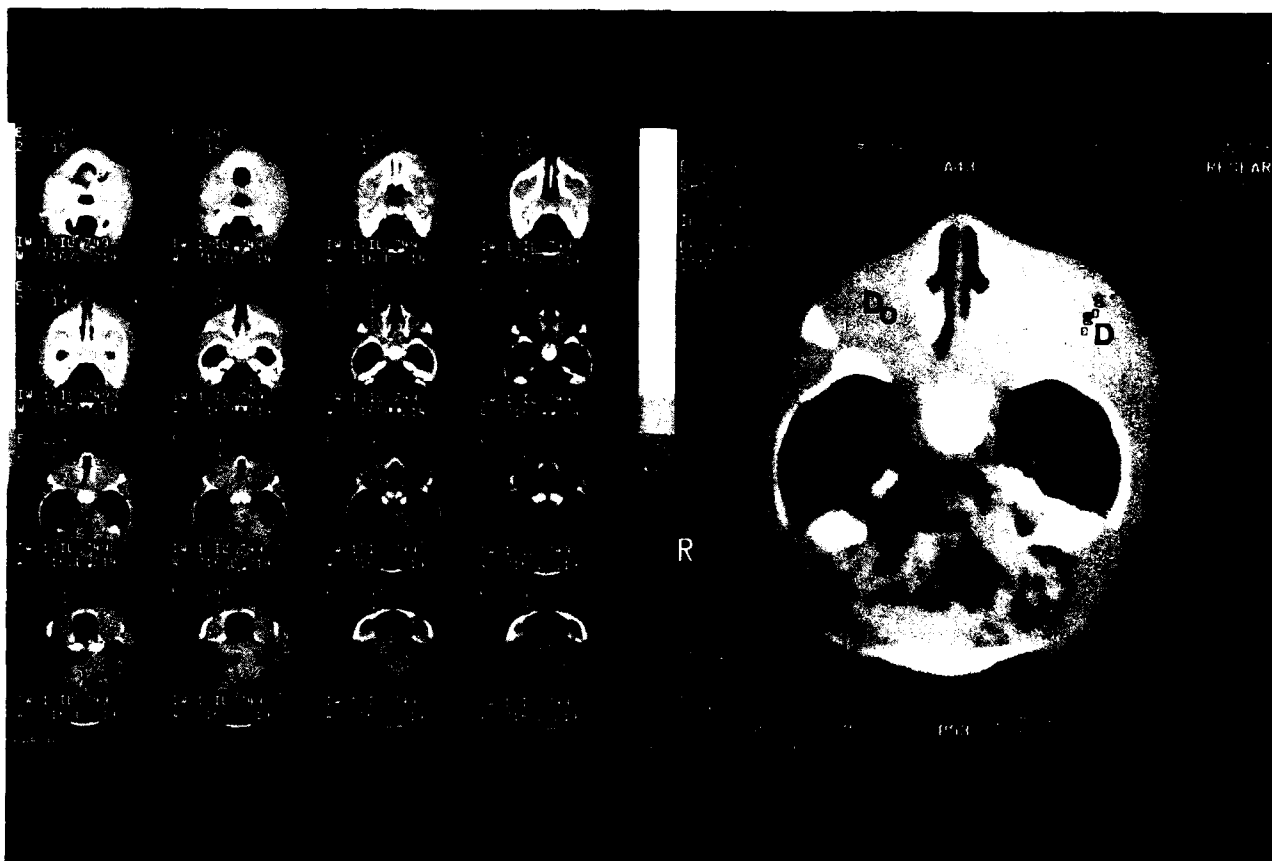
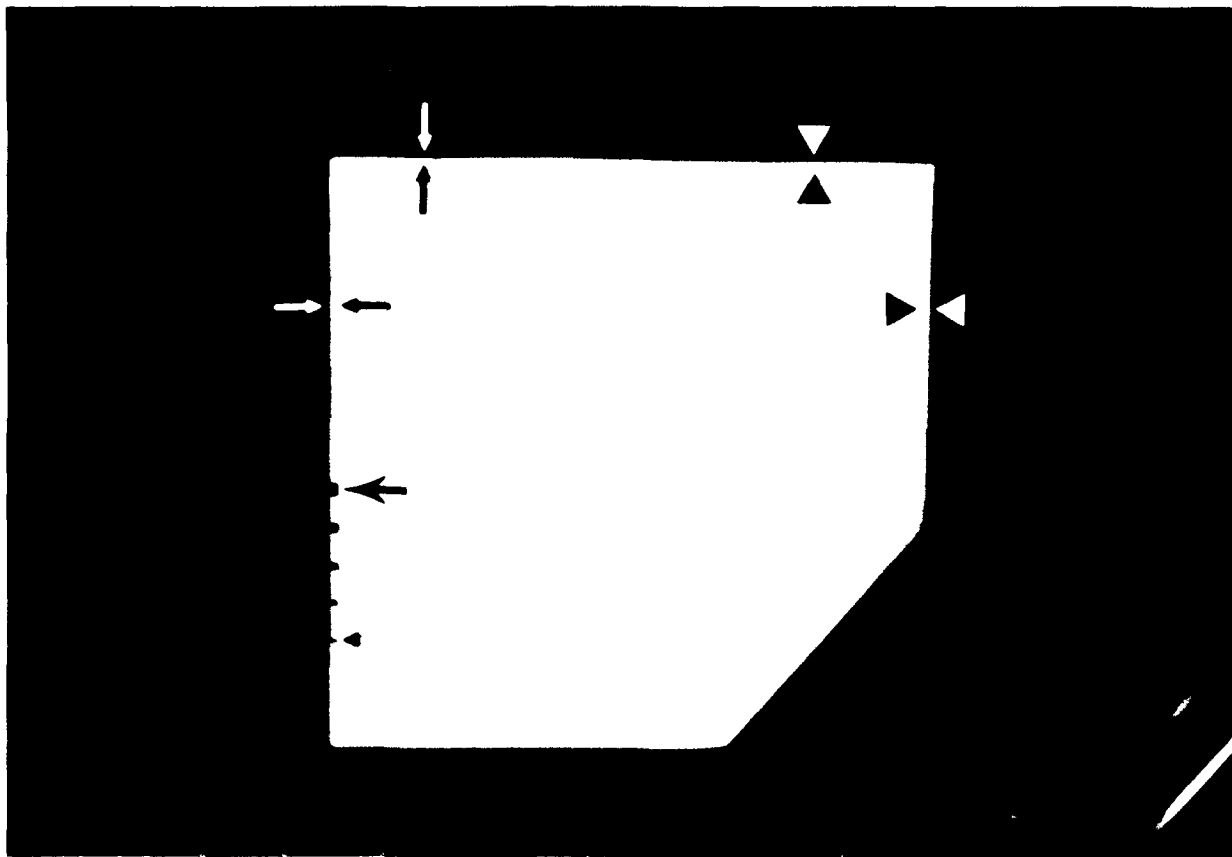
The most significant subjective element in this semiautomated approach is the selection of representative target and background tissues. This task is partially simplified by restricting the anatomic region of interest, and could be theoretically improved by using cluster plot analysis². Since this type of analysis is also subject to variation based upon population distribution of pixel densities, we are confident that an experienced technician or radiologist can select representative target and background densities based upon display options available on current CT scanners

¹ Richard A. Levy, M.D.
Assistant Professor of Radiology
University of Michigan Hospitals
Ann Arbor, MI 48109-0030

(Figure 2). When advances in imaging technology permit instantaneous cluster plot-type analyses of entire CT data sets, our thresholding algorithm could be applied to yield near real-time evaluation of CT data sets for craniofacial modeling.

We conclude that experimentation with a CT phantom can lead to semiautomated three dimensional craniofacial imaging and modeling. Further investigation of 2D CT craniofacial data sets is justified.





Legend to Figures

- Figure 1a** Photograph of a lateral view of the PVC phantom. Black arrowhead indicates slit of 0.375 mm width. Black arrow indicates slit of 1.1 mm width. Intermediate slits range from 0.55 to 0.94 mm.
- Figure 1b** Small black arrowhead and single black arrow correspond to slits in Figure 1a. Paired double black and white arrows indicate 0.375 mm-thick "shelves" forming one corner of the phantom base. Paired large black and white arrowheads indicate 0.75 mm-thick "shelves" forming another corner of the phantom base.
- Figure 2** Generation of 16 two-dimensional CT slices for the purpose of selecting D, the highest density target tissue in the anatomic region of interest. The "Identify" and "Multiply Display" options are used to initially select D which is verified via an ROI cursor (magnified CT image on the right.) In this setting, D_0 = the highest density background tissue in the anatomic region of interest (intraorbital soft tissue), was also selected using the "Multiple Display" option and measured with a ROI cursor.

References

1. Levy RA, Guduri S, Crawford RH. Preliminary experience with selective laser sintering models of the human temporal bone. AJNR (in print)
2. Kohn MI, et al. Analysis of brain and cerebrospinal fluid volumes with MR imaging. Radiology 1991; 178:115-122.

Appendix I

Since $T = (0.16) |D-D_0| + D_0$ for $|D-D_0| > 200$ HU

and $T = (0.5) |D-D_0| + D_0$ for $|D-D_0| < 80$ HU

a parametric expression for $80 \leq |D-D_0| \leq 200$ combining the above expressions was developed:

Thus $T = (t) [(0.16)(|D-D_0|) + D_0] + (1-t) [(0.5)(|D-D_0|) + D_0]$ for $80 \leq |D-D_0| \leq 200$

* Let $C = |D-D_0|$

Then $T = C[(0.5) - (0.34)(t)] + D_0$

When $t = 0$, $C \leq 80$

When $t = 1$, $C \geq 200$

Thus $t = (0.008) (C) - 0.64$ and

$T = C[(0.5) - (0.34)[(0.008) (C) - 0.64]] + D_0$

$= D_0 + (0.73) (C) - (0.003) (C)^2$

$= D_0 + (0.73) (|D-D_0|) - (0.003) (|D-D_0|)^2$

for $80 \leq |D-D_0| \leq 200$

HU = Hounsfield Units

Some Efficient Procedures for Correcting Triangulated Models

I. Mäkelä*

A. Dolenc

Helsinki University of Technology

Institute of Industrial Automation

July 1993

Abstract

This paper describes methods for handling efficiently a large class of problems encountered when dealing with 3D models represented by a collection of triangles in STL format. In spite of its drawbacks, the STL format has become a *de facto* industrial standard for transferring models to manufacturing processes generally known as Rapid Prototyping Techniques (RPT) or Solid Freeform Fabrication (SF²). As the accuracy and size of the workspace of such processes increases, so does the size of the models one wishes to manufacture. Therefore, the efficiency of application programs is an important consideration. Previous published work has focused on the problem of eliminating gaps in triangulated models. In addition to efficiency, this paper describes methods for dealing with other problems such as overlapping triangles and intersecting triangles. The algorithms have been implemented and tested in industry. The underlying data structures based on adaptive space subdivision also allow the development of other efficient tools such as slicing.

1 Introduction

Data transfer between CAD systems and RP processes is mainly based on data exchange formats capable of representing faceted models. The current *de facto* standard is the STL format [1] which allows one to represent triangulated models, *i.e.* each facet is a triangle.

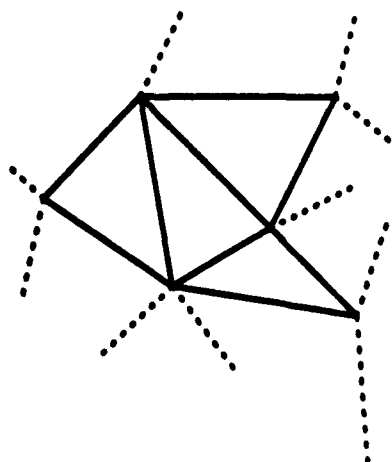


Figure 1: A correct triangulation.

In order for models to be correctly manufactured they must represent a collection of one or more non-intersecting solids. The manufacturer hopes to receive "well-behaved" STL-files such as the one outlined in Figure 1. In a correct STL-file, each triangle has exactly one neighbour along each edge and triangles are only allowed to intersect at common edges and vertices. Under these conditions, it is possible to distinguish precisely the inside from the outside of the model.

*Otakaari 1, SF-02150 Espoo, Finland. Tel:+358-0-4513372. Fax:+358-0-4513293. Email (Internet): ima@cs.hut.fi.

Unfortunately, quite often incorrect faceted models are used. The mistakes can be numerous (Figure 2). The models can contain **gaps** due to missing facets, facets may intersect at incorrect locations, the same edge may be shared by more than two facets, etc. Special cases of these errors may occur that require separate treatment, e.g. overlapping facets (coplanar facets whose intersection results in another facet). The reasons for such errors are related to the application that generated the faceted model, the application that generated the original 3D CAD model, and the user. Many STL interfaces in CAD systems fail to inform the user that the result is not correct and problems remain undetected until the manufacturer attempts to process the model.

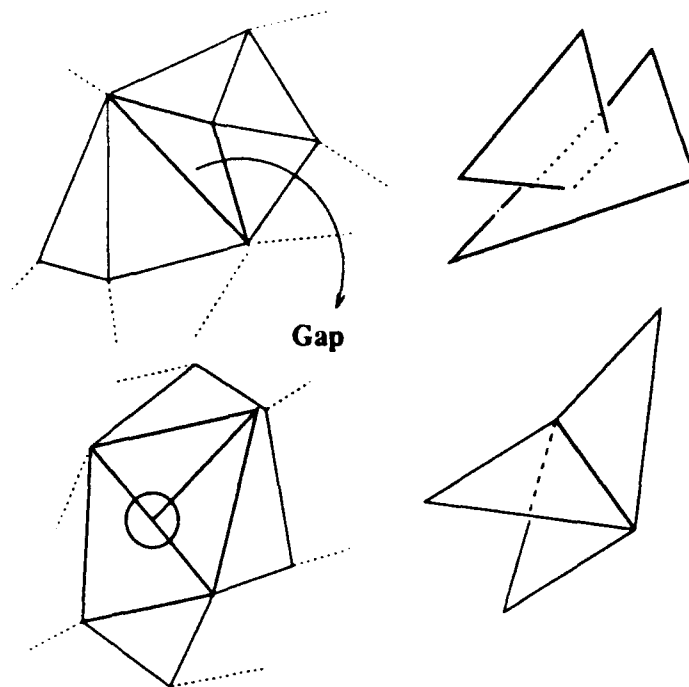


Figure 2: Incorrect triangulations.

The objective of this paper is to describe efficient algorithms for (i) verifying if the model is correct, (ii) detect the mistakes in the model, and (iii) automatically correct as many mistakes as possible. Additional requirements are portability and user friendliness, the latter implying that the parameters should be easy to understand and have a predictable effect on the output.

The paper is organized as follows. One of the key aspects are the data structures used so we begin with their description in Section 2. Next, in Section 3 we outline the algorithm used to process an STL-file. The algorithm for determining the **topology** of the model—i.e. the neighbours of a given triangles along its edges—is described in Section 4. Determining the correct orientation of the triangle normals—a requirement of the STL format—is described in Section 5. Detecting incorrect intersection and the handling of special cases of overlapping triangles is described in Section 6. Section 7 outlines a gap elimination algorithm for a restricted class of gaps. Related and future work is discussed in Section 8 and, finally, we state our conclusions in Section 9.

2 Data structures

Efficient handling of large geometrical data sets requires special data structures. We use an adaptive space subdivision scheme that reduces the amount of browsing involved when searching for objects nearby a given object, and adopted a method that is a variant of *quadtrees* [9]. The system is called *the CELL space subdivision system* (other data structures are also suitable for this application [9, 10]).

A bounding box, or *space*, surrounding the objects must be known in advance. Associated to each object is a bounding box of dimension n . The space is subdivided into smaller regions, or *cells*, until either each cell contains at most N objects or the depth of the subdivision reaches a maximum D . The subdivision is done by splitting the cell using iso-oriented hyperplanes of dimension $n - 1$ ¹ and always at the midpoint. The direction alternates at each level of subdivision.

¹The hyperplanes will correspond to lines in two dimensions and planes in three dimensions.

Figure 3 illustrates a space subdivision with six objects, $n = 2$ and $N = 3$. A suitable data structure for representing the space subdivision is a tree. In the example shown, white nodes are the internal nodes and the black nodes are the leaf nodes, or simply *leaves*. The information stored in the nodes is very simple. The internal nodes contain only pointers to the subtrees; it is not necessary to store bounding boxes or splitting directions because this information can be derived as the tree is searched. The leaves contain simply an array of pointers to the objects.

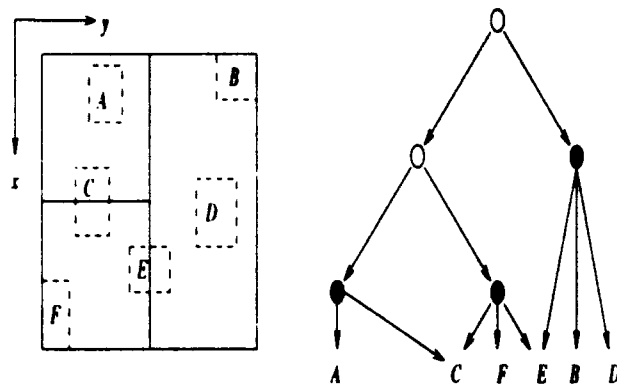


Figure 3: An example space subdivision and tree representation.

Finally, objects contain a bounding box, a query number and a reference to user data. Suppose a query Q , a rectangle, intersects the bounding box of object E . In order to avoid E being reported twice, the queries are numbered and objects that are reported by a given query are assigned the same number. If an object already has the same number as the current query then it is ignored. The query numbers of all objects would have to be reset only when the query counter overflows, an unlikely event if the platform uses 32-bit integer arithmetic.

When inserting a new object, it may happen that it is impossible to subdivide a cell such that only N objects remain, e.g. if $N + 1$ triangles share the same point. The default action is to subdivide until a maximum depth D is reached. Alternatively, the application programmer can supply a boolean function *Subdivide?* that will browse the objects and determine if it is worth attempting the subdivision.

Searching such a data structure is efficient because the number of possible neighbour candidates is usually small. We only have to check nearby objects, instead of going through the entire collection. Furthermore, in our applications the data structure is semi-static. After initial object insertion, objects added to the data structure do not change significantly the original bounding box of the space, and very few deletions are done. Thus, no reorganization of the data structure is needed during the processing.

Interface

The interface consists of four functions. *CellInit* creates the data structure according to the set of parameters already mentioned earlier, namely the bounding box, maximum cell occupancy, and maximum depth. *CellInsert* and *CellDelete* are used to update the data structure. Finally, *CellQuery* is a function that takes as arguments a bounding box and a query number and it returns a list of all objects that intersect the given bounding box.

Analysis

In general, the size of a CELL data structure is bounded by $O(2^D + n)$, where n is the number of objects. In our applications, we set D equal to $\lfloor \log_2 (\lfloor n/N \rfloor) \rfloor + 1$, so the size is bounded by $O(n)$ and the height of the tree by $O(\log n)$. Regarding the computation time for updates and queries, so far we have not made any attempt to analyse the complexity of the worst and average cases. However, experiments indicate that the performance is excellent.

Application-dependent data structures

Triangle records are referenced with an application data pointer from the CELL objects. The triangle record has pointers to the vertices and to the edge-neighbors. A field is reserved for a normal vector and a reference counter for memory management. The vertices are indicated by a set of pointers, $\{v_0, v_1, v_2\}$. Edge i is defined by the vertices $v_{i \bmod 3} v_{(i+1) \bmod 3}$, and associated to each edge is a pointer n_i to the corresponding neighbouring triangle.

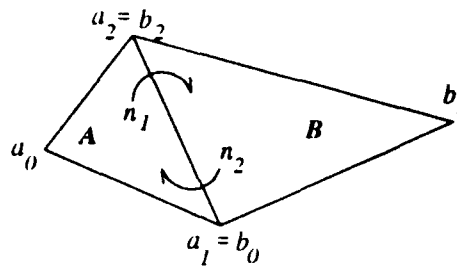


Figure 4: Two neighbouring triangles A and B.

The data associated to each vertex consist of three floating-point values defining the xyz -coordinates, a reference counter and a vertex id.

3 Outline of the algorithm

The CELL data structure is very flexible in the sense that when one is equipped with such a data structure there are various solutions to the problems laying ahead. We have chosen those that favour minimizing memory resources at the expense of computation time.

Before the CELL structures can be initialized, it is necessary to read the input file to gather the required information, *i.e.* the bounding box enclosing the model and the number of triangles. Next, two CELL structures are created, namely *TCell* will contain objects associated to the input triangles, and *ECell* will contain the edges with no neighbours and is used to construct the gaps. The user may supply the maximum occupancy for each of these CELL structures to override the internal defaults. Based on the maximum occupancy, the depth of the associated trees is bounded by a suitable constant to obtain a balance between the main resources, namely memory and computation time.

The first stage evaluates the topology of the model, detects gaps, exact duplicates, and degenerated triangles. *TCell* is used to collect vertices that are equal within a tolerance ϵ . Once the vertices have been merged and values have been assigned to the pointers v_i , then we proceed to detect the **edge-neighbours** and assign values to the pointers n_i . The triangle is now ready to be inserted into *TCell*. After all triangles have been inserted, it is possible to determine the existence of gaps but not their actual description.

The direction of the normals is now evaluated because this information is needed for correcting the gaps and other errors that might be detected subsequently. The next stage consist of verifying the model. The description of the gaps is evaluated and errors such as improper intersections and overlapping triangles are also detected. Some of these errors can be corrected whereas others can only be reported. Once errors have been corrected, the normals are oriented again because if gaps where present it is possible that the first orientation is incorrect. In fact, if the gaps have not been all eliminated, it is not possible to guarantee that the second attempt is successful either. Finally, the triangles and a description of the errors are written to files in the required format.

4 Creating the topology

Creating the topology for a model consists of collecting for each triangle t neighbourhood information about t . More specifically, it consists of detecting the triangles that share common vertices and edges with t . Naturally, the first step is to begin with the vertices.

4.1 Detecting vertex-neighbours

Let us assume that all triangles inserted so far into *TCell* have their corresponding v_i pointers already initialized to correct values. (In the sequel, the Euclidean coordinates of an unprocessed triangle are denoted V_i as opposed to the associated pointer which is denoted v_i .)

For each vertex $V_i \in t$ we apply the following procedure. The bounding box $BB_i \doteq \text{BoundingBox}(V_i) + \epsilon$ is evaluated, where ϵ is a small constant to account for rounding errors that probably occurred when the model was created. Next, the set of triangles $V\text{NeighbourCandidates} \doteq \text{CellQuery}(TCell, BB_i)$ is evaluated. The vertices V' of all triangles $t' \in V\text{NeighbourCandidates}$ are searched to find the closest one to $V_i \in t$. Once found, the associated pointer is assigned to v_i .

If a triangle collapses to a line or a point then it is deleted and is not inserted into $TCell$.

4.2 Detecting edge-neighbours

If a little more effort is done while finding the vertex-neighbours then enough information can be made available to easily detect the triangles that share a common edge with t . Let V_{min} be the closest vertex to V_i evaluated by the procedure outlined above. Since the entire set $V\text{NeighbourCandidates}$ is searched one can collect the triangles that already share the same pointer v_{min} .

Let us say that these triangles are placed in a set denoted by VN_i . For each $k = 0, 1, 2$ we compute $I \doteq NV_k \cap NV_{k+1 \bmod 3}$. If $|I| = 0$ then the neighbour of t along the edge k either does not exist or has not yet been inserted in $TCell$. In this case, no further action is taken. If $|I| > 1$ then a possible error condition has been detected, namely an edge is being shared by more than two triangles. The edge is tagged accordingly and the tag will be cleared if another edge from another triangle matches it. Edges shared by $2n$ triangles with $n > 1$ are reported as **warnings** whereas edges shared by $2n + 1$ triangles with $n \geq 0$ are reported as **errors**. We call the latter **odd-edges**. Finally, if $|I| = 1$ then the neighbour of t along edge k has been found. The pointer n_k is set equal to v_{min} and a global counter, *EdgeHit*, is incremented by one.

After all triangles have been inserted into $TCell$, the value of *EdgeHit* must equal $3N$, where N is the number of triangles. If $EdgeHit < 3N$ then the entire set of triangles is searched for the **odd-edges**. These are placed in $ECell$ for subsequent use during the gap elimination stage. Before a triangle is inserted, though, we verify if it is an exact duplicate, i.e. if all pointers n_i have the same value. In this case, the triangle is discarded because it is likely that it is the result of duplicate or coincident surfaces².

5 Orienting the triangles

An initial triangle t_0 is chosen arbitrarily and a queue of triangles U is initialized. A ray is cast in the direction of the normal vector \vec{N}_0 of t_0 . The direction of \vec{N}_0 is determined by the number of intersections between the ray and the model. The vertex pointers v_i are reordered according to the specifications of the STL format which states that as the fingers of the right-hand follow the vertices the thumb must be pointing towards the outside of the model. $TCell$ is used to minimize the number of ray-triangle intersection tests. Only the triangles that are located in cells that are hit by the ray need to be taken into consideration.

Once a triangle t has been oriented, all its edge-neighbours that have not yet been processed are placed in the queue U , if not already there. The next triangle to be processed is the one at the head of the queue. When the queue is empty we verify if all triangles in the model have been processed. If not then the next unprocessed triangle t'_0 is again chosen arbitrarily and the same procedure is applied once more.

At this point, we would like to introduce the concept of a **component**. Loosely speaking, a triangle t belongs to the same component as t' if one can be reached by the other by "walking" along edge-neighbours. (For precision purposes we include the following definition using concepts from Graph Theory. Let $G = (V, E)$ be a graph where each vertex $v \in V$ corresponds to a triangle and an edge $e = vw$ with $v, w \in V$ is an edge of G if the triangle associated to v is an edge-neighbour of the triangle associated to w . Because the property is reflexive, G is an un-directed graph. In a sense, the graph G is the "dual" of the triangulated model. A *path* in G is any connected set of edges. Two vertices are said to be in the same component C of G if a finite path can be found between them. Two triangles t_v and t_w are in the same component if the associated vertices $v, w \in V$ are in the same component of G . Finally, notice that the algorithm above corresponds to a breadth-first search—BFS, for short—on the graph G .)

²In some cases, discarding both is a better alternative.

Clearly, a "by-product" of the above algorithm is the set of components of the model. This information will be useful to detect more efficiently errors such as improper intersections.

It may happen that the orientation of a triangle is not consistent with all its neighbours. This happens when the model contains a non-orientable component such as a Moebius strip. The user is notified of such errors but no attempt is made to correct them.

It is possible to avoid one ray casting operation by choosing a suitable triangle as the first one. Let t_0 to be a triangle that is not parallel to the xy -plane and that touches the bounding box of the model. If the model is correct then such a triangle must exist. Let $V \in t_0$ be a vertex that touches the bounding box. Then the xy -projection of $\vec{V} + \vec{N}_0$ must be outside the projection of the bounding box onto the xy -plane. Experiments indicate that, in our case, this method did not improve significantly overall execution times.

We draw the attention of the reader to the fact that if the model is incorrect then it is not possible to guarantee that the direction of the normals is correct. However, one can state that the normals of the triangles associated to the same component are oriented consistently. This property is sufficient for correcting some errors in the model.

6 Checking the model

Errors are categorized into three classes. **Gaps** are detected during topology re-construction and their handling is described in the following Section. **Improper intersections** may exist even if no errors were detected in previous stages of the algorithm. **Overlapping triangles** are a special case of intersections and are dealt with separately. One type of overlapping triangles, namely duplicate triangles, was already dealt with during topology re-construction. Two triangles t and t' intersect improperly if their intersection is a line segment that does not correspond to a common edge. On the other hand, they overlap if their intersection is a facet.

These errors are expensive to detect and report even when using the CELL data structure. The first stage treats each component C of the model separately. The second stage handles pairs of intersecting components.

The first stage is as follows. For each triangle $t \in M$ the set

$$ICandidates \doteq CellQuery(TCell, BoundingBox(t))$$

is evaluated. The triangle t is checked for errors against those triangles in $ICandidates$ that are in the same component as t . In the case of improper intersections, one can also exclude the neighbours of t .

The second stage uses a CELL structure called $CCell$. The objects in $CCell$ are associated to the components of the model. For each component C the set $CCandidates \doteq CellQuery(CCell, BoundingBox(C))$ is evaluated. Next, for each $C' \in CCandidates, C' \neq C$ the following procedure is applied. The bounding box $I = BoundingBox(C) \cap BoundingBox(C')$ is evaluated. We now take from $TCell$ the triangles enclosed by this bounding box, i.e. the set $T = CellQuery(TCell, I)$ is evaluated. Finally, the triangles in this set that belong to the component C must be checked against those of C' , and vice-versa.

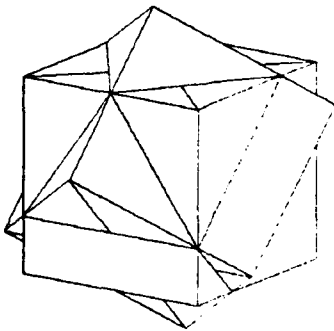


Figure 5: An incorrect model with improper intersections.

Consider the model shown in Figure 5. Each box forms one component. Although each box in isolation is correct, together they form an incorrect model because the result is ambiguous. Additional information from the user would be needed to correct the model and, therefore, improper intersections are reported but no attempt is made to correct them.

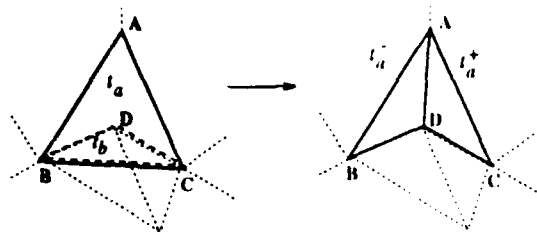


Figure 6: Special case of overlap removal.

Figure 6 illustrates a special case of overlapping triangles that is corrected. One of the overlapping triangles, $t_b = BCD$, is removed whereas another one, $t_a = ABC$, is split in two. This situation can occur for various reasons, e.g. it can be caused by errors in the triangulation of parametric surface models [5].

7 Filling gaps

A gap is a closed polyline composed of odd-edges. It is easy to find the gaps using the *EC*ell mentioned in previous Sections. However, filling the gaps, or gap elimination, poses many difficulties. One problem is choosing a set of “user-friendly” parameters. Another problem—which has no hope of being fully automated—is filling the gaps such that the original intentions of the designer are preserved. It cannot be fully automatic because given a model with more than one gap, it is not possible to decide algorithmically if triangles should be added such that each gap is filled separately or such that the gaps are joined. Finally, regardless of which choice is taken, we must find a method that adds triangles such that the result is a valid model.

The method we describe here can be applied to one individual gap. Triangles are added to the gap until it is closed or user-supplied tolerances prevent triangles from being added.

Consider a closed polyline P with n vertices, v_0, v_1, \dots, v_{n-1} , where $v_0 = v_{n-1}$. The distances d_{i-} and d_{i+} attached to a vertex v_i are the distance between the vertex v_i and vertices v_{i-2} and v_{i+2} , $d_{i-} = v_i - v_{i-2}$ and $d_{i+} = v_i - v_{i+2}$, respectively. Vertices are sorted in ascending order according to the smallest distances d_{i-} and d_{i+} , $i = 0, \dots, n-1$. Let us assume that the distance d_{i+} was the smallest. The triangle $t_{i+} = (v_i, v_{i+1}, v_{i+2})$ is added if the normal direction of the new triangle does not differ too much from the normals of those triangles which contribute to the edges $v_i v_{i+1}$ and $v_{i+1} v_{i+2}$. When a triangle is added to the model, one vertex is removed from P and all distances are re-evaluated for the remaining points in the polygon. In the above example, if the triangle t_{i+} was added then the point v_{i+1} is removed. The procedure is applied until the polyline P “shrinks” to a polyline with only five vertices or tolerances prevent further triangles from being added. The latter occurs when the smallest distance is greater than a user-supplied tolerance t_g . If P has only five vertices then it is triangulated using two triangles such that the area of the result is minimized.

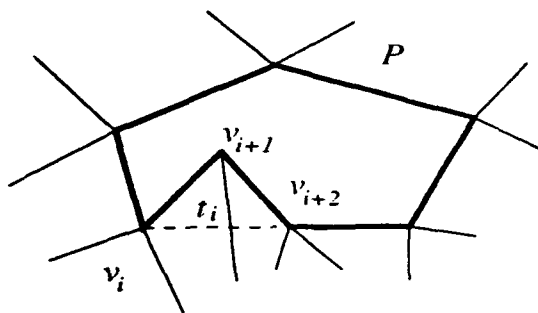
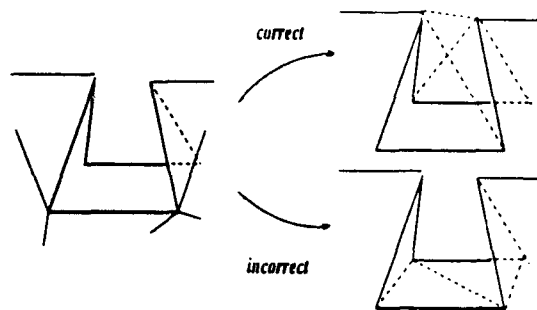


Figure 7: An erroneous fill triangle t_i .

The procedure uses an additional parameter t_a . This parameter is an upper bound on the angle between the normals of the original triangles and the fill triangles. Its main purpose is to avoid “cusps”, i.e. to create a smooth blend to fill the gap. It minimizes the chances of adding a triangle that will overlap or intersect neighbouring triangles. Consider the situation in Figure 7. Without normal checking, the algorithm might suggest to add the triangle t_i which is clearly an error.



Another example is shown in Figure 8. If the normals are taken into account then better results are usually obtained. The default value for t_a is 90 degrees.

Figure 8: The effect of using normal information.

8 Related and future work

Rock [8] described a method for generating topological information from an STL-file. The fundamental difference is the use of AVL-trees for vertex matching. Apparently though, this data structure is not appropriate for range queries [9] (e.g. *CellQuery* is an implementation of n -dimensional range queries). "Back-pointers" from merged vertices to the associated triangles are used to detect edge-to-edge relationships. We chose not to use such pointers in order to economize memory resources. A method for orienting the triangles is not described.

Barequet [2] describes the best method (so far) for eliminating gaps in faceted models. One of the ideas exposed is the use of global information to verify if adding a given set of facets would result in a valid solid. If the set fails this test then another one is taken until either a successful set is found or such a set cannot be computed such that tolerances are respected. The method used for finding an alternative set of matches is efficient. It is certainly an idea that could improve the algorithm described in this paper but significant changes would be necessary. The method described in this paper for filling gaps utilizes only local information.

Bøhn [3] categorizes gaps into five classes. Unlike Barequet, the gaps are apparently oriented prior to gap elimination. Gaps can be merged or connected if they share a common vertex and are located in different components (shells). In our opinion, this is not a general criterion. The method for adding triangles to fill the gap does not take into account the shape of the neighbouring triangles. The algorithm does not use any user-supplied tolerances although it is not difficult to include them in the algorithm described.

The problem of generating a triangulation to fill a gap can be related to the more general problem of generating a faceted model from a set of 3D points. In the case of gap elimination, some of the edges are already given. In this more general setting, O'Rourke [7] describes a method for generating a polyhedra of minimal area given a set of 3D points.

The algorithms described in this paper have been implemented by one of the authors and tested with numerous models from industry. It incorporates all the features described in this paper. It is written using the C language and is highly portable, being available on several different platforms. Several output formats are supported, namely binary and ASCII STL, Personal Visualizer WAVEFRONT (OBJ format), and IGES. Diagnostics (description of the gaps, non-manifold edges, improper intersections, etc) are reported in VDA-FS format. Full details can be obtained elsewhere [6]. The implementation is available as commercial product.

The CELL data structure has been used to implement other algorithms such as gap elimination in parametric surface models [4] and slicing.

We are exploring the possibility of using secondary storage to handle models with $O(10^4)$ triangles. The algorithms described in this paper could be easily generalized to facets but a significant portion of the implementation would need re-writing. Besides, our feeling is that the limits of a non-interactive tool have been reached and that the greatest benefits are to be gained by implementing appropriate interactive tools.

9 Conclusions

In this paper we have presented an efficient algorithm for handling polyhedra models represented in STL format. An algorithm for filling individual gaps that takes into account the shape of the neighbouring triangles was presented. In addition, we have explained how to generate the topology of the model, orient the facets, and detect all errors that can occur in the description of a model in addition to gaps. Special cases of these errors are automatically corrected. The efficiency of the algorithms is based on the usage of good data structures, namely binary trees associated to spatial subdivision. The algorithm has been successfully tested in industry and proven useful.

We would expect productivity to improve if a better data exchange format replaced the STL-format. Not that the problems discussed here would simply vanish; rather they would be minimized and occur less frequently. The "quality" of a model represented in a neutral file format is directly related to the capabilities of the format, the tool used to convert the model to the given format, and the user. Due to user expectations regarding RPT, it will always be necessary to verify and correct models regardless of the format chosen for data transfer.

10 Acknowledgements

This work was done within the INSTANTCAM project, an European Consortium of partners from both industry and research centers. Although not all partners have been directly involved in software development, they have all contributed in some way, either with suggestions, support, patience, or testing of the tools. The partners are, in alphabetical order, BIBA (G), Black&Decker GmbH (G), Danfoss A/S (DK), the Danish Technological Institute (DK), E&D Design (SF), Helsinki University of Technology (SF), Instituto Superior Técnico (P), NTH-SINTEF Production Engineering (N), Raufoss A/S (N), Oy Saab-Valmet Ab (SF), and Wilhelm Karmann GmbH (G). At HUT, we received the financial support of TEKES.

References

- [1] 3D Systems, Inc. *Stereolithography Interface Specification*, July 1988.
- [2] G. Barequet and M. Sharir. Filling Gaps in the Boundary of a Polyhedron. Under preparation, 1993.
- [3] J. H. Bøhn and M. J. Wozny. Automatic CAD-model Repair: Shell-Closure. In *Proceedings of Solid Freeform Fabrication Symposium*, pages 86–94, Austin, Texas USA, 1992.
- [4] A. Dolenc. Rapid recipes for parametric surface models. Submitted to *Computer-Aided Design*, 1993.
- [5] A. Dolenc and I. Mäkelä. Optimized Triangulation of Parametric Surfaces. Technical Report TKO-B74, Helsinki University of Technology, 1991. To be published in *Mathematics of Surfaces IV*.
- [6] Helsinki University of Technology, Otakaari 1, SF-02150 Espoo, Finland. *TR2STL User Guide, Opus 1.9d*, January 1993.
- [7] J. O'Rourke. Polyhedra of Minimal Area as 3D Object Models. In A. Drinan, editor, *Proceedings of the 7th Joint Conference on Artificial Intelligence (IJCAI-81)*, volume II, pages 664–666, August 1981.
- [8] S. J. Rock and M. J. Wozny. Generating Topological Information from a Bucket of Facets. In *Proceedings of Solid Freeform Fabrication Symposium*, pages 1–15, Austin, Texas USA, 1992.
- [9] H. Samet. *The Design and Analysis of Spatial Data Structures*. Addison-Wesley Publishing Company, Inc., 1989.
- [10] M. Tamminen and R. Sulonen. The EXCELL Method for Efficient Geometric Access to Data. In *ACM/IEEE 19th Design Automation Conference*, pages 345–351, June 1982.

ROBUST PROTOTYPING

Jana K. Chari
Dr. Jerry L. Hall

Department of Mechanical Engineering
Engel Manufacturing Laboratory
Iowa State University
Ames, IA 50011

Submitted for Publication in
Solid Freeform Fabrication Symposium, The University of Texas, Austin
August 1993

ABSTRACT

This paper presents a new prototyping system consisting of a computer interface based on IGES standard to represent and path plan objects with precise curve and surface definitions and a laser-metal deposition process for the prototype fabrication. The advantage of using the Non-Uniform Rational B-Splines (NURBS) data instead of the traditional triangular data is that it requires fewer data conversions as most standard analytical shapes (like lines, conics, circles, planes and quadratic surfaces) as well as free form curves and surfaces are represented with one common underlying mathematical form. By addressing this issue of improved data representation on the CAD file front-end and an improved processing technique, this research will significantly impact the output of rapid prototyping with functional parts of improved tolerance and surface finish capabilities. A detailed description of the implementation of the computer interface on different hardware platforms and an outline of the fabrication process are presented. We conclude that NURBS interfacing technique is a robust mathematical technique and offers great potential for precise rapid prototyping.

1. INTRODUCTION

Many engineering design and manufacturing situations involve the evolution of a new product and a rethinking of many manufacturing activities. The CAD systems allow designers to routinely develop computer models of parts to be fabricated. When coupled with CAM capability, the part specifications can be down loaded directly to the manufacturing equipment. Currently, several processes such as selective laser sintering, 3D laser cutting of sheet metals, stereolithography and rapid prototyping or solid freeform fabrication use such CAD/CAM systems. One advantage is the speed at which a conceptual design is converted to a form testable prototypes. Robust prototyping is one such challenging fabrication technique to convert conceptual designs to testable functional parts.

2. TECHNICAL BACKGROUND AND LIMITATIONS

The state-of-the-art systems currently available for solid freeform manufacturing perform many of the fabrication functions required. However their limitations include:

1. Metal parts have not been produced rapidly for functional testing.
2. Inaccuracies due to improper CAD representation result in limited application of the fabrication process.

Current prototyping or fabrication systems build three-dimensional shapes by incremental material buildup of thin layers of materials. These prototypes or models are used for form testing only. Functional testing cannot be done due to their fragility. There also seems to be no method available to fabricate metal parts directly using the same principle of successive solidification. NC fabrication of complex geometry remains expensive and time consuming.

These manufacturing systems are also limited in terms of geometric inaccuracies due to the approximation of CAD triangulation. The surfaces of the object are defined as a set of interfacing triangles (many CAD packages use such technique to draw surfaces of on-screen images). The triangles are defined by their vertices and a normal, which identifies which side faces out and which faces in. This planer faceted representation has inherent limitations in terms of its ability to approximate the original part design with acceptable precision.

3. PROBLEM DEFINITION

Although several parts of the problem of providing a computer interface for rapid prototyping have been attempted, there has been no attempt to provide an interface which uses the precise information from the solid modeling system for path planning the laser curing process. At the beginning of this research, the need for such a computer interface was identified. During the development of such an interface based on a CAD representation, a more fundamental understanding of the process of 2D path planning was obtained and this understanding prompted a reexamination of the concepts currently in use. It also seemed clear that the increasing need for functioning prototypes produced through rapid prototyping systems would necessitate more refined methods of geometric representation and advanced material fabrication techniques. The problem addressed in this paper can be defined as:

- **"Given a complete geometric description of the part to be prototyped, design appropriate techniques to retrieve precise cross-sectional information and automatically produce a cross-hatch pattern suitable for the laser post processor and develop methods to fabricate functional parts directly through successive solidification using laser-metal deposition techniques."**

4. OVERALL METHODOLOGY

The 3D computer models created in the CAD system have to be sliced into a stack of 2D cross-sections for laser path planning in rapid prototyping. In commercial systems the object is tessellated (triangulated) before it is sent to the rapid prototyping system and sliced by a special software there. This results in the error/inaccuracy introduced by the triangulation to propagate through the entire process.

The research initiative here is therefore to design and implement a "slicing program" that can be associated with any geometric model. This program can either be an external program or an internal program using the "section cutting" capabilities of the solid modeler. The overall methodology is to provide a system that will help users to extract the information of the cross-sectional profiles based on NURBS data and to then use it for the generation of 2D cross-hatch patterns. The following are the steps in providing such an interface:

1. Design the part using a solid model CAD system and orient it in the way that it would be built.

2. Run the slice program such that the set of cutting planes are defined perpendicular to the build direction. Output all the curves describing the cross-sections in IGES format.
3. Transform these IGES formatted files to the interface software.
4. Obtain the 2D cross-hatch pattern for each cross-section using the intersection algorithm.
5. Verify the correctness of the solution by simulating the laser curing and the part building process using a graphical user interface.

4.1 Obtaining The Cross-sectional Profiles

The cross-sectional profiles are obtained from the intersection calculations between the object and a regularly spaced stack of planar faces. The spacing between these planes can be varied. One or more profiles are created and stored by this operation. The profiles corresponding to a particular cross-section are retrieved and joined together to exactly represent the cross-section of the model. This cross-sectional information is output to an IGES file with the *Rational_B-Spline* option. IGES files are those which conform to the Initial Graphics Exchange Specifications [5].

4.2 Vector Scanning or 2D path planning

The 2D path planning is the task of designing a cross-hatch pattern to move the lase/scanner system over the cross-sectional profiles. This motion involves identifying the solid/hole areas for the laser light to be turned on/off. Normally the motion is specified by assigning a sequence of points between the initial and final points which are termed intersection points. Each of these intersection points specifies whether the light has to be turned on/off. Between these points the motion of the scanning system is defined to be a smooth function. The intersection calculations are based upon the Newton-Raphson method and cross-hatch pattern is generated using the Ray Casting method

4.3 Newton-Raphson Method

Many geometric algorithms include tests for intersection between geometric entities. For example, identification of the interior and skin-fill areas of the cross-sectional profile for laser curing applications involves intersection operations. The intersection between the cross-section and the cross-hatch grid identifies the vectors to be scanned by the

laser scanner system. The object boundaries for the laser are quickly found from the perimeter of the cross-sections. Similarly, the grids for the laser path planning are defined by the intersection of the perimeters of the cross-sections with the grid of line segments. A closed form solution for evaluating the surface/curve intersection points is difficult to get. Therefore this problem is solved numerically using the Newton-Raphson method. This algorithm used successive approximations and a general description of this method is given in [Nielson K.L. 1965].

4.4 Method of Ray Casting

Ray casting is a method normally performed by intersecting a ray (a semi-infinite line) against the curve/surface elements of a geometric model. In this case, this method is used to differentiate between solid and hole boundaries. Basically a two dimensional grid of semi-infinite lines are chosen that covers the cross-sectional profile being path planned. A ray (defined by its starting point q and its direction u) is cast along each of the lines on the grid and all the intersections between this ray the cross-sectional profile are obtained.

Having found the intersections points, they are classified as on/off toggle points for the laser scanner system to traverse the cross-sectional contours. Here it is assumed, that the starting point of the ray is outside the cross-sectional profile. Apart from the singular cases when the ray hits the cross-sectional profile in a single point or goes along its boundary curve, it will intersect the cross-sectional profile at an even number of points, denoted by t_1, t_2, \dots, t_n in cartesian space. With $k = 0, \dots, n/2$, the ray is within the solid area for the points $t_{2k} < t < t_{2k+1}$ and outside the solid area for the points $t_{2k+1} < t < t_{2k+2}$. When the number of intersections is odd, for $k = 0, \dots, n-1$, the ray is within the solid area for $t_k < t < t_{k+1}$ and outside otherwise. This information is utilized by the laser scanner system to turn on/off the beam according to whether the point is inside the solid area or outside.

5. LASER-METAL DEPOSITION TECHNIQUE

In the current rapid prototyping techniques, CAD models are used to produce parts for iterative design evaluation as well as form and fit testing. The research initiative here is to extend the idea of successive solidification to produce functional metal parts with engineering properties and dimensional tolerances comparable to conventionally produced parts.

The fabrication method involves the sequential buildup of laser melted and subsequently solidified metallic droplets to form continuous, bulk components. The process

involves the melting of continuous feed metallic wire under a fiber transmitted laser beam. The movement of the laser beam is controlled by a robot and the substrate on which the laser melt pool solidifies is moved by mounting it on a x-y-z CNC table driven by the CAD data. The subtasks that are being solved are:

- Controlling the melting and flow of metal wire feed
- Controlling the metal transfer mechanism to the substrate - spray, globules or tear drops
- Selecting the nature of the substrate - polymer, metal or ceramic
- Optimizing the laser control parameters.

The metal deposition and post processing are being automated using a robot and fiber optics assembly to control the deposition rate and energy sharing. Automated metal deposition will require the scheduling of the laser parameters and the selection of the robot path. The robotic processing will be enhanced through an off-line trajectory, kinematic and process planner to achieve consistent and predictable performance.

6. EXAMPLE : Model of a Fan and Shroud

An example is provided to explain the CAD interface and how it works with different computer models that have engineering applications. The example is a model of a high performance cooling fan for electronic equipment [figure 1]. The shroud around the fan is modeled from cross-section and are used to "skin" the solid object. This shroud illustrates a classic case of transitioning from a round section around the fan to a square mounting flange. The fan blades were modeled using different surfacing techniques. Seven blades are then combined with the rotor to make the completed fan. Figure 2 shows the cross-sectional profiles created by slicing operation. Figures 3 and 4 show the 2D curing pattern and the part building-up process. These figures also show the ability of the software to vary the mesh size. This is especially useful where a fine mesh is needed for high surface finish.

7. CONCLUSION

Rapid automated prototyping is complete when there exists a system for off-line creation, slicing and path planning of the 2D cross-sectional profiles of objects, and an online laser post processing system with feedback to control the curing process. This research provides a framework on which other interfaces can be built to close the feedback loop and

make it completely a CAD based automatic prototyping system. Important contributions by way of this research can be summarized as:

1. Current commercial rapid prototyping systems do not make use of the representational geometry of the solid modeling systems. This research for the first time has implemented a routine that uses the same underlying geometric representation (NURBS) for object creation, slicing and path planning the individual cross-sections.
2. The path planning (2D) is robust mathematical technique to obtain the cross-hatch pattern for the laser post processor and has great potential to be applied in future rapid prototyping systems.
3. Initial attempts are being made with 304 stainless steel wire (0.6mm diameter) with fiber transmitted Nd:YAG laser beam. The ultimate goal of this research is to develop an automated system capable of producing testable metal parts using an integrated CAD/CAM approach where both the geometric and process models share a common precise CAD (NURBS) representation.

8. ACKNOWLEDGMENTS

Funding for this work was provided by the R. A. Engel Laboratory, Department of Mechanical Engineering, Iowa State University and the Iowa Center for Emerging Manufacturing Technology. The authors would like to thank Dr. James Oliver and Dr. Molian for their insightful discussions and advice.

REFERENCES

- [1] Agarwal, P.K. 1991, *Intersection and Decomposition Algorithms For Planar Arrangements*, Delmer Publishers Inc., Albany, NY.
- [2] Guessel, T. 1989, "Affordable Prototypes Made Without Tooling," *Modern Plastics*, Vol. 66, no. 3, pp. 84-86.
- [3] Heller, T. 1990. "Software Enables Laser Stereolithography," *Laser Focus World*, Vol. 7, pp. 57-58.
- [4] IDEAS 1991. Solid Modeling User's Guide, SDRC Corporation, Milford, OH.
- [5] IGES, 1991. Initial Graphics Exchange Specification, American National Standard, Version 5.1, International TechneGroup Inc., Milford, OH.
- [6] McGeough J.A. 1988. *Advanced Methods of Machining*, Chapman and Hall Publishers, New York, NY.
- [7] Nielson K.L. 1965. "Methods in Numerical Analysis," The Macmillan Company, New York.

NURBS Based Computer Interface

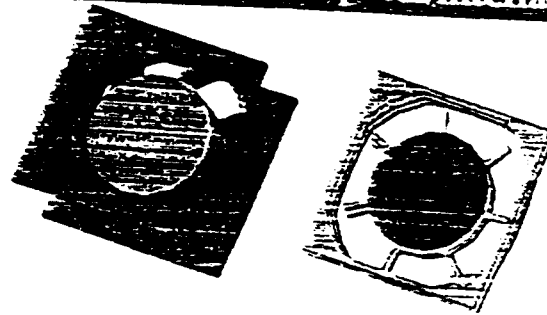
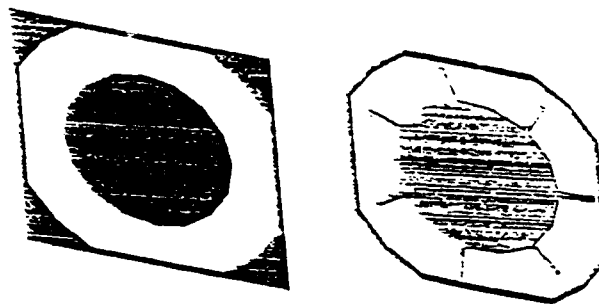


Figure 1: A Model of A Fan and Shroud & sectional profiles sketched together



Engel Laboratory

Figure 2: Cross-sectional Profiles

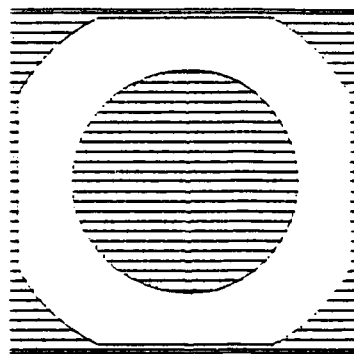


Figure 3: Cross-hatch Pattern of the rotor and the shroud profile

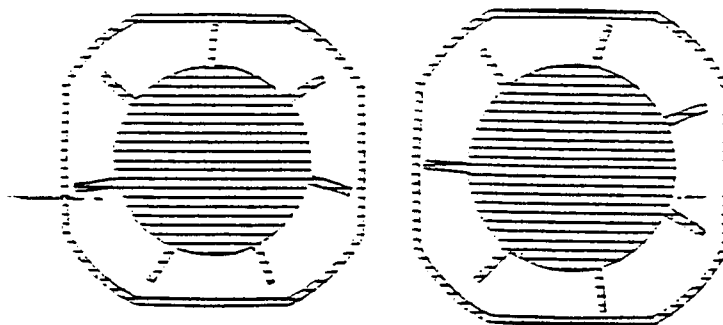


Figure 4: Cross-hatch pattern of the cover and the shroud profile

SIMULATION OF SOLID FREEFORM FABRICATION

Stuart Brown

**Department of Materials Science and Engineering
Massachusetts Institute of Technology
Cambridge, Massachusetts 02139**

Abstract

Solid freeform fabrication involves highly coupled, nonlinear, thermomechanical processes. This investigation simulates the formation of a simple SFF geometry, a right, rectangular prism with aspect ratios of 1:1:2. We include the effects of material variation, deposition path, and initial conditions to predict resulting distortion.

Introduction

Most SFF processes are constrained in their range of application by certain mechanical and microstructural phenomena. Thermally-induced distortion limits the dimensional precision of these processes due to several inherent characteristics. First, the high temperature, local sintering or solidification zone produces large thermal gradients that in turn cause plastic deformation and distortion. Second, the subsequent shrinkage cooling of the high temperature and previously porous material introduce further distortion. Certain processes also introduce distortion due to differential cooling of a polymer stream.

In the case of 3D Printing, where the heating is primarily isothermal, distortion still results due to spatial variation in capillary forces developed between the binder and powder particles. This distortion can occur in certain extensions of SLS technology, where the laser is used to bind metal and ceramic powders coated with a thermoplastic binder. Distortion also results from the uneven shrinkage of the printed, porous green body during sintering. Finally, stereolithography can experience shrinkage due to the polymerization reaction [Iwanaga, et al., 1992; Weissman, et al., 1992].

This temperature-, polymerization- and binder-induced distortion also introduce residual stresses during processing. Cooling of a local high temperature zone surrounded by a lower temperature material introduces tensile stresses in the local zone. Unless removed, these tensile stresses can

cause cracking and prevent the complete closure of pores. In some cases these tensile fields can introduce additional porosity by expanding smaller pores in the presence of a tensile hydrostatic state of stress.

These residual stress fields can act as the primary constraint on the application of components fabricated using any of these technologies. High strength requires low porosity and low residual stress states. The absence of either of these conditions significantly reduces the strength of any SFF component, as they would any porous body [Lakshminarayan and Marcus, 1992].

The relative amount of cohesion between different parts of fabricated components and the microstructure of components are deposition or sintering path dependent. Many nonlinear processes occur simultaneously in these technologies, for example: nonlinear thermal conduction, viscoplastic deformation, powder flow, grain growth, and capillary flow. Given these nonlinearities, it is very difficult to predict the best deposition/sintering path to produce a component with the least distortion and residual stress, and the best material properties.

The only work of which we are aware that has employed three dimensional modeling of any SFF technology is by Iwanaga [Iwanaga, et al., 1992], who appears to have used finite element analysis to simulate photolithography. Documentation of this Japanese effort is very limited, however. Hsu [Hsu, 1992] presents some preliminary simulation of sintering using finite element methods, but did not consider issues specific to transient SFF processes. Hsu also employed a rather simple constitutive model for sintering without including the effect of elasticity or residual stresses. To summarize, we are not aware of any three dimensional simulation of domestic SFF processes, including SLS and 3D Printing.

The following sections provide the details of the finite element analysis used to simulate the deposition of a right, rectangular prism. The effect of different materials, beam paths, initial conditions, and boundary conditions are given in the next section. The paper closes with discussion and conclusions.

Model Details

The finite element code ABAQUS is used to simulate a generic SFF process. Figure 1 illustrates the simple prism used in the analysis. The body is very small, consisting of 16 elements arranged in a prism with aspect ratios of 1:1:2. The body is held fixed at one corner and allowed to displace freely at all other points. Deposition and/or heating of powder material is simulated using an element activation capability in ABAQUS. Each beam path variation therefore activates elements in a different order. The simulation is a decoupled thermomechanical analysis, where the thermal history resulting from a thermal analysis is used as the loading for a subsequent mechanical analysis. The activation of elements in the mechanical analysis is delayed by one element activation

step to activate elements in their high temperature state, thereby eliminating any mechanical effect due to heating of loose powder. All analyses were performed using a DECstation 5000.

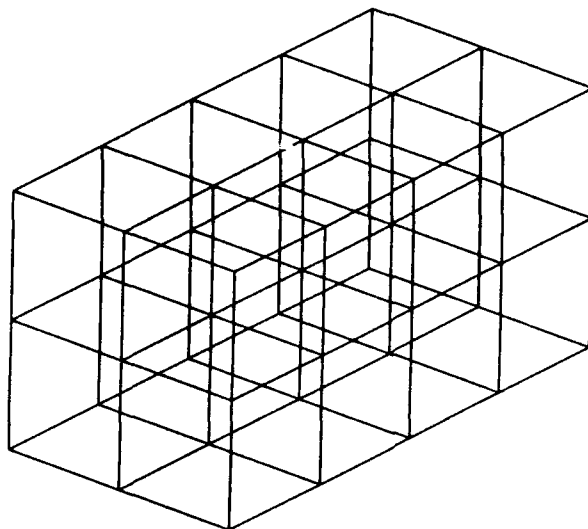


Figure 1 Finite element model of right, rectangular prism.

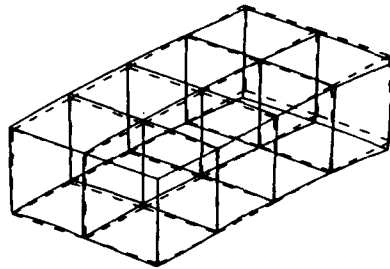
Two materials, a plain carbon steel and polycarbonate, were included in the analysis assuming elastic-plastic, rate-independent behavior. Our previous analyses of welding processes indicate that a rate-independent assumption works reasonably well for predicting metal distortion. The polycarbonate is most likely less accurately modeled using rate-independent models. Material properties (elastic moduli, specific heat, yield stress, thermal expansion coefficient, thermal conductivity) vary with temperature in the simulation. Behavior above the melting temperature was approximated by a very small value of yield stress.

The heating of the surface was simulated by the imposition of a uniform energy flux on the surface of a newly activated element. The magnitude of the flux was adjusted until the material within the element exceeded its melting temperature. Heat transfer is modeled approximately using film coefficients on the surfaces of the activated elements. Film coefficients were therefore assigned and eliminated as elements became activated and as elements were covered by previously unactivated elements.

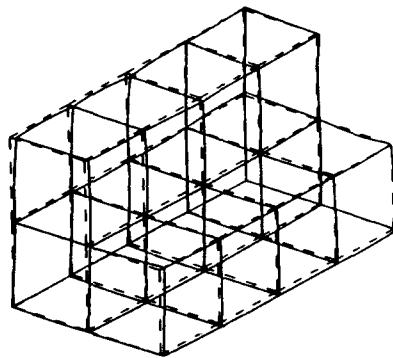
The simulations did not include the effects of radiation heat transfer, rate-dependent constitutive behavior, orientation dependence of the heat transfer coefficient, powder constitutive behavior, or effects due to capillary flow.

Experimental Results

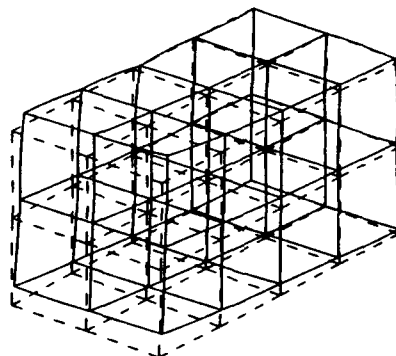
Figure 2 illustrates representative results for a simulation at different stages in the deposition of the full prism. This simulation employed steel constitutive behavior and deposited materials along the long axis of the prism. The dashed lines indicate the shape of the prism in the absence of any deformation. The solid lines indicate the shape of the prism at that stage. The final deformed shape corresponds to the final room temperature configuration.



First layer deposited



First row of second layer deposited



Final deposited geometry

Figure 2 Representative sequence of distortion resulting from steel prism simulation.

Table 1 summarizes the effect of different deposition (beam) paths and initial conditions for the steel deposition using the final, fully cooled, vertical displacement of a lower corner of the prism for comparison. The vertical displacement was much larger than displacements in the plane of deposition. The corner location is illustrated in figure 3. It is interesting that the simulations indicate that the path with the lower distortion also results in the lowest maximum principal tensile stress. Path selection therefore may offer promising opportunities in improving component properties. Increasing the ambient temperature (from 20 Celsius to 800 Celsius) produced significant reductions in residual stresses and displacements.

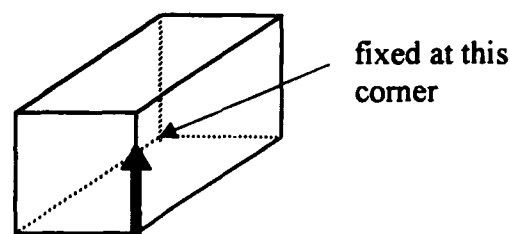


Figure 3 Location of point displacement used to compare different simulation cases.

Table 1: Comparison of beam paths and initial conditions

Simulation description	Beam path in each layer	Corner vertical displacement	Maximum principal tensile stress
Steel, beam path in one direction only along prism long axis.	⇒	0.12 mm	980 MPa
Steel, beam path in two directions along prism long axis.	⇔	0.12 mm	1000 MPa
Steel, beam path in one direction only along prism long axis.	⇓	0.10 mm	860 MPa
Steel, beam path in one direction only along prism long axis, initial and ambient temperature of 800 Celsius.	⇒	0.05 mm	98 MPa

The effect of change in materials was unremarkable. Displacements associated with the polycarbonate prism were within a factor of two of those associated with the steel. However, the polycarbonate is first, rate-dependent and is second, highly dependent on the particular manufacturer's

formulation. More accurate simulation of the polycarbonate therefore requires more accurate constitutive models for the polymer thermal and mechanical behavior.

Discussion and Conclusions

Given the guidance that such process modeling has provided to other processes, such as welding [Brown and Song, 1992], we expect even greater benefit to be derived in SFF. SFF processing is at a sufficiently early stage of maturity where many of the nonlinear process interactions are not well understood. We believe that accurate simulation capabilities will provide substantial assistance in understanding these nonlinearities.

The simulation work proposed here is not coupled to any one particular SFF technology, but instead is applicable to a number of SFF processes, including SLS, 3D Printing, Stereolithography and the Stratasys process. Consequently, the insights gained through this effort should assist the development of several competing processes.

Acknowledgments

This work was funded primarily by the Office of Naval Research (grant number N00014-90-J-1938). Additional support was provided by the Materials Processing Center at M.I.T. and the Richard P. Simmons Career Development Chair in the Department of Materials Science and Engineering.

References

- 1 Brown, S. and Song, H., "Implications of 3D Numerical Simulations of Welding of Large Structures," *The Welding Journal*, February 1992, pp. 55s-62s.
- 2 Brown, S. and Song, H., "Finite Element Simulation of Welding of Large Structures," *Journal of Engineering for Industry*, November 1992, pp. 441-451.
- 3 Cima, M., Sachs, E., *Proceedings of the Solid Freeform Fabrication Symposium*, University of Texas at Austin, 1991, pp. 187-194.
- 4 Cima, M., Lauder, A., Khanuja, S., Sachs, E., "Microstructural Elements of Components Derived from 3D Printing," *Proceedings Solid Freeform Fabrication Symposium*, August 3-5, 1992, University of Texas, Austin, Texas, pp. 220-227.
- 5 Crump, S.S., "The Extrusion Process of Fused Deposition Modeling," *Proceedings, Third International Conference on Rapid Prototyping*, June 7-10, 1992, University of Dayton, Ohio, pp. 91-100.
- 6 Hsu, M.B., "Numerical Simulation of Viscous Sintering under Mechanical Loads," *Proceedings Solid Freeform Fabrication Symposium*, August 3-5, 1992, University of Texas, Austin, Texas, pp. 188-195.

- 7 Iwanaga, S., Ohkawa, M., Igarashi, K., Kurihara, F., "Influence of Material Characterization on Dimensional Stability," Proceedings, Third International Conference on Rapid Prototyping, June 7-10, 1992, University of Dayton, Ohio, pp. 77-89.
- 8 Jacobs, P.F., "Rapid Prototyping and Manufacturing," Society of Mechanical Engineers, 1992.
- 9 Lakshminarayan, U. and Marcus, H.L., "An Experimental Study of the Relationship between Microstructure and Mechanical Properties of a Ceramic Composite Fabricated by Selective Laser Sintering," Proceedings Solid Freeform Fabrication Symposium, August 3-5, 1992, University of Texas, Austin, Texas, pp. 44-53.
- 10 Marcus, H.L., Beaman, J.J., Barlow, J.W. and Bourell, D.L., "From Computer to Component in 15 Minutes: Integrated Manufacture of Three Dimensional Objects," Journal of Metals, April, 1990, p. 8.
- 11 Weissman, P., Bolan, B., and Chartoff, R., "Measurements of Linear Shrinkage and the Residual Stresses Developed During Laser Photopolymerization," Proceedings, Third International Conference on Rapid Prototyping, June 7-10, 1992, University of Dayton, Ohio, pp. 103-112.

AUTOMATED 4 AXIS ADAPTIVE SCANNING WITH THE DIGIBOTICS LASER DIGITIZER

INTRODUCTION

The DIGIBOT 3D Laser Digitizer is a high performance 3D input device which combines laser ranging technology, personal computing, and Microsoft Windows in an attractive desktop package.

With its full four-axis scanning capabilities, the DIGIBOT provides a simple, accurate, and quick way to copy or inspect complex, sculpted surfaces. The DIGIBOT provides an effective solution for many industrial and academic problems involving 3D design, inspection, replication, analysis, and visualization/animation. By measuring sequential points and producing a standard list of x/y/z coordinates, the DIGIBOT interfaces to any CAD/CAM/CAE imaging or animation software that reads 3D points, contours, or triangular facets.

UNIQUE BENEFITS OF THE DIGIBOT SYSTEM

The following unique benefits are provided by the DIGIBOT technology:

- DIGIBOT's ranging system measures individual surface points without using complex, non-linear imaging optics or sophisticated detector-array processing techniques.
- The ranging system provides high resolution and accuracy while maintaining a small, fixed triangulation angle across a large work volume.
- Unlike camera-based ranging devices, the Digibot Ranging System has a very long ranging length with a small stand-off and does not suffer from focal problems such as lens aberrations and depth-of-field issues.
- Systems can be mechanically configured to provide up to two rotations and two translations between the object and the ranging system.
- Advanced positioning capabilities make possible the complete, one-scan measurement of complex objects.
- Adaptive 4 axis scanning procedures minimize shadowing effects, provide optimal measurement orientations, and produce homogenous point spacing with no measurement redundancy.
- Semi-adaptive, systematic, and interactive scanning procedures provide efficient alternatives for less sculpted, more regular surfaces. A complete library of C-based system functions can be used to develop custom scanning procedures.
- The system is a peripheral device which interfaces to an IBM compatible PC through a controller board located inside the PC. The system is self-orienting and maintenance free. The Digibot calibration/registration procedure is quick and easy to perform. This procedure is much less complicated than the calibration/registration processes used for camera-based systems.

- DIGIBOT systems are easy to set up and move because of their small size and low weight.
- Digibot's windows-based software provides a conventional, intuitive interface to the scanning procedures and a variety of data processing utilities, including contour editing, surface editing, polygonal surface generation, adaptive surface filtering, 3D viewing, and data formatting.

DIGITIZING DESCRIPTION

Digitizing an object begins by first mounting the object on the platter in front of the laser scanning system. The operator then uses the Windows interface to select from a variety of scanning procedures, each of which will be more or less appropriate for a given object. Once selected, the operator instructs the system to execute the scanning procedure. Typical scanning procedures, systematic or adaptive, provide sampling rates on the order of 10,000-100,000 points per hour. A course sampling grid can be executed in minutes while high resolution sampling of complex surfaces can take hours.

DATA (GEOMETRY AND TOPOLOGY)

The DIGIBOT device, including the control software resident on the customer's host computer (IBM PC), is essentially an automatic data acquisition system. Typically, the next step after acquiring data with the digitizer is to manipulate the data for some purpose such as graphical display or numerical analysis. At this time the user must understand and appreciate the 'art and science' of using a set of discrete surface points to mathematically represent a surface. In essence, the 3D coordinate values of individual surface points only provide information about the geometry of a surface. A complete surface representation also requires topology (i.e. information about how each point is connected to its neighboring points). The selection of one scanning procedure over another will typically have a great influence on the amount of explicit topology information that can be acquired during the digitizing process. Some scanning procedures can provide complete topology while others provide only partial or no topology. Any data that is lacking in topology information must typically be subjected to some form of mathematical topology generator. A procedure of this type must attempt to establish topology from the available geometry. In general, the user must be aware that the selection of one scanning procedure over another also involves a conscious decision to use one data processing procedure over another.

ADAPTIVE SCANNING AND FILTERING

When measuring an analog subject, it is generally a good idea to perform a high resolution sampling procedure so that high frequency components are adequately resolved. This principle is appropriately applied when digitizing a 3-dimensional object. The representation of a sharp edge will typically require a dense grid of closely spaced surface points. Although essential, high resolution scanning procedures also present a problem. Slowly curving surfaces, which can be represented with relatively

few widely spaced surface points, tend to be over-sampled producing excessive amounts of unnecessary data. The solution to this problem is provided by introducing some form of filtering mechanism which uses the local rate of surface curvature to adaptively adjust the spacing between neighboring surface points. With the DIGIBOT system, a filtering procedure of this type can be introduced in two ways. When digitizing, an adaptive scanning procedure can be executed so that the spacing between consecutive measurements is decreased for increasing rates of surface curvature. After digitizing, the acquired data can be subjected to a flexible filtering procedure which removes unnecessary points in over-sampled surface regions. Generally, the second approach is the most attractive and flexible (i.e. it is the best to over-sample the object and then use a data filter to selectively remove a desired set of surface points).

POINT MEASUREMENT BY TRIANGULATION

Individual range measurements are obtained using an active triangulation method. The ranging system is composed of a laser source and a translating photo-direction detector. The laser source and the photo-direction detector are positioned at two corners of a right triangle formed by the orthogonal intersection of the laser line and the base line. At the third corner of the triangular system the laser beam illuminates a small surface producing a diffuse point-source of light. The photo-detector is translated until the illuminated surface point enters the detector's field of view. At this time the system can accurately determine the distance and the angle θ from which the range can be computed.

Active triangulation requires that the surface be a relatively diffuse reflector and that the angle of incidence between the laser line and the surface normal be within limits. Polished surfaces cannot be measured because, in most orientations, no light will be reflected back toward the photo-detector. Increasing incident angles will tend to illuminate an increasingly larger surface area while decreasing the amount of light reflected back toward the photo-sensor.

There is a limit to the effectiveness of a triangulating range system. As surface concavity increases, the photo-detector's view of points located within concave regions becomes increasingly obstructed, producing increasing limited laser/photo-sensor orientations. Reduced probing angles provide improved probability but tend to decrease measurement resolution and accuracy. Typical applications will use a 30 degree probing angle.

RELATIVE MOTIONS (DOFs) BETWEEN LASER BEAM AND OBJECT

Assuming that the ranging device has a long ranging length and does not need to move toward or away from an object, there remains four forms of relative motion between an object and a laser beam needed to illuminate a point on any exposed surface of a 3-dimensional object. More specifically, a 3D digitizer needs two translational and two rotational degrees-of-freedom (DOFs) between the ranging system and object to provide full 3D sampling capabilities. DIGIBOT offers two translational DOFs and one rotational DOF. This is also known as four axis scanning. The laser can be

translated vertically and horizontally while the object can be rotated about a vertical axis. By not providing the fourth DOF (i.e. rotation of the object about a horizontal axis), DIGIBOT is not capable of measuring points along vertical facing surfaces. For most applications, the practicality of using a 4-DOF digitizer is questionable due to mechanical, operational, and data processing difficulties. The fourth DOF can, however, be partially realized by digitizing the same object multiple times in different orientations. This approach requires that the multiple data sets be merged to form a single surface mesh.

By using different combinations of its three DOFs, DIGIBOT is capable of performing three types of 3D scanning procedures:

1. two DOF scan using two translational DOFs,
2. two DOF scan using translational DOF and rotational DOF, and
3. three DOF scan using two translational DOFs and one rotational DOF.

Each of these three scanning options is useful for different types of objects. Flat objects are best digitized using two translational DOFs while convex objects are best digitized using both translation and rotation. Three DOF scanning offers a very attractive method for digitizing complex objects with non-axial geometry, multiple contours, and concavities. The following three discussions provide a more detailed description of when and how the different scanning options can be used to digitize different types of objects.

SCANNING WITH TWO TRANSLATIONAL DOFs

Probably the simplest scanning procedure that can be performed with DIGIBOT employs two translations of the ranging system. As a result, this type of scanning option should be used to measure relatively flat surfaces. Once the user has decided which combination of motions are appropriate for a given application, a decision must be made to perform either a systematic scanning procedure or an adaptive scanning procedure.

The surface mesh generated from adaptive data is very attractive because it produces a homogeneous, evenly spaced set of points on all exposed regions of a surface. An adaptive mesh can also be optimized to provide more points in high frequency regions and fewer points in regions where high sample density is unnecessary. Though the data produced by adaptive scanning procedures is attractive, in practice it is generally more practical for simple-shaped objects to employ fully systematic procedures with only two DOFs. The reasoning for this is two fold:

1. the grid topology of systematic data is provided implicitly while the mesh topology of adaptive data must, by some method, be explicitly specified and recorded (this can be difficult), and
2. systematic data from a high density grid can be adaptively filtered to produce an adaptive surface mesh that is very similar in quality to that produced by adaptive scanning procedures.

Though adaptive scanning methods are used for most applications, systematic scanning procedures should be used whenever possible because they are easy to perform and they provide structured data that can be flexibly filtered to provide an

optimal data sub-set. Another advantage to using high frequency systematic sampling procedures is realized when the user decides that more data is needed. It is generally easier to refilter a set of data than to re digitize an object.

SCANNING WITH ONE TRANSLATIONAL DOF AND ONE ROTATIONAL DOF

A very popular form of 2-DOF scanning utilizes both rotation and translation. By first positioning the laser line to pass orthogonal through the center of rotation, a set of radial measurements can be obtained by rotating the object and vertically translating the ranging system. This scanning configuration is useful for convex objects because acceptable incident angles are possible only at locations where the surface normal does not depart significantly from the radial direction. When choosing between systematic versus adaptive scanning procedures, the very same reasoning, introduced in the previous discussion describing 2-translation scanning, can again be used. A systematic scanning procedure will produce a data-grid (with complete topology and filtering capabilities) by incrementally rotating the object and incrementally translating the ranging system. Some subtle properties of rotation contour sampling are:

- points with a surface tangent that passes through, or near, the center of rotation cannot be measured,
- negative radiuses can be measured because the active range of the ranging system extends past the center of rotation,
- closer spacing between measurements occurs along contours that are closer to the center of rotation,
- off-center objects are sampled during two portions of a complete rotation causing partial loss of topology and partial loss of the contour on two sides where large incident angles make measurement impossible, and
- most concave surfaces cannot, or can only partially, be measured.

Two DOF scanning procedures are very attractive because they are easy to perform and they produce data that is easy to work with. Unfortunately, the type of object that can be digitized using 2-DOF methods is limited. With its third DOF, DIGIBOT is capable of digitizing much more complex objects, including off-center contours, multiple contours, and concavities. However, as a general rule, 2-DOF scanning procedures should be used whenever possible to take advantage of gridded data and to avoid the difficulties associated with the processing and compatibility of 3-DOF data. The reasoning behind this rule will become clearer after reading the following description of 3-DOF scanning.

SCANNING WITH ALL THREE DOFs (4 AXIS SCANNING)

The work volume generated using all three DOFs (i.e. rotation of the object and both vertical and horizontal translation of the laser line) will be cylindrical in shape. With three DOFs, DIGIBOT provides a work volume with an 18" diameter and a 18" height. The advantage of using a third DOF is two fold:

1. the surface normal at any given point is limited only by the requirement that it not depart significantly from the horizontal, and
2. each individual point can be measured from a variety of different perspectives (i.e. the laser beam can illuminate a single surface point from a variety of different directions).

Complex contours can be better sampled along a horizontal plane by both rotating the object and translating the ranging system. Deep concavities and multiple contours can only be measured using both rotation and translation while, for complex contours of this type, rotations by itself will yield comparatively poor results.

An efficient 3-DOF procedure for sampling contours along a horizontal cross-section requires adaptive feedback control. The direction and rate of curvature along a contour are computed using previously acquired points to help predict the location and surface normal of a target point (i.e. the next point to be measured). In this way, the object is rotated and the ranging system is translated to provide an optimal measurement perspective (i.e., the laser as normal as possible to the surface) for each consecutive target point as the system adaptively tracks a contour. For convex surfaces, the optimal measurement perspective is obtained with a zero incident angle between the laser beam and the surface normal. For concave surfaces, optimal measurement perspectives are obtained when the laser line is closely pivoted about the outer edges of the concavity. Orientations of this type will typically produce non-zero incident angles. A very useful result of adaptively moving along a contour can be seen by measuring consecutive points. The system effectively acquires complete topology information (i.e. the points are connected in the same order in which they are acquired) and, when multiple contours exist, each contour is scanned separately (i.e. once started, the systems attempts to complete a contour by pivoting around any other obstructing contours.)

Though two DOFs are used to scan adaptively within a horizontal plane, the third DOF is typically used to systematically position the ranging system at vertically displaced planes. For this reason, this type of 3-DOF scanning could be referred to as 'semi-adaptive.' It is important to recognize that adaptive scanning along planar cross-sections provides complete contour topology in the horizontal direction. This is a great advantage but, by blindly moving to vertically displaced planes, semi-adaptive scanning will provide no vertical topology between neighboring cross-sections (i.e. no information is provided to establish how points in one planar contour are connected to points in a corresponding, vertical-displaced planar contour). As a result, a procedure for vertical topology generation must be employed before a valid surface mesh can be obtained from semi-adaptive data.

A filtering mechanism can be incorporated into the procedure for semi-adaptive scanning to provide a flexible way to discriminate between rapid and slow rates of surface curvature. By using the local rate of surface curvature to adjust the spacing between consecutive measurements, a relatively small number of measurements are needed to define a contour containing sharp corners and slow curving sides. Without a filtering mechanism, a contour of this type must be sampled frequently to guarantee that the sharp corners will be adequately resolved. Such a procedure will require significantly more time and will, in this case, produce an over-abundant amount of data along slow curving surfaces.

There is, unfortunately, a competing disadvantage to using an adaptive filtering mechanism along planar cross-sections when performing a semi-adaptive scanning procedure. By systematically stepping to consecutive planes, no filtering mechanism is applied in the vertical direction producing a non-homogenous surface mesh composed of long, skinny polygons. This problem can be resolved by employing a vertical filter either during or after the scanning procedure. When scanning, a fully adaptive procedure is fast and concise but it is difficult to implement and the resulting data must explicitly specify topology. After scanning, a vertical data filter must first be applied to produce a homogenous surface mesh which will also require explicit topology information. As a consequence, unless time is a factor, or for some other specific reason, it is generally more practical to execute a semi-adaptive scanning procedure with equal sample spacing in both the vertical direction and along horizontal contours. The data produced from such a procedure can be subjected to a vertical topology generator, and then filtered to extract the desired data subset.

SUMMARY

The Digibot 3D Laser Digitizer is a high performance 3D input device which combines laser ranging technology, personal computing, and Microsoft Windows in a desktop package. With its full four-axis scanning capabilities, the Digibot provides a simple, accurate, and quick way to copy or inspect complex, sculpted surfaces. The Digibot provides an effective solution for many industrial and academic problems involving 3D design, inspection, replication, analysis, and visualization/animation. By measuring sequential points and producing a standard list of x/y/z coordinates, the Digibot interfaces to any CAD/CAM/CAE imaging or animation software that reads 3D points, contours, or triangular facets.

The DIGIBOT uses a unique triangulation technique that does not use complicated imaging optics or array detectors. The scan head resides outside of the scan region and does not move back and forth from the object to maintain focus of the laser beam spot. Consequently, scanning is simple and efficient. Adaptive scanning procedures intelligently position the beam spot on the object's surface while effectively walking from one point to the next. For complex objects, this technique, unique to the DIGIBOT, can reach into deep concavities, undercuts, and between surfaces to produce a complete, homogeneous data mesh. Simple systematic scanning procedures produce grid data for single faced (i.e., flat-faced) objects or convex, cylindrical shaped objects.

Three dimensional modeling is becoming the technology of choice for the majority of designers and manufacturers. In order to be effective, many industries need to automate the acquisition of 3D geometry into the computer. The Digibot solves this need with industry leadership in technology, usability, and affordability.

StereoLithography 1993:

QuickCast™

Drs. Thomas H. Pang and Paul F. Jacobs
Research and Development Department
3D Systems, Inc.
26081 Avenue Hall
Valencia, California 91355

Abstract

Previously, StereoLithography (SL) generated solid patterns had limited success in highly accurate shell investment casting applications. The majority of the failures involved the cracking of the ceramic investment casting shell. However, the recent invention of the QuickCast™ build-style and the development of a new epoxy resin, XB 5170, led to an unprecedented level of success in the burnout process of SL patterns from investment casting shells. Unlike conventional SL building techniques, QuickCast involves the building of SL patterns with essentially hollow structures. When the low viscosity liquid epoxy resin is drained from the interior of the pattern, voids are formed, allowing the cured resin to collapse inwards during the autoclave and burn-out stages. This effectively prevents the shells from cracking as the result of outward thermal expansion. 3D Systems formed QuickCast teams with three respected foundries to test shell investment casting using SL patterns. A test part having relatively complex geometries (i.e. a Boeing 737 cargo door bracket) was selected. To date, this SL part has been successfully cast in aluminum, titanium, beryllium-copper, and stainless steel, with RMS surface finish as low as 1 micrometer, without any subsequent finishing operations.

Background

Recently, one of the authors visited a large foundry that has specialized in investment casting for decades. Until just a few years ago, typical projects involved highly complex geometries in hundred to multi-thousand lot quantities for various aerospace applications. On such projects, the development of the tooling typically cost from \$ 30,000 to as much as \$ 200,000. Obviously, this was a lot of money. However, considering the critical characteristics of the final components, investment casting was often the least expensive production method capable of satisfying the specifications and was commonly the preferred approach. Furthermore, the amortized cost of the tooling, on a per part basis, was quite reasonable.

As a consequence of the profound changes in the aerospace business within the past two years, the situation has altered significantly. This foundry is now receiving hundreds of requests for quotation (RFQs) on projects involving one, two, or three prototype parts. Obviously, if traditional methods were used, the amortized cost of the tooling could be tens to hundreds of

thousands of dollars per component. This is clearly not very economical. It is also not especially competitive. As a result, the company has been forced to no-bid hundreds of RFQs. Under the best of conditions this would not be desirable, but in a serious recession, sustained non-responsiveness could be critical to their future viability.

An economical means to produce accurate patterns with a smooth surface finish was clearly needed. Further, these patterns must be sufficiently robust to allow handling, assembly, and ceramic shell investing without breakage. Also, the pattern material must have characteristics that allow for excellent burnout without damage to the shell. And finally, prototype quantities should require minimal initial pattern generation expense. Stereolithography can be a solution if a process can be developed to address all these elements. While definitely ambitious, 3D Systems has advanced considerably towards this goal. Much of the progress has been led by improved photopolymers working in concert with still newer part building methods discussed below.

New Epoxy Resin XB 5170

Ciba-Geigy (Switzerland) and the Research and Development Department at 3D Systems have been involved in a program of joint SL photopolymer research and development since 1988. Ciba-Geigy, one of the leading chemical companies in the area of epoxy chemistry, had been looking at SL epoxy resins for sometime. In July, 1993, Ciba-Geigy released a new resin for the SLA-250 based on epoxy chemistry. The epoxy resin has an excellent set of physical, mechanical, and dimensional properties that exceed those of acrylate resins in almost every single category.¹ Namely, XB 5170 has

- 1) very low viscosity
- 2) high laser-cured (green) modulus
- 3) high postcured modulus
- 4) good elongation at break
- 5) good impact strength
- 6) substantially reduced thin flat slab distortion
- 7) almost twice the overall UserPart accuracy compared to XB 5081-1 acrylate resin (Note: XB 5081-1 was formerly the most accurate SL resin until XB 5170 was introduced.)
- 8) negligible curl during the SL building process
- 9) superb dimensional stability in the laser-cured state.

It is clear that XB 5170 possesses many of the key stereolithography characteristics needed for the generation of substantially more accurate parts. The combined properties make this epoxy resin, XB 5170, the resin of choice, especially for the new QuickCast™ build style.

QuickCast™

Previously, stereolithography generated patterns were successfully used for so-called flask investment casting, as shown by the results of Texas Instruments working with two foundries: Cercast Group and Shellcast Foundries, Inc., both of Montreal, Quebec, Canada.² In this method the stresses generated as a result of the thermal expansion of the resin during burnout are resisted by the solid metal flask as well as the considerable thickness of the ceramic material. However, this technique can only be used efficiently for a limited range of part geometries.

Unfortunately, attempts to use solid SL parts as patterns for the more general *shell* investment casting technique had achieved only modest success.³ In numerous cases the heating of the pattern during burnout would cause significant thermal expansion of the resin, in excess of that of the ceramic material. This would lead to the development of substantial internal stresses and possible cracking of the shell. Special purpose Investment Casting Resins were also only marginally successful. The concept involved the addition to the resin formulation of a non-reactive volatile diluent. In principle, subsequent to polymer crosslinking, the volatile diluent would escape from the pattern upon heating, resulting in a loss of mass and a corresponding shrinkage that would hopefully offset the thermal expansion of the polymer.

Since this process hinges upon the diffusion of the volatile component to the surface, its effectiveness clearly depends upon the local surface to volume ratio. While thin sections might work well, thick sections could become diffusion limited, with the effects of thermal expansion occurring before those of mass loss. This was indeed what was observed. Parts having section thicknesses less than 2.5 mm worked well, with little or no tendency to generate shell cracks. For parts with section thicknesses between 2.5 and 4 mm, the method was marginal, showing occasional shell cracking. However, for parts with section thicknesses in excess of 4 mm, major shell cracking was observed.⁴ Thus, despite some initial positive results, it became clear that solid patterns would not work in all cases.

Recognizing that the problem involved the thermal expansion of thick, solid sections of cured resin, it was reasoned that *quasi-hollow* patterns generated from a resin with good burnout characteristics might well allow the shell to survive. The key idea was that if the pattern was mostly hollow and made from a resin that softened at a relatively low temperature, it might collapse inward upon itself before sufficient stress had been developed to crack the ceramic shell. However, in order to generate quasi-hollow patterns, it became essential to devise a means by which the residual uncured liquid resin could be drained from within.

The heart of the QuickCast™ method depends upon a novel interior part structure capable of providing effective resin drainage. Mathematically, QuickCast™ involves building patterns in a *topologically simply connected* manner. Subject only to the limitations of viscous and surface tension forces, in principle no matter how complicated the pattern geometry, the resin should be able to flow from any location within the part to any other location within the part.

Clearly, if the second location is an opening, then the pattern could be drained of uncured liquid resin. In addition to the small openings for resin drainage, known appropriately as *drains*, other small openings known as *vents* are also required. The vents enable air to enter the evacuated volumes, thereby avoiding any flow retardation due to the creation of reduced pressure regions.

The vents and drains are later sealed with investment casting wax, at the foundry, to insure that the ceramic slurry will not invade the interior of the pattern. Experience with QuickCast™ has shown that the time required to thoroughly drain a part is a function of:

- The part geometry
- The resin viscosity
- The resin surface tension
- The spacing of the QuickCast™ interior hatch vectors.

Extremely convoluted parts will take longer to drain than simple cubes. Resins with lower viscosity drain faster. Smaller resin surface tension reduces capillary effects. Finally, larger interior triangles greatly speed drainage. However, if the triangles are made too large, upfacing and downfacing surfaces may sag, leading to reduced pattern accuracy. Clearly, optimum parameters must be established for each resin. Figure 1 is a photomicrograph of an interior portion from a QuickCast™ part, showing the quasi-hollow, triangular hatch structure characteristic of this build style.

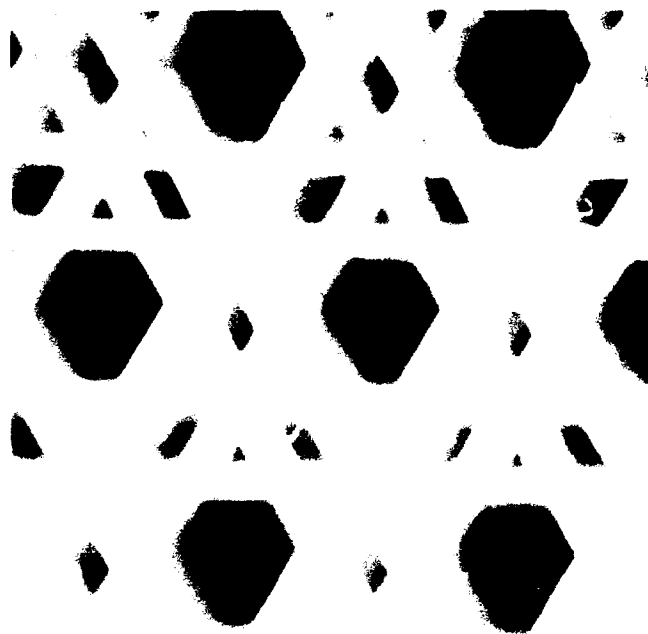


Figure 1. The interior hatch pattern used in the QuickCast™ build style.

A CAD model of the pattern is initially developed in the usual manner. Next, the part is sliced using the new QuickCast™ software proprietary to 3D Systems. This software provides instructions for the SLA system to generate the appropriate interior topology that is fundamental to the QuickCast™ method.

Upon completion of the SLA building process, the pattern is allowed to drain under the influence of gravity. With the new epoxy resin, XB 5170, simple parts drain within 30 minutes, while even the extremely complicated geometries require only a few hours. Subsequent to drainage, the part is simply wiped clean. XB 5170 leaves little residual photopolymer on exterior surfaces after about 45 minutes. The part is then postcured in a standard PCA for 1 hour.

Next, the pattern is wrapped in bubble-pack, boxed and shipped to an appropriate foundry that is thoroughly familiar with QuickCast™. The foundry will then seal the vents and drains with a thin coating of investing casting wax, add their usual wax gating, etc., and apply pretested ceramic shell coatings that have proven to be fully compatible with the resin used to fabricate the QuickCast™ pattern. This is one of the reasons that prior testing and approval of the foundry is essential for success.

At this point the wax gating is removed in an autoclave. During the early testing of QuickCast™ this step was problematic. However, over the past six months we have learned that successful autoclaving (i.e. removing the wax gating without pattern expansion causing damage to the ceramic shell) depends upon:

- The type of resin used to build the pattern
- The spacing of the interior hatch vectors
- How well the resin has been drained from the pattern.

All three of these items affect the so-called void ratio, or R_v , defined by the relation

$$R_v = 1 - [M_q/M_s]$$

where M_q is the mass of the QuickCast™ pattern, and M_s is the mass of a solid STAR-WEAVE™ part of identical size. Obviously, when the parts have not been drained at all, and $M_q=M_s$, then $R_v=0$. Conversely, the smaller the value of M_q the higher the value of R_v . Observations from numerous foundry autoclaving tests have shown that the greater the value of R_v , the higher the probability of successful autoclaving. Recently, using XB 5170, void ratios as high as 0.67 have been achieved. As a result, successful autoclaving is now occurring for about 80 % of the patterns tested. Further improvements in this ratio are anticipated as experience with QuickCast™ increases.

Subsequent to autoclaving, the shell is cured and the QuickCast™ pattern is burned out all in one step. Here the shell is elevated from room temperature to roughly 1,000°C within about 2 hours in a fully aspirated furnace. The shell is then maintained at this temperature for another 1 - 2 hours and finally allowed to cool. Since the resin is almost entirely hydrocarbon based, if the burnout is done in a sufficiently oxygen rich environment, the vast majority of the pattern material will be converted to carbon dioxide and water vapor. Any residual ash should be removed with compressed air or fluid rinsing and drying.

Next, the appropriate metal is poured into the ceramic shell mold and allowed to cool. In the case of either titanium or magnesium this must be done under vacuum to avoid oxygen contamination and subsequent damage to the surface of the casting. For aluminum, ferrous metal and beryllium-copper alloys conventional methods apply.

Finally, the shell is broken away, the gates removed and the usual finishing steps taken such as grinding, sandblasting, milling, etc. The end result is then a precision shell investment cast *metal part* produced directly from a stereolithography generated pattern; bypassing the traditional requirements for expensive and time consuming hard tooling.

Results to Date

3D Systems formed QuickCast™ teaming arrangements with three respected North American foundries in May-June 1992. These were the following:

- Solidiform, Inc. Fort Worth, Texas, USA
- Precision Castparts Corp., Portland, Oregon, USA
- Cercast Group, Montreal, Quebec, Canada.

QuickCast™ patterns were generated in five different resins: three for the SLA-250 and two for the SLA-500. These patterns involved a variety of different hatch spacings, drainage intervals, and post processing methods.

Early in the testing phase it was found that the most critical step involved the removal of wax gating during the autoclave process. A resin that softens at elevated temperature is definitely beneficial. Further, a very high correlation was found between successful autoclaving and the extent to which the pattern had been drained of excess resin. In all cases those patterns with the highest void ratios, always produced the best results.

After some initial trial and error, all three foundries have now achieved successful results using QuickCast™ patterns for shell investment casting. To date, a Boeing 737 cargo door bracket has been successfully cast in the following metals:

- | | |
|-------------------------|------------|
| • A-356 Aluminum | Solidiform |
| • A-357 Aluminum | Cercast |
| • TI 6 Al-4V Titanium | PCC |
| • C-20 Beryllium-Copper | Cercast |
| • 304 L Stainless Steel | PCC |

Figure 2 shows a QuickCast™ pattern of the cargo door bracket, and examples of the final metal parts in stainless steel, beryllium-copper and aluminum.



Figure 2. QuickCast™ pattern of the Boeing 737 cargo door bracket and final metal parts in stainless steel, beryllium-copper, and aluminum.

Also, a complex, six-bladed, centrifugal impeller has been successfully shell investment cast in A-357 aluminum directly from an SLA QuickCast™ pattern, shown in Figure 3. The actual A-357 impeller casting is shown in Figure 4. Each of the three foundries is currently testing larger, more geometrically complex castings.



Figure 3. QuickCast™ SL pattern for the six-bladed centrifugal impeller.



Figure 4. The six-bladed centrifugal impeller cast in A-357 aluminum from the QuickCast™ SL pattern.

To date, the amount of residual ash has been measured in the range of about 10-30 micrograms per gram of initial pattern weight. The lower value corresponds to resin XB 5170.

Three additional benefits of QuickCast™ in XB 5170 are:

- *Substantial photopolymer savings.*
With a hatch spacing of 3.8 mm, QuickCast™ requires only 33% of the resin needed to build the same object with STAR-WEAVE™.
- *A modest throughput increase.*
Based on the test data from a representative range of parts, QuickCast™ builds about 10-20% faster in XB 5170 than an equivalent part in XB 5149 using STAR-WEAVE™. The mildly reduced photospeed of XB 5170 is more than offset by the substantial decrease in the required volume of material to be photocured. Additionally, reduced Z-wait intervals are possible as a result of the low viscosity of the new epoxy resin.
- *Thinner Layers.*
With XB 5170, 0.1 mm layer thickness is optimum for both speed and surface quality.

Summary

In 1993, current and future stereolithography users can anticipate the following key advances:

- Further continued and significant improvements in part accuracy, to the point where 90% of all measurements of an SLA generated object will be within 120 microns of the intended CAD dimensions.
- The release of an epoxy resin for the SLA-500. With its greatly reduced curl, shrinkage, creep and slab distortion, this new photopolymer will result in a further quantum jump in overall stereolithography part quality.
- The ability to generate accurate patterns for rapid, low cost, small lot, shell investment casting applications using the new QuickCast™ technique. This will enable customers to fabricate functional metal parts in prototype quantities much more economically than with traditional methods requiring hard tooling.

References

- ¹ Pang, T. H., "*StereoLithography Epoxy Resin Development: Accuracy and Dimensional Stability*", Proceedings of the Solid Freeform Fabrication Symposium, University of Texas at Austin, August 9-11, 1993.
- ² Blake, P., and Baumgardner, O., Chapter 12, "*Rapid Prototyping & Manufacturing: Fundamentals of StereoLithography*", Society of Manufacturing Engineers, Dearborn, Michigan, July 1992.
- ³ Cromwell, W. E., "*Prototype Casting Fabrication by StereoLithography*", Proceedings of the Second International Conference on Rapid Prototyping, Dayton, Ohio, June 23-26, 1991, pp. 103-148.
- ⁴ Schulthess, A., "*Eighth Report on Formulations for Investment Casting*", Ciba-Geigy research Report No. 185,035, Marly, Switzerland, November, 1992.

FFF at Ford Motor Company

Sean B. O'Reilly
Ford Motor Company
Alpha Simultaneous Engineering
24500 Glendale Avenue
Redford, Michigan 48239

Introduction. Ford's effort in Free Form Fabrication (FFF) began in 1987 with the formation of an internal consortium, composed of a dozen different activities, whose purpose was to evaluate and apply, where possible, this emerging technology. Each of the consortium members agreed to contribute some money and, more importantly, one or more people to work on this project. By the following year (1988) the first machine, an SLA-1, had been installed at the Alpha Manufacturing Development Center and formed the cornerstone of the FFF Lab.

An Early Success. By the end of the year a number of successful parts had been built. One of the most dramatic was a rocker arm for the 1992 5L engine. The story of this arm has been told several times in articles and presentations but, nonetheless, bears repeating. A young engineer had designed this arm and had sent the design out to suppliers for quotes. (This particular part is purchased from outside.) Normal practice at that time was to use a 2-D detailed drawing to describe the part to be quoted. The initial round of quotes had already been completed based on the information contained in the drawing. Four suppliers had been contacted and asked to quote. Three of the four had responded with per-unit prices and the fourth had come back with a "No-Bid". The engineer was assigned to the FFF lab, built a 3-D Solid model of the part and then used the model to build a stereolithography

prototype. It was only upon inspection of the prototype that he discovered a problem with the design. He corrected the design and built a second prototype to verify that the problem had been solved. Since the design had changed, a second round of quoting was initiated. This time, however, plastic stereolithography prototypes were sent to the suppliers in place of revised drawings. Each of the suppliers came back with a lower quote than on the first round and the supplier who had "no-bid" first time around, came in at a price roughly 50 cents lower than any one else. This reduction amounted to several million dollars of savings per year.

Fundamental Value of FFF. The rocker arm story illustrates the basic value of FFF technology. The ability to take a computer model and build an accurate prototype of it in a few hours or days provides a new, high-bandwidth medium of communication for information about parts. Consider the process by which 2-D drawings are produced today: the engineer conceptualizes the part in his head; makes a few rough 2-D sketches and passes these along to a designer or detailer who must first get an accurate concept of the part, then, conceptually pass planes through the conceptualized part at various angles and then accurately conceptualize how these cross-sections would look; then he begins drawing these conceptualized cross-sections. This is a very complex and error-prone process. Once the drawings are complete, they are sent to a manufacturer who must then reverse the process conceptually and reconstruct the original design intent from the drawn cross-sectional information - an even more complex and error-prone process. All of this conceptual gyrating is completely short-circuited by FFF. The FFF prototype becomes the primary method of communicating all of the geometric intricacies

of the part. In a sense, representations of the part are replaced by the part itself. It is never easy to quantify the benefits of improved communications, but the millions in savings spawned by the plastic rocker arm certainly indicate that "...there's gold in them thar hills!!!!..."

FFF and Prototyping. Prototypes have been in the mainstream of invention, engineering and product development since Alley Oop first laid chisel to stone in search of the wheel. In the past, the role of prototyping has been severely limited by our inability to produce prototypes rapidly and cost-effectively. FFF holds out the prospect of being able to provide prototypes at virtually every stage of product development. Let me emphasize that this ability is not here today, but is coming. Prototypes seem to fall into three main categories, related to the stage of development of the product: "touch - feel" prototypes, "form, fit, limited function" prototypes and fully functional prototypes.

"Touch-Feel" Prototypes: Like the rocker arm cited above, these prototypes are used in the early stages of design for a number of purposes - concept verification, communication of design intent, even for verifying the CAD representation of the part. We have seen numerous examples where the FFF prototype showed up a flaw in the CAD model that was not detectable on the screen. This is the area where FFF currently has its greatest impact.

"Form, Fit, Limited Function" Prototypes: Components designed by different activities must often be assembled to form an integrated system. The ability to build each component quickly and accurately is of tremendous value in assembly studies, in finding interferences and in discovering problems early enough that they are easily handled. Again FFF prototypes are having a

tremendous impact in this arena. Fig. 1. shows a partial engine block, made in an SLA 500. This block was sent to the plant which was to manufacture it. The plastic block was used to check out tooling, fixturing, material handling equipment and dunnage. A number of potentially costly problems were discovered and corrected before the final specification for the plant equipment. Fig. 2. shows an experimental intake manifold made on a Cubital solidier. This manifold was attached to an engine and run through several power cycles to determine the effect of the design on engine performance. We have made many such manifolds on Cubital and SLA machines. The ability to actually test a new design within a few days is a capability that our engineers have never had before. This is an example of a "limited functionality" prototype. Several of our divisions now make this type of prototype where the functionality is primarily due to the geometry. Manifolds, throttle bodies, pump housings, alternator housings and AC housings are all examples of this kind of application.

"Full Functionality" Prototypes: For the most part, FFF-generated parts do not have the material properties required for full functionality. In this case, the FFF part is used as a model or pattern in a more traditional type of manufacturing process. Fig. 3a shows a stereolithography transmission case and Fig. 3b shows the aluminum casting that was made in our experimental foundry. Figs. 4a and 4b show a stereolithography crankshaft and the iron on made from it. In both instances, our engineers have gotten functional prototypes in a fraction of the time it would have taken using conventional methods. Sand, plaster and investment casting of metals and molding of some plastics (e.g. silicone rubber molding of polyurethane) are all sped up

dramatically by the use of FFF models as patterns. Significant time reductions (at least 50%) in the prototyping process are almost universal.

FFF and Tooling. A recent study has estimated that there are 1200 PARTS THAT MUST BE DESIGNED AND MANUFACTURED FOR EACH PART THAT GOES INTO THE AVERAGE FORD VEHICLE. Tooling, fixtures, material handling and dunnage all fall into this category. A similar study by GM came up with an estimate of about 1800 such parts. Since work on these parts can't seriously begin until the product design is reasonably stable, it seems evident that the application of FFF to this arena will be essential to reduce time to market. We are currently carrying out work to develop ways of making tools (molds and dies) directly from FFF parts. Fig. 5 shows an FFF part in the right foreground. It is actually a sand core which will be assembled into a sand mold to make an aluminum engine block. This particular core will be an internal oil drain passage. To the left of the part is a stereolithography prototype of the part sitting in a mold half. This was produced by designing the mold half on a CAD station with the part embedded. In the background are two epoxy mold halves which were formed as follows: the right mold half was formed directly from the stereolithography piece. The left half was then formed from the right half with the part inserted.

FFF Limits. These few examples illustrate the variety of parts and applications that we have completed. Where applicable FFF gives a tremendous advantage in terms of time savings and cost savings. However, not all of the parts the Ford Motor Company makes can be successfully prototyped today using FFF. The most obvious limit is the size of a part that can be built in one piece. Many of our parts must be built in two or more pieces and then

joined. In many cases this is a perfectly satisfactory process, producing acceptable prototypes. However, this approach doesn't work, for example, in the area of large sheet metal parts. No machine available today can build a durable hood or fender out of any material. Along with size, the layering process appears to be an impediment in very thin but extended parts.

Compared to more traditional processes for making prototypes, FFF is nothing short of a miracle. After a while however, speaking of limits, one begins to become impatient with the build speed of today's FFF machines. (An example of the infinite perversity of homo sapiens? - They're NEVER satisfied.)

Given the rapid (and seemingly accelerating) pace of development in the FFF arena and the fact that the industry is still in its infancy, we can expect to see many of today's limits overcome in very short order.

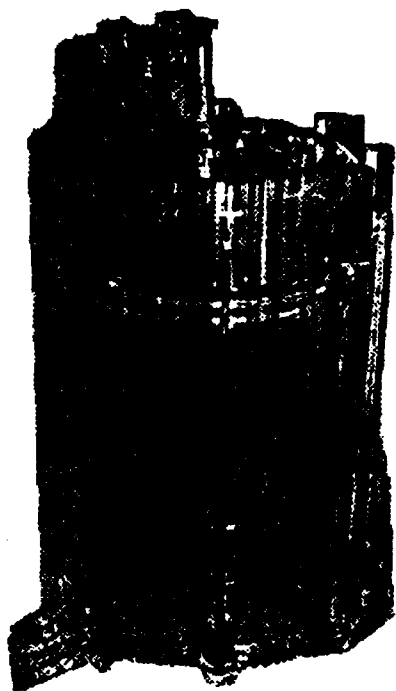


Figure 3a.
Stereolithography
Transmission Case

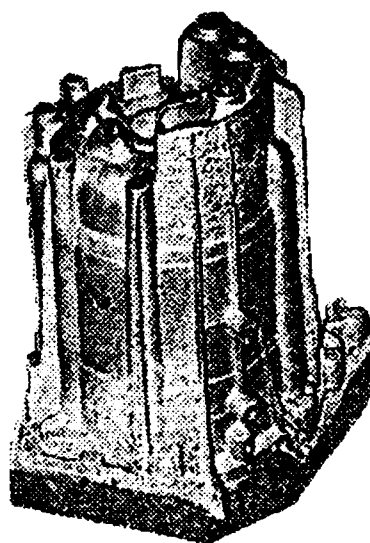


Figure 3b.
Cast Aluminum
Transmission Case

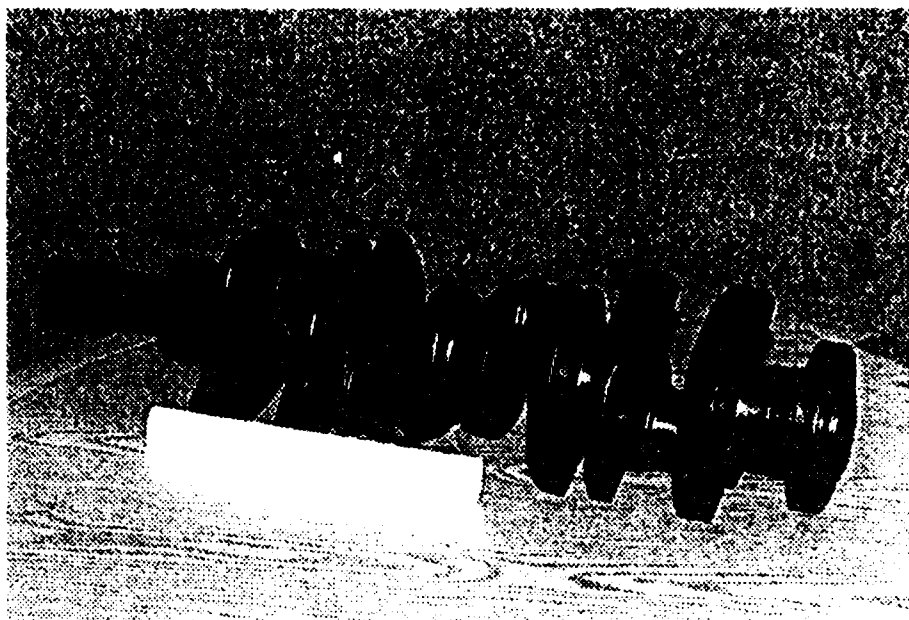


Figure 4a.
 Stereolithography
 Crankshaft (Cont'd)

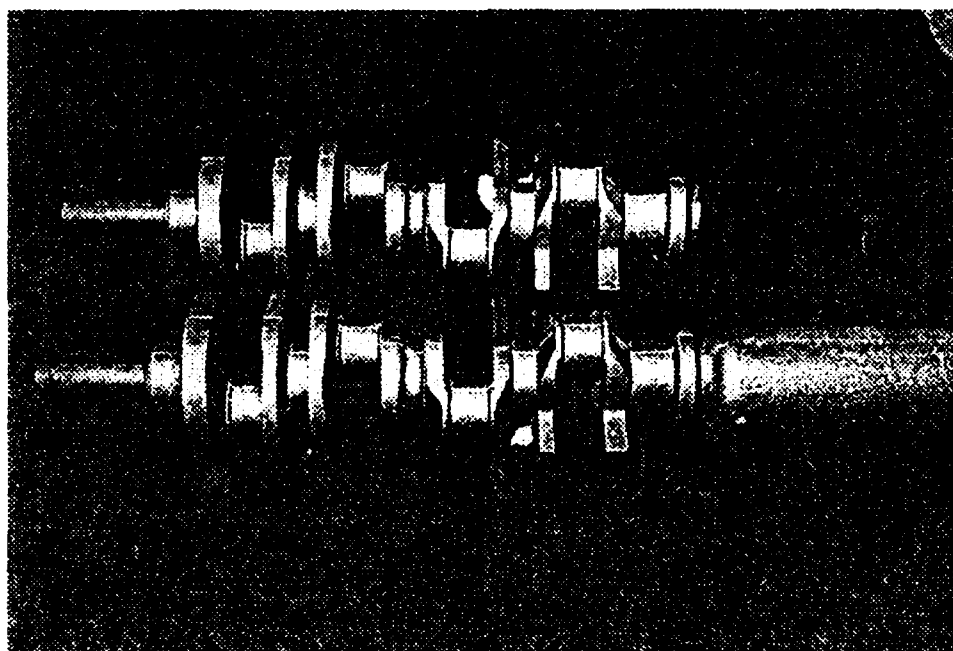


Figure 4b.
 Iron Crankshafts cast
 using SLA part as pattern.

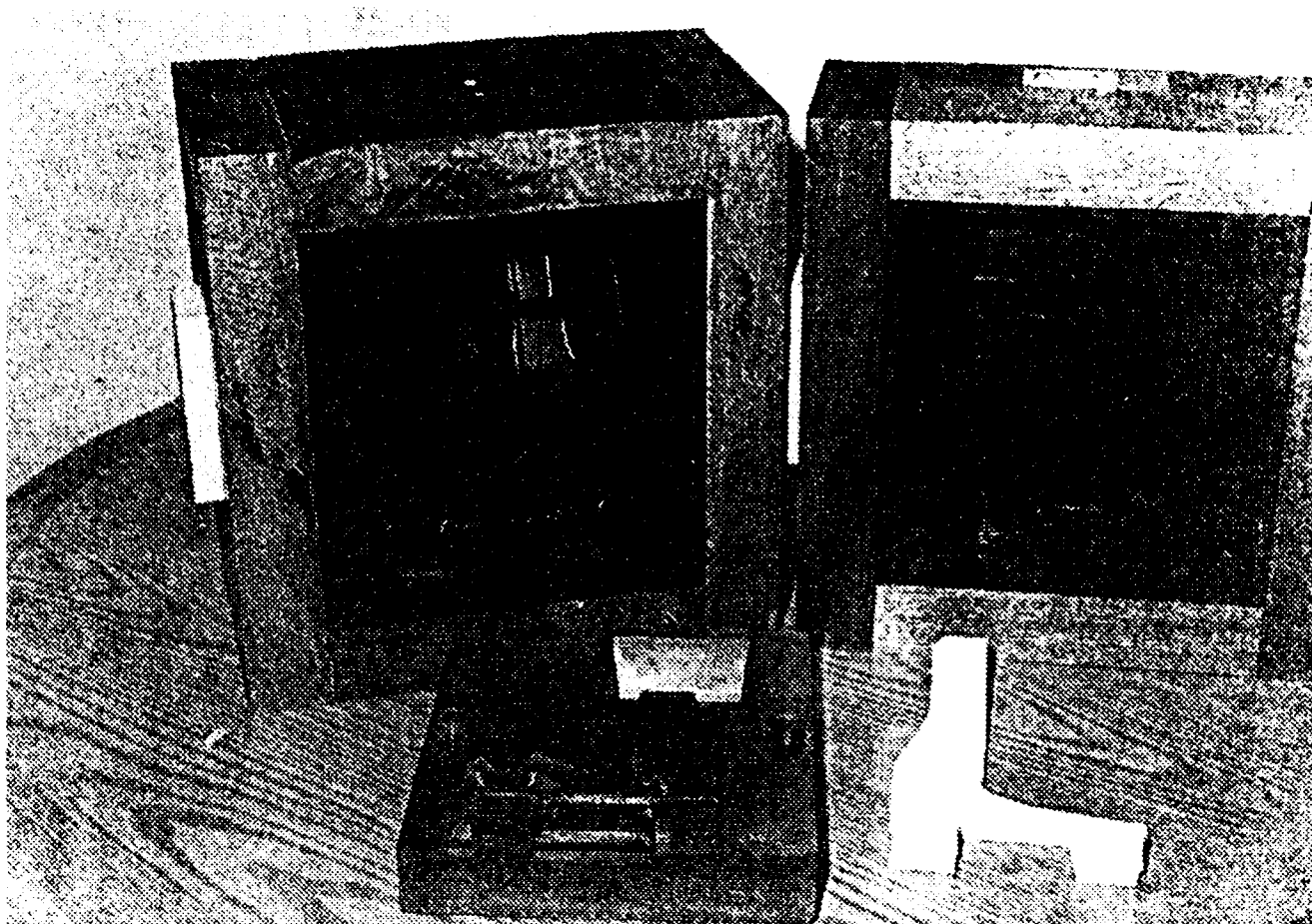
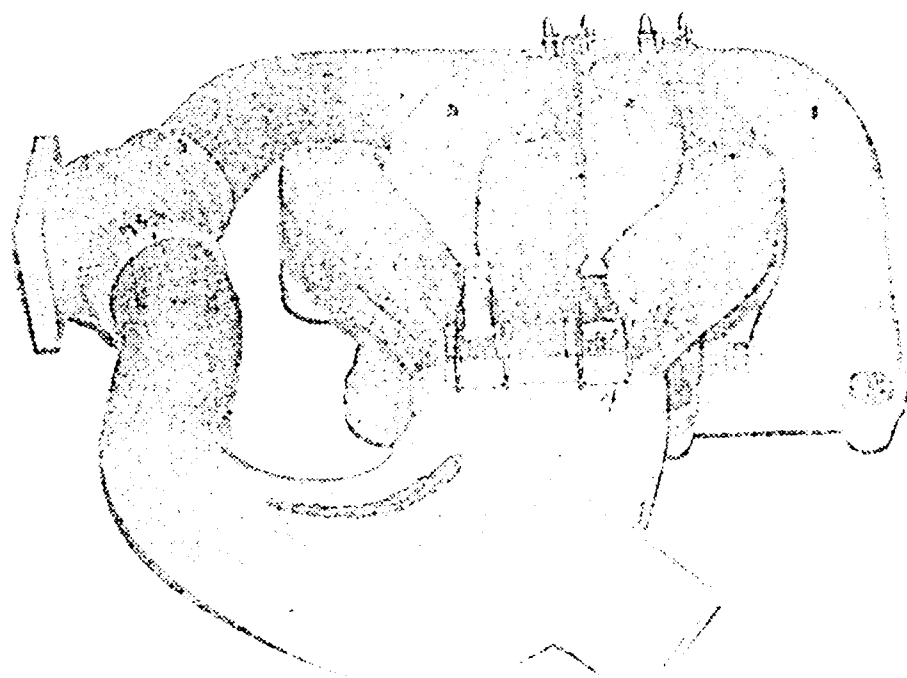


Figure 5.

Right foreground: FFF model of oil drain sand core.
Center foreground: SIA model of core embedded in mold half.
Background: Epoxy mold made directly from SIA model.



An Experimental Study of the Parameters Affecting Curl in Parts Created Using Stereolithography

Leslie Horton*, Edward Gargiulo**, Michael Keefe*

* Mechanical Engineering Department, University of Delaware, Newark, Delaware 19716.

** E.I. duPont de Nemours & Co., Inc., Wilmington, Delaware, 19880.

Abstract:

This paper describes an experimental study of some stereolithography build parameters to determine their effect on curl deformation. The test parts were slabs 2 inches long by 0.375 inch wide and 0.185 inch thick. Parts were imaged with consideration of five parameters: hatch type, layer thickness, hatch spacing, hatch overcure, and fill cure depth. However, because of the failure to create viable pieces with certain combinations of the parameter values, statistically significant results were obtained only for a TRIHATCH build with a 0.010 inch layer thickness. Results indicate a primary dependence of curl on hatch spacing with the need to consider combined effects of the parameters.

INTRODUCTION

Stereolithography is a photopolymer solid imaging process for rapid-prototyping and manufacturing that involves scanning a laser beam to sequentially draw or print cross sections of a model on the surface of a photo-curable liquid polymer.[1] With an installed capital investment exceeding \$60 million dollars in the United States alone, there is considerable incentive to make full and efficient use of this technology.

One of the most challenging goals of rapid prototyping is the generation of accurate and dimensionally stable parts. The ultimate dimensions of a part built on a layer by layer basis depend on many factors that must be carefully balanced to produce accurate parts. The inability to understand and control the parameters leads to many problems including post-cure shrinkage, swelling, cantilever curl distortion, vertical wall post-cure distortion and horizontal slab distortion [2]. An unfortunate fact of acrylate polymerization is shrinkage and attendant residual stresses which reside in the cured parts. These stresses often result in distortion of the work-piece.[3]

The problem of curl distortion has been discussed by several authors and a number of ways to minimize it have been proposed. Curl may be defined as any out-of-plane deflection of a flat layer and is the result of interlayer shear stresses residual to the solidification process. 3D Systems, Inc., has studied this problem extensively and has developed a diagnostic test to measure curl in terms of the distortion distance and cantilever length. [4] Although models for quantifying the curl parameter have been proposed and various parameters identified, the relative importance of the parameters and a theoretical model for curl distortion still needs to be developed.

The purpose of this study was to experimentally determine the parameters that are most important in minimizing curl and warp deformation. A designed experiment was used to statistically determine the relative importance of the parameters.

THEORY

In the course of preparing a part for stereolithography as many as twenty parameters may have to be selected that will govern the imaging process and the qualities of the final object. Five essential parameters were selected for inclusion in this study:

Layer Thickness,
Hatch Style,
Hatch Cure Depth,
Hatch Spacing, and
Fill Cure Depth.

Three-dimensional objects are "sliced" into series of constant thickness, two-dimensional layers to be printed in solid imaging processes. Layer thicknesses are chosen to balance the need to minimize geometric errors in the build direction caused by the inevitable "contouring" of curved surfaces against the desire to achieve a reasonable build time. A few practitioners regularly build parts with thicknesses as thin as 0.0025 inches, but most select a thickness near 0.010 inches.

Each two-dimensional layer is imaged on the photopolymer surface with a specific hatch style selected by the user. Hatching is used to photopolymerize the liquid in the interior regions of a part. The hatch style affects the sequence and amount of polymer solidification in the part and therefore its physical properties and internal stress distribution. Several hatch styles have been developed for photopolymer solid imaging, but only two will be considered here.

The TRIHATCH style images vectors in three directions (0, 60, and 120 degrees relative to the x-axis) to form equilateral triangles, Figure 1. The vectors are imaged without offsets between layers and with cure depths greater than the layer thickness to assure layer to layer adhesion. Up- and down-facing skin fills trap an amount of liquid in the triangular prisms that are formed. The volume of residual liquid resin is related to the spacing and linewidth of the hatch vectors. TRIHATCH imaging was the first commercialized with acrylate resins and systems with low power and short life He-Cd lasers to provide a fast and efficient imaging process. TRIHATCH imaged parts exhibit low curl, but may suffer from postcure warping and swell distortion.

Weave hatch styles image parallel vectors first in the x-direction, followed by parallel vectors in the y-direction. Hatch spacing is selected to be greater than the cured linewidth so the parallel vectors do not interact. Cure depths may be chosen to be less than or greater than the layer thickness depending on the hatch spacing. The STARWEAVE variation of this style, Figure 2, offsets the vectors in sequential layers (STagger), alternates the order of x and y vector writing (Alternating), and alternately stops the vector imaging short of the opposing borders (Retraction). The cure depth in this hatch style is usually less than the layer thickness. The principal advantages of Weave imaging styles are the elimination of swell and post-cure warp distortions. Curl distortions are not universally improved with these styles

Curl distortion can occur in all rapid-prototyping methods that build parts in successive layers where the solidifying material undergoes shrinkage. This shrinkage causes distortion and internal stresses. [5] Figure 3 shows the sequence of steps leading to curl distortion. When a single layer is first imaged on the liquid surface, it is free to shrink without inducing stresses. However, the second and subsequent layers that are drawn are each bonded to the layer below that has already shrunk. If there is shrinkage of these upper layers after they have become bonded to the layers below, a bending moment is introduced that can cause upward displacement of the unsupported ends of the layer. Curl distortion is typically measured in terms of a curl factor [4] defined as the vertical distortion distance, h , divided by the length of the free layer L .

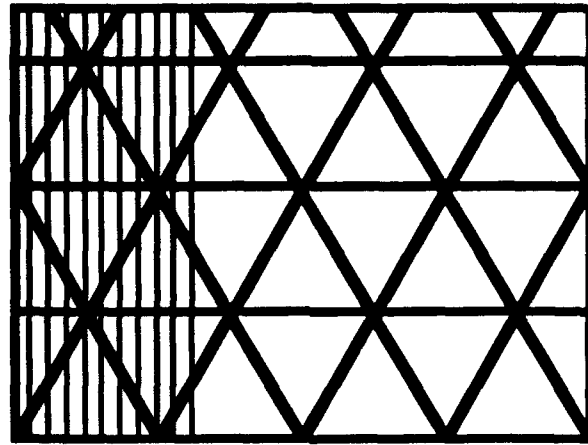


Figure 1: TRIHATCH Imaging Style

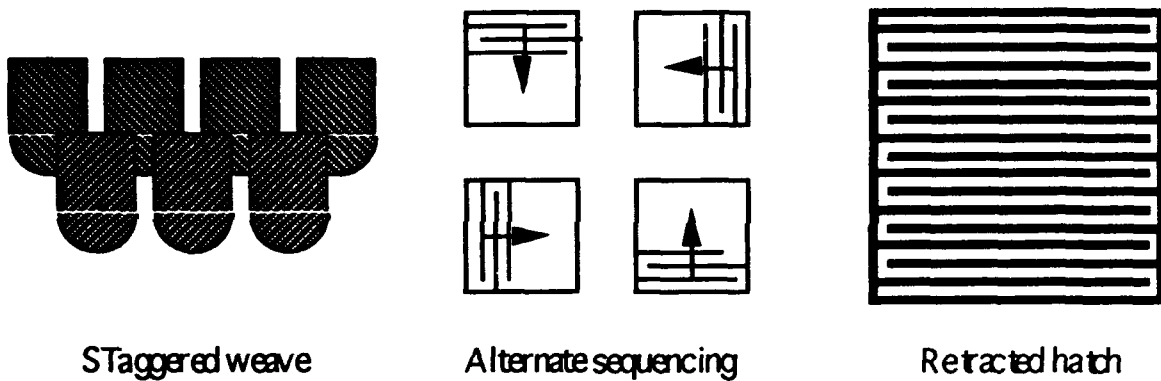


Figure 2: STARWEAVE Imaging Style

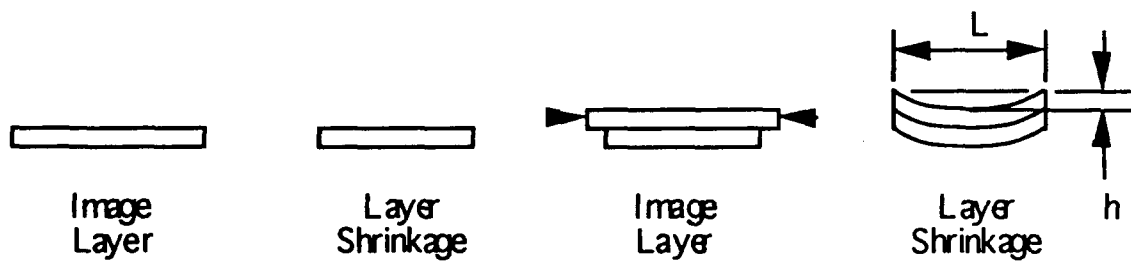


Figure 3: Layer by Layer Build Process

EXPERIMENT

The purpose of our experiment was to statistically determine the relative importance of various build parameters on the curl distortion. The parameters studied were hatch type, layer thickness, hatch spacing, hatch overcure and fill cure depth. The experiment was divided into four sets of parts. Each set consisted of one hatch type and one layer thickness with three different

values for each of the three remaining parameters. Thus there were 27 parts for each of the four sets for a total of 108 parts built. Table I summarizes the experiments.

Table I: Ranges of Experimental Parameters

<u>Experiment Number</u>	<u>Hatch Type</u>	<u>Layer Thickness</u> mil	<u>Hatch Spacing</u> mil	<u>Hatch Overcure</u> mil	<u>Fill Cured Depth</u> mil
1	TRIHATCH	10	10,30,50	-2, 2,6	5,15, 25
2	TRIHATCH	5	10,30,50	-2, 2,6	5,15, 25
3	STARWEAVE	10	10,15,20	-2,-1,0	0,12.5,25
4	STARWEAVE	5	10,15,20	-2,-1,0	0,12.5,25

(1 mil = 0.001 inch)

Figure 4 shows the solid model geometry used to create the test pieces. Since the geometry is identical for all the pieces, the curl distortion is proportional to the chord height, h . A dial indicator depth gage was used to measure that height for each experimental piece and that value was recorded as a measure of the curl distortion.

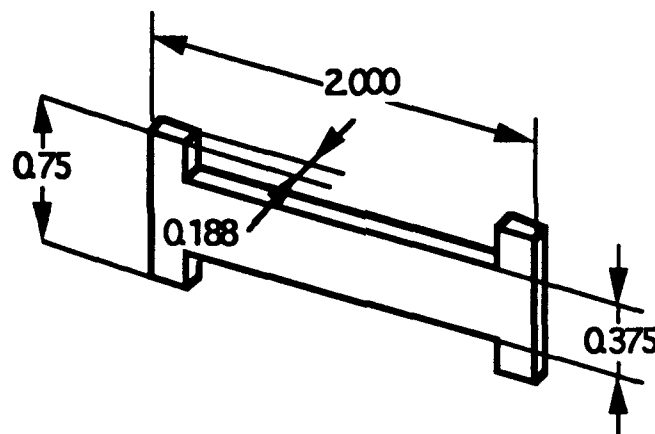


Figure 4: Test Part

The two hatch types chosen were TRIHATCH and STARWEAVE™. The TRIHATCH pattern leaves a large portion of the part in the liquid state. Post curing must be used to solidify the honeycomb trapped volumes and results in internal stresses. The STARWEAVE hatch style was developed to reduce those internal stresses. The pattern is formed by creating orthogonally alternating layers of fingers that are not all attached to their respective ends. Furthermore, the hatch overcure is selected so the layers are not completely attached. Since curl distortion is related to the extent of shrinkage after contact with the previous layer, the delayed shrinkage is expected to reduce curl distortion.

Layer thicknesses of 5 and 10 mils were chosen for this study. These values are commonly used by many users and they are usually selected to meet accuracy and build speed requirements.

Hatch spacing is the distance between parallel vectors used to hatch the interior of the part. If the hatch spacing is very small, the solidifying vectors will overlap causing a completely solid layer. Large hatch spacings allow liquid polymer to be trapped in the part to be solidified in the

postcuring operation. Values were selected for each hatch style to avoid complete vector overlap and show the postcure effects.

Hatch overcure is the depth that one cured vector "string" pierces into the lower adjacent layer. This is what keeps the individual layers connected together to form a complete part. Although the major portion of the STARWEAVE vectors are not intended to overlap, multiple exposures at vector intersections are expected to "nail" the layers together at points. The TRIHATCH construction superimposes vector scans creating a line connection between layers. Hatch overcures were selected to try to make sure the parts had sufficient layer overlap to prevent delamination and give good "green" strength. Nominal hatch overcures of 6 mils are usually recommended for TRIHATCH and a -1 mil overcures (1 mil undercure) is a common starting point for STARWEAVE.

Fill cure depth is the depth of the solid layers formed on the upper and lower faces of the solid. This holds the remaining liquid inside the part for subsequent post-curing. Skin fill s are required for the TRIHATCH style , but are sometimes eliminated in STARWEAVE.

Many other parameters need to be defined for a complete build. These remaining variables were all held constant. The Appendix gives the complete setup for the 3D Systems SLA-250 used to create the parts.

RESULTS

The following tables show the chord height for each of the pieces made as measured by a dial depth gage. Positive values indicate an upward curl as shown in Figure 3, while negative values indicate sag. An "X" indicates that the style was not able to produce a viable solid (e.g. insufficient green strength or delamination). All dimensions are in mils (0.001 inches).

Tables III through V show a large number of failures and thus there was not enough data to make a complete statistical evaluation. However, some qualitative observations can be made. For the TRIHATCH with 5 mil layer thickness, one can estimate that the 30 and 50 mil hatch spacings were too far apart, with 30 mils close to the upper limit. Therefore, more experiments need to be

Table II: 10 mil Layer TRIHATCH

Hatch Spacing:	10			30			50		
Hatch Overcure :	-2	-2	-6	-2	-2	-6	-2	-2	-6
Fill Cure Depth:									
5	24	20	17	-6	-13	21	X	-16	-7
15	11	13	16	4	0	0	16	35	0
25	15	18	21	-8	0	10	-12	-6	-7

Table III: 5 mil Layer TRIHATCH

Hatch Spacing:	10			30			50		
Hatch Overcure :	-2	-2	-6	-2	-2	-6	-2	-2	-6
Fill Cure Depth:									
5	13	22	18	X	-17	4	X	X	-10
15	7	14	18	X	-8	-8	X	X	1
25	5	20	15	X	-7	6	X	X	11

Table IV: 10 mil Layer STARWEAVE

Fill Cure Depth:	0			12.5			25		
Hatch Overcure :	-2	-1	0	-2	-1	0	-2	-1	0
Hatch Spacing:									
10	31	37	29	14	21	21	13	16	10
15	X	X	4	11	15	29	3	2	-10
20	X	X	X	15	13	3	10	55	43

Table V: 5 mil Layer STARWEAVE

Fill Cure Depth:	0			12.5			25		
Hatch Overcure :	-2	-1	0	-2	-1	0	-2	-1	0
Hatch Spacing:									
10	X	39	25	22	24	16	X	2	11
15	X	X	X	X	X	4	10	9	X
20	X	X	X	X	X	25	X	X	X

performed with hatch spacings between 10 and 20 mils. For the STARWEAVE style, the curl values are all fairly large. It seems that the range of parameter values chosen were not appropriate for the STARWEAVE pattern. More experiments need to be performed with different parameter values or perhaps different parameters. This indicates more understanding and practical experience with the TRIHATCH pattern.

The only set to give enough data was the TRIHATCH with 10 mil layer thickness. Qualitatively, Table II indicates curl minimization near the 30 mil hatch spacing which matches our experience. To study the data, we first performed a three-way layout with one observation per cell analysis of variance. The three factors were hatch spacing, hatch overcure and fill cure depth:

$$h(i,j,k) = K + A(i) + B(j) + C(k)$$

where K is a translational constant and A, B, C represent the effects of the three parameters: hatch spacing ($i=1,2,3$ corresponds to 10,30,50 mils), hatch overcure ($j=1,2,3$ corresponds to -2,2,6 mils) and fill cure depth ($k=1,2,3$ corresponds to 5,15,25 mils) respectively. Unfortunately, a simple linear model with just those three variables was able to account for less than 40% of the total variance between the model and the data; $R = 0.35$, where R is the typical correlation coefficient used in least-squares analyses. Next, the three-way layout was performed with the model:

$$h(i,j,k) = K + A(i) + B(j) + C(k) + AB(i,j) + AC(i,k) + BC(j,k)$$

where again, K is a constant and A B C represent the effects of the three parameters, but now AB, AC and BC represent the effects of the combined parameters of hatch spacing with hatch overcure, hatch spacing with fill cure depth and hatch overcure with fill cure depth respectively. This model was able to account for over 80% of the variance ($R = 0.90$) and thus gives a reasonable model estimate of the data. However, an estimate of the standard deviation of the experimental curl observations is fairly large at 5.637 mils and indicates the need for more experiments. Nevertheless, we have enough data to determine the relative importance of the various effects (A, B, C, AB, AC and BC) by testing the hypothesis that all values of any specific parameter are 0; that is the parameter has no effect on the curl. Table VI shows the probability that the particular parameter has no effect on the curl.

Table VI: Relative Importance of Parameters

<u>Source</u>	<u>Probability of NO effect</u>
Hatch Spacing	2.15%
Hatch Overcure	89.28%
Fill Cure Depth	39.02%
Hatch Spacing x Hatch Overcure	28.75%
Hatch Spacing x Fill Cure Depth	19.46%
Hatch Overcure x Fill Cure Depth	25.69%

From this, we can conclude that the most statistically significant parameter is the hatch spacing.

Given the results from the analysis of variance, we attempted to fit the experimental data to a quadratic function of the three variables; that is:

$$h = K0 + K1*x + K2*y + K3*z + K4*x*y + K5*x*z + K6*y*z + K7*x*x + K8*y*y + K9*z*z$$

where the K0, K1, ... K9 constants were determined by a least-squares minimization of error and the variables x,y,z represent hatch spacing, hatch overcure and fill cure depth respectively. Unfortunately, this model can only account for a little over 40% of the variance ($R = .64$) and thus indicates the need for more experiments to get better statistical curl information for the parameters and/or the need for a different mathematical model to predict curl.

An additional source of error in these experiments could have been the cleaning of the test pieces. No solvents were used in cleaning the parts because of their known influence on curl and swell. Some parts were very delicate and could have been damaged when their supports were removed.

Recommendations for further experiments are to:

1. Rebuild pieces to obtain statistical measures of curl for a single set of build parameters,
2. Build the TRIHATCH pieces with more hatch spacing values between 10 and 20 mils, and
3. Build more STARWEAVE pieces to determine more appropriate build parameters.

CONCLUSION

In this paper we experimentally studied the effect of various parameters on the curl distortion in parts built using stereolithography. From our experiments, only the TRIHATCH build with 10 mils layer thickness had enough data for statistical evaluation. However from observation, our experiments indicate that it is difficult to produce good parts with no fill cure depth. More parts need to be built with the STARWEAVE style to determine how those build parameters affect curl. Our results for the 10 mil TRIHATCH show that there are important cross relationships between the hatch spacing, the hatch overcure and the fill cure depth. In addition, the hatch spacing is the single most important parameter affecting the curl. We were not able to generate an acceptable quadratic model for our experimental data and suggest further experiments.

REFERENCES

1. SLA-250 User Guide, 3D Systems, Inc., April 1991.
2. Richter, J. and P.F. Jacobs, "The Present State of Accuracy in Stereolithography," Proceedings of the Second International Conference on Rapid Prototyping, Dayton, Ohio, 1991.
3. Murphy, E.J., Ansel, R.E. and J.J. Krajewski, "Reduced Distortion in Optical Freeform Fabrication with UV Lasers," Stereolithography Users Group Meeting, 1988.
4. Jacobs, P.F., Rapid Prototyping and Manufacturing - Fundamentals of Stereolithography, Society of Manufacturing Engineers, 1992.
5. Weissman, P.T, Bolan, B.A., and Chartoff, R.P., "Measurements of Linear Shrinkage and the Residual Stresses Developed During Laser Polymerization," Proceedings of the Third International Conference on Rapid Prototyping, Dayton, Ohio, 1992.

APPENDIX

Model:

Create Solid Model (Using Aries Software, Version 4)
 Create Support Structure
 Create Array of Test Parts
 Orient and Position Parts
 Convert to SLA Interface File
 Transfer File to SLICE Computer

Slice: (SLA-250 3D Stereolithography System Version 1.8 Release 3.82.1, copyright 1990, 3D Systems, Inc.)
 Select SLICE Parameters

<u>Parameter</u>	<u>TRIHATCH</u>	<u>STARWEAVE</u>
Scale Factor	1	1
Slice Resolution	5000	5000
Layer thickness	fixed	fixed (0.01 or 0.005)
X hatch space	variable	variable
Y hatch space	0	0
X skin fill	0.004	0.004
Y skin fill	0	0
Min. Surf. Angle	0	50
Beam Comp.	0	0
Slice Axis	Z	Z
Staggered hatch	OFF	ON
Alt. Sequence	OFF	ON
Retracted hatch	OFF	ON

Execute slice

Process:

Import Slice file to SLA-250 machine
 Select files to be merged and offset
 MERGE: Create vector layer parameter range files
 Select range parameters
 Add ranges: define 3100 for 10 mil and 3075 for 5 mil
 Recoater
 Range 1: NS 0; ZA .5; ZV .5; ZW 5; PD 1
 Range 2: NS 1; ZA .5; ZV .5; ZW 10; PD 1; P1 17
 Vector Cure Depths
 Border overcures: 0.008 supports, 0.006 parts
 Hatch overcures: 0.008 supports, (Table I) parts
 Fill cure depths: (Table I) parts
 Update range file
 Set-up machine:
 Verify laser beam power (18mW)
 Verify material (DuPont SOMOS™ 3110)
 Verify vat conditions (fill level and 30C temperature)

Build parts

Finish:

Drain parts over vat
 Remove parts from SLA
 Remove excess resin from parts:
 absorbant swab, NO solvent used
 Remove parts from platform
 Remove supports
 Continue excess resin removal
 Post-cure: UV oven for ten minutes per side

Homogenization Design and Layered Manufacturing of a Lower Control Arm in Project MAXWELL

**Roy Johanson
Noboru Kikuchi
Panos Papalambros**

Department of Mechanical Engineering
& Applied Mechanics
The University of Michigan
Ann Arbor, MI 48109

and

**Fritz Prinz
Lee Weiss**

Engineering Design Research Center
Carnegie Mellon University
Pittsburgh, PA 15213

Abstract

We briefly describe a new methodology for the design and manufacture of mechanical components and demonstrate the process for the design of an automobile suspension component. The methodology is a unique coupling between advanced technologies for product design and manufacture, which leads to the rapid realization of superior products. The concurrent design and analysis strategy yields information about the optimal structural layout, as well as details about the material composition. The fabrication of such designs requires unconventional manufacturing processes, such as layered manufacturing. Project MAXWELL, therefore, offers the possibility for the integration of layered manufacturing into the mainstream product development and fabrication process.

1. INTRODUCTION

Project MAXWELL embodies a methodology that provides a rigorous technique for the concurrent design of material composition and shape of components, and a new manufacturing process for their realization. At the University of Michigan (U-M), a new methodology has been developed for designing the form and material composition of mechanical and structural components based only on a description of the loading conditions and packaging requirements. At Carnegie Mellon University (CMU), a new manufacturing process has been developed for the free-form fabrication of parts from single or composite materials by thermal spray shape deposition. The goal of Project MAXWELL is to demonstrate the validity of an integrated approach for the rapid realization of superior components. Such components will possess superior structural and mechanical properties, and will satisfy packaging and assembly requirements.

The current application domain is in the design and manufacture of automobile components. The design methodology has been applied to the design of stiffened sheet

metal/component panels, suspension components, and a variety of other structures. Ongoing work involves the extension of the methodology to other applications.

In this paper, we briefly discuss the concurrent design of layout and material using the homogenization method. After describing the Recursive Mask and Deposit (MD*) process, we then demonstrate the MAXWELL methodology for the design of a lower control arm for an automobile suspension.

2. TOPOLOGY DESIGN IN MAXWELL

A fundamental approach to the thermo-mechanical characterization of general composite materials was first put forth by James Clerk Maxwell (1831-1879) and was later generalized as the theory of mixtures to provide a rigorous foundation for studying the mechanics of composite materials (see, e.g. [FUN65]). Project MAXWELL aims at transforming those early ideas into engineering reality.

The necessity of topological design in addition to size and shape design is widely recognized by structural engineers. If topological changes are not allowed, size and shape optimization procedures can improve a design by roughly 5-15%. Topological modifications can often yield 30-50% improvement. The homogenization method is a rigorous methodology to perform topology optimization. The problem is reformulated as a problem involving material distribution. Given an initial design domain, we discretize the domain and introduce microscale voids throughout the structure. The optimization problem then becomes the determination of the size and orientation of the microscale voids inside the initial design domain. If an area is highly stressed, the voids in that area will tend to zero -- the method will force solid material there. By removing material completely from portions of the domain densely packed with voids, the optimum shape of the structure is identified, while its topology is determined by accounting for the number of "global" holes (see also Figure 1).

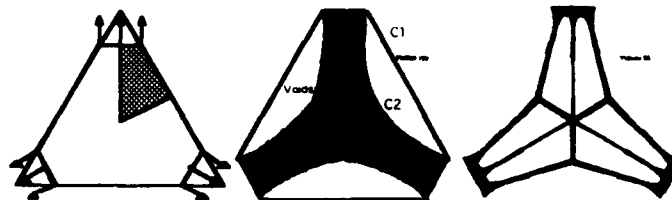


Figure 1: Identification of the Shape and Topology

This intuitive method of "sculpting" a structure is based on the theory of homogenization -- a method developed in the mid-1970's for the study of mechanics of composite materials. Applied mathematicians in France, Italy, and the former Soviet Union [LUR84, SAN80, TAR77] developed the homogenization theory to derive the constitutive equation of a composite material.

Although the optimization process often yields homogeneous solids, we consider the design domain to be a very specialized, fictitiously constructed composite material consisting of solids and voids. In order to determine the best microstructure, we allow the design domain to include other composite materials, e.g., ones that can improve strength, toughness, vibrational characteristics, and other measures of structural performance. Such structures have not been realized in practice due to the lack of an attractive manufacturing process that delivers non-homogeneous and anisotropic materials. For example, it is

impossible to create internal voids within a component by conventional NC machining. In MAXWELL, we use CMU's MD* process where the component is built up layer by layer, allowing the possibility of creating and orienting the voids as desired. Therefore, MD* allows serious consideration of these unusual and highly efficient structures for the first time.

3. FABRICATION BY THE MD* PROCESS

In the MD* (recursive Mask and Deposit) process developed at CMU, parts are manufactured by successively spraying cross-sectional layers. Each layer may contain several different materials. The geometry of the part is not constrained and its shape and material composition can be changed continuously during fabrication. To create a part, its geometric model is first sliced into cross-sectional layers, typically 0.001 to 0.005 inches thick. For each material in a layer, a disposable mask is made that exposes the area where that material occurs. The mask is placed upon the top layer of the growing part shape and a robotically manipulated thermal spray gun traverses the areas exposed by the mask. Masks are made from paper stock cut with a laser. Several alternative strategies are feasible for creating support structures for the part as it grows, including retaining a part of the mask or spraying the support material in place after the primary materials are deposited. A more detailed description of the MD* method can be found in [WEI92]. Two features of MD* make it particularly attractive in the context of Project MAXWELL: the ability to perform selective material deposition, and the prospect of a robust process for the forming and joining of composite structures. Availability of the MD* manufacturing process provides the requisite technology for the realization of novel designs (at the macro and microscale level) generated by the homogenization method. Additionally, MD* has the potential to create dense and laminate structures of arbitrary geometric complexity, while masking also enables selective material deposition. Therefore, different regions within a layer can be composed of different materials. Beck [BEC92] describes the manufacture of an integrated electro-mechanical structure created with the MD* process.

4. EXAMPLE: LOWER CONTROL ARM DESIGN

As an example of the integrated design and manufacturing process of project MAXWELL, a lower control arm was designed using the homogenization process and fabricated using MD*. This component is typical of vehicle chassis structural components; their design is typically driven by stiffness requirements. Phase I of the MAXWELL process begins with the description of an appropriate design domain and boundary conditions, shown in Figure 2. In this particular example, packaging requirements for other suspension and wheel components severely limit the allowable design space. In addition, appropriate attachment material for the strut must be provided in the final design. Translational displacements are constrained at the two pivots (to the right in Figure 1), and loads are applied at the strut and at the ball joint. Three separate loading conditions are considered, with the primary load case being vertical (z-direction) loading at the strut attachment point.

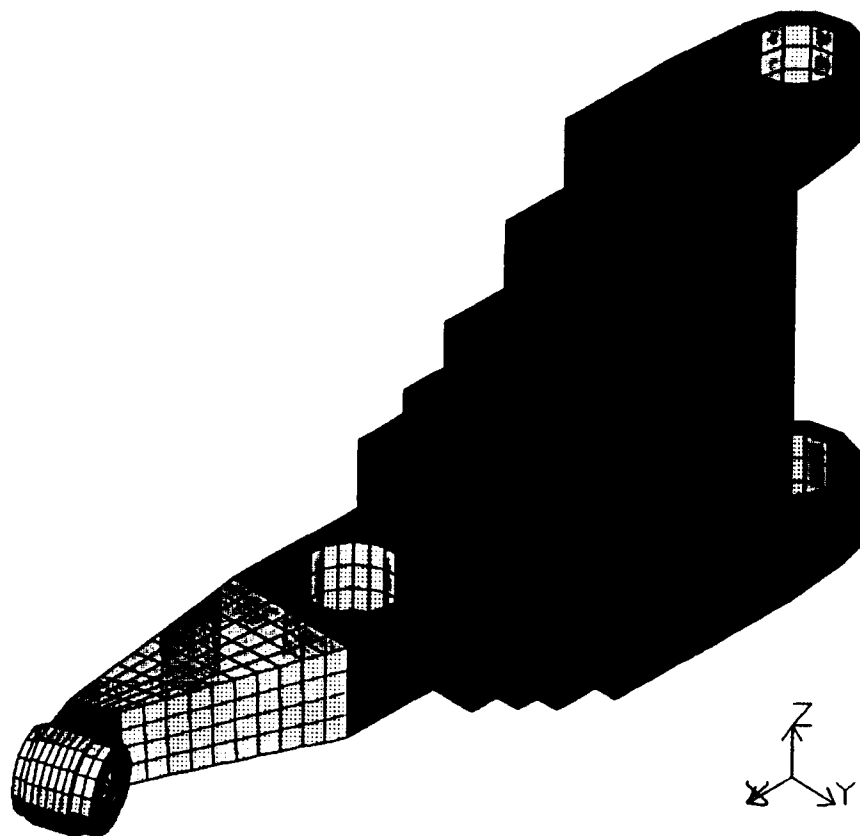


Figure 2: Design Domain for Lower Control Arm

The homogenization process produces a topology which possesses the maximum stiffness for a (user-supplied) constraint on the percentage of the design domain to be filled with material. Figures 3 and 4 show the result of the homogenization process, showing two cross-sections of the resultant structure. Note that the optimal topology which is designed using the homogenization procedure would be difficult to manufacture using traditional techniques.

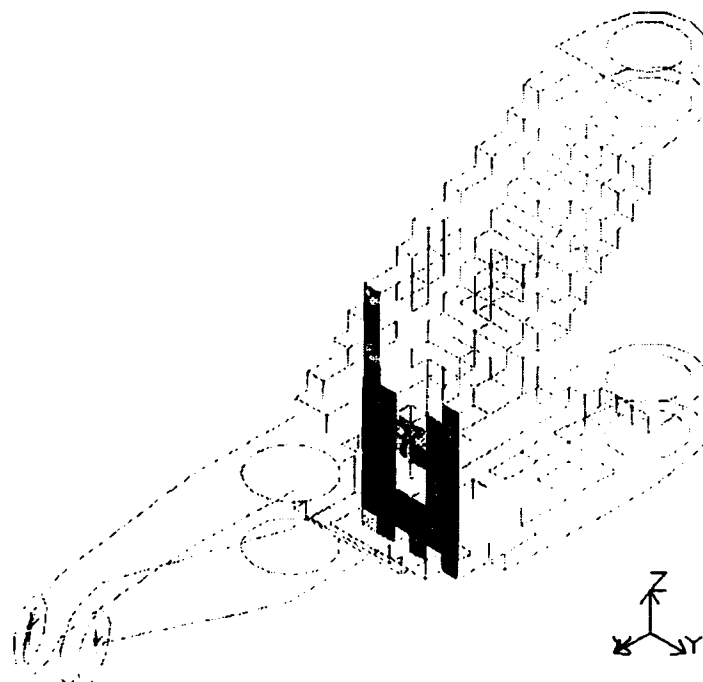


Figure 3: Cross-Section of Lower Control Arm at 45% Section

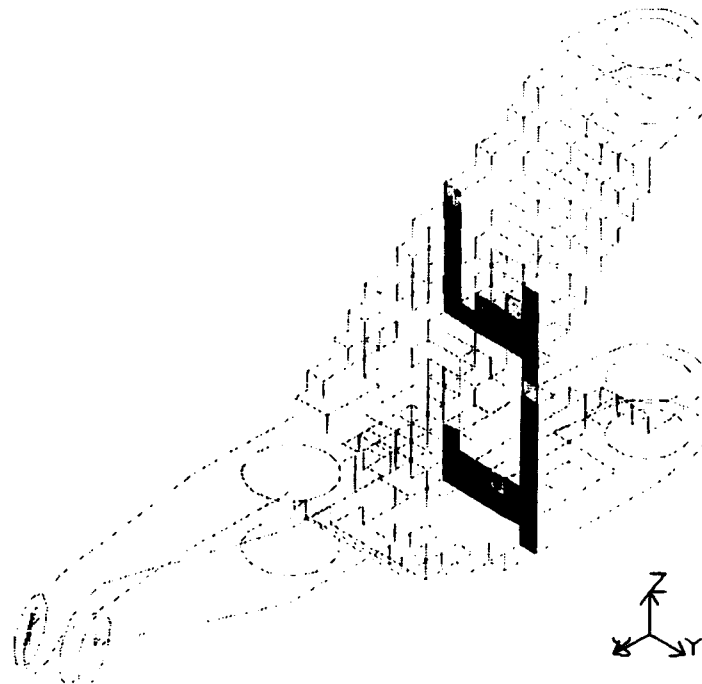


Figure 4: Cross-Section of Lower Control Arm at 60% Section

Often, the results from the homogenization procedure are smoothed, and detailed local structural constraints on allowable stresses and deflections are added and evaluated in a second sizing optimization procedure. In this example, however, we proceeded directly to the fabrication of the component using the MD* process. The data was transferred directly from the homogenization output to the MD* process through a standard stereolithography file. The control arm was interpreted as an isotropic component composed of one material, i.e., individual elements in the structure were interpreted as either all material (solid) or all void (holes), and the control arm was fabricated from a zinc alloy.

5. CURRENT STATUS AND FUTURE GOALS OF PROJECT MAXWELL

Project MAXWELL is a synergistic integration of two novel research efforts, one in design and the other in manufacturing, for the purpose of establishing a sound methodology for the rapid realization of superior products. Basic research directly relevant to MAXWELL has been ongoing at the participating institutions for over four years. The UM results to date can be summarized as the development of an integrated three-phase system for the concurrent design and analysis of superior structural components.

Phase I: Based on the specified boundary conditions (type and magnitude of loads) and designable space (packaging specifications) the homogenization method is applied to derive a gray scale representation of the material composition and distribution that is optimal relative to some desired measure of structural performance.

Phase II: Using computer vision and geometric modeling techniques, this image is interpreted and translated into a realistic structure.

Phase III: A parametric optimization model based on finite element analysis is formulated and solved to determine a complete dimensional and material description of the structure.

Phase IV: The manufacture of the Phase III output (i.e., discrete parts of arbitrary geometry and possibly varying material composition) using the MD* process is performed.

Phase V: The final phase in MAXWELL is the testing phase, where the Phase IV products will be subjected to various mechanical tests. Qualitative indices of performance in Phase V will include measures such as weight to stiffness ratio, impact energy absorption rates, and fatigue life.

Currently the UM system can develop structural layouts for 2D, 2.5D and full 3D components. A major area of current research is appropriate geometric representation of optimal topologies in three dimensions. Ongoing research at CMU directly relevant to MAXWELL can be summarized as the development of the MD* process for the rapid manufacture of single or multi-material components.

ACKNOWLEDGMENTS

The UM research was partially funded by the National Science Foundation. CMU has received partial support from the National Science Foundation Engineering Research Center

REFERENCES

- [ASH91] Ashley, S. "Rapid Prototyping Systems" *Mechanical Engineering*, 113(4), 34-43 (1991)
- [BEC92] Beck, J.E., F.B. Prinz, D.P. Siewiorek, and L.E. Weiss. "Manufacturing Mechatronics using Thermal Spray Shape Deposition." in Proceedings of Solid Freeform Fabrication Symposium, The University of Texas at Austin, August, 1992, pp. 272-279.
- [BEN86] Bennet, J.A. and Botkin, M.E., The Optimum Shape: Automated Structural Design, Plenum Press, New York, 1986.
- [BEN88] Bendsoe, P.M. and Kikuchi, N., "Generating Optimal Topologies in Structural Design Using a Homogenization Method". *Comp. Meth. Appl. Mech. Eng.*, Vol 71, 197-224, 1988.
- [BOT85] Botkin, M.E. and Bennet, J.A., "Shape Optimization of Three Dimensional Folded Plate Structures" *AIAA J.*, 23(11) 1804-1810, 1985.
- [BRE91] Bremicker, M. Chirehdast, M. Kikuchi, N. Papalambros, P.Y., "Topology and Shape Optimization in Structural Design." *J of Mechanics of Structures and Machines*
- [DUT92] Dutta, D. et. al. "Project MAXWELL: Towards Rapid Realization of Superior Products" in Proceedings of Solid Freeform Fabrication Symposium, The University of Texas at Austin, 1992., pp. 54-62.
- [FUN65] Fung, Y.C. Foundations of Solid Mechanics, Prentice-Hall, Englewood Cliffs, NJ, 1965
- [LUR84] Lurie, K.A. and Cherakev, A.V. "Exact Estimates of Conductivity of Composites formed by two Isotropically Conducting Media taken in Prescribed Proportion". *Proc Royal Soc. Edinburgh*, 99A, pp. 71-78, 1984.

- [SAN80] Sanchez-Palencia, E. "Non-homogeneous media and vibration theory", *Springer Lecture Notes in Physics*, Berlin, 1980.
- [TAR77] Tartar, L. "Estimation de coefficients homogeneises, *Springer Lecture Notes in Mathematics*, Berlin, pp.364-373, 1977.
- [WEI91] Weiss, L.E., Prinz, F.B. and Siewiorek, D.P. "A Framework for Thermal Spray Shape Deposition in the MD* System" in Proceedings of Solid Freeform Fabrication Symposium, The University of Texas at Austin, August, 1991.
- [WEI90] Weiss, L. Guroz, E.L., Prinz, F.B. Fussel, P.S., Mahalingham, S. and Patrick, E.P., "A Rapid Tool Manufacturing System Based on Stereolithography and Thermal Spraying" *Manufacturing Review*, 3(1), 40-48, 1990.
- [WEI92] Weiss, L. E., F. Prinz, D. Adams. "Solid Freeform Fabrication by thermal spray shape deposition" in *ASM International Thermal Spray Conference*, Orlando, FL, June 1992.

AN EVALUATION OF THE MECHANICAL BEHAVIOR OF BRONZE-NI COMPOSITES PRODUCED BY SELECTIVE LASER SINTERING

Mukesh K. Agarwala, David L. Bourell, Benny Wu, and Joseph J. Beaman.
Center for Materials Science and Engineering, and Department of Mechanical Engineering,
The University of Texas at Austin, Austin, Texas 78712.

ABSTRACT

Mechanical properties of Bronze-Nickel composites produced by Selective Laser Sintering (SLS) were evaluated by constant displacement tension tests. These were studied as a function of SLS process parameters - laser power density, scan speed, scan spacing, scan direction and layer thickness. The strength data was then correlated to the microstructure and the part bulk density. To further enhance the part densities and the mechanical properties, post-SLS sintering was studied. The relationships between SLS process parameters, post-SLS sintering parameters and the resulting microstructures, part bulk density and the mechanical properties will be described.

INTRODUCTION

Markets for rapid prototyping continue to grow as the demand for functional parts and prototype tooling increases. Several novel approaches exist to meet this demand. In recent years, Selective Laser Sintering (SLS) has emerged as one such process which can, not only produce parts from polymers successfully, but also is capable of producing parts from high temperature materials like metals and ceramics directly, without the aid of any low temperature binders (1,2).

Direct SLS of metals is extremely desirable as it avoids the time consuming and often tedious step of binder removal associated with indirect fabrication of metals and ceramics parts. This makes the production of prototype patterns, molds and dies for casting and injection molding, fast and economical.

However, any structural part produced, either by direct SLS or any other technique, is of little consequence unless it has the structural integrity to withstand the complex loading conditions that its use may require. In this study, the mechanical behavior of direct SLS Bronze-Nickel parts were evaluated, as this alloy system is being developed for use as molds in injection molding.

EXPERIMENTAL PROCEDURE

Sub-size tension test bars of Bronze-Nickel were made in the high-temperature SLS workstation developed at The University of Texas at Austin (3,4). The dimensions and geometry of the bars used in this study is shown schematically in Figure 1., which conforms closely with the ASTM Standard E8 (5) and the standard MPIF tension test bars for powder metallurgy materials (6).

Prealloyed, 90 Wt.% Cu - 10 Wt.% Sn, Bronze powders of particle size 30-50 μm and Ni powders of particle size 75-150 μm were mixed and SLS processed at laser powers of 35 W, 45 W, and 56 W with beam diameters of 0.875 mm, 1.06 mm, and 1.224 mm, respectively. Scan speeds in the range 0.2 to 1.5 inch/second were used. Layer thickness and scan spacing were kept constant at 0.01 and 0.02 inch, respectively. Scanning was done along the transverse and longitudinal directions of bars and layers were built in the thickness direction.

Post-SLS sintering was done for a series of tension test bars processed at 56 W laser power and scan speeds of 0.3"/sec. and 1.5"/sec. Post-SLS sintering of the bars was done at temperatures ranging from 900°C to 1100°C in flowing hydrogen for time periods varying from 1 to 10 hours. All tension testings were done in a constant displacement testing machine at a crosshead speed of 1 mm/min. Densities were measured by direct volume measurement. Phase

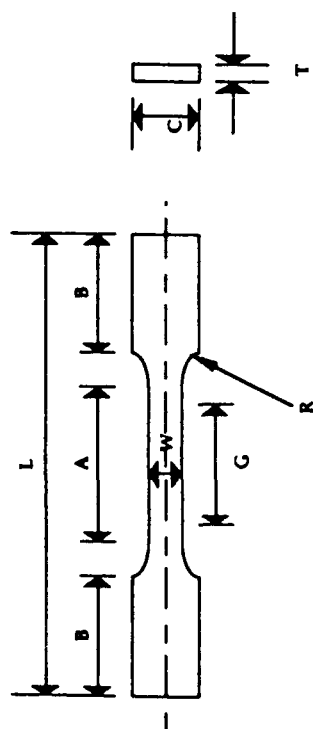


Figure 1. A Schematic of Tensile Bar Geometry Used to Make SLS Bronze-Ni Samples. ($L=3"$, $B=0.7"$, $A=1"$, $G=0.75"$, $W=0.2"$, $C=0.5"$, $R=0.375"$, and $T=0.25"$)



Figure 3. SEM of Fracture Surface of SLS Bronze-Ni Part Showing Melting of Bronze With No Melting of Ni.

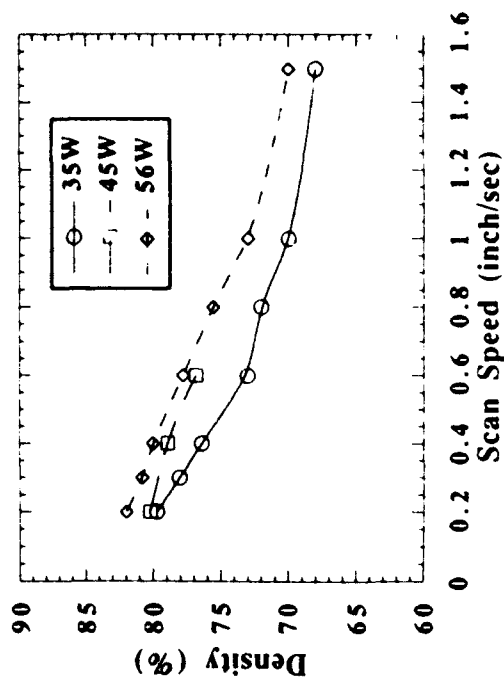


Figure 2. Fractional Density of SLS Bronze-Ni Parts as a Function of Scan Speed and Laser Power.

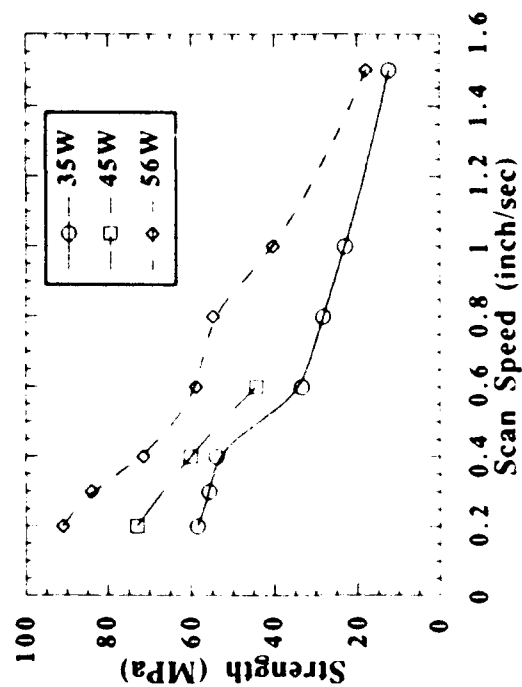


Figure 4. Tensile Strength of SLS Bronze-Ni Parts as a Function of Scan Speed and Laser Power.

analysis and microstructural analysis of the material was done at every step of processing by X-ray diffraction, optical microscopy, EDS and SEM.

RESULTS AND DISCUSSION

Preliminary experiments were done to investigate the effect of scan direction and layer thickness. From these experiments it was found that strengths were considerably lower when scanned in the longitudinal direction when compared to transverse direction. This is due to a better sintered part when the scan vector is short. Nelson, et al (7) have shown that a series of short scan vectors would receive more net energy than a series of longer scan vectors because of less delay between successive pulses.

As expected, lowering the layer thickness from 0.02" to 0.01" resulted in higher strength. However, on further lowering the layer thickness to 0.005" resulted in difficulty in spreading fresh layers without disturbing the previously sintered layers. This is especially the case during the early build-up of the part. Therefore, all further experiments were done at a constant layer thickness of 0.01" and all scanning was done along the short-transverse direction.

EFFECT OF SCAN SPEED AND LASER POWER

As shown in Figure 2, for a given laser power, density of the SLS Bronze-Nickel parts increased as the scan speed decreases. Also, the density is found to increase with increasing laser power, at a constant scan speed. Higher density is achieved with slower scan speed and higher laser power due to an increased amount of energy input to the powder surface. A higher amount of energy to the powders increases the temperature high enough to result in a larger amount of liquid phase formation. Bronze, which melts incongruently between 870°C (solidus) and 1030°C (liquidus), exhibits a higher degree of liquid formation as the temperature above the solidus increases. Also, as temperature increases, the viscosity of molten bronze decreases, facilitating more efficient densification with the solid nickel particles. An increase in temperature also lowers the wetting angle between liquid bronze and solid nickel to result in better wetting characteristics and improved densification. Figure 3 shows the fracture surface of a typical Bronze-Nickel part showing melting of bronze particles while the nickel particles are present without any significant melting. However, at very high laser powers and slow scan speeds (0.2"/sec. - 0.8"/sec.), significant amount of "curling" phenomenon was observed in the parts, as observed by Zong et.al. also (1). Experiments with varying bed temperatures showed that "curling" can be minimised by using high bed temperatures while keeping laser power high enough with slow scan speeds necessary for high density parts. However, at bed temperatures above 450°C, the entire powder bed undergoes light sintering and forms a "cake" around the SLS part. This makes it difficult to remove the SLS parts from the surrounding powder bed. Therefore, all experiments in this study were done at a bed temperature of 450°C.

Strength, which is primarily a function of fractional density (or porosity) (8), exhibited a similar trend as density with respect to scan speed and laser power, Figure 4. Pores reduce the effective load carrying capacity of a material. Also, pores act as stress concentrators and as effective crack initiation sites. Therefore, a sample with density less than 100% is expected to have a strength less than that of a fully dense wrought material. In addition to fractional density, the strength of such porous compacts depends on various powder characteristics such as particle size, particle size distribution and particle shape. The strength of porous compacts is expected to vary with fractional density ρ of the compact as follows :

$$\sigma = C \sigma_0 f(\rho) \quad (I)$$

where σ is the strength of compact, σ_0 is the wrought strength and $f(\rho)$ is a fractional density dependance function. Several studies have attempted to correlate strength with ρ by various forms of $f(\rho)$. The most commonly used relationship is of the form :

$$\sigma = C \sigma_0 \rho^m \quad (II)$$

where C and m are empirical material constants and ρ is the fractional density.

POST-SLS PROCESSING OF BRONZE-NICKEL PARTS

In an attempt to further densify and hence improve strength, the SLS Bronze-Nickel tensile coupons were further processed by Liquid Phase Sintering (LPS) in hydrogen above the solidus temperature (870°C) of bronze. Before looking at the results of post-SLS processing, it is important to review the basic concepts of LPS (9) to better understand the results, especially with respect to Bronze-Nickel system. Liquid phase sintering in Bronze-Nickel system occurs in three stages :

STAGE I : At temperatures above the solidus temperature 870°C, bronze melts partially and above the liquidus 1030°C it melts completely. In this stage of LPS, the liquid bronze flows into the pores and a rearrangement of the solid nickel particles takes place. This stage leads to rapid shrinkage and increase in density and hence strength. Most of the densification in LPS is achieved in this stage. If sufficient amount of liquid is formed with low enough viscosity to flow freely, then the final density at the end of stage I is independent of the starting density, which is determined by laser power and scan speed. The amount of liquid phase formed and the viscosity of the liquid formed depends on the sintering temperature. Higher the sintering temperature, higher is the amount of liquid phase formed with lower the viscosity. But a very high sintering temperature can lead to very high amount of liquid phase with very low viscosity which can result in loss of shape. Particle size of solid phase and rate of heating also determine densification at this stage.

STAGE II : In this stage of LPS, normal densification is accompanied by chemical homogenization between bronze and nickel. Bronze, predominantly copper (90 Wt.%), and nickel homogenize at high temperatures, either by interdiffusion if the homogenization is between solid bronze and solid nickel or by solution-precipitation if the homogenization is between liquid bronze and solid nickel, to form a homogeneous solid solution. In either case, the bronze phase disappears completely leaving behind pores in its place and an expanded solid solution of Cu in Ni. This happens due to a faster diffusion rate of Cu into Ni than that of Ni into Cu, which results in the Kirkendall effect. Therefore, the pores created at this stage are referred to as Kirkendall porosity. Kuczynski has demonstrated the influence of the Kirkendall effect upon sintering in a series of model experiments (10). Therefore, in this stage, normal densification is dominated by the growth or swelling of the part due to Kirkendall porosity.

Detailed investigations of LPS have shown that similar material transport mechanisms prevail during stage I as well as stage II. Therefore, a sharp distinction between these stages is not justified. Whether stage I or stage II predominates the process depends on the particular circumstances. Powder particle size, starting density, sintering temperature, time and rate of heating are most influential in determining this. Effect of some of these variables on LPS will be discussed later with respect to SLS Bronze-Nickel parts. Figure 5 shows the microstructural changes observed with the different stages of LPS and Figure 6 shows the peak broadening occurring due to formation of a homogeneous solid solution of Cu-Ni.

STAGE III : Once homogenization has occurred, only normal shrinkage due to sintering occurs. But now, the sintering occurs in solid state as the temperature is below the solidus of the newly

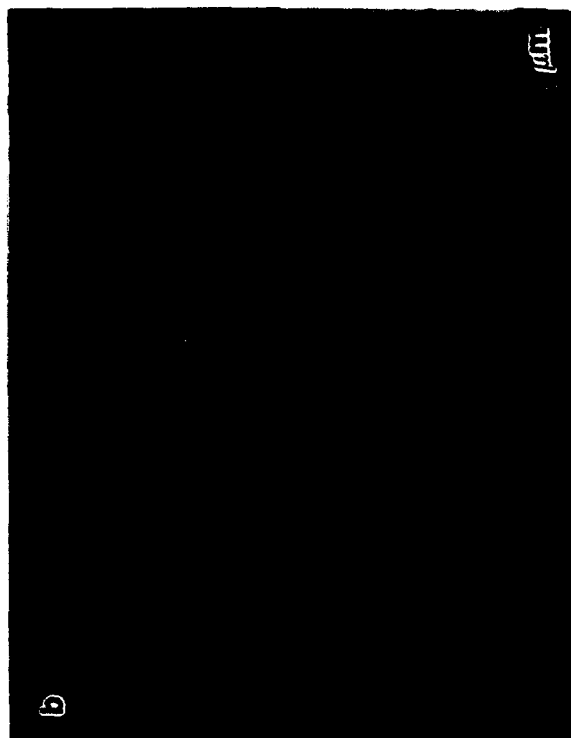
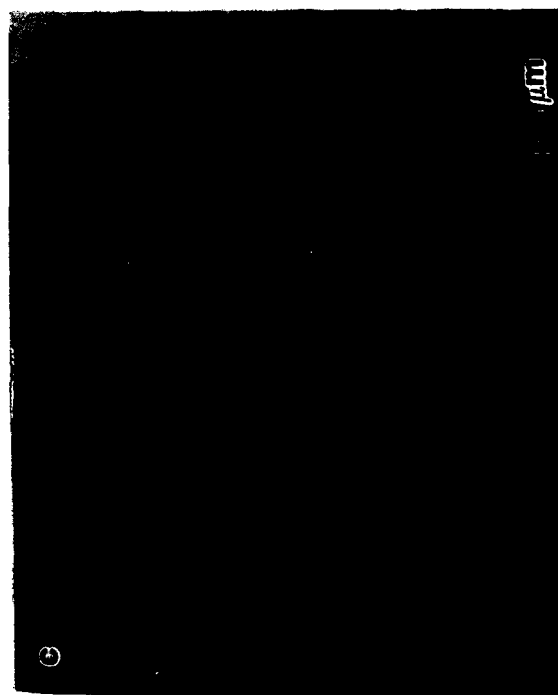


Figure 5. Optical Micrographs of (a) SLS Bronze-Ni Part (56W, 0.3 inch/sec) Showing Bronze and Ni as Separate Phases and High Porosity, (b) Post-SLS Stage II LPS Bronze-Ni Part (56W, 0.3 inch/sec., 950°C, 1 hour) Showing Nearly Homogeneous Phase of Cu-Ni With Some Residual Bronze and High Porosity, (c) Post-SLS Stage I LPS Bronze-Ni Part (56W, 0.3 inch/sec, 1030°C, 1hour) Showing Nearly Homogeneous Phase of Cu-Ni With Some Residual Bronze and Low Porosity



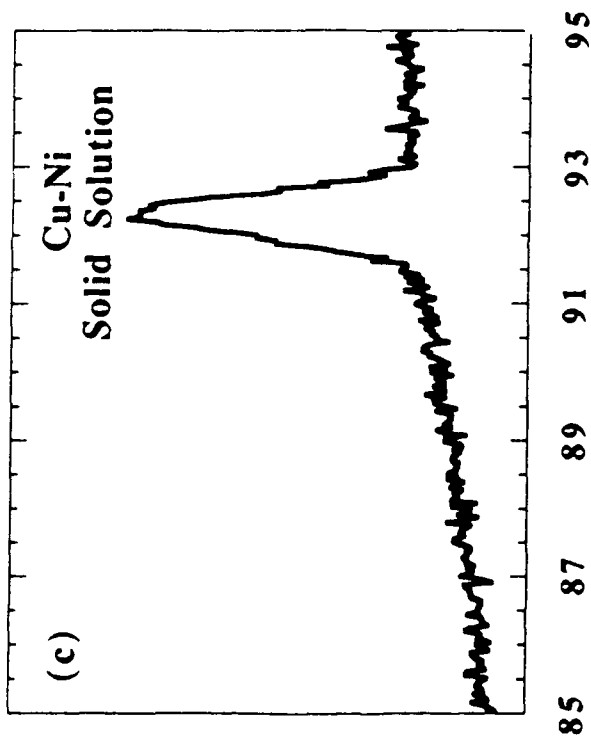
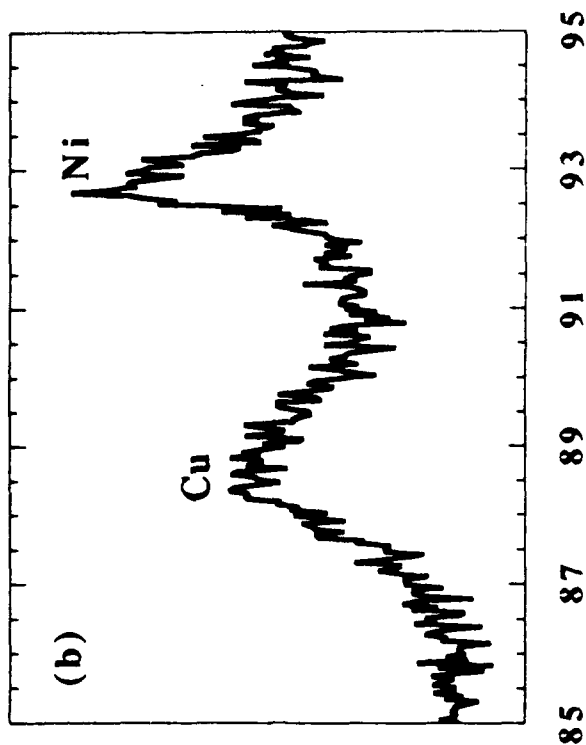
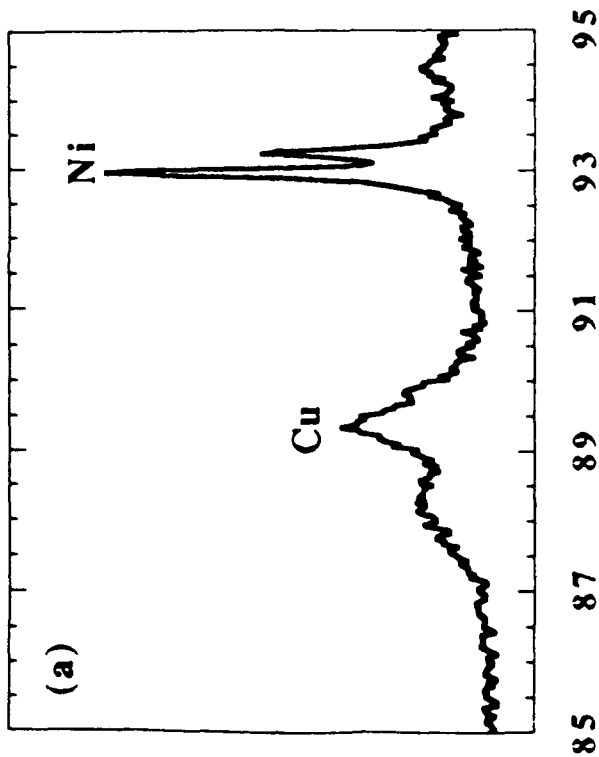


Figure 6. XRD patterns of (311) peaks of Bronze and Nickel Showing Peak broadening due to Homogenization (a) SLS Bronze-Ni Part (56W, 0.3 inch/sec) Showing Cu and Ni as Separate Phases (b) Post-SLS Stage II LPS Bronze-Ni Part (56W, 0.3 inch/sec., 950°C, 1 hour) Indicating Partial Homogenization of Cu and Ni (c) Post-SLS Stage II LPS Bronze-Ni Part (56W, 0.3 inch/sec, 950°C, 6hour) Indicating Complete Homogenization of Cu and Ni.

formed solid solution of Cu-Ni ($\sim 1100^{\circ}\text{C}$). Therefore, even for prolonged periods of times, shrinkage or densification during this stage is very small, leaving an overall expansion or shrinkage in the samples, depending on whether first stage or second stage of LPS dominates.

EFFECT OF SINTERING TEMPERATURE AND TIME

As shown in Figures 7, at temperatures below 1000°C the density and strength of SLS parts decrease irrespective of starting densities. The density and strength reach a minimum and then increase slowly to nearly starting densities. At such low temperatures, amount of liquid phase formed is very small with high viscosity which prevents any significant densification normally associated with stage I LPS. Instead, stage II dominates the LPS initially and then stage III continues till the end of the process.

At 1060°C , a temperature well above the liquidus of bronze, bronze is completely in liquid state and has sufficiently low viscosity to allow stage I LPS to dominate. Therefore, the density and hence the strength of the SLS parts increase rapidly at short times of 1 hour. Following this rapid gain in density and strength, there is a slight loss of density and strength due to stage II LPS when the density and strength decrease due to Kirkendall porosity. Some of this loss in density and strength is regained in stage III of LPS due to solid state sintering of Cu-Ni solid solution. At such a high temperature the flow of liquid in stage I is free of any restriction due to low enough viscosity. Therefore, the final density and strength at the end of stage I is independent of starting density and strength. At temperature above 1060°C , the SLS parts exhibited loss of shape even at small times due to significantly lower viscosity of the liquid bronze.

At the liquidus temperature of 1030°C , liquid bronze is more viscous than at 1060°C . Therefore, flow of liquid into pores and rearrangement of solid nickel particles is less dominant. Therefore, the density and strength in stage I at 1030°C is lower than that at 1060°C . In a high-starting-density part, the rigid network of solid nickel particles restrict the flow further and prevent their rearrangement. While in a lower-starting-density part the liquid is more free to flow and rearrange the solid particles. Also, the interdiffusion lengths in a high-starting-density part is smaller, thereby promoting stage II LPS and thus resulting in lower final strengths and density than that for a lower-starting-density part. This effect is more pronounced at 1000°C when the stage II homogenization completely dominates over the stage I densification for a higher-starting-density part. Therefore, at 1000°C , while a high-starting density part exhibits worsening of density and strength, a low-starting-density part exhibits improvements in density and strength.

ANISOTROPIC LINEAR DIMENSIONAL CHANGES

Net volume changes (expansion or shrinkage) of SLS parts during LPS was in accordance with the observed density and strength changes. However, the linear dimensional changes, $\Delta L/L_0$, was not same in all three directions (11). They exhibited some rather interesting trends reflecting the anisotropy in SLS parts.

In general, parts that exhibited swelling or growth during LPS, had a net volume expansion exceeding 10% and was mostly of the order of 15%, resulting in a decrease in fractional density of the order of 8% to 12%, as seen earlier. In accordance with stage II LPS, this decrease was observed over a relatively short period of time followed by a nearly constant density, as would be expected in stage III of LPS. However, the linear dimensional expansion in these parts was anisotropic with least expansion ($\sim 2\%-3\%$) in the thickness direction, i.e. direction normal to the sintering plane. Most of the expansion (5%-9%) was confined to the transverse direction (scan direction), Figure 8 (a). A higher degree of sintering along the scan direction, during SLS, results in better density along the transverse direction, thus forming a rigid network of solid nickel and decreasing the interdiffusion lengths. Therefore, stage I LPS is suppressed and stage II LPS dominates along the scan direction yielding a high linear expansion. While a lower degree of

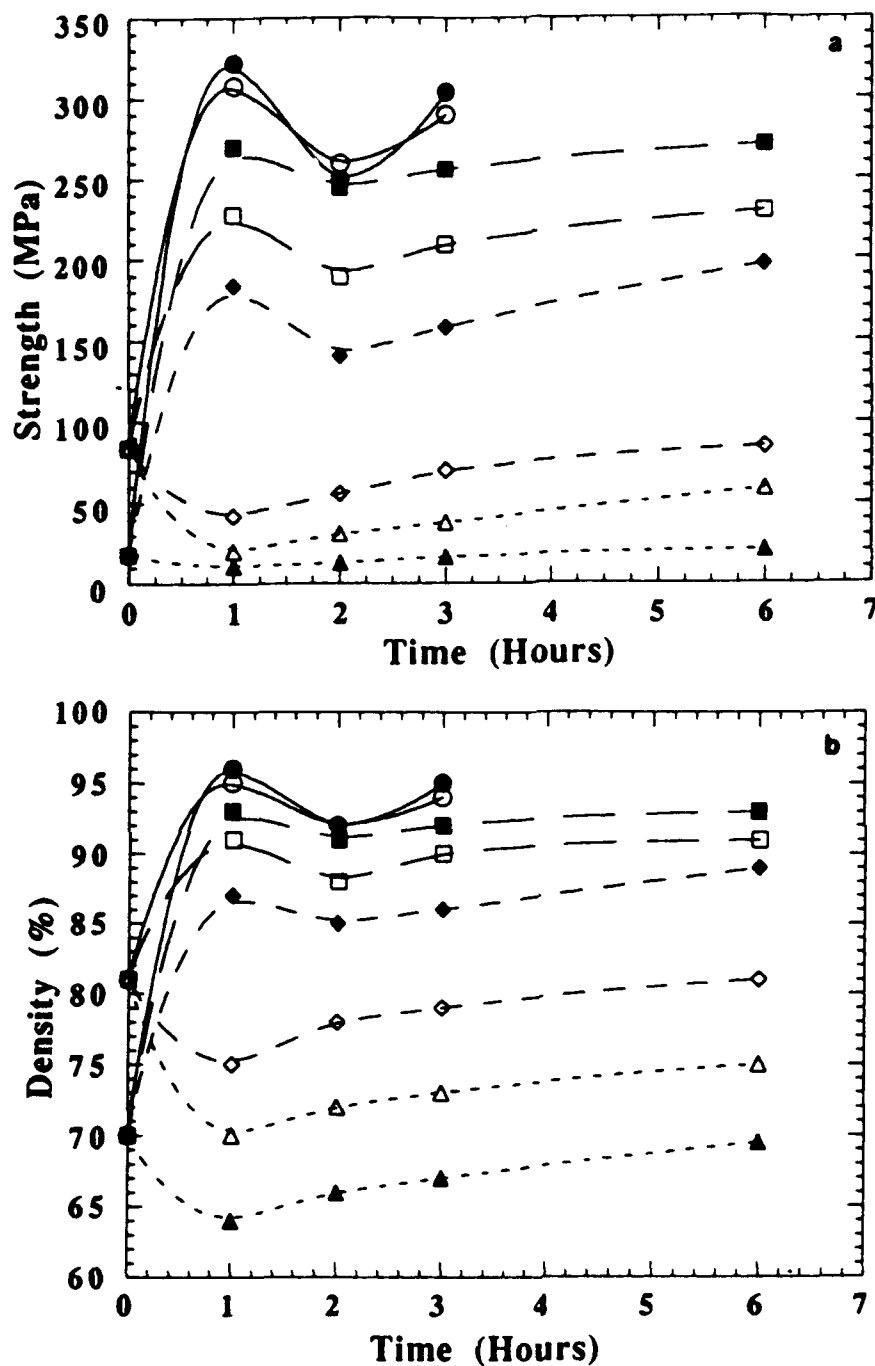
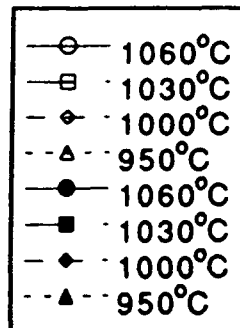


Figure 7.(a) Strength of Post-SLS LPS Bronze-Ni Parts Showing the Effect of LPS Time and Temperature and Starting Density, (b) Fractional Density of Post-SLS LPS Bronze-Ni Parts Showing the Effect of LPS Time and Temperature and Starting density. (Open Symbols - Samples SLS at 0.3 inch/sec. Starting Density 81% and Closed Symbols - Samples SLS at 1.5 inch/sec. Starting Density 70%)



sintering normal to the sintering plane results in poor density between layers leaving a loose network of solid nickel and large interdiffusion lengths. Therefore, stage I LPS is less suppressed and stage II LPS is less dominating between the layers resulting in considerably lower linear expansion. Also, flow of liquid bronze in stage I along the thickness direction is aided by gravity as the samples were post processed with the thickness direction along the direction of gravity.

Like the parts which exhibited growth, the parts exhibiting overall shrinkage or densification also exhibited volume changes according to changes in density, but the linear dimensional changes in the three directions were different. As explained above, since stage I LPS is more dominant along the thickness direction than along the scan direction, higher linear shrinkage was observed in the thickness direction than along the transverse direction. Shrinkage in the longitudinal direction was comparable but higher than along the transverse direction, Figure 8(b).

STRENGTH VARIATION WITH DENSITY

As discussed earlier, pores reduce the effective load carrying capacity of a material, thus decreasing the strength of the material. Equation II relates the strength to the fractional density empirically, based on the premise that pores reduce the load bearing capacity of the material. Based on the discussions of results thus far, it can be seen that both the strength as well as density of SLS parts increased with increasing laser power and decreasing scan speed. Therefore, it seems reasonable to relate the strength and density of SLS parts irrespective of the laser power or scan speeds at which they were processed. As shown in Figure 9, a near perfect fit was obtained for the strength and density by relating them using the power law Equation II, with the empirical constants $C\sigma_0$ and m as 590.8 and 9.43 respectively. A high exponent factor, m , of 9.43 indicates large gains in strength for small incremental gains in density. This makes it possible to produce less than fully dense yet structurally sound parts of Bronze-Nickel by direct SLS, without any post-processing. Small incremental gains in density are achievable by increasing the laser power and/or decreasing the scan speed. The "curl" phenomenon associated with high laser power and slow scan speeds can be overcome by using higher bias temperatures in the high-temperature workstation, if light sintering of the powder bed can be avoided or minimised.

Liquid Phase Sintering (LPS) of the SLS Bronze-Ni parts results in an increase or decrease in density and strengths simultaneously as a function of LPS time and temperature, as discussed earlier. Therefore, relating strength with density using the power law form given by Equation II, yields a near perfect fit with the empirical constants $C\sigma_0$ and m as 527.94 and 8.73 respectively, Figure 9(b). From comparison of the empirical constants $C\sigma_0$ and m for SLS Bronze-Nickel parts and for post-SLS LPS Bronze-Nickel parts, it is clear that density and strength vary in a similar way irrespective of the processing. During SLS scan speed and laser power determine the density and strength, while during LPS time and temperature determine the density and strength. SLS laser power is analogous to the LPS temperature as it determines the processing temperature. Similarly, SLS scan speed is analogous to the LPS time as it determines the time of processing. Therefore, by careful manipulation of these four variables it is possible to produce high density, structurally sound parts with no "curl" by direct SLS followed by LPS in very short processing time periods.

CONCLUSIONS

Direct SLS of Bronze-Nickel parts was studied by evaluating the density and strength of the parts as a function of SLS process parameters : laser power, scan speed, scan direction, and layer thickness. Post-SLS processing of the parts was done by Liquid Phase Sintering (LPS) to further enhance the density and strength. LPS of the SLS parts was studied as a function of time and temperature. The relationships between the SLS processing parameters, LPS parameters and the resulting microstructures, density and strengths can be summarized as follows :

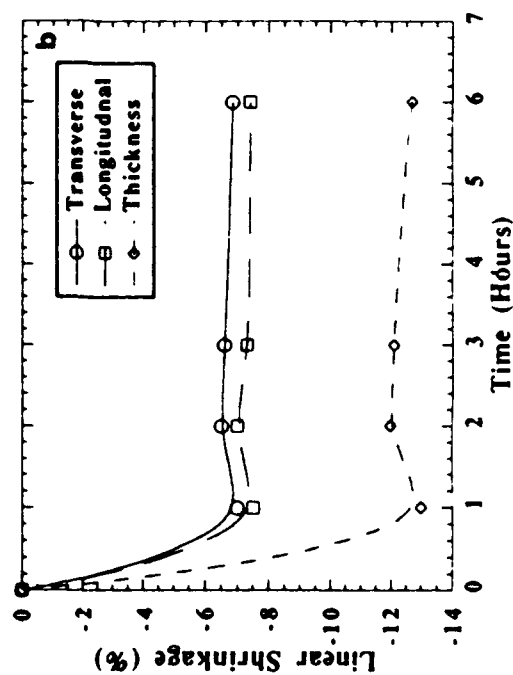
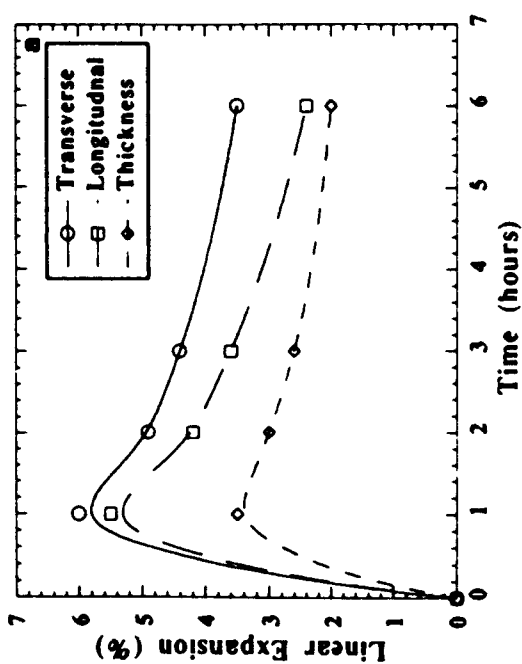


Figure 8. Linear Dimensional Changes Showing Anisotropic Changes (a) Expansion in 56W, 0.3"/sec. SLS Part, LPS at 950°C (b) Shrinkage in 56 W, 1.5"/sec.SLS Sample, LPS at 1030°C.

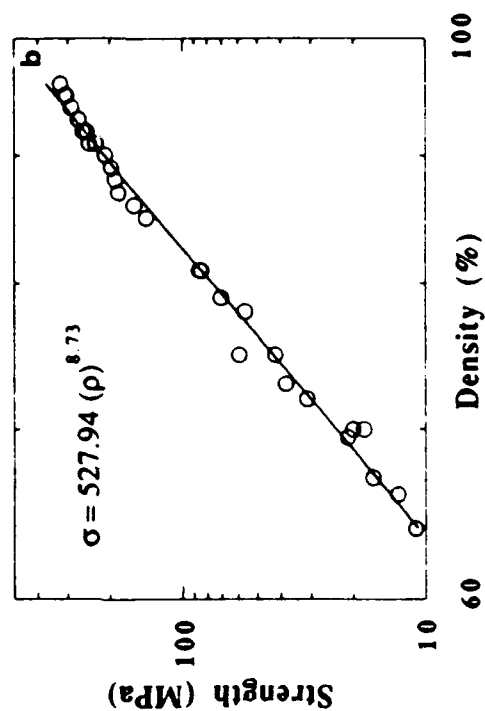
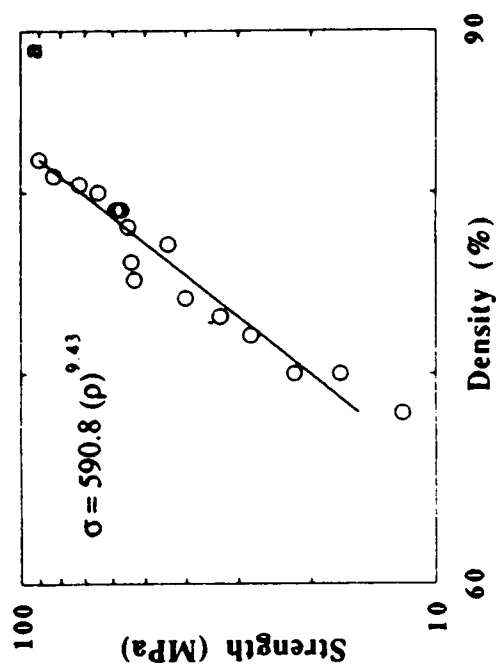


Figure 9. Strength vs. Density Using Equation II for (a) SLS Bronze-Ni Parts Without Post-SLS Processing (b) Post-SLS LPS Bronze-Ni Parts.

1. Density and strength increase as the layer thickness decreases, scan speed decreases and laser power increases.
2. Scanning in the short transverse direction yielded best results.
3. Strength and density of SLS Bronze-Nickel parts show a very strong power law dependence.
4. LPS of SLS Bronze-Nickel parts improved density and strength at temperatures well above the liquidus temperature of bronze.
5. By LPS at temperatures well below the liquidus temperature of Bronze, density and strength of SLS Bronze-Nickel parts decreased due to Kirkendall porosity resulting from the homogenization of Bronze and Ni.
6. Linear dimensional changes during LPS were anisotropic.
7. Strength and density of post-SLS LPS Bronze-Nickel parts show a similar power law dependence as the SLS Bronze-Nickel parts.

ACKNOWLEDGMENTS

The authors gratefully acknowledge research grants from DTM Corporation, Austin, Texas and NSF Small Grant for Exploratory Research, Grant # DDM-9312603.

REFERENCES

1. G.Zong, Y.Wu, N.Tran, I.Lee, D.L.Bourell, J.J.Beaman, and H.L.Marcus, "Direct Selective Laser Sintering of High Temperature Materials," Proc. of the SFF Symp., Austin, Texas, Aug 3-5, 1992.
2. D.L.Bourell, H.L.Marcus, J.W.Barlow, and J.J.Beaman, "Selective Laser Sintering of Metals and Ceramics," Int. J. Powder Met., 28(4), 369, 1992.
3. S.Das, J.C.McWilliams, Y.Wu, and J.J.Beaman, "Design of a High Temperature Workstation for the Selective Laser Sintering Process," Proc. of the SFF Symp., Austin, Texas, Aug , 1991.
4. J.McWilliams, C.Hysinger, and J.J.Beaman, "Design of a High Temperature Process Chamber for the Selective Laser Sintering Process," Proc. of the SFF Symp., Austin, Texas, Aug 3-5, 1992.
5. ASTM, "Standard Methods of Tension Testing of Metallic Material," 1977 Annual Book of ASTM Standards, Part 6 : Copper and Copper Alloys, ASTM Designation : E8-77, 898-917, 1977..
6. Metals Handbook, Vol.7, 9th Ed., American Society of Metals, Metals Park, OH.
7. J.C.Nelson, and J.W.Barlow, "Relating Operating Parameters Between Selective Laser Sintering Machines which have Different Scanner Geometries and Laser Spot Sizes," Proc. of the SFF Symp., Austin, Texas, Aug 3-5, 1992.
8. R.M.German, "Powder Metallurgy Science," Metal Powder Industries Federation, Princeton, NJ.
9. F.V.Lenel, "Powder Metallurgy - Principles and Applications," Metal Powder Industries Federation, Princeton, NJ.
10. G.C.Kuczynski, "Model Experiments and the Theory of Sintering." From "Sintering - Key Papers," Ed. by S.Somiya and Y.Moriyoshi, Elsevier Applied Science, London and New York.
11. J.C.Nelson, N.K.Vail, M.M.Sun, and J.W.Barlow, "Post-Processing of Selective Laser Sintered Polycarbonate Parts," Proc. of the SFF Symp., Austin, Texas, Aug , 1991.

Silicon Carbide Preforms for Metal Infiltration by Selective Laser Sintering™ of Polymer Encapsulated Powders

N.K. Vail[†], J.W. Barlow[†], and H.L. Marcus[‡]

[†]. Department of Chemical Engineering

[‡]. Center for Materials Science and Engineering
The University of Texas at Austin

Abstract

A polymer encapsulated silicon carbide system has been developed for use with Selective Laser Sintering. Extensive studies with this material have provided information pertaining to processing and material parameters which most affect the strengths and densities of resulting green parts. The important parameters considered were particle size distribution of the powders, laser scanning conditions, and laser beam diameter. Simple and complex shapes were easily produced with this material using optimized parameters. Green objects were infused with metal by Lanxide using their pressureless infiltration process to produce both metal matrix and ceramic matrix composites.

(Key Words: Silicon Carbide, Encapsulation, Polymer, Selective Laser Sintering, Composites).

Introduction

Polymer encapsulated, high temperature powder material systems for Selective Laser Sintering have been under development at The University of Texas for the past few years^{1,2}. These materials offer a convenient path to complex ceramic and metal preforms via SLS. Several systems, including glass³, alumina and silica-zircon⁴, and copper², have been demonstrated to be viable materials for the fabrication of preforms.

Recent work has focused on investigating possible applications for the material systems under development. Additionally, it is desired to compare the performance of SLS preforms against that of other, more conventional preform manufacturing methods during post-processing steps. To this end, a polymer encapsulated silicon carbide system has been developed to produce preforms for use with Lanxide's pressureless infiltration process^{5,6,7}. The results of the infiltration will be described in a separate paper in this symposium.

Materials and Methods

Four particle size distributions of silicon carbide were provided by Lanxide Corporation. These powders were designated L-1000, L-800, L-500, and L-220, according to their specified grit sizes. Figure 1 shows the particle size distributions of these powders as measured by a

Coulter Multisizer. A poly(methylmethacrylate) latex polymer was produced as described elsewhere⁸. This polymer was formulated to have a specified melt flow index (ASTM D1238) of 30 g/10 min as measured using a Kayness Galaxy I capillary rheometer at conditions of 200°C and 75 psi. The polymer had an actual melt flow index of 32.2 g/10min. The glass transition temperature, T_g , of the polymer was determined to be 105°C using Differential Scanning Calorimetry.

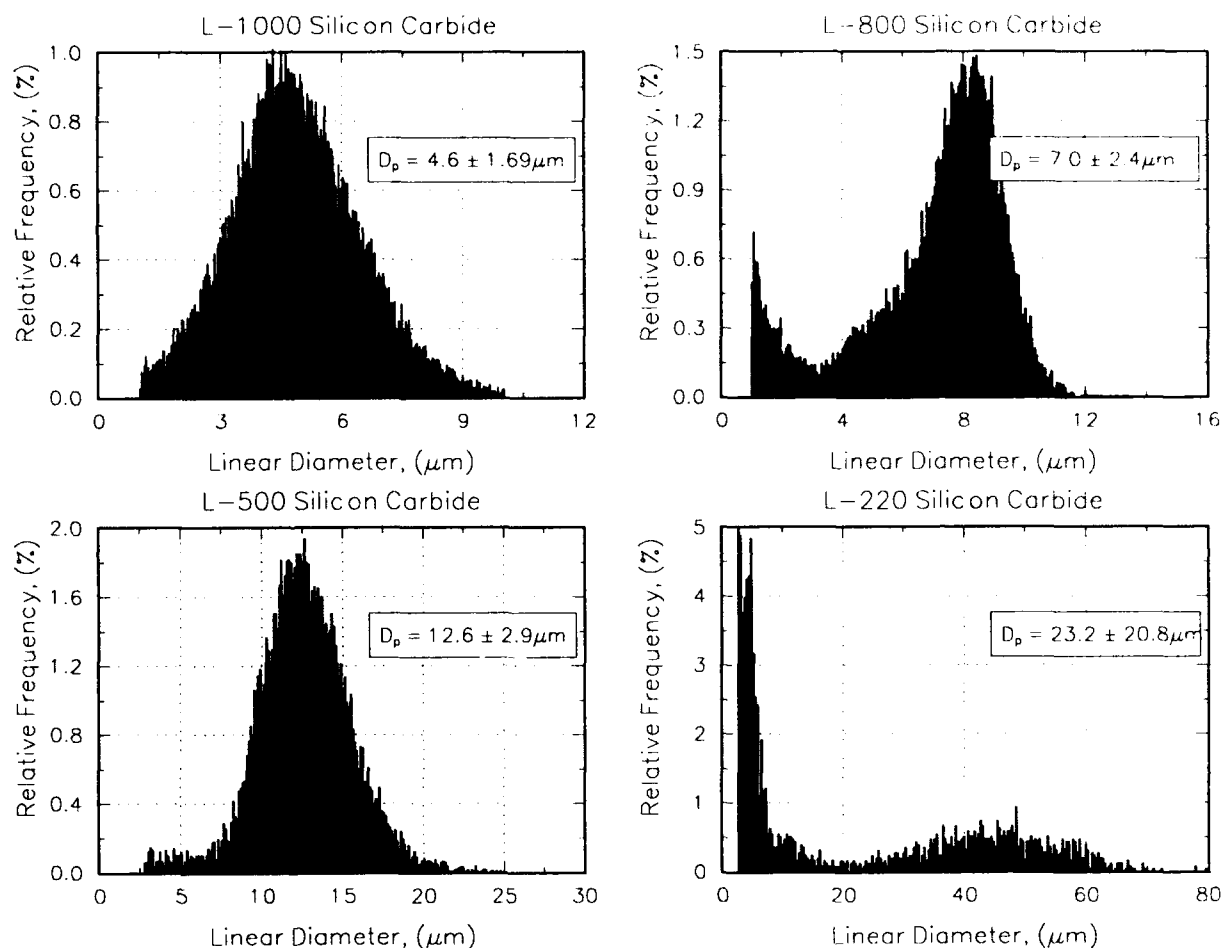


Figure 1. Particle size distributions of silicon carbide powders.

Two batches of polymer encapsulated silicon carbide, each consisting of a different particle size distribution, were prepared by spray drying according to methods described previously¹. The drying conditions were maintained to yield an agglomerated particle morphology. The initial batch was encapsulated to obtain a polymer composition of 30 vol. % (13.8 wt. %). The second batch was encapsulated to obtain a polymer composition of 25 vol. % (11.1 wt. %). The resulting encapsulated powders were admixed with pure silicon carbide powder to reduce the polymer content to 20 vol. % (8.5 wt. %). It has been shown that mixtures

of encapsulated powders with pure materials increases the apparent packing density of the powder³. Polymer compositions of all powders were determined by Thermal Gravimetric Analysis (TGA). Figure 2 shows an electron micrograph of the initial batch of polymer encapsulated silicon carbide.



Figure 2. Polymer encapsulated L-500 silicon carbide powder prior to admixing of pure silicon carbide L-500.

The initial samples were prepared from a single particle size distribution consisting of the L-500 powder. The second set of samples used a quadmodal particle size distribution composed of all four supplied powder sizes according to the composition shown in Table 1. Figure 3 shows the particle size distribution for the premixed quadmodal powder as supplied by Lanxide Corp. This distribution was verified using a mixture of the component powders.

Table 1. Quadmodal distribution powder composition.

Powder	Amount, (wt. %)
L-220	47.0
L-500	25.0
L-800	16.0
L-1000	11.0

Selective Laser Sintering of Materials

Both batches of materials were processed at the DTM Corp. using an SLS™ Model 125

workstation equipped with a calibrated 25 watt CO₂ laser. The laser beam profile and diameter were determined using a beam profilometer. Processing was conducted in a nitrogen environment, less than 2% O₂, with a gas flow rate produced by a pressure differential of 0.04 in. H₂O. Surface bed temperatures were maintained at 119°C as determined by a infrared sensor using an emissivity, ϵ , of 0.90.

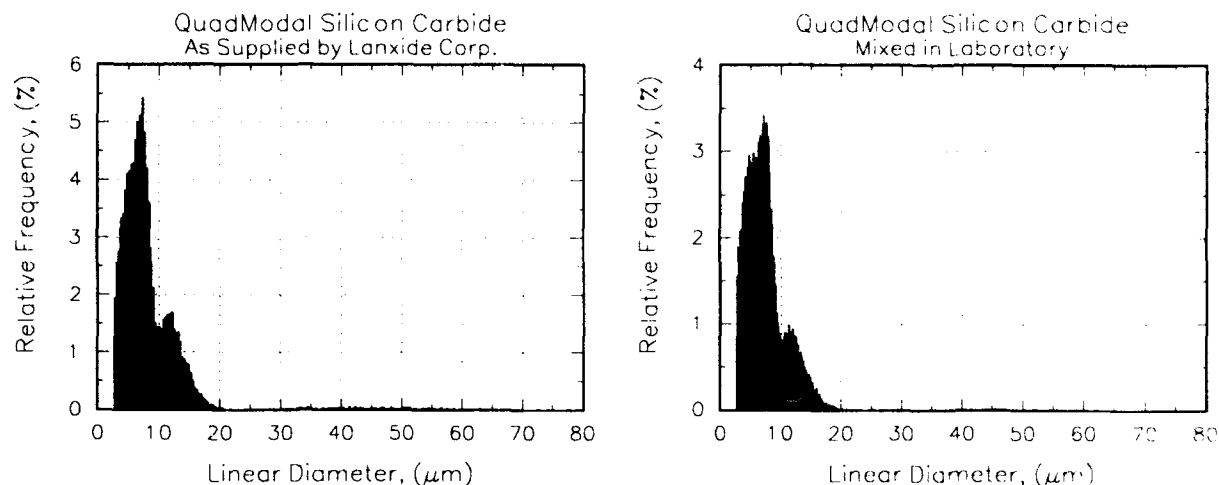


Figure 3. QuadModal particle size distribution.

Table 2 lists SLS operating parameters for the materials studied. 2"x2"x0.3" coupons for metal infiltration tests and 1"x3"x¼" coupons for characterization of green part properties were produced using the full range of SLS operating parameters. Complex shapes consisting of a thin walled electrical packaging box and an engine cowling were produced using optimized SLS operating parameters.

Table 2. Range of Selective Laser Sintering operating conditions.

Laser Power, (W)	Scan Speed, (ips)	Beam Spacing, (mils)	Layer Thickness, (mil)
6 - 16	50 - 100	2 - 5	4.5

Characterization of SLS Parts

Powder bed densities were measured using the method of density cups. Cups having a wall thickness of 3/16" and a volume 1.5" in diameter by 1" depth are produced by SLS using optimized operating parameters. Bed density is determined from the contained volume of powder. Cups are made at different bed locations to observe positional density variance. Part densities were determined from volume and mass measurements. Part green strengths were measured by three point bend analysis. Fracture planes of the bend specimens were examined by Scanning Electron Microscopy (SEM). Polymer content of the green parts were measured by TGA.

Results and Discussion

Monodistribution Powder

Initial experiments with this material were concerned with determining the effects of laser power, laser scan speed, and beam spacing on the strength and density of green parts. Nelson has shown, however, that these three critical SLS parameters are coupled and it is better to consider them as such when examining their influence on properties of objects produced by SLS⁹. Starting from scanning geometry and laser beam characteristics, Nelson derived the following expression for the laser power density

$$A_N = \frac{k' P}{BS * SCSP} \quad (1)$$

where A_N is the Andrew Number typically expressed in cal/cm², k' is a geometry specific constant, P is the laser power, BS is the beam speed, and $SCSP$ is the scan spacing. Eq. (1) provides a convenient means of lumping the major SLS parameters and can be used to correlate green part properties such as strength and density. Furthermore, from Eq. (1), it follows that similar part properties may result for constant A_N with varying combinations of laser power, beam speed, and scan spacing.

Table 3. Effect of laser scanning parameters on part properties.

A_N , (cal/cm ²)	Laser Power, (W)	Scan Spacing, (mil)	Scan Speed, (ips)	Density, (g/cm ³)	Green Strength, (psi)
0.41	7	5	125	1.35	9.1
0.47	8	5	125	1.37	12.1
0.74	8	4	100	1.37	76.1
0.79	8	3	125	1.38	73.4
0.79	8	5	75	1.40	72.4
1.32	8	5	75	1.40	183.2
1.35	12	3	110	1.37	170.3
1.74	13	3	92	1.33	186.0
1.74	12	4	64	1.35	186.4
1.74	12	3	85	1.32	192.9
2.27	14	3	76	1.35	205.2
2.28	12	3	65	1.34	205.8

Table 3 shows the influence of fixed power densities, A_N , with varying laser power, beam speed, and scan spacing on resultant densities and strengths of three point bend specimens. The data clearly show green strength to be related to the power density and not to be influenced

significantly by the respective operating parameters. The data also show green strength to increase with A_N . As energy input is increased it is expected that sintering of polymer binder within the layer would increase as would the likelihood of fusing the layer to previous layers, thus, increasing green strength. At the point where interlayer bonding is achieved further increases in power density would no longer be expected to improve green density. In fact, further increases in power density would cause degradation of the polymer binder reducing green strength.

Figure 4 shows the influence of the scan density, A_N , on green strength. The trend is as suggested although no decrease in green strength is observed for the range of energy densities studied. A transition in green strength occurs at about $A_N \approx 1.20 \text{ cal/cm}^2$ where the rate of strength increase diminishes to roughly 20% of the previous rate of strength development. Figure 5 and Figure 5 are SEM micrographs of green part fracture planes. In Figure 5, where $A_N < 1.2$, the layered structure of the part is very noticeable, whereas in Figure 5, where $A_N > 1.2$, the layered structure is noticeably absent.

Changes in the rate of strength development with energy input may be further attributed to changes in part density and thermal degradation of the polymer binder. Figure 8 shows density of the green parts to increase in manner similar to that of green strength. Increases in density are known to cause increases in material strength^{10,11}. Figure 7 shows the effect of power density on the polymer content. The polymer volume content decreases nearly 15% over the range of A_N studied. This binder loss combined with power density saturation may contribute to the decrease of green strength development shown in Figure 4.

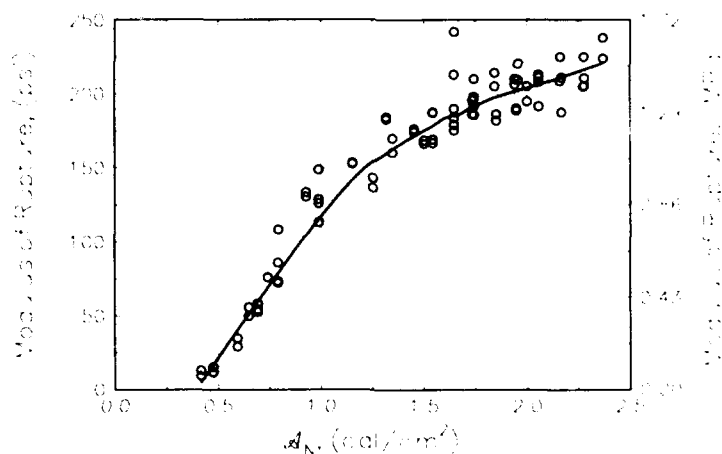


Figure 4. Influence of scan density on green strength.

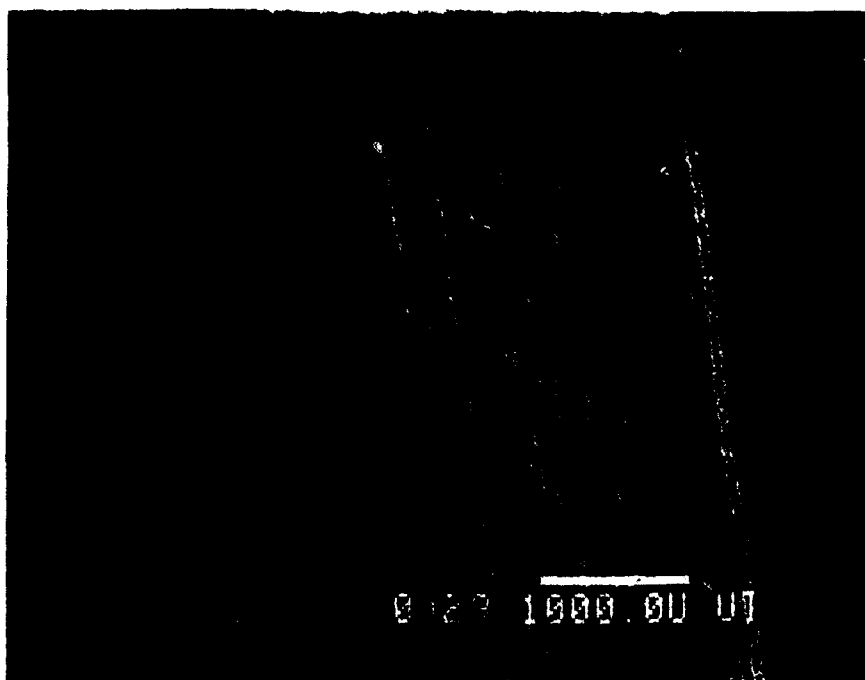


Figure 5. Poor interlayer bonding. $A_N = 0.69 \text{ cal/cm}^2$. Scan conditions: 7W, 75 ips, and 3 mil beam spacing.

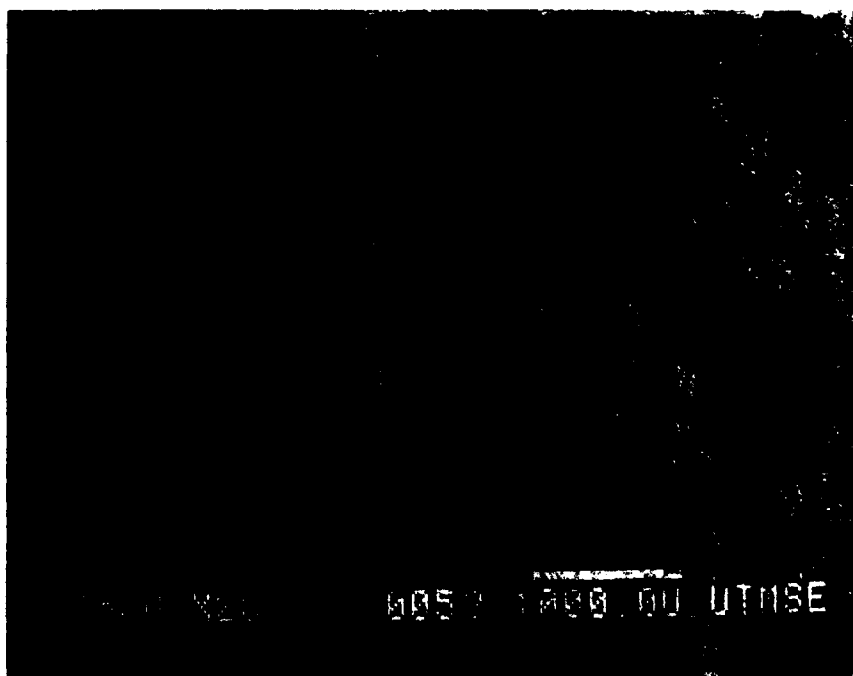


Figure 6. Good interlayer bonding. $A_N = 2.00 \text{ cal/cm}^2$. Scanning conditions: 12W, 74 ips, and 3 mil beam spacing.

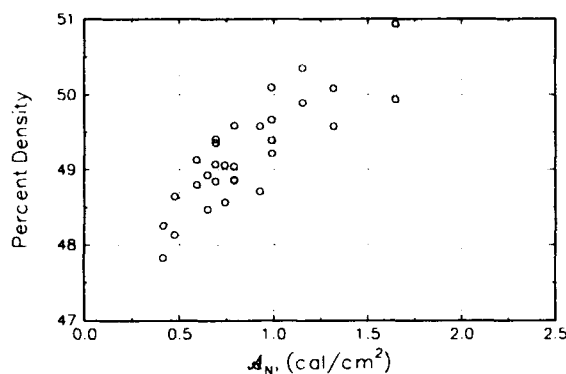


Figure 7. Influence of scan density on green density.

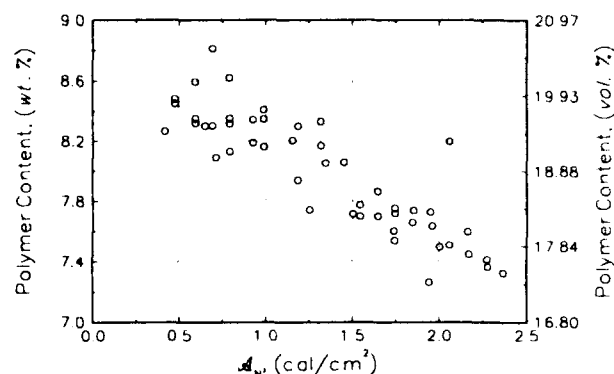


Figure 8. Effect of scan density on polymer content of green parts.

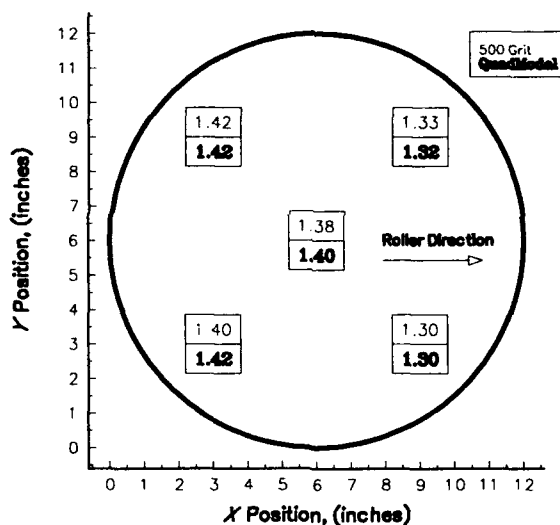


Figure 9. Influence bed position on powder bed density.

QuadModal Distribution Powder

This material, without binder, has an apparent tapped density of 62% compared to 52% for that of the L-500 powder. Therefore, it was hoped the quadmodal distribution material would improve green part density thereby increasing ceramic loading of the part. In practice, however, green densities were unchanged, still ranging from 48 to 51% as observed for the L-500 material. Tapped densities of the encapsulated powders were determined to be 57% and 59% for the quadmodal and L-500, respectively. Figure 9 shows the powder bed densities to be lower than the tapped densities, 46% (1.30 g/cm³) to 50% (1.42 g/cm³), and to decrease in the direction of the roller. This problem does not occur in the SLS Sinterstation™ 2000, the commercial machine, since the roller spreads powder in both directions¹². Density changes across the bed are evident in the green parts, too.

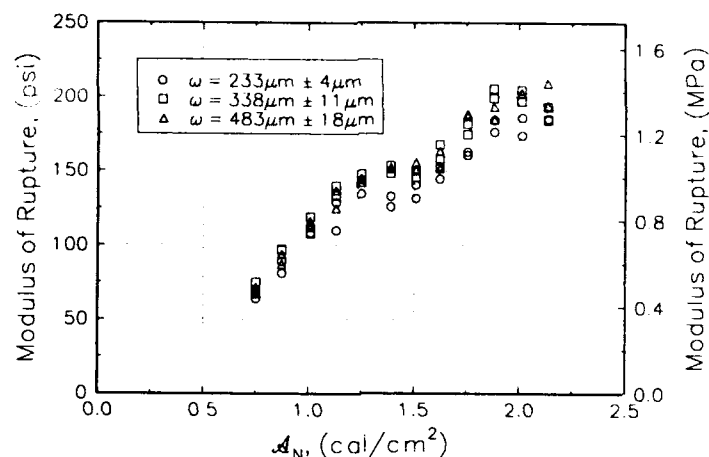


Figure 10. Effect of laser power density on strength of Quadmodal powder preforms.

Figure 10 shows the strength of green parts to develop with increasing Andrew Number, A_N , in a manner similar to the L-500 material. Additionally, the influence of laser beam diameter was investigated with this material. For the range of beam diameters studied, it can be seen that no appreciable effect on part strength is observed.

Conclusions and Further Work

The polymer encapsulated powders studied here were found to produce green shapes with good strength, surface finish, and dimensional accuracy. Figure 11 shows complex preforms produced from these materials. A broad range of SLS scanning conditions were determined suitable for producing parts with green strengths sufficient for processing by Lanxide Corporation. Typically, parts with green strengths greater than 125 psi ($A_N > 1.0 \text{ cal/cm}^2$) were preferred since delamination was not observed during the infiltration process.

The quadmodal distribution powders did not perform as expected and further work is required to explain this result. It is possible the distribution is adversely effected by the encapsulation process. If this is indeed true, it may be advisable to encapsulate a one or more of the individual size fractions and then mix these with other individual size fractions to achieve a high packing material, thus, increasing the ceramic loading.

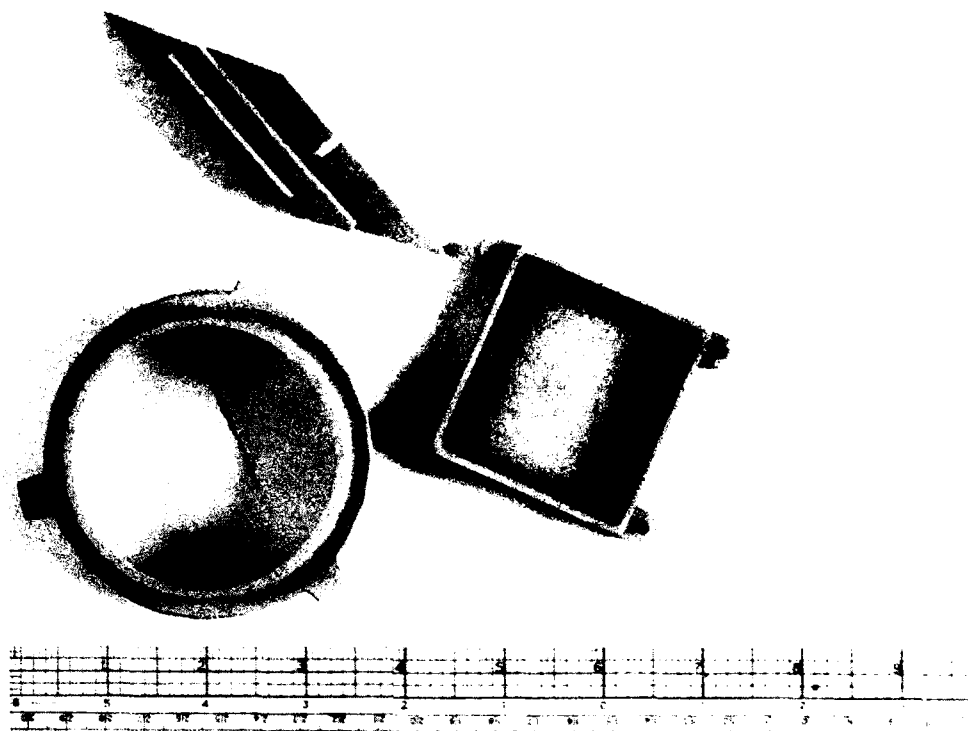


Figure 11. Silicon carbide preforms.

This research was supported by DARPA/ONR grant N000 14-92-J-1394 and DARPA grant MDA 972-92-J-1026 through Lanxide Corporation. DTM Corporation made available the SLS™ Model 125 workstation for these studies. Appreciation is given to Mike Durham, of the Austin Service Bureau, for his cooperation in obtaining experiment time on the workstation.

References

1. N.K. Vail and J.W. Barlow, *Solid Freeform Fabrication Symposium Proceedings*, **1**, 1 (1990).
2. B. Badrinarayan and J.W. Barlow, *Solid Freeform Fabrication Symposium Proceedings*, **3**, 141 (1992).
3. N.K. Vail and J.W. Barlow, *Solid Freeform Fabrication Symposium Proceedings*, **2**, 195 (1991).

4. N.K. Vail and J.W. Barlow, *ibid*, ref 2, p. 124.
5. B.W. Sorenson, G.H. Schiroky, and A.W. Urquhart, *Turbomachinery International*, [9] (1990).
6. A.W. Urquhart, *Advanced Materials and Processes*, [7] (1991).
7. S. Ashley, *Mechanical Engineering*, [7] (1991).
8. N.K. Vail and J.W. Barlow, "Development of a Poly(methyl methacrylate - co - *n*-butyl methacrylate) Copolymer Binder System", *in press*.
9. J.C. Nelson, Ph.D. Dissertation, The University of Texas at Austin, 1993.
10. U. Lakshminarayan, Ph.D. Dissertation, The University of Texas at Austin, 1992.
11. M. Yu. Bal'shin, *Doklady Akademi Science, USSR*, 67 [5], 831.
12. U. Lakshminarayan, Ph.D., DTM Corporation, *Private Communication*.

Fabrication of Ceramic and Metal Matrix Composites From Selective Laser Sintered Ceramic Preforms

Lucy Deckard and T. Dennis Claar
Lanxide Corporation
Newark, Delaware

Abstract

This paper will discuss the tool-less fabrication of functional advanced composites by infusion of a ceramic or metal matrix into Selective Laser Sintered (SLS) porous ceramic preforms using Lanxide's patented matrix infusion processes. The fabrication of porous preforms of particulate ceramics by SLS at the University of Texas at Austin is described in a companion paper. The PRIMEX™ pressureless metal infiltration process was used to infiltrate aluminum matrices into both SiC and Al₂O₃ particulate SLS preforms to make metal matrix composites without the use of tooling. Also, SiC_p/Al₂O₃ ceramic matrix composites were fabricated using the DIMOX™ directed metal oxidation process to grow an Al₂O₃ matrix into porous SiC particulate SLS preforms. Measured properties and microstructures of the resulting composites will be presented and compared to similar composites made using conventionally fabricated preforms. The rapid prototyping of a SiC_p/Al MMC electronic power package to near-net shape from an SLS preform will also be described.

Introduction

Lanxide's matrix infusion processes for fabricating ceramic and metal matrix composites are near-net shape processes in which a matrix is infused into a porous ceramic preform. The final composite shape is dictated by the shape of the preform; therefore, a critical step in the process is the fabrication of a porous preform to near-net shape. Preforms typically have been made using a variety of standard ceramic processing methods, including tape casting, injection molding, green machining, dry pressing, etc. Many of these conventional processes either do not have the complex shape-making capabilities needed or require tooling that is expensive and time-consuming to fabricate for prototypes or small production runs. The newly-emerging Solid Freeform Fabrication technologies, and in particular Selective Laser Sintering (SLS), appear to be ideally suited to fill the need for a method to fabricate porous preforms to near-net shape quickly and without the use of tooling.

One of the objectives of the current work is to evaluate the feasibility of fabricating Ceramic Matrix Composites (CMCs) and Metal Matrix Composites (MMCs) using preforms formed to net shape using SFF processes. Fabrication of the SLS ceramic preforms is described in a companion paper; the results of work to convert these preforms to CMCs and MMCs via Lanxide's matrix infusion processes are discussed below.

Lanxide's Matrix Infusion Processes

The DIMOX™ directed metal oxidation process for fabricating ceramic matrix composites (Fig. 1) and the PRIMEX™ pressureless metal infiltration process for metal matrix composites (Fig. 2) are similar. In both processes, a ceramic preform is made from the desired reinforcing material, which can be ceramic particulates or fibers. In the current work, SiC and Al₂O₃ particles ranging in size from 1 μm to 60 μm, which are typical reinforcing materials, were used (fibers were beyond the scope of this work). The preform is formed to the desired shape of the final part, a barrier is applied to the upper surfaces to stop infiltration and retain shape, and the preform is placed in contact with the growth alloy which is typically an aluminum alloy. In the CMC process,

the alloy is heated above its melting point to temperatures of 900°C - 1000°C in air, and the alloy wicks into the preform while simultaneously oxidizing to form an Al_2O_3 matrix. This wicking and oxidizing process (referred to as "matrix growth") continues, filling the entire preform until the growth barrier on the top surface is reached. The resulting Ceramic Matrix Composite part, consisting of a reinforcement phase and an Al_2O_3 matrix with small interconnecting channels of Al, is removed from the alloy. The process for fabricating MMCs is similar, except that the alloy is heated above its melting point to temperatures of only 750°C to 850°C in a nitrogen atmosphere; no oxidation of the aluminum occurs as it wicks into the preform to form an aluminum matrix composite. No pressure is required to aid infiltration of the alloy into the preform.

The chief advantages of these processes are:

- near-net shape capability (less than 1% shrinkage compared to preform dimensions)
- uses comparatively inexpensive raw materials and equipment
- no part-specific tooling required after fabrication of preforms

Experimental Work

As described in the companion paper, Marcus, et. al. supplied Lanxide with both Al_2O_3 and SiC particulate SLS preforms made using a variety of sintering parameters. Initially, preforms were supplied in the form of 2" x 2" x 1/4" coupons, then after composition and sintering parameters were established, complex-shaped preforms were fabricated. These preforms were evaluated for compatibility with Lanxide's matrix infusion processes. Initially, preforms were made using either 20 μm Al powder or spray-dried PMMA as a binder. We were able to successfully make MMCs and CMCs from both types of preforms; however, the microstructures of the composites made with preforms using the PMMA binder were much more uniform. It was therefore decided that further work would employ the PMMA binder only.

Table 1 gives the properties measured to date for MMCs and CMCs made from SLS preforms. Although SLS preforms were fabricated from both Al_2O_3 and SiC particulate, work concentrated on SiC because both the CMC and MMC demonstration components were to be fabricated using SiC particulate reinforcement. The reinforcement particle loadings of the SiC preforms ranged from 40 to 46 vol%. At least one preform from each set (specimens fabricated using the same SLS parameters) was infiltrated using Al alloy to make an MMC, and another preform from the set was grown to make a CMC. The SiC preforms generally infiltrated well; no significant differences in matrix infusion behavior for either the CMC or MMC processes were observed for specimens made with the various SLS parameters tested. The main effect observed in preforms fabricated using different SLS parameters was variation in green strength which affected ability to withstand handling. Figure 3 shows a microstructure for the MMC; it can be seen that there is almost no visual evidence of layering of the SiC. However, a relatively large amount of fine porosity (approx. 8 vol% as measured by QIA) was evident, resulting in lower thermal conductivity than would normally be expected. Work is currently concentrating on adjusting infiltration parameters to reduce the occurrence of this porosity.

Figure 4 shows a plot of modulus as a function of particle loading for SiC/Al MMCs made at Lanxide using a variety of preforming techniques; it can be seen that MMCs fabricated from SLS preforms have elastic moduli comparable to MMCs made using other preforming techniques, taking into account the vol% particle loading. Figure 5 shows a similar graph of CTE as a function of loading, and again it can be seen that MMCs made using SLS preforms behave similarly to composites made using conventional preforms.

These results indicate that it should be possible to make fully functional MMC components from SLS preforms. However, many MMC applications require composites with higher reinforcement

loadings than those attained to date. For example, many electronics applications require a CTE of $\leq 7.0 \text{ ppm/}^\circ\text{C}$, which translates into a particle loading of at least 60 vol%. Less demanding electronics applications require a CTE of approximately $8 \text{ ppm/}^\circ\text{C}$, or approx. 55 vol% reinforcement. The most highly loaded MMCs fabricated to date from SLS preforms have had 44 vol% reinforcement. Increasing the reinforcement loading is therefore the most important issue to address in developing functional and commercially viable MMCs made from SLS preforms. Since the reinforcement loading in the composite is a direct function of the preform density, efforts were made to increase the SLS preform density by using a blend of four particle sizes to increase packing efficiency. These initial efforts, described in the companion paper, were unsuccessful; however, it is expected that optimization of the binder system and spray drying parameters may allow the fabrication of higher density SLS preforms.

SLS $15 \mu\text{m}$ SiC particulate preforms were also subjected to the DIMOXTM directed metal oxidation process to form a $\text{SiCp/Al}_2\text{O}_3$ CMC. Figure 6 shows a photomicrograph of the resulting CMC; it can be seen that the microstructure is quite uniform and there is little evidence of layering. As in the case of the MMCs, most SiC_p-reinforced CMC applications typically require reinforcement loadings from 55 vol% to 60 vol% or greater. Therefore, increasing the preform density is also important to the fabrication of functional SiC_p-reinforced CMC components.

The SLS Al_2O_3 ($15 \mu\text{m}$ nominal particle size) preforms with PMMA binder had Al_2O_3 loadings of 37 - 38 vol% as determined by green density and TGA measurements, and contained approximately 8 wt% binder. The preforms were successfully infiltrated with two aluminum alloys commonly used for automotive MMC applications. Filler loadings in the composites measured by Quantitative Image Analysis (QIA) were around 35 vol% with 1.4 vol% porosity. Figure 7 shows the microstructure of a typical MMC made using an SLS preform. Only slight evidence of layering of the Al_2O_3 is visible in the SLS composite; the homogeneity of this microstructure is encouraging. It should also be noted that the particle loadings are within the range of loadings needed for many of the automotive applications.

Fabrication of Demonstration Articles

As part of the RAPTECH-CMC program, two demonstration articles were selected for fabrication from SLS preforms. The first article was a generic electronic power package to be fabricated from SiC/Al MMC using an SLS preform. The second article was a turbine engine tip shroud to be fabricated from SiC/Al₂O₃ CMC using an SLS preform. As discussed in the companion paper, preforms for both articles were successfully fabricated using SLS. The preform for the generic power package was successfully infiltrated to form a near-net shape MMC part (Fig. 8). Lateral dimensions of the infiltrated MMC part were consistently 17% to 18% larger than the specified drawing dimensions. The thickness of the part was within the $\pm .005$ " specification. These dimensional differences were due to oversized dimensions of the SLS preform; the infiltration process causes a small (<1%) shrinkage compared to the preform dimensions. Since this part was among the first of this design to be fabricated using SLS, it is expected that dimensional accuracy will improve as more preforms are fabricated. Work to fabricate the CMC tip shroud from the preform is currently in progress.

Conclusions

The results to date indicate that Selective Laser Sintering may in the future be used as a fast, tool-less route to obtaining preforms for prototypes and small production runs. Furthermore, based on the properties measured to date, if the preform density can be improved it is very possible that the resulting composite properties could be fully interchangeable with composites made using more conventional preforming methods. This would mean that parts for prototypes

and small production runs could be made using SLS preforms, and then if a larger production run is required high volume preforming methods could be used to make essentially the same material.

Acknowledgements

This work was performed under ARPA-sponsored Precompetitive Technology Grant MDA 972-92-J-1026. The authors wish to thank Dr. William Coblenz for his encouragement and guidance.

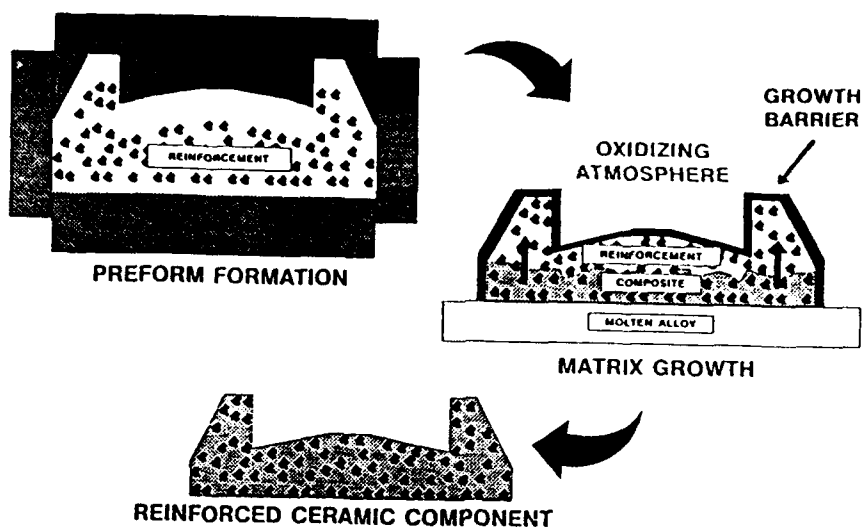


Figure 1. A Schematic of the DIMOX™ directed metal oxidation process for making CMCs

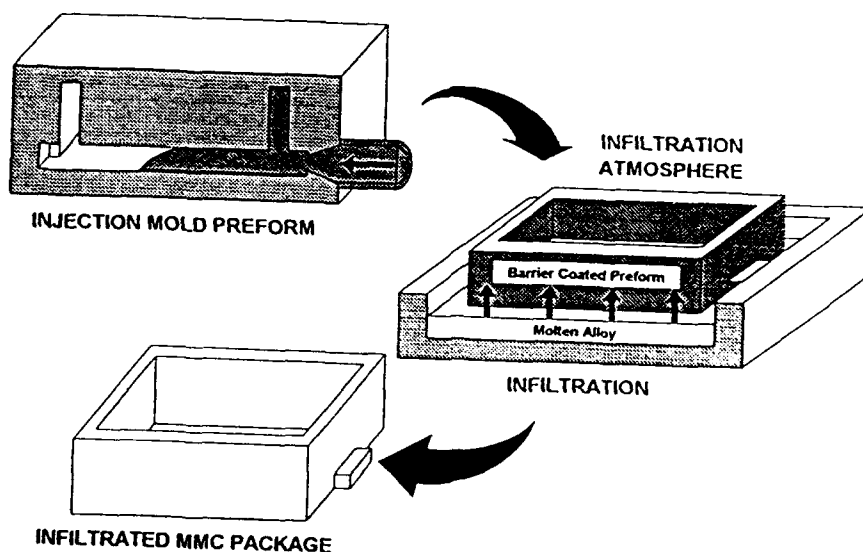


Figure 2. A Schematic of the PRIMEX™ pressureless metal infiltration process for making MMCs

Table 1. Properties Measured for Composites Fabricated from SLS Preforms

	$\text{Al}_2\text{O}_3/\text{Al MMC}$	$\text{SiC}_p/\text{Al MMC}$	$\text{SiC}_p/\text{Al}_2\text{O}_3\text{-CMC}$
Quantitative Image Analysis			
Reinforcement Loading	38 vol%	45 vol%	41 vol%
Porosity/Other phases	1 vol%	8 vol%	3 vol%
Metal	61 vol%	47 vol%	20 vol% (residual metal)
Al_2O_3 matrix (CMC)			36 vol%
Density	3.12 g/cm ³	2.95 g/cm ³	3.47 g/cm ³
Sonic Modulus	130 GPa	180 GPa	286 GPa
CTE (25°C - 100°C)	14.5 ppm/°C	9.1 ppm/°C	7.5 ppm/°C
Thermal Conductivity	67 W/m-K (Al - 7 Mg) 83 W/m-K (Al-4.5 Cu-4 Mg)	115 W/m-K	----
Fracture Toughness	-----	8.3 MPa-√m	8.0 MPa-√m
Flex Strength (4-point)	-----	275 MPa	260 MPa

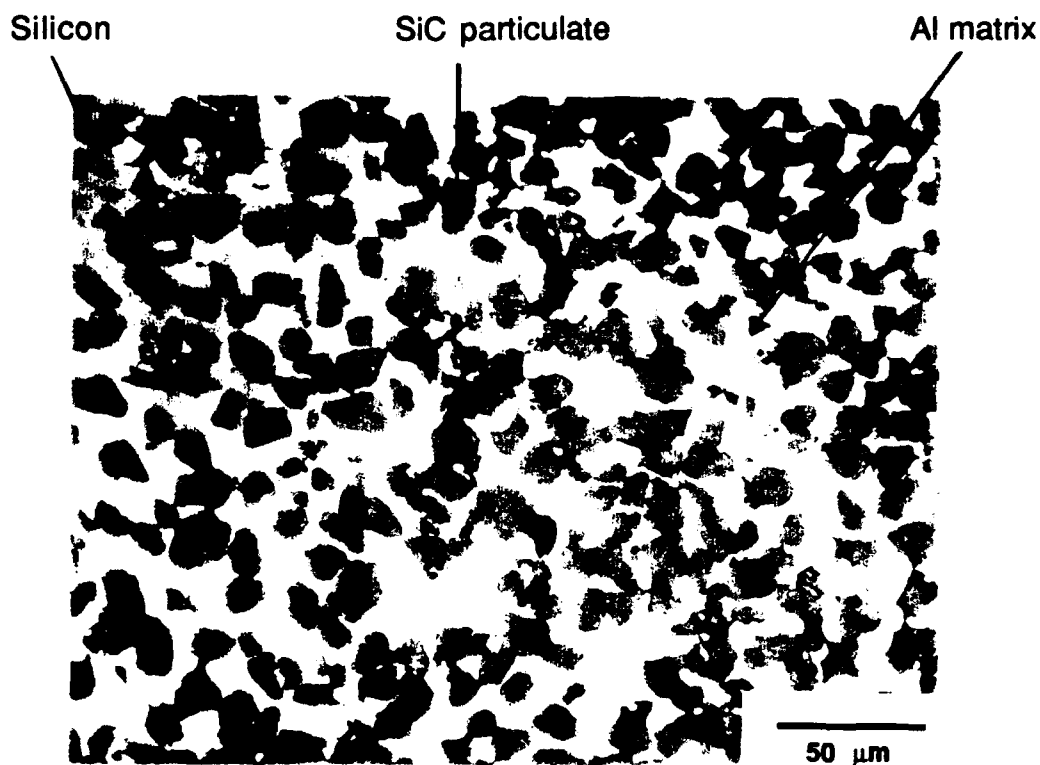


Figure 3. Microstructure of SLS $\text{SiC}_p/\text{Al MMC}$

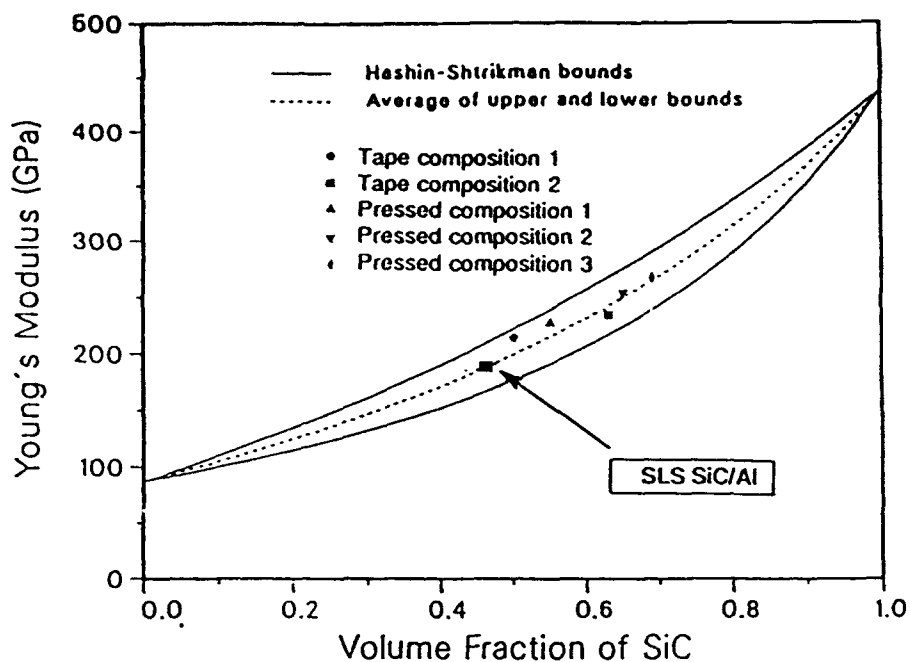


Figure 4. Elastic Modulus as a Function of Loading in SiC_p/Al MMC

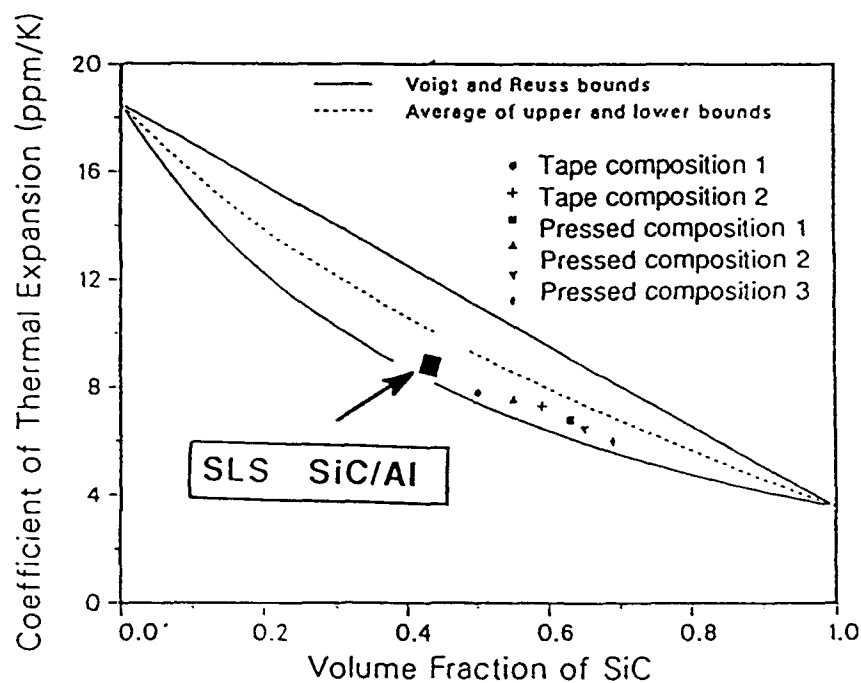


Figure 5. CTE as a Function of Loading for Lanxide's SiC_p/Al MMCs

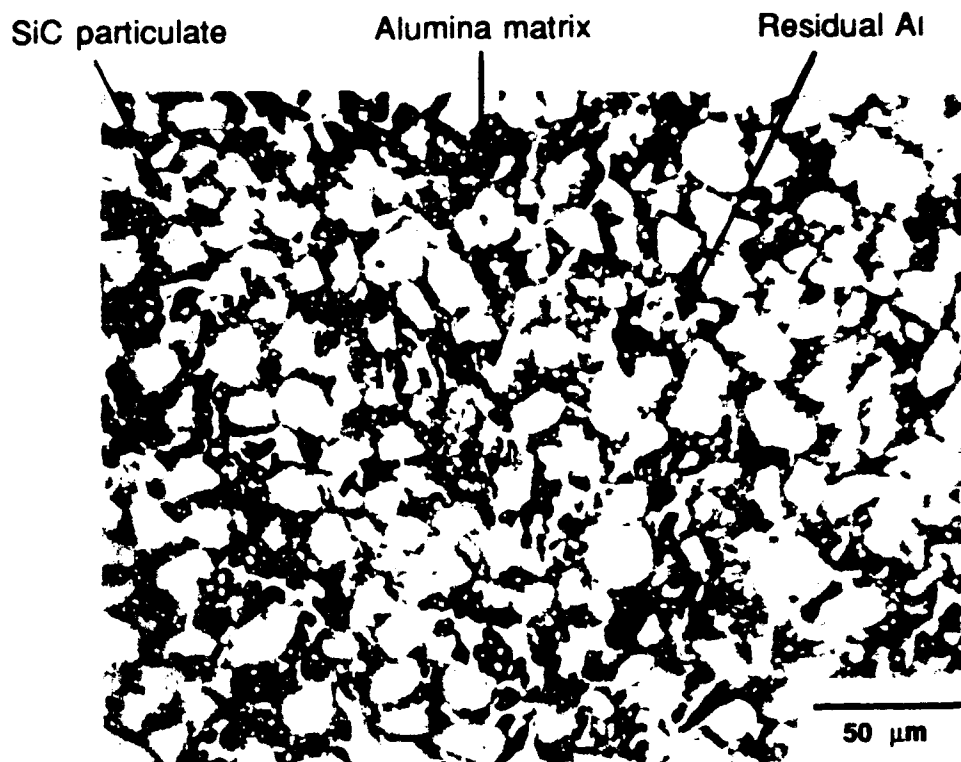


Figure 6. Microstructure of SLS $\text{SiC}_p/\text{Al}_2\text{O}_3$ CMC

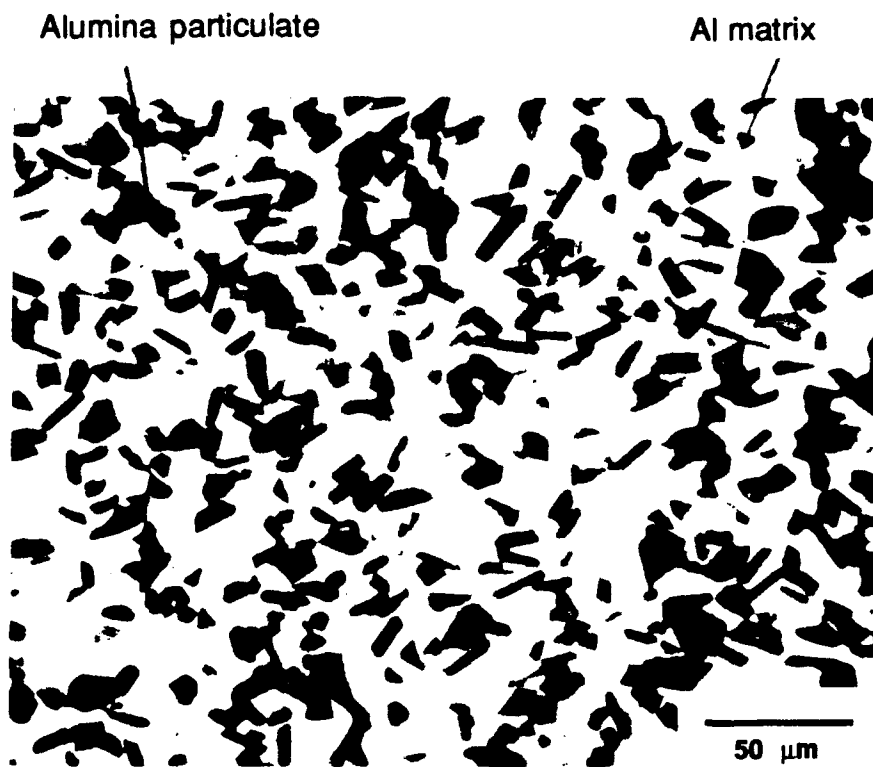


Figure 7. Microstructure of SLS $\text{Al}_2\text{O}_3p/\text{Al}$ MMC

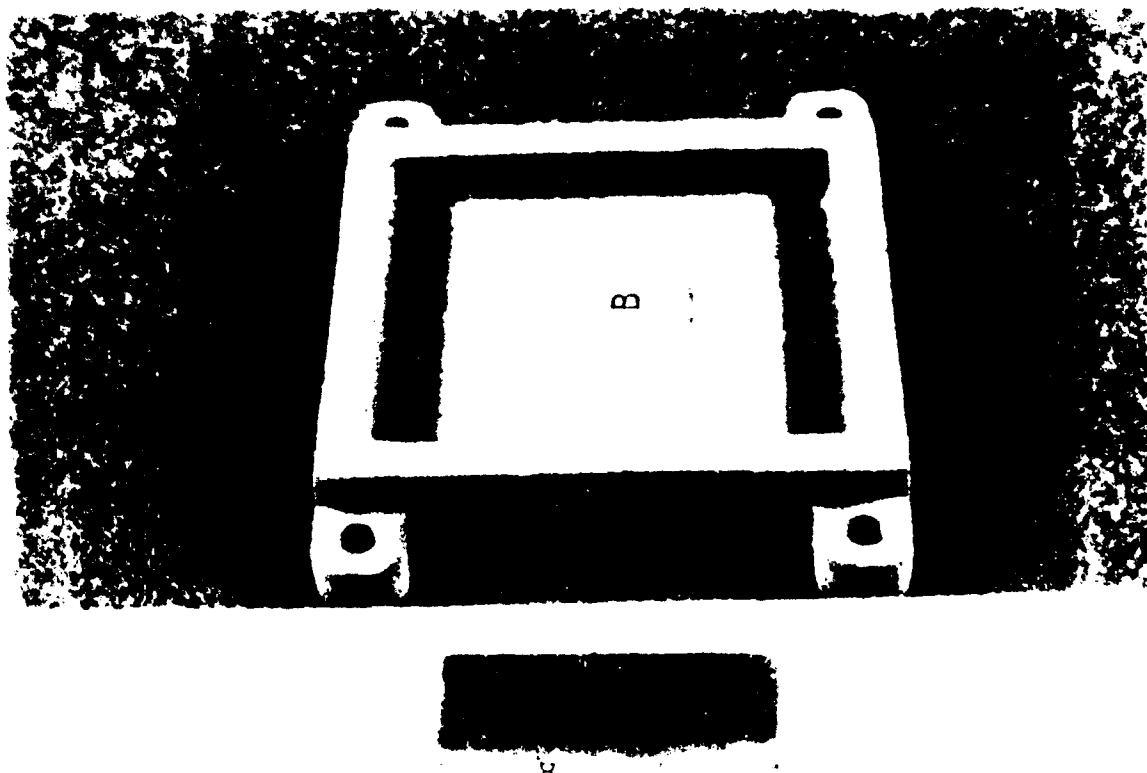


Figure 8. SLS Preform for Electronic Power Package

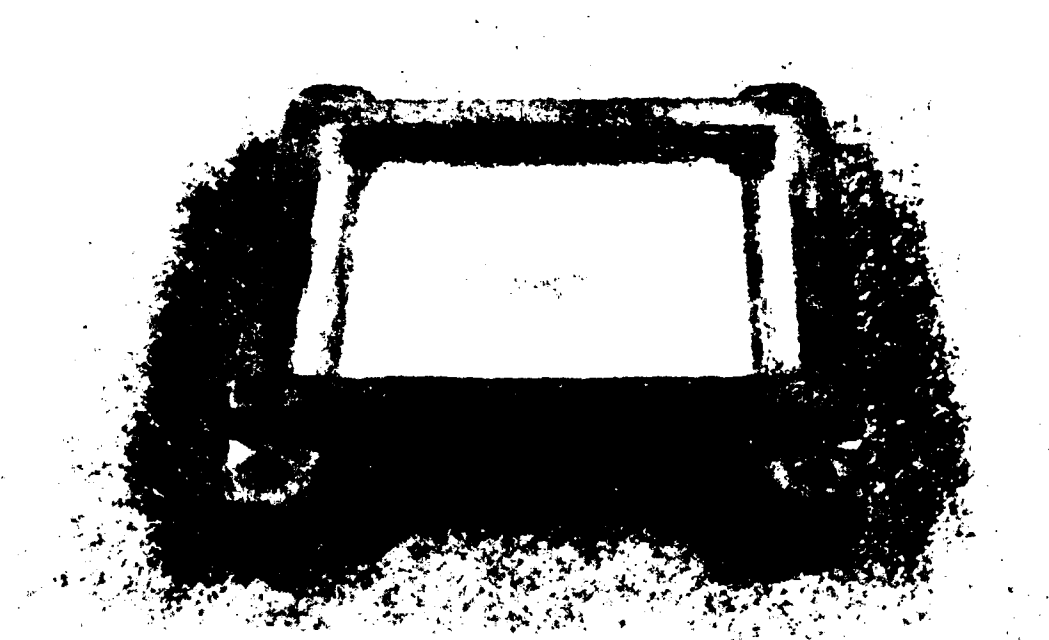


Figure 9. SLS Preform Shown in Figure 8 Infiltrated to Form MMC

POWDER LAYER POSITION ACCURACY IN POWDER-BASED RAPID PROTOTYPING

Sang-Joon John Lee Emanuel Sachs Michael Cima

Department of Mechanical Engineering
Department of Materials Science and Engineering

Massachusetts Institute of Technology
Cambridge, Massachusetts 02139

Abstract

Layer position accuracy in powder-based processes such as Three Dimensional Printing and Selective Laser Sintering is a fundamental concern for dimensional control in the vertical direction. Ideally, each powder layer is generated at a vertical position that remains fixed at a prescribed distance from the floor of the powder bed. However, the powder bed beneath any given layer is compressible. Loads imparted to the top of that layer may cause it to displace downward. The weight of subsequent layers is an inherent source of load, that increases with the number of layers added. Other possible causes for position error include mechanical forces applied during powder spreading and powder densification from vibration.

Vertical displacements at various levels within powder beds have been measured for a set of aluminum oxide powders, using the layering process of 3D Printing. The mean displacement in a 76.2 mm deep bed ranged from 23 microns for a 30-micron platelet-shaped powder to over 260 microns for a 9-micron platelet-shaped sample. In all cases, position errors were most severe in the middle regions of the powder beds, with diminishing magnitude toward the top and bottom.

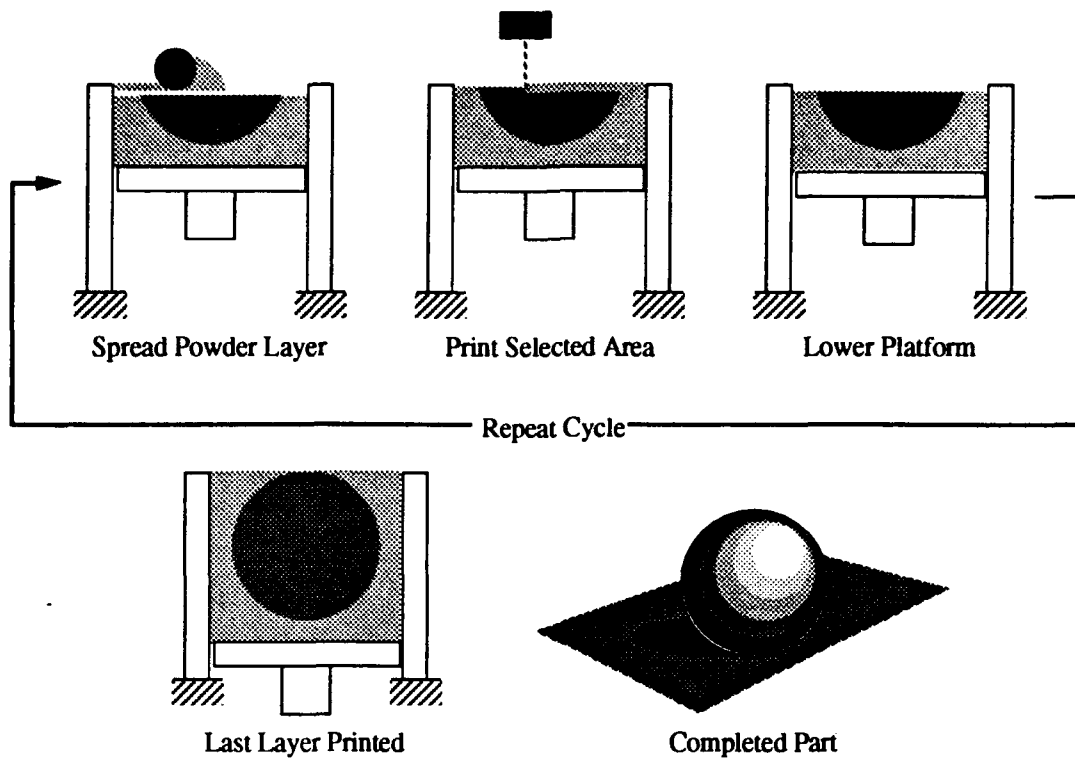
A model for layer displacement has been examined using experimental data for compressibility and applied load. Predictions made from the model captured the relative magnitudes of actual errors at various positions within layered powder beds.

Introduction

Several rapid prototyping technologies fabricate solid freeforms in a layer-by-layer sequence, with each layer representing a two-dimensional "slice" of the final part [Wohlers]. Processes known as Three Dimensional Printing [Sachs] and Selective Laser Sintering [Deckard] create the slices by joining selected areas of thin powder distributions.

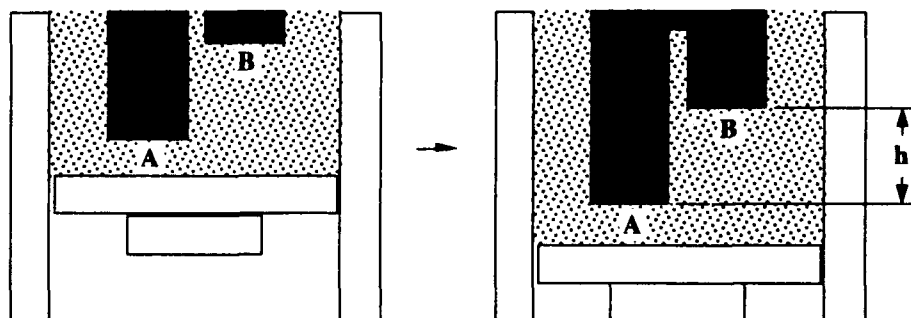
Figure 1 shows the basic operating sequence of 3D Printing. Each cycle begins with fine powder, spread into a thin layer. A slicing algorithm draws detailed information for every layer, from a CAD representation of the desired part. Then a raster-scanning printhead (using a technology similar to ink-jet printing) selectively applies a binder material to join particles where the object is to be formed. A piston that supports the powder bed lowers so that the next powder layer can be leveled and selectively joined. The layered building cycle repeats until the part is completed. After a heat treatment, removal of the unbound powder reveals the finished part.

Figure 1. Three Dimensional Printing Process



The stability of dry-powder layer positions may be critical to dimensional accuracy in the vertical direction. Loads applied from above each layer, combined with the inherent compressibility of the powder bed below, may cause a layer to deviate from its original position (with respect to the powder bed floor). The vertical position of a layer is relatively secure within the bulk region of a part, because the particles above and below it are bound in place. However, a delicate or weakly-supported feature may suffer a change in position if the powder beneath it compresses when loaded from above. Figure 2 shows an example in which the vertical spacing between two regions of a part may be inaccurate because the powder beneath each of them compresses by different amounts.

Figure 2. Example of the Significance of Powder Layer Position Accuracy



The experiments described in this paper uses the 3DP layering process to study some examples of powder layer displacement, and to develop a basic understanding of the interaction between load and compressibility. *Dry* conditions are examined as a worst-case scenario for layer displacement, presuming that layers mutually supported by binder are less prone to changing position. Although particle morphology is not studied formally, four samples of aluminum oxide are used to roughly compare particles that differ in size and shape.

Figure 3 details the steps of the 3D Printing layering sequence. Each complete cycle involves two passes over the powder bed. In the first pass, a bead of powder is spread into a uniform distribution, while applying counter-rotation and vibration. The rotation enhances particle flow, while the vibration increases packing density and breaks agglomerates. The second pass strikes a clean surface onto which binder may be printed. Rotation and vibration of the spreading device are made possible by the configuration shown in Figure 4.

Figure 4. Powder Layering Sequence for 3D Printing (Side View)

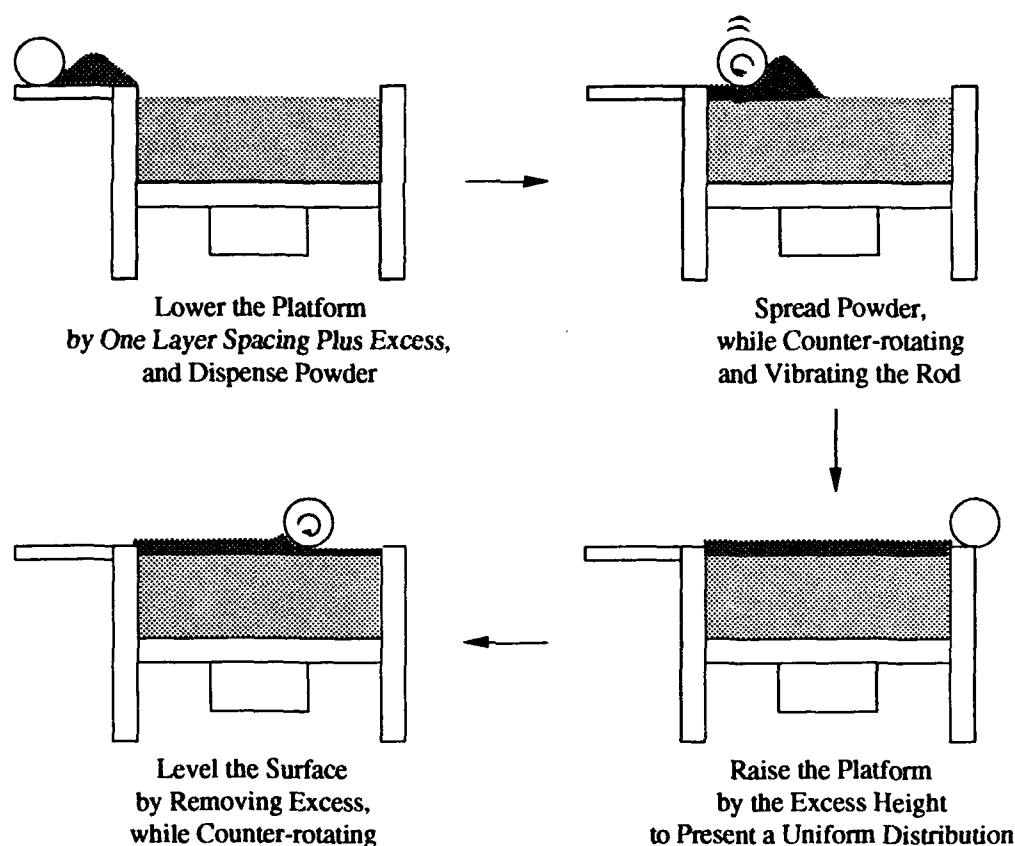
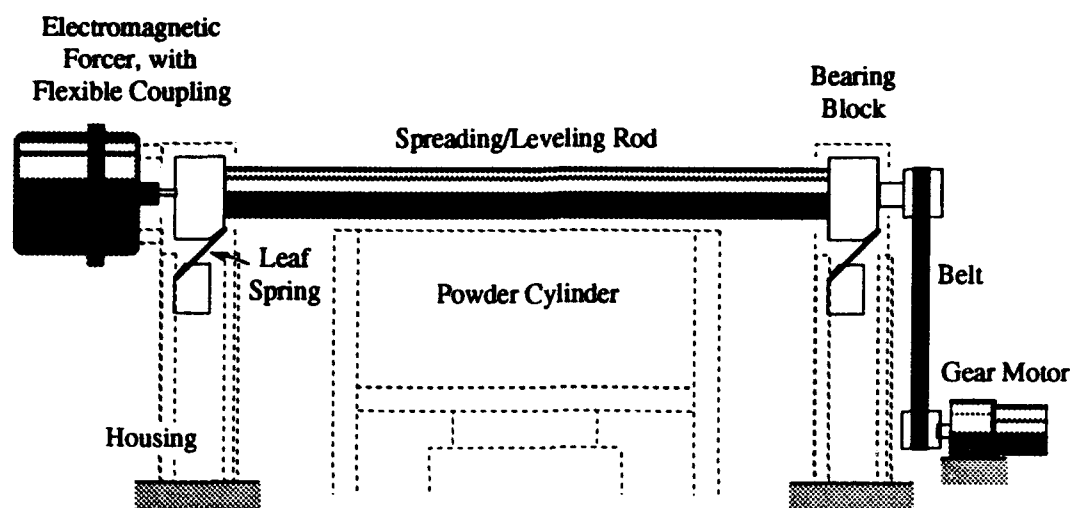


Figure 4. Powder Spreading Apparatus (Front View)

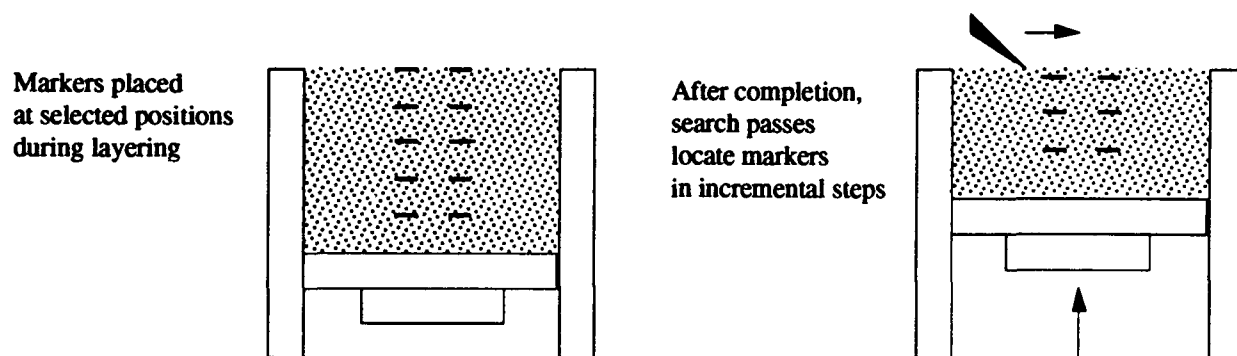


Before beginning layer position measurements, operating conditions that favor high packing density were studied by performing a designed experiment. A description of the factorial design is provided as an appendix. High packing density at every layer is desirable for minimizing compressibility [Fayed] and reducing compaction from incidental vibration.

Layer Displacement Measurements

A powder bed that is not fully dense will compress to some degree when loaded from above. Consequently, the vertical position of layers within the bed will displace downward. To measure the magnitude of this effect, graphite needles were placed at selected positions during experimental layering runs. As layers were added, the needles moved with the powder particles and thereby marked the change in layer position (see Figure 5). After completion of all layers, incremental search passes with a scraper blade would locate the altered positions of the markers.

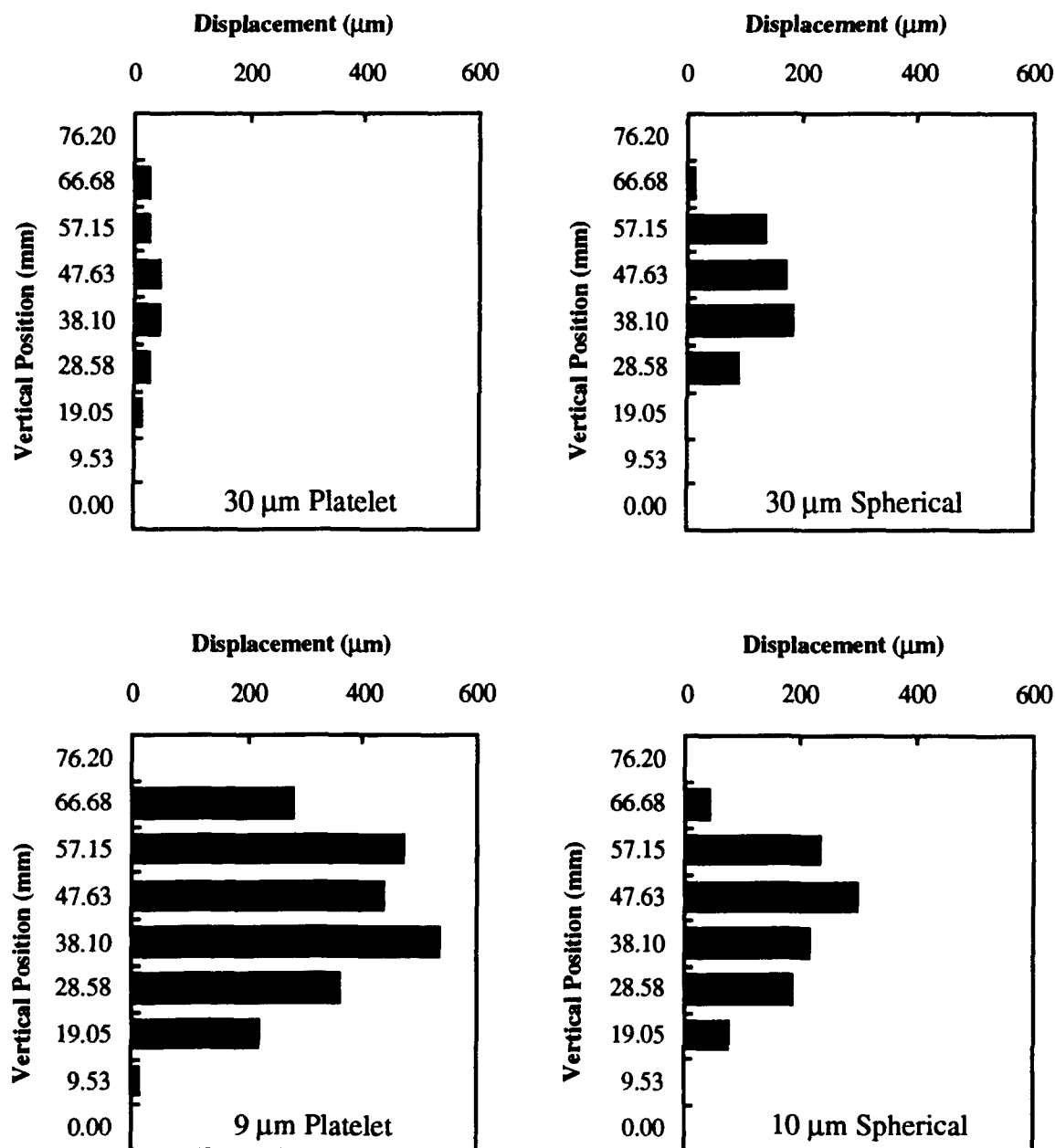
Figure 5. Layer Displacement Measurement



The experiments were conducted in a bed 76.2 mm deep, with a 90 mm x 90 mm cross-sectional area. Layers were spaced 190.5 microns apart. The spreader was traversed at 50 mm/s, with a counter-rotation speed of 75 mm/s on the outer diameter of the rod. Vibration was applied at 250 Hz with 50-micron peak-to-peak amplitude. Alumina powder was used in two sizes (about 10 and 30 microns, typical diameter) and two shapes (platelet-shaped or spherical).

Marker trace experiments generated the results shown in Figure 6. The plots are oriented such that the bottom of each plot corresponds to the bottom of the powder bed, and the magnitude of the bars correspond to the amount of *downward* displacement for each of the measured layers.

Figure 6. Measured Errors in Layer Position



Each of the powder samples exhibited the greatest displacement in the middle region of the bed. Smaller displacement error was observed near the top and bottom. The error profiles can be interpreted as resulting from the combined effect of load and compressibility. The layers near the bottom have significant weight above, but show little error because they are near the floor of a rigid platform. Although the layers near the top have much material to compress below, they also have small error magnitudes because there is very little load from above. In contrast, the middle layers have the greatest error magnitudes because they have substantial loading from above, and a sufficient quantity of powder to compress below.

Experiments were conducted to examine load and compressibility more closely. Measurements for load and compressibility were then combined to generate error predictions. Comparison of the predictions with actual displacement measurements provides a means of understanding the mechanics that affect vertical position accuracy in powder-based processes.

Compressibilities Of Powder Beds

A powder bed is an assembly of a large number of particles with a significant fraction of void space. A bed of powder will exhibit some compression under load [Dallavalle], even at relatively high packing density. The apparatus shown in Figure 7 was used to make compressibility measurements. An opaque mask was attached to a thin latex membrane, which in turn covered a small pressure chamber. When pressure was applied to the chamber, the membrane and mask moved downward with the top surface of the powder. A (stationary) solar cell was calibrated to measure displacement as the mask exposed more light. Pressure was applied from zero to 1250 Pa (1250 Pa simulates the weight of a typical full powder bed), onto a 50-layer powder bed (at 190.5 micron layer thickness). The membrane was chosen over a rigid platform because its compliance more closely simulates the movement of a powder layer.

Figure 7. Compressibility Measurement Apparatus

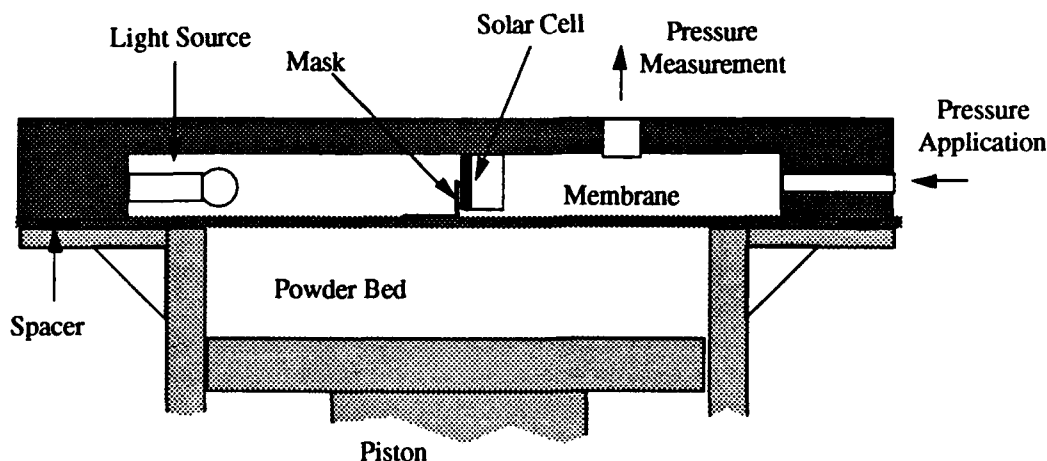
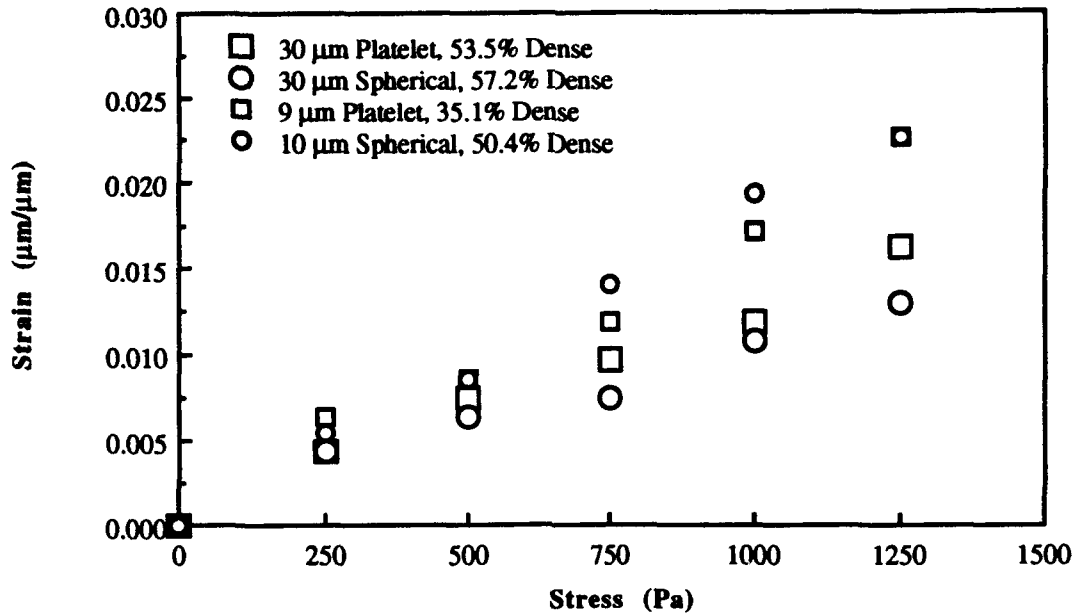


Figure 8 presents the compressibility data for the four powders, tested in a bed of 190.5 μm layers, stacked 9.525 mm deep. Compressibility is expressed in strain vs. stress, where the strain is the displacement divided by the stack height and the stress is the pressure applied to the top surface.

Figure 8. Compressibility Data



In this paper, compressibility is interpreted as the slope of a fitted line through the strain-stress data. High compressibility means that a powder bed will have a large change in height for a given load. The compressibilities of the sample powders are:

Large Platelet	1.15×10^{-4}	Pa^{-1}
Large Spherical	9.30×10^{-5}	Pa^{-1}
Small Platelet	1.62×10^{-4}	Pa^{-1}
Small Spherical	1.75×10^{-4}	Pa^{-1}

Expressing measurements in terms of strain presumes that the compression of a bed scales linearly with stack height. That is, for a given load, a stack twice as high as another will compress twice as much. This assumption should be valid as long as the powder does not approach tap density. However, when load is applied in large increments, the combination of wall friction and extensive inter-particle bridging may reduce the compression of taller beds. Therefore, the relatively shallow 9.525 mm stack height was used in these measurements. In the actual layering process, small load increments (typically 5 Pa) and vibration during spreading minimize non-linearity caused by wall friction and inter-particle bridging.

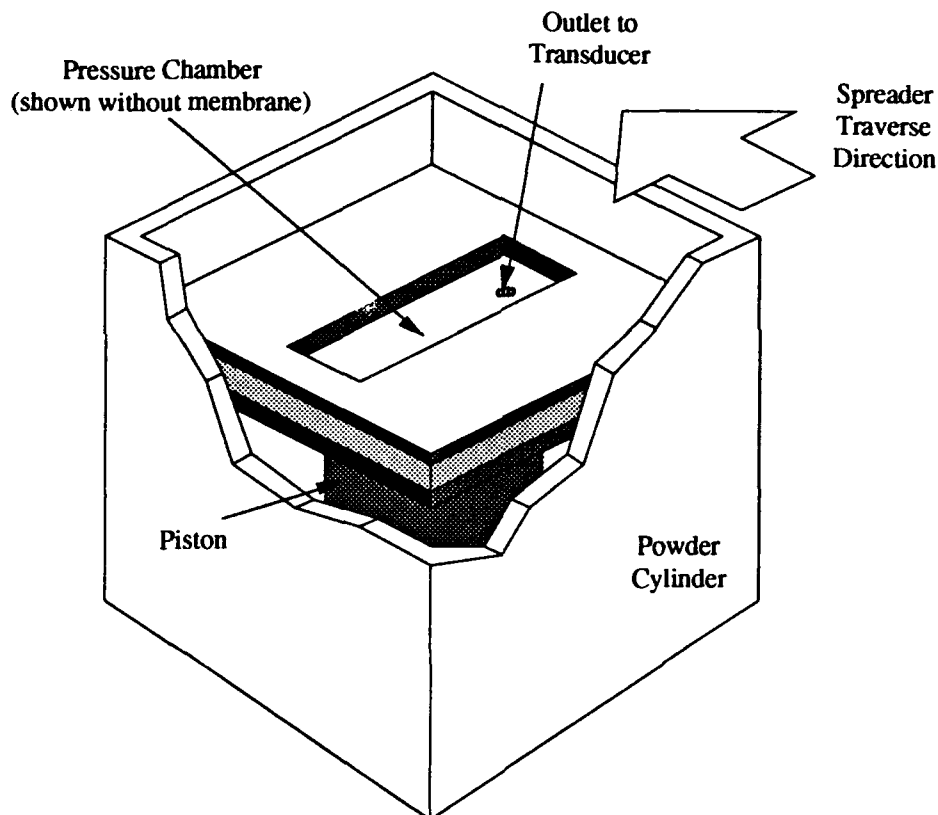
Now having a measure of how a powder bed responds to load, the loads are measured in the following set of experiments.

Loads Applied To Powder Layers

Each layer within a powder bed will be subjected to vertical loading. An inherent source of load is the weight of subsequent powder layers. A secondary compressive load may arise if a significant quantity of powder is trapped under the spreader rod as it traverses the powder surface. The weight can be calculated easily from packing density and volume, but a special technique was required to check the significance of loads during actual spreading.

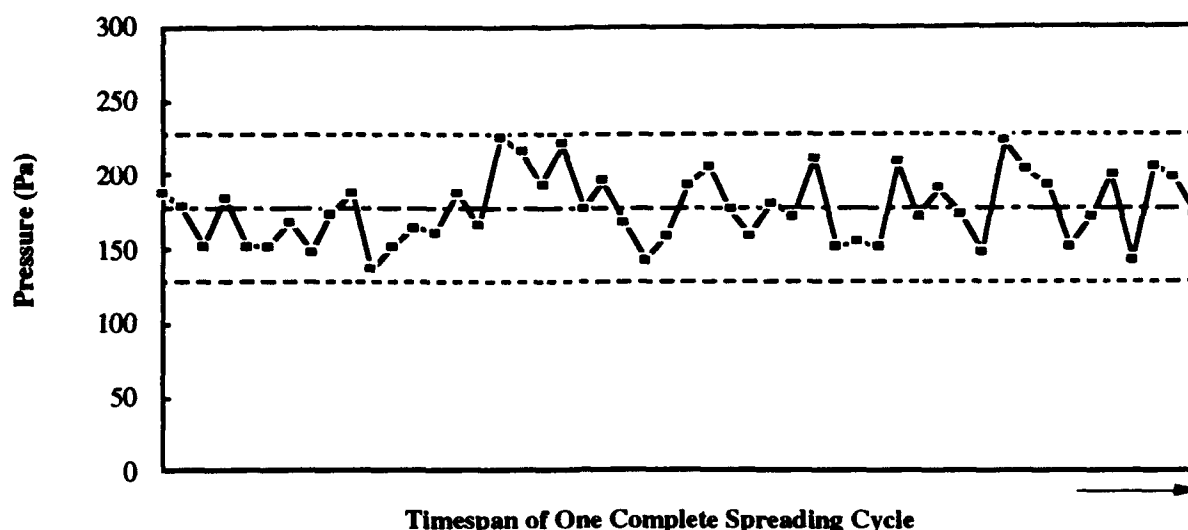
A pressure sensor was designed to measure the force exerted on a powder bed during traversal of the spreader rod. As Figure 9 shows, a shallow pocket connected to a silicon pressure transducer was imbedded into the piston floor. The pocket was covered with a thin latex membrane and filled with oil to act as a load sensor. The pocket was oriented such that its signal would show a peak if the spreader rod caused a significant pressure increase as it passed over the bed.

Figure 9. Powder Bed Load Measurement Device



No significant pressure increase could be detected as the spreader rod traversed over the powder bed under a wide range of conditions. Traverse speeds were varied between 20 mm/s and 100 mm/s and rotation speeds varied between 20 mm/s and 100 mm/s on the circumference. Bed depths as shallow as 1 mm and as deep as 67 mm were examined. Figure 10 shows typical real-time pressure measurements as the spreader rod makes one back-and-forth traverse across a bed of 10-micron spherical alumina.

Figure 10. Pressure Measurements during Spreader Traverse



A standard deviation was computed from long runs of data while the spreader was at rest. Upper and lower limits are set at 3 standard deviations from the mean. If the spreader rod increased pressure significantly, the plots would show two peaks (for each of the pass over the bed). The results suggest that the dominant source of load upon a given layer is simply the weight of subsequent layers.

Error Predictions

Displacement predictions for a layer can be made using the compressibility of the powder by assuming the static weight of layers above is the primary source of load. Compressibility from experimental data and load computed from density and volume lead to the following key relationships for a prediction of layer displacement:

$$\text{Compressibility} = \frac{\text{Strain}}{\text{Stress}} \quad \text{Strain} = \frac{\text{Displacement}}{\text{Vertical Position}} \quad \text{Stress} = \frac{\text{Load}}{\text{Interface Area}}$$

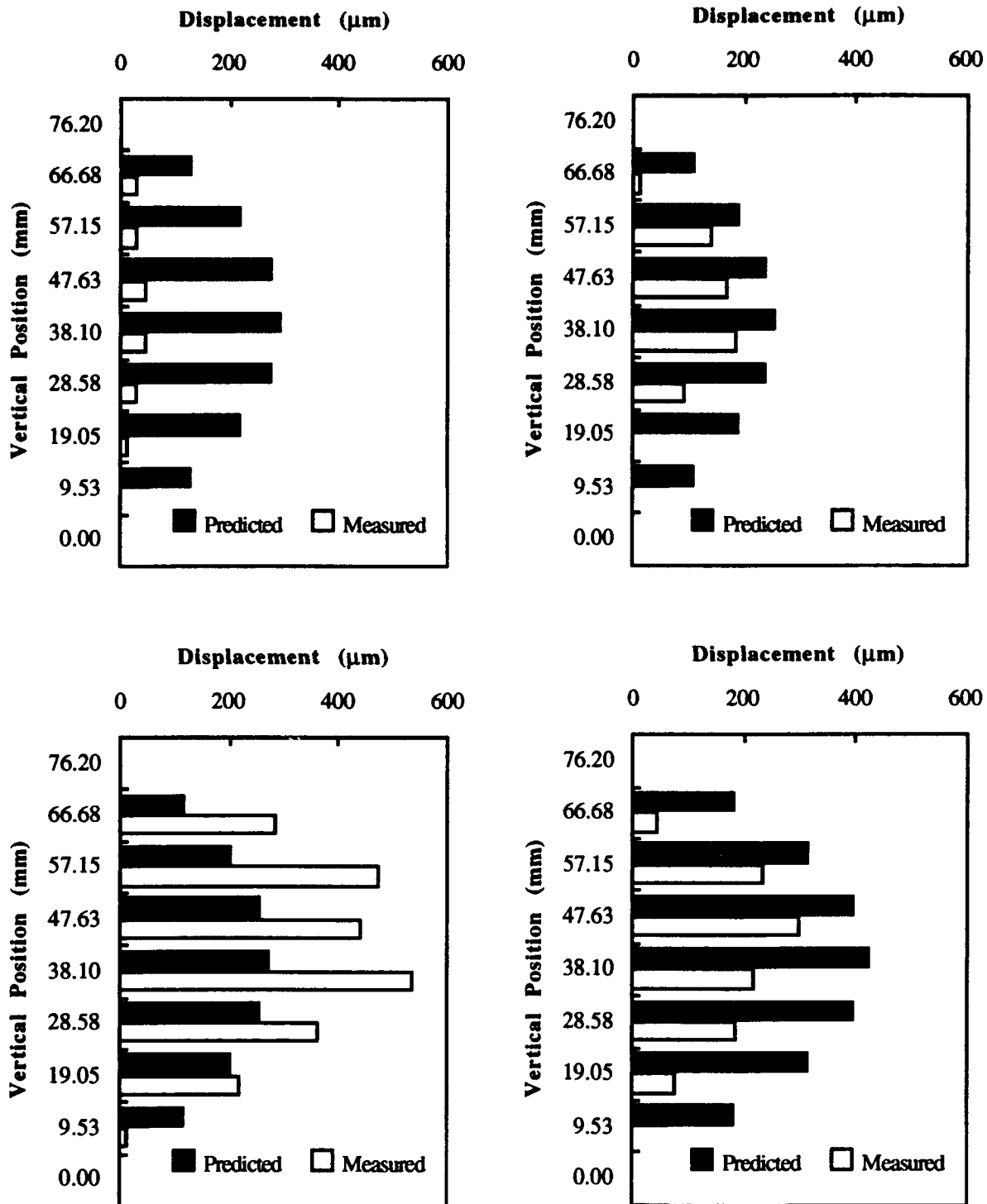
$$\text{Load} = \text{Density} \cdot (\text{Total Height} - \text{Vertical Position}) \cdot \text{Interface Area}$$

Letting C = Compressibility, ρ = Density, and H = Total Height, layer displacement Δy is shown to be a quadratic function of vertical position (y) from the bed floor:

$$\Delta y = (\rho C H) y - (\rho C) y^2$$

Figure 11 shows the layer displacement predictions for the four powder samples, superimposed upon the error traces from direct measurement.

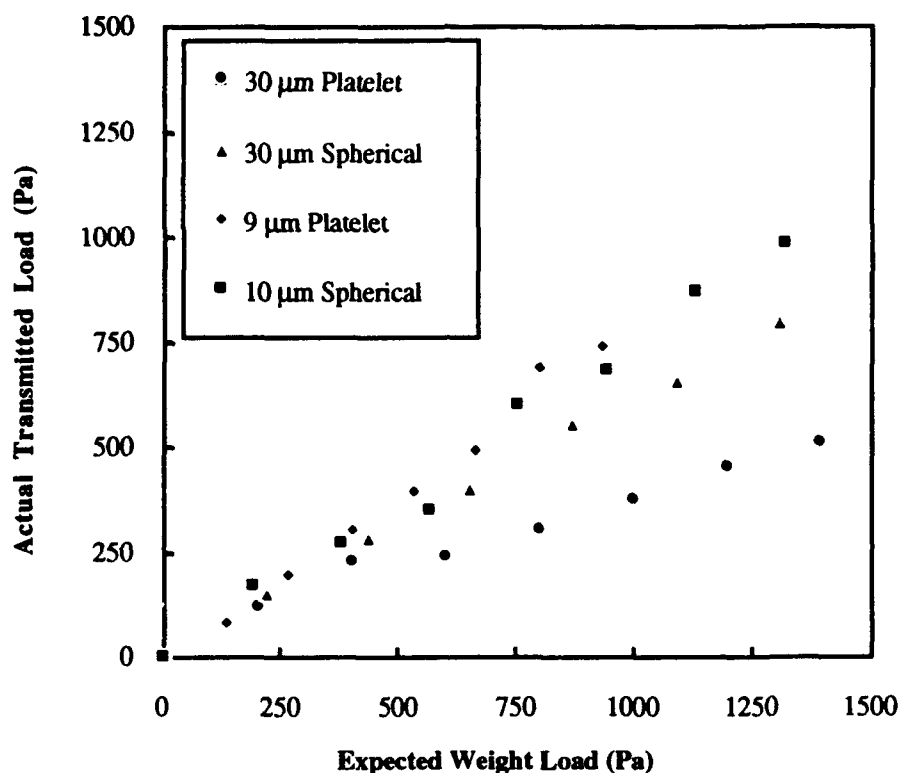
Figure 11. Layer Displacement Predictions



The results show that the compressibility and load data indeed capture the quadratic shape of the measured error profiles. The spherical powder samples also showed close agreement between predicted and measured magnitudes. The platelet-shaped particles showed less predictability with respect to magnitudes.

The over-estimation for the large disk-shaped powder may be the result of wall friction and internal bridging of particles. Figure 12 compares expected weight versus the weight measured using the pressure sensor. The measurements show that the full load of the powder stack is always slightly less than the expected load. The largest deviation was experienced by the 30-micron platelet powder, which also exhibited the largest discrepancy between measured and predicted vertical displacement.

Figure 12. Actual Transmitted Load versus Expected Weight



Conclusions

The following conclusions can be made based on measured layer displacements and experiments on compressibility and load: (1) Layer displacements in a dry powder bed may have significant magnitude compared with layer spacing. (2) Layer displacements have a characteristic parabolic profile, with greatest errors for middle layers and diminishing magnitude for top-most and bottom-most layers. (3) The weight of subsequent powder appears to be the dominant source of load on any given powder layer. (4) Predictions based on weight and compressibility make fair approximations to actual errors in layer position. (5) Results are highly material-dependent. Particle geometry and packing density affect the magnitudes of errors. (6) In some cases, wall friction may significantly reduce the powder weight that is transmitted to lower layers.

A suggestion for accuracy improvement is the investigation of techniques that help to fix particles in place. Procedures such as misting with water or a temporary chemical agent could reduce compressibility and thereby reduce layer displacements.

Acknowledgements

NSF Strategic Manufacturing Initiative
MIT Leaders for Manufacturing
ARPA
Three Dimensional Printing Consortium
3M
AMP
Ashland Chemical
Boeing
E-Systems
Hasbro
Howmet
Johnson & Johnson
National Center for Manufacturing Sciences
Procter & Gamble
Sandia National Labs
United Technologies

References

- Brown, R. L. & Richards, J. C., *Principles of Powder Mechanics*, Pergamon Press, Oxford, 1970.
- Dallavalle, J. M., *Micrometrics: The Technology of Fine Particles*, 2nd ed., Pitman Publishing Corporation, New York, 1948.
- Deckard, C. & Beaman, J., "Recent Advances in Selective Laser Sintering," *Fourteenth Conference on Production Research and Technology*, University of Michigan, Oct. 1987, pp. 447-452.
- Fayed, M. E. & Otten, L., eds., *Handbook of Powder Science and Technology*, Van Nostrand Reinhold Company, New York, 1984.
- Iinoya, K., Gotoh, K., Higashitani, K., eds., *Powder Technology Handbook*, Marcel Decker, Inc., New York, 1991.
- Sachs, E., Cima, M., Williams, P., Brancazio, D, and Cornie, J., "Three Dimensional Printing: Rapid Tooling and Prototypes Directly From a CAD Model," accepted for publication in the *Journal of Engineering for Industry*, 1990, p. 13.
- Wohlers, T., "Creating Parts by Layers", *Cadence*, April 1989, pp. 73-76.

Appendix: Designed Experiment to Maximize Packing Density

Experimental design has been implemented to characterize the powder layering process in terms of how input parameters affect layered packing density. To address many factors in a reasonable number of experiments, only two levels (low and high) were examined for each control variable.

A $1/8$ fractional design (2^{7-3}) [Montgomery: *Statistical Quality Control*] is used to reduce the number of experiments to a reasonable number. The parameters in Table A1 were selected as control variables to understand the conditions affecting layered packing density.

Table A1. Layered Packing Density Control Variables

Variable	Symbol	Low	High	Units
Layer Spacing	S	127	254	μm
Traverse Speed	T	50	100	mm/s
Rotation Speed	R	1.5	2.0	rev/s
Vibration Frequency	F	125	400	Hz
Vibration Amplitude	A	25	50	μm zero-to-peak
Moisture Exposure	M	35	80	% sat @ 25 °C
Spreading Excess	E	31.75	127	μm

The 2^{7-3} experimental array for a given powder is shown in Table A2, with (-1) representing low levels and (+1) representing high levels of the control variables.

Table A2. 2^{7-3} Fractional Factorial Design

Run	S	T	R	M	F	A	E
1	-1	-1	-1	-1	-1	-1	-1
2	+1	-1	-1	-1	+1	-1	+1
3	-1	+1	-1	-1	+1	+1	-1
4	+1	+1	-1	-1	-1	+1	+1
5	-1	-1	+1	-1	+1	+1	+1
6	+1	-1	+1	-1	-1	+1	-1
7	-1	+1	+1	-1	-1	-1	+1
8	+1	+1	+1	-1	+1	-1	-1
9	-1	-1	-1	+1	-1	+1	+1
10	+1	-1	-1	+1	+1	+1	-1
11	-1	+1	-1	+1	+1	-1	+1
12	+1	+1	-1	+1	-1	-1	-1
13	-1	-1	+1	+1	+1	-1	-1
14	+1	-1	+1	+1	-1	-1	+1
15	-1	+1	+1	+1	-1	+1	-1
16	+1	+1	+1	+1	+1	+1	+1

Under a customized control program for powder layering experiments, powder layers were built to a total bed depth of 12.7 mm, with a corresponding volume of 102.87 ml. Samples were weighed on a digital balance.

A convenient way of summarizing the data of such a design is to express the results in terms of main effects. The main effect of a factor X is the average of all occurrences where X is high minus the average of all occurrences where X is low [consult Montgomery for details]. Figures A1 and A2 display the differences in output caused by the two levels of each input variable, for two sample powders. Each line segment is centered about the grand mean. For each pair of points and the corresponding control factor, the higher one is calculated as the grand mean plus half the main effect, and the lower is the grand mean minus half the main effect.

Figure A1. Layered Packing Density Main Effects for Alumina 30 μm

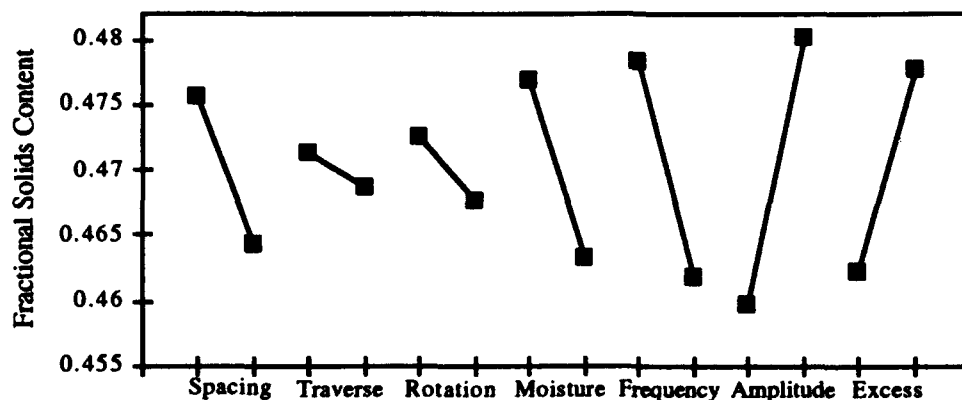
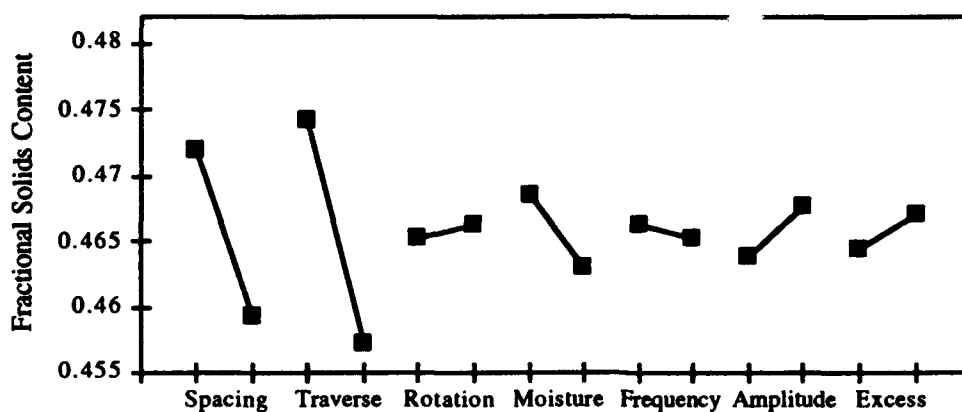


Figure A2. Layered Packing Density Main Effects for Alumina 10 μm



A simple verification experiment was run for the standard 3DP powder (30 μm alumina), using the main effects that predicted highest density. FSC values were 0.520 and 0.521, for an average of 0.521, higher than all values in the experimental design array.

The Physics of Digital Microfabrication with Molten Microdrops*

Fuquan Gao and Ain A. Sonin

Department of Mechanical Engineering
Massachusetts Institute of Technology
Cambridge, MA 02139

1. Introduction

Precise deposition of molten microdrops under controlled thermal conditions provides a means of 3D "digital microfabrication", microdrop by microdrop, under complete computer control, much in the same way as 2D hard copy is obtained by ink-jet printing. This paper describes some results from a study of the basic modes of microdrop deposition and solidification (Gao & Sonin, 1993). The conditions required for controlled deposition are discussed, and some experimental results and theoretical analyses are given for various basic deposition modes. These include columnar (i.e. drop-on-drop) deposition at low and high frequencies, sweep deposition of continuous beads on flat surfaces, and repeated sweep deposition for buildup of larger objects or materials.

2. Experimental Conditions

We are concerned with systems in which individual molten droplets are dispensed on demand and delivered ballistically to a target location where they impact and solidify. To avoid drop breakup or splattering at impact, and thus set the stage for precise control over the deposition process, we use conditions where capillarity forces dominate during impact. This requires that, roughly, $We = \rho V^2 a / \sigma < 10$, where We is the Weber number based on droplet density ρ , impact speed V , droplet radius a and surface tension σ .

In our experiments individual droplets of molten wax with diameter $2a \approx 50 \mu\text{m}$ were ejected at controlled frequencies in the range 0-15 kHz from a heated, piezoelectrically driven drop-on-demand generator (an adapted ink-jet print head) and directed to a target located typically 3-5 mm away, where they impacted at a speed V of the order of 3 m/s. The ambient air and the target were maintained at a temperature below the melt's solidification point. In-flight cooling of the droplets was typically insignificant, and the drops arrived at the target in superheated liquid form with essentially the temperature they had at the generator.

Two types of waxes were used in the experiments referred to in this paper. One was a candelilla wax with a solidification temperature of 70°C, and the other a microcrystalline petroleum wax (Reed 6882) with a solidification temperature of 91°C.

3. Deposition of Single Droplets; the Solidification Angle

Figure 1 shows the impact of a single melt droplet on a surface (in this case plexiglas), recorded through a microscope objective with the aid of strobe lighting. The drop impacts with essentially its source temperature T_0 . The impact occurs in this case with $We=10$. The droplet touches the surface, wets it, showing some inertial distortion

* © F. Gao & A. A. Sonin, 1993. Correspondence should be addressed to Prof. Ain A. Sonin, Room 3-256, MIT, Cambridge, MA 02139, USA. Tel: (617) 253 2247. Fax: (617) 258 8559.

about 20 μs after impact, but quickly assumes a spherical-cap shape under the action of capillarity forces, reaching what appears to be a state of mechanical equilibrium with finite contact angle long before it solidifies. The entire spreading process takes only about 40 μs in this case. The droplet's solidification time on plexiglas, on the other hand, can be estimated (Gao & Sonin, 1993; Hill & Kucera, 1983) as about 20 ms, three orders of magnitude longer than the spreading time.

The contact angle which the drop assumes before solidifying is not an equilibrium property. The drop spreading occurs under thermally nonequilibrium conditions, with the bulk of the liquid superheated and the target surface subcooled. Nevertheless, we have observed that under conditions where the drop spreading on the target is completed in a time much shorter than the solidification time, as in Fig. 1, the molten drop appears to possess an apparent (nonequilibrium) contact angle which is, at least approximately, a property of the melt material, the target material and the characteristic temperatures involved, but independent of the spreading process. A melt droplet stops spreading when it reaches this "melt contact angle", having apparently attained a mechanical but not thermal equilibrium, and then freezes on a much longer time scale while maintaining this angle. The solidification angle is in such cases equal to the (nonequilibrium) melt contact angle, and thus, like that angle, appears to be a property of the melt material, the target material and the characteristic temperatures, but independent of the spreading process (Gao & Sonin, 1993). Our studies with waxes have shown that for the case where the target is the same material as the melt, the solidification angle depends largely on the target temperature and tends to increase as the target's subcooling is increased.

4. Columnar Deposition

The letters "MIT" in Fig. 2 are about 300 μm tall and stand upright on a plastic surface. They are fabricated by precise deposition of molten microdrops from above, at a frequency low enough for each droplet to solidify by heat transfer to the ambient atmosphere before the next one arrives.

Figure 3 shows the effect of frequency on the solid structures formed by columnar deposition. Here, 25 consecutive droplets have been deposited on top of each other at various frequencies ranging from 0 to 10 kHz. At sufficiently low frequencies — below about 10 Hz in this case — a distinct *dropwise solidification* takes place where identical, vertical pillars of solidified droplets are formed independent of frequency, much like in Fig. 2. A transition away from dropwise solidification occurs as the frequency increases to the point where there is insufficient time for the previous droplet to completely solidify and cool down to ambient temperature before the next one arrives. As a result the next droplet hits a "target" with higher than ambient temperature, the solidification angle between the arriving droplet and the previous droplet is reduced, and the 25-drop pillar becomes shorter and stouter. The effect increases as the frequency rises, until successive droplets begin to melt together.

At frequencies greater than about 50 Hz, there is insufficient time for solidification before the next drop arrives. The impinging droplets coalesce into a hemispherical liquid cap, and solidification takes place below the shoulder of the cap. If the deposition is continued instead of being curtailed after 25 drops, there results a continuous growth mode where the liquid tip moves upward as the new drops arrive, leaving behind a solid rod with diameter larger than the individual droplets (Fig. 4). At still higher frequencies — above 200 Hz, say, in Fig. 3 — the whole burst of 25 droplets coalesces into a spherical drop which solidifies only after the salvo stops. The droplet delivery rate affects the base radius of the large drop, the base radius increasing (solidification angle decreasing) as the liquid delivery rate increases. This can be attributed to the fact that the delivery time of the 25-droplet liquid volume is in this case longer than the solidification time, and the contact line freezes and becomes arrested on its way cutward before it can attain the apparent

mechanical equilibrium displayed in Fig. 1. Note that all the large drops formed by high frequency deposition would in fact grow into solid rods as in Fig. 4 if droplet deposition were continued.

5. Low Frequency Dropwise Deposition

Three parameters characterize a "vertical" pillar produced in the low-frequency regime: (i) the radius r measured at the maximum point (Fig.5), (ii) the length h which is added to the pillar by each deposited drop, and (iii) the maximum frequency at which the deposition is frequency-independent.

Mass conservation and the fact that the drop's radius of curvature is constant (the Bond number is small at the microscale) allow the first two of these quantities to be derived straightforwardly in terms of the incoming drop radius, a , and the solidification angle θ of the droplet after impact on subcooled solid material of its own kind (Gao & Sonin, 1993). This reduces the problem of the geometry of dropwise columnar solidification to that of establishing the solidification angle θ of the droplets: the smaller the contact angle, the shorter and stouter the column. The solidification angle will depend on the properties of the melt material and the temperatures of the incoming droplet and the previously solidified material on which it lands.

The maximum frequency f_{\max} at which dropwise deposition is independent of frequency can be estimated from the time required for the tip of the pillar to cool back to ambient temperature after a drop is deposited. The derivation is lengthy, in part because the pillar acts as a heat transfer fin (Gao & Sonin, 1993), and we will not give it here, but for the data of Fig. 3 one obtains $f_{\max}=12$ Hz, in good agreement with the observations.

The free-standing letters in Fig. 1 were created in the dropwise solidification mode. Note that even a "horizontal" member can easily be made with this technique by deposition from "above", since capillarity forces dominate over inertial forces at impact. The "horizontal" center-to-center separation between two consecutive droplets simply has to be adjusted so that the next drop will touch the last solidified one, grab onto it by capillarity and spread partly over it, and solidify. By adjusting the ratio of the horizontal center-to-center drop spacing, w , to the incoming droplet radius, a , one can give a pillar of droplets any slope β between 0° and 90° (Fig. 5). The precise relationship between w/a and β depends on the apparent contact angle (and possibly also somewhat on the Weber number at impact, if that number is not sufficiently small). If inertial effects are insignificant compared with capillarity forces (i.e. the Weber number $\rho V^2 a / \sigma$ is not too large) one would expect that

$$\frac{w(\beta)}{h} = \cos\beta \quad (1)$$

where h is the height added to a vertical pillar by each drop and can be calculated easily in terms of a and θ . Equation (1) is in good accord with our observations (Fig. 6).

6. High Frequency Columnar Deposition: the Continuous Solidification Mode

A gradual transition away from dropwise solidification occurs in Fig. 3 as the frequency increases from about 10 Hz to 50 Hz. At sufficiently high frequencies there is insufficient time between droplets for any solidification. The first of the arriving droplets coalesce on the target surface into a larger, spherical-cap liquid drop (surface tension dominates at this scale) which spreads as more liquid arrives, maintaining at first a spherical cap shape. As this coalesced drop grows, however, its contact line advance rate over the cool target surface slows and eventually becomes so slow that solidification sets in

at the contact line and arrests the spreading. The point at which this occurs depends on deposition frequency (spreading speed), material properties and the characteristic temperatures. After contact line arrest the large drop grows for a while more by bulging out over the frozen contact line, maintaining an approximately spherical-cap shape, but then the solidification spreads upward from the base and begins also at the sides as a result of heat loss to the ambient air. Eventually an asymptotic state results (see Figs 4 and 7) where a hemispherical liquid cap rises upward at a steady rate, fed from above by the arriving droplets and chased from below by a solidification front, leaving behind it a continuous, cylindrical solid rod of constant diameter. The diameter of the solid is controlled by the enthalpy flux associated with the melt deposition and by the heat flux from the hemispherical cap to the ambient air: a steady state is attained when interfacial solidification sets in precisely at the shoulder of the liquid cap.

This *continuous solidification mode* will invariably result if the deposition frequency is high enough and if the deposition is continued long enough to form an adequate solid base and establish a steady state growth. This mode is, in essence, a microscale version of the Verneuil crystal growth process.

We have derived a simple, approximate model for continuous deposition based on the model sketched in Fig. 7. Hot melt arrives at the top as droplets of radius a and temperature T_0 impact at frequency f . In steady state, the column's radius R adjusts itself so that air cooling of the hemispherical liquid cap brings the melt's temperature to precisely the fusion point T_f at the cap's base. Solidification starts below the cap at the column's outer surface and proceeds inward, leaving the column with a liquid core the length of which depends primarily on the Stefan number $c(T_f - T_a)/L$ where T_a is the ambient air temperature, c is the melt's specific heat, and L the latent heat of fusion. The model gives the column radius as

$$R \approx \frac{2pa^3fc}{3k_{air}Nu} \ln \left(\frac{T_0 - T_a}{T_f - T_a} \right). \quad (2)$$

where $Nu = qR/k_{air}(T - T_a)$ is the Nusselt number based on the heat flux q from the cap to the ambient air, the local liquid temperature T , the conductivity of the air k_{air} , and the cap radius R . The shape of the solidification zone below the liquid cap is parabolic and can also be expressed in analytic form.

Figure 8 shows some data for R obtained with two different waxes over a range of deposition frequencies, and compares them with Eq. (2) taking $Nu \approx 1$ (rigorous for a spherical body in still air, and a good approximation here for the small scale involved). Except at the lower frequencies, the agreement is quite good, given the simple nature of the theory. Video and visual observations using translucent waxes showed the liquid cap as a smooth, transparent hemisphere with a semi-opaque solid afterbody inside which a faintly visible molten region could be seen, much like the parabolic prediction sketched in Fig. 7, with λ/R apparently somewhat greater than 2. The visibility was not, however, adequate for an accurate comparison of λ with the model.

7. Continuous Bead Deposition on Flat Surfaces

When a generator dispenses liquid droplets at a frequency f while moving over a flat target at a speed U (Fig. 9), the droplets will overlap and tend to form a continuous bead if

$$\frac{f(2a)}{U} > F(\theta) \quad (3)$$

where θ is the solidification angle and $F(\theta)$ is a function which can be derived from geometry (Gao & Sonin, 1993). Bead deposition has potential uses such as laying down electrically conductive (or resistive) lines on a substrate. A model for the bead's geometry as a function of operating conditions and material properties can be written in terms of the material's solidification angle θ , the assumption being that this angle can, over a range of conditions where the melt spreads to a quasi-equilibrium condition much faster than it solidifies, be considered an empirical property of the melt and target materials and the temperatures involved. This yields the bead's width W , for example, as

$$\frac{W}{2a} = \left(\frac{2\pi \sin^2 \theta}{3(\theta - \sin \theta \cos \theta)} \frac{f(2a)}{U} \right)^{1/2} \quad (\theta < \pi/2) \quad (4)$$

Figure 10 shows a comparison of the model with experimental data of sweep deposition using candelilla wax on plexiglas with $2a=50.5 \mu\text{m}$, $U=0.293 \text{ ms}^{-1}$, $T_0=90^\circ\text{C}$, and $T_a=58^\circ\text{C}$. The onset of bead formation at about $f(2a)/U=0.6$ is in good agreement with Eq. (3) and the bead's width as a function of frequency is in agreement with Eq. (4), provided we take $\theta=53^\circ$. This value is exactly consistent with the solidification angle observed for the separate individual drops deposited at low sweep speeds, i.e. at $f(2a)/U < 0.6$.

8. Repeated Sweep Deposition

Figure 11 shows a "wall", about $1500 \mu\text{m}$ tall and $65 \mu\text{m}$ thick, built by repeated sweep deposition at speed $U=0.84 \text{ m/s}$ and deposition frequency $f=13.9 \text{ kHz}$, which correspond to $f(2a)/U=0.83$. The building rate was 10.8 cm^2 of wall per minute. The frequency in repeated sweep deposition can be very high, much higher than that in dropwise columnar deposition, because the time available for solidification is controlled by the interval between sweeps rather than by the deposition frequency. It is important, however, to maintain correct conditions related to sweep speed, deposition frequency and characteristic temperatures, as well as the precision of the deposition. Otherwise, structural irregularities (instabilities) will arise and grow as the next layers are laid down.

9. Concluding Remarks

This paper describes some of the basic modes of precise molten microdrop deposition — dropwise columnar deposition, continuous columnar deposition, sweep deposition of continuous beads on surfaces, and repeated sweep deposition — and provides for each mode some understanding of the required operating conditions and analytical methods for predicting the solid shapes.

Our experiments were done with waxes, but through analysis it is possible to generalize the results to other materials. It should be noted, however, that most of our results are obtained under conditions where the droplet deposition (i.e. impact and spreading) occurs on a much shorter time scale than solidification, with the result that the drops first establish a quasi-equilibrium liquid shape on the target and solidify thereafter on a much longer time scale. The apparent contact angle of the liquid after deposition, but before solidification, is an important parameter, for it determines the solid shapes that result from droplet deposition. This nonequilibrium contact angle is not well understood, and further studies are warranted.

Acknowledgements

This research was supported by the National Science Foundation under Grant No. CTS-9122123, and initiated with the aid of grants from the Charles E. Reed Faculty Initiative Fund and the Hewlett Packard Corporation.

References

Gao, F. and Sonin, A. A., 1993, Precise Deposition of Molten Microdrops: the Physics of Digital Microfabrication. Submitted for publication in *Proc. Roy. Soc. A*.

Hill, J. M. and Kucera, A., 1983 Freezing a Saturated Liquid Inside a Sphere. *Int. J. Heat Mass Transfer* 26, 1631-1637.

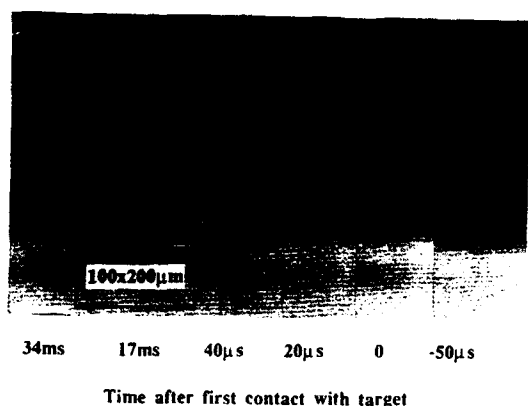


Figure 1 Impact of a single microdrop of candelilla wax on a plexiglas target. $T_0=90^\circ\text{C}$, $T_a=30^\circ\text{C}$, $V=2.6\text{ ms}^{-1}$.

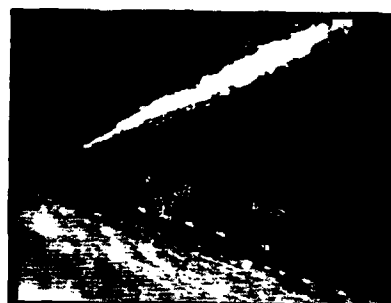


Figure 2 Freestanding 300 μm tall letters produced by dropwise deposition of molten wax microdrops. The conical object is the tip of a common pin; the rectangle measures 200x600 μm .



Figure 3 Structures produced by depositing 25 microdrops on top of each other at various frequencies. Candelilla wax, $T_0=100^\circ\text{C}$, $T_a=38^\circ\text{C}$.

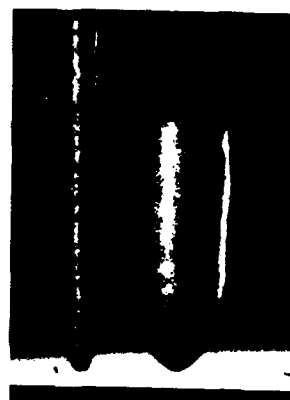


Figure 4 The continuous solidification mode. Candelilla wax, $T_0=90^\circ\text{C}$, $T_a=33^\circ\text{C}$. Frequency, from left: 200 and 1000 Hz. Rectangle: 200x600 μm .

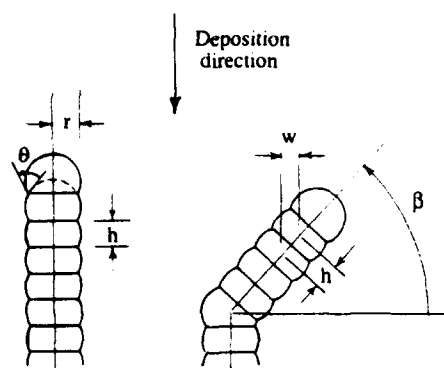


Figure 5 Parameters of vertical and inclined pillars produced by low-frequency dropwise deposition from above.

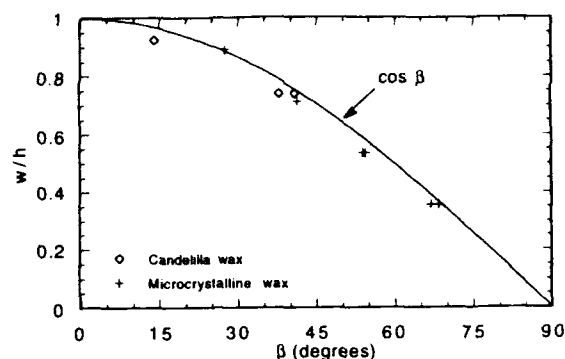


Figure 6 The relationship between a pillar's slope β and the horizontal center-to-center deposition spacing w .

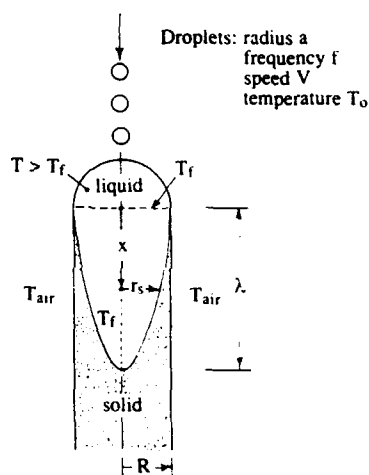


Figure 7 Cross section of continuously growing column in the high-frequency mode.

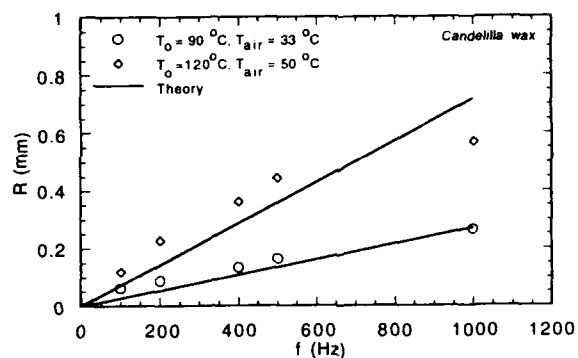


Figure 8 Column radius in the continuous solidification mode: experiment vs theory.

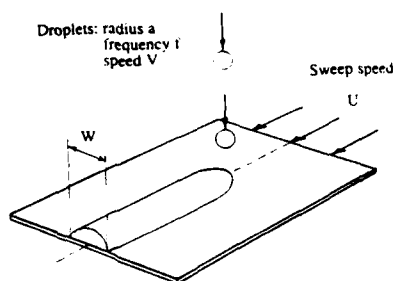


Figure 9 Parameters in sweep deposition of smooth beads.

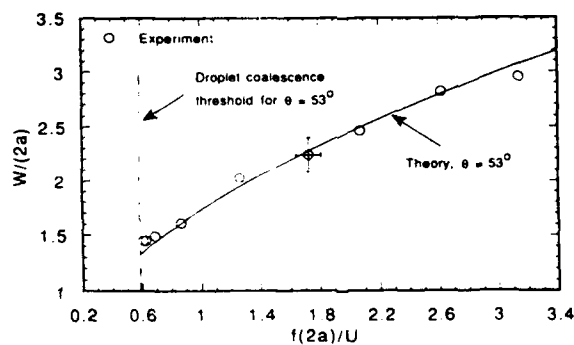


Figure 10 Bead width in sweep deposition: experiment vs theory.

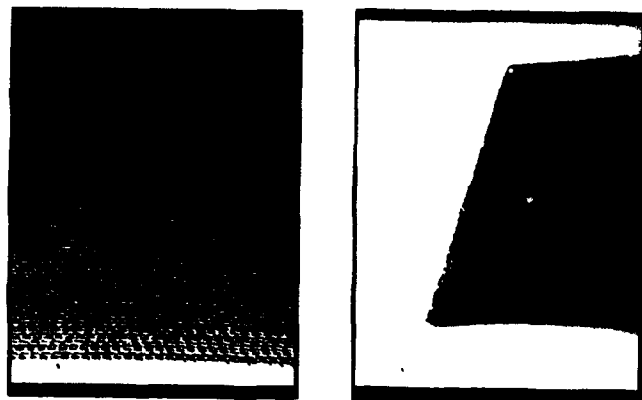


Figure 11 Wall built up by repeated sweep deposition. Candelilla wax, $T_o=100^{\circ}\text{C}$, $T_a=43^{\circ}\text{C}$. At right is a view in perspective after the wall was cut. Rectangle: $200\times 600\text{ }\mu\text{m}$.

MATERIAL AND PROCESS PARAMETERS THAT AFFECT ACCURACY IN STEREOLITHOGRAPHY

Richard P. Chartoff, Lawrance Flach,
and Peter Weissman*
University of Dayton
Rapid Prototype Development Laboratory and
Center for Basic and Applied Polymer Research
Dayton, Ohio 45469-0130

ABSTRACT

Experimental real time linear shrinkage rate measurements simulating stereolithography are used in an analysis of shrinkage during line drawing in stereolithography. While the amount of shrinkage depends on the polymerization kinetics, shrinkage kinetics and overall degree of cure, it also depends on the length of time to draw a line of plastic. A line drawn slowly will exhibit less apparent shrinkage than one drawn very quickly because much of the shrinkage is compensated for as the line is drawn. The data also indicates that a typical stereolithography resin in the green state may shrink to only 65% of its maximum, thus retaining considerable potential for shrinkage during post-cure. This information can be used to predict the amount of shrinkage to be expected under certain exposure conditions and to formulate overall strategies to reduce shrinkage and subsequent warpage that causes shape distortion.

INTRODUCTION

In order to better understand the shrinkage-related problems associated with stereolithography, and to minimize their effect, it is essential to understand the relationship between the polymerization kinetics, shrinkage kinetics, total shrinkage, and the laser scan rate. These variables directly affect the amount of shrinkage that will occur in a line of plastic drawn by the stereolithography apparatus (SLA) and ultimately in the warpage and shape distortion of the final part. In this paper we discuss the results of a series of real time shrinkage rate measurements (in an apparatus that simulates stereolithography) and use the rate data in an analysis of the shrinkage that occurs when a single strand of material is formed. The analysis indicates that the rate of shrinkage rather than shrinkage itself is the key parameter for controlling shrinkage-related dimensional effects.

EXPERIMENTAL

Real time shrinkage measurements were performed on "full line" exposures of three photopolymers: Ciba XB5081-1, UD experimental formulas 60.1 and 61.1. The so-called "full line" exposure is performed by exposing an approximately 7 mm long by 0.2 mm wide line to a focused Argon-Ion UV laser beam. The apparatus and procedures for making these measurements have been described elsewhere [1,2]. The current experiments were designed to

* Current Address: UCB Radcure, Inc., 200 Lake Park Drive, Smyrna, GA 30080-7611.

compare the shrinkage rates as well as the shrinkage occurring under both short term and long term laser illumination. This was accomplished by exposing a line of polymer to a single 40 m sec pulse (short term exposure) and subsequently a series of successive 40 m sec pulses until maximum shrinkage was achieved.

Real time shrinkage measurements were made, in duplicate, for the three polymers. The laser power was varied for each so that a cure depth (C.D.) of 0.85 mm was obtained. The energy densities 76.9, 65.2, and 66.5 mJ/cm² were used to obtain a uniform specified cure depth for XB5081-1, 60.1, and 61.1, respectively. The total shrinkage was noted five minutes after the first exposure. Each sample was then exposed again the standard amount and the additional shrinkage noted after five minutes. This procedure was repeated to obtain the desired number of exposures. Each material was subjected to five consecutive exposures with a five minute pause between each. XB5081-1 was tested using eight consecutive exposures.

DISCUSSION OF EXPERIMENTAL RESULTS

The real time shrinkage data for the six samples (three polymers in duplicate) that were exposed once are shown in Figure 1. Resins 60.1 and 61.1 show a shorter induction time, steeper slope, and higher shrinkage than XB5081-1.

The data of Figure 2 indicate that 60.1 and 61.1 complete a greater percentage of their ultimate shrinkage after the first exposure than does the XB5081-1. Table I tabulates the percentage of maximum shrinkage that has occurred after each individual exposure. The change in shrinkage due to additional exposures became very small after the fifth exposure for 60.1 and 61.1. However, for XB5081-1 the change in shrinkage with continued exposures does not decrease significantly until the eighth exposure. Therefore, the maximum shrinkage for 60.1 and 61.1 was taken as that which had occurred after the fifth exposure, while for XB5081-1 it was taken as that which had occurred after the eighth exposure.

Additional data on the density changes for the three photopolymers measured after long term cure under Hg vapor lamp exposure indicates that approximately 15-25% of the total shrinkage that occurs is missed by the real time shrinkage apparatus. This is the amount that occurs before gelation and does not affect the dimensions of a line actually drawn by a laser. Further density characterization of full line specimens after long term laser exposure is now being carried out to determine more exactly the amount of initial shrinkage not detected in the real time shrinkage measurements.

SHRINKAGE ANALYSIS

The amount of shrinkage observed when a line of plastic is drawn by the SLA is determined by the polymerization kinetics, the shrinkage kinetics, and the laser scan rate. A detailed analysis is required in order to determine the inter-relationships between the appropriate variables. There are two shrinkage components that must be considered. These are: (1) cure related shrinkage arising due to a change in chemical bond distances in the unpolymerized monomer relative to the polymer, and (2) thermal expansion/contraction due to temperature

changes in the resin on polymerization. The latter is assumed negligible as discussed elsewhere [2]. The analysis incorporates the experimental shrinkage rate data described previously.

The basis for the analysis is that any shrinkage that occurs before completing the laser scan for a particular line of plastic will be compensated for at least partially by the fact that the laser still scans a line of the correct length. The actual shrinkage that will be observed should be based on the amount of shrinkage that will occur at each point along the line **at the time the line is completed**. At that time the line is the correct length (due to a scan of the correct length) and any change in length is a result of polymerization and shrinkage occurring after completion of exposure.

If L is the desired length of a line of plastic drawn by the SLA, then the overall linear shrinkage (fraction) due to cure for the line of plastic will be given by:

$$F_c = \frac{1}{L} \int_0^L f_r(x) dx \quad (1)$$

where $f_r(x)$ is the residual shrinkage (fraction) at position x along the line, i.e. the amount of shrinkage that will occur at that point after completion of the line as indicated in Figure 3.

The residual shrinkage, $f_r(x)$, can be obtained from experimentally determined shrinkage vs. time data, or can be estimated from model-based predictions of the degree of cure along the line of plastic. If t_s is the time taken for the laser to scan from position x to the end of the line L , and $f_{ts}(x)$ the fractional shrinkage that has occurred up to time t_s at position x , then the residual shrinkage is just

$$f_r(x) = f_\infty - f_{ts}(x) \quad (2)$$

where f_∞ is the maximum fractional shrinkage that occurs at $t \rightarrow \infty$ (see Figure 4).

Using the fact that

$$f_\infty = f(t) \quad \text{as } t \rightarrow \infty \quad (3)$$

and

$$f_{ts}(x) = f(t) \quad \text{at } t = \frac{L-x}{s} \quad (4)$$

where s is the laser scan (draw) rate and $f(t)$ the shrinkage vs. time curve, eqn. (2) can be transformed to a time integral as follows:

$$F_c = f_\infty - \frac{s}{L} \int_0^{L/s} f(t) dt \quad (5)$$

In this expression L/s is just the time required for the laser to scan (draw) the line of plastic of length L , so eqn. (5) can be written as:

$$F_c = f_{\infty} - \frac{1}{t_{\text{scan}}} \int_0^{t_{\text{scan}}} f(t) dt \quad (6)$$

where t_{scan} is the scan time ($= L/s$).

SCAN RATES, SCAN TIMES AND SHRINKAGE

Modification of the scan (draw) rate typically requires that laser power be adjusted in order to maintain the same actinic exposure levels. This is necessary if use is to be made of a single shrinkage curve valid at a particular exposure level only. In all further discussions thus, when reference is made to scan rate adjustment, it should be understood that this is accompanied by appropriate laser power level adjustments.

A computer program was developed to investigate the relationship between the shrinkage and laser scan rate (for a line of plastic of constant length), and between shrinkage and line length (for a constant scan rate). The shrinkage data used for the investigation are those shown in Figure 1 for Cibatool XB5081-1 stereolithography resin and the faster curing experimental formulation F61.1. The program utilizes eqn. (6) to estimate the shrinkage that will occur when drawing a line of plastic of a specified length at a specified scan rate. Results were computed for two test cases. In the first, the scan rate was varied for a line of plastic of length 10 cm, and in the second, the line length was varied for a scan rate of 10 cm sec⁻¹. Typical operating laser scan rates for XB5081-1 are in the range 10-200 cm sec⁻¹. Results for the two tests can be found in Figures 5 and 6. As can be seen the shrinkage increases with increasing scan rate and decreasing line length. In both cases the maximum shrinkage value of f_{∞} is attained when the scan is completed during the shrinkage induction time, i.e. before any measurable shrinkage occurs. Note that the shrinkage does not depend independently on the two parameters, scan rate and line length, but on the single parameter t_{scan} (as revealed by eqn. (6)) which is a combination of the two parameters (eqn. (4)).

A number of interesting facts are revealed when considering the results of this analysis for a single shrinkage data set:

1. F_c will always be equal to or less than f_{∞} .
2. If the scan is very rapid or the line of plastic is very short ($t_{\text{scan}} \rightarrow 0$), then $F_c \rightarrow f_{\infty}$.
3. If the scan is very slow or the line of plastic is very long ($t_{\text{scan}} \rightarrow \infty$), then $F_c \rightarrow 0$.
4. f_{∞} is constant for a particular set of shrinkage data.
5. The integral part of eqn. (6) is simply the cumulative shrinkage that occurs during the laser scan and as such is subtracted from the maximum shrinkage that could occur.

6. Inspection of eqn. (6) reveals that for any particular shrinkage curve (resin, exposure combination), the measured shrinkage that occurs during the drawing of a line of plastic depends on the scan time only, i.e. on the combination of line length and scan rate, and not on the individual parameters.

It is an important consideration that experimentally measured shrinkage data, such as that in Figure 1, represent the composite effect of polymerization kinetics and shrinkage kinetics relative to the conversion.

When comparing results for different resins which exhibit different shrinkage rates and different final amounts of shrinkage, f_{∞} , some interesting observations can be made. The F61.1 resin shrinks considerably faster than the XB5081-1 and exhibits a higher final shrinkage. Figures 5 and 6, however, reveal that the shrinkage expected to occur when drawing a line of plastic is less for the faster curing and higher shrinking resin for certain scan rates and line lengths. This is a result of the compensating effect of shrinkage that occurs during the drawing process.

In lieu of a measured shrinkage curve, the mathematical process models developed for stereolithography [3], together with a kinetic shrinkage model such as that proposed by Bowman and Peppas [4], would allow estimation of the shrinkage that might be expected to occur when drawing a line of plastic. Eqn. (6) would still be required to compute the overall shrinkage. A procedure for using such an "a priori" approach will be discussed in a future report.

CONCLUSIONS

The conclusions that can be drawn from the above experiments and analysis is the following:

1. A significant amount of shrinkage occurs during cure prior to gelation that is not measured in linear shrinkage experiments that simulate stereolithography. This amounts to around 20% (or more) of total volume shrinkage and does not impact the stereolithography process. Thus volume shrinkage data will overestimate the actual SLA shrinkage.
2. The amount of shrinkage, warpage, and dimensional inaccuracies for stereolithography produced parts may be reduced by using very low scan rates (and low laser power) or, alternatively, developing a resin that shrinks rapidly compared to typical scan rates. The former of these two conclusions appears contrary to the concept of a rapid prototype technique, but should be considered when, for example, a high precision part is required. Selection of an optimum scan rate would be based on a compromise between the dimensional accuracy required and the speed of prototype production. The second conclusion is one that has influence on resin formulation. A fast curing, fast shrinking resin would be desirable for stereolithography use. A resin with a greater final shrinkage (f_{∞}) could be tolerated if the shrinkage occurred rapidly compared to the scan rate.

3. During the SLA part drawing process hatch vectors should not be attached until shrinkage is largely completed, i.e. for a fixed length vector, the scan rate should be adjusted to minimize F_C (use low scan rates).
4. Another aspect of the shrinkage/warpage problem that might be addressed by implementation of a fast curing, fast shrinking resin is residual post cure shrinkage. Resins such as F60.1 and F61.1 that shrink and cure more fully during the initial laser exposure will lead to less residual shrinkage and warpage during post cure.

NOMENCLATURE

$f(t)$	shrinkage function (fractional linear shrinkage vs. time)
$f_r(x)$	residual shrinkage at position x
$f_{ts}(x)$	shrinkage at position x at time t_s
f_∞	maximum shrinkage expected ($t \rightarrow \infty$)
F_C	overall fractional shrinkage in a line of plastic
L	length of line of plastic (cm)
s	laser scan rate (cm sec^{-1})
t_s	time for laser to scan from position x to L (sec)
t_{scan}	total laser scan time, L/s (sec)
x	position along line of plastic (cm)

ACKNOWLEDGEMENTS

The authors gratefully acknowledge the financial support of the State of Ohio Edison Materials Technology Center (EMTEC), the United States Air Force and an industrial consortium of companies. The contributions of Stanley Rodrigues who assisted with shrinkage measurements and Shwn-Meei Linden who helped with resin preparation are acknowledged.

REFERENCES

1. Weissman, P.T., B.A. Bolan, and R.P. Chartoff, "Measurements of Linear Shrinkage and the Residual Stresses Developed During Laser Photopolymerization," Proc. 3rd Int. Conf. Rapid Prototyping, Dayton, OH, June 7-10, 1992.
2. Weissman, P.T., R.P. Chartoff, S.J. Rodrigues, and S.-M. Linden, "Real Time Measurements of Linear Shrinkage During Laser Photopolymerization: Implications Concerning Post Cure Shrinkage," Proc. 4th Int. Conf. Rapid Prototyping, Dayton, OH, June 14-17, 1993.
3. Flach, L. and R.P. Chartoff, "Laser Photopolymerization in the Stereolithography Process: Model-Based Predictions," J. Rad. Curing/Rad. Curing, 19, No. 4, 4-9, 1992; also paper accepted for publication in Polymer Eng. and Sci.
4. Bowman, C.N. and N.A. Peppas, "Coupling of Kinetics and Volume Relaxation During Polymerizations of Multiacrylates and Multimethacrylates," Macromolecules, 24, 1914-1920, 1991.

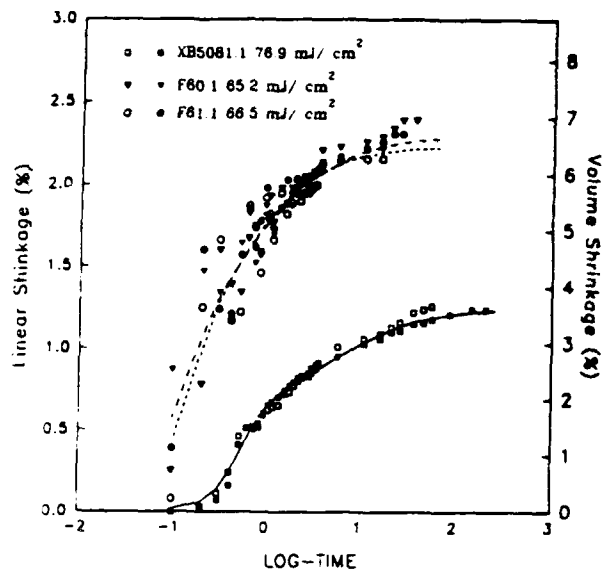
TABLE 1

SHRINKAGE AFTER MULTIPLE 0.040 SECOND EXPOSURES (DATA ARE NORMALIZED BY THE MAXIMUM SHRINKAGE FOR EACH POLYMER)

Exposure	XB5081-1 (%)	60.1 (%)	61.1 (%)
1	64.4	89.5	88.8
2	81.4	93.6	94.6
3	86.6	96.3	97.7
4	90.7	99.5	98.8
5	94.3	100	100
6	97.4	---	---
7	99.4	---	---
8	100	---	---
Ultimate Volumetric Shrinkage	6.0	6.4	7.5

Full Line Exposure

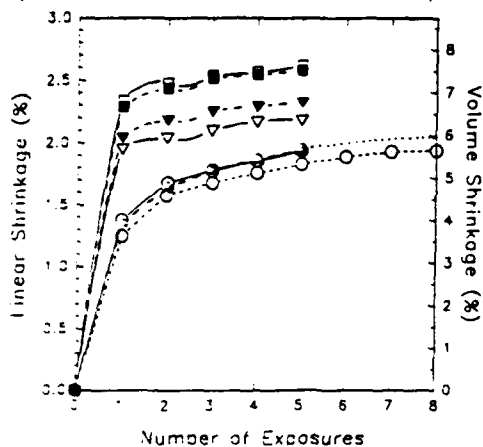
(0.04 sec. exposure, C.D.=0.85)



Real Time Shrinkage Data for XB5081-1, 60.1, and 61.1.

Figure 1

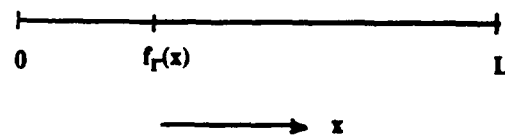
Shrinkage
After Multiple 0.04 Second Exposures
(Measurements taken 5 minutes after each exposure)



○ XB5081-1 76.9 mJ/cm²/expo.
▽ F60.1 65.2 mJ/cm²/expo.
■ F61.1 66.5 mJ/cm²/expo.

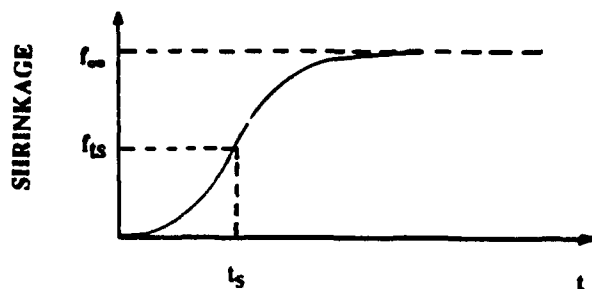
Multiple 0.040 Second Exposures in the Real Time Shrinkage Apparatus.

Figure 2



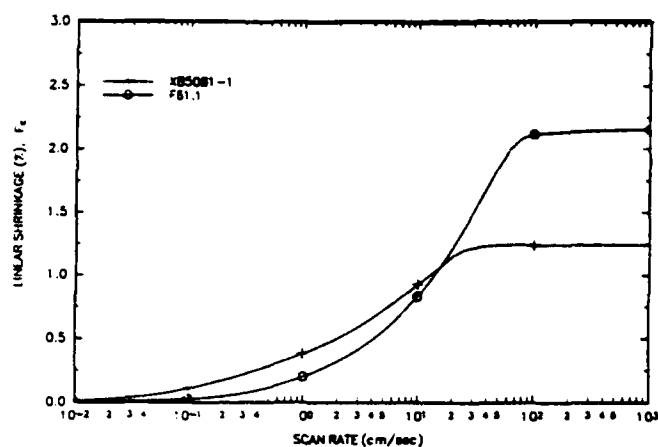
RESIDUAL FRACTIONAL SHRINKAGE
ALONG LINE OF PLASTIC

Figure 3



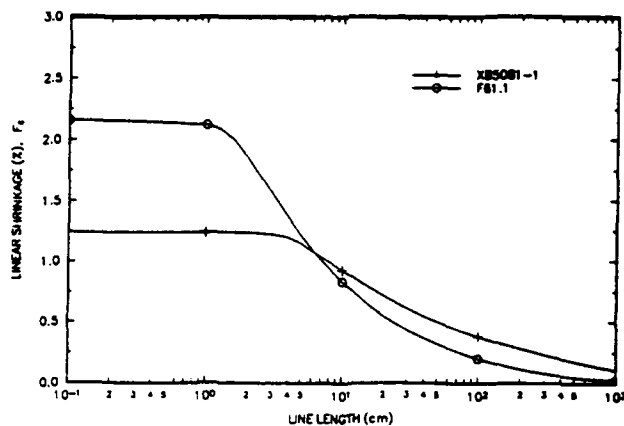
SHRINKAGE VS. TIME CURVE INDICATING
VARIABLES USED TO CALCULATE
RESIDUAL SHRINKAGE

Figure 4



Shrinkage vs. scan rate for a 10 cm line of plastic.
(Actinic exposure level constant.)
(Computer generated curves.)

Figure 5



Shrinkage vs. length of line of plastic when
drawn at a fixed scan rate of 10 cm sec⁻¹.
(Computer generated curves.)

Figure 6

Thermal Analysis and Modeling of Steady-State Rod Growth During Gas-Phase Solid Freeform Fabrication

James L. Maxwell
Joseph Pegna
Alexandar G. Ostrogorsky
Rensselaer Polytechnic Institute
Troy, New York

Abstract: *An analysis of the steady-state growth of rods during gas-phase solid freeform fabrication is presented. It is demonstrated that heat transfer controls the evolution of shape during laser-induced pyrolysis of slender 3-D structures. Insulating and conductive deposit materials were studied, using both simple analytic and numerical simulations to demonstrate how steady-state rod growth is achieved.*

Keywords: LCVD, SALD, Microfabrication.

1 Introduction

Laser-induced Chemical Vapor Deposition, or LCVD—also known as Selective Area Laser Deposition, or SALD—has been used extensively in the microelectronics industry for the fabrication of custom IC interconnects. While its use in the solid freeform fabrication of millimeter-length rods was first demonstrated by Bauerle et. al. [1],[2], only recently has the process been applied to the microfabrication of other 3-dimensional structures [3],[4]. We assert that LCVD holds great promise as a general-purpose manufacturing tool for micro- and millimeter-scale mechanical systems.

Compared with traditional microfabrication processes, LCVD offers the potential for a highly flexible manufacturing tool. It possesses many of the same advantages found in other SFF processes, namely:

1. One-step fabrication, where the entire structure is created directly under computer control.
2. Complex structures with internal features can be created as easily as simple block structures.

In addition, LCVD has other benefits inherent to the scale at which the process is applied; these are not-necessarily found in all SFF processes:

1. The need for assembly of small mechanical components is eliminated.
2. In-situ fabrication is possible. (No handling of fragile components during the process, and increased technological integration).

3. Fabrication of non-homogenous materials is fully realizable: one can blend one material into another in a continuous manner. This property is potentially useful for the fabrication of functionally graded materials, which fully exploit the properties of the materials employed.
4. A wide variety of metals and ceramics can be deposited, often with the same apparatus.
5. Complete integration with existing IC interconnection/package technology is possible.
6. The process works over a wide range of scales: from nanometric to millimetric dimensions.
7. Great dimensional control should be possible--to several hundred nanometers or more.
8. Hardware costs for this process can be much less than that of photolithographically-based methods, as multiple processing steps can be performed within a single environment.

For LCVD to become a useful Solid Freeform Fabrication (SFF) tool, sufficient understanding and control of the process must be attained. Our goal is to develop a working model of Laser-Induced pyrolysis which allows prediction of deposit geometry versus time for a continuum of process conditions and a wide variety of substrate and precursor materials. In the long term, this model would be used to control an actual LCVD-based microfabrication system for production of custom micro mechanical parts from CAD geometry information. To this end, this paper represents an initial attempt at simulating the LCVD of slender rods and cones—which are the simplest 3-D structures.

2 Methodology

Pyrolytic LCVD is a thermally driven process. Heat transfer in the deposit and substrate dictate the surface temperature, which in turn drives the deposition rate. From a thermophysics viewpoint, LCVD is a two-phase heat and mass transfer problem akin to freezing front. However, due to the characteristic size and control of this process, few predictive models are available for controlling SALD. A model for SALD layered fabrication was proposed by Jacquot et al. [5] and later Zong et al.[6]. Our paper differs from previous work in the type of structures addressed, namely slender 3-dimensional rods. This type of structure is the most commonly grown LCVD spatial structure. As we shall see, this difference in shape may lead to different heat transfer and deposition modes.

In this paper, we shall survey in the following order the three basic mechanisms involved in shaping the deposit:

1. The precursor transport mechanism,
2. Heat transfer in the deposit, and
3. the material build-up.

The precursor transport mechanisms are discussed in section 3

The rest of this paper stems from a common experimental observation illustrated by Figure 4. When a fixed laser beam is focused onto a substrate in an LCVD experiment, the deposit takes the form of a rod growing toward the beam. Moreover, if the beam direction is changed while its focus is

kept onto the rod tip, the rod will keep growing in the beam's direction as illustrated by Figure 3. This observation holds for a wide variety of precursors, substrate and environmental conditions.

Based on this observation, Section 4 will develop the thermal analysis of a rod on a substrate subjected to a Gaussian flux at its tip. For lack of a closed-form solution for the surface temperature, we derive an empirical model from a numerical simulation presented in Section 5. This empirical model is then used to drive the growth process in Section 6.

3 Physical Parameters Limiting LCVD

Figure 1 outlines the key parameters which determine the outcome of a LCVD process, and which must be controlled. Note that there are three distinct regimes in LCVD [3]: (1) the kinetically limited regime, controlled by heat transfer at the deposition surface and characterized by an activation energy [2]; (2) The mass transport regime, where passage of reactants to and from the reaction zone determines the process rate [7]; and (3) the nature of the chemical reaction itself. As illustrated by Figure 2, the absolute deposition rate is determined by the slowest of these 3 "cogs" in the process, and for a given chemistry, the rate depends directly upon the surface temperature, precursor pressure and (sometimes) flow rate. In most cases, the latter two (pressure and flow rate) are fixed during an LCVD session, and only the surface temperature varies--which depends on the evolving surface geometry and the amount of heat flux absorbed at the laser focus.

For our analysis of rod growth, we have assumed that the reaction occurs entirely within the kinetically-limited regime, and that no transport limitation applies. While this may not be true in all cases of rod growth, it is certainly true that rods may be grown under this condition, as suggested by Boman et. al. [8] in the LCVD of boron and silicon rods.

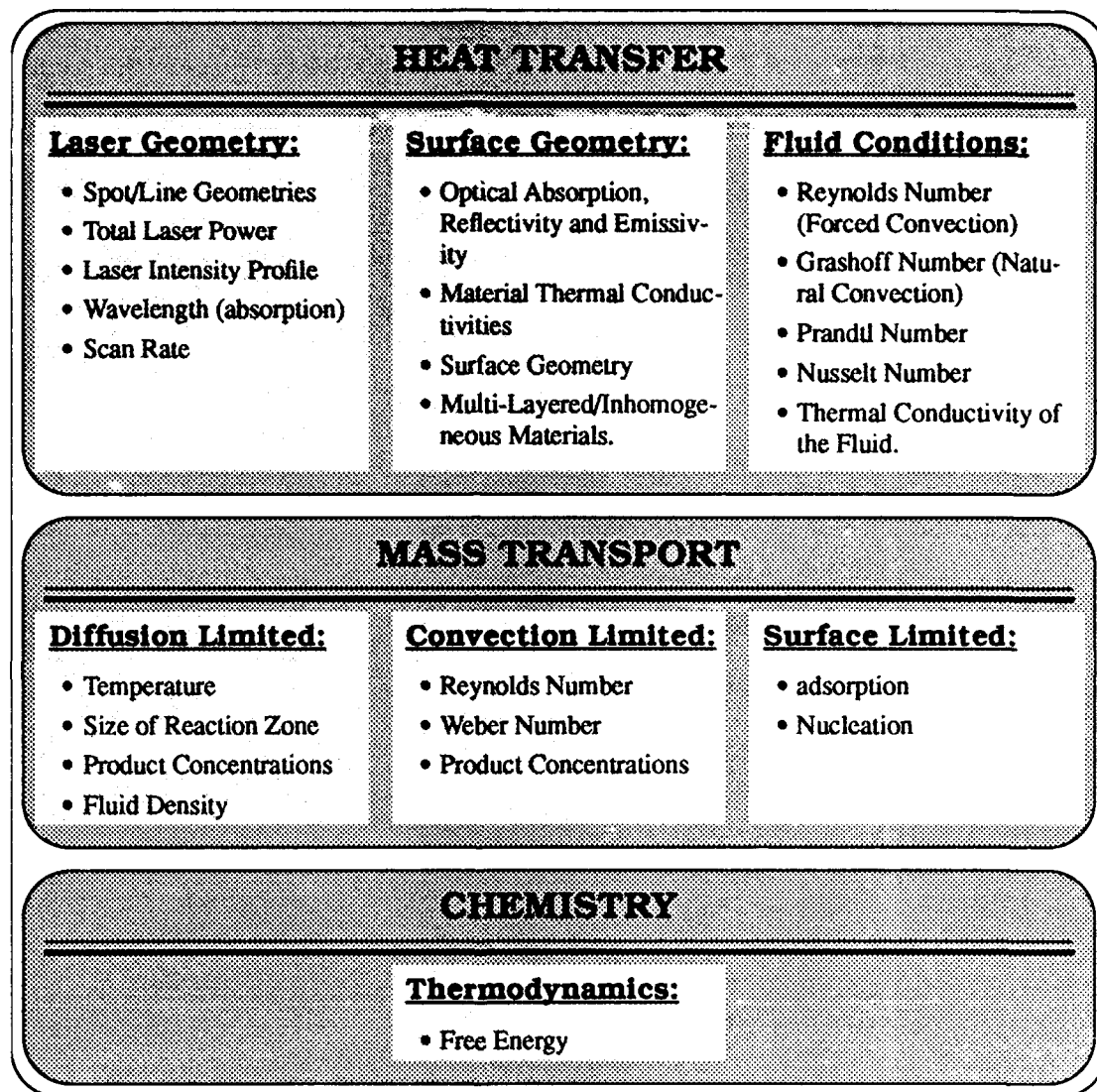
Boman et al. [8] grew, from Silane at a partial pressure of 12 torr, a Silicon rod 200 microns in diameter (Figure 3.) The growth rate was 1.2 $\mu\text{m/s}$. Using a reaction efficiency of 20%, this translates to a required reaction flux of $j_{\text{reaction}} \sim 6 \times 10^{11}$ molecules/ $\mu\text{m}^2 \text{ s}$.

We estimate the diffusion flux at the surface of the rod to be nearly two orders of magnitude higher: $j_{\text{diff}} \sim 1 \times 10^{13}$ SiH_4 molecules/ $\mu\text{m}^2 \text{ s}$. This estimate was obtained using the hemispherical diffusion model developed by Ehrlich [7], assuming a laser beam diameter, $w_0 = 21 \mu\text{m}$ and diffusion coefficient for Silane in Argon of $D = 1.2 \text{ cm}^2/\text{s}$. The diffusion coefficient was derived from equation (1) [10], where the temperature T is in Rankine Units, the pressure P is in atm., and v and molwt are the atomic volumes and molecular weights of the precursor and buffer gases respectively:

$$D = 1.78 \times 10^{-3} T^{3/2} \sqrt{\frac{1}{\text{molwt}_1} + \frac{1}{\text{molwt}_2}} \frac{1}{P (v_1^{1/3} + v_2^{1/3})^2} \quad (\text{EQ 1})$$

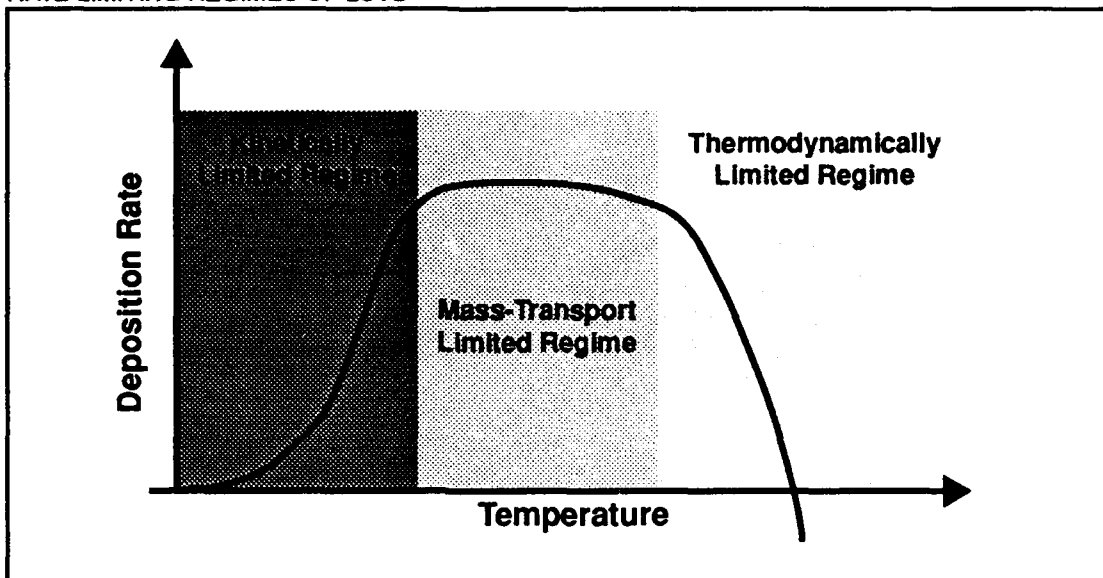
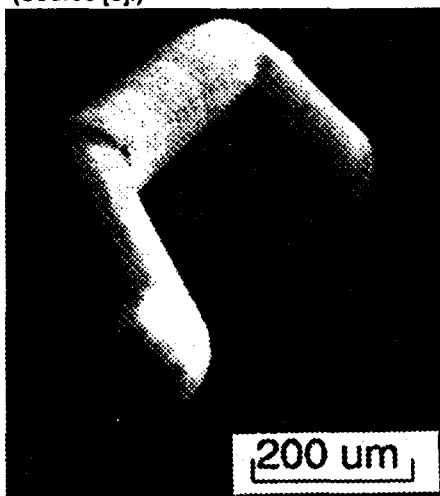
FIGURE 1.

PROCESS PARAMETERS CHART



Since j_{reaction} is much less than j_{diff} , this rod, at least, was grown in the kinetically-limited regime (as the authors claim). Boman [8] also grew boron rods in the kinetically-limited regime, noting the laser flux and surface temperature at which the rods became mass transport limited.

Comparable rods of Carbon were deposited by Marcus et al. [11]. The carbon rod shown in Figure 4 were grown at or near the mass transport limited regime, since, using the hemispherical model presented above, we found that the diffusion and reaction fluxes at the rod tip are nearly equivalent ($j_{\text{diff}} \sim 2 \cdot 10^{12}$ molecules/ $\mu\text{m}^2 \text{ s}$, $j_{\text{reaction}} \sim 0.1 \times 10^{12}$ molecules/ $\mu\text{m}^2 \text{ s}$) The diffusion coefficient used for Acetylene was $3.4 \text{ cm}^2/\text{s}$.

FIGURE 2.**RATE LIMITING REGIMES OF LCVD****FIGURE 3.****THREE-DIMENSIONAL SILICON ROD STRUCTURE GROWN BY LCVD (Source [8].)****FIGURE 4.****EXAMPLE OF CARBON RODS GROWN BY LCVD (Source [11].)**

The similarity in shape of the Silicon and Carbon rods (the tips are rounded and lengths nearly cylindrical—the only observable difference being the taper of the carbon deposit at its base) indicates that, under normal conditions, mass transport has little effect on the essential characteristics of a rods' geometry. It also indicates that the shape of a rod depends primarily on the kinetics of the system, whose rate is determined by the local surface temperature. Hence, the study of rod development can be treated as a heat transfer problem. This will be the subject of the next section.

4 Thermal Analysis

The 4 mechanisms that may contribute to heat transfer in LCVD are shown schematically in Figure 1. Laser power absorbed—estimated to 1.5 Watts—at the rod tip may be dissipated by:

- i) absorption through the free energy of the gas decomposition;
- ii) radiation from the rod's surfaces;
- iii) convection from the rod's surfaces to the surrounding precursor gases and;
- iv) conduction down the rod into the substrate.

For typical LCVD parameters, numerical simulations indicate that heat conduction may be the primary mode of heat transfer for short rods. This is similar to the findings of [5] and [6] in the case of layered fabrication. This will be discussed for the example of the carbon rod in Figure 4, using the physical characteristics table Table 1, which are derived from [3] and [12]. We will discuss each mode of heat transfer in turn.

I) Heat of Formation

The pyrolysis of acetylene is an exothermic reaction. Using the heat of formation and deposition rate given above, the heat generated is:

$$Q_{kin} = 2.3 \text{ mW},$$

which is two orders of magnitude less than the absorbed laser flux. In the growth of Carbon rods, then, the heat of formation has a very negligible effect on the surface temperature distribution.

II) Radiation

In the case of radiation from the rod, we can quickly calculate the total power loss, assuming that the *entire* rod is at an elevated temperature of 2000 K. The radiative loss is [13]:

$$Q_{rad} = Ah_{rad}(T_{ave} - T_{amb}), \quad (\text{EQ 2})$$

$$\text{where } h_{rad} = 4\epsilon\sigma T_{ave}^3. \quad (\text{EQ 3})$$

TABLE 1. PHYSICAL CHARACTERISTICS USED IN THE NUMERICAL SIMULATION.

Diameter = 250 μm	Total Input Laser Power = 5W
Length = 1000 μm	Bulk Reflectivity of Graphite = 0.70, (10 μm CO ₂ Laser)
Surface Area = 0.0078 cm^2	Emissivity of Graphite = 0.80 @ 2000 K
Acetylene Precursor Pressure = 200 torr	Total Absorbed power = 1.5 W
Acetylene Vol. Coef. of Expan. = $3.0 \times 10^{-3}/\text{K}$	Beam 1/e Radius = 75 μm
Thermal Conductivity of C ₂ H ₂ = $66. \times 10^{-3} \text{ W / m K}$	Rod Peak Surface Temp. = 2600 K
Kinematic Viscosity of C ₂ H ₂ = $30. \times 10^{-6} \text{ m}^2/\text{s}$	Rod Average Surf. Temp. = 2000 K
Heat of Formation = 230 kJ/mol	Ambient Temperature = 473 K
Deposition Rate = 2.4 $\mu\text{m/s}$	

Here, T_{rod} and T_{amb} are the average rod temperature and ambient temperature, and ϵ and σ are the emissivity and Stephan-Boltzman constants, respectively. Substituting the above parameters yields:

$$h_{rad} = 0.15 \text{ W/cm}^2\text{K}^4 \text{ and } Q_{rad} = 1.74 \text{ W};$$

which is of the same order of magnitude as the laser input (1.5 W absorbed power). Thus, radiation can have a significant effect on the overall temperature distribution in the rod, and cannot be neglected. Numerical simulations not described in this paper seem to indicate that for a well-developed rod, radiative heat transfer becomes dominant and prescribes the final radius of a rod, as well as the steady-state peak temperature which is attained at the rod tip.

III) Convection

We can also show that the amount of heat removed by convection Q_{conv} , is much lower than the amount of heat removed by radiation. We will derive the heat transfer coefficient h_{conv} in:

$$Q = Ah_{conv}(T_{eff} - T_{amb}), \quad (\text{EQ 4})$$

in which h_{conv} can be determined from the dimensionless Nusselt number, Nu, which determines the ratio of convection to conduction losses:

$$Nu = h_{conv} \frac{L}{k} = 0.68 + \frac{0.67Ra^{1/4}}{\left(1 + \left(\frac{0.492}{Pr}\right)^{9/16}\right)^{4/9}} \quad (\text{EQ 5})$$

In equation (5), Ra and Pr denote respectively the Rayleigh and Prandtl numbers. The Rayleigh number, is given by equation (6). The Prandtl number Pr, which is the ratio of momentum and thermal diffusivity, has an approximate value of 0.7 at atmospheric pressure.

$$Ra = \frac{g\beta Pr (T_s - T_{inf}) L^3}{\nu^2} \quad (\text{EQ 6})$$

Taking the *entire* rod (1 mm long) to be at $T_{eff} = 2000 \text{ K}$, the Rayleigh number is $Ra \approx 35$.

Hence, we can derive the Nusselt number $Nu \approx 2$ and the convection coefficient $h_{conv} \approx 0.013 \text{ W/cm}^2\text{K}$

Using the surface area of the rod, the maximum heat loss which could be derived via convection is: $Q_{conv} \approx 300 \text{ mW}$, which is an order of magnitude less than the laser power input.

Note that we have greatly overestimated the length scale over which convection would occur, as well as the pressure. Convective losses (typically an order of magnitude or two smaller than the laser input) have a minor effect on the temperature distribution, and will be considered negligible in our further analysis.

iv) Discussion

The primary modes of heat transfer are, therefore, conduction to the substrate and radiation. This leads to some surprising conclusions, which will be elucidated below. If we consider heat conduction in a rod to be purely 1-D axial flow, i.e. we temporarily neglect radiation and assume that the rod is slender, we can see what happens during the initial stages of rod growth. This approximation is only valid when the rod is small and slender, and the surface area of the rod is insufficient to support large radiative losses. In this case, we can solve for the temperature distribution simply. We can model the problem as a 1-D rod with constant flux at one end and conduction to the substrate at the other. This problem is treated in the literature [14]. Let L be the length of the rod, R_0 be the steady-state rod radius, R_i be the radius of the rod at the base, Q_{las} be the constant laser flux, and K_s and K_d be respectively the thermal conductivities of the substrate and deposit. The steady-state solution is then given by equation (7).

$$T = T_{amb} + Q_{las} \left(\frac{(L-x)}{K_d \pi R_o^2} + \frac{8}{3\pi^2 K_s R_i} \right) \quad (EQ 7)$$

This states that, neglecting the 2-dimensional effects of a rounded tip and non-uniform flux, the temperature should drop linearly from a peak temperature of:

$$T_{peak} = T_{amb} + Q_{las} \left(\frac{L}{K_d \pi R_o^2} + \frac{8}{3\pi^2 K_s R_i} \right) \quad (EQ 8)$$

at the rod tip ($x=0$) to the rod base temperature of $T_{base} = T_{amb} + (8Q_{las}/3\pi^2 K_s R_i)$ at $x=L$. Note that the base temperature depends inversely on the deposit and substrate thermal conductivities. Thus, for an insulating deposit on a highly conductive substrate ($K_d \ll K_s$), the first term above will dominate the temperature distribution, and a large linear gradient over the rod will result, while if we have a conductive deposit on an insulating substrate, i.e. $K_d \gg K_s$, the base temperature will be high and little gradient will occur over the rod. In the latter case, resolution of the LCVD process would suffer, since the entire rod (sides as well as tip) would grow outward, broadening the rod. In the extreme case, it would be impossible to grow a rod as no temperature gradient would occur across the rod, and the rod would tend to grow as a hemisphere on the substrate.

Most importantly, however, this model predicts the peak temperature is a function of the rod length. As a rod evolves, the peak temperature should rise with its length, the LCVD growth rate increasing exponentially, until the rod begins to melt at its tip. This effect is most pronounced for insulating deposits--as the slope of increase for a given laser input is $1/K_d$.

Finally, note that for sufficiently long rods ($L \rightarrow \infty$), the rod temperature varies as R_o^{-2} , so that a small increase in rod diameter causes a large decrease in temperature. In fact, if we impose the condition that the peak temperature becomes a constant for large L , the rod radius would of necessity converge to $R_\infty = A\sqrt{L}$, where A is a constant. The increase in rod radius with L would slow with time. While this is close to reality, it does not predict an asymptotic radius, as is seen in practice, and clearly some physics is missing.

In reality, a mechanism exists which provides sufficient heat loss to stop the linear rise in peak temperature--and which provides for an asymptotic rod radius $R_0=R_f$ --as carbon rods up to 4 mm in length [11] have been grown at a uniform rate. The only likely mechanism is radiation. In essence, as a rod begins to form, the temperature distribution is largely determined by conduction, the peak temperature rising rapidly; however, as sufficient surface area becomes available, radiation becomes the dominant heat loss mechanism, and the peak temperature approaches a constant. This will be the subject of an upcoming publication.

5 Two-Dimensional Numerical Simulation

To further elucidate the nature of rod growth, we also performed a finite-element 2-D simulation which included the effects of gaussian flux, reflection at the rounded tip, rod geometry, and substrate cooling. The finite element package used for this simulation is Nekton. Several geometric variations on this mesh were also developed to demonstrate the effects of rod length, steady-state diameter, and the diameter of the rod at its base. Material properties, such as thermal conductivity, reflectivity, and emissivity were also varied, as well as laser parameters such as total power, and 1/e beam width. The objective, of course, was to find an accurate temperature profile on a rod surface, so that a 2-D model of rod growth could be constructed.

The heat flux at the tip of the rod was specified as a function of radial distance from the center-line and the angle of incidence to the surface normal, alpha, as:

$$Q_{las} = (1 - R) P_o e^{-\frac{y^2}{w_o^2}} \cos^2 \alpha ; \quad (EQ 9)$$

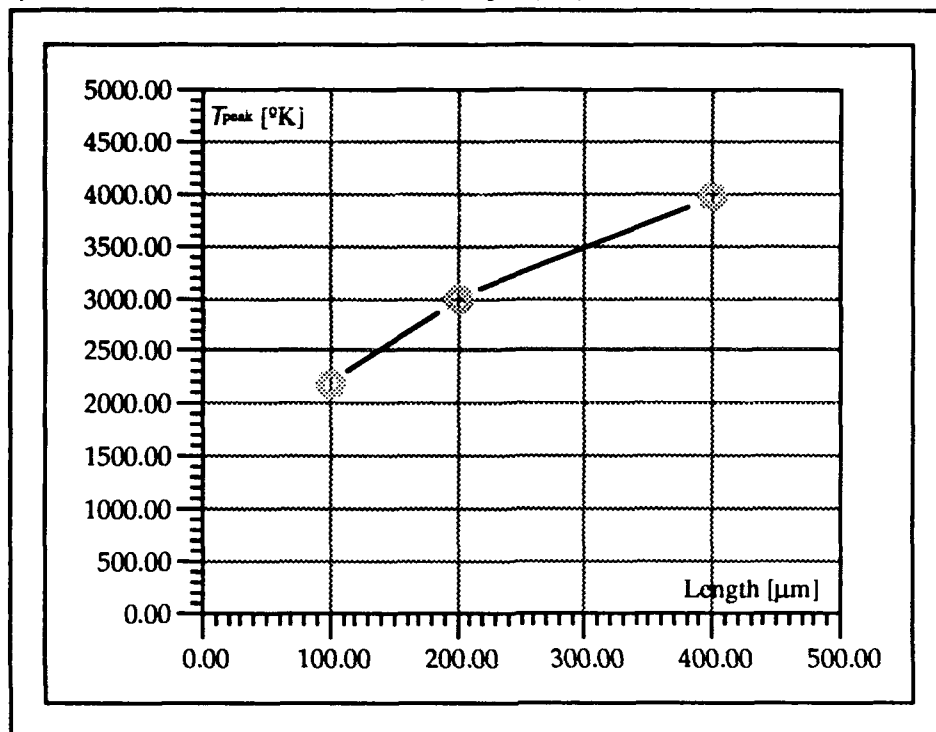
where P_o is the total laser power, R is the reflectivity of the deposit at the laser wavelength in question, and w_o is the 1/e beam radius. The reflection attenuation term $\cos^2 \alpha$, was used as a first approximation to the true reflection attenuation given by [15]:

TABLE 2. THERMOPHYSICAL PROPERTIES OF MATERIALS USED IN NUMERICAL SIMULATIONS (T=500°K, Source [16] and [17].)

Material	Mass Density (ρ)	Diffusion	Conductivity	Specific Heat-Cp	ρ Cp
Units	kg/cm ³	cm ² /s	W/cm K	J/kg K	J/cm ³ K
Silicon	0.00233	0.37	0.74	850	1.98
Graphite	0.00195	0.01445	0.020	709	1.38
Aluminum	0.002702	0.87	2.35	1000	2.7
Alumina	0.003970	--	0.20	1035	4.11

FIGURE 5.

PEAK TEMPERATURE VERSUS ROD LENGTH (PYROLITIC GRAPHITE ON ALUMINA, Absorbed power $5.7 \cdot 10^3 \text{ W/cm}^2$, rod radius: $100\mu\text{m}$, $w_o=75\mu\text{m}$.)



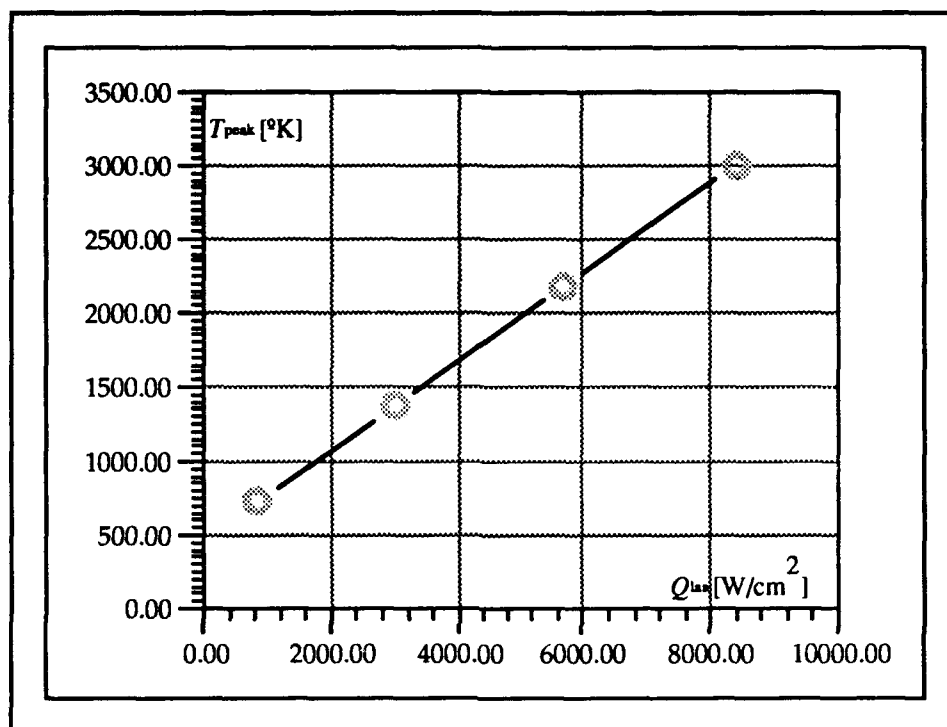
$$R(\alpha) = \frac{1}{2} \left\{ \left[\frac{\cos \alpha - \sqrt{n^2 - \sin^2 \alpha}}{\cos \alpha + \sqrt{n^2 - \sin^2 \alpha}} \right]^2 + \frac{n^2 \cos \alpha - \sqrt{n^2 - \sin^2 \alpha}}{n^2 \cos \alpha + \sqrt{n^2 - \sin^2 \alpha}} \right\}; \quad (\text{EQ } 10)$$

where α is the angle of incidence, and the deposit index of refraction n , can be derived from Snell's law and the normal-incidence reflection coefficient. This expression is valid for a randomly polarized beam. We chose to simply use a \cos^2 attenuation function since the profile of a rod tip has not been detailed in the literature—nor the polarization used in most experiments—these are necessary to precisely model the reflection. We used a hemispherical rod tip.

Table 2 below gives the physical constants employed in the simulations. As predicted from our 1-D conduction model, the peak temperature rose with rod length in the 2-D model; however, the relationship is not now entirely linear. This can be seen in Figure 5, where the results for several simulations are summarized, and a curve fit to the data.

In addition, we found that the tip temperature rose linearly with increasing absorbed laser power, as Figure 6 shows. This is an important, although obvious result. Its importance lies in the fact that the absorbed power depends linearly on the reflection coefficient, and a linear increase in surface reflectance should lead to a *linear* decrease in temperature. In addressing the issue of how the peak

FIGURE 6. PEAK TEMPERATURE VERSUS ABSORBED POWER (PYROLITIC GRAPHITE ON ALUMINA, Length=100 μ m, R_0 =100 μ m, w_0 =75 μ m.)



rod temperature experimentally levels off to a constant steady-state value, an increase in surface reflectance with temperature would be a potential solution. However, what this analysis shows is that, not only would the reflectance need to increase with rising temperature, but it would need to do so continually—the longer the rod became, the greater the reflectance would need to be. It is unlikely that any physical mechanism exists which could produce such a perfect balance—unless some gradual phase change at the rod tip occurs.

In varying the material thermal conductivities during the 2-D simulation, we found some very interesting conjectures. Two typical contour plots are shown in Figure 7 and Figure 8 for pyrolytic graphite on an Alumina substrate, and Aluminum on Alumina, respectively. As expected, the more conductive aluminum has the least temperature gradient, most of the gradient being over the substrate. The carbon rod, in contrast, has a very large gradient, its base temperature being less than 7% above that of the ambient. In general, we find that for a fixed deposit/substrate combination and sufficiently-developed rods (i.e. $L \gg w_0$), the temperature *gradient* remains largely unchanged regardless of peak temperature or absorbed power, and for a fixed geometry, the base temperature is a set fraction of the peak temperature.

Of greatest importance in the graphite-rod case is the nature of the isotherms near the rod tip. Here, as the deposit widens, the flow diverges rapidly, and the temperature drops to 64% of T_{peak}

FIGURE 7. TEMPERATURE CONTOUR PLOTS FOR PYROLITIC GRAPHITE ROD ON ALUMINA SUBSTRATE

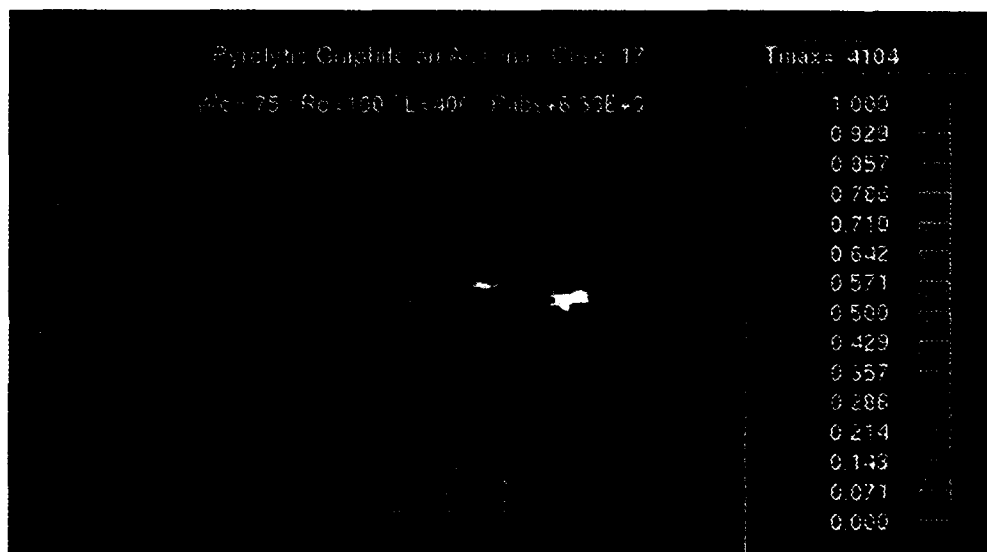
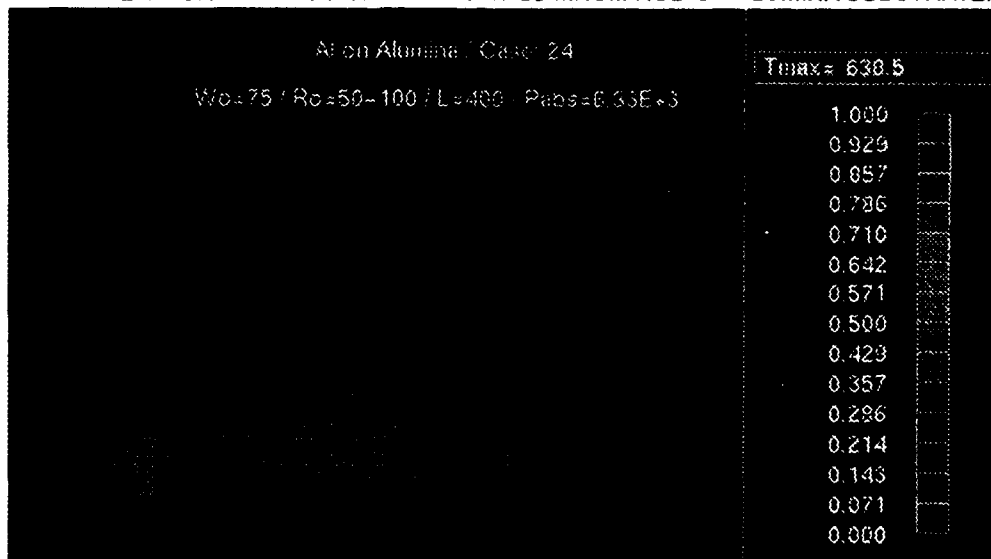
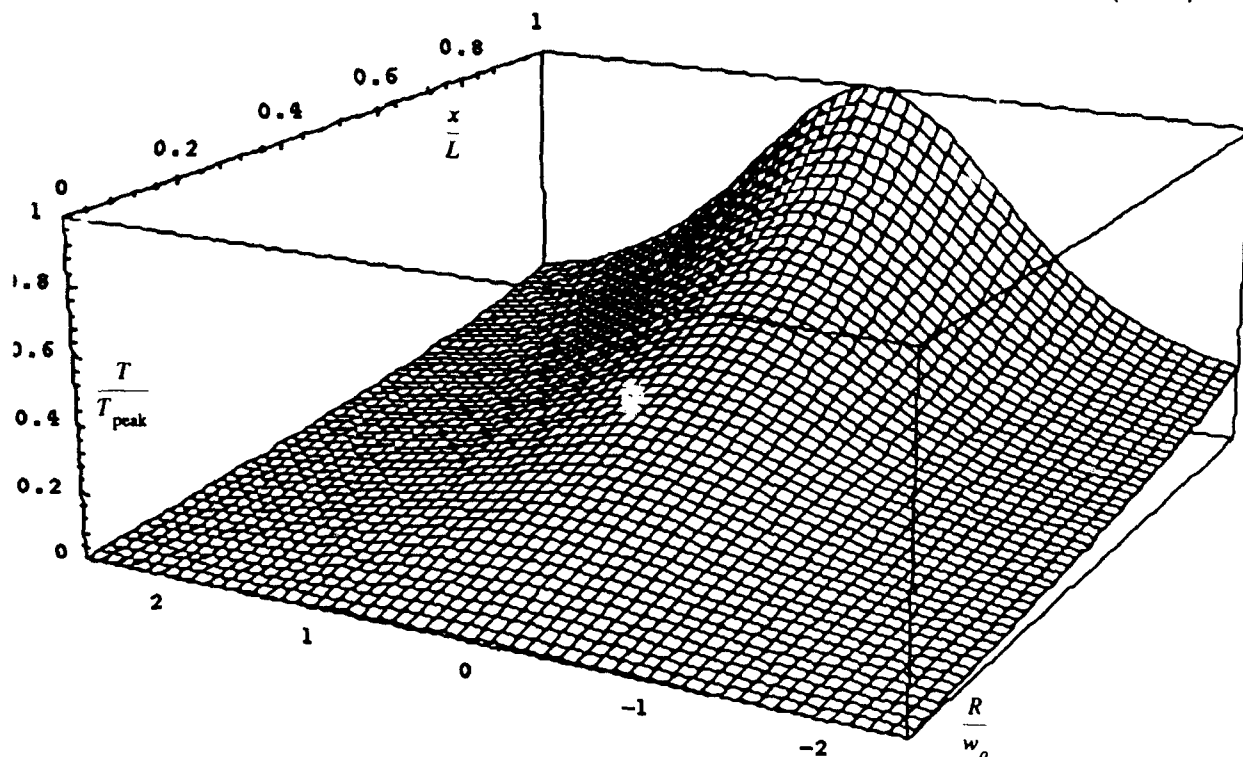


FIGURE 8. TEMPERATURE CONTOUR PLOTS FOR ALUMINUM ROD ON ALUMINA SUBSTRATE.



within $1.4 w_0$ radii along the surface (regardless of overall rod length--provided $L \gg w_0$). The isotherms are very similar to those obtained in the solution of a gaussian source on a semi-infinite solid. Beyond the tapered area of the tip, the gradient quickly transforms into a linear solution similar to that presented above in equation (7). The constriction at the base, typical of many rods grown via LCVD,

FIGURE 9. 3-D PLOT OF EMPIRICAL TEMPERATURE FOR THE CONDUCTIVE ROD MODEL (EQ 12)



also warps the thermal gradient, however, we will ignore this effect for now, as the temperature has dropped sufficiently at this point that little deposition is likely to occur.

Based on these two regimes, we developed an empirical formulation for the 2-D surface temperature profile which employs a linear combination of the "broadening solution" and the "linear solution"; as a first approximation for the tip's temperature profile. We used the solution given by Lax [18] for a gaussian flux absorbed completely at the surface of a semi-infinite solid. Letting J_0 and I_0 be the Bessel and Modified Bessel functions, and x and R be the axial and radial directions from the source, respectively, the dimensionless solution is:

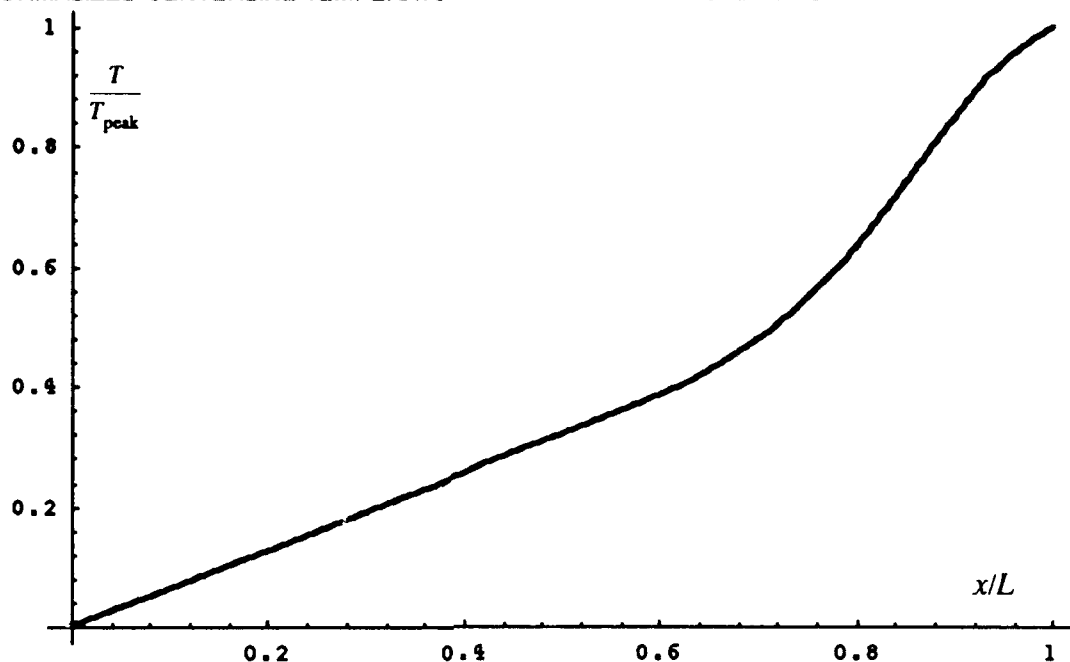
$$\bar{T}_1(x, R) = \int_0^{\infty} J_0(\lambda R) e^{-\lambda x} e^{-\frac{\lambda^2}{4}} d\lambda \quad (\text{EQ 11})$$

On the surface of the solid, i.e. when $x = 0$, this has the simplified solution:

$$\bar{T}_1(R) = I_0\left(\frac{R^2}{2}\right) e^{-\frac{R^2}{2}} \quad (\text{EQ 12})$$

FIGURE 10.

NORMALIZED CENTERLINE TEMPERATURE VERSUS NORMALIZED LENGTH.



The conductive models of an insulated fin (EQ 7) and a Gaussian source (EQ 11) were blended to obtain an empirical model of the surface temperature distribution.

$$\bar{T} = \left[I_o \left(\frac{R^2}{2} \right) e^{-\frac{R^2}{2}} \right] \cdot \left[u_1(x) \cdot x + u_2(x) \cdot e^{-\beta(1-x)^2} \right] \cdot (T_{\text{peak}} - T_{\text{base}}) + T_{\text{base}} \quad (\text{EQ 13})$$

In equation (12) we fit the exponent β , to account for the axial decay in the peak temperature near the rod tip, and the constant α to scale the decay in the radial direction. The functions u_1 and u_2 , are used to blend the linear and broadening solutions. A sample 3-D plot of this function is shown in Figure 9, the cross-section along the rod centerline being given in Figure 10.

Note that for T_{peak} in equation (12), one may use a constant temperature, assuming that the experimental evidence suggests this, or employ the curve fit derived from the numerical simulations.

6 Growth Modeling

With a simple temperature model in hand, we are now ready to create a 2-D moving boundary simulation to account for the development of a kinetically-limited rod. The purpose of this simulation was to address two as-yet unresolved questions, namely:

1. If the peak temperature does/does-not vary with length, how would this effect the growth profile of a rod?
2. Since a large portion of a rod behind the tip is still at an elevated temperature, what profile would result from this distribution?

Using the principle that instantaneous CVD growth always occurs in the direction of the unit surface normal, we generated a set of seed points distributed over a flattened disc (representing a thin film on a substrate). The distribution was weighted to generate more points in the vicinity of the maximum growth. For each point, we then applied the temperature function in equation (12) to the kinetic rate equation, which for an activation energy ΔE , C_2H_2 partial Pressure P , and time-step δt , is:

$$\delta N = R_0 P^{1.02} e^{\frac{-\Delta E}{R} T} \delta t \quad (\text{EQ 14})$$

This is the rate equation fit by Zong [3] to data for the deposition of graphite from acetylene, given that $R_0 = 3.31 \cdot 10^6 \mu\text{m/s}$. Due to the exponentially-increasing growth rate, it was necessary to scale the time step of each iteration, so that sufficiently small spatial deposition steps could be obtained--for accuracy--and so that we could plot the results! Additionally, points were added to the seed set with each iteration to prevent portions of the deposit profile from becoming too sparse.

The results of this simple Mathematica simulation can be seen in Figure 11 and Figure 12. The first plot employs the increasing peak temperature curve derived from the numerical simulation, while the second uses a peak temperature profile that initially rises rapidly, then levels off at a constant temperature. In both cases, the rod grows from a narrow neck smaller than w_0 , then widens with time. In the latter case, however, the width appears to approach an asymptotic width--which would be the steady-state width of the rod. Note the similarities between the second plot and the rod shown in Figure 4.

These results would indicate that steady-state rod growth truly occurs at a constant peak temperature, else the rods thus grown would continue to widen and grow as cones. Additionally, it implies that it should be possible to fabricate tapered rods of increasing or decreasing diameter by gradually raising or lowering the peak temperature. The beam waist diameter, w_0 , also appears to have a great influence on the final radius of the rod. The base neck radius and the initial angle at which the deposit begins to broaden, however, are only weak functions of the absorbed laser power and w_0 . These are controlled by the activation energy of the reaction and the thermal conductivities of deposit and substrate (due to conduction being the principle mode of heat transfer at this stage).

7 Conclusions

Selective Area Laser Deposition (a.k.a. Laser-Induced Chemical Vapor Deposition) is a proven technology for the direct write of custom IC interconnects. Recent attempts at using gas-phase SFF have met with success in the fabrication of small 3-D structures with simple geometry. For

FIGURE 11. GROWTH SIMULATION WITH INCREASING PEAK TEMPERATURE (Conductive model, pyrolytic on alumina.)

time = 0.0000
Tpeak = 500.

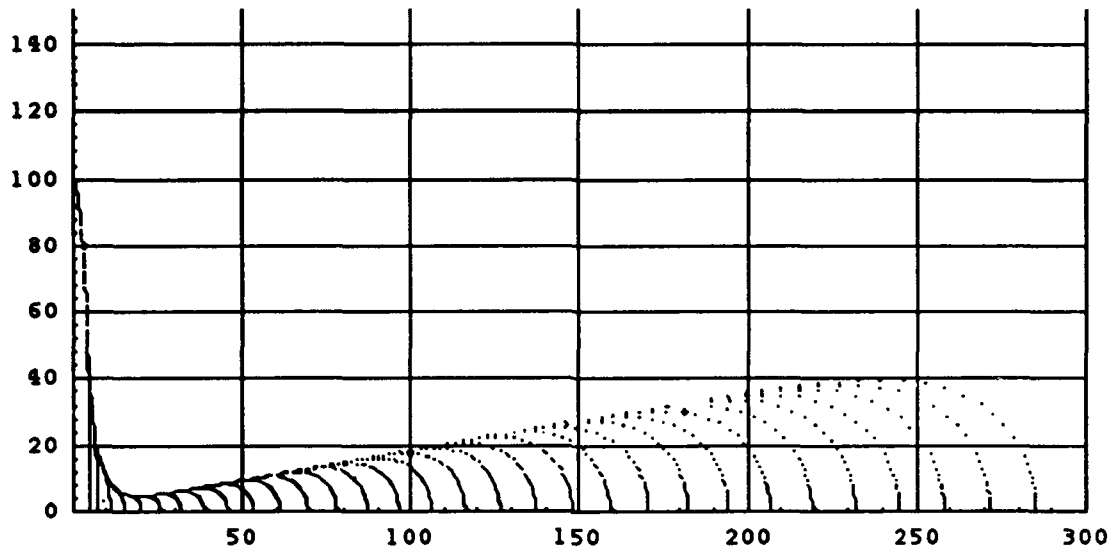


FIGURE 12. GROWTH SIMULATION FOR STEADY STATE PEAK TEMPERATURE (Pyrolytic graphite on Alumina.)

time = 0.0000
Tpeak = 500.

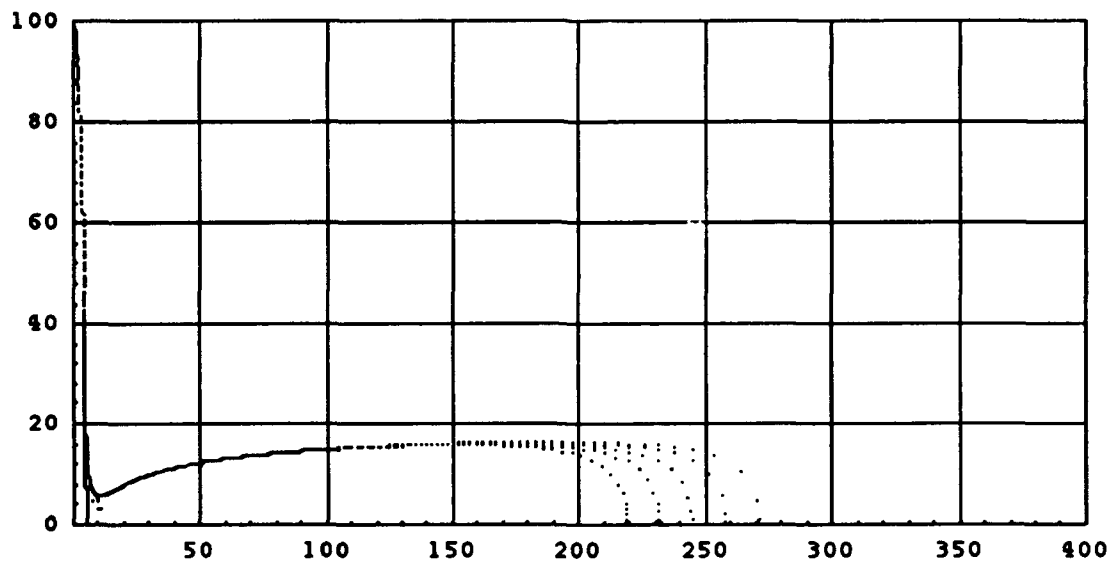
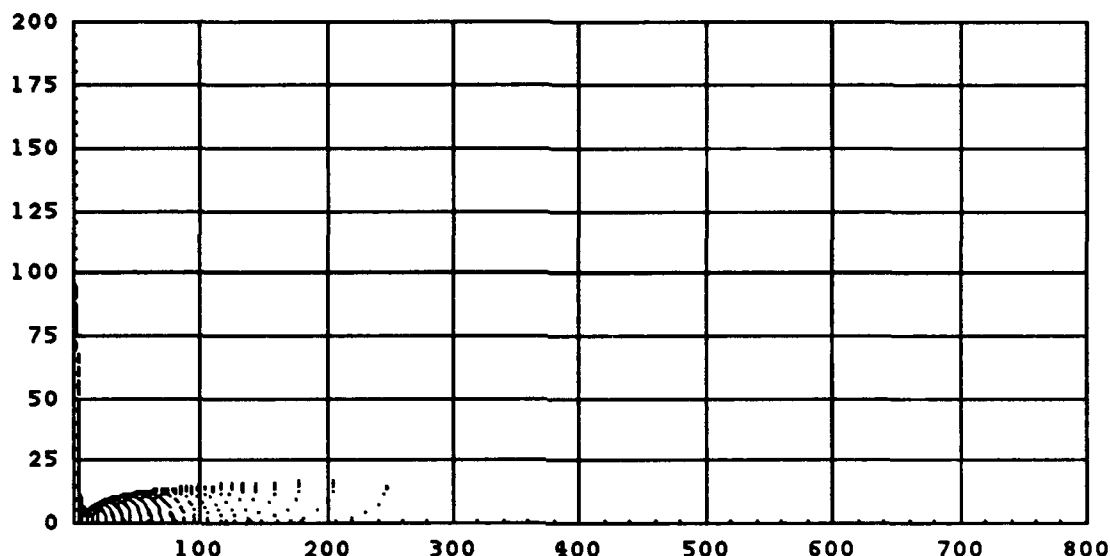


FIGURE 13.**SIMULATION OF INITIAL GROWTH SHOWING THE BROADENING OF THE ROD (Pyrolytic graphite on Alumina.)**

time = 0.0000

Tpeak = 500.



LCVD to become a useful microfabrication tool however, sufficient understanding and control of the process must be achieved.

This paper presents an initial attempt at simulating LCVD growth of slender structures. From this study, it appears that the process is thermally driven. Conduction to the substrate dominates early in the growth with radiative heat transfer superseding it if and when a steady-state growth is reached.

Our modeling effort shows that a rod grows initially as a hemisphere due to nearly uniform temperature gradient across the initial bump. The rod diameter then broadens until the temperature gradient at the tip becomes sufficiently large that the fringes of the tip cease to grow as rapidly, the length-wise temperature gradient—becoming linear at some point near the same location. Steady-State growth of uniform diameter rods is due to a constant peak temperature at the tip, radiation from the surface, and the exponential growth rate/large temperature gradient at the tip combining to induce growth in the beam direction.

8 Acknowledgments

The theoretical part of this work was made possible in part with support from the Society of Manufacturing Engineers, Engineering Education Foundation, the General Electric Corporate Research and Development, and the National Science Foundation under grant DDM9057059. The

numerical simulation was performed with the NEKTON™ thermal analysis software from the NEKTONICS Corporation. Experimental support is provided by an equipment grant from the General Electric Corporation, a National Science Foundation Small Grant for Exploratory Research (ECS 9314071). The clean room laboratory facilities were provided by the Center for Integrated Electronics at Rensselaer. All contributors to the *Rensselaer Freeform Microfabrication Project* are gratefully acknowledged.

9 References

- [1] Leyendecker, G., Bauerle, D., Geittner, P. and Lydtin, H., "*Laser Induced Chemical Vapor Deposition of Carbon*," Applied Physics Letters, Vol. 39, p. 921 (1981).
- [2] Bauerle, D., "*Laser-Induced Chemical Vapor Deposition*," Laser Processing and Diagnostics, Springer Series in Chemical Physics 39, (1984) pp. 166-181.
- [3] Zong, G., "*Solid Freeform Fabrication Using Gas-Phase Selective Area Laser Deposition*," Ph.D. Thesis, U. Texas at Austin (1991)
- [4] Bloomstein, T. M., Ehrlich, D. J., "*Stereo Laser Micromachining of Silicon*," Appl. Phys. Lett., 61, (6), (Aug. 1992), pp. 708-710.
- [5] Jacquot, Y., Zong, G., and Marcus, H.L., "*Modeling of Selective Area Laser Deposition for Solid Freeform Fabrication*," Proceedings of the Solid Freeform Fabrication Symposium, Edited by J.J. Beaman, H.L. Marcus, D.L. Bourell, and J.W. Barlow, Austin, Texas, August 6-8, 1990, pp. 74-82.
- [6] Zong, G., and Marcus, H.L., "*Moving Boundary Transport Phenomena in Selective Area Laser Deposition Process*," Proceedings of the Solid Freeform Fabrication Symposium, Edited by H.L. Marcus, J.J. Beaman, J. W. Barlow, and D.L. Bourell, Austin, Texas, August 12-14, 1991, pp. 279-287.
- [7] Zeiger, H. J., Ehrlich, D. J., Tsao, J. Y., "*Transport and Kinetics*," Laser Microfabrication. Thin Film Processes and Lithography, ed. Ehrlich, D. J., Tsao, J. T., Academic Press, 1989, pp.299-329
- [8] M. Boman, H. Westburg, "*Helical Microstructures Grown by Laser-Assisted Chemical Vapor Deposition*," Proc. Micro Electro Mechanical Systems (Feb 1992), p. 162-167.
- [9] Zeiger, H. J., Ehrlich, D. J., Tsao, J. Y., "*Transport and Kinetics*," Laser Microfabrication. Thin Film Processes and Lithography, ed. Ehrlich, D. J., Tsao, J. T., Academic Press, 1989, pp.299-329
- [10] Rohsenow, W. and Choi, H., "*Heat, Mass, and Momentum Transfer*", p. 383, Prentice Hall (1964)
- [11] Zong, G., Thompkins, J.V., Thissel, W.R., Sajot, E., and Marcus, H.L., "*Processing Problems Associated with Gas-Phase Solid Freeform Fabrication Using Pyrolytic Selective Area Laser Deposition*," Proceedings of the Solid Freeform Fabrication Symposium, Edited by H.L. Marcus, J.J. Beaman, J. W. Barlow, and D.L. Bourell, Austin, Texas, August 12-14, 1991, pp. 271-278.
- [12] Incropera, F., and DeWitt, D., "*Introduction to Heat Transfer*", John Wiley and Sons, 1990, Appendix A.
- [13] Kern, D. and Kraus, A., "*Extended Surface Heat Transfer*," McGraw-Hill, 1972, p. 44.

- [14] Carslaw, J. and Yeager, J., "*Conduction of Heat in Solids*," 2nd edition, Clarendon Press, Oxford, 1959, p. 125.
- [15] Dichburn, R.W. , *Light*, Dover, 1991.
- [16] Toukoulis, Y.S. and Ho, C.Y. Eds. "*Thermophysical Properties*," Thermophysical Properties Research Center, Purdue University, ISI/Plenum New York, 1972, Vol. 1-13.
- [17] CRC Handbook of Chemistry and Physics, 72nd Edition, 1991/1992.
- [18] Lax, M. , "*Temperature Rise Induced by a Laser Beam II, The Non-Linear Case*," Applied Physics Letters, Vol. 33, #8, 15 Oct. 1978, pp. 786-788.
- [19] NEKTON™ user's manual, Nektonics Corporation.

Potential Application of Solid Free-Form Fabrication (SFF) Process in Ceracon P/M Forging

R. V. Raman, S. V. Rele, and R. L. Anderson

Ceracon, Inc.

1101 N. Market Blvd., Suite 9

Sacramento, California 95834

The Ceracon Process

The Ceracon Process is a patented^[1], low cost powder metallurgy process for achieving near-net-shape, full density parts. It is a simple consolidation technique which utilizes conventional powder metallurgy equipment and set-up. The Ceracon Process is a quasi-isostatic, hot consolidation technique, that utilizes a ceramic particulate material as a pressure transmitting medium instead of a gas media as is used in hipping. Pressures up to 200 Ksi can be used and a broad range of metallic, ceramic, and polymeric materials and composites have been successfully processed^[2-6].

The CeraconTM Process steps are schematically detailed in Figure 1.

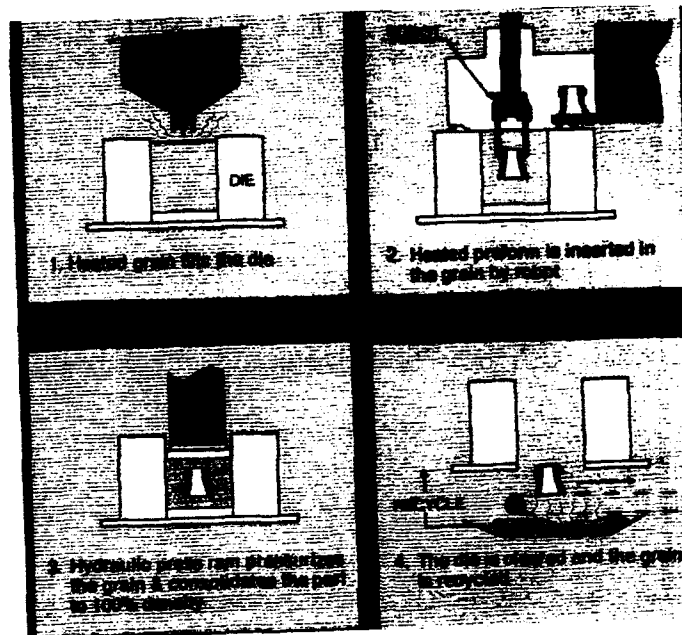


Figure 1: The Ceracon Process^[1]

Ceracon has licensed its technology to several companies including Reed Tool Company of Houston, Texas. Reed Tool is currently setting up to manufacture these parts. The five step process used by Ceracon and Reed in producing the rolling cutter rock bit is shown above in Figure 2 and outlined below:

1. An engineering drawing is prepared from anticipated deformation in the Ceracon process.
2. An aluminum mold pattern of this engineering design is made.
3. A flexible elastomer tool (rubber bag) is fabricated around the aluminum tool.
4. The rubber bag is filled with metallic powder and pressurized via a hydrostatic medium in a pressure vessel, to obtain a preform that is 80% of theoretical density.
5. The preform is consolidated by Ceracon forging process to 100% of theoretical density.

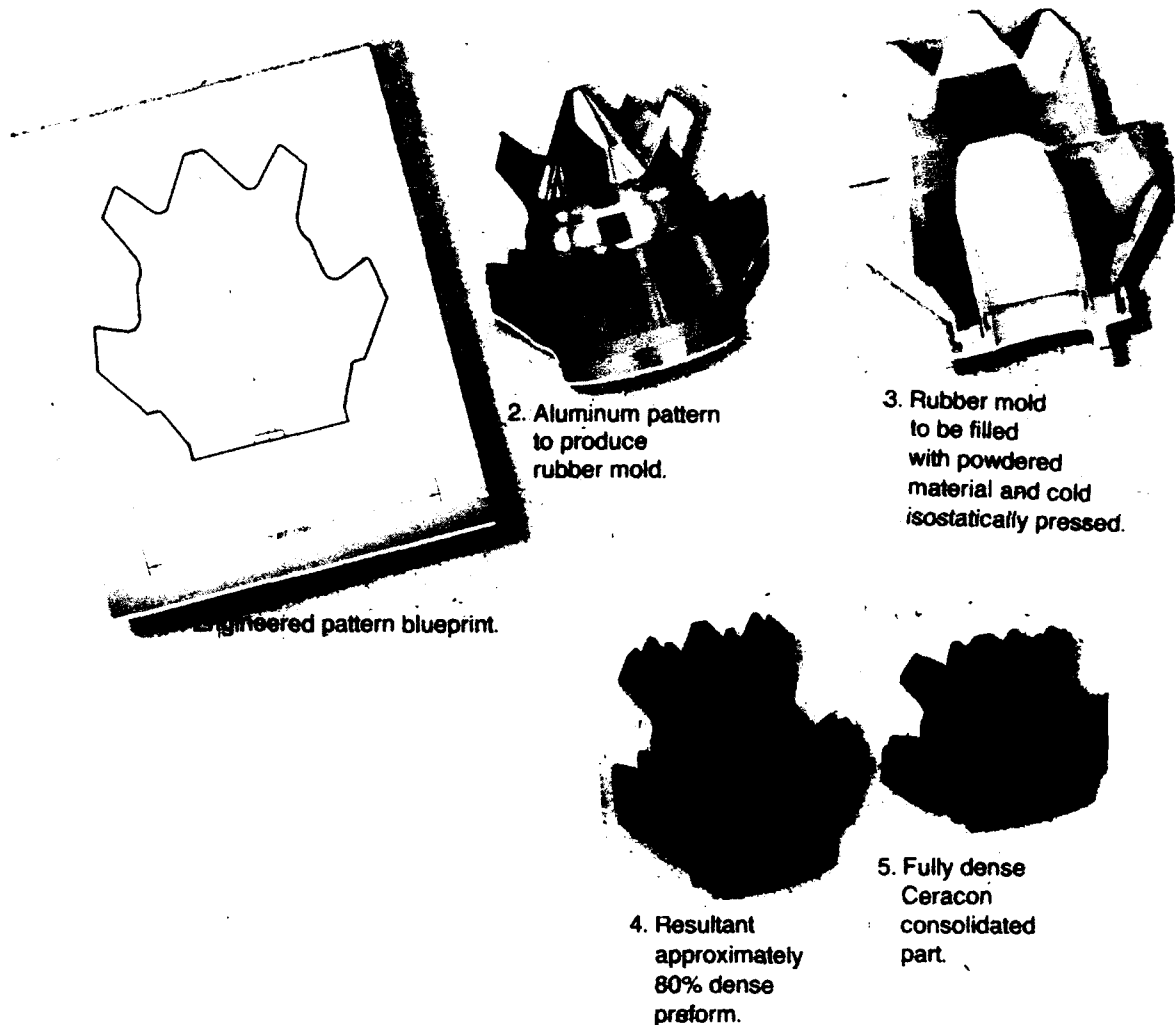


Figure 2: Five Step Process Used for the Rolling Cutter Rockbit

The conventional processing technique previously used for manufacturing this part required significant machining and welding. The Ceracon powder metallurgy approach not only significantly reduced the machining required, but also eliminated the welding step. The Ceracon process has allowed reduction of cost to manufacture the part, while also enhancing drilling performance.

The solid free form (SFF) process^[1] was developed by the University of Texas at Austin by Marcus and colleagues. This process as shown schematically involves layer by layer application of polymeric powder, and superimposing of a laser beam driven by CAD/CAM program to etch out melt polymer particles, and bond to each layer. This process is commercially being provided by DTM Corp. of Austin, Texas, under a license of U.T., Austin (Figure 3).

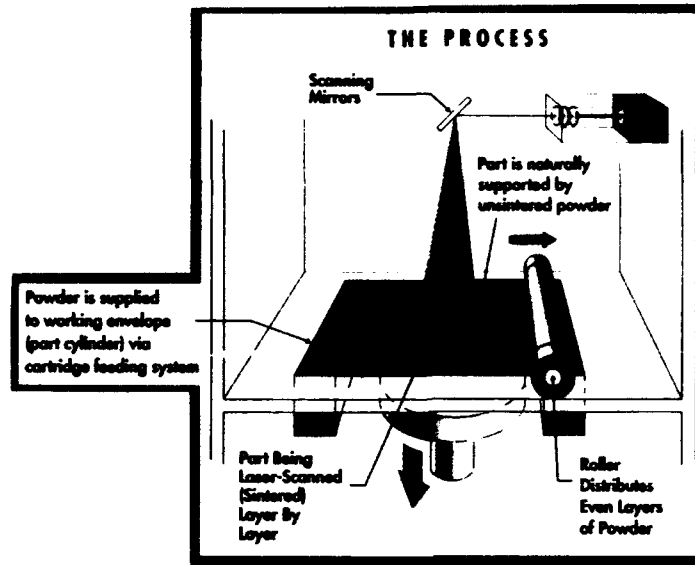


Figure 3: The Solid Free Form Process^[7]

The solid free form (SFF) process offers a potential to be integrated into the preform fabrication steps of the Ceracon forging process. The ultimate goal is to build the preform directly in one step via SFF. But, the SFF process has not been developed to a level of being feasible for direct forming of steel preforms. The current state-of-the-art of the SFF technology allows only for low temperature and small specimens. While the ultimate goal is to use a preform made by the SFF process directly in the Ceracon process, there are other areas in the preform fabrication process, i.e., mold and tooling where the SFF process appears to have potential and could be evaluated for feasibility. One such area is the elastomeric bag used in the cold isostatic processing (CIP) method. Currently, the bag is molded from a metallic mold. The SFF process has already shown that it can produce complex shaped preforms from nylon powder. Thus, the substitution of nylon by polymer for use in the fabrication of CIP bags, and applying the Ceracon process to make the part should enable bypassing of the metallic mold making operation. Thus significant reduction in machining of molds and iterations required in the process could be obtained.

In conclusion, the preforming capability of the SFF process could be coupled with the complimentary full-density capability of the Ceracon forging process. This should result in significantly reducing the time required time for prototype and manufacturing of net-shape powder metallurgy parts. The Ceracon forging powder metallurgy process and the SFF process appears to offer complimentary capabilities for rapid prototype of powder metal parts for a variety of applications.

References:

1. The Ceracon Process is protected by 25 U.S. patents.
2. Oxidation Resistance of Powder Metallurgy Zirconium Aluminide Densified Using the Ceracon Process, R.V. Raman, S.V. Rele, and D.L. Hunn, presented at the International Conference & Exhibition on Powder Metallurgy & Particulate Materials, May 16-19, 1993.
3. A Novel Processing Route for the Fabrication of Monolithic and Composite Silicon Nitride, R. V. Raman and S. V. Rele, Proceedings of the MRS Meeting, Vol. 289, April, 1993.
4. In-Situ Synthesis and Rapid Consolidation of MoSi_2 to Full Density, R. V. Raman, S V. Rele, and M. J. Paskowitz, Journal of Metals, January, 1993
5. Advances in Full Density Consolidation of Engineered Materials, R. V. Raman, Advances in Powder Metallurgy and Particulate Materials - Vol. 2, 1992, Pages 401-420
6. Powder Consolidation In The 1990's: Recent Advances at Ceracon, Inc.", Powder Metal Report, April, 1990 issue entitled, "Advances in Powder Consolidation".
7. DTM Corporation Brochure, "The SLS Process, Rapid Prototyping and The Selective Laser Sintering Process".

Machine Vision for Rapid Geometric Modeling

V. Koivunen and R. Bajcsy
GRASP Laboratory
University of Pennsylvania
300C 3401 Walnut Street
Philadelphia, PA 19104-6228

Abstract

A method is presented for constructing geometric design data from noisy 3-D sensor measurements of physical parts. A complete 3-D data set have to be produced from several partial data sets. Model building tools for free form surfaces as well as irregular and standard geometric shapes are presented. In particular, NURBS, superellipsoids and Delaunay triangulations are employed. The data interpretation should be able to map the recovered shape of the part to appropriate design primitives. The resulting model description is a procedural CAD model which can represent the structural properties of a part in addition to low level geometric primitives. Finally, the model is translated to standard product data exchange format to enable data sharing.

1 Introduction

Sculptured surfaces are widely used, for example, in designing car and ship parts. The design of free form shapes, however, is relatively time consuming and requires typically extensive knowledge about the modeling primitives, such as splines. The task could be made easier by constructing a model automatically using sensory measurements, for example, from a clay model of a part. We propose here an approach for integrating an intelligent sensory system into a CAD system in order to produce an initial geometric model rapidly. The designer should be able modify the obtained model which is often necessary because the design changes during the development process.

We are employing non-contact optical sensors for data acquisition to be able to acquire dense data set fast. Dense data are required for modeling sculptured surfaces accurately. In order to model solid objects we have to obtain a complete 3-D data set. Laser range finders, however, produce only partial data from a single viewpoint at the time and the complete data have to be combined from partial data sets acquired from different viewpoints. The problem requires estimation of relative translation and rotation parameters between partial data sets obtained from different vantage points as well as combination of data into a common coordinate frame. The data interpretation part constructs a geometric model from the data by fitting models. The obtained representation of the data is compatible with the representations employed in modeling systems and product data exchange formats.

Our approach constructs *procedural CAD models* in order to represent low level geometry of the part as well as convey its overall structure. Structural information is vital for analysis, simulation and process planning purposes. Procedural models are also relatively easy to modify. They are also convenient in representing intersections

of parametric surfaces. The intersection is described in the procedure and it can be approximated in the level of required accuracy when it is actually needed. The constructed model should employ the model primitives used in CAD systems. It must be translated into standard product data exchange format to enable data sharing, and consequently, concurrent engineering [5]. The proposed system is depicted as a part of concurrent engineering environment in Figure 1.

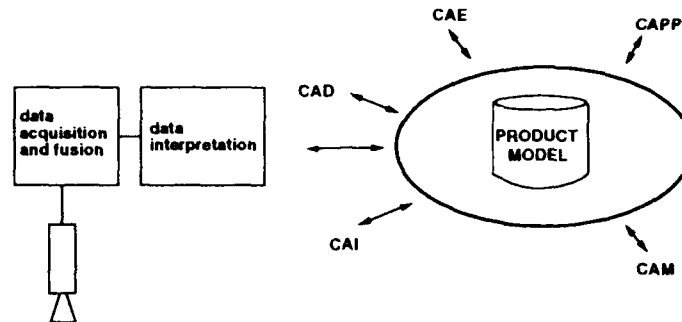


Figure 1: The proposed system as a part of a concurrent engineering environment. The CAX processes are Design, Engineering, Process Planning, Manufacturing and Inspection.

The organization of this paper is as follows. In section 2 we address shape representation issues in machine vision and CAGD. Section 3 outlines the proposed approach and describes briefly some methods used in model construction. In section 4 we show some examples of data interpretation using real and simulated range data. Finally, in section 5 we conclude and discuss some areas requiring future research.

2 Representation of shape

Constructive Solid Geometry (CSG) and Boundary Representation (B-rep) are widely used in solid modeling systems [13]. Several CAD-systems are hybrid systems that employ multiple representations in order to provide efficient tools for different design tasks and to overcome the shortcomings of each single representation. For instance, Alpha-1 [1] uses NURBS for designing free form shapes and allows CSG type Boolean operations on solids as well as design by manufacturing features.

It seems, analogous to the design, that there is no single representation in Computer Vision that could be used for recovering an appropriate shape description from sensor data in all situations. In general, the representations can be classified into surface, volumetric and sweep representations [3]. In order to facilitate modeling of different shapes from sensor data we are employing multiple representations. An optimal triangulation is generated for modeling polygonal and complicated irregular shapes which may have arbitrary topology. It can also serve as a worst case representation, if no other method is appropriate. NURBS are used for modeling free form surfaces because of their continuity and local control properties. In addition, trimmed surfaces are used when rectangular arrangement of tensor product surfaces is not suitable. Furthermore, they are included in IGES product data exchange standard which facilitates data sharing and concurrent engineering. Superellipsoid models are used to detect overall part

structure which allows us to use more efficient model primitives that are helpful in part analysis and process planning.

3 An overview of the proposed system

The data acquisition is performed by a laser range finder. The accuracy of such sensory system is suitable for measuring artifacts of large scale. Optical non-contact sensors measure only from bounding surfaces of an object, hence the interior of solids are not modeled. A multipart artifact must be disassembled if one wants to produce a description of the joints as well. Otherwise, data have to be segmented into meaningful parts. Physical measurements are subject to various noise effects. In the case of laser range finders, the noise process deviates from Gaussian and there may occur outliers. We apply nonlinear RLTS filters [8] based on robust estimation theory for separating the desired part in degraded data from the undesired part while preserving the structure of the signal.

In order to produce a complete 3-D data set, the transformation between partial data sets have to be estimated and the data combined into common coordinate frame. This is done by combining the data sets from each viewpoint incrementally. A method based on iterative closest point procedure [4] is used for solving the rotation and transformation which minimizes the distances of points from the surfaces in the model constructed so far. A more thorough description of the view registration and preliminary experimental results are given in [16, 10].

The 3-D data set is represented as a collection of triangles. In particular, a 2/3 Delaunay triangulation is generated. The triangulation process is based on the algorithm given in [7]. It is refined so that the accuracy meets a user defined tolerance value [10]. Triangulations convey very little structural information but can be used as a worst case representation if no other method is appropriate, e.g., in the case of natural objects that do not consist of smooth surfaces. Moreover, the resulting triangulation can be used as an input to more advanced surface approximation procedures as well as an initial mesh for analysis and simulation processes.

The CAD model building strategy is chosen based on the obtained volumetric and surface data descriptions and their quality. The basic idea is to find out if the part is approximately a standard primitive solid or has structure such as symmetry. A superellipsoid model [2, 15] is recovered for each part to capture both overall structure and global deformations. An implicit equation for superellipsoid surface is defined as follows:

$$f(x, y, z) = \left(\left(\frac{x}{a_1} \right)^{\frac{2}{\varepsilon_2}} + \left(\frac{y}{a_2} \right)^{\frac{2}{\varepsilon_2}} \right)^{\frac{\varepsilon_2}{\varepsilon_1}} + \left(\frac{z}{a_3} \right)^{\frac{2}{\varepsilon_1}} = 1, \quad (1)$$

where a_1 , a_2 , and a_3 define the size in x-, y- and z-axis direction. ε_1 and ε_2 are the shape (squareness) parameters in the latitude and in the longitude plane, respectively. The obtained shapes are classified into categories so that an appropriate CAD modeling primitive can be selected [9]. The superellipsoid method does not give the part dimensions very accurately. In the case of rotationally symmetric objects, for instance, the accurate dimensions are obtained by fitting conic sections [12].

The surfaces are approximated using NURBS surfaces because of their good continuity and local control properties. NURBS is defined as a bivariate polynomial function

of parameters u and v as follows:

$$S(u, v) = \frac{\sum_{i=1}^n \sum_{j=1}^m h_{i,j} B_{i,j} N_{i,k}(u) M_{j,l}(v)}{\sum_{i=1}^n \sum_{j=1}^m h_{i,j} N_{i,k}(u) M_{j,l}(v)} \quad (2)$$

where $N_{i,k}$ and $M_{j,l}$ are the basis functions, $h_{i,j}$ are the weights, and the $B_{i,j}$'s are the control points. n and m identify the number of control point vertices in each direction. The complexity of the underlying surface is determined by a local surface characterization process. An appropriate size for control point mesh is estimated based on the number of geometrically homogeneous surface patches detected in the characterization process [9]. The locations of the control points $B_{i,j}$ are estimated by minimizing error in least squares sense. The approximation is refined to meet a user given tolerance value by knot insertion [11]. Surface discontinuities are detected where rapid changes in surface normal occur. B-splines are subdivided where discontinuities take place [6].

The obtained model data is represented both in procedural modeling language and in standard product data exchange format (IGES) to be able to share the model with other subsystems. Some of the obtained model primitives can be directly mapped to primitive manufacturing operations in computer aided process planning (CAPP). Rotationally symmetric parts can be mapped to a manufacturing stage performed on a CNC lathe, for example. Novel manufacturing processes, such as MD* [17], can fabricate very complicated shapes easily with less structural information. The process planning is basically independent from part complexity because 3-D shapes are build incrementally from cross-sectional layers. Each layer is then sprayed using a disposable mask which has a shape of cross-section.

4 Examples

In this section we show some examples of building CAD models from simulated and real range data. Constructed models of standard geometric and free-form shapes as well as surfaces of arbitrary topology are shown. The test pieces are illustrated in Figure 2 where the Cylindrical Pin is simulated data and the Face Mask image and the Hand image are from NRCC [14] range image library.

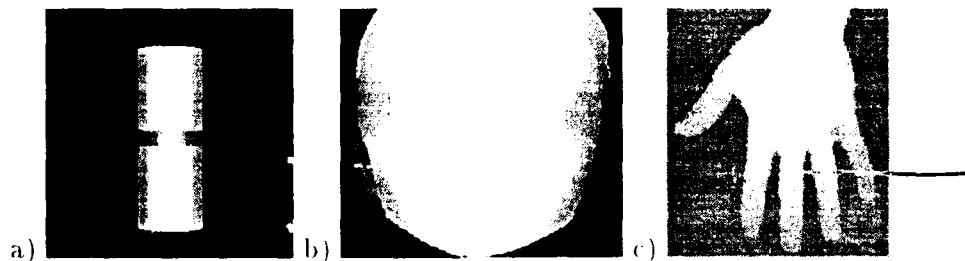


Figure 2: Example test data: a) The Cylindrical Pin is rotationally symmetric shape, b) the Face Mask is a free form shape and c) the Hand is a free-form shape with several branches.

Noise attenuation and especially outlier rejection are important to be able to obtain reliable results from least squares fitting procedures. Robust RLTS filtering is

performed to recover the signal structure from noisy observations. Filtering examples are given in [8, 9].

2/3 Delaunay triangulation is performed on test data. Triangulations are employed in modeling polygonal objects and irregular shapes where the surfaces may not be smooth. Example triangulations of the Face Mask and Hand data are shown in Figure 3.

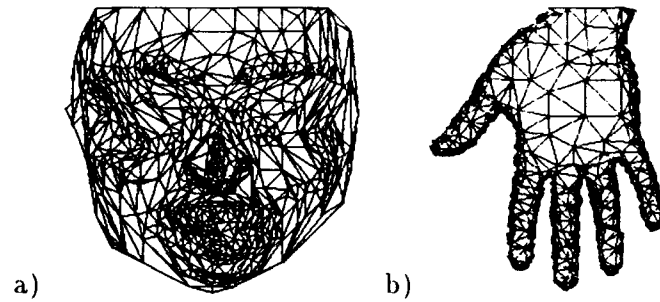


Figure 3: Delaunay triangulations of a) the Face Mask and b) the Hand data using tolerance value 0.4 mm.

The superellipsoid model recovery is used to reveal global shape properties. The obtained shape parameters are used as a hypothesis to invoke the appropriate model building procedure. The superellipsoids for test pieces are depicted in Figure 4. The shape parameters reveal the rotational symmetry of the Cylindrical Pin. The quality of the fit is also high, hence surface of revolution modeling primitive is selected. The quality of the fit is low for the Face Mask and the Hand data and they are modeled as a collection of bounding surfaces.

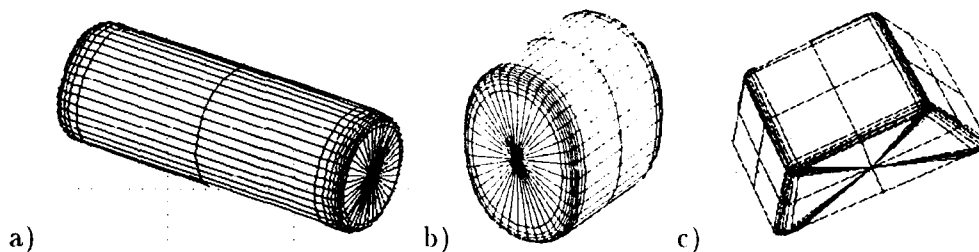


Figure 4: The obtained superellipsoid models of the test pieces: a) the Cylindrical Pin, b) the Face mask, and c) the Hand

The free-form surfaces are approximated by NURBS. The locus of the control points is solved minimizing least squares error norm. Rectangular arrangement of tensor product surfaces is not appropriate in all situations. Trimmed surfaces provide a convenient engineering tool for modeling surfaces of arbitrary topology. Boundaries of the surface are used to compute trimming curves which divide the surface into valid and invalid parts. Approximating NURBS surfaces for test pieces are depicted in Figure 5. The surface description is refined to meet user defined tolerance value by inserting knots and, as a consequence, more control points. An example of the refinement by knot insertion for a profile from the Face Mask is depicted in Figure 6.

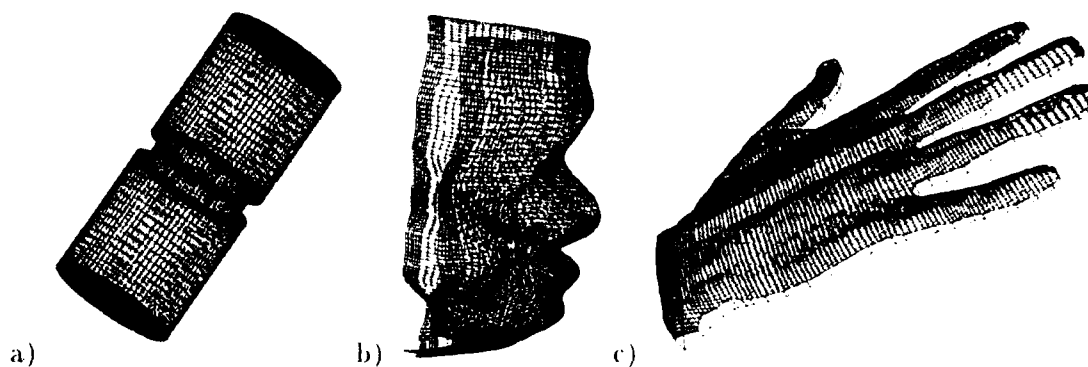


Figure 5: Approximating NURBS surfaces for the test pieces: a) The Cylindrical Pin is modeled as a surface of revolution, b) the Face Mask is a tensor product surface and, c) the Hand is a trimmed surface.

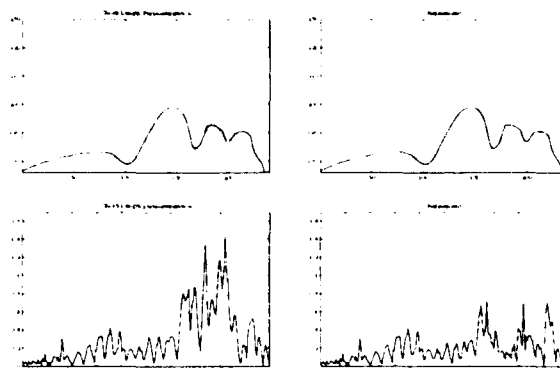


Figure 6: A profile from the Face Mask data and its B-spline approximation (dotted line) before (left) and after (right) the refinement by knot insertion. A tolerance value of 1 mm is used. The corresponding error distances are depicted below.

The obtained model procedure which generates the part geometry is imported into Alpha-1 [1] solid modeling system. Procedural models are able to convey information about the part structure, for example, the rotational symmetry of the cylindrical pin. Moreover, the surface intersection in the trimming operation for the Hand data is described in the procedure and the intersection can be approximated only when needed: less accurately for display purposes and very accurately for toolpath generation. A part of a model procedure generating a solid of revolution and a part of the corresponding IGES file are illustrated in Figure 7.

5 Conclusion

We presented a computer-aided engineering tool where an intelligent sensory system is integrated into a design automation environment. The task at hand is to build an initial geometric model of a part using 3-D sensor data. In particular, modeling of sculptured shapes could benefit from rapidly produced geometric models. It is important that the initial model can be modified because the design typically evolves.

```

p12 := prujpc(0.00000,00.61196,27.174069,1.0);
p13 := prujpc(0.00000,100.26072,27.123450,1.0);
p14 := prujpc(0.00000,120.61196,27.100613,1.0);
p15.1 := prujpc(0.00000,129.00000,27.140000,1.0);
p15.2 := prujpc(0.00000,129.00000,27.140000,1.0);
p15.3 := prujpc(0.00000,129.00000,27.140000,1.0);
p15.4 := prujpc(0.00000,129.00000,27.140000,1.0);
p16 := prujpc(0.00000,129.00000,0.00000,1.0);
}

Reveur := curve(garminfo(cubic,ex_spos,MyEntList);
list(p0, p1.1, p1.2, p1.3, p1.4, p2, p3, p4, p5.1, p5.2,
p5.3, p5.4, p6.1, p6.2, p6.3, p6.4, p7, p8, p9, p10.1,
p10.2, p10.3, p10.4, p11.1, p11.2, p11.3, p11.4, p12, p13, p14,
p15.1, p15.2, p15.3, p15.4, p16));
RevSurf := exOffRevolucion(Torix,Reveur,m1,m1);
ModSolid := shell(RevSurf);
}

```

```

IGES OUTPUT FROM Rapid Prototyping System
10,10,,,12H symnavy.igs,20H Rapid Prototyping .5M1.0.0.32.30.6.30.15.,G 1
1.,2,2HMM,32.5.,13H920821.120414,0.00001,1000.0000,2HVK.,9.0,G 2
162 1 0 1 0 0 0 00000001D0000001
162 0 0 1 0 0 0 0 1D0000002
126 2 0 1 0 0 0 0 1D0000003
126 0 0 32 0 0 0 0 1D0000004
162,3,1,0,0,0,0,0,0,0,0,0,1,0,0,0,
126,34,3,0,0,0,0,0,
000.00000,000.00000,000.00000,000.00000,000.03125,000.06250,
000.09375,000.12500,000.15625,000.18750,000.21875,000.25000,
50000001
1D0000002
3P0000002
3P0000003
3P0000004

```

Figure 7: Model data for the Cylindrical Pin: a part of the Alpha.1 model (left), and a part of the IGES description (right).

Physical measurements are subject to noise which must be attenuated without distorting the underlying signal in order to make accurate model construction possible. Data have to be acquired from several viewpoints and fused into a complete 3-D data set in a common coordinate frame. The data interpretation is produced by fitting models. Multiple representations are employed in order to model different shapes efficiently. The aim is to obtain a representation of the part geometry using CAD modeling primitives. The result is a procedural CAD model which is able to convey structural information about the part in addition to low level geometric data. Furthermore, the designer can modify the procedure and refine the model as the design evolves. The model is translated to standard product data exchange format to facilitate concurrent engineering.

The ongoing and future research is directed toward refining and extending the data acquisition process in order to register free form shapes accurately. Furthermore, the integration of engineering analysis tools into the system is under development.

Acknowledgements

We want to thank Dr. Beth Cobb and Prof. Rich Riesenfeld for providing us Alpha.1 system, and for their help and hospitality while studying it. The Academy of Finland, The Foundation Suomen Kulttuurirahasto, and the University of Oulu, Finland are gratefully acknowledged for financial support. The facilities were partly provided by Navy Grant N00014-92-J-1647, AFOSR Grant 88-0296; Army/DAAL 03-89-C-0031PRI; NSF Grants CISE/CDA 88-22719, IRI 89-06770, and ASC 91 0813; and Du Pont Corporation

6 REFERENCES

- [1] Alpha.1 User's Manual (1992) University of Utah. USA.
- [2] Barr, A., "Superquadrics and Angle Preserving Transformations", IEEE Computer Graphics and Applications, Vol. 1, pp. 11-23, 1981.
- [3] Bhanu, B., Ho, C., "CAD-Based 3-D Object Representation for Robot Vision", IEEE Computer, August, pp. 19-35, 1987.
- [4] Besl, P., McKay, N., "A Method for Registration of 3-D Shapes", IEEE Transaction on Pattern Analysis and Machine Intelligence, Vol. 14, No. 2, pp. 239-256, 1992.
- [5] Carver, G., Bloom, H., "Concurrent Engineering through Product Data Standards", In: Control and Dynamic Systems, Vol. 45: Manufacturing and Automation Systems: Techniques and Technologies, Academic Press, pp. 31-109, 1992.

- [6] Cohen, E., Lyche, T., Riesenfeld, R., "Discrete B-Splines and Subdivision Techniques in Computer Aided Geometric Design and Computer Graphics", *Computer Graphics And Image Processing*, 14, pp. 87-111, 1980.
- [7] Field, D., "A Generic Delaunay Triangulation Algorithm for Finite Element Meshes", *Adv. Eng. Software*, 1991, Vol. 13, No. 5/6 combined, pp. 263-272, 1991.
- [8] Koivunen, V. "Robust Approach to Filtering of Scalar and Vector Valued Signals". *IEEE Workshop on Image and Multidimensional Signal Processing*, Cannes, France, 1993.
- [9] Koivunen, V., Bajcsy, R., "Geometric Methods for Building CAD Models from Range Data". In: *Geometric Methods in Computer Vision II*, SPIE Vol. 2031, San Diego, 1993.
- [10] Koivunen, V., Vezien J-M., Bajcsy, R., "Multiple Representation Approach to Geometric Model Construction from Range Data", Technical Report MS-CIS-93-66, University of Pennsylvania, 1993.
- [11] Piegl, L., "Modifying the shape of rational B-splines. Part 2: Surfaces", *Computer Aided Design*, Vol. 21, No. 9, pp. 538-546, 1989.
- [12] Pratt, V., "Direct Least-Squares Fitting of Algebraic Surfaces" *Computer Graphics* 21, No. 4, pp. 145-152, 1987.
- [13] Requicha, A., Voelcker, H., "Solid Modeling: A Historical Summary and Contemporary Assessment", *IEEE Computer Graphics and Applications*, Vol. 2, No. 2, pp. 9-24, 1982.
- [14] Rioux, M., Cornoyer, L. "The NRCC Three Dimensional Image Data Files". CNRC 29077, National Research Council of Canada, 1988.
- [15] Solina, F., Bajcsy, R., "Recovery of Parametric Models from Range Images: The case of Superquadrics with Global Deformations", *IEEE Transactions on Pattern Analysis and Machine Intelligence*, PAMI-12, No. 2, pp. 131-147, 1990.
- [16] Vezien J-M, "Data Acquisition and Registration of Range Images for Reverse Engineering Applications", Technical Report, University of Pennsylvania, Department of Computer Science, July, 1993.
- [17] Weiss, L., Prinz, F. & Siewiork, D., "A Framework for Thermal Spray Shape Deposition: The MD* System", *Solid Freeform Fabrication Symposium*, Austin, Texas, USA, 1991.

STRATEGY FOR COMPOSITE DEVELOPMENT IN RAPID PROTOTYPING

R. Charan and A. Bagchi
Department of Mechanical Engineering

T. Renault and A.A. Ogale
Department of Chemical Engineering

Intelligent Design and Rapid Prototyping Laboratory
Center for Advanced Manufacturing
Clemson University
Clemson, SC 29634

ABSTRACT

The polymeric parts built with a stereolithography apparatus (SLA) have good dimensional accuracy, but they cannot be used as functional prototypes because of their low mechanical properties. This paper describes the concept of fabricating fiber composites by 3-D photolithography. In this process, the strength and stiffness of parts are improved over stereolithography by adding fiber reinforcement to the resin. An automated desktop photolithography unit (ADPU) was designed and built in-house, to add continuous E-glass or quartz fibers in situ to the photoresin. The first composite parts made by 3-D photolithography are presented in this paper, the feasibility of curvilinear addition of fibers is demonstrated, and strategies for selective reinforcement are discussed.

INTRODUCTION

The emergence of solid freeform fabrication (SFF) techniques has reduced the processing time of prototypes as compared with those of conventional manufacturing processes. SFF methods create parts by slicing its three-dimensional (3-D) computer aided design (CAD) representation into layers of finite thickness. The part is built layer by layer from the bottom up, by adhering each freshly developed layer to the part, until a three dimensional object is fabricated. Therefore, SFF techniques use selective material addition, whereas conventional methods build parts by material removal. Extensive part dependent tooling and fixtures required in conventional manufacturing make the process time consuming. The absence of tooling and pre/post processing reduces SFF process lead time and allows complicated parts to be built with relative ease.

A true prototype must have required dimensional accuracy and mechanical properties. The dimensional accuracy of an SFF part is achieved by proper selection of slice thickness. However, its mechanical properties are much lower than those developed by conventional manufacturing processes. The mechanical properties of SFF parts are limited by the polymers used in many of these processes [1-3], such as selective laser sintering and fused deposition modeling.

The fabrication of composite prototypes by SFF was first developed at Clemson for photolithography. It was easier to handle liquid thermoset resins and continuous fiber tow reinforcements than powdered thermoplastics (in selective laser sintering [4]) or molten thermoplastics (in fused deposition modeling [3]). The feasibility of integrating fiber

reinforcements with stereolithography was demonstrated by fabricating manually test coupons, which were tested for tensile strength, stiffness, and impact strength [6, 7]. We have shown earlier that parts with mechanical properties similar to those of aluminum can be obtained with stereolithography resins by adding 20 vol% of glass or quartz fibers [7]. The next step, automatically adding reinforcement to the resin in a selective and controlled manner, to produce fiber composite prototypes by 3-D photolithography is presented in this paper.

COMPOSITE PROTOTYPE DEVELOPMENT

The preliminary study used two commercial stereolithography resins, Ciba Geigy Cibatoool XB5081 (CG) and Desotech Desolite SLR 806 (DS). Both resins were polyacrylates and the main difference between the two resins was the high viscosity of CG (3000 cP at room temperature) as compared to DS (300 cP at room temperature). Most of the newer resins have slightly better mechanical properties, and are notably less brittle, yet none of these resins attain sufficient strength and stiffness for functional applications [8]. The chemistry is the limiting factor, and the easiest way to improve the mechanical properties of these resins by one order of magnitude appears to be with the addition of fibers to the resins.

In a preliminary study, continuous glass and quartz fibers were wound around aluminum plates and impregnated with resin [6]. The mechanical properties of the resins were found to improve by a factor of 10 with approximately 20 vol% of fibers [7]. Discontinuous E-glass and quartz fibers were also used as reinforcements, but the improvement in terms of mechanical properties was found to be smaller [7, 9]. Also, it was not possible to premix the fibers and the resin because of the very high viscosity of the blend. Consequently, short fibers would have to be selectively dispensed in a piecewise continuous fashion, resulting in a smaller improvement. For these reasons the 3-D photolithography for fabrication of composite prototypes have been developed using continuous fibers only. The increase in mechanical properties of the composites depend upon the mechanical properties of the fiber and the resin, volume fraction, fiber orientation, aspect ratio and wetting properties of the fiber in the resin.

We have addressed in previous studies that (a) the influence of the fibers on the photocure of the resin and (b) the wetting of the fibers by the resin are critical to the process. Since the resins have to be exposed to UV light to cure, the choice of the reinforcing fibers is critical. Glass and quartz fiber are completely transparent to UV light at 325 nm, the wavelength used to cure the resin. It was shown that they did not influence the cure kinetics of the resin, and that they could be used as reinforcements [11]. On the other hand, the cure of the resin could not be completed with carbon fibers because of its opacity to UV light. The wetting of the fibers by the resin has also been studied, because if the fibers are not properly wetted, the bond between the fiber and the resin will be poor and result in low mechanical properties. It was found that the main parameter for the wetting process is the viscosity of the resin [12]. If a viscous resin like CG is used the time needed for the resin to impregnate a tow with 800 glass fibers is 2 minutes whereas for a low viscosity resin like DS, it is only 10 seconds. With a long wetting time, the process is slowed down making it unattractive for part production. With low viscosity resins, however, only a few seconds are needed to wet the fibers, and this step is not a problem for 3-D photolithography.

The fabrication of composites by 3-D photolithography is a unique process when compared compared with the traditional techniques used to manufacture composites. Pultrusion, injection molding, resin transfer molding, compression molding, hand lay-up and filament winding all need some kind of tooling, be it a die, mold or a mandrel. Fabricating composites by 3-D

photolithography therefore combines the advantages of SFF methods with the improved mechanical properties of composite materials. Another advantage of 3-D photolithography for the fabrication of composite materials is that until recently composites were developed with fibers laid out straight and parallel to each other on any plane, e.g., a 0/90/0 orientation. Although these parts displayed improved mechanical properties, they did not take advantage of the full potential of the fibers. Studies have indicated that for a given volume fraction fibers, laying them in a curvilinear format yields best results [13]. The part will be selectively reinforced with greater percentage of fibers placed in the high stress region. The idea of building parts using fibers laid out in curvilinear format has been hampered by the inability to implement such a design. However, with the development of 3-D photolithography it is now possible to selectively lay down fibers along any curve.

AUTOMATED DESKTOP PHOTOLITHOGRAPHY UNIT

The automated desktop photolithography unit (ADPU) was designed and built in-house to allow *in situ* addition of fibers. A schematic of the current setup of the ADPU is shown in Figure 1. The part is built on an aluminum platform which is immersed in a rectangular vat containing monomeric resin. The platform and the vat are positioned manually to control the thickness of the resin over the plate and the distance of the top layer from the light source. The unique feature of the ADPU is the fiber dispensing device which is used to automatically dispense the continuous fibers into the resin. The light source consists of an optical fiber with a focusing lens connected to a 100W mercury lamp. The light source and the fiber dispensing device are mounted on a circular plate which can traverse in the X-Y direction and rotate about the Z axis. Because the fibers dispensed in the resin have to be wetted before the resin is polymerized, the light source is located at the center of the plate while the fibers are dispensed 1cm off the center. A traverse speed of 1 mm/s allows the fibers to be wetted for 10 s before cure. The translational motion is provided by the X-Y positioning table and the rotation by the rotational drive mounted on the positioning table. The three controllers for positioning table (X, Y) and the rotational drive (theta) are supervised by a computer. The motion of the X and Y axes can be combined to develop any curvilinear path, while the rotation ensures that the fibers are dispensed ahead of the lamp and along the desired path. Each axis is set in motion as soon as a command is received from the supervisory program. With this setup it is possible to dispense fibers in the resin and polymerize the composite in any desired orientation on any layer.

The first step in part building is the creation of data file which consists of the coordinates of all the points that are to be joined sequentially. The location and the order of these points depend on part geometry and loading conditions. This data file along with the translational/rotational speed of each axis form the input to the program to create motion commands for each controller. The output of this program is fed to a supervisory program resident in the computer which distributes the information between the two controllers.

PART BUILDING

Test coupons were built to compare the tensile strength of parts with and without fibers. The samples were 100 mm x 10 mm x 1.5 mm, and were reinforced by 20 fiber tows placed along its length. The concept of curvilinear fiber layout was demonstrated by building a circular ring with one, two, and three concentric passes of fiber, 24, 27, and 30 mm in diameter, respectively. The data

file for each circular motion was created by approximating a circle into 36 equal sectors of 10° each joined together. A plate of 100 mm by 40 mm with a centrally placed hole of dia 20 mm was built from pure resin. On top of this plate three concentric rings of DS/quartz composites were built. The desired paths for the fiber dispenser and the lamp are shown in Figure 2 for all these parts.

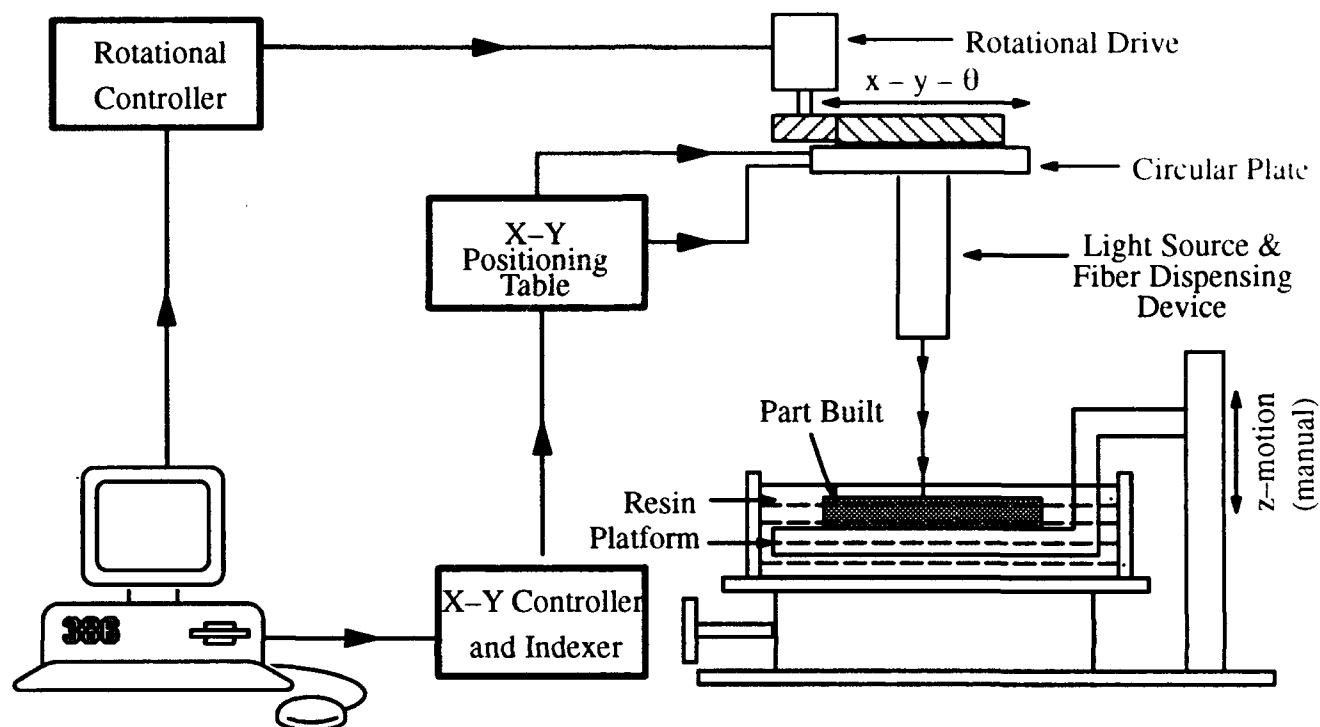


Figure 1. Automated Desktop Photolithography Unit (ADPU)

RESULTS AND DISCUSSION

A photo of a pure DS sample and of a DS/quartz composite is shown in Figure 3. The pure DS resin samples (100 mm x 10 mm x 1.5 mm) built in the ADPU were found to have a tensile strength of 22 ± 2 MPa. The next batch of samples was a one layer DS/quartz composites with a volume fraction of 5 %. The tensile strength of these samples was 42 ± 5 MPa. This strength is much lower than the 300 MPa obtained in the preliminary study for samples processed manually with 20 vol% of fibers, and it shows not only a nearly 100% improvement in tensile strength but also the need for incorporating higher volume fraction of fibers. The volume fraction of fibers can be increased either by adding more fibers or by limiting the thickness of the resin. The tensile strength of these samples was measured by dividing the load at break by an average width and thickness of the sample. As shown in Figure 3, because the surface of the composite is not as smooth as that of the pure resin sample, the average thickness is only a rough estimate and the strength of these

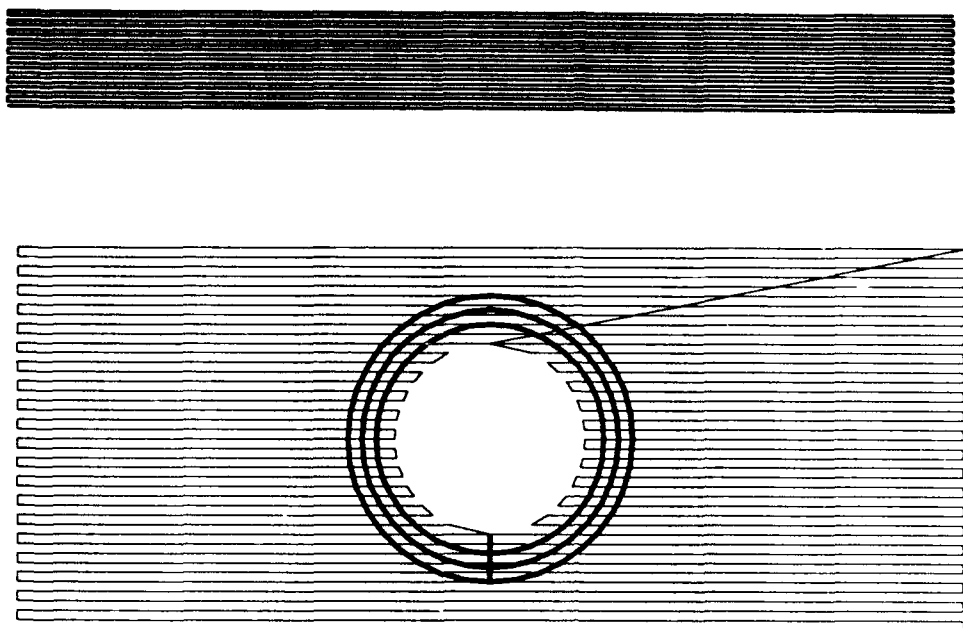


Figure 2. Path of the lamp and the fibers generated by computer simulation for
 (a) composite tensile test coupon
 (b) ring with three concentric passes of fiber (thick lines) over a layer of
 plate with hole in the center



Figure 3. Tensile test coupons of pure DS resin (top) and DS/ Quartz composite
 (bottom) made in ADPU

composites might actually be higher than the 42 MPa reported here. To get a better estimate of the cross sectional area, an image analysis technique will be used to measure the cross-section of the samples. The surface of the composites samples can be greatly improved if layers of pure resin are added at the bottom and on top of the composite. Samples with one layer of DS/quartz composite between 2 layers of pure DS resin were built, but the volume fraction of fibers was limited to 1%. The tensile strength of these samples was therefore similar to pure resin.

The rings with one, two, and three passes of fibers are shown in Figure 4. These rings demonstrate that it is possible to add fibers along a curvilinear path with good accuracy and repeatability. The 'beads' on the rings are due to the pauses that were imposed between each translation and rotation. As shown in Figure 5, they are also present at both ends of the plate made of resin. A ring with three passes was built on this plate with a hole. This is the first step towards the reinforcement of a plate with a hole. In future, fibers will be dispensed along the stress contours, and the mechanical properties of this part with and without fibers will be compared.

In this study the concept of reinforcement is applied to parts built by photopolymerization of resins used in the SLA. Like stereolithography, other SFF techniques also build parts layer by layer. However, Cubital's solidex cures the resin in bulk through a mask and Helysis's laminated object manufacturing cuts the paper in the required shape. Since the layers are not prepared by hatching, *in situ* fiber reinforcement can be difficult for these processes. Nevertheless, it is feasible in concept to fabricate reinforced composites with other freeform fabrication processes such as DTM's selective laser sintering and Stratasys's fused deposition modeling, which prepare layers in a process similar to stereolithography. In selective laser sintering, the thermoplastic powders used would have to be melted by the laser to impregnate the fibers, a process that is theoretically feasible, but might be difficult to implement experimentally. A better method might be to use fiber tows that are precoated with thermoplastics, although these materials might be too stiff to bend at sharp corners. The process might be more readily suited for fused deposition modeling, where a wire of thermoplastic is fused and deposited through a tip.

CONCLUDING REMARKS

A new process to fabricate composite prototypes by 3-D photolithography is presented in this paper. This method is unique because it can process composite parts with improved mechanical properties without the need for tooling. Also the fibers can be added selectively and in a curvilinear path. A new automated desktop photolithography unit (ADPU) was used to automatically build fiber reinforced parts by 3-D photolithography. At the present time, the fiber content added to the resin was limited to 5 vol%, and the improvement in the mechanical properties was limited; future work will attempt to increase the fiber volume fraction. Parts with fiber dispensed in a curvilinear format were fabricated to prove the feasibility of the concept. However the issues pertaining to identification of optimum curvilinear fiber layout still need to be addressed.

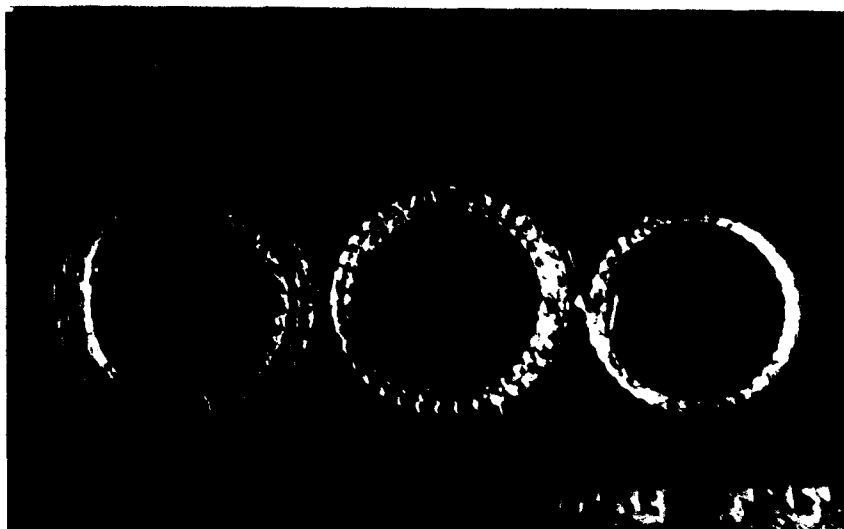


Figure 4. DS/ Quartz composite rings fabricated on the ADPU. From right to left fibers were laid down in:

- (a) one circle of 24 mm dia.
- (b) two concentric circles of 24 and 27 mm dia.
- (c) three concentric circles of 24, 27 and 30 mm dia.

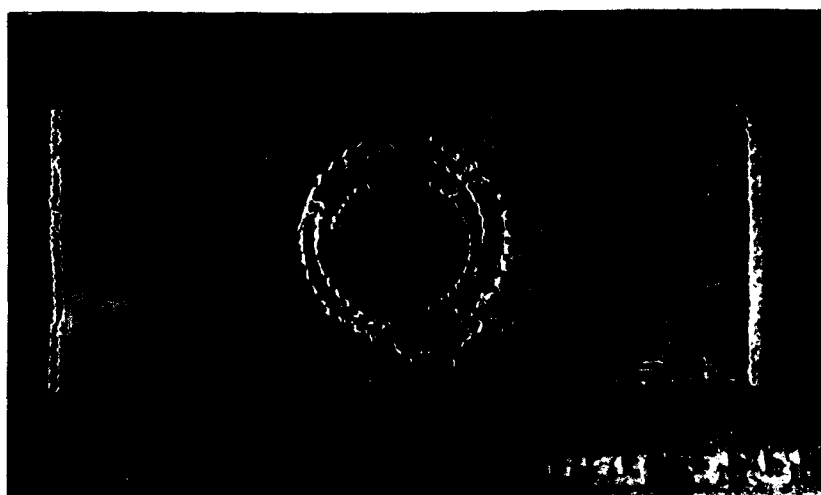


Figure 5. DS/ Quartz composite ring made of three concentric circles over a plate of pure resin with a hole made in ADPU

REFERENCES

1. Deitz, D., "Stereolithography Automates Prototyping," Mechanical Engineering, Feb 1990, pp.34-9 (1990).
2. Feygin, M., "LOM System goes into Production," Proc. of Second International Conference on Rapid Prototyping, pp. 351-7 (1991).
3. Crump, S., "The Extrusion Process of Fused Deposition Modeling," Proc. of Third International Conference on Rapid Prototyping, pp. 91-102 (1992).
4. Barlow, J. W., "Metallic and Ceramic Structures from Selective Laser Sintering of Composite Powders," Proc. of Third International Conference on Rapid Prototyping, pp. 73-6 (1992).
5. Sachs, E., M. Cima, and J. Cornie, "3-D Printing: Ceramic Shells and Cores for Casting and Other Applications," Proc. of Second International Conference on Rapid Prototyping, pp. 39-54 (1991).
6. Renault, T., A. A. Ogale, R. L. Dooley, A. Bagchi, and C. C. Jara-Almonte, "Photolithography for Composites Manufacturing: Continuous Glass Fiber/Polyacrylate Composites," SAMPE Quarterly, 22 (2), pp. 19-25 (1991).
7. Renault, T. and A. A. Ogale, "3-D Photolithography: Mechanical Properties of Glass and Quartz Fiber Composites," Proceedings ANTEC 92, Detroit, Michigan, May 3-7, pp.745-7(1992).
8. Chartoff, R. P., P. T. Weissman, and S. M. Linden, "Advances in Polymer Technology for Stereolithography," Proc. of Second International Conference on Rapid Prototyping, pp. 55-68 (1991).
9. Ogale, A. A., T. Renault, A. Bagchi, C. C. Jara-Almonte and R. L. Dooley, "3-D Photolithography for Composites Development: Discontinuous Reinforcements," SAMPE Quarterly, 23 (1), pp. 28-38 (1991).
10. Charan, R., A. Bagchi, T. Renault, and A.A. Ogale, "Fabrication of Composite Prototypes by 3-D Photolithography," Proc. of Fourth International Conference on Rapid Prototyping, pp. 15-23 (1993).
11. Renault, T., A. A. Ogale, and M. J. Drews, "Influence of Reinforcements on Photocuring: Photo Dynamic Mechanical Analysis," Proceedings ANTEC 93, New Orleans, May 9-13, pp.1252-4 (1993).
12. Ogale, A. A., T. Renault, A. Bagchi, C. C. Jara-Almonte and R. L. Dooley, "Processing of Composites by 3-D Photolithography," Proceedings of International Conference on Transport Phenomena in Processing, S. Guceri, Ed., Waikiki, Hawaii, March 22-26, pp.1342-52 (1992).
13. Hyer, M.W. and R.F. Charette, "Use of Curvilinear Fiber Format in Composite Structure Design," AIAA Journal, 29(6), pp. 1011-15 (1991).

Direct Generation of Contour Files from Constructive Solid Geometry Representations

Sashidhar Guduri, Research Assistant
Richard H. Crawford, Assistant Professor
Joseph J. Beaman, Professor
Department of Mechanical Engineering
The University of Texas at Austin
Austin, TX 78712

Abstract

Geometry processing for layer-based Solid Freeform Fabrication consists of at least two steps: slicing the geometry to obtain the part contours for each layer, and scan-converting the layers for laser scanning (or other device-dependent in-layer processing). This paper discusses the generation of contour files directly from Constructive Solid Geometry (CSG) representations for the Selective Laser Sintering process. Previous work at The University of Texas focused on slicing CSG representations composed of quadric primitives. This paper extends previous work at UT to include the torus, a fourth degree surface, as one of the CSG primitives. Slicing a torus results in a fourth degree equation in two variables, which represents a curve in two-dimensional real space. For some special cases, this fourth degree equation may be sub-divided into two second degree equations. For the cases where the fourth degree equation cannot be sub-divided, a method is presented to approximate the fourth degree curve with second degree curve segments.

Introduction

Solid Freeform Fabrication (SFF) techniques manufacture solid objects directly from three-dimensional computer models. Most SFF processes produce parts on a layer-by-layer basis. The process begins by slicing the geometric description of the part into layers. The slicing operation generates the contours of the part for each layer. The contours are then processed in a manner dependent upon the particular SFF technology. For instance, for Selective Laser Sintering (SLS) the contours are discretized into "toggle points" at which the laser beam must be modulated to produce the desired solid.

The geometric description used to represent solid objects significantly affects the accuracy and quality of the final parts produce with SFF. One way to improve the final accuracy and definition of SFF parts is to improve the geometric descriptions that represent three dimensional objects. As described in [1], Constructive Solid Geometry is one geometric description where the accuracy of the final contours can be improved as compared to present geometric representations. A method was presented in [1] for generating contour files from Constructive Solid Geometry representations composed of quadric objects. This paper extends that work to include higher degree surfaces (degree greater than two) in the primitive set. Special attention is given to the torus, a fourth degree surface.

Slicing a higher degree surface results in a boundary curve whose degree may be greater than two. A curve of degree greater than two is parametrizable if the genus (g) of the curve is zero. The genus of a curve is defined by

$$g = \frac{(N-1)(N-2)}{2} - \sum_i \delta(p_i), \quad (1)$$

where N is the degree of the equation and the $\delta(p_i)$ operator appropriately counts the number of times that the curve comes in contact with itself at each singular point p_i . All quadratic curves are genus zero and are therefore parametrizable. A limited set of curves of degree greater than two are parametrizable. Unfortunately, the algebraic equations produced by many geometric design applications are not generally genus zero. It therefore becomes necessary to approximate higher degree curves with lower degree curve segments. These curve segments are then parametrized individually.

The method presented in this paper approximates curves of degree greater than two using second degree curve segments. There are two advantages to using second degree curves. First, all second degree curve segments are parametrizable. Second, the intersection of two second degree curves (required for Boolean set operations) can be computed by well-known, stable algorithms. If curve segments of degree greater than two are used as approximations, calculating the intersection of two curves becomes computationally expensive. The algorithm for generating the approximation is based on degree reduction of the triangular Bernstein form of the curve. The next section of the paper illustrates the representation of the torus as a CSG primitive and gives the equations involved in calculation of the implicit equation of the torus. Following this section, a method for determining the Bernstein coefficients of the implicit curve is described. The remainder of the paper describes the steps in the approximation algorithm: parametrization, approximation and error estimation, subdivision, and resolution of singularities. Examples are presented at the end of the paper.

Torus as a CSG Primitive

The equation of a torus generated by sweeping a circle about the y axis, with the origin at the center, is given by:

$$(x^2 + y^2 + z^2 + R^2 - r^2)^2 - 4r^2(x^2 + z^2) = 0 \quad (2)$$

As a CSG primitive the torus is represented using a base point, an axis vector and two radii, as illustrated in Figure 1.

Given the above information, the equation of the torus can be generated by translating the base point of the torus to the origin and rotating about x and z axes such that the resulting axis of the torus is aligned with the y axis. This procedure is summarized below:

1. Normalize the axis vector of the torus.
2. Translate the base of the torus to the origin.
3. Rotate about the x axis by an angle of $-\tan^{-1} \left(\frac{z_a}{y_a} \right)$.
4. Rotate about the z axis by an angle of $\tan^{-1} \left(\frac{x_a}{\sqrt{z_a^2 + y_a^2}} \right)$.

If the above steps are applied the following transformations are obtained

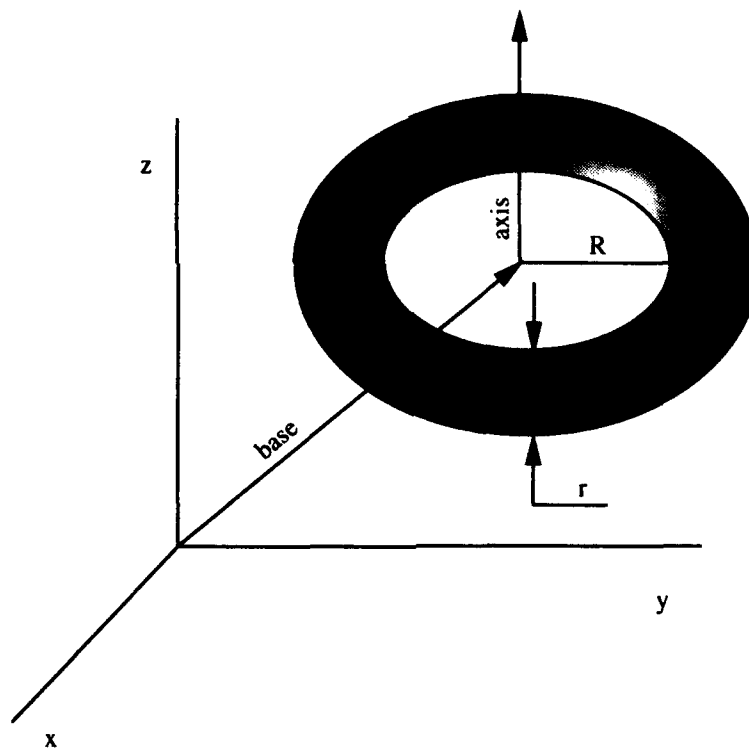


Figure 1. Representation of a torus.

$$\begin{aligned}
 x &= \sqrt{1-x_a^2}(X-x_b) - \frac{x_a y_a}{\sqrt{1-x_a^2}}(Y-y_b) - \frac{x_a z_a}{\sqrt{1-x_a^2}}(Z-z_b) \\
 y &= x_a(X-x_b) + y_a(Y-y_b) + z_a(Z-z_b) \\
 z &= \frac{-z_a}{\sqrt{1-x_a^2}}(Y-y_b) + \frac{y_a}{\sqrt{1-x_a^2}}(Z-z_b)
 \end{aligned} \tag{3}$$

where X, Y and Z define the coordinate system local to the torus. Substituting these equations into equation 2 gives the fourth degree equation of the torus in x, y and z . Substituting the z value of the slicing plane gives a fourth degree equation in x and y that is the implicit equation of the contour for that slicing plane.

Conversion of Algebraic Equations to Triangular Bernstein Form

This section describes a method for converting an algebraic equation in two unknowns to Bernstein form over arbitrary triangular regions [2]. Use of the Bernstein simplifies the task of degree reduction and degree elevation of algebraic curves. The triangular form simplifies subdivision of the curve. A method to do this is also presented in this paper. The general form of a bivariate polynomial of degree N is given by:

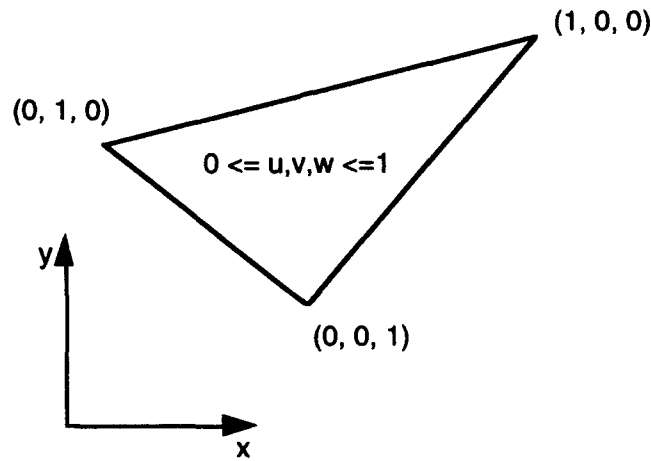


Figure 2. Barycentric coordinate system.

$$P^N = \sum_{i,j=0}^{i+j \leq N} a_{i,j} x^i y^j \quad (4)$$

A triangle can be defined by the three points P_{00} , P_{N0} and P_{0N} . The coordinates of any point inside the triangle can be computed from its barycentric coordinates (also referred to as area or trilinear coordinates) u , v and w , where $u+v+w = 1$. An arbitrary point P in the triangle is expressed in terms of barycentric coordinates by:

$$P = wP_{00} + uP_{N0} + vP_{0N} \quad (5)$$

The coefficients of the bivariate polynomial are used to compute the elements of a four dimensional array C , as given by the following equations:

$$C_{00}^{r0} = a_{N-r,r} \text{ and } C_{ij}^{rk} \equiv 0, \quad i, j < 0 \text{ and } i+j > k$$

$$C_{ij}^{rk} = C_{i-1,j}^{r,k-1} Y_{N0} + C_{i,j-1}^{r,k-1} Y_{0N} + C_{ij}^{r,k-1} Y_{00} + P(k,i,j) a_{N-r,r-k} \quad (6)$$

where $k = 0, \dots, r$ and $i, j \geq 0$ and $i+j \leq k$ and

$$P(a,b,c) = \frac{a!}{b! c! (a-b-c)!} \quad (7)$$

The elements of C are used to calculate a tetrahedral array D :

$$D_{ij}^k = 0, \quad (8)$$

where $i, j < 0$ and $i+j > k$ and $k = 0, \dots, N$

$$D_{ij}^k = D_{i-1,j}^{k-1} X_{N0} + D_{i,j-1}^{k-1} X_{0N} + D_{ij}^{k-1} X_{00} + C_{ij}^{kk} \quad (9)$$

where $k = 0, \dots, N$ and $i, j \geq 0$ and $i+j \leq k$. Finally the Bernstein coefficients are given by:

$$b_{ij}^N = \frac{D_{ij}^N}{P(N, i, j)} \quad (10)$$

After the Bernstein coefficients are obtained, the algorithm proceeds with approximation, as described in the next section.

Approximation of Higher Degree Curves

The algorithm for approximating algebraic curves of degree greater than two consists of four stages [3]. The parametrization stage builds a parametric definition. The approximation stage attempts to build a degree $N-1$ equation that matches the given degree N expression within acceptable error. The subdivision stage partitions the region where the curve is defined into smaller regions, if the region is not already too small. In the fourth stage, the algorithm resolves singularities. The complete algorithm is summarized as follows:

Stage 1: Parametrization

An attempt is made to parametrize the curve $f(x, y) = 0$ if the degree is less than 3. Should the degree be greater than 2, the algorithm proceeds with the approximation stage, where the degree of the equation is reduced to two.

Stage 2: Approximation

If the degree k function $f(x, y)$ monotonically increases or decreases with respect to any one edge of the domain triangle, estimate the error present in the $k-1$ approximation. If the error is within limits, return the approximation to stage 1 of the algorithm; if not, proceed with the subdivision stage.

Stage 3: Subdivision

If the size of the triangular region is smaller than a preset limit, assume the region contains a singularity and proceed to stage 4. Otherwise, divide the triangle into subregions and return to stage 1.

Stage 4: Resolution of Singularities

Using quadratic transformations for resolving singularities, generate an approximation for the curve segment through the given region.

Parametrization

If the degree of an equation is less than three, it can be parametrized. The procedure consists of two steps. First, the Bernstein equation is transformed into standard polynomial form (eqn. 4). Then the parameter values are calculated at the intersections of the triangle and the curve. The Bernstein equation is a function of parameters u and v . The coordinates x and y vary linearly with respect to u and v according to the following equations:

$$\begin{aligned}
x &= wX_{00} + uX_{N0} + vX_{0N} \\
y &= wY_{00} + uY_{N0} + vY_{0N}
\end{aligned}
\tag{11}$$

Transforming the above equations such that u and v are obtained in terms of x and y and substituting these equations for u and v in $f(u,v)$, we get a bivariate polynomial equation in terms of x and y .

$$\begin{aligned}
u &= \frac{x(Y_{01} - Y_{00}) - y(X_{01} - X_{00})}{(X_{10} - X_{00})(Y_{01} - Y_{00}) - (Y_{10} - Y_{00})(X_{01} - X_{00})} \\
v &= \frac{x(Y_{10} - Y_{00}) - y(X_{10} - X_{00})}{(X_{01} - X_{00})(Y_{10} - Y_{00}) - (Y_{01} - Y_{00})(X_{10} - X_{00})} \\
f(x,y) &= f(u,v)
\end{aligned}
\tag{12}$$

The parametrization algorithm is described in [4]. The intersection points of the curve and the Bernstein triangle are calculated and the appropriate curve segments are taken by determining if the curve segment lies inside the triangle or not.

Approximation

In this stage of the algorithm approximations of degree $N-1$ are generated for degree N curves and the characteristics such as convex hull property of the Bernstein polynomial basis are exploited to estimate the maximum error present in the approximation. This section describes the equations involved in degree reducing and degree elevating Bernstein polynomials.

Given a degree N algebraic curve in Bernstein form, an exact representation of this curve can be created using a degree $N+1$ Bernstein polynomial basis [5]. Mathematically, this means the expression

$$\sum_{i,j=0}^{i+j \leq (N+1)} \frac{(N+1)!}{i!j!(N+1-i-j)!} x^i y^j (1-x-y)^{N+1-i-j} h_{ij}
\tag{13}$$

is equivalent to

$$\sum_{i,j=0}^{i+j \leq N} \frac{N!}{i!j!(N-i-j)!} x^i y^j (1-x-y)^{N-i-j} b_{ij}
\tag{14}$$

This degree augmentation process, shown in the following equations, defines the coefficients of the degree $N+1$ expression in terms of those from the degree N equation:

$$h_{N+1,0,0} = b_{N,0,0},$$

$$h_{0,N+1,0} = b_{0,N,0},$$

$$h_{0,0,N+1} = b_{0,0,N}$$

$$h_{i,j,k} = \frac{i * b_{i-1,j,k} + j * b_{i,j-1,k} + k * b_{i,j,k-1}}{N+1}, i+j+k = N+1, \quad (15)$$

Similarly, the Bernstein polynomial formulation can be used to produce a lower degree polynomial approximation [6]. The degree reduction process is summarized below:

$$l_{N-1,0,0} = b_{N,0,0},$$

$$l_{0,N-1,0} = b_{0,N,0},$$

$$l_{0,0,N-1} = b_{0,0,N}$$

$$l_{i-1,j,k}^1 = \frac{N * b_{i,j,k} - j * l_{i,j-1,k}^1 - k * l_{i,j,k-1}^1}{i}, i \neq 1 \text{ and } i \geq j, k$$

$$l_{i,j-1,k}^2 = \frac{N * b_{i,j,k} - i * l_{i-1,j,k}^2 - k * l_{i,j,k-1}^2}{j}, j \neq 1 \text{ and } j \geq i, k$$

$$l_{i,j,k-1}^3 = \frac{N * b_{i,j,k} - i * l_{i-1,j,k}^3 - j * l_{i,j-1,k}^3}{k}, k \neq 1 \text{ and } k \geq i, j \quad (16)$$

Unlike degree elevation, the coefficients in degree reduction are defined only in terms of previously computed coefficients, and all coefficients with negative subscripts are zero. When any two or all three indices are equal, the components given by each of the corresponding equations are averaged to define a single value. Note that if the degree of a polynomial is first elevated and subsequently lowered, the original polynomial coefficients are retrieved.

Once the degree reduction procedure has been applied to the algebraic curve $f(x, y) = 0$ and an approximation $g(x, y)$ is generated, an estimate of the approximation error is required. An upper bound on the error can be derived from a combination of difference values ($\Delta z = f - g$) and directional derivative information taken from the two single valued surface equations $z = f(x, y)$ and $z = g(x, y)$ [7].

To begin, the degree elevation procedure is invoked to ensure f and g have the same polynomial degree, thereby assuring the same control point lattice over the triangle. Applying the convex hull property, the maximum difference between the two surfaces $z = f(x, y)$ and $z = g(x, y)$ is bounded by the largest difference found between the two control nets:

$$|\Delta z_{\max}| = \max |f_{ij} - g_{ij}| \quad (17)$$

Tangent plane and normal information can be derived from the surface equations [5, 8]. This information is used to relate the largest surface difference, given in the above equation, to the difference between the two algebraic curves. If point P is located on the curve approximation $g = 0$, the corresponding point on $f = 0$ has to be located. Figure 3 illustrates that there must exist

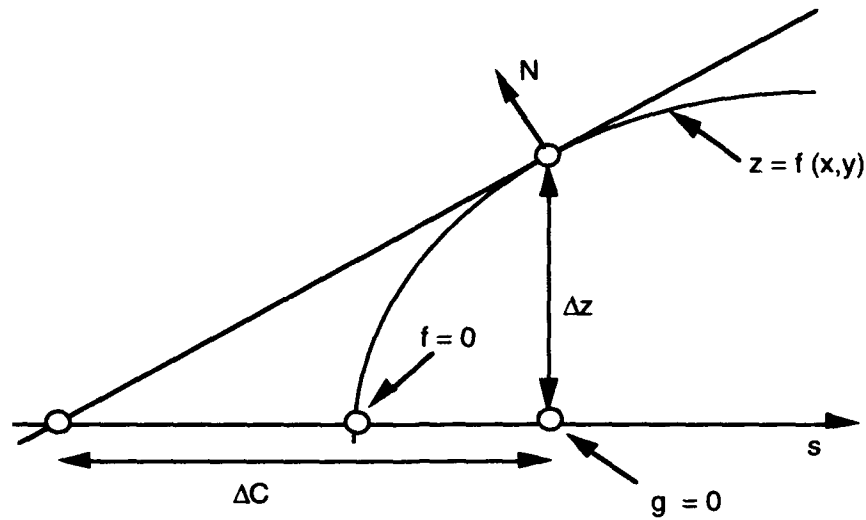


Figure 3. Error estimation.

a point on $f = 0$ at least within a distance ΔC , where θ is the smallest angle between the tangent plane and a direction s defined in the x - y plane, and ΔC is given by the equation

$$\Delta C = \frac{\Delta z}{\tan \theta} \quad (18)$$

Since the surfaces are single valued, $\tan \theta$ defines the value of the directional derivative, $\frac{dz}{ds}$, of the function $z = f(x, y)$ with respect to the direction s . If the original Bernstein triangle with its Bernstein coefficients is called the original patch, then the Bernstein coefficients of the directional derivative patch can be calculated from the original patch using the following equation (for direction s shown in Figure 4):

$$b_{i,j} = N * (B_{i,j+1} - B_{i,j}), \quad (19)$$

where $i+j \leq (N-1)$ and N is the degree of the original patch.

The convex hull property is applied to the directional derivative patches of $f(x, y)$ and $g(x, y)$ to determine a minimum value for $\tan \theta$. Combining the maximum surface difference with the minimum value of $\tan \theta$, a single error bound is produced:

$$e_{\max} \leq \Delta C = \frac{|\Delta z_{ij}|_{\max}}{|(dz_{ij}/ds)_{\min}|} \quad (20)$$

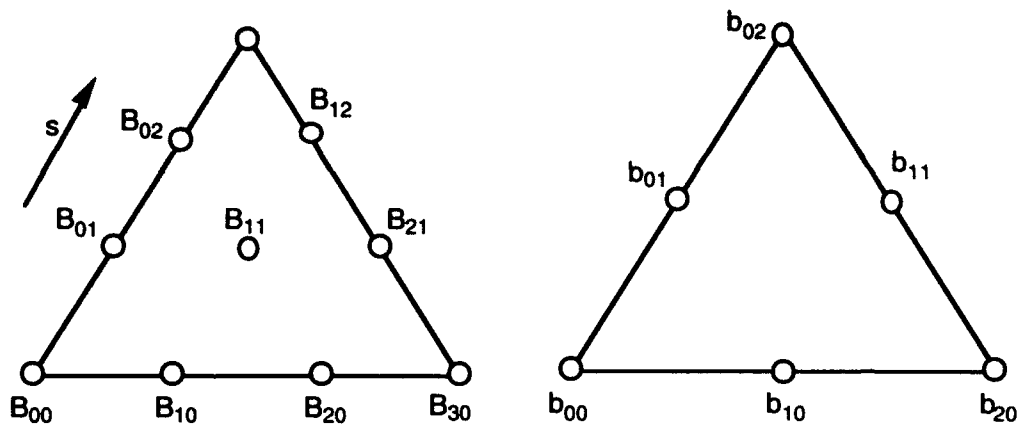


Figure 4. Original patch and its directional derivative patch.

A tighter error bound, but computationally more expensive, can be obtained by calculating the error at all the control points. If the error estimate is not within the specified limits, the triangle must be subdivided. Subdivision techniques are discussed in the next section.

Subdivision

The subdivision stage of the algorithm is reached under two sets of circumstances. When the given function is not monotonic with respect to any edge of the triangle, the triangle is subdivided to generate new sets of edges. The second condition is reached when an unacceptable approximation error is present. The following equations define the procedure for calculating Bernstein coefficients after subdivision [7]:

$$b_{i,j,k}^0(u,v,w) \equiv b_{i,j,k}, \quad (21)$$

where $i+j+k = N$, and

$$b_{i,j,k}^m(u,v,w) = ub_{i+1,j,k}^{m-1}(u,v,w) + vb_{i,j+1,k}^{m-1}(u,v,w) + wb_{i,j,k+1}^{m-1}(u,v,w) \quad (22)$$

where $i+j+k = N-m$.

The geometric interpretation of the recursion process is shown in Figure 5. In general, sets of control points from a degree k control net are combined three at a time, weighted by the barycentric coordinates, to generate a degree $k-1$ control net. This process is repeated N times for a degree N Bernstein surface, ultimately producing a single value which is the desired point on the surface. The three sets of vertices $b_{0,j,k}^i(u,v,w)$, $b_{i,0,k}^j(u,v,w)$ and $b_{i,j,0}^k(u,v,w)$ define the control nets for the new surface patches generated by subdividing the surface at the point with barycentric coordinates (u,v,w) .

Resolution of Singularities

A singular point is a point on the curve where the function and its first partial derivatives vanish. One may assume that a region contains a singularity if the side of the triangle becomes smaller than the approximation tolerance. When a region is discovered to be near a singularity, the following quadratic transformation is used:

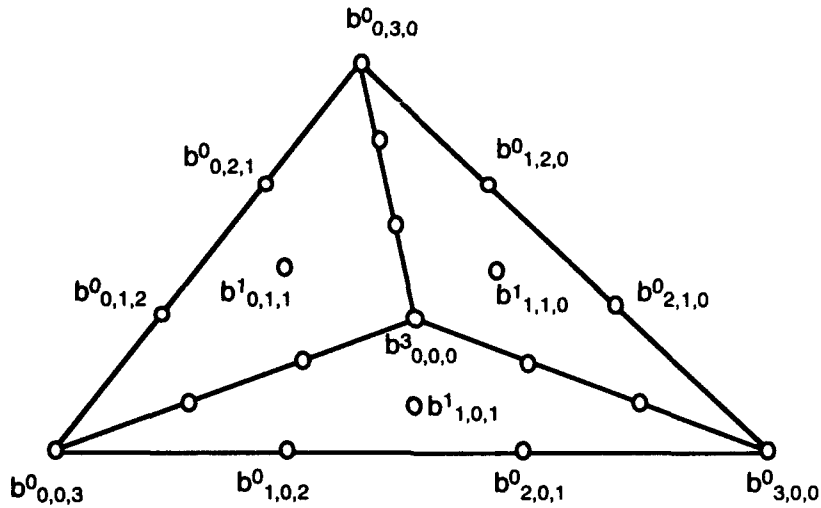


Figure 5. Subdivision of a bivariate Bernstein polynomial.

$$x = x$$

$$y = \frac{y}{x} \quad (23)$$

A piecewise linear approximation is generated near singularities by numerically marching along the various branches of the proper transform. The sequence of points generated are then mapped back to the original coordinate system by reversing the quadratic transformation.

Examples

Examples are presented in this section demonstrating the approximation of a cross-section of a torus using a collection of second degree curves. The curve traces were generated using a collection of procedures written in the C programming language and executed on a SunTM SparcStation 2. In each of the examples, approximation is developed over a triangular region enclosing the closed curve.

The torus used for slicing is centered at (0, 0, 0) and the axis of the torus is straight line given by the equation $y = x$. The radius of the torus is 3, and the radius of the disc rotated about the axis to generate the torus is 0.7.

Figure 6 shows the cross-section of the torus at $z = 2.2$. The number of quadratic curve segments in this approximation is 306.

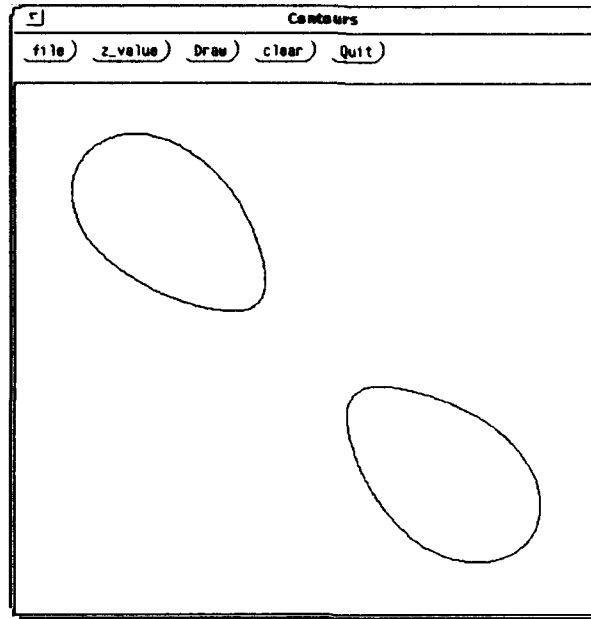


Figure 6. Torus sliced at $z = 2.2$.

Figure 7 shows the cross-section of the torus at $z = 2.3$ (the singularity case). The number of quadratic curve segments in this approximation is 318.

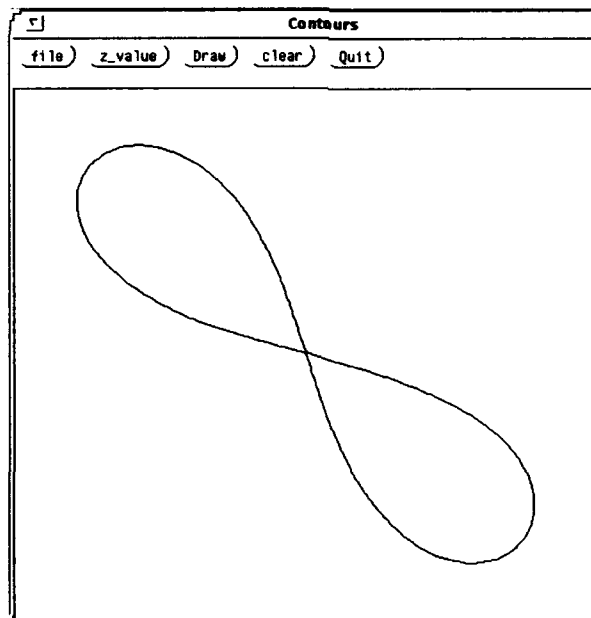


Figure 7. Torus sliced at $z = 2.3$.

Conclusions

This paper discusses a method to directly process Constructive Solid Geometry representations and obtain contour files. Aspects involved in slicing higher degree surfaces, in particular the torus, are highlighted. The algorithm is applicable to other higher degree surfaces

as well, including rational bicubic parametric surfaces. The algorithm provides a rational basis for approximating geometry for SFF applications.

References

1. Sashidhar, Guduri., Crawford, Richard H. and Beaman, Joseph J., "A Method to Generate Exact Contour Files for Solid Freeform Fabrication", *Proceedings of Solid Freeform Fabrication Symposium*, 1992, Marcus, Harris L., Beaman, Joseph J., Barlow, Joel W., Bourell, David L., Crawford, Richard H., eds., Austin, TX, August 3-5. pp. 95-101.
2. Waggenspack, Warren N. Jr., Anderson, David C., "Converting Standard Bivariate Polynomials to Bernstein Form Over Arbitrary Triangular Regions", *Computer Aided Design*, Vol. 18, No 10, 1986. pp 529-532.
3. Waggenspack, Warren N. Jr., Anderson, David C., "Piecewise Parametric Approximations for Algebraic Curves", *Computer Aided Geometric Design*, 1989. pp 33-53.
4. Abhayankar, Shreeram S. and Bajaj, Chanderjit, "Automatic Rational Parametrization of Curves and Surfaces I: Conics and Conicoids", *Computer Aided Design*, Vol. 19, No 1, 1987. pp 11-14.
5. Farin, Gerald, "Triangular Bernstein-Bezier Patches", Department of Mathematics, University of Utah, Salt Lake City, Utah, USA, 1986.
6. Peterson, Carl S., "Adaptive Contouring of Three-Dimensional Surfaces", *Computer Aided Geometric Design*, Vol. 1, 1984. pp. 61-74.
7. Sederberg, Thomas W., "Planar Piecewise Algebraic Curves", *Computer Aided Geometric Design*, Vol. 1, No 4, December 1984. pp 241-255.
8. Farin, Gerald, "Bezier Polynomials Over Triangles and Construction of Piecewise C^1 Polynomials", Tech Report TR/91, Department of Mathematics, Brunel University, Uxbridge, Middlesex, UK, 1980.

Indirect Metal Composite Part Manufacture Using the SLS Process

James R. Tobin¹, B. Badrinarayan², J. W. Barlow², J. J. Beaman¹, and D. L. Bourell^{1,3}

1. Department of Mechanical Engineering

2. Department of Chemical Engineering

3. The Center for Materials Science and Engineering

ABSTRACT

As a near term alternative process to direct metal sintering, an intermediate polymer binder is combined with powder to produce green preforms with the Selective Laser Sintering (SLS) process. To produce parts with desirable strength and dimensional control, the binder is gradually removed from the green preform (obtained from the SLS process), and the remaining form is lightly bonded. This porous part is then infiltrated. Final part density, shrinkage, and strength data are presented. An injection mold insert was fabricated from this material and used to mold ABS, PMMA, polyester, and polycarbonate parts. To date, the mold insert has survived 176 shots at injection pressures up to 35,000 psi and melt temperatures of up to 300°C.

INTRODUCTION

Molds to be used for the injection molding of thermoplastics are traditionally manufactured from cast metal by precision metal cutting devices. The machining and polishing times are quite extensive and the costs are correspondingly high. These high costs and production times effectively preclude the preparation of prototype plastic parts by injection molding. Prototype plastic parts are consequently usually manufactured by other processes. Unfortunately, the properties of such parts may not be truly representative of those of injection molded parts due to the thermal stresses and molecular orientation inherent to the injection molding process.

Clearly, there is a great need for low cost, low production time molds which could produce the 50 - 500 plastic parts needed to prove a design. The University of Texas at Austin is presently investigating new material systems and processes that potentially permit the rapid fabrication of molds by SLS and subsequent processes. In addition to cost and time savings, potential advantages to mold making by the SLS process include: incorporation of custom cooling channels and other features that are not easily machined, ease of manufacturing duplicate molds, opportunity to evaluate the runner system prior to machining a production mold, and ease of cavity design by use of commercial CAD solid modelers.

Two of the important goals of the material system and process include: minimal, predictable, shrinkage from original CAD design, and sufficient strength for withstanding injection pressures and temperatures. With most powder processes, there is usually a trade-off between minimal shrinkage and strength. In an attempt to minimize shrinkage issues and still have enough strength, a powder/infiltrant system was chosen as the first material system for investigation.

DISCUSSION

The target process for manufacturing molds in the SLS process is outlined in figure 1:

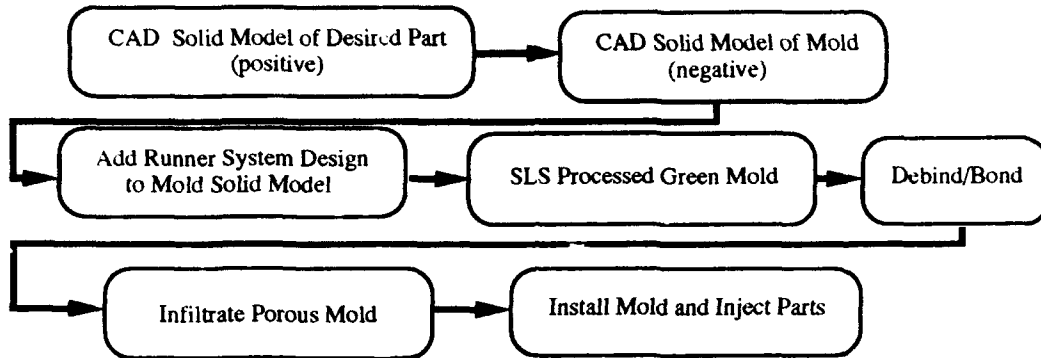


Figure 1. Process for fabricating molds

In an effort to arrive at this process, the material system and bonding cycle performance needed to be evaluated. To determine preferred bonding cycle and material system, green three point bend bars and 1 1/4" thick blocks were fabricated with different powders. Different bonding cycles were evaluated to determine shrinkage and strength of the fired bars prior to infiltration. Strength measurements were also taken on three point bend bars that were infiltrated with a total of four different infiltrant systems.

An initial preferred powder/infiltrant system was selected. Prior to fabrication of the mold insert using the SLS process, a mold insert was fabricated with the process outlined in figure 2. The insert was fabricated in this manner because the selective laser sintering equipment available at the university is not capable of manufacturing parts of the required scale. However, strength tests on bars made both in the SLS process and in the oven show the resultant material systems to be effectively the same.

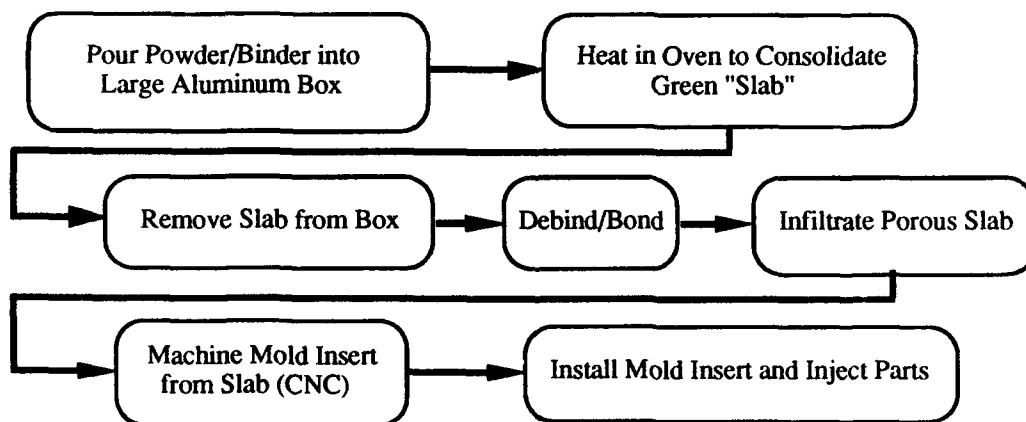


Figure 2. Process for fabricating molds for material evaluation

Figure 3 shows a photograph of a completed mold assembly. For testing purposes, a standard Master Unit Die plaque mold was modified by replacing the steel plaque cavity with the insert. As shown in the foreground, the insert is 8.4" x 5.3" x 0.6" and the part cavity is 5" x 2.5" x 0.25". It is equipped with seven standard ejector pins (4 through holes in the part cavity, and 3 through holes in the runner cavity). The runner is 1/4" in diameter and the letters are 1/16" deep. The insert was not channeled for water cooling. For this reason, the cooling times were kept long (near 55 seconds).

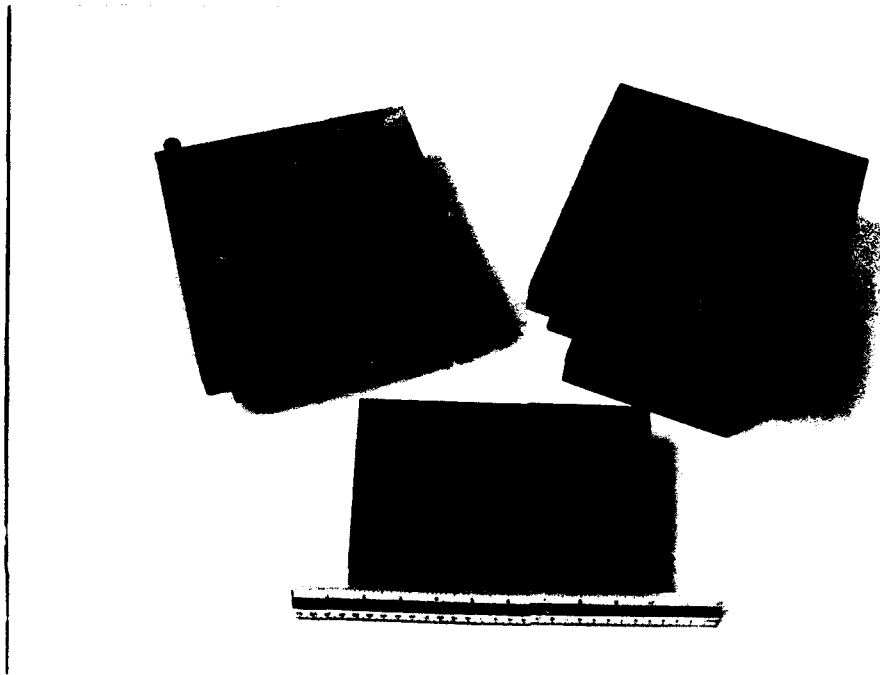


Figure 3. Mold Assembly

RESULTS

Table 1 shows the average density and strength measurements taken on 10 SLS processed three point bend bars with the same material used to fabricate the tooling insert.

TABLE 1
SLS Processed Three Point Bend Bar Data

	Relative Density (%)	Modulus of Rupture (psi)
Green:	51	421
Porous :	32	95
Infiltrated:	98	3,841

These same bars demonstrated linear shrinkages of 0.45% in the X direction, 0.82% in the Y direction, and 1.41% in the Z direction. To date, the 1 1/4" thick blocks have also shown linear shrinkages of less than 2% in all directions after bonding.

Table 2 shows the molding conditions used to inject the first 176 shots into the mold insert.

TABLE 2
Molding Conditions

Polymer	# of Shots	Peak Inj. Press. (psi)	Temperature (°C) zones 1, 2, 3, & 4	Injection Time (sec)
ABS	101	8000	200, 190, 200, 200	3
PMMA	28	35000	175, 170, 160, 160	3
Kodak A150	22	35000	275, 275, 275, 275	4
PC	25	35000	245, 275, 300, 300	4

Additionally, for all plastics, the injection hold pressure time was set to 2 seconds and the cooling time was set to 55 seconds.

Observations of the molded parts show only 2 defects during the 176 shot run. Both of these defects occurred while molding PMMA. At shot 105 a hairline fracture (perhaps surface) started at one of the ejector pins and grew over the next 25 shots to a total length of approximately one inch. The crack did not noticeably propagate further after that point and did not affect the performance of the mold other than the faint mark left in the moldings. At shot 123, a small but noticeable chip of material around another ejector pin broke loose. This breakage progressed through shot 127 to a total size of approximately 1/16" x 3/16" x 1/16". This defect, similar to the hairline fracture, did not grow further. We are currently in the process of evaluating mold erosion by measuring dimensions of the molded parts.

CONCLUSIONS

The generally low shrinkages associated with post processing green shapes suggest acceptably good geometric fidelity for successful molding of plastic parts. Our evaluation of the mold material is presently incomplete, however, these initial results are most encouraging. They suggest that even materials with relatively low strengths can be adequate for prototype insert service, provided reasonable care is exercised in the overall tool design. Mold erosion does not qualitatively appear to be significant. The deficiencies seen near 2 out of 7 ejector pins are of some concern. We are presently developing a higher strength material that could correct this problem. Ejector pin sleeves could also be installed in future designs.

We intend to prepare new inserts with cooling channels and various geometric features to gain additional understanding of the relationships between insert material properties, mold design, and molding conditions

ACKNOWLEDGMENTS

The authors gratefully acknowledge the financial and general support of the DTM Corporation, Austin, Texas, for portions of this work. J. Tobin especially wishes to thank Brian Carr of the DTM Corporation and Hank Franklin of the UT Austin Mechanical Engineering Machine Shop for their assistance.

Solid Freeform Fabrication of Silicon Carbide Shapes by Selective Laser Reaction Sintering (SLRS)

B.R. Birmingham and H.L. Marcus

*Center for Materials Science and Engineering
The University of Texas at Austin
Austin, Texas 78712*

Abstract

This paper describes an investigation of the production of silicon carbide shapes by Selective Laser Reaction Sintering (SLRS). One type of SLRS process, which combines laser sintering of silicon with acetylene decomposition, is briefly outlined, and the mechanisms important to the process are discussed. A series of test shapes are made at different acetylene pressures to determine pressure effects on conversion to silicon carbide. X-ray diffraction spectroscopy is used for bulk analysis of the shapes, and Auger electron spectroscopy is used for surface analysis. The results indicate that acetylene pressure does have a strong effect on silicon conversion to silicon carbide, and SLRS can be used successfully to make silicon carbide shapes.

Introduction

Selective Laser Reaction Sintering as a Solid Freeform Fabrication (SFF) technique and the processing equipment used for this study have been previously reported [1]. Briefly, the technique uses a scanning laser to selectively sinter a thin layer of powder. Laser sintering is accompanied by a reaction between sintering powders or sintering powder(s) and a gas precursor. The sintering/reaction combination results in a solid layer of material compositionally different from the powder source(s). Successive layers of powder are spread and selectively laser reaction sintered to build up the desired shape.

The purpose of this study is to determine if silicon carbide shapes can be made by a powder/gas precursor type SLRS process. For this study, the source powder is -325 mesh (<44 μ m), >99.5% purity silicon powder, and the gas precursor is high purity acetylene (C₂H₂). The basic mechanisms of the process are discussed with emphasis on possible rate limitations. A series of tests are run to determine the effect of one process variable, gas pressure, on the overall process. Results are presented and discussed.

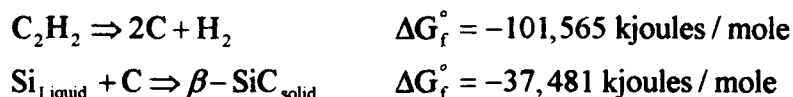
The Silicon-Acetylene SLRS Mechanism

The proposed mechanism can be summarized as follows.

- 1) A scanning CO₂ laser locally heats the silicon powder bed.
- 2) The silicon powder is heated and melted.
- 3) C₂H₂ gas is adsorbed onto the liquid silicon surface where it decomposes to carbon and hydrogen.
- 4) Hydrogen gas desorbs as H₂.
- 5) Adsorbed carbon diffuses rapidly into the liquid silicon.
- 6) Carbon reacts with liquid silicon and solidifies as SiC.

It is important to note here that step two (2) is crucial to the success of this process. The typical material being selectively laser sintered has seconds to bond and densify. Solid state sintering mechanisms are ineffective in this time frame because solid-state diffusion effects, which are five or six orders of magnitude slower than liquid diffusion rates, are negligible [2,3]. The formation of a liquid phase, in this case liquid silicon, is critical because it can lead to solution-reprecipitation processes that are rapid enough to achieve particle bonding and densification in a SLRS time frame. A thermal model of the laser sintering system used in this study indicates surface temperatures in excess of 2000°C are readily achievable at the laser beam's focal point [4]. Silicon has a melting temperature of 1413°C. Therefore, a liquid phase can easily be created.

Thermodynamically, the decomposition of C₂H₂ and the reaction between liquid silicon and carbon to form SiC are both energetically favorable. Using 2000°C as the reaction temperature, the free energies of formation are [5];



Basic kinetic requirements of the C₂H₂ decomposition and carbon deposition steps can be established using a simple model of a laser beam moving across a surface, see

Figure 1. This model establishes a beam residence time of one second for a single pass of the laser. Scan overlap increases total beam residence time to approximately ten seconds.

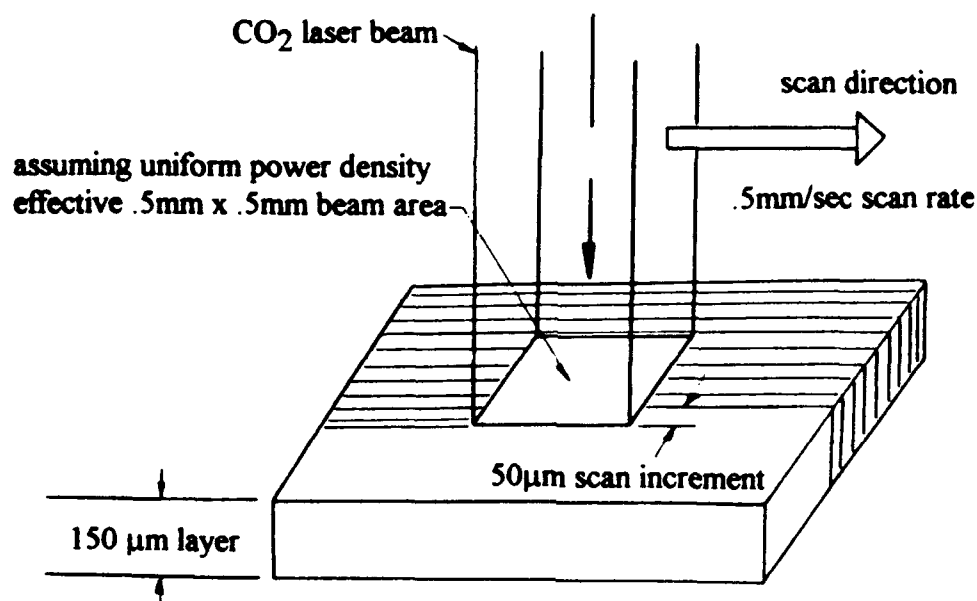


Figure 1: A simple scanning model used to determine required carbon deposition rate

Assuming a typical sintered layer thickness of 150μm and a powder porosity of 50 percent, the model indicates that a carbon deposition rate of 3μm/sec is necessary to supply the volume of silicon under the beam with enough carbon to allow full conversion to SiC. Leyendecker et al. [6] report laser induced carbon deposition rates from acetylene of 2-10μm/sec when at the temperatures and pressures used for this SLRS study, and Zong [7] reports localized rates as high as 1mm/sec. Comparing the reported rates with those required by the model, it appears that carbon deposition rate will not limit the overall process. However, it should be noted that both studies indicate that carbon deposition decreases as pressure decreases. It follows that there is some low precursor pressure below which carbon deposition rate becomes the overall rate limiting factor.

The rate that surface carbon diffuses into liquid silicon can be determined using a relationship that describes a concentration profile created by unsteady state diffusion in a single phase [8].

$$\frac{C_t - C_o}{C_s - C_o} = 1 - \text{erf}(y / \sqrt{Dt})$$

y = distance into the bulk,

C_s = surface concentration

D = diffusivity of carbon in liquid silicon = $2 \times 10^{-4} \text{cm}^2/\text{sec}$ [2]

The silicon-carbon phase diagram [9], Figure 2, suggests behavior that will allow the final step of this process, the conversion of silicon and carbon to SiC.

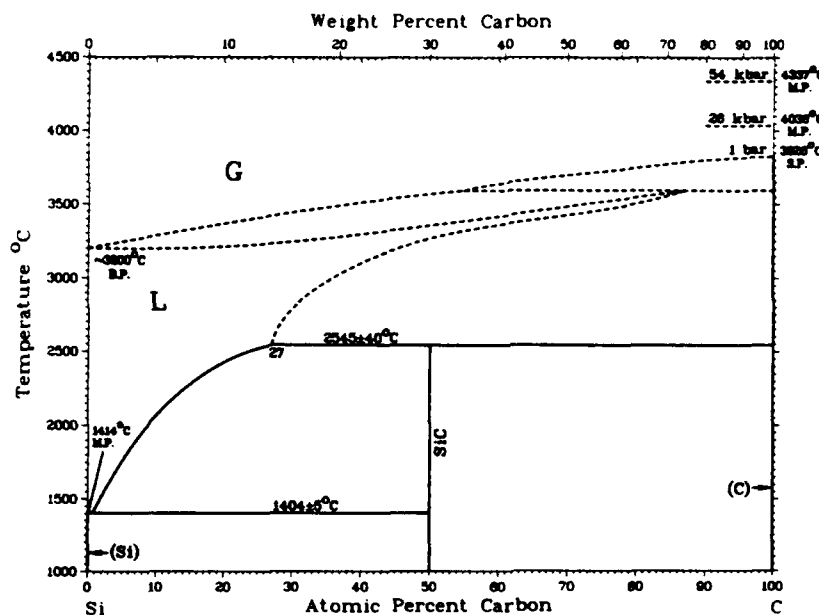


Figure 2: Silicon-Carbon binary phase diagram [9]

Above the eutectic reaction temperature at 1404 °C, carbon solubility in the liquid silicon phase dramatically increases. At 2000 °C, the Si-C phase diagram indicates a carbon solubility of approximately ten atomic percent in the liquid phase. Because of this high solubility, adsorbed carbon can diffuse into the liquid phase and react to form SiC. As predicted by the lever rule, the conversion of the saturated liquid silicon phase to SiC would continue as the liquid phase cooled. Because of scan overlap the same region will be exposed to near maximum temperatures repeatedly. Each time, some of the remaining silicon will melt and react with diffusing carbon to form more SiC. It is difficult to quantitatively predict the total amount of conversion, but amounts in excess of 50 atomic percent might be expected.

Experimental Setup

A series of single layer test coupons were produced to determine the effects of an acetylene atmosphere on the laser sintering of silicon. All operating parameters were held constant except atmosphere. The laser was scanned at 500 μ m/sec with a 50 μ m spacing between scan lines to generate a rectangular 5mm x 5mm scanned area. Each coupon area was scanned twice, using an out and back type scan, with laser power held at 1.8watts and 2.8watts, respectively. The atmosphere was provided by first evacuating the system to $<10^{-3}$ Torr and then filling with acetylene to the desired pressure. Five different pressures of acetylene were used.

Coupon 1:	700 Torr C ₂ H ₂	(1 atmosphere = 760 Torr)
Coupon 2:	380 Torr C ₂ H ₂	
Coupon 3:	200 Torr C ₂ H ₂	
Coupon 4:	100 Torr C ₂ H ₂	
Coupon 5:	50 Torr C ₂ H ₂	

Results

X-ray diffraction spectroscopy was used for bulk phase analysis of the sintered test coupons. Figure 3 shows the diffraction pattern taken from coupon 4 .

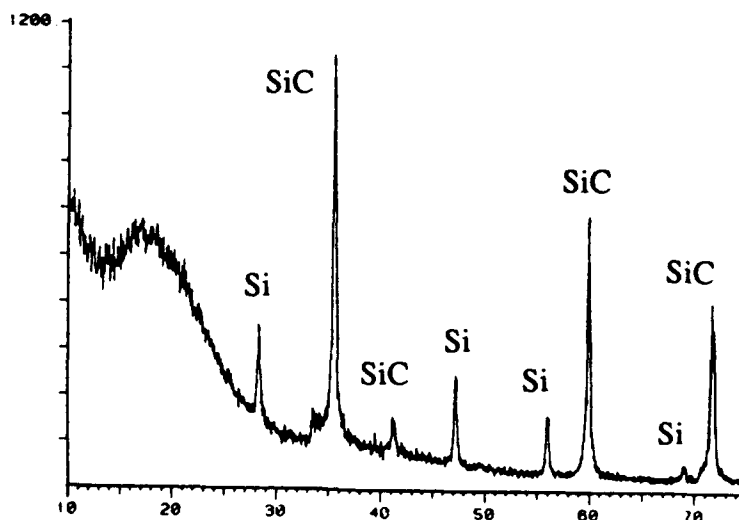


Figure 3: X-ray diffraction pattern taken of coupon 4 using Cu_Kα x-rays.

Diffraction peaks for silicon and β -SiC are present. SiC conversion was semi-quantitatively determined for each coupon by comparing diffraction pattern relative peak

heights to a silicon/SiC standard run on the same x-ray equipment. Figure 4 shows a plot of SiC conversion versus pressure data obtained from the coupons.

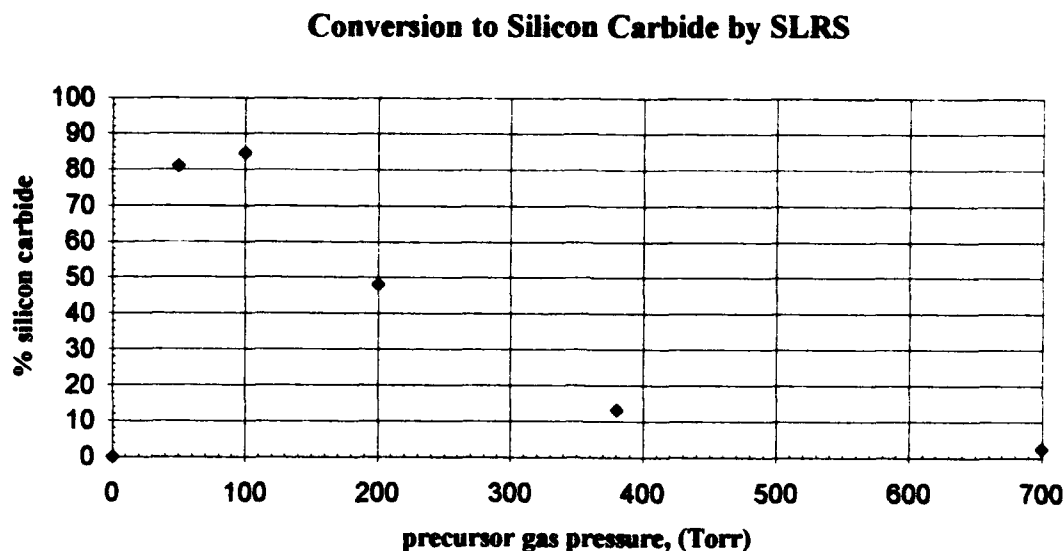


Figure 4: SiC conversion versus acetylene pressure.

Auger electron spectroscopy was used to determine the surface chemistries of the coupons. Surface spectra were taken, and then the samples were sputtered to determine concentration profiles into the bulk. Figure 5 is a plot of chemical concentration versus sputter time for coupon 4.

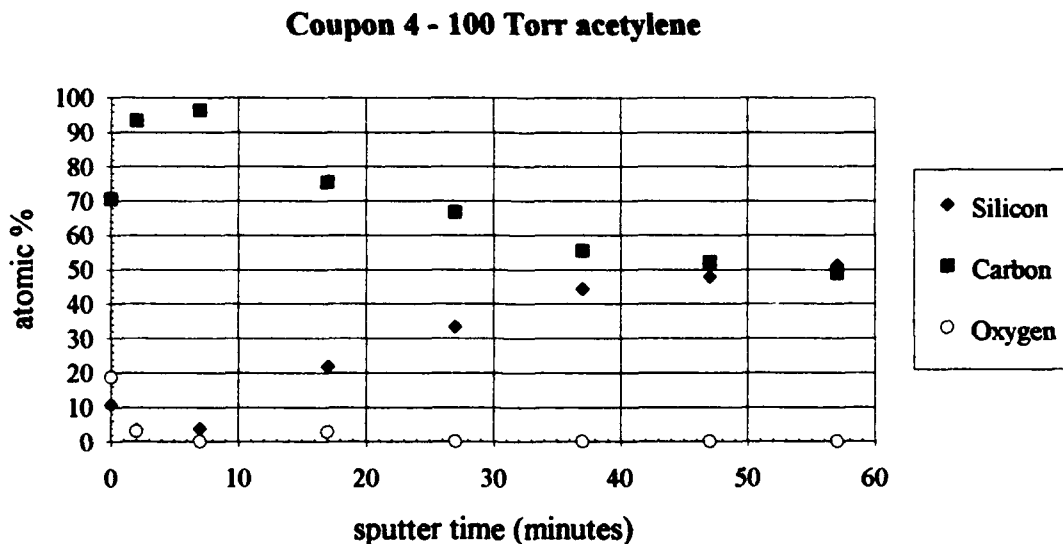


Figure 5: Chemical concentration versus sputter time for coupon 4.

The concentration profile indicates that a predominantly carbon surface gradually gives way to SiC stoichiometry. Auger peak shape and energy changes characteristic of carbon in SiC [10] were observed as stoichiometry was approached. All five coupons showed the same general behavior.

Discussion

The plot of conversion rate versus precursor pressure, Figure 4, clearly shows a maxima occurring at ~ 100 Torr C_2H_2 pressure. The decrease in conversion below this pressure can be attributed to the decrease in carbon deposition with pressure as predicted by Leyendecker et al [5]. The reduction in conversion rate as pressure increases above 100 Torr is more difficult to explain. One explanation could be that higher pressures generate initially high carbon deposition rates that cause the formation of a solid diffusion barrier at the surface of the coupons. The barrier could be SiC or carbon or a mixture of both. This barrier would then prevent further conversion of silicon to SiC by limiting the diffusion of carbon and/or silicon. The validity of this mechanism is dubious because of the lack of evidence of an increase in carbon coverage with pressure. If carbon deposition on the surface had increased with pressure as predicted, but conversion to silicon carbide was diminished because of limited diffusion, then there would have been increasing accumulations of carbon on the surfaces of the coupons. This was not detected by x-ray or Auger analysis. Another explanation focuses on a reduction in temperature at the beam focus. Initially high deposition rates might promote a surface structure with reduced infrared absorptivity and/or increased thermal conductivity. Reduced absorptivity would reduce the effective power of the laser beam. Increased thermal conductivity would increase heat flow away from the beam area. Both of these effects would lower subsequent surface temperatures, and thereby reduce carbon deposition and conversion to SiC.

Structurally, the test coupons had successfully been laser sintered to create porous 5mm x 5mm squares approximately 150 μ m thick. No mechanical testing was performed, but the coupons exhibited sufficient strength for handling. Figure 6, a SEM micrograph of coupon 3, reveals the carbon coated surface structures typical of all the coupons. A sputtered region of the same coupon, seen in Figure 7 reveals the underlying material. Note the crystalline structures indicative of a solution-reprecipitation process.



1 μm

Figure 6: Surface of coupon 3



1 μm

Figure 7: Underlying surface of coupon 3

As an additional test of this SLRS process, the operating parameters which yielded highest conversion to SiC in the single layer tests were used to make a multiple layer structure. The seven layer rectangular solid can be seen in Figure 8.



Figure 8: 5mm x 5mm x 1mm SiC shape made by SLRS, 100 Torr C_2H_2 pressure

Conclusions

Single layer and multiple layer shapes with high SiC content were fabricated using silicon/acetylene SLRS. Precursor gas pressure was discovered to have a large but yet unexplained effect on the conversion of silicon to SiC. Work will now proceed to better

understand the mechanisms of the process so that operating parameters can be controlled to produce denser, stronger, more fully converted multiple layer SiC shapes.

Acknowledgments

Thanks go to the Office of Naval Research, grant # N00014-92-J-1514, for support of this work.

References

1. B.R. Birmingham, J.V. Tompkins, G. Zong, and H.L. Marcus, "Development of a Selective Laser Reaction Sintering Workstation," Proceedings of the Solid Freeform Fabrication Symposium, Austin, Texas, August, 1992, pp 147-153.
2. *Silicon Chemical Etching*, edited by J. Grabmair, Berlin, Springer-Verlag, 1982, p 62.
3. *Ibid*, p 28.
4. G. Zong, "Solid Freeform Fabrication Using Gas Phase Selective Area Laser Deposition," Ph.D. Dissertation, The University of Texas at Austin, Austin, Texas, 1991, pp 90-105.
5. *JANAF Thermochemical Tables*, 2nd edition, edited by D.R. Shull and H. Prophet et al., NSRDS-NBS37, U.S. Department of Commerce, National Bureau of Standards.
6. G. Leyendecker, H. Noll, D. Bauerle, P. Geittner, and H. Lydtin, "Rapid Determination of Apparent Activation Energies in Chemical Vapor Deposition," Journal of Electrochemical Society: Solid-State Science and Technology, January, 1983, pp 157-160.
7. G. Zong, "Solid Freeform Fabrication Using Gas Phase Selective Area Laser Deposition," Ph.D. Dissertation, The University of Texas at Austin, Austin, Texas, 1991, p 76.
8. F.D. Richardson, *Physical Chemistry of Melts in Metallurgy Vol. 2*, London, Academic Press, 1974, pp 398-399.
9. *Binary Alloy Phase Diagrams*, 2nd edition, T.B. Massalski editor-in-chief, Ohio, ASM International, 1990, pp 882-883.
10. J.C. Riviere, *The Analyst*, **108**, 1983, p 649.

SUPERSOLIDUS LIQUID PHASE SELECTIVE LASER SINTERING OF PREALLOYED BRONZE POWDER

Gopalakrishna B. Prabhu and David L. Bourell,
Center for Materials Science and Engineering,
The University of Texas at Austin, Austin TX 78712.

Abstract

The use of Selective Laser Sintering (SLS) as a method of Solid Freeform Fabrication (SFF) in the direct sintering of metal powders to form the final part has been investigated earlier [1,2,3]. The phenomenon of supersolidus liquid phase sintering (SLPS) is studied using prealloyed bronze powder. The influence of laser parameters, bed temperature and secondary heat treatment on the density and the dimensional stability of the final product are discussed.

Introduction

Supersolidus Liquid Phase Sintering (SLPS) involves heating prealloyed powder to a temperature between the solidus and the liquidus to attain partial melting [4]. Densification occurs by capillary-induced rearrangement and solution reprecipitation in the partially liquid particles and is shown in Figure 1. Liquid forms along grain boundaries and regions of contact. The sintering temperature and alloy composition are thus the most important process variables needing optimization since they dictate the liquid fraction. A typical amount of liquid is 30% which is slightly higher than that observed in liquid phase sintering of mixed powders [5,6,7]. The requisites for a material system include a higher concentration of the alloying element and steep solidus and liquidus lines. A higher concentration in general gives a larger separation between the solidus and the liquidus and so a larger temperature range to investigate. Steep solidus and liquidus lines are desirable because temperature control becomes less critical as the volume fraction of the liquid does not change rapidly. Taking into account these requisites and making use of phase diagrams, the Cu-Sn system with a nominal composition of 89Cu-11Sn was chosen for study. The phase diagram of the Cu-Sn system is shown in Figure 2.

Experimental Procedure

The SLS technique and the workstations used have been described elsewhere [8,9]. In the present study, the prealloyed bronze powder was sintered using either a Nd-YAG or a CO₂ laser. The main laser parameters are listed in Table 1.

Initial experiments were conducted in a room temperature environment to establish optimum laser parameters. Multilayer parts were made with a laser power of 35 watts and a scan speed of 2.5 cm/sec. Attempts to make parts with higher powers were unsuccessful because of excessive curling of the part due to the presence of residual stresses in the part when it cooled down to room temperature. The next set of experiments were run using a high temperature bed in order to alleviate the residual stresses and to

unsuccessful because of excessive curling of the part due to the presence of residual stresses in the part when it cooled down to room temperature. The next set of experiments were run using a high temperature bed in order to alleviate the residual stresses and to reduce the curling seen earlier. Bed temperatures of 300-500 °C and nitrogen at a flow rate of 60 lit/min were used. Parts were made using both the Nd-YAG and the CO₂ lasers. Post processing heat treatments were performed on some of the parts and the effect on part density was studied. Post-processing involved long-term (12-15 hr) heat treatments at different temperatures (700-800°C) and short-term heat treatments(15 min-1hr) at 830-1000°C in either flowing hydrogen or forming gas (96 N₂ - 4 H₂).

Results and Discussion

Selective Laser Sintering:

Prealloyed bronze powder of nominal composition 89Cu-11Sn shown in Figure 3 with a mean particle size of -150# was used to study supersolidus sintering. The best parameters for laser sintering using a room-temperature bed were determined to be a power of 35 watts, a scan speed of 2.5 cm/sec and a layer thickness of 300 µm. The top surface of the part made is shown in Figure 4. Wetting is not very good. Poor interlayer bonding is seen (Figure 5). This is attributed to the use of low power in sintering the bronze powder. Higher powers could not be used because of the excessive curling of the individual layers on sintering. Sintering carried out in a high-temperature environment yielded much better results. Figure 6 shows the top surface of the part made at 400°C using a laser power of 100 watts and a scan speed of 2.5 cm/sec. Good wetting is seen. The end view of the part made with a bed temperature of 350°C is shown in Figure 7. The layers are barely distinguishable indicating that a high-temperature bed and a higher laser power help in improving interlayer bonding. The densities of the parts were determined. The parts made in a room-temperature environment have densities ranging from 4.21 to 4.27 g/cm³, while those made in a high-temperature environment ranged from 4.75 to 5.65 g/cm³. The influence of bed temperature on part density was studied. The results are shown in figure 8. As the bed temperature increased, the density of the part also increased. This can be attributed to less curling observed because of a decrease in residual stress. However 500°C seemed to be an upper limit of temperature for bed heating, as levelling problems were encountered due to caking of the whole powder bed.

Post-Processing Heat Treatments:

From the phase diagram, prealloyed bronze powder of composition 89Cu-11Sn starts melting at 830°C and melts completely at 1025°C. However, because of the non-equilibrium cooling experienced when powders are produced by atomization, these temperatures for the prealloyed bronze powders may not be very accurate. The list of heat treatments with the post-processing density and physical characteristics are shown in Table 2.

Among the long-term heat treatments involving solid-state diffusion, 800°C for 15 hours was the best heat treatment giving the highest density. For the short-

term heat treatments involving liquid phase formation, 850 °C for 15 minutes was the best heat treatment. Beyond 850 °C swelling and loss of shape were observed. Swelling occurred due to the presence of an excess amount of liquid which causes compact slumping, non-uniform densification and pore coalescence [5,10].

Conclusions

The feasibility of Supersolidus Liquid Phase Sintering has been demonstrated using prealloyed bronze powder. The parts that were produced in a high-temperature environment had improved density and surface finish as compared to parts that were made in a room-temperature environment. Post-processing heat treatments to optimize the part density have been determined. The use of a wetting agent to increase the as-laser-sintered part density and the influence of a higher starting density on post-processed part density needs further study.

Acknowledgements

This research was funded by the DARPA-ONR grant # 26-0679-7750 and DTM Corporation.

References

1. J.A.Manriquez-Frayre and D.L.Bourell, "Selective Laser Sintering of Cu-Pb/Sn solder powders", Solid Freeform Fabrication Symposium Proceedings, 1991.
2. Wendy Weiss and D.L.Bourell, "Selective Laser Sintering to produce Ni-Sn intermetallics", Solid Freeform Fabrication Symposium Proceedings, 1991.
3. Paul W. Haase, Masters Thesis, "Selective Laser Sintering of Metal Powders", The University of Texas at Austin, December 1989.
4. R.M.German, "Supersolidus Liquid Phase Sintering Part-1: Process Review", International Journal of Powder Metallurgy, 26[11], p 23-35.
5. R.M.German, "Powder Metallurgy Science", Metal Powder Industries Federation, 1984, p 146.
6. R.M.German, "Phase Diagrams in Liquid Phase Sintering Treatments", JOM, August 1986, pp 26-29.
7. R.M.German, "The Use of Phase Diagrams in Predicting Sintering Behavior", Conference Proceedings, Horizons of Powder Metallurgy Part-2, 1986 International Powder Metallurgy Conference and Exhibition.
8. Harris L. Marcus, Joseph J. Beaman, Joel W. Barlow and David L. Bourell, "Solid Freeform Fabrication: Powder Processing", American Ceramic Society Bulletin, 69[6], 1990 pp 1030-1031.

9. Harris L. Marcus, Joseph J. Beaman, Joel W. Barlow and David L. Bourell, "From Computer to Component in 15 Minutes: The Integrated Manufacture of Three Dimensional Objects", JOM, 42[4], 1990, p 8.
10. R.M.German, "Liquid Phase Sintering", Plenum Press, New York & London, 1985.
11. Binary Alloy Phase Diagrams, Second Edition, ASM International, 1990.

Table 1: Laser Parameters

Laser	Nd-YAG	CO ₂
Wavelength	1.06 micron	10.6 micron
beam diameter	0.5 mm	4.5 mm
Laser power used	20-60 watts	90-110 watts

Table 2: Post-Processing Heat Treatments

Heat treatment	Starting density (p/pth)	Final density (p/pth)	Physical characteristics
700 °C - 15hrs	45.5 %	54.2%	shape retained
750 °C - 15hrs	45.5%	59.1%	shape retained
800 °C - 15hrs	50%	74.2%	shape retained
830 °C - 15min	48.5%	70.5%	shape retained
850 °C - 15min	47%	73.5%	shape retained
875 °C - 15min	46.5%	-	loss of shape
850 °C - 30min	47%	-	loss of shape
850 °C - 15min	59%	78.1%	shape retained
875 °C - 15min	59%	-	loss of shape

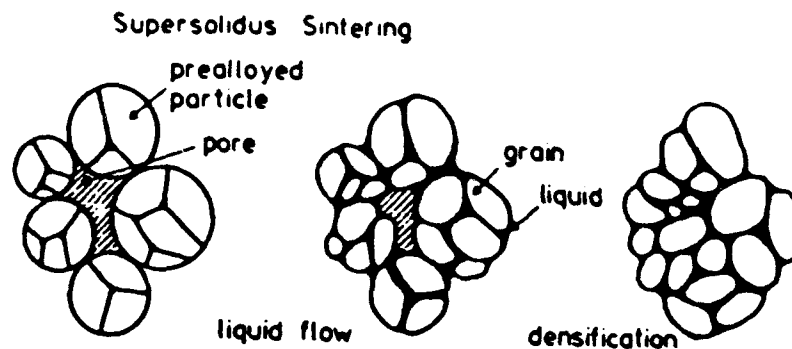


Figure 1: Supersolidus sintering involves the formation of a liquid along the grain boundaries in a prealloyed powder which leads to densification [4].

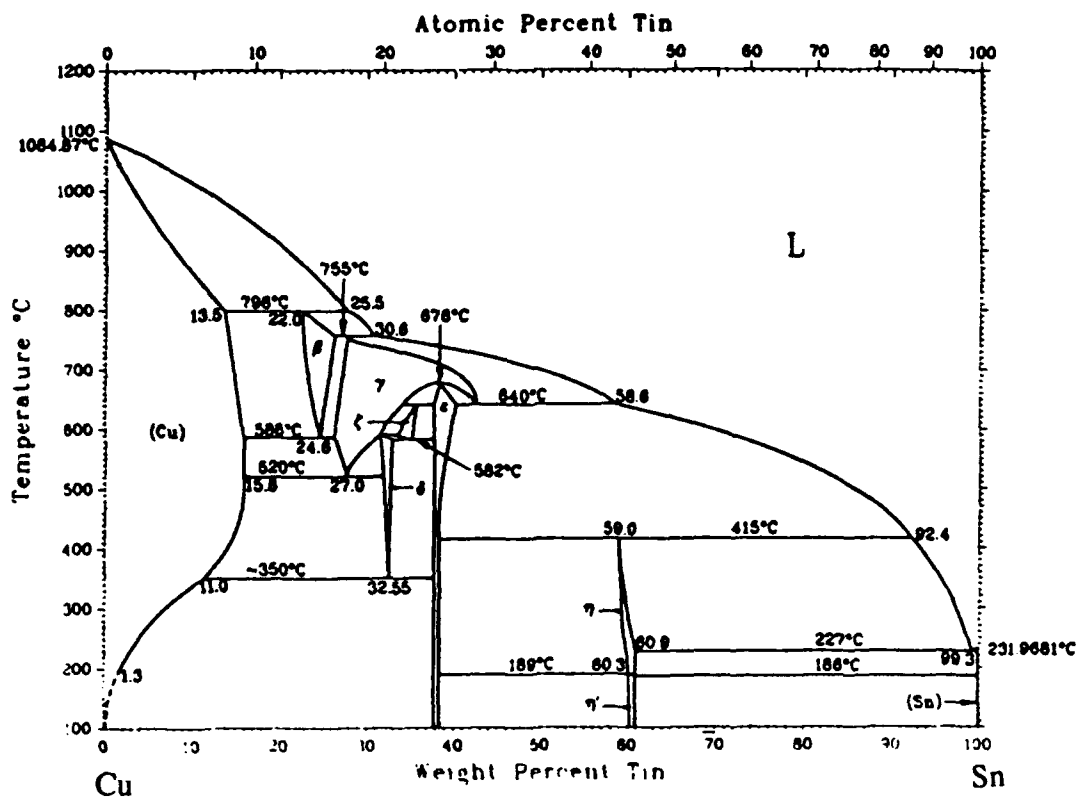


Figure 2: The Cu-Sn phase diagram [11].

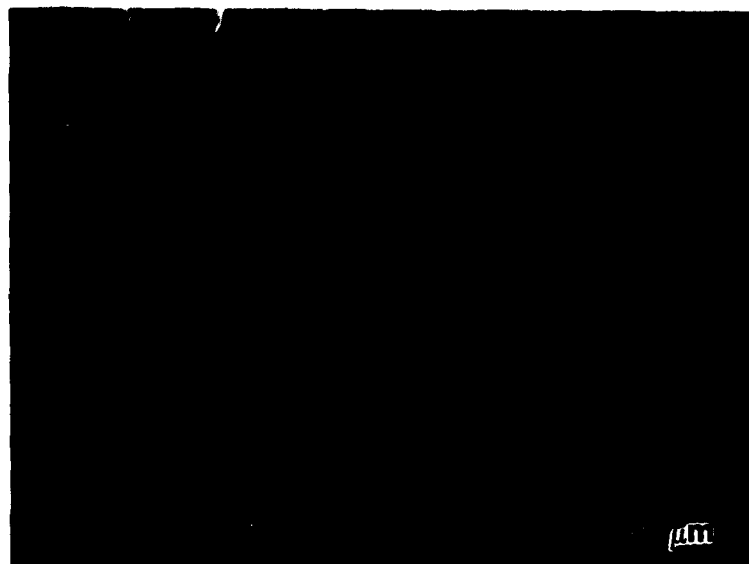


Figure 3: Scanning Electron Micrograph of as received Bronze (89Cu-11Sn) powder.

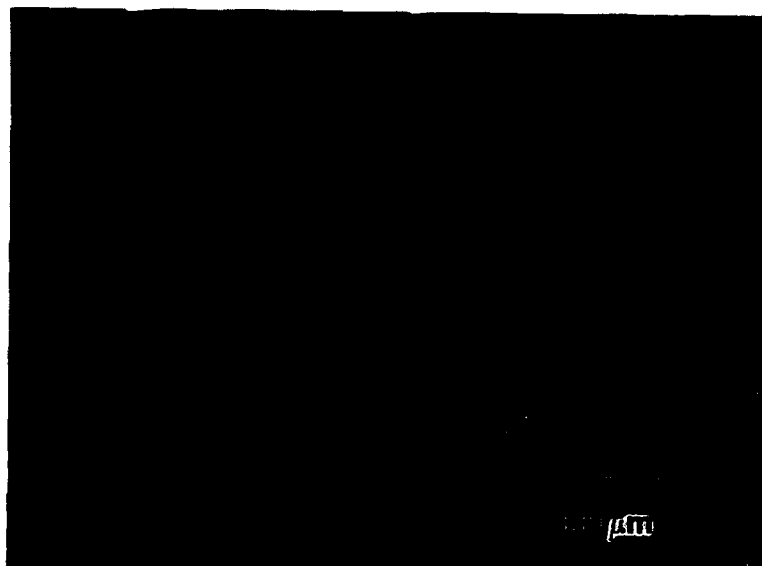


Figure 4: Top surface of the part made in a room-temperature environment shows poor wetting. Laser Power = 35 Watts, Scan Speed = 2.5 cm/sec.

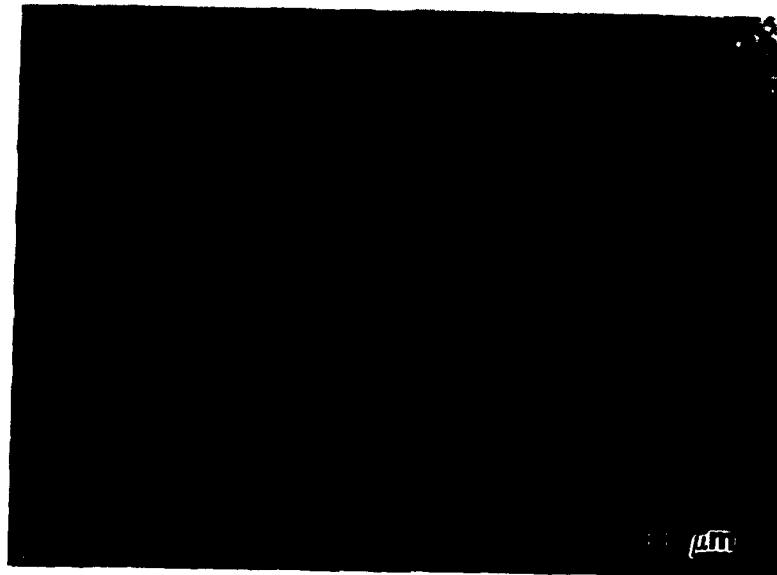


Figure 5: End-view of the part made in the room-temperature environment shows poor interlayer bonding. Laser Power = 35 Watts, Scan Speed = 2.5 cm/sec.

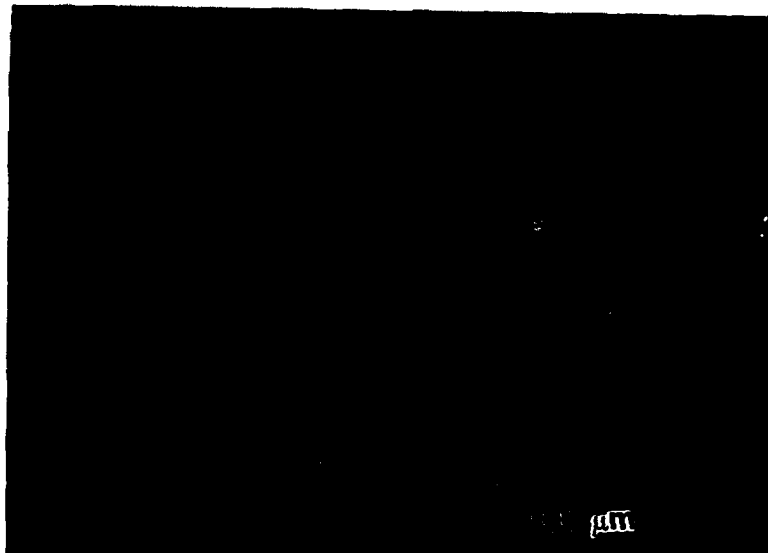


Figure 6: Top surface of the part made with a bed temperature of 350°C shows better wetting than before. Laser Power = 100 Watts, Scan Speed = 2.5 cm/sec.

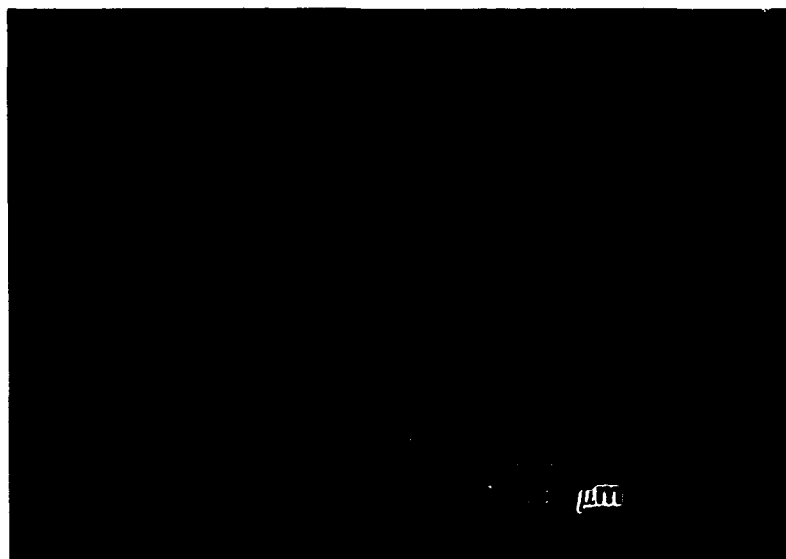


Figure 7: End-view of the part shown in Figure 6. The layers are barely distinguishable. Laser Power = 100 Watts, Scan Speed = 2.5 cm/sec.

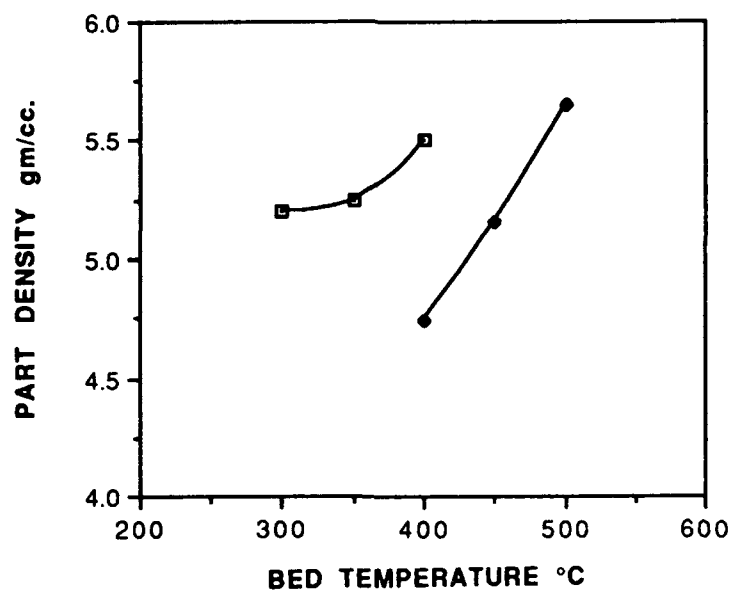


Figure 8: Part density versus bed temperature.

Selective Area Laser Deposition of Silicon Carbide

James V. Tompkins and Harris L. Marcus

*Center for Materials Science and Engineering
The University of Texas at Austin*

Abstract

Selective Area Laser Deposition (SALD) is a Solid Freeform Fabrication approach which uses a moving laser beam to deposit solid material from a precursor gas. We have achieved a deposition rate of 1.5 mm/min for silicon carbide within the focused laser beam, sufficient for constructing three dimensional objects. Use of tetramethylsilane vapor yielded freestanding rods and uniform single layers. Critical issues include the effect of nucleation rate on material quality, thermal shock complications, and non-uniform growth.

Selective Area Laser Deposition

The ability to develop a mature Solid Freeform Fabrication industry depends in part on materials processing technologies which can quickly and inexpensively produce three dimensional objects. Currently, many of the established rapid prototyping systems employ solid materials (often as powders) [1,2,3], and liquids (especially photopolymers) [4] for rapid prototyping applications.

Selective Area Laser Deposition (SALD) uses gas exclusively to produce solid material [5]. In this method, a focussed laser beam causes a precursor gas to chemically react to produce solid material only where the beam strikes a substrate. As the beam moves over the substrate, it leaves behind a trail of the material, which one may use to build up a solid object.

SALD offers several advantages. It can use a relatively simple mechanical system since it doesn't require precision powder or liquid delivery systems. SALD also offers spatial resolution which is not limited by powder grain size or finite thicknesses of powder layers. Further, depositing from a gas minimizes the porosity inherent with powders, suggesting full strength, structural parts are possible. SALD is not limited to successive planar cross sections of uniform composition. In principle, it offers a nearly unlimited ability to produce internal variations in composition by switching precursor gases, or possibly even to create internal voids or ducts.

The largest obstacle to making objects from gases is the low growth rates associated with conventional chemical vapor deposition (CVD), usually on the order of 100-1000 $\mu\text{m/hr}$. SALD requires a deposition process with a much higher growth rate. Other important requirements are a deposit profile which is uniform both along and perpendicular to the scanning direction, and a good interface between scan lines.

Silicon Carbide

Previous work on SALD investigated the pyrolysis of acetylene to deposit carbon [6]. This research focused on silicon carbide, as its extreme hardness and high melting temperature (2540 C) limit the conventional machining or casting of parts. Most silicon carbide parts are sintered at high temperature and pressure from silicon carbide powder with boron added as a binding agent. The rapid production of fully dense objects from silicon carbide without the costly processing steps and without the impurity of a binder material demonstrates unique advantages of the SALD process.

This study used tetramethylsilane ($\text{Si}(\text{CH}_3)_4$) as a precursor to deposit silicon carbide. It is a liquid which boils 26 C, giving a vapor pressure close to one atmosphere at room temperature, and makes a safe, convenient source of vapor. High purity tetramethylsilane is commonly used as a nuclear magnetic resonance (NMR) standard, making it readily available.

Experimental Procedure

Fig. 1 shows a schematic of the SALD system. All depositions occurred within a vacuum chamber flushed with nitrogen and evacuated to a 5 mTorr base pressure. All experiments used tetramethylsilane vapor at 125 torr, drawn from a flask of liquid at room temperature outside the chamber. The chamber was not heated.

To selectively deposit silicon carbide, we used the focussed infrared beam from a 25W CO_2 laser. A 4.5 W beam focussed to a diameter of 1mm on an unheated substrate gave a bright plume of light at the substrate surface, indicating the presence of a thermal plasma [7]. We did not measure temperature within the plasma, although rough visual estimates are in excess of 1000 C.

The deposition chamber was translated on a computer controlled X-Y table, with the substrate moving relative to a fixed beam. Scan rates varied from 0 (stationary) to 400 $\mu\text{m/sec}$. A stationary beam produced rods of material roughly the same diameter as the laser beam. The growth rates reported below came from dividing the resulting rod length by the elapsed time.

Alumina substrates were used because of their high temperature resistance and their lack of both silicon and carbon. Both solid sheets and powders were

tried, with powders having the advantage that they allowed a lower laser intensity to initiate growth. This is possibly due to greater absorption of the beam through internal reflection, or lower thermal conductivity.

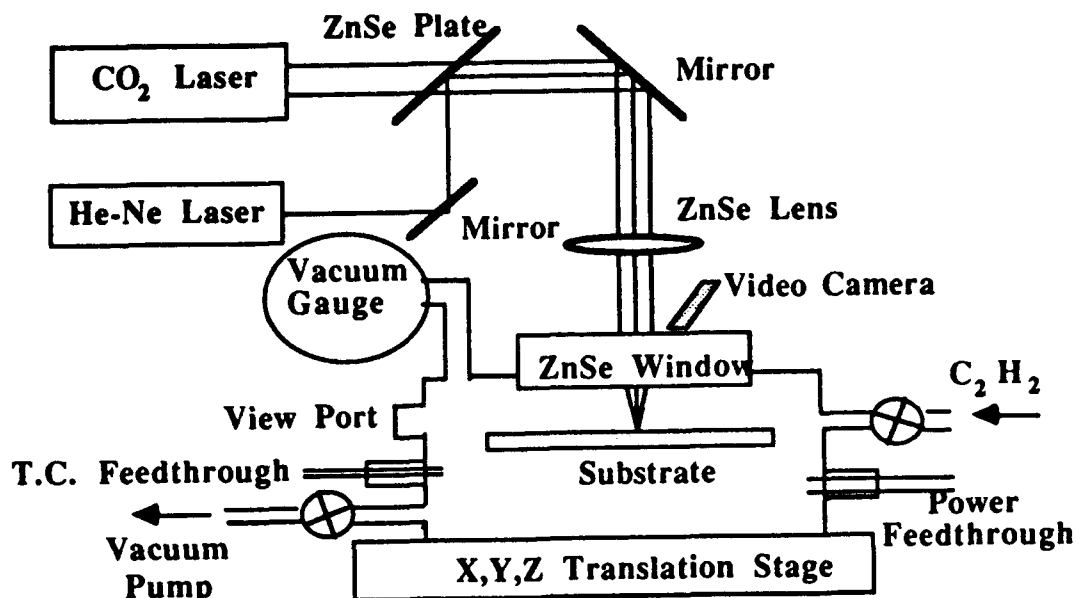


Fig 1. SALD System, Zong *et al* [8]

Results

The above conditions led to growth of a glossy black material. Measurement of rods grown in a stationary beam indicated growth rates of 1.5 mm/min, or 90,000 $\mu\text{m/hr}$. This is approximately 180 times greater than the 470 $\mu\text{m/hr}$ [9] to 510 $\mu\text{m/hr}$ [10] reported for conventional CVD of silicon carbide from tetramethylsilane in hydrogen.

Several analytical results for the deposited material were consistent with those for amorphous silicon carbide. X-ray diffraction studies of the resulting material indicated that the material was amorphous, with no crystalline silicon, graphite, or silicon carbide peaks present. The material was also found to be harder than polycrystalline alumina in a scratch test. Auger spectra of the deposited material were compared qualitatively with a hot-pressed silicon carbide standard and showed a silicon to carbon ratio within six percent of the standard. In an additional experiment, samples placed in a furnace at 850 C in air for twenty hours showed a unmeasurable (0.001 g) weight loss while a similar quantity of graphite was completely consumed in less than two hours.

Slow scanning of the laser beam (20 $\mu\text{m/sec}$) produced curved or articulated rods, showing that growth could be produced at least 45 degrees from the vertical direction of the laser beam. Faster movement of the beam (100-400

um/sec) gave a uniform line of material on the substrate surface. Rastering of the laser beam produced a square deposit as seen in Fig. 2. The interface between successive scans cannot be discerned after sputtering of the surface.

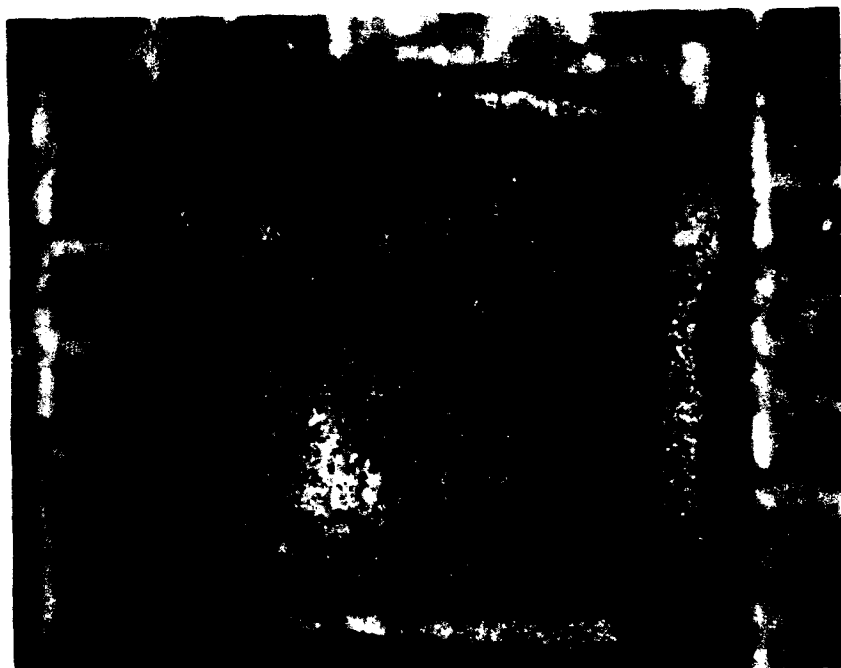


Fig. 2 Square from 3X3mm Raster, 400 um/sec,
100 um Line Spacing

Discussion

The material deposited from tetramethylsilane appears to be amorphous silicon carbide. The material is a very shiny black, and under a microscope interference colors indicate a very thin film which we believe is a self passivating layer of silica associated with residual oxygen in the system. We also hypothesize that the presence of the thermal plasma contributes to the high growth rates in a manner related to plasma enhanced CVD, although the higher partial pressure of tetramethylsilane and lack of hydrogen gas may also be responsible. Another factor may be the opportunity for diffusion of reactant to the deposition point in three dimensions, instead of the conventional diffusion through a boundary layer.

The nearly stoichiometric silicon to carbon ratio was remarkable. Tetramethylsilane contains four times the stoichiometric amount of carbon. However, the carbon is contained in methyl groups, and the molecule contains just enough hydrogen atoms for the methyl groups to ideally leave as methane. We anticipate that adding excess hydrogen would lower the carbon content further, possibly at some expense to the growth rate.

The apparent amorphous character of the material was not expected, however, we may speculate on its origin. The high growth rate would be consistent with a rapid nucleation rate during deposition. The large number of nucleation sites might occur due to the high concentration of tetramethylsilane or due to the activated species in the thermal plasma. A large number of nucleation sites would prevent the growth of large, ordered crystals in the material. The absence of an X-ray diffraction pattern for crystalline beta-silicon carbide is consistent for amorphous material or very small crystals. SEM images of the material showed rounded structures without facets expected of crystalline material as seen in Fig. 3. For high resolution in SFF applications, the glassy, isotropic nature of amorphous material might be an advantage, since facets or preferred growth directions interfere with smooth planar growth.

After a short inert ion sputter in a Scanning Auger Microprobe, the oxygen content in the deposited material was below the detection limit. The low oxygen content was encouraging, indicating an absence of a SiO_x phase in the bulk material. Although alumina was chosen to isolate the material from possible sources of carbon or silicon, alumina is susceptible to decomposition at high temperature, yielding free oxygen.



Fig. 3 SEM of SALD Silicon Carbide Rod, 4.5 Watts

We encountered two obstacles when we attempted to deposit thick or multiple layers of silicon carbide to produce three dimensional objects. First, when scanning over an existing layer, the steep, rapidly moving temperature gradient caused severe cracking in the underlying layer. The thermal shock combined with any residual stresses in the first layer cannot be resisted by the thin silicon carbide, even though silicon carbide has a good thermal shock resistance for a ceramic material. Several approaches may have to be employed in the future to alleviate this problem: First, the entire deposition area may be heated to a high temperature, reducing the thermal gradient needed. Secondly, a deposition chemistry which can use a lower temperature may be employed.

Another problem encountered is non-uniform growth in thick or multiple layers. Although the uniformity in a single layer seems quite good, the smallest projection from the surface becomes excessively hot during subsequent heating with the laser beam. This rise in temperature accelerates growth, making any microscopic projection unstable for extended growth. This is separate from the problem of localized growth due to a nucleation barrier observed by Zong in the SALD of pyrolytic carbon [11].

Conclusion

We have successfully produced silicon carbide rods and single layers using the SALD process, demonstrating its potential as a rapid prototyping tool as well as a method for producing structural parts. The lack crystallinity may be explained by the extremely high growth rates achieved, and may be desirable where high resolution is needed. Thermal shock considerations may be solved in the near future using proposed techniques, but the instability of microscopic irregularities in the first layer will require further study.

The authors acknowledge the support of ONR grant N00014-92-J-1514 in funding this research. The assistance of Britton Birmingham and Steve Lin in this work is greatly appreciated.

References

- [1] Proceedings of the Solid Freeform Fabrication Symposium, edited by J.J. Beaman, Harris L. Marcus, David L. Bourell, and J. W. Barlow, The University of Texas at Austin, Austin, Texas, August 6-8, 1990
- [2] Proceedings of the Solid Freeform Fabrication Symposium, edited by Harris L. Marcus, Joseph J. Beaman, David L. Bourell, and Richard H. Crawford, The University of Texas at Austin, Austin, Texas, August 12-14, 1991.
- [3] Proceedings of the Solid Freeform Fabrication Symposium, edited by Harris L. Marcus, Joseph J. Beaman, Joel W. Barlow, David L. Bourell, and Richard H. Crawford, The University of Texas at Austin, Austin, Texas, August 3-5, 1992.
- [4] Jacobs, Dr. Paul F., and Jan Richter, "Advances in Stereolithography Accuracy", Proceedings of the Solid Freeform Fabrication Symposium, edited by Harris L. Marcus, Joseph J. Beaman, David L. Bourell, and Richard H. Crawford, The University of Texas at Austin, Austin, Texas, August 12-14, 1991.
- [5] Zong, G., Yves Jacquot, W. Richards Thissell, and H.L. Marcus, "Solid Freeform Fabrication Using Selective Area Laser Deposition", Plasma and Laser Processing of Materials, edited by K. Upadhyay, The Minerals, Metals, and Materials Society, 1991.
- [6] Zong, G., J.V. Tompkins, W.R. Thissell, E. Sajot, and H.L. Marcus, "Processing Problems Associated With Gas Phase Solid Freeform Fabrication Using Pyrolytic Selective Area Laser Deposition", Proceedings of the Solid Freeform Fabrication Symposium, edited by Harris L. Marcus, Joseph J. Beaman, David L. Bourell, and Richard H. Crawford, The University of Texas at Austin, Austin, Texas, August 12-14, 1991, p.271
- [7] Radziemski, Leon, and David A. Cremers, Laser Induced Plasmas and Applications, Marcel Dekker Inc., New York, NY, 1989 pp 327-9

- [8] G. S. Zong, R. Carnes, H. G. Wheat, and H. L. Marcus, "Solid Freeform Fabrication by Selective Area Laser Deposition", Proceedings of the Solid Freeform Fabrication Symposium, edited by J.J. Beaman, Harris L. Marcus, David L. Bourell, and J. W. Barlow, The University of Texas at Austin, Austin, Texas, August 6-8, 1990

- [9] Figueras, A., S. Garelik, J. Santiso, R. Rodriguez-Clemente, B. Armas, C. Combescure, R. Berjoan, J. M. Saurel, R. Caplain, "Growth and Properties of CVD-SiC Layers Using Tetramethylsilane", *Materials Science and Engineering*, Volume B11, Nos 1-4, January 15, 1992, pp 83-88.

- [10] Figueras, A., R. Rodriguez-Clemente, S. Garelik, J. Santiso, B. Armas, C. Combescure, A. Mazel, Y. Kihn, J. Sevely, "Influence of H₂ Partial Pressure on the Morphology and Crystallization of SiC Layers Obtained by LPCVD Using Tetramethylsilane", *Journal de Physique IV*, Colloque C2 Supple. au Journal de Physique II, Volume I, September 1991, pp C2-225-232

- [11] Zong, G., J.V. Tompkins, W.R. Thissell, E. Sajot, and H.L. Marcus, "Processing Problems Associated With Gas Phase Solid Freeform Fabrication Using Pyrolytic Selective Area Laser Deposition", Proceedings of the Solid Freeform Fabrication Symposium, edited by Harris L. Marcus, Joseph J. Beaman, David L. Bourell, and Richard H. Crawford, The University of Texas at Austin, Austin, Texas, August 12-14, 1991, p.271

Drying of Colloidal Binder Infiltrated Ceramic Green Parts Produced by Selective Laser SinteringTM

M. Glazer[†], N.K. Vail[‡], and J.W. Barlow[‡]

[†]. Department of Mechanical Engineering

[‡] Department of Chemical Engineering
The University of Texas at Austin

Abstract

Colloidal ceramic binders have been used to strengthen ceramic green shapes produced by Selective Laser Sintering. This paper focuses on the effectiveness of the colloid infiltration with respect to the physical properties of the colloidal binder. Mass gains, strength gains, and dimensional changes resulting from infiltration were monitored. Controlled drying experiments were conducted to predict the factors influencing drying times for complex shapes.

(Key Words: Alumina, Silica Colloid, Drying)

Introduction

Ceramic preforms can be produced by Selective Laser Sintering of ceramic powders that have been encapsulated with a fugitive polymer binder. In this process, the polymer binder sinters producing a composite ceramic matrix. However, the polymer binder must be replaced because it does not have sufficient strength nor the thermal resistance necessary for functional ceramic objects. This paper discusses the infiltration of these preforms with ceramic colloids to improve strength and temperature capabilities. Green alumina coupons were infiltrated with colloids of varying solids content and then dried under controlled conditions. Physical properties of the coupons were determined prior to and following colloidal infiltration.

Materials

The polymer encapsulated ceramic used in this study is the same as that used in a previous study¹. This material consists of a high purity, electronical grade aluminum oxide, provided by Lanxide Corporation, coated with a polymethylmethacrylate polymer having a specified melt flow index of 20g/10min as measured by a Kayness Capillary Rheometer at 200°C and 75 psi (ASTM D1238). Figure 1 shows the mean particle size of the uncoated alumina to be 10.3µm, as measured by a Coulter Multisizer. The particles were observed to be regular in shape using a scanning electron microscope.

Samples of LudoxTM colloidal silica, grade TM, were provided by Dupont Corporation. This colloid is 50% wt. silica and consists of particles having a mean diameter of 22nm. A sample of Dupanol ME, a sodium dodecyl sulfate based emulsifier, was also provided by Dupont Corporation.

Methods

SLS Production of Test Coupons

Test specimens were produced using an SLS Model 125 workstation equipped with a 25 watt CO₂ laser. Fabrication of parts was conducted in an inert nitrogen environment using the

parameters listed in Table I. A number of rectangular coupons 1"x1"x0.25" (Group 1), 1"x1"x0.5" (Group 2), and 1.25"x1.25"x0.25" (Group 3) were produced for drying studies. Additional coupons 1"x3"x0.25" were produced for strength measurements. Densities of these coupons were determined by mass and dimensional measurements.

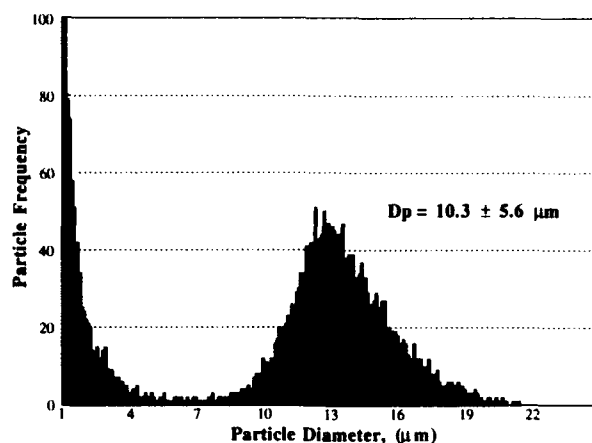


Figure1. Particle size distribution of Lanxide alumina.

Table I. SLS parameters for test specimens used in this study.

Laser Power, (W)	Layer Thickness, (mil)	Beam Spacing, (mil)	Beam Speed, (ips)	Bed Temperature, (°C)
10	4	2	50-110	65

Post-processing of preforms

Each coupon size was infiltrated with colloids of varying silica content. The stock colloid was diluted with deionized water to produce samples with 10%, 20%, 30%, and 40% wt. silica. Emulsifier was added to each colloid sample to aid infiltration in an amount of 1.0% wt. based on total water content.

Infiltration was accomplished by placing a coupon in a pool of colloid and allowing it to draw up the colloid. When the colloid reached the top of the coupon additional colloid was dripped on to the top surface. The coupon was then transferred to a paper towel and excess colloid was drawn off. When no further colloid could be drawn off, colloid was dripped on the top of the coupon. Infiltration was considered complete when a wet spot appeared on the paper towel.

Following infiltration the coupons were weighed, measured, and transferred to a drying chamber. Figure 2 shows the constant humidity drying chamber used in this study. Temperature and relative humidity in the chamber were monitored with a thermohygrometer. Temperature was maintained at the room temperature of 24°C. Relative humidity was maintained at 64±2% with a sodium dichromate salt solution². An air flow rate of 45 ft/s, measured by a Alnor Velometer, was provided by an electric fan controlled by a rheostat. Laminar air flow was created by forcing the air through a group of narrow, adjacent tubes.

In the chamber, the coupons were placed on a platform suspended from a cantilever balance. The balance was connected to an LVDT which sent a signal to a data acquisition system. The initial and final masses of the sample provided the calibration of the LVDT. The data was used to observe the changing moisture content of the part as a function of time. After drying, the bars were removed from the chamber, weighed, measured, baked at 200°C for 1 hr. to remove residual water and then weighed again.

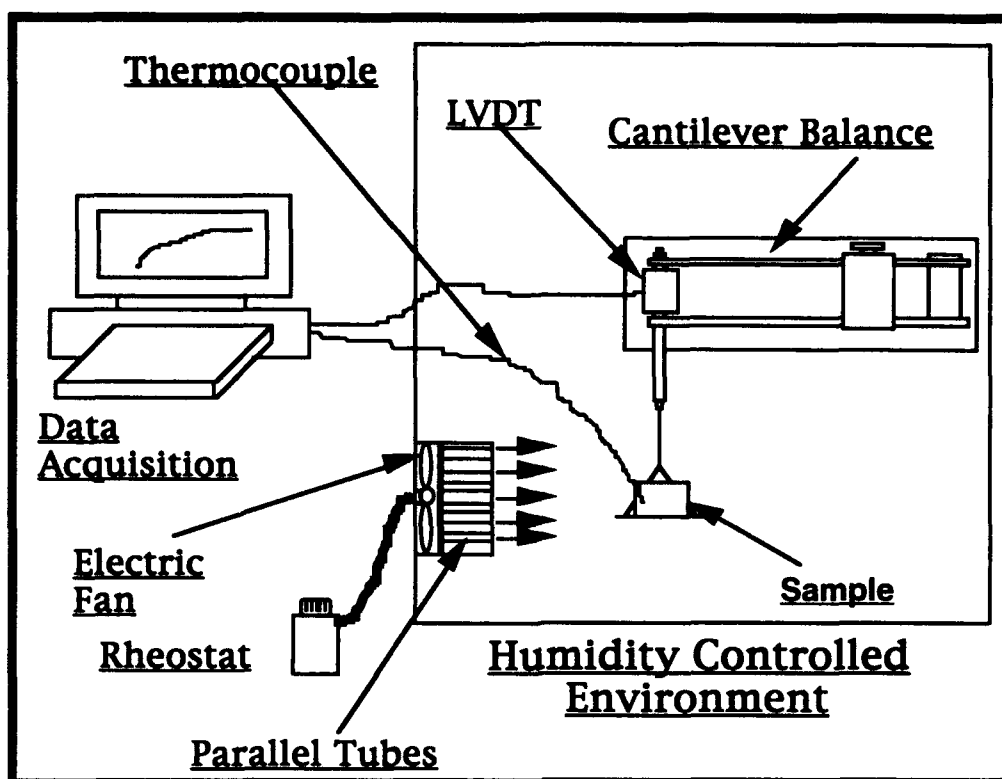


Figure 2. Drying chamber and data acquisition system.



Figure 3. (left). Pure alumina powder. (right). Silica infiltrated alumina coupon with polymer removed by burnout at 400°C for 1 hour.

Results and Discussion

Prior to conducting drying tests, a set of experiments was performed to verify the effectiveness of the colloidal infiltration described above. This was done by introducing a dye into the colloid and observing cross-sections of wet coupons. Discoloration of cross-sections was observed to be homogeneous. Furthermore, x-ray mapping of cross-sections by scanning electron microscopy showed silica to be present at the center-line and a slight concentration gradient to exist. These two methods proved the infiltration method to be effective. Figure 2 shows SEM micrographs comparing pure alumina powder to silica infiltrated alumina. The figures clearly show an accumulation of material in the infiltrated sample.

Figure 4 shows resultant densities of square coupons. Prior to colloid infiltration, all coupons had an initial density of approximately 1.55g/cm^3 . As would be expected coupon density increases with increasing silica content in a nearly linear fashion. From mass balance considerations the observed increases in density are a result of silica infiltration. Dimensional fluctuations of the processed coupons were within experimental error with most exhibiting no more than 0.5% deviations.

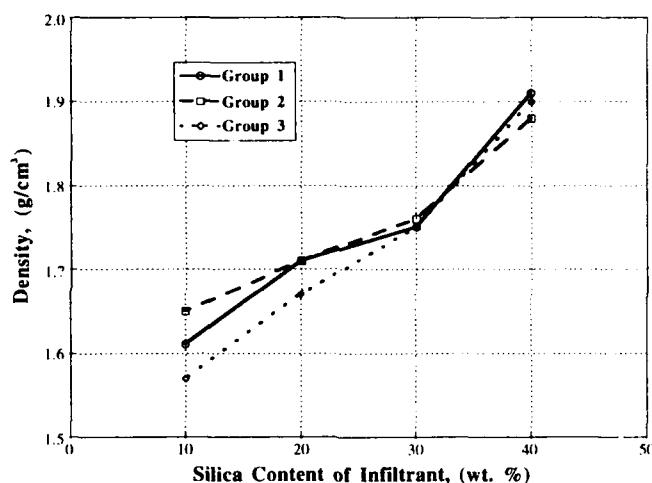


Figure 4. Density of test bars baked at 200°C .

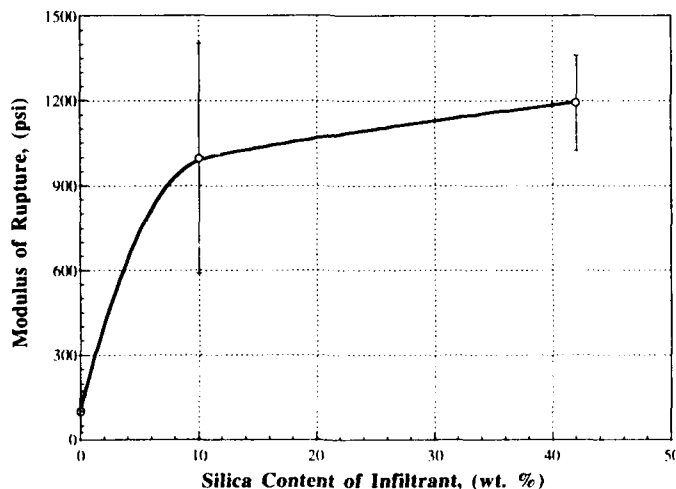


Figure 5. 3-point bend breaking strength of test coupons after baking at 200°C .

Figure 5 shows the modulus of rupture of test coupons which have been infiltrated, dried, and baked at 200°C for 1 hr.. Colloids that were 10 and 42 wt.% silica were used to determine the strengths which could be obtained by infiltration. The data shows a large gain in the green strength which appears to be independent of the amount of silica beyond 10 to 15 wt.% silica.

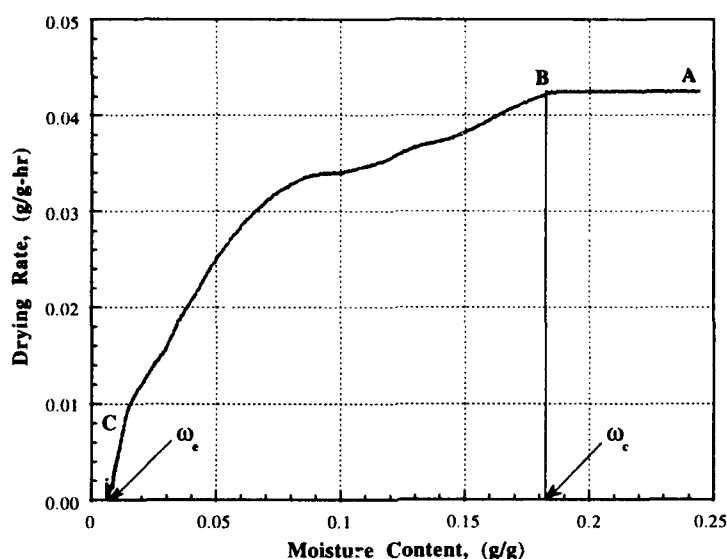


Figure 6. Drying data from infiltrated bar placed in drying chamber.

Figure 6 shows a typical drying curve for a coupon. This curve is similar to drying patterns observed by other authors and is indicative of drying of a hygroscopic material³. The rate curve is characterized by the constant rate period (AB) and the falling rate period (BC). During the constant rate period equilibrium of the drying surface is maintained by diffusion of excess moisture to the surface. At the critical moisture content, ω_c , the rate falls as the drying front recedes into the part. Analysis of these curves for the coupons studied here indicate the drying rate to be influenced by both coupon thickness and the solids content of the infiltrant. Using the analysis of Perry and Green⁴, it was determined that the drying process is controlled by diffusion and capillary moisture transport. A rigorous analysis of the data is in progress.

Cracking of coupons was observed to increase as the thickness of the part increased. Cracking also increased as the solids content of the infiltrant increased. In a separate set of experiments, coupons, that were infiltrated with water then dried under similar conditions, did not develop cracks. Cracking appears to be related to stresses induced by drying of the colloid and to the initial strength of the green coupon. Scherer⁵ has shown that ceramic colloids tend to shrink and crack during controlled drying. Therefore, as the drying front proceeds in to the coupon, stress gradients that exceed the green strength of the coupon may develop. Thicker coupons would necessarily experience larger stress gradients and be more likely to crack.

To examine the influence of initial green strength a set of coupons with similar dimensions but with different strengths were processed. Coupons having strengths of 45psi, 100psi, and 160psi were infiltrated with 30 wt. % colloid and dried under similar conditions. The low strength bar cracked severely, the high strength bar did not crack, and the moderate strength bar developed hairline cracks.

Conclusions/Further Work

Infiltration with silica colloids is an effective method for increasing strength and density of polymer bound prototypes produced by Selective Layer Sintering. Strength gains of the coupons were nearly independent of the solids content of the infiltrant. However, high solids infiltrants increased cracking, especially in parts with low inherent green strength.

Further study is required to optimize the infiltration and drying processes. Additional strength measurements need to be conducted on coupons from which the polymer binder has been removed. It may be necessary to subject the coupons to an additional colloid infiltration following binder removal to further increase density and strength. The strength of fired bars need to be studied, also.

A detailed analysis of stresses during the drying period, which includes the contributions of capillary and diffusion induced drying, is in progress. Infiltration with other ceramics could provide improved strength, temperature, and drying characteristics.

Acknowledgments

The authors gratefully acknowledge support of this work by the University of Texas SFF Industrial Associates Program.

References

1. N.K. Vail and J.W. Barlow, "Ceramic Structures by Selective Laser Sintering of Microencapsulated, Finely Divided Ceramic Materials," *Solid Freeform Fabrication Symposium Proceedings*, 3 (1992), pp. 124-130..
2. A. Wexler and S. Hasegawa, "Relative Humidity-Temperature Relationships of Some Saturated Salt Solutions in the Temperature Range 0° to 50°C," *Journal of Research of the National Bureau of Standards*, vol. 53, no. 1 (1954), pp. 19-25.
3. C. Strumillo and T. Kudra, *Drying: Principles, Applications and Design*, Gordon and Breach Science Publishers, Switzerland (1986), pp. 69-97.
4. R.H. Perry and D. Green, *Perry's Chemical Engineering Handbook*, 6th ed., McGraw-Hill, St. Louis (1984), pp. 20.9-20.14.
5. G.W. Scherer, "Drying Gels," *Journal of Non-Crystalline Solids*, 87 (1986), pp. 199-225.

SYNTHESIS, SELECTIVE LASER SINTERING AND INFILTRATION OF HIGH T_c DUAL PHASE $\text{Ag-YBa}_2\text{Cu}_3\text{O}_{7-x}$ SUPERCONDUCTOR COMPOSITES.

Mukesh K. Agarwala, David L. Bourell, Arumugam Manthiram,
Britton R. Birmingham, and Harris L. Marcus.
Center For Materials Science and Engineering.
The University of Texas at Austin, Austin, Texas 78712.

ABSTRACT

Fine, homogeneous dual phase $\text{Ag-YBa}_2\text{Cu}_3\text{O}_{7-x}$ composite powders were prepared by a simple colloidal sol-gel co-precipitation technique. Silver did not react with or degrade $\text{YBa}_2\text{Cu}_3\text{O}_{7-x}$. Bulk porous samples of pure $\text{YBa}_2\text{Cu}_3\text{O}_{7-x}$ and $\text{Ag-YBa}_2\text{Cu}_3\text{O}_{7-x}$ were made from powders by Selective Laser Sintering. The porous parts were further densified by infiltrating silver into pores, resulting in a dense, structurally sound dual phase superconducting composite. Laser processing parameters were varied to obtain optimum microstructure. The laser sintered parts required oxygen annealing after infiltration to restore the orthorhombic, superconducting structure. X-ray diffraction and T_c measurements indicate some impurity phases present in samples processed under aggressive laser conditions.

INTRODUCTION

Since the discovery of high T_c ceramic superconductors (1) much work has been devoted to develop them for practical applications. Considerable success has been achieved in the area of thin films (2). However, prototype applications in bulk form are still being investigated. The major obstacles in making practical bulk shapes from these materials are their inferior current carrying capacity in bulk form and poor mechanical properties. Numerous synthesis and fabrication techniques have been attempted to tackle these issues, but with limited success.

In the synthesis of these materials, several elements and compounds have been incorporated in the $\text{YBa}_2\text{Cu}_3\text{O}_{7-x}$ ceramic superconductor either as substitutional elements in the $\text{YBa}_2\text{Cu}_3\text{O}_{7-x}$ structure or as dispersoids in the $\text{YBa}_2\text{Cu}_3\text{O}_{7-x}$ matrix (3,4). Noble metals, gold and silver, are one such class of additives that have been widely investigated and found to be promising (3-6). Due to its inertness, silver does not react with and degrade the superconducting properties of the ceramic $\text{YBa}_2\text{Cu}_3\text{O}_{7-x}$ and has, therefore, been used as an appropriate second phase and as a sheath or cladding material in bulk fabrication (3,6). Silver doping has been found to improve the critical current density, due to the presence of silver at voids between the $\text{YBa}_2\text{Cu}_3\text{O}_7$ grains (5,6). A further problem associated with the $\text{YBa}_2\text{Cu}_3\text{O}_{7-x}$ superconductors is incomplete oxygenation during processing or gradual loss of oxygen subsequently, especially at grain boundaries. Due to high solubility of oxygen in silver and presence of silver at grain boundaries, it is an efficient source of oxygen for the $\text{YBa}_2\text{Cu}_3\text{O}_{7-x}$ superconductor matrix.

Similarly, in an attempt to improve the critical current density and mechanical properties, several fabrication techniques have been studied to make bulk parts from pure $\text{YBa}_2\text{Cu}_3\text{O}_{7-x}$ or $\text{Ag-YBa}_2\text{Cu}_3\text{O}_{7-x}$ powders. High critical current density parts have been made by melt texturing (7) that results in oriented grained structures necessary for high critical current density. Other fabrication techniques such as cold pressing and sintering (8), tape casting (8), and powder-in-tube rolling (9), have used Ag and $\text{YBa}_2\text{Cu}_3\text{O}_{7-x}$ powder mix to improve the mechanical properties. Most of the studies done on fabrication employing $\text{Ag-YBa}_2\text{Cu}_3\text{O}_{7-x}$ systems have employed the powder metallurgy route of mixing elemental silver powder with $\text{YBa}_2\text{Cu}_3\text{O}_{7-x}$ powder in different proportions (5,6). This technique may result in rather non-homogeneous distribution of silver in $\text{YBa}_2\text{Cu}_3\text{O}_{7-x}$ matrix. In contrast to the powder metallurgy route of mixing powders, sol-gel co-precipitation provides a homogeneous distribution of various phases in composites.

In this study, we report on a technique for synthesizing fine, homogeneous Ag-YBa₂Cu₃O_{7-x} composite powders by extending the citrate sol-gel technique proposed by Kakihana et al (10) to make single phase YBa₂Cu₃O_{7-x} powders. We have also made an attempt to produce structurally sound dense parts of Ag-YBa₂Cu₃O_{7-x} which have the potential of carrying high current densities. Porous preforms of YBa₂Cu₃O_{7-x} were made, which were then infiltrated with silver to give dense parts. The porous preforms of near net shape were made by the rapid prototype technique - Selective Laser Sintering (SLS) (11,12).

SLS is a pressureless sintering process which usually involves a liquid phase (13). Partial liquid phase is formed and solidified as the laser beam is scanned across the powder bed in a directional fashion. Such directional formation and solidification of liquid phase can result in an oriented-grained structure. Since YBa₂Cu₃O_{7-x} melts incongruently (14,15), it is possible to form partial liquid phase by careful control of the laser power density to induce interphase melting. Other laser processing parameters that affect the microstructure and hence the properties are : laser scan speed, scan spacing and the layer thickness. These laser processing parameters have been studied extensively for various ceramic, metals and polymer systems (12,13). By careful manipulation of these parameters and the powder characteristics such as particle size, desirable microstructure with optimum properties can be obtained.

EXPERIMENTAL PROCEDURE

SYNTHESIS OF YBa₂Cu₃O_{7-x} And Ag-YBa₂Cu₃O_{7-x} POWDERS

Metal nitrates, Y(NO₃)₃, Ba(NO₃)₂, Cu(NO₃)₂ and AgNO₃, were dissolved in water in required amounts. 1.9 g citric acid to 1 g of Ba(NO₃)₂ was dissolved in the nitrate solution. This was followed by addition of 10 ml of ethylene glycol per 1 mmol of Y. The ratios of citric acid to Ba(NO₃)₂ and ethyleneglycol to Y are same as that proposed by Kakihana et al (10) as the process is insensitive to pH. The amounts of various nitrates were varied to produce 10g batches of Ag-YBa₂Cu₃O_{7-x} composite powders with compositions in the range 0 - 60 weight percent silver. All the solutions were heated on a hot plate at 100°C - 150°C to obtain a brown-black solid which was ground into powder and referred to as "precursor". The precursor was calcined at 900°C in oxygen for 10-12 hours followed by furnace cooling. The calcined powder was ground and its structure and purity were assessed by x-ray diffraction. Following calcination, the powders were oxygen annealed at 600°C for 6 hours.

SELECTIVE LASER SINTERING

The Selective Laser Sintering workstation system developed and described by Birmingham et al (13) was used to carry out the sintering. Pure YBa₂Cu₃O_{7-x} and Ag-YBa₂Cu₃O_{7-x} powders of compositions 20% and 30% by weight of silver, were used in this study. All SLS processing were carried out in air at room temperature. A 25 Watt CO₂ laser was used with a beam diameter of 700 µm. Three dimensional square parts of 8 mm side dimension were made layer by layer to final thicknesses ranging from 1 to 3 mm. Laser power density was varied from 500 W/cm² to 1300 W/cm². Laser scan speeds of 1 to 3 mm/second were employed. Scan spacing was kept constant at 100 µm for all runs. Layer thickness was varied from 250 µm to 150 µm. Initial layers were thicker (200-250 µm) to avoid displacement of the previously sintered layers by the roller action during the spreading of powder to lay fresh layers for sintering. As subsequent layers were sintered the layer thickness was gradually reduced to 150 µm. The final thickness of the sample was thus controlled by the layer thickness and the number of layers.

INFILTRATION

The porous parts obtained by SLS were infiltrated with silver to fill up the pores and provide a reinforcing ductile phase. Silver infiltration was accomplished by placing the samples in an alumina boat with sufficient silver powder (0.7-1.3 μm) atop the samples (16). The boat with the sample and infiltrant was heated in a vertical tube furnace at 970°C in air for 10 to 30 minutes. The process was continuously monitored to allow melting of silver and its infiltration, by capillary effect, into the porous $\text{YBa}_2\text{Cu}_3\text{O}_{7-x}$ samples while avoiding any significant melting of the $\text{YBa}_2\text{Cu}_3\text{O}_{7-x}$ which would result in loss of shape.

CHARACTERIZATION

The SLS porous parts and the silver infiltrated dense parts were annealed at 930°C for 8 to 10 hours in flowing oxygen and slow cooled in flowing oxygen. Structural phases of the powders synthesized by sol-gel and of parts fabricated by SLS and infiltration were investigated at each stage of processing by X-ray diffraction. Critical transition temperatures were measured by a SQUID magnetometer. Samples were weighed before and after silver infiltration to determine the volume fraction of porosity at each stage and to find the degree of silver infiltration. A Micromeritics Accupyc 1330 pycnometer was used to determine the degree of open versus closed porosity. The sample microstructures and the distribution of silver were studied by SEM.

RESULTS AND DISCUSSION

POWDER SYNTHESIS

Submicron ($\sim 100\text{nm}$) size $\text{YBa}_2\text{Cu}_3\text{O}_{7-x}$ and Ag- $\text{YBa}_2\text{Cu}_3\text{O}_{7-x}$ powders were synthesized by the citrate sol-gel technique. X-ray diffraction spectra of Ag- $\text{YBa}_2\text{Cu}_3\text{O}_{7-x}$ composites with different weight percents silver are shown in Figure 1. The x-ray diffraction patterns show the orthorhombic $\text{YBa}_2\text{Cu}_3\text{O}_{7-x}$ structure for all samples. The x-ray peaks for silver are present as separate peaks suggesting that the silver is present as a separate crystalline phase in the $\text{YBa}_2\text{Cu}_3\text{O}_{7-x}$ matrix. However, in some samples of Ag- $\text{YBa}_2\text{Cu}_3\text{O}_{7-x}$, reflections from Y_2BaCuO_5 and/or BaCuO_2 are present. Presence of these impurity phases arise due to greater difficulty in complete and efficient removal of CO_2 evolved from the decomposition of citrate gel complexes during heat treatments. $\text{YBa}_2\text{Cu}_3\text{O}_{7-x}$ reacts strongly with CO_2 and the reaction products depend on the CO_2/O_2 ratio and the annealing temperature (17).

$\text{YBa}_2\text{Cu}_3\text{O}_{7-x}$ precursor derived from the gel decomposition requires calcination and oxygen annealing to obtain the superconducting orthorhombic structure. In this study, it was noticed that presence of silver had a significant effect on the degree of oxygen annealing required to obtain complete oxygenation of the $\text{YBa}_2\text{Cu}_3\text{O}_{7-x}$ structure. Batches of Ag- $\text{YBa}_2\text{Cu}_3\text{O}_{7-x}$ containing less than 30 weight percent silver required oxygen annealing following calcination to obtain superconducting orthorhombic structure. No such oxygen annealing was necessary for developing a completely oxygenated structure when batches of Ag- $\text{YBa}_2\text{Cu}_3\text{O}_{7-x}$ contained 30 weight percent or more silver. X-ray diffraction of powder samples from Ag- $\text{YBa}_2\text{Cu}_3\text{O}_{7-x}$ containing 20 and 30 weight percent silver without any oxygen annealing, Figure 2., indicate an incompletely oxygenated tetragonal structure for the lower silver content sample but completely oxygenated orthorhombic $\text{YBa}_2\text{Cu}_3\text{O}_{7-x}$ structure for the higher silver content sample. Table I shows the heat treatments required to obtain completely oxygenated orthorhombic $\text{YBa}_2\text{Cu}_3\text{O}_{7-x}$ structure in Ag- $\text{YBa}_2\text{Cu}_3\text{O}_{7-x}$ composites with different silver contents. Oxygenation of the $\text{YBa}_2\text{Cu}_3\text{O}_{7-x}$ structure occurs by diffusion during the heat treatment and subsequent cooling of the precursor. In this study it was seen that the process of diffusion is slow in bulk samples with low silver content while the diffusive process is enhanced by increasing the silver content. Also, it seems possible to decrease the time of calcination with increasing silver content.

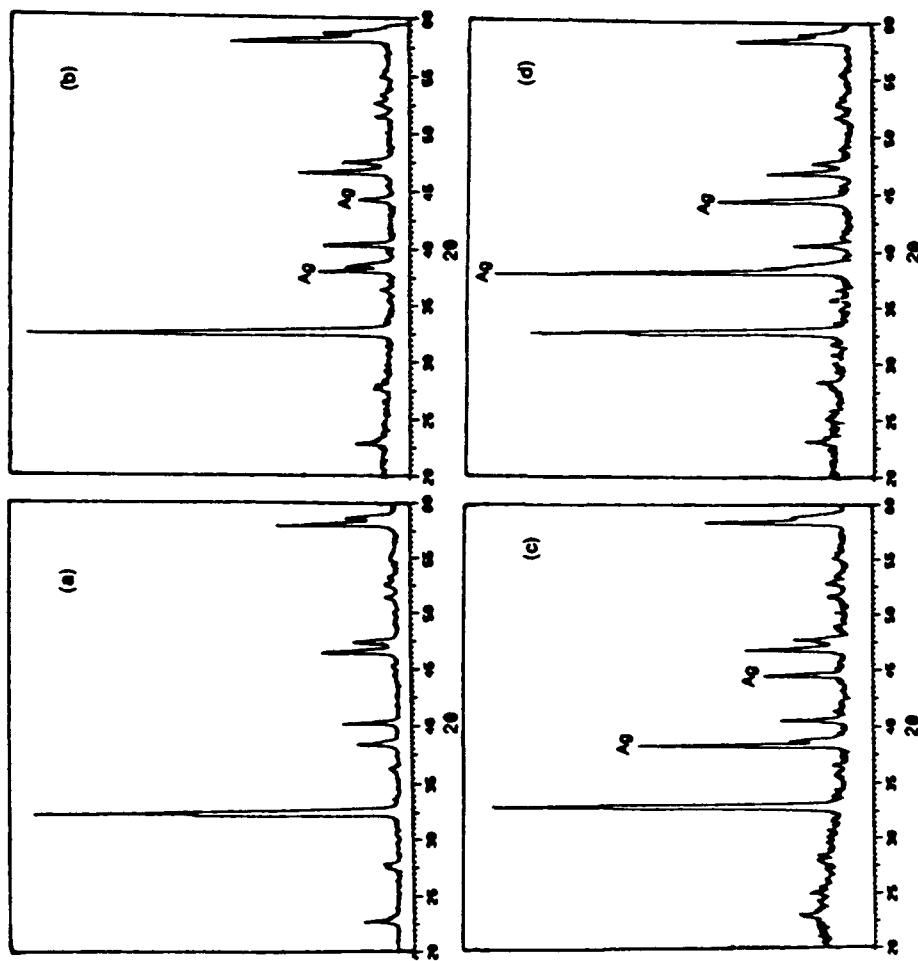


Fig. 1. XRD Patterns of Ag-YBa₂Cu₃O_{7-x} Composite Powders With Different Silver Contents Prepared by Sol-Gel Co-Precipitation (a) Pure YBa₂Cu₃O_{7-x} (b) 20 Wt.% Ag - 80 Wt.% YBa₂Cu₃O_{7-x} (c) 40 Wt.% Ag - 60 Wt.% YBa₂Cu₃O_{7-x} (d) 60 Wt.% Ag - 40 Wt.% YBa₂Cu₃O_{7-x}

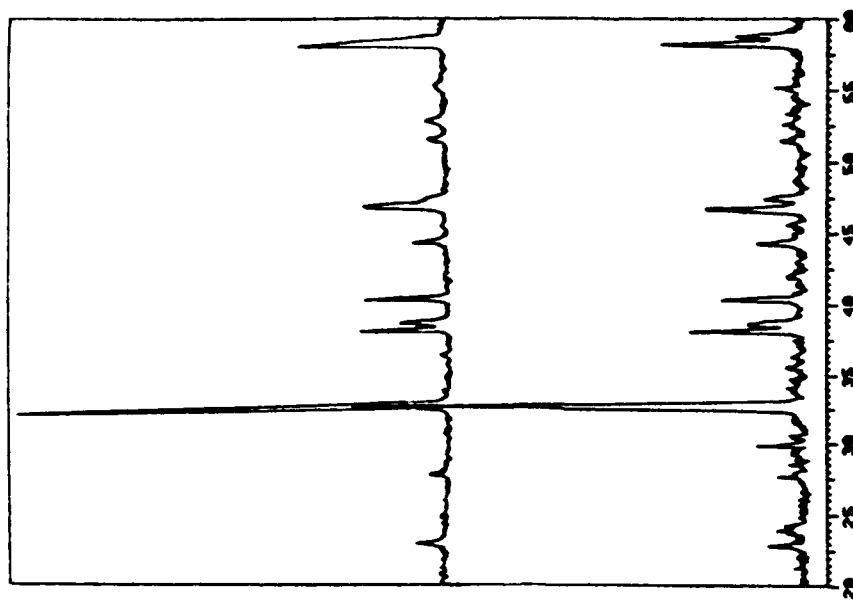


Fig. 2. XRD Patterns of 20 Wt.% Ag - 80 Wt.% YBa₂Cu₃O_{7-x} (top) and 30 Wt.% Ag - 70 Wt.% YBa₂Cu₃O_{7-x} (bottom), Both Having Undergone Calcination Prior to Oxygen Annealing.

The results of T_C measurements made on the Ag-YBa₂Cu₃O_{7-x} powder composites with different silver contents are shown in Figure.3. As indicated in Table I, the onset T_C remains unaffected up to a silver content of 40 weight percent and decreases slightly above 40 weight percent. There is a slight broadening of the transition width with increasing silver content. Broadening of transition width is usually associated with presence of bulk second phase, silver in this study, especially at grain boundaries. However, in all cases, the materials exhibited zero T_C at temperatures well above liquid nitrogen temperature (77K).

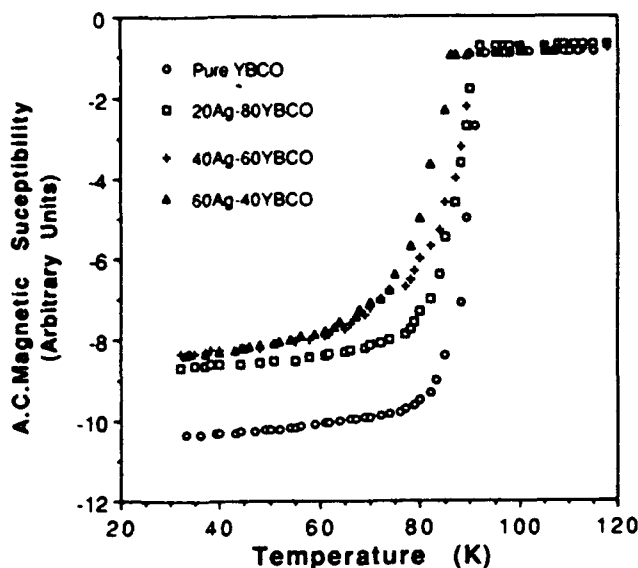


Fig.3. A.C. Magnetic Susceptibility measurements as a function of temperature for Ag-YBa₂Cu₃O_{7-x} composite powders.

Table I : Heat Treatments for Ag-YBa₂Cu₃O_{7-x} Powders

Amount of Silver Wt %	Vol %	Heat treatment	Onset T_C (K)
0	0	Calcination And Oxygen Annealing	93
20	13.1	Calcination And Oxygen Annealing	92
30	20.62	Calcination Only	92
40	28.78	Calcination Only	91
50	37.74	Calcination Only	88
60	47.63	Calcination Only	86

SELECTIVE LASER SINTERING

Partial liquid phase, necessary for SLS, was created by providing sufficient laser power density to produce a temperature above the peritectic decomposition temperature of YBa₂Cu₃O_{7-x}, producing Y₂BaCuO₅ and a liquid phase, "L" according to the reaction (14,18) :



The amount of liquid phase, "L", formed depends on degree of peritectic superheating.

Single layer and multilayer tests of Ag-YBa₂Cu₃O_{7-x}, with 20 and 30 weight percent Ag, done at various scan speeds and laser power density did not produce a structurally sound part that could be handled successfully. However, similar tests with pure YBa₂Cu₃O_{7-x} powder produced structurally sound parts at laser power densities above 500W/cm². Lack of structural integrity in Ag-YBa₂Cu₃O_{7-x} parts may be due to a decreased ratio of liquid to solid phase.

As shown in Figure 4(a), XRD patterns of selectively laser sintered parts did not exhibit significant crystallinity, irrespective of the laser processing parameters, but did indicate a breakdown of the YBa₂Cu₃O_{7-x} structural phase into various phases, such as Y₂BaCuO₅, BaCuO_{2-x} and BaCu₂O₂. The existence of metastable, noncrystalline phases is expected after SLS due to rapid melting and solidification of the ceramic YBa₂Cu₃O_{7-x} in the process. However, following SLS, crystallinity and the superconducting phase, YBa₂Cu₃O_{7-x} were restored in the SLS parts by oxygen annealing and slow, controlled cooling [Figures 4(b) and 4(c)]. Small

amounts of impurity phases of Y_2BaCuO_5 , BaCu_2O_2 and BaCuO_{2-x} were still found in the samples. As shown in Figures 4(b) and 4(c), samples processed at high laser power density ($>1000 \text{ W/cm}^2$) had higher degree of non-superconducting phases present in them even after oxygen annealing. Higher laser power density raises the powder temperature enough to result in complete melting which leads to significant chemical segregation and complete breakdown of the $\text{YBa}_2\text{Cu}_3\text{O}_{7-x}$ structure. Such severe breakdown in structure makes it more difficult for the stoichiometric, orthorhombic structure to be regained completely during oxygen annealing at 930°C for 8 to 10 hours. Lower laser power density ($<1000 \text{ W/cm}^2$) results in partial melting of the powders, according to the above mentioned peritectic reaction, resulting in partial breakdown of the $\text{YBa}_2\text{Cu}_3\text{O}_{7-x}$ structure and less chemical segregation. Therefore, nearly phase pure $\text{YBa}_2\text{Cu}_3\text{O}_{7-x}$ is easily regained by a simple oxygen annealing when the laser power density produces only a partial melting of the $\text{YBa}_2\text{Cu}_3\text{O}_{7-x}$ powders.

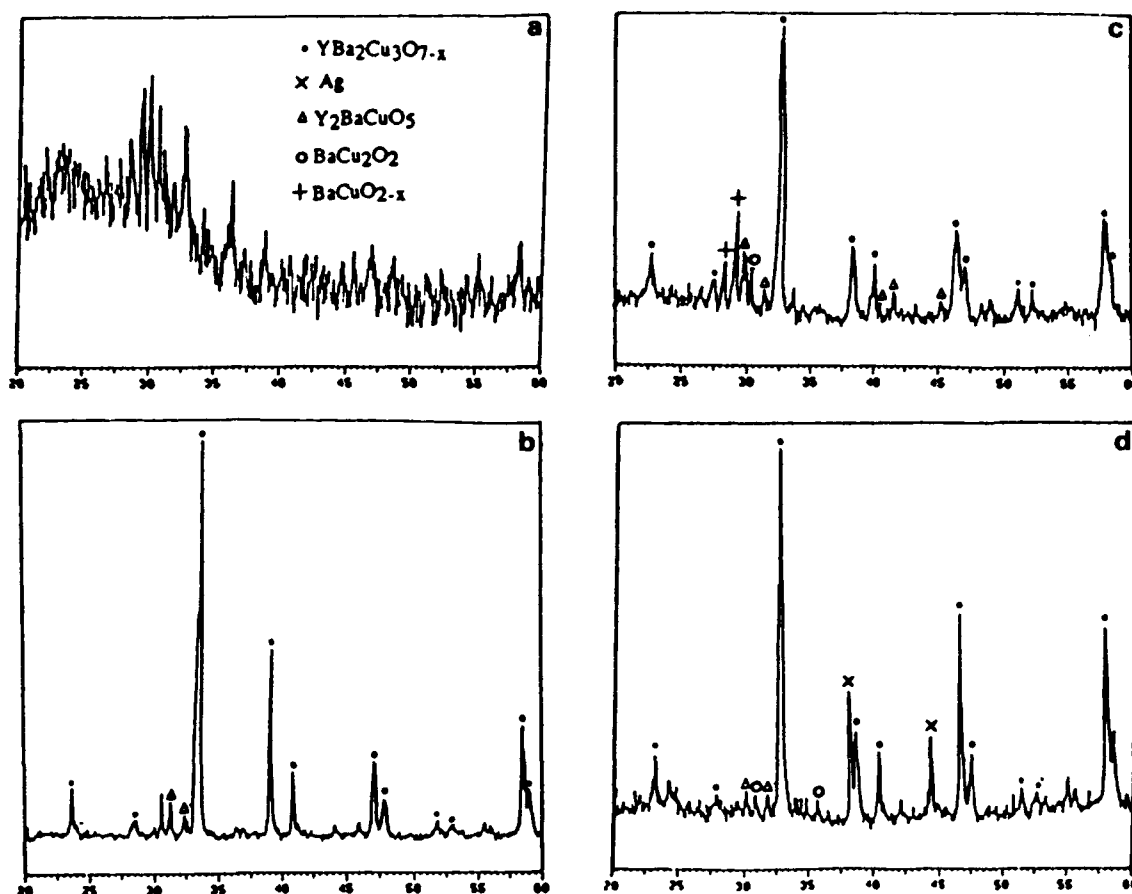


Figure 4. XRD Patterns of (a) SLS $\text{YBa}_2\text{Cu}_3\text{O}_{7-x}$, (b) SLS and O_2 Annealed $\text{YBa}_2\text{Cu}_3\text{O}_{7-x}$, Sample B, (c) SLS and O_2 Annealed $\text{YBa}_2\text{Cu}_3\text{O}_{7-x}$, Sample D, and (d) SLS, Silver Infiltrated and O_2 Annealed $\text{YBa}_2\text{Cu}_3\text{O}_{7-x}$, Sample H.

Bulk density of various SLS metal and ceramic parts has been found to be affected by laser processing parameters. In this study, bulk density of the laser sintered $\text{YBa}_2\text{Cu}_3\text{O}_{7-x}$ parts varied from 55% to 75% of theoretical density as the laser power density increased from 500 W/cm^2 to 1300 W/cm^2 at a constant scan speed of 1 mm/second (Figure 5). Bulk density also varied from 55% to 65% as the scan speed decreased from 2 to 1 mm/second at a constant power density of

750W/cm² (Figure 6). Reduced layer thickness was found to improve the bulk density significantly. However thick layers had to be used in the initial build-up of the structure to prevent displacement of the layers by the traversing roller. Density of the YBa₂Cu₃O_{7-x} samples was also measured using the helium gas pycnometer. Using the theoretical density of YBa₂Cu₃O_{7-x} and from the densities determined by the pycnometer, it was concluded that the porous, SLS parts had predominantly open, interconnected porosity with only 1% - 2% closed porosity.

Localized heating of the powder bed results in a temperature gradient along the scan line during SLS. If the temperature gradient is large, residual stresses appear in the sample which can lead to macrocracks and debonding of the layers. As shown in Figures 7(a) and 7(b), the surface and cross-section of a laser sintered part of YBa₂Cu₃O_{7-x} show some macrocracks but no significant debonding of layers. High laser power density and low scan speeds, which tend to aggravate this problem, also produced no significant debonding of layers in YBa₂Cu₃O_{7-x}. Figures 7 also show high degree of open porosity on surface and cross-section which is most desirable for further densification by infiltration.

INFILTRATION

Oxygen annealing of SLS parts at 930°C for 8 to 10 hours restored the desired orthorhombic YBa₂Cu₃O_{7-x} structural phase, but did not improve the bulk density of the samples significantly. Higher annealing temperatures (>940°C), for similar time periods, increased the bulk densities moderately but not significantly, but at a cost of partial or complete loss of shape. Partial liquid phase formation can occur in YBa₂Cu₃O_{7-x} above 900°C by a eutectic reaction arising due to CuO and/or BaO enrichment in the stoichiometry. The temperature at which this eutectic occurs and the amount of liquid phase formed depends on the deviation from stoichiometry. Therefore, prior to oxygen annealing, densification of the porous SLS parts was achieved by infiltrating silver into the open interconnected pores. Infiltration was done at 970°C to insure melting of the silver (melting point at 960°C) for efficient infiltration. Higher infiltration temperatures lead to shape loss due to excessive melting of the YBa₂Cu₃O_{7-x}. For the same reason the infiltration process at 970°C was continuously monitored and the process was stopped in 10 to 30 minutes when all the silver atop the YBa₂Cu₃O_{7-x} samples had melted and infiltrated into the pores. Keeping the time periods for infiltration short prevented any loss of shape, even though the infiltration temperature (970°C) was above the eutectic temperature. This is probably due to relatively small amount of liquid phase formed. However, such short time periods of infiltration did not result in restoration of the YBa₂Cu₃O_{7-x} phase in the parts. Therefore, following SLS and silver infiltration, the samples were oxygen annealed at 930°C for 8 to 10 hours.

As shown in Figure 8, infiltration occurred throughout the cross-section of the sample with large, continuous pores being infiltrated completely by silver while infiltration into micropores was limited. This is probably due to the relatively high viscosity from the small superheating of the molten silver, thus hindering infiltration into micropores. The bulk density of the samples after silver infiltration was found to be 85% to 90%. The volume fraction of silver in the samples varied from 30% to 45% depending on the volume fraction of pores before infiltration and the extent of infiltration.

SQUID magnetometer T_c measurements for different samples are shown in Figure 9. T_c (onset) under zero field conditions for all the samples is approximately 88K to 90K. There is a slight broadening of the transition width for samples processed under aggressive laser conditions and also for the silver infiltrated parts. Transition width broadening is usually associated with the presence of bulk second phases. Parts processed under aggressive laser conditions have some impurity second phase, as evidenced from X-ray diffraction, which results in transition width broadening. Silver infiltrated parts have continuous networks of silver as a second phase causing

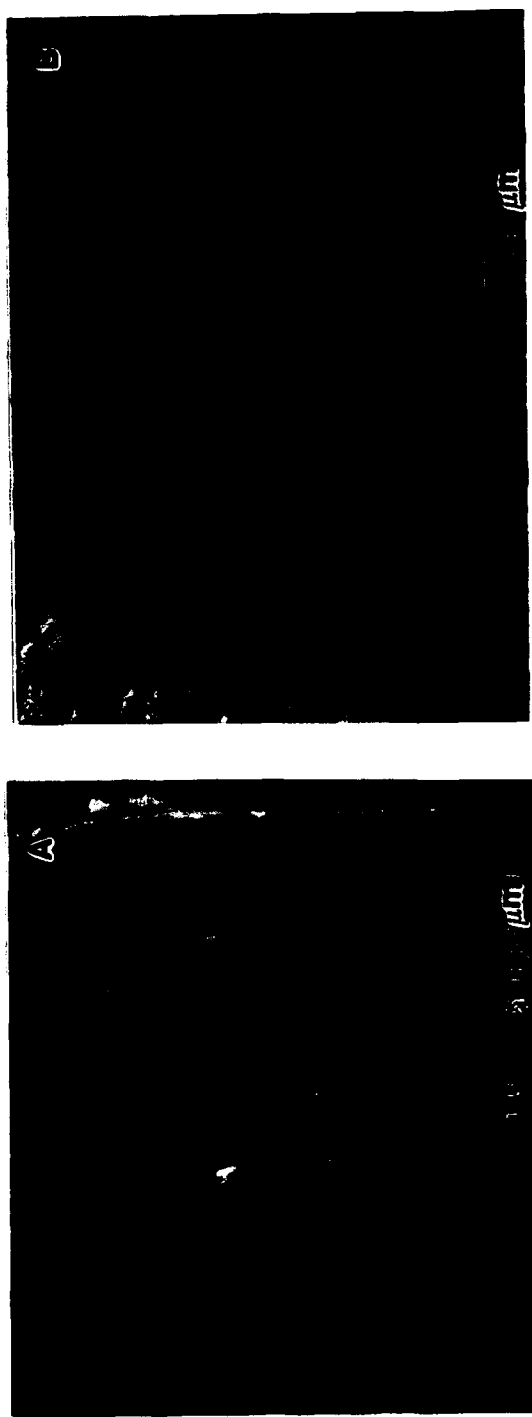


Figure 5. SEM Micrographs of a SLS $\text{YBa}_2\text{Cu}_3\text{O}_{7-x}$ Sample (A) Surface and, (B) Cross-section.

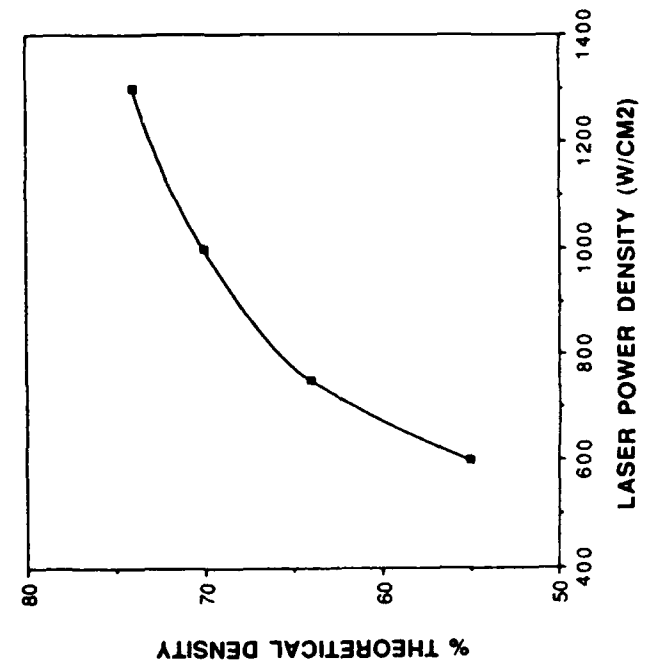


Figure 6. Bulk Density as a Function of Laser Power

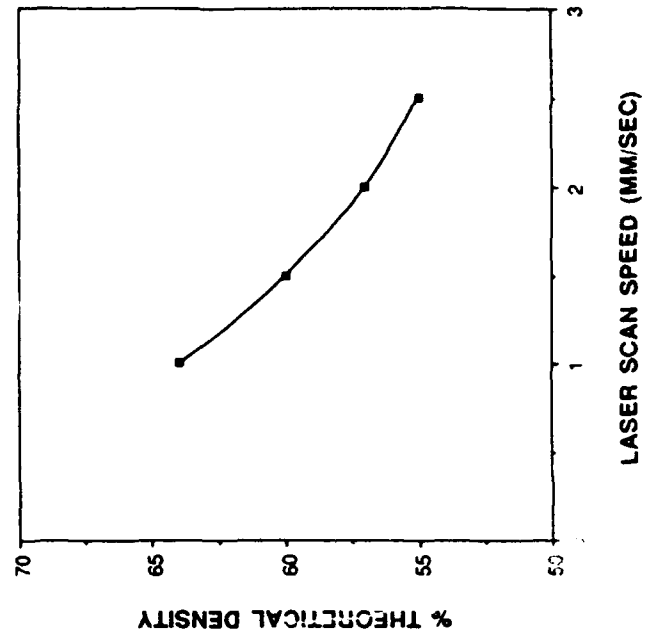


Figure 7. Bulk Density as a Function of Laser Scan Speed.



Figure 8. SEM Micrographs of SLS and Silver Infiltrated $\text{YBa}_2\text{Cu}_3\text{O}_{7-x}$ Samples.

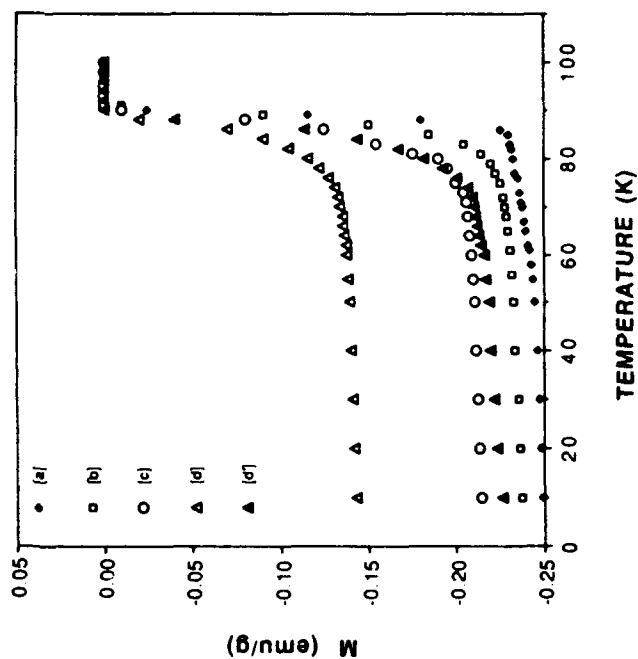


Figure 9. Field-Cooled (20 Gauss) Magnetization Data versus Temperature for [a] As Prepared $\text{YBa}_2\text{Cu}_3\text{O}_{7-x}$ Powders, [b] Low Laser Power SLS and O₂ Annealed $\text{YBa}_2\text{Cu}_3\text{O}_{7-x}$, Sample B, [c] High Laser Power SLS and O₂ Annealed $\text{YBa}_2\text{Cu}_3\text{O}_{7-x}$, Sample D, [d] Low Laser Power SLS, Silver Infiltrated and O₂ Annealed $\text{YBa}_2\text{Cu}_3\text{O}_{7-x}$, Sample H, and [d'] Data of curve (d) divided by (1- Ag weight fraction).

the broadening. However, in all cases, T_c^{zero} occurs well above the liquid nitrogen temperature of 77K. Comparison of diamagnetic signals of samples processed by SLS and oxygen annealing (Figures 9b and 9c) with that of as prepared $YBa_2Cu_3O_{7-x}$ powders (Figure 9a) reveals that SLS followed by oxygen annealing does not result in any significant reduction in the fraction of superconducting phase. This is in good agreement with the XRD data which shows very small quantities of non-superconducting phases after SLS and oxygen annealing. Similarly, comparison of Figures 9d' and 9a shows that silver infiltration in conjunction with SLS does not cause in any significant fraction of non-superconducting phases. This is also in good agreement with the XRD data and indicates that no chemical reaction occurs during silver infiltration to result in any non-superconducting phases, as also observed by other studies on Ag- $YBa_2Cu_3O_{7-x}$ composite studies (5,19).

TABLE II. SLS Processing Parameters and Post-SLS Processes Used.

Sample	Laser Power (W/cm ²)	Speed (mm/sec)	Ag Infiltration (970°C)	O ₂ Anneal (930°C)
A	600	1.0	No	Yes
B	750	1.0	No	Yes
C	1000	1.0	No	Yes
D	1300	1.0	No	Yes
E	750	1.5	No	Yes
F	750	2.0	No	Yes
G	600	1.0	Yes	Yes
H	750	1.0	Yes	Yes
I	1000	1.0	Yes	Yes

CONCLUSIONS

Fine (~100 nm) powders of superconducting $YBa_2Cu_3O_{7-x}$ and Ag- $YBa_2Cu_3O_{7-x}$ were successfully synthesized by a simple sol-gel technique. Presence of silver in the $YBa_2Cu_3O_{7-x}$ aided in the oxygenation of the superconductor necessary during annealing. The fine powders were then successfully fabricated into bulk, porous shapes by selective laser sintering which were subsequently densified by silver infiltration. The relationships between laser processing parameters and the resulting physical and superconducting properties can be summarised as follows :

- (1) Bulk density of SLS $YBa_2Cu_3O_{7-x}$ parts improves with increased laser power density, reduced scan speed, and reduced layer thickness.
- (2) Oxygen annealing restored nearly phase pure orthorhombic $YBa_2Cu_3O_{7-x}$ structure in parts processed under lower laser power density (<1000 W/cm²).
- (3) Silver was found to infiltrate successfully into large, continuous pores, improving the bulk density, while micropores were infiltrated partially.
- (4) $T_{c\text{onset}}$ for SLS parts and silver infiltrated parts were 88 K - 90K.
- (5) Broad transition widths were observed for parts processed under high laser power and for those infiltrated with silver.

ACKNOWLEDGEMENTS

The authors thank Konrad Bussman and Laura Henderson for their help in A.C.magnetic susceptibility and Pycnometer density measurements respectively. The authors also acknowledge the research grants from Texas Advanced Research Project Grant # 003658-063 and DTM Corporation, Austin, Texas

References

1. J.G.Bednorz, and K.A.Muller, "Possible High- T_c Superconductivity in the Ba-La-Cu-O System," *Z. Phys. B: Condens. Matter* 64, 189, (1986).
2. T.Venkatesan, X.D.Wu, B.Dutta, A.Inam, M.S.Hegde, D.M.Hwang, C.C.Chang, L.Nazar, and B.Wilkins, *Appl. Phys. Lett.*, 54, 6, (1989).
- 3.R.C.Sherwood, S.Jin, T.H.Tiefel, R.B.Van Dover, R.A.Fastnacht, M.F.Yan and W.W.Rhodes, "Superconducting Properties of $YBa_2Cu_3O_{7-x}$ Doped with Various Metals and Oxides," *Mat. Res. Soc. Symp. Proc. Vol. 99*, 503-506 (1988).
4. M.F.Yan, W.W.Rhodes, and P.K.Gallagher, "Dopant Effects on the Superconductivity of $YBa_2Cu_3O_7$ Ceramics," *J. Appl. Phys.* 63(3) 821-828 (1988).
5. Y.Matsumoto, J.Hombo, Y.Yamaguchi, M.Nishida, and A.Chiba, "Origin of the Silver Doping Effects on Superconducting Oxide Ceramics," *Appl. Phys. Lett.*, vol. 56 No. 16 1585-1587 (1990).
6. M.Itoh, H.Ishigaki, T.Ohyama, T.Minemoto, H.Nojiri, and M.Motokawa, "Influence of Silver on Critical Current of the Y-Ba-Cu-O Superconductor," *J. Mater. Res.* 6[11] 2272-2279 (1991).
- 7.S.Jin, T.H.Tiefel, R.C.Sherwood, R.B.Van Dover, M.E.Davis, G.W.Kammlott, and R.A.Fastnacht, "Melt Textured Growth of Polycrystalline $YBa_2Cu_3O_{7-x}$ with High Transport J_c at 77K," *Phys. Rev. B*, 37, 7850, (1988).
8. J.P.Singh, H.J.Leu, R.B.Poepfel, E.van Voorhees, G.T.Goudey, K.Winsley, and D.Shi, "Effect of Silver and Silver Oxide Additions on the Mechanical and Superconducting Properties of $YBa_2Cu_3O_{7-x}$ Superconductors," *J. Appl. Phys.*, 66(7), 3154, (1989).
9. S.Sen, I.Chen, C.H.Chen, and D.M.Stefanescu, "Fabrication of Stable Superconductive Wires with $YBa_2Cu_3O_x/Ag_2O$ Composite Core," *Appl. Phys. Lett.*, 54(8), 766, (1989).
10. M.Kakihana, L.Borjesson, S.Erikson, P.Svedlindh, and P.Norling, "Synthesis of Highly Pure $YBa_2Cu_3O_{7-x}$ Superconductors Using a Colloidal-Processing Technique," *Physica C*, 162, 931, (1989).
11. D.L.Bourell, H.L.Marcus, J.W.Barlow, and J.J.Beamon, "Selective Laser Sintering of Metals and Ceramics," *Int. J. Powder. Met.*, 28(4), 369, (1992).
12. Proceedings of the Solid Freeform Fabrication Symposium, 1991. Edited by H.L.Marcus, J.J.Beamon, J.W.Barlow, D.L.Bourell, and R.H.Crawford, Aug. 12-14, 1991, The University of Texas at Austin, Austin, Texas.
13. Proceedings of the Solid Freeform Fabrication Symposium, 1992. Edited by H.L.Marcus, J.J.Beamon, J.W.Barlow, D.L.Bourell, and R.H.Crawford, Aug. 3-5, 1992, The University of Texas at Austin. Austin, Texas.
14. K.Oka, K.Nakane, M.Ito, M.Saito, and H.Unoki, "Phase-Equilibrium Diagram in the Ternary System Y_2O_3 -BaO-CuO," *Jpn. J. Appl. Phys.*, 27(6), L1065, (1988).
15. N.Nevriva, P.Holba, S.Durcok, D.Zemanova, E.Pollert, and A.Trisk, "On the Melt Equilibria in the Y-Ba-Cu-(O) System," *Physica C*, 157, 334, (1989).
16. R.M.German, "Phase Diagrams in Liquid Phase Sintering Treatments," *J. Metals*, 38(8), 26, (1986).
17. Y.Gao, K.L.Merkle, C.Zhang, U.Balachandran and R.B.Poepfel, "Decomposition of $YBa_2Cu_3O_7$ During Annealing in CO_2/O_2 Mixtures," *J. Mater. Res.* 5[7] 1363-1367 (1990).
18. N.Ozkan, B.A.Glowacki, E.A.Robinson, and P.A. Freeman, "Infrared Zone Melting Process for $YBa_2Cu_3O_{7-x}$ Wires," *J. Mater. Res.*, 6(9), 1829, (1991).
19. B.Ropers, R.Canet, F.Carmona, and S.Flandrois, "Transport Properties and Percolating Behavior of $YBaCuO/Ag$ Random Composites Above and Below T_c ," *Solid State Comm.*, 75(10), 791, (1990).

Selective Laser Sintering of Al_2O_3 .

P. Kamatchi Subramanian, G. Zong, N.K. Vail,
J.W. Barlow and H.L. Marcus
Center for Materials Science and Engineering,
The University of Texas at Austin

Abstract

Selective Laser Sintering (SLS) of Al_2O_3 with an organic binder to create the green part is reported. The effect of processing parameters on the strength and density of parts produced by SLS are examined. The effect of particle size on the process and resulting green strength was studied. Two methods of applying the polymer binder to the ceramic powder, i) spray drying and ii) mixing, are compared.

Introduction

Selective Laser Sintering (SLS) has been employed as a method of forming parts from Al_2O_3 . Three approaches to SLS of Al_2O_3 may be employed to make parts. These are i) use an inorganic binder^{1,2,3} to bond the Al_2O_3 particles, ii) use an organic binder such as poly methyl methacrylate⁴ (PMMA) to bond the alumina and iii) direct sintering of the Al_2O_3 powder. This paper describes the experiments done on the laser sintering of Al_2O_3 powder of various sizes with organic binders and reports the properties of the green SLS parts.

When an organic binder is used the binder may be removed completely at a later stage by burnout. Thus, with the proper choice of the binder, it has the advantage of little material contamination and of being a low temperature SLS process.

Experiments

Three kinds of Al_2O_3 powder were investigated for this study. The characteristics are shown in table I. The $2\mu\text{m}$ and $8\mu\text{m}$ powders contained some flocculants that were removed by heating to 800°C .

Agglomeration of the particles as received was observed only for 8 μ m particles. The 2 μ m particles had limited agglomeration following the 800C thermal treatment.

Table I

Sample Ave. Particle size	Composition	Agglomeration
2 μ m	99.5% Al ₂ O ₃	Some
8 μ m	85%Al ₂ O ₃ , 2%CaO 1%MgO, Bal SiO ₂	Particles were in 70-100 μ m agglomerates.
15 μ m	99.5% Al ₂ O ₃	None

Two methods of applying the PMMA to the powder were used: i) mixing the polymer powder with the ceramic powder and ii) Spray drying the ceramic powder with the polymer emulsion using conditions shown in table II. The polymer powder used for the mix was obtained by spray drying the polymer emulsion.

The 2 μ m powder was spray dried with poly methyl methacrylate (PMMA) emulsion to 35 and 25 vol% respectively according to conditions listed in table II.

Table II Spray drier conditions

Inlet temperature (°C)	Outlet temperature (°C)	Atomizer speed (RPM)
250	90 to 105	30,000

The agglomerates of the 8 μ m powder were mixed with PMMA powder produced by spray drying and processed by SLS. Three volume fractions 20, 30 and 40 vol% of PMMA were employed. These exhibited good green strengths after SLS.

The agglomerates of the 8 μ m material were also spray dried with PMMA to 30 vol% after adding a viscosity enhancer (Xanthan

gum , 0.5%) and tested by SLS. The Xantham gum was necessary to reduce the settling of the agglomerates.

The 70-100 μ m agglomerates of 8 μ m particles were broken down using an attritor. This attrited powder was processed both by mixing with PMMA powder and also by spray drying with PMMA.

The 15 μ m powder was spray dried with PMMA to 30 vol% and the uncoated 15 μ m ceramic was added to dilute the concentration of PMMA to 25 vol%. Parts were made and density and bend strength determined. As a comparison the 15 μ m was also mixed with PMMA powder to 25 vol% and parts made by SLS and density and bend strength determined.

The following processing parameters were used for the SLS experiments. The powder bed was maintained at a temperature of about 85°C and laser power kept a constant at 10W. The scan line spacing was fixed at 0.005". The layer thickness was fixed at 0.007". The beam speed was varied to alter the power density incident on the layer. Power density is defined as the amount of energy incident on the layer per unit area in cal/cm². Specimens were tested for both bend strength and density. The volume of the specimen was determined by mensuration to estimate the density. The bend strength was determined with a three point bend test using a INSTRON constant displacement rate machine.

Results and discussion.

SLS of parts from the 2 μ m powder at both 25 and 35 vol% produced low strength green parts. Strong green parts were produced when the agglomerates of 8 μ m powder was mixed with PMMA powder and processed by SLS. The variation of bend strength and density with power density of these samples are shown in Figure 1 and Figure 2. When the agglomerated powder was spray dried with PMMA the agglomerates broke down during spray drying. Strong parts were not produced by SLS from the spray dried powder. When the 8 μ m powder is deagglomerated it does not form

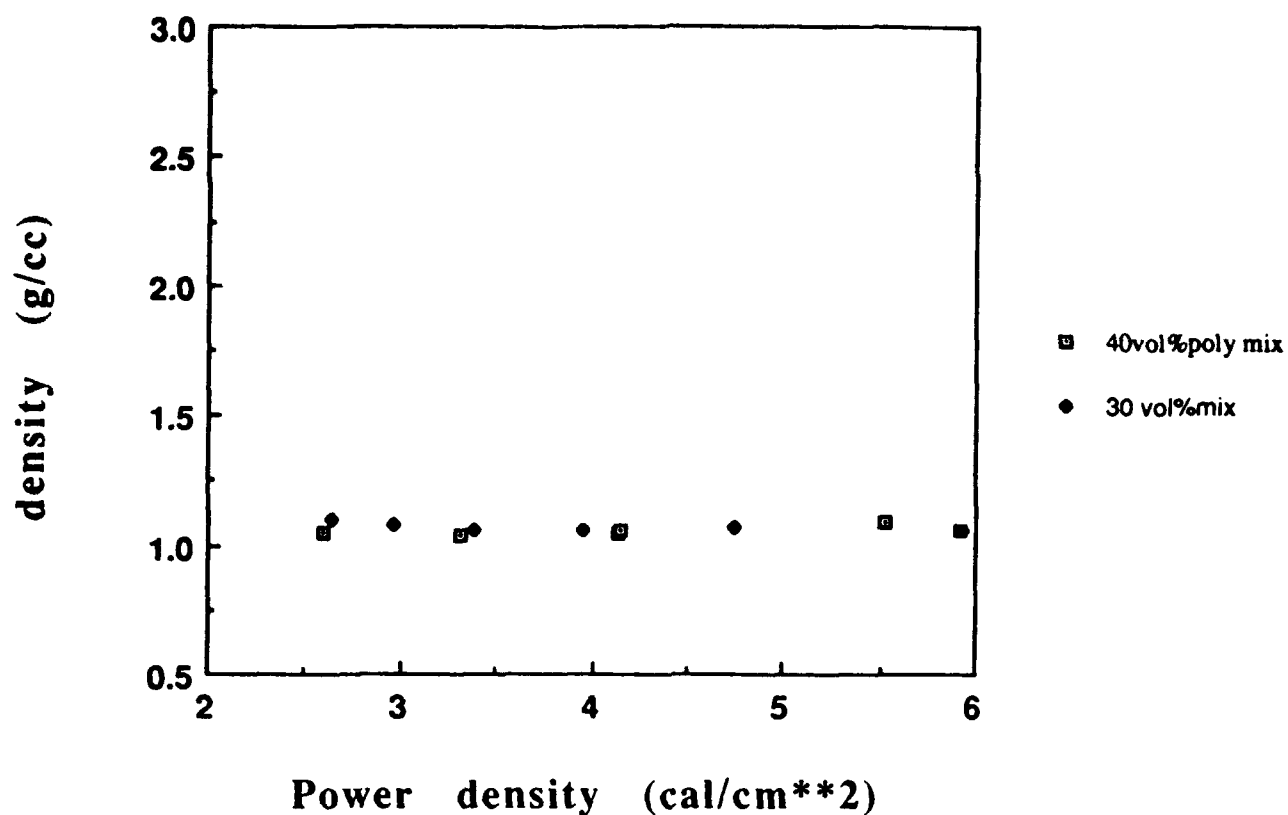


Fig.1. Effect of power density and binder volume fraction on density of parts from agglomerates of 8 μ m powder by SLS

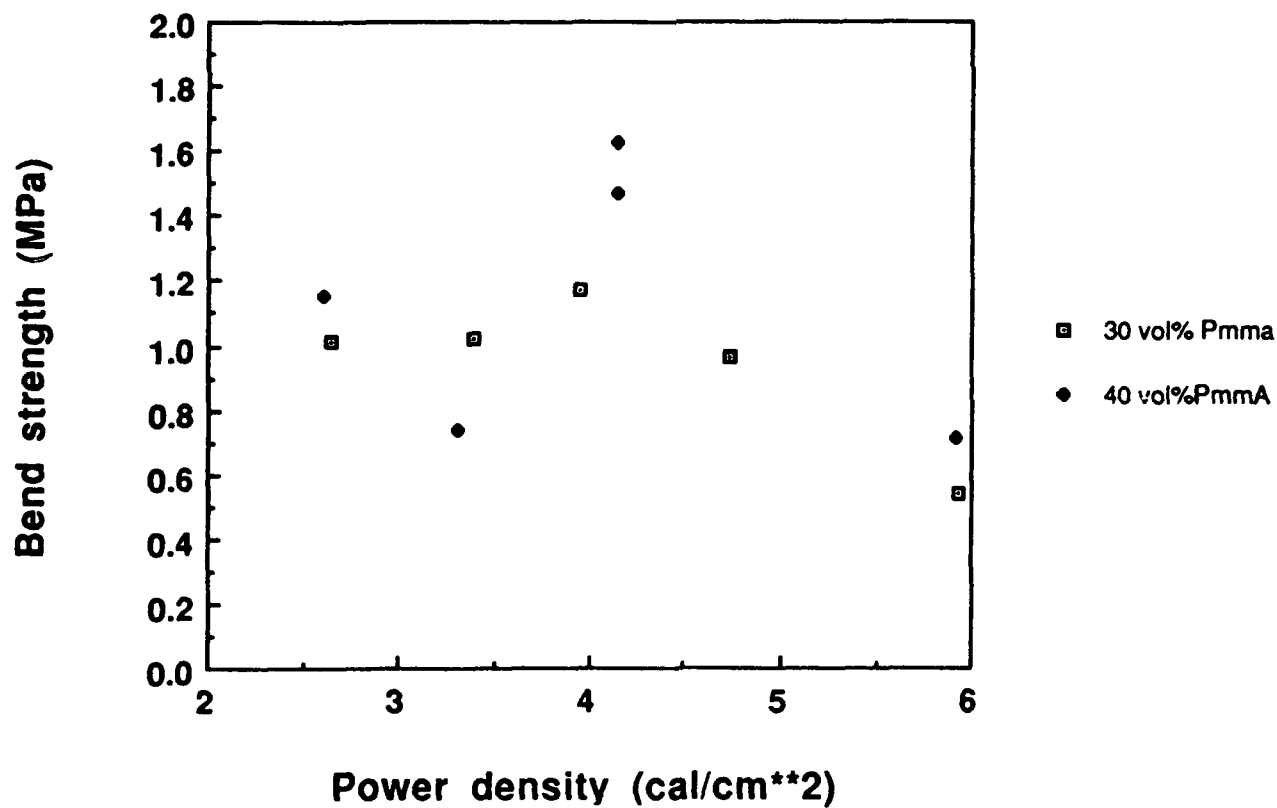


Fig.2 Effect of power density and binder volume fraction on bend strength of parts from agglomerates of 8 μ m powder by SLS

strong parts when mixed or spray dried with PMMA partly due to the nonuniform coating of the powder. The 15 μ m powder mixed and spray dried produced reasonable green strengths. The bend strength and density of the samples from 15 μ m powder are shown in Figure 4 and Figure 5.

Effect of binder content on strength.

Equation 1 relates the effect of binder content to the strength of composite⁵.

$$\sigma = k (V_b/V_p)^{0.75} (\gamma E/G)^{0.5} \quad (1)$$

where σ = strength of porous material, k = constant, V_b = volume content of binder phase, V_p = volume content of primary phase,

γ = Surface fracture energy, E = Young's modulus and G = Grain size. This equation was derived for brittle materials built up of particles joined at points of contact. A curve fit of the strength to the V_b/V_p ratio for three volume fractions of the polymer in the case of

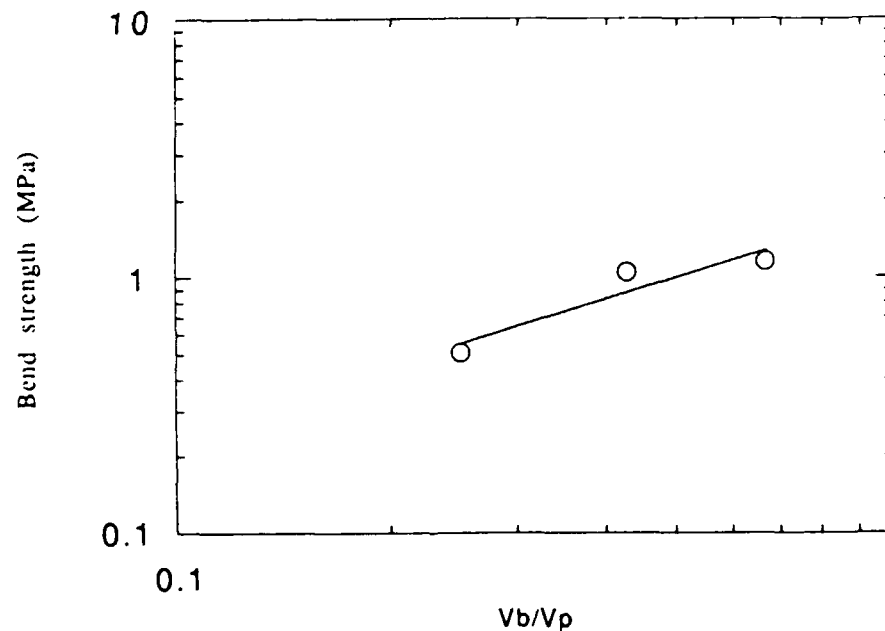


Figure3. Effect of binder volume fraction on bend strength

the agglomerates of 8 μ m powder is shown in Figure 3. The exponent according to the curve fit is 0.86 with $R=0.92$. Further experimentation is necessary to establish an appropriate model.

This result that the bend strength will decrease with decreasing content of polymer binder is expected since all the strength is associated with the binder and binder/ceramic interaction.

Effect of binder content on density.

There is not much variation in observed density of the parts with binder content. At a higher volume fraction of polymer there is sufficient polymer to melt and flow and cause an increase in density beyond the powder bed density. At low volume fractions of polymer this is not the case. Hence even though the theoretical density of powder mixtures of 20 and 40 vol% PMMA is 3.41 and 2.86, respectively, the density of parts made from them is approximately the same, 1.05g/cc.

Effect of power density on strength.

At low power densities insufficient melting and flow of binder occurs causing poor strength. At high power densities decomposition of the polymer occurs over a wider area causing a reduction in the strength. An intermediate value of the power density gives a higher strength. This may be seen in Figure 2 and Figure 5.

Effect of particle size on the process.

As the particle size decreases the strength of the part decreases. This is due to the greater surface area that the binder has to contact. If the binder is spread uniformly on all particles this will give rise to a thinner layer of the polymer with decreased particle size. Therefore there will be a smaller bonding area resulting in decreased strength. This may be seen from the fact that both 2 μ m and 8 μ m particle sizes do not form strong parts. The 8 μ m powder when present as agglomerates of 70 - 100 μ m size forms strong parts

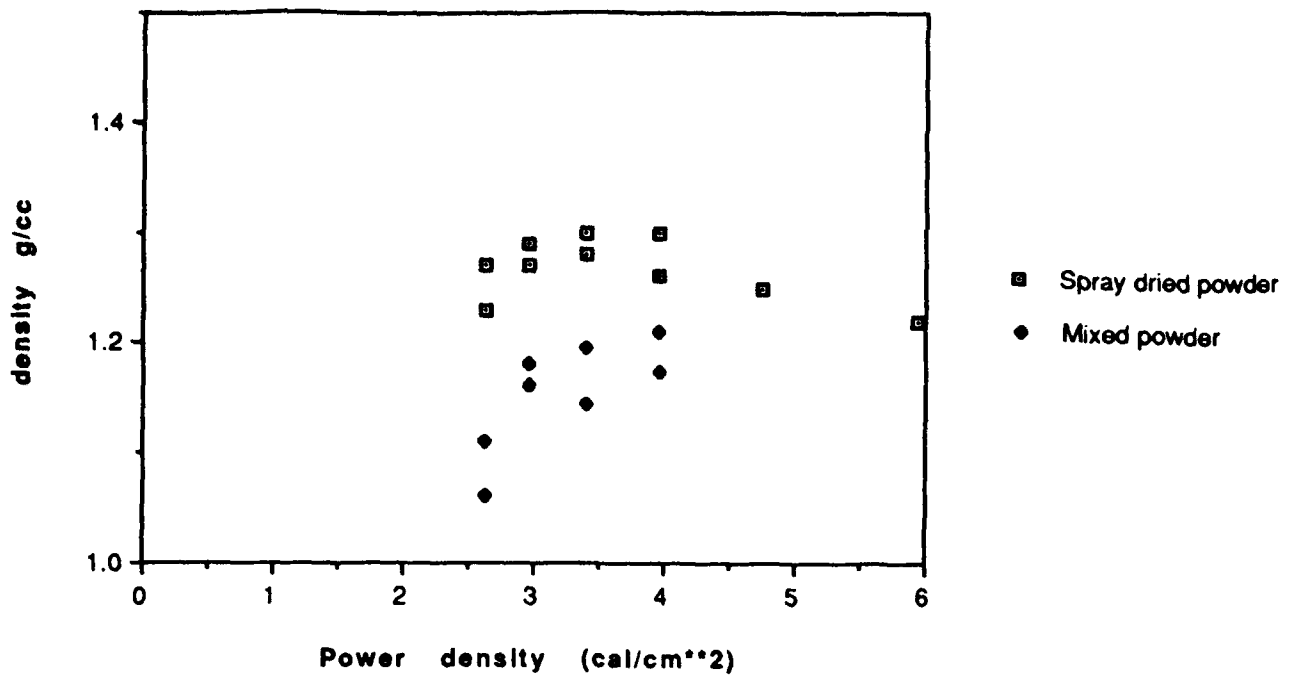


Figure 4. Effect of spray drying .vs. mixing on density of SLS samples for the 15 μ m Al₂O₃.

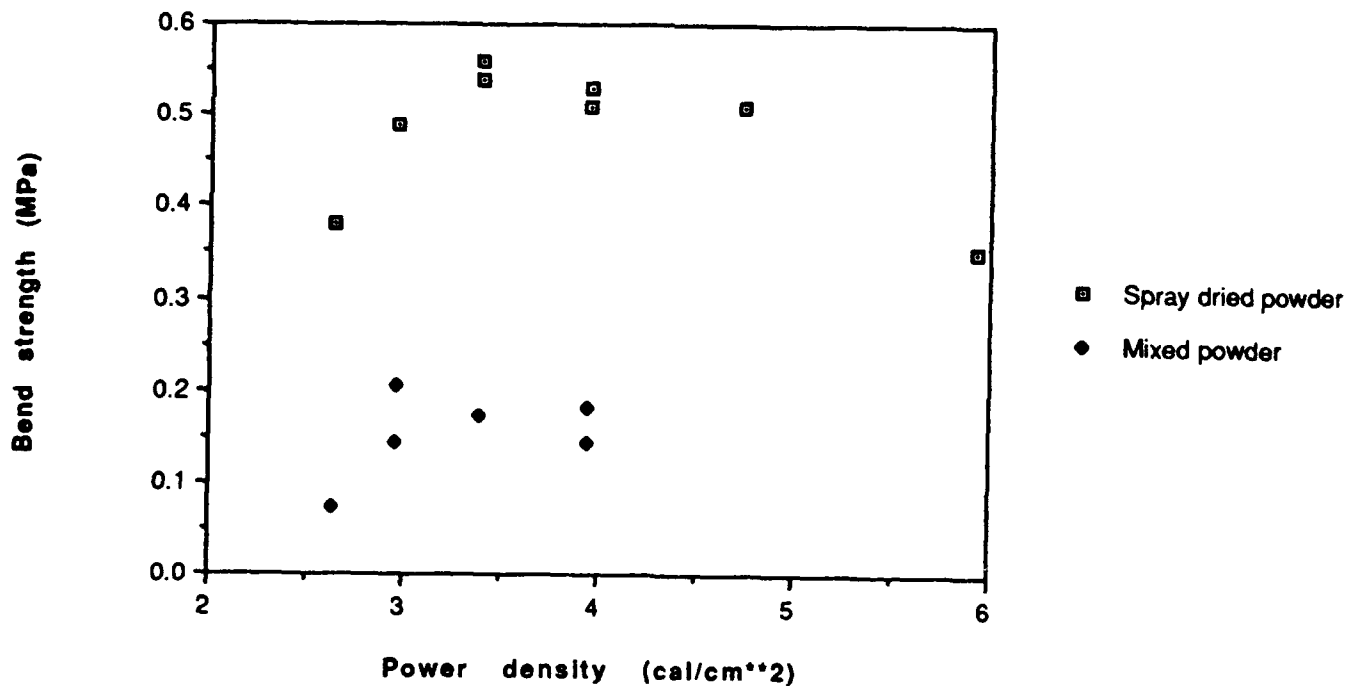


Figure 5. Effect of spraydrying .vs. mixing on bend strength of SLS samples for the 15 μ m Al₂O₃.



(a)

Figure 6. Microstructure of parts made from agglomerates of 8 μ m Al_2O_3 . a) Low magnification b) High magnification



(b)

when mixed with the polymer. This effect is partially due to the nonuniform coating associated with the spray drying.

Effect of spray drying vs mixing of the polymer.

The effect of spray drying vs mixing for the $15\mu\text{m Al}_2\text{O}_3$ may be seen in Figure 4 and Figure 5. Under identical conditions the strength for samples from spray dried powder is almost twice the strength for samples from the mixed powder. In the case of spray dried powder the polymer is more homogeneously distributed and the powder more uniformly coated. The $15\mu\text{m}$ powder is present as $50\mu\text{m}$ polymer/ Al_2O_3 agglomerates in the case of spray dried powder. The density of parts produced by SLS is also higher for spray dried powder as shown in Figure 4.

Microstructure of the composites.

These composites have interconnected porosity with the alumina particles bonded together by the polymer. The polymer envelopes the alumina particles. This may be seen from Figure 6 which shows the surface of a part made by SLS from the agglomerates of $8\mu\text{m}$ powder.

Summary.

The variables involved in the SLS of alumina using an organic binder are examined. The strength of the green parts produced increases with the volume fraction of the binder. The strength of the parts produced decreases with decreasing particle size. At high laser power density the strength of the parts produced is reduced. Spray drying homogenizes the polymer distribution and strengthens the parts.

References.

1. U. Lakshminarayan and H. L. Marcus, Proceedings of the Solid Freeform Fabrication symposium, Ed. J.J. Beaman, H.L. Marcus, D.L. Bourell, J.W. Barlow and R.H. Crawford, 1991, p.205

2. U. Lakshminarayan and H. L. Marcus, Proceedings of the Solid Freeform Fabrication symposium, Ed. J.J. Beaman, H.L. Marcus, D.L. Bourell, J.W. Barlow and R.H. Crawford, 1992, p.44
3. P.K. Subramanian, G. Zong and H.L. Marcus, Proceedings of the Solid Freeform Fabrication symposium, Ed. J.J. Beaman, H.L. Marcus, D.L. Bourell, J.W. Barlow and R.H. Crawford, 1992, p.63
4. N.K. Vail and J.W. Barlow, Proceedings of the Solid Freeform Fabrication symposium, Ed. J.J. Beaman, H.L. Marcus, D.L. Bourell, J.W. Barlow and R.H. Crawford, 1992, p.124
5. H.H. Bache, Journal of American Ceramic Society, 53 (12), 1970, p.654

Acknowledgments

We acknowledge financial support of this work from DARPA-ONR grant N0014-92-J-1394. We also acknowledge the assistance of Mr. B. Balasubramanian in some stages of this work.

Laser Sintering Model for Composite Materials

J. C. Nelson, N. K. Vail and J. W. Barlow
Department of Chemical Engineering
The University of Texas at Austin

Abstract

A computer model for the sintering of ceramic/polymer composite materials has been established based on empirical sintering rate data. The model calculates sintering depths which result from variations in the operating parameters which include laser power, beam speed, scan spacing, scan vector length, and initial temperatures of the powder and surroundings. Sintering depths measured in multiple layer parts made of polymer coated ceramic powders are compared to sintering depths calculated by the sintering model.

Introduction

In this paper, the development of a sintering model for composite materials is examined. The sintering model for composites is based strongly on a previously developed model which calculates the extent of sintering and subsequent densification of amorphous polymer powders in response to Selective Laser Sintering (SLS) operating conditions and scanning parameters [Nelson, 1993].

Composite materials are comprised of a non-sintering phase, ceramic or metal, and a sintering phase, polymer. The non-sintering phase is either mixed or coated with the polymer prior to sintering. As the laser scans the composite powder during the part build, the polymer is selectively melted, and upon cooling, solidifies binding the non-sintering phase together. Post-processing of green¹ SLS part removes the polymer phase and bonds the ceramic or metal in a homogeneous phase.

The material system examined in this paper is a ceramic/polymer composite. The ceramic is Silicon Carbide (SiC), and the polymer is poly(methyl methacrylate). The polymer is polymerized in emulsion form, and in a subsequent step, the SiC powder is coated with a thin layer of polymer in a spray dryer. Twenty-five volume percent polymer is applied to the ceramic powder in the spray drying step, then uncoated ceramic is added to reduce the polymer content to twenty volume percent.

Sintering Model

The development of a computer model is crucial in the understanding and future automation of the SLS process. The sintering model is used as a tool to investigate how the various process variables (i.e. scan speed, laser power, and scan spacing) effect the quality of the finished SLS parts. A sintering model also allows one to perform a

¹A "green" part refers to the state of the SLS object after removal from the sintering machine but before undergoing any post-processing steps.

parametric analysis to study how variations in one parameter affect the sintering depths within a powder layer.

The first building block, used to model the thermal gradients in the SLS powder bed, is the differential equation for thermal diffusion. The differential equation is written in one-dimension as follows:

$$\rho_{(\epsilon)} C_{P(T)} \frac{\partial T_{(z,t)}}{\partial t} - \frac{\partial}{\partial z} \left(K_{(T,\epsilon)} \frac{\partial T_{(z,t)}}{\partial z} \right) = G_{(z,t)} \quad (1)$$

$$-K \frac{\partial T}{\partial z} = Q_{(0,t)} + h(T - T_{\infty}) \quad \text{at } z = 0, \quad t > 0 \quad (2)$$

$$-K \frac{\partial T}{\partial z} = 0 \quad \text{at } z = L, \quad t > 0 \quad (3)$$

where ρ is the bed density at position z , C_p is the specific heat, K is the thermal conductivity, T the temperature, t the time, G is the internal heat source, Q the heat source term at the surface, and h the heat transfer coefficient which includes contributions from both convection and radiation transfer at the surface, and T_{∞} the ambient temperature. The flux term, Q , represents the energy input from the laser as a function of the laser power, laser spot size, scan speed, and scan spacing.

The thermal-diffusion equation, Equation (1), is used to calculate the thermal profiles within a solid region as a function of the thermal properties of the material and the boundary conditions. However, during sintering the material properties change as a function of the void fraction, or porosity, within the solid. Therefore, the material properties are calculated as a function of both temperature and void fraction. The porosity is related to the bed density, ρ , and the material solid density, ρ_s , by the expression,

$$\epsilon = \frac{(\rho_s - \rho)}{\rho_s} \quad (4)$$

and is a function of the powder size distribution, the powder aspect ratio, and the fraction of sintering that has occurred.

The second building block is the sintering model which is used to calculate the change in void fraction as a function of temperature. Several theoretical models are available to model sintering; however, these models are not adequate for powders with broad particle size distributions, or more importantly for composite materials. The sintering rate used in this study is an empirical rate measured using an oven sintering apparatus, [Nelson, 1990; Nelson 1993]. Sintering rate data is acquired at several temperatures 10 to 50 K above the T_g or T_m of the material. The temperature dependence of the sintering rate is calculated, and the rate data is extrapolated into the regime where sintering occurs during laser processing.

This method works very nicely for homogeneous polymeric materials (i.e. polycarbonate), however, because the composite material is primarily a ceramic phase, which sinters at very high temperatures relative to the polymer phase, the total densification during oven sintering at the highest operating temperatures was only about 5 percent. Since the amount of sintering was so small, the uncertainty in the extrapolated

rate data was large. For this reason, we measured the sintering rate of a sample of polymer binder in powder form.

Therefore, instead of measuring the rate at which the composite material sinters, we obtained the sintering rate of the binder. Our next task, was to relate the polymer sintering rate to the composite sintering rate. After proposing several models for the interactions that may occur during the sintering of ceramic agglomerates coated with a polymer binder, we settled on a very simple model. Basically, the ceramic and the polymer are treated as two separate powders, and the change in void fraction only occurs in the polymer phase. By this approximation, if the polymer phase completely sinters to full density, the overall change in void fraction is proportional to the amount of polymer present. In our study, the complete sintering of polymer results in the complete sintering of 20 percent of the composite material.

The two building blocks described above, the thermal diffusion equation and the sintering rate equation, are combined in a one-dimensional finite element program optimized to model powder sintering. This transient model calculates the temperature profiles within the powder bed during SLS processing. Within each time step, the temperature profile is used to compute the degree of sintering at each node, and any changes in porosity are calculated. The simulation is complete when the temperature of the powder bed drops below the softening temperature of the polymer where sintering no longer occurs.

Material Properties

In order to model sintering and the subsequent densification during SLS processing, four pieces of information about the material system must be known which are the thermal conductivity, specific heat, density, and sintering rate of the composite material. Traditionally, the thermal properties of powders are not readily available, therefore, methods of measurement and calculation of the thermal properties must be examined. Calculation of the thermal properties of a powder poses several challenges. The fact that the material system focused upon in this paper is a composite, increases the difficulty of calculation. Techniques for measurement and prediction of the thermal properties needed for the development of a sintering model are presented below.

Density

The solid density of the composite material is calculated as a function of densities of the individual materials,

$$\rho_s = \phi \rho_{pmma} + (1 - \phi) \rho_{SiC} \quad (5)$$

where ϕ is the volume fraction of polymer binder. For our material system, the polymer comprises 20 percent of the total volume and has a density of 1.2 g/cm³. The ceramic, Silicon Carbide has a solid density of 3.217 g/cm³. Therefore the solid density of the composite material is 2.81 g/cm³ by Equation (5).

The density of the agglomerated powder is calculated as a function of the solid density and the powder porosity, Equation (4). The initial porosity of the powder bed is 0.5, which corresponds to a density of 1.41 g/cm³. As the porosity decreases, the density of the powder bed approaches the solid density of the composite.

Specific Heat

The specific heat of the composite is calculated as the mass average of the specific heats of each phase,

$$C_p = \xi C_{P(\text{pmma})} + (1 - \xi) C_{P(\text{SiC})} \quad (6)$$

where ξ is the weight fraction of polymer binder. For the composite material system, the weight fraction of polymer is 0.085, which corresponds to a volume fraction of 0.20 polymer. The weight fraction and the volume fraction are related by the following,

$$\phi_1 = \frac{\rho_2 \xi_1}{\rho_2 \xi_1 + \rho_1 (1 - \xi_1)} \quad (7)$$

where the two components are designated by the subscripts 1 and 2.

The specific heat of a material can be readily measured using a DSC (Differential Scanning Calorimeter) or similar apparatus. Figure 1 presents specific heat data for each phase (solid lines) and for the composite (dashed line). The specific heat of PMMA was unavailable at the time of the simulation, therefore, the specific heat of polycarbonate was used in the calculations. The specific heat of the polymer is double that of the silicon carbide. The specific heat of the composite calculated from a mass average of the two components agrees fairly well with the measured data.

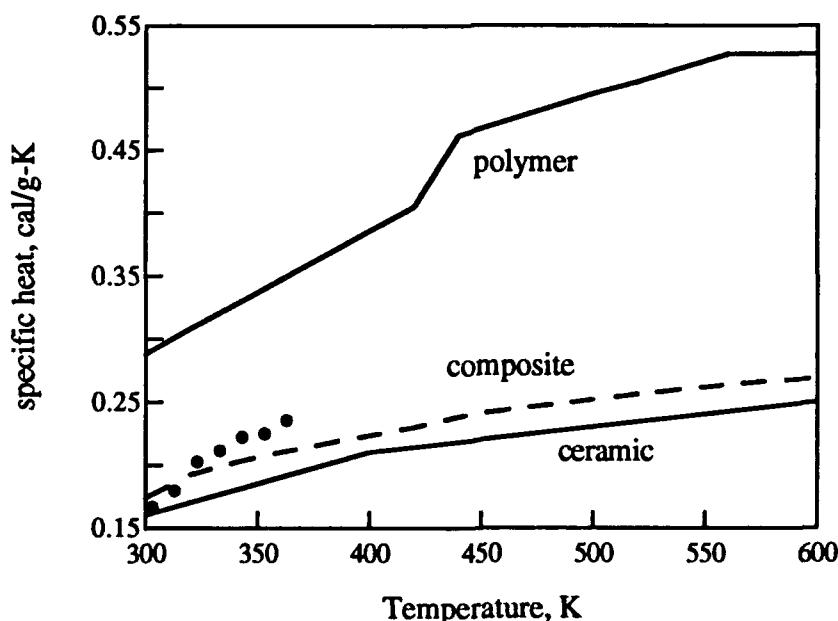


Figure 1 Effective specific heat of the powder bed. The markers (●) represent data measured using a DSC. The specific heat of the composite calculated by a mass average is represented by a dashed line.

Thermal Conductivity

For most solid materials, thermal conductivity data is reported at one or more temperatures. However, the thermal conductivity data for powders is not readily available. Therefore, the properties of powder must be measured or modeled. The transient heat conduction method [Naumann, 1983] is one method used to measure thermal conductivity of a powder. The transient method is used by Xue, [Xue, 1991], to measure thermal conductivity of powders used in the SLS process. The data reported below for the SiC/PMMA system was measured by Xue using a water bath method and a laser-heated method, [Shi, 1993]. In Figure (1), thermal conductivity data measured by both methods is reported for the composite material at a bed void fraction, ϵ , of 0.53. The water bath method and the laser heating method are represented by circles (●) and diamonds (◆), respectively. The water bath method is limited to temperatures below 100 °C; however, the laser heat method allows the measurement of thermal properties at higher temperatures. The sharp increase in thermal conductivity above 100 °C is due to the sintering of the polymer, and the improved contact between Silicon Carbide (SiC) particles.

The model considered for the calculation of the thermal conductivity was published in 1957 by Sakae Yagi and Daizo Kunii [Yagi, 1957] at The University of Tokyo. Yagi and Kunii presented a theoretical model for the effective thermal conductivity of packed beds. The influence of both packing characteristics and temperature on the effective thermal conductivity was studied by comparisons with experimental data. The general equation derived is reduced to the following in the case of gas-filled voids in a motionless fluid:

$$\frac{k_e}{k_g} = \frac{\beta(1-\epsilon)}{\gamma\left(\frac{k_g}{k_s}\right) + \frac{1}{\frac{1}{\phi} + \frac{D_p h_{rs}}{k_g}}} + \epsilon\beta \frac{D_p h_{rv}}{k_g} \quad (8)$$

where k_e is the effective thermal conductivity of the powder, k_g and k_s are the thermal conductivity of the gas and the solid respectively, ϵ is the void fraction of the powder bed, D_p is the average particle diameter, h_{rv} and h_{rs} are the radiation heat transfer coefficients for void to void and solid surface to solid surface, and the remaining variables describe the geometry of the packing. The factor γ is defined as the effective length of solid relating to thermal conduction, divided by the mean diameter of the solid. The factor β is defined as the ratio of the average length between the centers of two neighboring solids in the direction of heat flow, to the mean diameter of the packing. The factor ϕ is defined as the ratio of the effective thickness of fluid film through which heat is conducted to the mean diameter of the packing material. The geometric factors were found by analyzing experimental data reported for effective thermal conductivity, and correlating the data with the theoretical equations. Values of ϕ are calculated as a function of void fraction, ϵ , from experimental data previously reported for air. The data conforms to Equation (9).

$$\phi = 0.1927 \times \epsilon^{1.8544} \quad (9)$$

The values of both β and γ are approximately unity, for all cases where the packing particles were either spherical or cylindrical.

Table 1 summarizes the solid and gas thermal conductivity data used to calculate the thermal conductivity of the powder. Because the Yagi-Kunii model, Equation (8), considers only one material, the thermal conductivity of the ceramic and the polymer must be consolidated into an effective thermal conductivity, $k_{s,eff}$, of the solid composite material. The effective thermal conductivity of the composite is then used to calculate the effective thermal conductivity of the powder. Two methods are used to calculate the effective thermal conductivity of the solid. First, a simple volume average of the solid thermal conductivity data is considered, Equation (10). As shown in the fifth column of Table 1, this method heavily weights the thermal conductivity of the ceramic. The second method consists of a more complex means of calculating an equivalent thermal conductivity. Based on the assumption that each ceramic particle is evenly coated with polymer, a one-dimensional resistance model is defined, and the effective thermal conductivity is calculated by integrating the thermal conductivity through the particle, [Badrinarayan, 1990]. This method heavily weights the thermal conductivity of the polymer, because all of the heat conducted through the particle must pass through a thin film of polymer. As the thickness of the polymer coating increases, the effective thermal conductivity of the particle approaches that of the polymer.

$$k_{s,eff} = (\phi)k_{s,pmma} + (1 - \phi)k_{s,SiC} \quad (10)$$

Table 1 Thermal conductivity data used in calculate the effective thermal conductivity in Figure 2. The composite material is 20 percent by volume polymer. thermal conductivity, k (W/m-K)

Temperature, K	solid material, k_s		gas, k_g	composite material (SiC/PMMA), $k_{s,eff}$	
	SiC	PMMA	Air	volume average	equivalent conductivity [‡]
300 (27 °C)	456.3	0.195	0.026	368.3	3.04
370 (97 °C)	383.4	0.248	0.031	309.5	3.64
440 (167 °C)	310.6	0.30 [†]	0.036	250.7	4.23

[†] extrapolated

[‡] method derived by Badrinarayan, 1990

Figure 2 compares the measured and calculated effective thermal conductivity of a randomly packed bed of coated ceramic particles. The lines represent the thermal conductivity calculated using the Yagi-Kunii model in conjunction with the effective thermal conductivity of the solid listed in Table 1. The void fraction of the powder bed is decreased linearly from 0.53 (370 K) to 0.41 (420 K) to account for sintering of the polymer phase. The change in void fraction is based on density measurements made by Xue. Although there is a significant difference between the effective thermal conductivity of the composite, the effective thermal conductivity of the powder differs by approximately 20 percent. However, the thermal conductivity model fails to capture the true temperature dependence of the composite material.

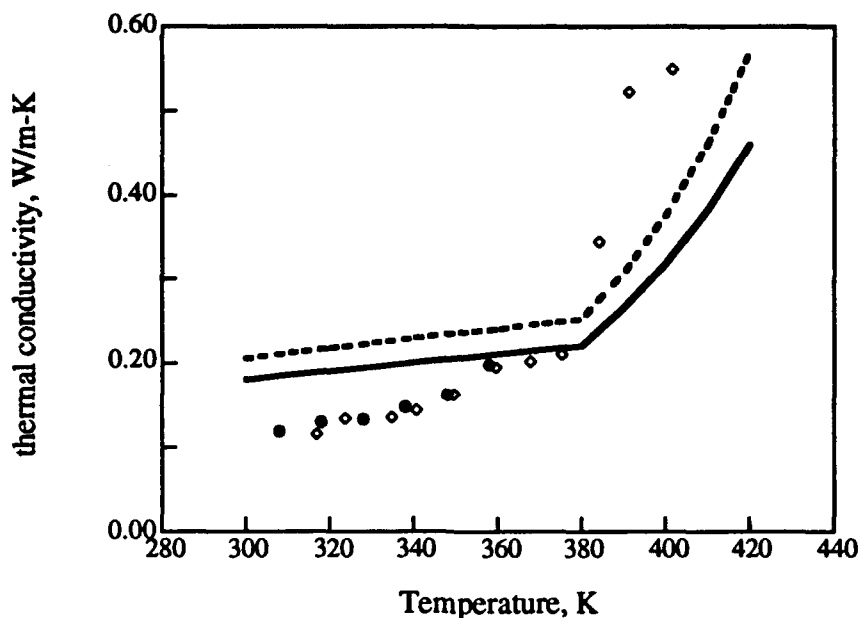


Figure 2 Effective thermal conductivity of the powder bed where the SiC particles are coated with 20 % by volume PMMA, and the void fraction is 0.53. The markers represent data measured by the (●) water bath method, and the (◊) laser heating method. The lines represent values of thermal conductivity calculated using the Yagi-Kunii model. The solid thermal conductivity used in the model is either (---) a volume average, or (—) an equivalent conductivity, see Table 1.

Sintering Rate

The sintering rate measurement is a key element in the sintering model. Figure 3 shows rate data for both pure PMMA powder and for the composite spray dried powder. The data points represent isothermal rate measurements made using an oven sintering apparatus. The temperatures at which the experiment was performed ranged from 100 to 150 °C. The temperature range used is dependent on the softening temperature of the binder (low value) and the viscosity of the binder (high). Below the softening temperature no sintering occurs. And at higher temperatures, sintering occurs too quickly, and may finish before the sample reaches an equilibrium temperature. Typically, the operating range is between 10 to 50 °C above the softening temperature of the binder.

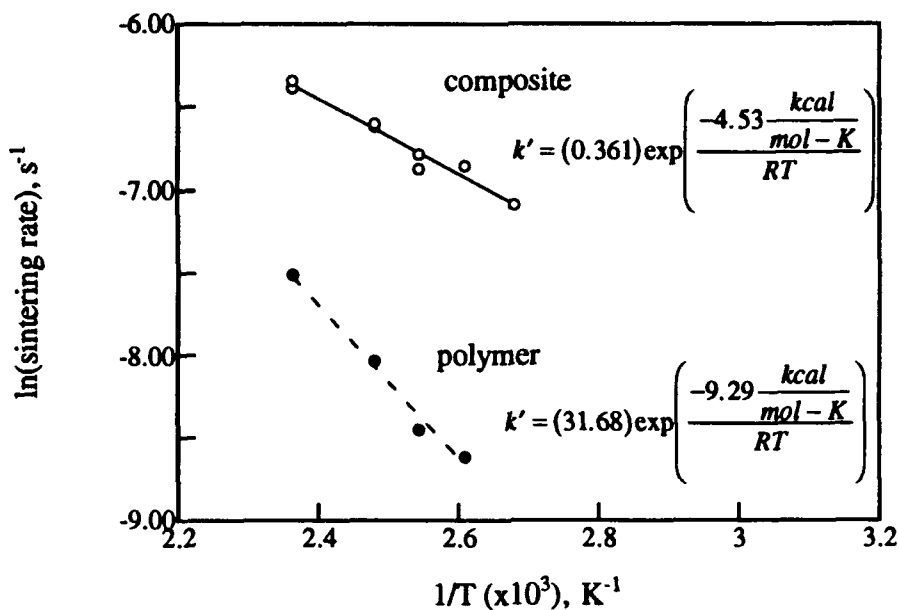


Figure 3 Sintering rate data for both polymer (PMMA) powder and composite (SiC/PMMA) spray dried powder.

Results and Discussion

Analyzing the results posed several challenges. First, during the actual SLS processing of the composite material, there is no noticeable change in density. Consequently, the density of the green part is the same as that of the unsintered powder. This negligible change in density during SLS processing prevents the direct comparison of sintering model results to the experimental data. For example, in the case of the amorphous sintering model [Nelson, 1993], a direct comparison was made between the density of a SLS part to the density calculated by the sintering model. However, this correlation cannot be made for the composite materials.

Therefore, another means of comparing model results to a measurable parameter has to be established. Bending strength data is available for SiC/PMMA composite SLS parts as well as pictures of the fracture surfaces, [Vail, 1993]. In order to compare the sintering model results to this experimental data, the SLS operating parameters used to make the composite parts via SLS, are used to calculate the surface boundary condition in the model. For the sintering model, a void fraction profile is obtained after the sintering is complete.

To reduce the number of variables in the analysis, the SLS operating parameters are reduced to an energy per unit area, \mathcal{A}_N (cal/cm²), Equation (11). Figure 4 compares both the bending strength of SLS green parts and the percent change in void fraction of the fusible material to the energy flux.

$$\mathcal{A}_N = \frac{\text{laser power}}{(\text{beam speed})(\text{scan spacing})} \quad (11)$$

Both curves increase as the energy flux increases, which is the expected response. In Figure 4a, the change in the initial void fraction of the polymer phase is plotted versus the energy input. As the energy flux is increased, the powder reaches higher temperatures leading to more sintering. In Figure 4b, as the energy flux increases, the strength of the SLS parts increases leveling off at higher values of A_N .

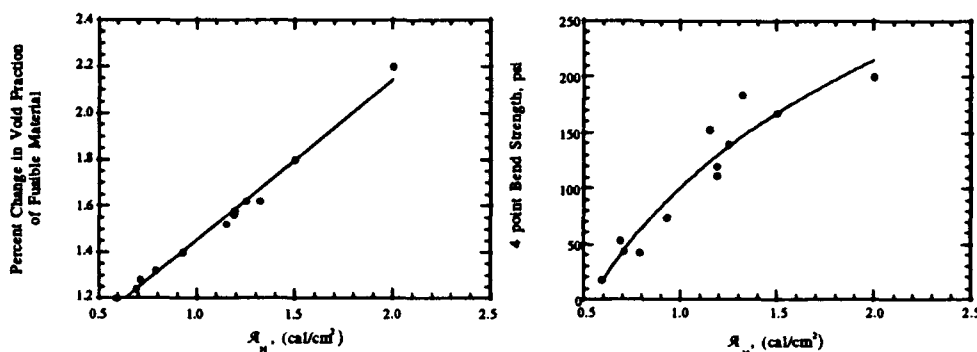


Figure 4 Effects of an increase in the energy per unit area delivered by the laser during a part build. The predicted change in void fraction (left), and the measured bending strength of test bars via SLS processing (right).

The data in Figure 4 can be replotted by relating the two curves by their common variable, A_N . Based on the assumption that the strength increases as the void fraction decreases, the sintering model accurately predicts the expected trends.

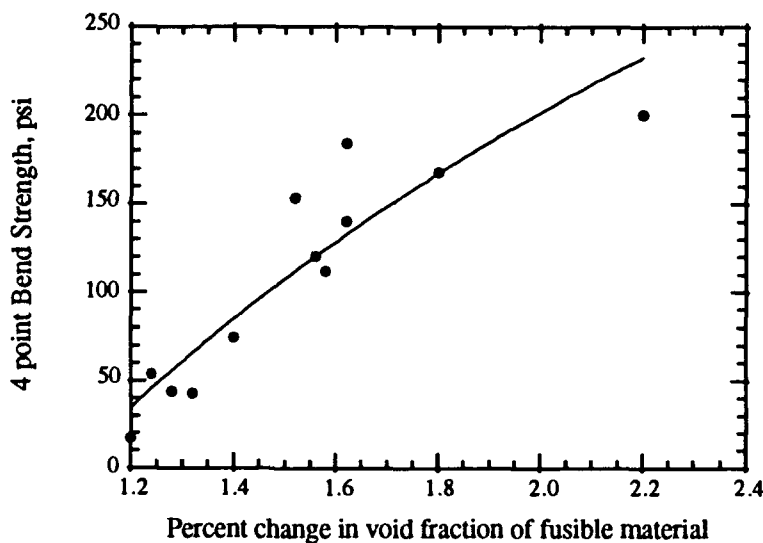


Figure 5 Comparison of model results to measured bending strengths.

Summary

The task of developing a laser sintering model for composite materials has presented several challenges. A very simple sintering model to explain void reduction is used because of a lack of information about the sintering of polymer coated agglomerates. The thermal properties of the composite material are calculated from the material properties of each phase. The material properties and the sintering rate data for the composite material are combined in a sintering model which calculates temperature and void fraction profiles in one-dimension. The results of the numerical analysis compare favorable to the measured bending strengths of composite test bars via SLS. The general trends of increasing strength and decreasing void fraction are compared over a range of SLS operating parameters. Future modeling should focus on the interactions between particles and agglomerates during two phase sintering.

References

Badrinarayan, B. and Barlow, J. W., "Prediction of the Thermal Conductivity of Beds which Contain Polymer Coated Metal Particles", In *Solid Freeform Fabrication Symposium Proceedings*, pp. 91-98, 1990.

Naumann, D. and Seydel, K., "Messung der Wärmeleitfähigkeit von Pulvern (Measurement of Thermal Conductivity of Powders)," *Plaste and Kautschuk*, 30, pp. 233-234, 1983.

Nelson, J. C. and Barlow, J. W., "Sintering Rates in the Selective Laser Sintering Process" In *Solid Freeform Fabrication Symposium Proceedings*, pp. 164-170, 1990.

Nelson, J. C., *Selective Laser Sintering: A Definition of the Process and an Empirical Sintering Model*, Ph.D. dissertation, The University of Texas at Austin, 1993.

Shi, S. (Xue) and Barlow, J. W., "Measurement of the Thermal Conductivity of Powders by Two Different Methods," In *Solid Freeform Fabrication Symposium Proceedings*, 1993.

Vail, N. K., Barlow, J. W., and Marcus, H. L., "Silicon Carbide Preforms for Metal Infiltration by Selective Laser Sintering of Polymer Encapsulated Powders," In *Solid Freeform Fabrication Symposium Proceedings*, 1993.

Xue, S. and Barlow, J. W., "Models for the Prediction of the Thermal Conductivities of Powders," In *Solid Freeform Fabrication Symposium Proceedings*, pp. 62-69, 1991.

Acknowledgments

We acknowledge financial support of this work from DARPA-ONR grant N0014-92-J-1394.

MEASUREMENT OF THE THERMAL CONDUCTIVITY OF POWDERS BY TWO DIFFERENT METHODS

Samuel S. Sih and Joel W. Barlow
Chemical Engineering Department
University of Texas at Austin

Abstract

The thermal diffusivities and thermal conductivities of powders, especially PMMA-coated silicon carbide, at various temperatures, have been tested by two different dynamic methods, the water-bath method and the laser-heated method. The thermal conductivity data found by these two techniques are found to be consistent with each other.

A Review of the Two Techniques

A Differential scanning calorimeter (DSC), DSC-7 made by the Perkin-Elmer Company, has been used [1] to measure the heat capacities at various temperatures for all of the powders used. The heat capacities of the powders were found to be functions of temperature. The specific heats of all the powders are found to be the same as those of the corresponding solids.

The thermal conductivities of powders are measured by an unsteady state method with two water baths of small temperature differences[1,2,3]. The range of the temperatures investigated, limited by the boiling point of water in the water-bath method, was mainly from 30-90°C, i.e. below the sintering temperatures of the powders. During the process of raising the temperature, sometimes bubbles of air were seen to adhere to the outside surface of the sample tube which obviously decreases the rate of the transfer of heat. The authors found that the formation of air bubbles may be avoided by the addition of some soap solution into the water baths to decrease the surface tension of the water used. Only small changes in temperature, typically 10°C, are used. This is necessary to account for the temperature dependent thermal properties at the powder beds.

As the temperatures used during the SLS process are not limited to the ambient temperatures, a laser-heated method [5,6,7] was adopted to study thermal conductivity at the higher temperatures. This technique uses a laser to heat the surface of a sample powder bed while a thermocouple at a certain depth inside the powder bed records the rise of temperature against time.

Figure 1 shows the basic experiment. The powder bed is contained in a 1 inch diameter by 5 inch long glass tube. The bed temperature is maintained at the desired temperature by a 675 watt Tempco Co. coil heater (MHS1255BL02). That is controlled by a pulsed DC output temperature controller (Omega CN76120). The pulsed output is used to switch a solid state relay connected to the heater AC power line. The powder samples completely fill the sample tube. The center temperature, 1 cm below the bed surface, is measured with a thermocouple. The tube is wrapped with thin aluminum foil and placed inside the coil heater.

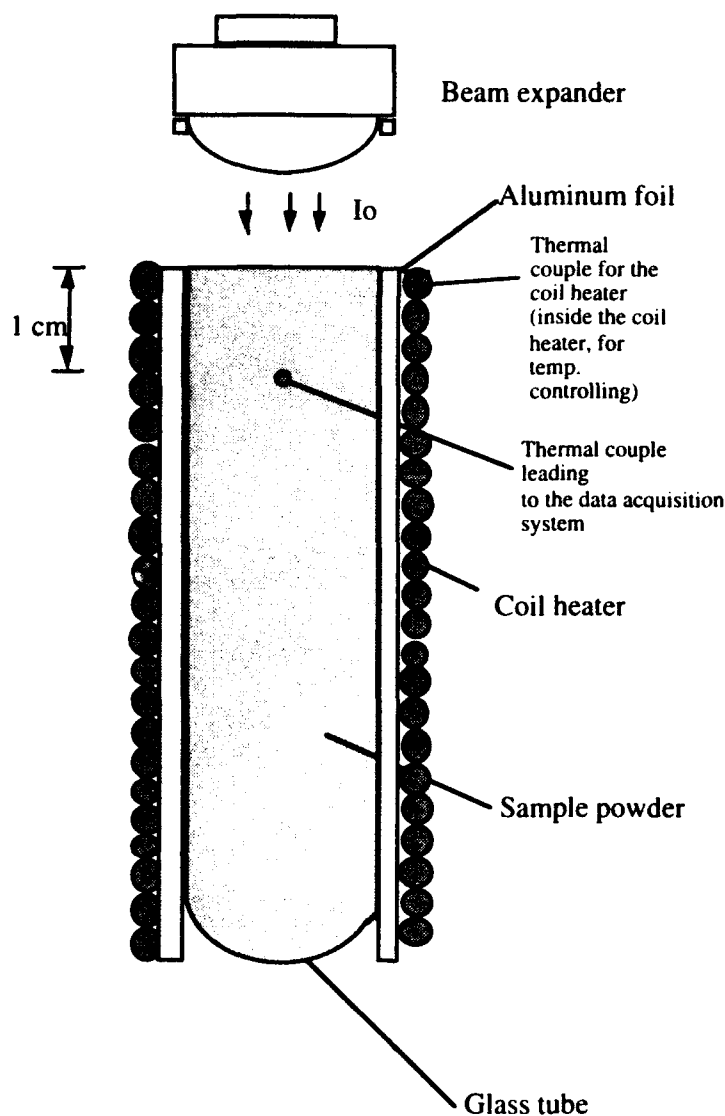


Figure 1. The laser and the powder sample

One might have the worry whether the heat energy supplied through the coil heater might interfere with the energy supplied by the laser power. But actually, with the short incidence of the laser light (from 1 min. to about 4 min.) and with the small change in temperature caused by the laser, the coil heater generally sends in little energy, if any.

Experimental Results

The PMMA-coated SiC, prepared by Neal Vail, has 19.3 vol% of the polymer. The solid density for PMMA is 1.2 g/cc, the solid density of SiC is 3.217 g/cc. So the solid density of the PMMA-coated SiC is 2.827 g/cc. The bulk density of the powder sample we used for the water bath method was 1.328 g/cc. Consequently, the porosity of the powder sample was 0.530. The temperature range for the water bath method was 30-59°C. One of the temperature vs. time curve of water bath runs is shown below. (See Figure 2.)

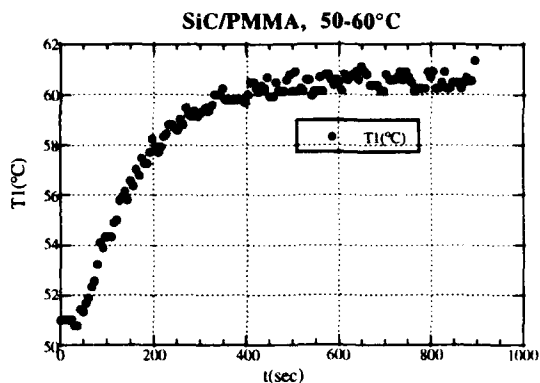


Figure 2. PMMA-coated SiC powder temperature rising curve, 50-60°C

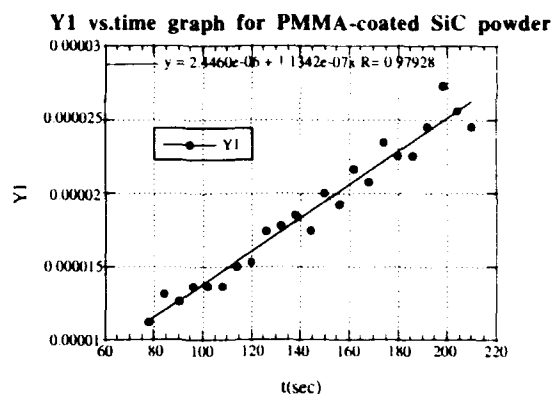


Figure 3. Y1 vs time graph for the same powder and same heating cycle

The analysis of the water bath data is done according to the procedure discussed before. [1] The Y1 vs time graph for the PMMA-coated SiC powder, from 50-60°C is shown in Figure 3. (See Figure 3.)

The heat capacity of the PMMA-coated SiC powder vs. temperature is shown in Figure 4. (See Figure 4.) The resulting thermal conductivity of the PMMA-coated SiC powder vs temperature is shown in Figure 5.

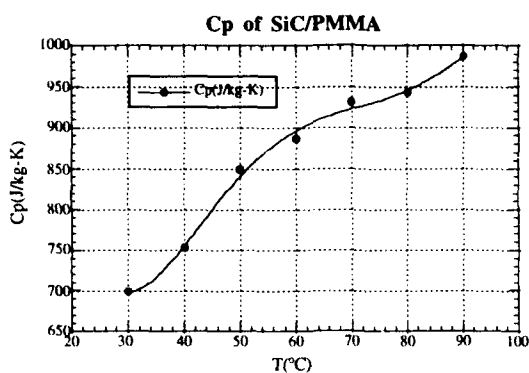


Figure 4. The heat capacity vs. temperature curve of PMMA-coated SiC powder

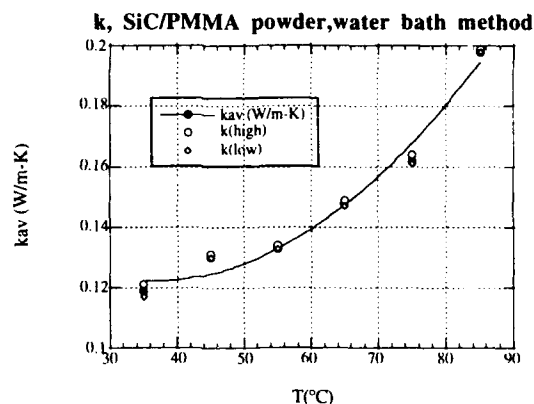


Figure 5. The thermal conductivity vs. temperature curve of PMMA-coated SiC powder

The porosity of the powder of the PMMA-coated SiC which we tested through the laser-heated method was also 0.530. The temperature rise vs. time curve of one of the runs of the laser-heated method is shown in Figure 6.

k for PMMA-coated SiC powder, laser-heated method

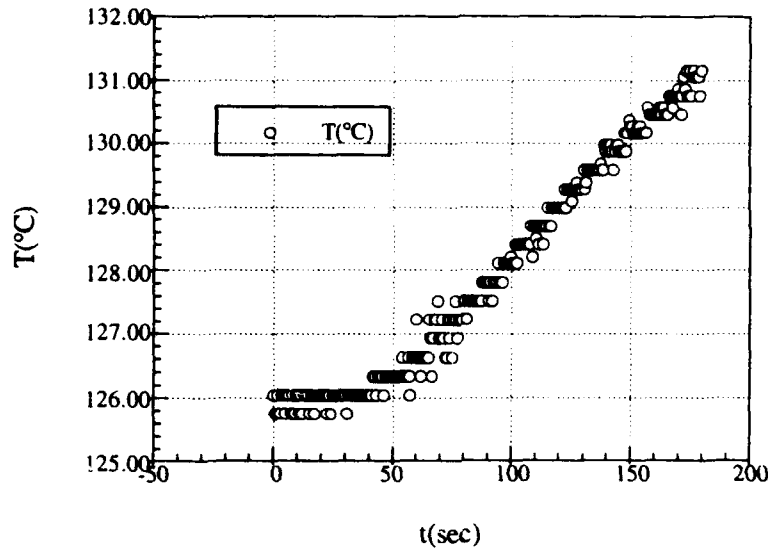


Figure 6. The temperature rise vs. time curve of PMMA-coated SiC powder in the laser-heated method.

The data are analyzed by the ratio method as discussed before [5]. For the run of Figure 6, the reading of the temperature at 90 sec. was 127.82°C, and the reading of the temperature at 180 sec. was 131.15°C. (The reading of the numbers were obtained not through the graph, but through the output of the data acquisition system.) As the initial temperature of the run was 126.05°C, the ratio, R , of the two temperature differences at the two time periods is

$$R = \frac{131.15 - 126.05}{127.82 - 126.05} = 2.88 \quad (1)$$

The mathematical solution for this semi-infinite 1-D heat conduction problem [5] is

$$\begin{aligned} \Delta T(z, t) &= \frac{2\epsilon I_0}{k} \sqrt{\alpha t} \operatorname{ierfc}\left[\frac{z}{2\sqrt{\alpha t}}\right] \\ R &= \frac{\Delta T(L, 2t_1)}{\Delta T(L, t_1)} = \frac{T_2 - T_0}{T_1 - T_0} = \frac{\sqrt{2} \operatorname{ierfc}\left[\frac{L}{2\sqrt{\alpha t_2}}\right]}{\operatorname{ierfc}\left[\frac{L}{2\sqrt{\alpha t_1}}\right]} \\ &= \frac{\sqrt{2} \operatorname{ierfc}\left[\frac{1}{2\sqrt{2}\sqrt{Fo}}\right]}{\operatorname{ierfc}\left[\frac{1}{2\sqrt{Fo}}\right]} \quad (2) \end{aligned}$$

In the above equation, the Fourier number, $Fo = \alpha t_1/L^2$, and L is the depth of the point beneath the surface at which the thermocouple is placed.

The authors wrote a Fortran program for the above relationship and got a table to find out the value of Fo for every definite R value, in Equation (2). For the value of $R = 2.88$, we found $Fo = 0.322$. Therefore,

$$\alpha = \frac{Fo \cdot L^2}{t_i} = \frac{0.322 \cdot 1^2}{90} = 0.000000358 \text{ m}^2 / \text{sec}, \quad (3)$$

at the average temperature of 128.6°C. At this temperature, $C_p = 1155.78 \text{ J/kg} \cdot ^\circ\text{K}$ (from extrapolation). The bulk density of the powder bed, $\rho = 1328 \text{ kg/m}^3$. Therefore, $k = 0.549 \text{ W/m-K}$.

The thermal conductivity data of the PMMA-coated SiC powder vs. temperature curve, obtained through the laser-heated method is shown in Figure 7.

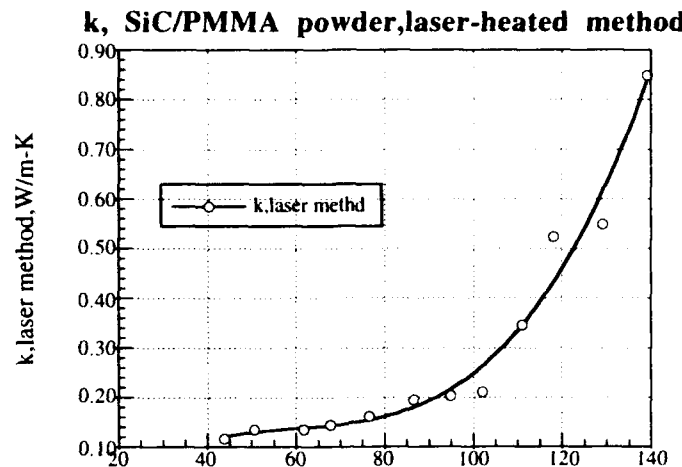


Figure 7. The thermal conductivity of PMMA-coated SiC powder vs. temperature curve through the laser-heated method

Two sets of the thermal conductivity data vs. temperature of the PMMA-coated SiC powder by the laser-heated method, together with the set of data of the same powder by the water bath method are shown together in Figure 8.

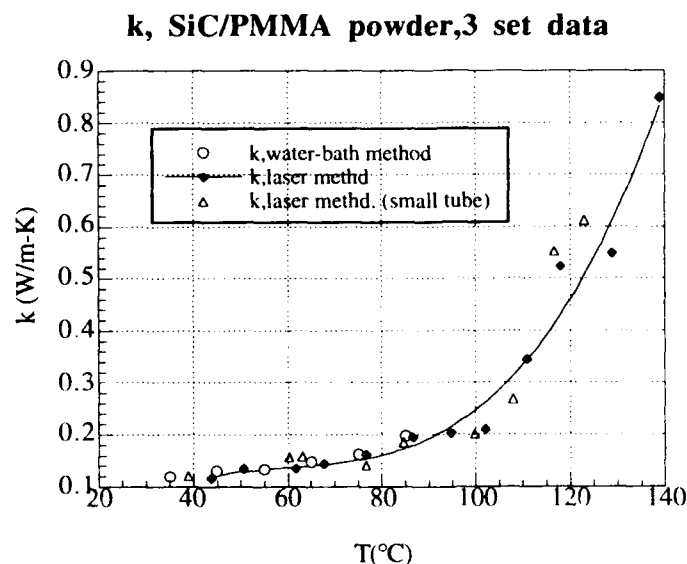


Figure 8. The thermal conductivity of PMMA-coated SiC powder vs. temperature data by three sets of experiments, porosity = 0.530

It may be seen that the data of the thermal conductivity of the PMMA-coated SiC powder obtained by us through the water bath method and the laser-heated method are very consistent.

Just for the sake of reference, the thermal conductivity of pure SiC powder ($\epsilon = 0.4357$) has also been tested by the authors by using the water bath method. It increases from 0.24 W/m-K to 0.32 W/m-K as the temperature changes from 35°C to 85°C. This agrees well with the reported value of the thermal conductivity of SiC powder in air (porosity = 0.425) of 0.263 W/m-K (0.226 kcal/m-h-K). [9,10,11]

Summary and Conclusions

The water-bath method used by the authors for the investigation of the thermal properties of powders is limited to a temperature range below 100°C. The laser-heated method shows similar results for thermal conductivity tests of the PMMA-coated silicon carbide powder samples below 100°C to those obtained by the water-bath method. This suggests the validity of the laser-heated method for the investigation of the properties of powders near the sintering temperatures of the powders.

Acknowledgments

The authors gratefully acknowledge support for this work by the University of Texas SFF Industrial Associates Program and by Lanxide Corporation.

References

1. Xue, Samuel S. and Barlow, J.W., 'Thermal Properties of Powders', in the Solid Freeform Fabrication Symposium Proceedings, the University of Texas at Austin, Austin, Texas (1990), pp. 179-185.
2. Xue, S.S., Master's thesis, The Thermal Properties of Polymer Powders, the University of Texas at Austin, December, 1991, pp. 69-71, 76.
3. Dieter Naumann and Klaus-Jürgen Seydel, "Messung der Wärmeleitfähigkeit von Pulvern," Plaste und Kautschuk, vol. 30, no.4 (1983), p. 233-234.
4. Carslaw, H.S., and J. C. Jaeger, Conduction of Heat in Solids, Oxford University Press, Oxford, 1959, p.112; 256-263.
5. Xue, Samuel S. and Barlow, Joel W., 'The Measurement the Thermal Properties and Absorptances of Powders near their Melting Temperatures,' in the Solid Freeform Fabrication Symposium Proceedings, the University of Texas at Austin, Austin, Texas (1992), pp. 131-140.
6. Taniguchi, N., Ikeda, M., Miyamoto, I., and Miyazaki, T., Energy-Beam Processing of Materials, Clarendon Press, Oxford, 1989.
7. Ikeda, M. et al., 'Basic Techniques of Laser Processing,' Precision Machinery, (in Japanese) vol.51 (1985), no. 12, pp. 2253-2258.
8. Tavman, Ismail, 'Flash Method of Measuring Thermal Diffusivity and Conductivity,' in Convective Heat and Mass Transfer in Porous Media, edited by Sadik Kakaç, et al., Kluwer Academic Publishers, London, 1991, pp. 923-936.
9. Kannuluick, W.G., and Martin, L.H., 'Conduction of Heat in Powders,' Proc. Royal Soc. (London) **A141**, 144 (1933).
10. Wilhelm, R.H., Johnson, W.C., Wynkoop, R. and Collier, O.H., 'Reaction rate, heat transfer and temperature distribution in fixed-bed catalytic converters,' Chem. Engineering Progress, vol. 44(2), 105 (1948).
11. Krupiczka, R., 'Analysis of Thermal Conductivity in Granular Materials,' International Chemical Engineering, vol.7, no. 1, January 1967, pp. 122-144.

Selective Laser Sintering of Bioceramic Materials for Implants

Goonhee Lee and J.W. Barlow
Department of Chemical Engineering
The University of Texas at Austin

ABSTRACT

Selective Laser Sintering (SLS) process is employed for fabrication of bioceramics for orthopedic implants. Hydroxyapatite and Calcium Phosphate ceramics are coated with polymer as a intermediate binder by using a spray drier. Polymer coated materials are SLS processed to make green parts, which are infiltrated and fired to remove the polymer. SLS processed green parts of hydroxyapatite have low density due to the small particle size with large specific surface area. This paper discusses the possibilities and problems in free-form fabrication of bioceramic.

INTRODUCTION

Many attempts have been made to find material that will assist in the regeneration of bone defects and injuries. Calcium phosphate ceramics, particularly hydroxyapatite (HA), $\text{Ca}_5(\text{OH})(\text{PO}_4)_3$, has received special attention as potential bone implant material because of its biocompatibility with the tissue and its compositional similarities to human bone and tooth. Many studies and methods, from powder compaction sintering to hot isostatic pressing, have been reported for the fabrication of HA. However, sintered HA materials by conventional techniques are as weak as sea coral even at high compacting pressure, because HA decomposes at temperatures lower than the required temperature for sintering.

Selective Laser Sintering (SLS) processes for preparing ceramic green parts with polymer as intermediate binder and post processing with the aid of ceramic cement have been discussed in detail in literature [1]. One advantage of SLS process for fabrication of bioceramic is the accurate construction of a complete facsimile bone structure from the geometric information obtained from either patient computed tomographic (CT) data or a computer Aided Design (CAD) software package [2]. Another advantage is the ability to controlling pore structure for biogenesis through control of polymer content.

MATERIALS and METHODS

HA, obtained from Monsanto Inc. as Tricalcium Phosphate, TCP, was used as starting material. HA powders are very cohesive and consist of very porous agglomerates with mean particle size of 1 to 2 μm and bulk density of less than 0.4 g/cm^3 [3]. The surface area determined by Mercury intrusion analysis is about 60 m^2/g , suggesting very small particles. Stoichiometric HA contains constitutional water in the form of OH^- ions. This water can be driven off at 1200 $^\circ\text{C}$. Figure 1 shows the microstructure of finely divided HA powders.



Fig.1 : Scanning Elctron Micrograph of HA (X1000)

Two intermediate polymeric binders, UCAR 430 Acrylic Polymer Latex (obtained from Union Carbide Corporation) and PMMA emulsion copolymer, designed to depolymerize completely to gaseous product when heated above 400°C were investigated. Inorganic ceramic cement, Cerama Bind™ 542 was obtained from Aremco Products Inc. This inorganic cement is an alumino-phosphate material that can react to form phosphate bonded HA material.

Polymer was deposited on the HA powder by spray drying a slurry of the powder with polymer emulsion in "Pulvis Mini Spray" drier. To determine the required amount of polymer binder, the coated powder was heated in air to 150 °C to fuse the polymer. Afterwards, the powder was cooled and qualitatively examined. More than 20 % (45 vol.%) of UCAR 430 was required to produce a cake that barely permit handling. While PMMA copolymer coated materials showed better properties at 20 % coating, cakes could still be easily crumbled. These problems were attributed to the high surface area of the finely divided HA powder.

In an attempt to modify surface area, 50 g HA was reacted with 100 ml of 5 M ortho-phosphoric acid(H_3PO_4), and heated to 150 °C to form a cake. The cake was then ground back to finely divided powder by a Szegvari attritor system, type 1HSA. The morphology of the reacted HA powder is shown in Figure 2. The powder was spray dried and examined as before. The oven sintered cake showed much improved strengths, enough to permit rough handling, with the 14% (30 vol.%) of PMMA copolymer.

Based on the oven tests, we scaled up the coating of reacted HA powders with the 14 % of PMMA copolymer by using an Anhydro Laboratory Spray Drier #1 [4]. The operating conditions are as follows:

Solid content	: 45 wt.%
Inlet temperature	: 175 °C
Outlet temperature	: 110 °C
Atomizer speed	: 30,000 rpm

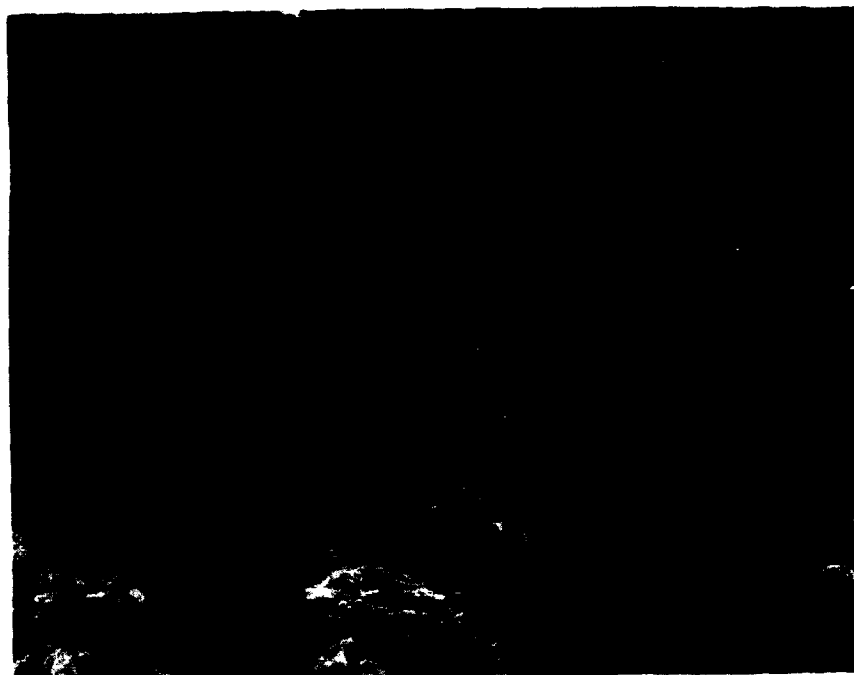


Fig 2 : S.E.M. of 5 M reacted HA (X 1000)

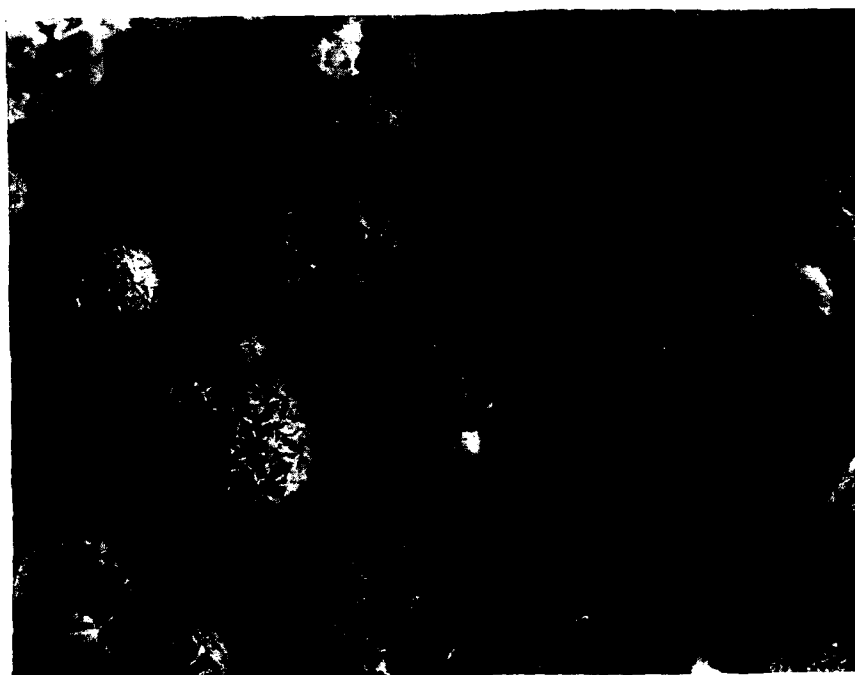


Fig 3 : S.E.M. of a polymer coated powder (X800)

Figure 3 shows the Scanning Electron Micrograph of a polymer coated powders. Spray dried powders are SLS processed using an University of Texas SLS machine. The operating conditions are presented in Table 1.

Table 1 : Operating condition of SLS machine

Power (W)	Bed Temp.(°C)	Layer Thickness	Scan Space (mil)	Scan Speed (inch\sec)
5	120	8 mil	5	15

SLS processed parts were infiltrated with the phosphoric acid based inorganic cement. High surface tension was observed on infiltration which prevented effective penetration by the cement. Diluted methanol and Witcolate D51-51 surfactant (Witco Corporation) were used to reduce the surface tension. Infiltrated green parts were dried for 5 days in ambient condition. Upon drying, the parts were cured in the oven at 200 °C raised at 50 °C/hr. As a final step, green parts were fired up to 700 °C in the furnace for 2 hours to burn off the polymer.

RESULTS AND CONCLUSIONS

Oven tests and some preliminary SLS work(not discussed) showed that parts made with polymer coated non-reacted HA, could not achieve acceptable green strengths. Low bulk density due to very large specific surface area caused by very small particle sizes and large porosity is believed to be the reason for this behavior.

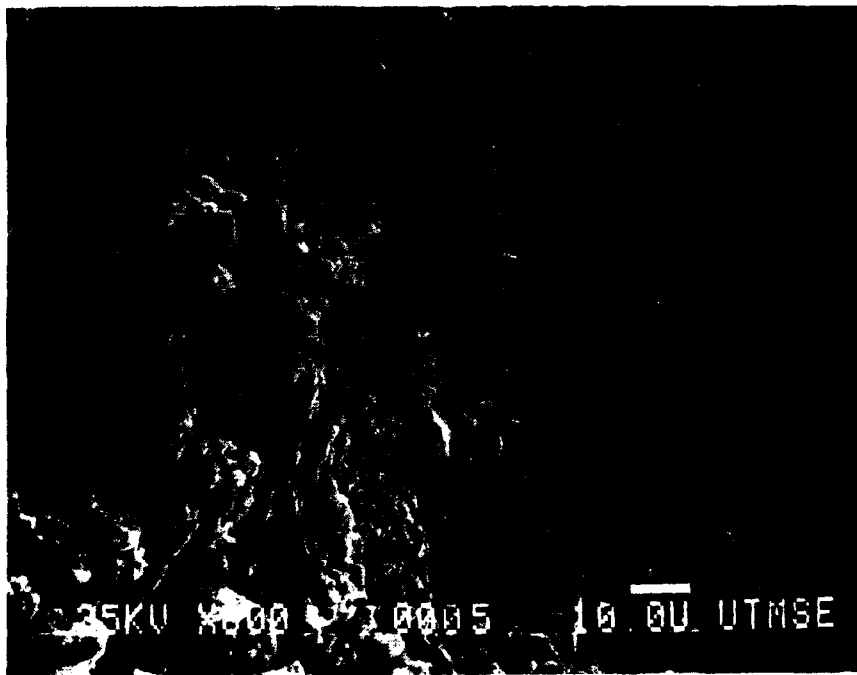


Fig 4:Scanning Electron Micrograph of sintered Surface (X800)

While HA in its pure form has bulk density of less than 0.4 g/cm^3 , HA reacted with 5 M phosphoric acid shows increased density over 0.7 g/cm^3 . SLS processed part made of reacted HA has sufficient strengths for rough handling as oven tests of sintered cakes predicted. The strengths of post-processed bioceramic parts have shown even more promise and are currently being evaluated.

While the SLS processed parts have promising strengths with sufficient pores, biological and mechanical limitations are still prevalent in bioceramics. The implant material should be not only strong enough to be compatible with its use, but also biologically acceptable. The material's porosity should be suitable for bone tissue growth to fix the prosthesis with connecting bones. Fig 4. shows a fractured surface of a part that was post processed and fired. Clearly, there is considerable porosity, and we believe that this interconnected porosity should be sufficient for ingrowth of fibulious tissue. The strengths of these porous structures are currently being evaluated. We believe that the strengths will be sufficient for low-load bearing implants.

REFERENCES

1. N.K. Vail and J.W.Barlow, "Ceramic Structures by Selective Laser Sintering of Microencapsulated, Finely Divided Ceramic Materials", Solid Freeform Fabrication Symposium Proceedings, 3, 124-130(1992)
2. Richard A. Levy, "Preliminary Experience with Selective Laser Sintigraphic (SLS) Models of the Human Temporal Bone", Solid Freeform Fabrication Symposium Proceedings, 3, 161-173 (1992)
3. T.Hattori and Y.Iwadate, "Hydrothermal Preparation of Calcium Hydroxyapatite Powders" J. Am. Ceram. Soc., 73(6) 1803(1990)
4. N.K. Vail and J.W.Barlow, "Effect of Polymer Coatings as Intermediate Binders on Sintering of Ceramic Particles", Solid Freeform Fabrication Symposium Proceedings, 2, 195-205 (1991)

Key Word Index

- 3 Degrees of Freedom scanning (150)
- 3D imaging and modeling (121)
- 3D laser digitizer (150)
- 3D Systems (11, 158))
- abrasives (27)
- accuracy (11, 245)
- acetylene (308)
- acrylate photopolymers (178)
- acrylic polymers (60)
- acrylic resins (27)
- active triangulation (150)
- adaptive 4 axis scanning (150)
- adaptive surface filtering (150)
- alternative to STL (135)
- alumina (40, 60, 333, 350, 370)
- aluminum (158)
- amorphous (325)
- angled wax builds (94)
- anisotropy (193)
- applications (168)
- bend strength (350, 370)
- Bernstein form (291)
- beryllium (158)
- Boeing 737 cargo door bracket (158)
- burn out process (158)
- CAD (102)
- cantilever (11)
- carbon fibers (60)
- Ceracon Forging Process (271)
- ceramic (360)
- ceramic matrix composites (215)
- ceramic shell (158)
- chemical vapor deposition (325)
- Ciba-Geigy (11, 158)
- co-precipitation (339)
- composite (283, 360)
- composites (204)
- Constructive Solid Geometry (291)
- contour editing (150)
- convex hull (291)
- copper (158)
- creep (11)
- creep rate (11)
- curl (11)
- curl distortion (178)
- degree elevation (291)
- degree reduction (291)
- densification (193)
- density (350)
- design for SFF (102)
- design primitives (275)
- designed experiment (178)
- desk-top VR (113)
- diagnostic test (11)
- Digibot (150)
- digital microfabrication (237)
- dimensional control (223)
- dimensional stability (11)
- direct metal fabrication (135)
- directional derivative (291)
- distortion (11)
- drying (333)
- DTM wax process (94) improvements (94)
- efficient data structures (126)
- elastomeric (86)
- electronics (215)
- encapsulation (204)
- Epoxy resin (11)
- expansion (193)
- FDM® (86)
- feed bypass boxes (94)
- fiber reinforcement (283)
- filament (86)
- finishing (27)
- finite element simulation (143)
- Fused Deposition Modeling (FDM®) (86)
- gap elimination (126)
- geometric design (275)
- geometry (102)
- hard tooling (158)
- hard waxes (237)
- homogenization (193)
- Hot Isolastic Pressing (HLP) (51)
- Hydroxapatite (376)
- IGES (275) standard (135)
- implant sintering (376)
- infiltration (215, 339, 376)
- injection molding (303)
- ink-jet printing (81)
- iron (51)
- laminate (74)
- laser (308, 360)
- laser cutting (74)
- laser machining (74)
- laser welding (74)
- latex binder (40)
- layer displacement (223)
- layered manufacturing (1)
- LCVD (253)
- liquefier (86)
- liquid phase sintering (193, 317)
- MD* process (186)
- mechanical forces (223)
- mechanical properties (40, 283, 303)
- melting (1)
- metal (51)
- metal matrix composites (215)
- metals (158)

Microfabrication (253)
 mixing (350)
 model (360)
 modeling (143)
 molds (271)
 molten microdrops (237)
 monomers (60)
 multi material structures (1)
 nanocomposites (64)
 net-shape (271)
 new directions (168)
 NURBS (275)
 NURBS based precise geometry (135)
 organic binder (370)
 oxygenation (339)
 particle size (350, 370)
 photolithography (283)
 polyamide (86)
 polygonal surface generation (150)
 polymer (204, 360)
 polymerization (60)
 polyolefin (86)
 position errors (223)
 post-processing (317)
 powder density (370)
 powder processing (64)
 powder-based processes (223)
 prealloyed bronze powder (317)
 precursor (325)
 preform (271)
 process control (102)
 process modeling (102)
 process parameters (245)
 product design (113)
 product development (113)
 quasi-hollow structure (158)
 QuickCast (158)
 range queries (126)
 rapid prototyping (11, 158, 178)
 reaction sintering (308)
 residual stress (1)
 residual stresses (143)
 robust prototyping (135)
 SALD (253)
 selective area laser deposition (325)
 selective laser reative sintering (64)
 selective laser sintering (51, 64, 204, 215)
 SFF (143)
 shell investment casting (11, 158)
 shrinkage (193, 245, 303)
 shrinkage rate (245)
 silica colloid (333)
 silicon carbide (204, 308, 325)
 silver (339)
 sintering (1, 360)
 slurry viscosity (60)
 software (126)
 sol-gel (339)
 sol-gel synthesis (64)
 solder (81)
 solid freeform fabrication (81, 168, 271, 308, 325)
 spray drying (350, 376)
 stainless steel (158)
 StereoLithography (11, 158, 178, 245)
 STL-files (126)
 strength (193)
 stress cracking (1)
 submicron powders (40)
 superconductors (339)
 superellipsoids (275)
 supersolidus (317)
 surface editing (150)
 surface roughness (27)
 systematic scanning (150)
 tension test (193)
 tetramethylsilane (325)
 thermal conductivity (360)
 thermal modeling (1)
 thermal spray deposition (186)
 Three Dimensional Printing (3DP) (40, 223)
 three dimension geometry (143)
 thresholding algorithms (121)
 titanium (158)
 tooling (271, 303)
 topology design (186)
 topology reconstruction (126)
 triangulation (275)
 ultrasonic finishing (27)
 UserPart (11)
 vibratory bowl abrasion (27)
 virtual reality (113)
 volumetric flow rate (86)
 wax build designed experiments (94)
 XB 5170 (11, 158)

Author/Attendee List

akesh Agarwala (193, 339)
e University of Texas at Austin
inter for Materials Science & Engineering
201
stin TX 78712

John A. Benda
United Technologies Research Center
411 Silver Lane MS 129-39
East Hartford CT 06108
203 727-7215 fax: 203 727-7852

David Bunnell
The University of Texas at Austin
Center for Materials Science & Engineering
62201
Austin TX 78712
512 471-3578

ark Atkeson
ited Technologies Research Center
1 Silver Lane, MS 129-48
st Hartford CT 06108
3 727-7409 / fax: 203 727-7880

Britton R. Birmingham (64, 308, 339)
Center for Materials Science & Engineering
The University of Texas at Austin
62201
Austin TX 78712

Marshall Burns
ENNEX Fabrication Technologies
549 Landfair Avenue
Los Angeles CA 90024
310 824-5185 (voice & fax)

nt Atwood
india National Laboratories
O. Box 5800, Org. 2484-1
uquerque NM 87185
5 844-0816 fax: 505 844-5589

Paul Blake
Texas Instruments
P. O. Box 405, MS 3428
Lewisville TX 75067
214 462-3015/ fax: 214 462-2684

Dan Cain
Lockheed Aeronautical Systems Co.
86 S. Cobb Drive
Marietta GA 30132
404 494-1671/ fax: 404 494-1436

nit Bagchi (283)
echnical Engineering Department
emson University
x 340921
emson SC 29634-0921
3 656-5641/ fax: 803 656-4435

Rick Booth
DTM Corporation
1611 Headway Circle, Bldg. 2
Austin TX 78754

Paul Calvert (60)
University of Arizona
Arizona Materials Labs
4715 East Ft. Lowell Road
Tucson AZ 85712

idrinarayan Balasubramanian (303)
partment of Chemical Engineering
ie University of Texas at Austin
400
stin TX 78712
2 471-5838

David L. Bourell (193, 303, 317,
339)
The Center for Materials Science and Engr.
The University of Texas at Austin
Austin TX 78712
512 471-3170

I. Campbell
Dept. Man. Eng. & Ops. Mangmt.
The University of Nottingham
University Park
Nottingham, NG7 2RD UNITED KINGDOM
44 602 514 063/ fax: 0602 514 000

el Barlow (204,303,333,350,
360,370,376)
partment of Chemical Engineering
ie University of Texas at Austin
stin TX 78712
2 471-1271

Walter Bradley
Texas A & M University
Department of Mechanical Engineering
College Station TX 77843

William T. Carter, Jr. (51)
GE Research & Development Center
P. O. Box 8
Bldg. K1, Room 235 MB
Schenectady NY 12301
518 387-6452/ fax: 518 387-7495

ven Baumgardner
exas Instruments
O. Box 405
S 3471
wisville TX 75067
4 462-4462/ fax: 214 462-5610

Bob Brown (113)
BPM Technology Inc.
1200 Woodruff Rd.
Suite A19
Greenville SC 29607
803-297-7700/ fax 803-297-7711

Robert S. Chambers
Sandia National Laboratories
Org. 1561, P. O. Box 5800
Albuquerque NM 87185
505 844-0771 fax: 505 844-9297

seph Beaman (193, 291, 303)
ie University of Texas at Austin
aterials Science & Engineering
201
stin TX 78712
2 471-3058

Robert L Brown
Director
Advanced Process and Control R&D
The Gillette Company
Gillette Park
617 463-2315 fax: 463-2527

Jana K. Chari (135)
Iowa State University
1051 Black Engineering Bldg.
Engel Manufacturing Laboratory
Ames IA 50010
515 294-0569 fax: 294-3261
jana@iastate.edu

on Beha
E Research & Development Center
O. Box 8
dg. K1, Room 235 MB
henectady NY 12301
8 387-7648/ fax 518 387-5576

Stuart B. Brown (143)
MIT
Dept. of Materials Science & Engineering
Bldg 8-106
Cambridge MA 02139
617 253-2100 fax: 253-8669

Richard P. Chartoff (245)
University of Dayton
Rapid Prototype Development Laboratory
300 College Park Avenue
Dayton OH 45469-0001
513 229-2517/ fax: 229-3433

Feng Chi (64)
Center for Materials Science and Engineering
The University of Texas at Austin
Austin TX 78712

A. De Filippi
Politecnico Di Torino
Dipartimento di Sistemi di Produzione
Ed Economia Dell'Azienda
Corso Duca Abruzzi 24
39 11-5647268/ fax 564-7294

Mark Ganninger
DTM Corporation
1611 Headway Circle, Bldg. 2
Austin TX 78754
512 339-2922/ fax: 512 339-0634

Michael J. Cima (40, 223)
Ceramics Processing Research Laboratory
MIT
77 Massachusetts Ave.
Room 12-011
617 253-6877 fax: 612 258-6936

Carl Deckard
DTM Corporation
1611 Headway Circle, Bldg. 2
Austin TX 78754

Edward P. Gargiulo (178)
DuPont Medical Products
Glasgow Business Community # 713
P. O. Box 6101
Newark DE 19714
302 451-9577 fax: 328-5693

T. Dennis Claar (215)
Lanxide Corporation
1300 Marrows Road
P. O. Box 6077
Newark DE 19714-6077

P. M. Dickens (27)
Dept. Man. Eng. & Ops. Mangmt.
The University of Nottingham
University Park
Nottingham NG7 2RD UNITED KINGDOM
602 515151/ fax: 602 51400

Ian Gibson (113)
Department of Manufacturing Engineering
and Operations Management
The University of Nottingham
University Park
011 0602 514018 fax: 0602 514000

Richard C. Cobb (27)
Dept. Man. Eng. & Ops. Mangmt.
The University of Nottingham
University Park
Nottingham, NG7 2RD UNITED KINGDOM
44 602 514 063/ fax: 0602 514 000

Michael A. Ervin
DTM Corporation
1611 Headway Circle
Austin TX 78754
512 339-2922 / fax: 512 339-0634

Paul Gillette
Hercules Research Center
500 Hercules Road
Wilmington DE 19804-0001
302 995-3815/ fax: 302 995-4121

Ed Coggins
Reliance Electric
P. O. Box 499
Greenville SC 29602
803 281-2248/ fax 803 281-2487

Brian Fabes
Arizona Materials Lab
4715 E. Fort Lowell
Tucson AZ 85712
602 621-6372/ fax: 322-2993

Dan Girouard
DTM Corporation
1611 Headway Circle, Bldg. 2
Austin TX 78754
512 339-2922/ fax: 512 339-0634

Robert Connelly
Motorola, Inc.
8000 W. Sunrise Blvd.
Ft. Lauderdale FL 33322
305 475-6148/ fax: 305 475-5584

Steven G. Fishman
Program Manager
Office of Naval Research
800 N. Quincy St.
Arlington VA 22217-5000
703 696-0285/ fax: 696-0285

Marc Glazer (333)
Department of Mechanical Engineering
The University of Texas at Austin
62200
Austin TX 78712
512 471-5838

Richard Corden (94)
DTM Corporation
1611 Headway Circle, Bldg. 2
Austin TX 78754

Paul Forderhase (94)
DTM Corporation
1611 Headway Circle, Bldg. 2
Austin TX 78754
512 339-2922 fax: 339-0634

Jeffrey A. Graves
Rockwell Science Center
1049 Camino Dos Rios
Thousand Oaks CA 91360
805-373-4438/ fax 805-373-4775

Richard H. Crawford (102, 291)
The University of Texas at Austin
Department of Mechanical Engineering
ETC 4.138
Austin TX 78712
512 471-1504

Douglas W. Freitag
Loral Vought Systems
P. O. Box 650003, M/S WT-21
Dallas TX 75265-0003
214 603-1632 fax: 214 603-0419

Sashidhar Guduri (291)
Department of Mechanical Engineering
The University of Texas at Austin
62200
Austin TX 78712

Stephen C. Danforth
Rutgers University
Center for Ceramic Research
P. O. Box 909
Brett and Bowser Roads
908 932-2211 fax: 932-3258
danforth@silicon-nitride-rutgers.edu

Paul S. Fussell
Alcoa Labs
100 Technical Drive
Alcoa Center PA 15069-0001

Tommy R. Guess
Sandia National Labs
P. O. Box 5800
Albuquerque NM 87185
505 845-9748/ fax: 505 844-1110

Jerry Lee Hall (135)
Iowa State University
1051 Black Engineering Bldg.
Engel Manufacturing Laboratory
Ames IA 50010
515 294-0569/ fax: 515 294-3261

James Hetzner
General Motors Corporation
Powertrain Division
1629 N. Washington
Saginaw MI 48605
517 757-0015/ fax: 517 757-1484

Leslie Horton (178)
2537 Park Heights Terrace
Baltimore MD 21215
410 542-7709

Chris Hysinger
Department of Mechanical Engineering
The University of Texas at Austin
MC 62200
Austin TX 78712

Kevin Jakubenas
The University of Texas at Austin
Center for Materials Science & Engineering
62201
Austin TX 78712

Anand Jog
Department of Mechanical Engineering
The University of Texas at Austin
MC 62200
Austin TX 78712

Roy Johanson (186)
University of Michigan
2250 G.G. Brown
Ann Arbor MI 48103
313-936-2624

Lloyd Johnson
Center for Materials Science and Engineering
The University of Texas at Austin
Austin TX 78712

Dale Karr
University of Michigan
Dept. of Naval Architecture & Marine Engineering
Ann Arbor MI 48109-2145

Luke L. Kimble
Market Development Manager
DTM Corporation
1611 Headway Circle, Bldg. 2
Austin TX 78754

Chuck Kirschman
BPM Technology, Inc.
1200 Woodruff Rd.
Suite A19
Clemson SC 29607

Ron Knight
Loral Vought Systems
P. O. Box 650003 M/S WT-21
Dallas TX 75265-0003

Visa Koivunen (275)
General Robotics and Active Sensory Perception
(GRASP) Laboratory
University of Pennsylvania
300C 3401 Walnut Street

Uday Lakshminarayan
DTM Corporation
1611 Headway Circle, Bldg. 2
Austin TX 78754

Thomas S. Latham
United Technologies Research Center
411 Silver Lane
East Hartford CT 06140
203 727-7409 / fax: 203 727-7880

Allen Lauder
E-Systems
7700 Arlington Blvd.
Falls Church VA 22046
(703) 560-5000 fax: 703 280-4627

Goonhee Lee (376)
The University of Texas at Austin
Department of Chemical Engineering
MC 60400
Austin TX 78712
512 471-5828

Insup Lee
Center for Materials Science & Engineering
The University of Texas at Austin
62201
Austin TX 78712

Sang-Joon John Lee (223)
MIT
35-231
77 Massachusetts Ave.
Cambridge MA 02139
617 253-2606/ fax 617 253-2123

Richard Levy (121)
Department of Radiology
The University of Michigan Medical Center
1500 E. Medical Center Drive
Ann Arbor MI 48109-0030
313 936-9878 fax: 764-2412

Brent Looby
Department of Mechanical Engineering
The University of Texas at Austin
MC 62200
Austin TX 78712

Ismo Mäkelä (126)
Helsinki University of Technology
Institute of Industrial Automation
Otakaari 1
SF-02150 Espoo FINLAND
358 0 4513372/ Fax: 358 0 451 3293

Arumugam Manthiram (64, 339)
The University of Texas at Austin
Center for Materials Science & Engineering
62201
Austin TX 78712
512 471-1791 fax: 471-7681

Harris Marcus (64, 204, 308,
325, 339, 350)
The University of Texas at Austin
Center for Materials Science & Engineering
62201
Austin TX 78712
512 471-3188 fax: 471-7681

Ronald E. Marusak (81)
MicroFab Technologies, Inc.
1104 Summit, Suite 110
Plano TX 75074
214 578-8076 / fax: 423-2438

Kevin McAlea
DTM Corporation
1611 Headway Circle, Bldg. 2
Austin TX 78754
512 339-2922/ fax: 512 339-0634

Larry Melvin
Department of Mechanical Engineering
The University of Texas at Austin
MC 62200
Austin TX 78712

Robert Merz (1)
Carnegie Mellon University
5000 Forbes Avenue
Pittsburgh PA 15213
412 268-3788 fax: 412 268-5229

Theo Pintat
Fraunhofer-IFAM
Lesumer Heerhersee 36
(Lesum)
D-2820 Bremen 77 GERMANY
49 4216383153/ Fax: 421-6383190

Emanuel Sachs (40, 223)
MIT
35-231
77 Mass Avenue
Cambridge MA 02139
617 253-2606/ fax 617 253-2123

Nathan Moore
Department of Mechanical Engineering
The University of Texas at Austin
MC 62200
Austin TX 78712
512 471-5838

Gopalakrishna Prabhu (317)
The University of Texas at Austin
Center for Materials Science & Engineering
62201
Austin TX 78712
512 471-3170 fax: 471-7681

Greg Sanders
General Motors Corporation
30300 Mound Road
Mail Drop A/MD36
Warren MI 48090-9040
313 986-9057

Anthony Mulligan (60)
Advanced Ceramics Research
841 E. 47th Street
Tucson AZ 85713
602 792-2616/ fax: 602 792-2635

William R. Pratt
Sr. Programmer Analyst
Techmedica, Inc.
3760 Calle Tecate
Camarillo CA 93012
805 987-0466/ fax: 987-4111

Don Sifford
Texas Instruments, Inc.
P.O. Box 405
MS 3412
Lewisville TX 75067
214 462-2151/ fax: 214 462-5610

Ulrike Naerger
Daimler-Benz TEP/M
P. O. Box 2360
U'm GERMANY 89013
49 731-505 2913 fax: 49 731-5054212

Mark S. Pridham (74)
University of Dundee
Dept. of Applied Physics & Electronic
and Manufacturing Engineering
Dundee DD1 4HN UNITED KINGDOM
011 44 382 23181/ fax: 02830

Manfred Sindu
Fraunhofer-Institut fur Angewandte
Materialforschung
Lesumer-Heerstrabe 36
D-2820 Bremen/77(Lesum) GERMANY
0421 6383-0/ fax: 0421 6383 190

Christian Nelson (360)
DTM Corporation
1611 Headway Circle, Bldg. 2
Austin TX 78754
512 339-2922/ fax: 512 339-0634

William R. Priedeman (86)
Stratasys, Inc.
14950 Martin Drive
Eden Prairie MN 55343
612 937-3000

Ain A. Sonin (237)
MIT
Department of Mechanical Engineering
Room 3-256
Cambridge MA 02139
617 253-2247 fax: 258-8559

Kurt O'Connor
Allison Gas Turbine
2001 South Tibbs Ave.
Indianapolis IN 46241
317 230-6282 fax: 230-2990

Fritz Prinz (1, 186)
Director, EDRC
Carnegie Mellon University
5000 Forbes Avenue
Pittsburgh PA 15213
412 268-2499 fax: 412 268-5229

Dieter Steinhauser
Dr. Ing. h.c.F. Porsche AG
Porschestrasser
71287 Weissach GERMANY
7044352142/ fax: 7044352058

Sean O'Reilly (168)
Ford Motor Company
Manufacturing Development Center
Operations Engineering
24500 Glendale Avenue
fax 313 592-2381

Ramas V. Raman (271)
Ceracon, Inc.
1101 N. Market Blvd. # 9
Sacramento CA 95834
(916) 928-1933/ Fax: 928-1934

Jim Stewart
Allison Gas Turbine
2001 South Tibbs Ave.
Indianapolis IN 46241
317 230-4337 fax: 230-2990

Thomas Pang (11, 158)
3D Systems
26081 Ave. Hall
Valencia CA 91355
(805) 295-5600/ fax: 805 257-1200

Sandra Rider
Xerox
800 Phillips Road 208-04H
Webster NY 14580
716-422-9354/ fax 716-422-9435

Brent Stucker
Texas A & M University
Department of Mechanical Engineering
College Station TX 77843

Joseph Pegna (253)
Rensselaer Polytechnic Institute
Department of Mechanical Engineering,
Aeronautical Engineering & Mechanics
Troy NY 12180
(518) 276-6999 fax: 276-2623

D. Romano
Politecnico Di Torino
Dipartimento di Sistemi di Produzione
Ed Economia Dell'Azienda
Corso Duca Abruzzi 24
39 11-564-7268/ fax 564-7294

Kevin Stuffle (60)
Advanced Ceramics Research
841 E. 47th Street
Tucson AZ 85713
602 792-2616/ fax: 602 792-2635

P. Kamatchi Subramanian (350)
Center for Materials Science & Engineering
The University of Texas at Austin
62201
Austin TX 78712

Lee Weiss (1, 186)
Carnegie Mellon University
5000 Forbes Avenue
Pittsburgh PA 15213
412 268-7657 / fax: 412 258-5016

Martin Sun
3M
6801 River Place Blvd A 146-1503
A146-5S-03
Austin TX 78726-9000
(512) 984-5496 fax: 984-7258

Eric M. Weissman
BF Goodrich R&D
9921 Brecksville Road
Brecksville OH 44141
216 447-5420/ fax: 216 838-4413

Rich Thissell
The University of Texas at Austin
Center for Materials Science & Engineering
62201
Austin TX 78712

Bernd Wiedemann
University of Stuttgart-IUP
Pfaffenwalddoing 32
Stuttgart, Valingen GERMANY
0211 685-2678/ fax: 0211 685-2066

James R. Tobin (303)
Department of Mechanical Engineering
The University of Texas at Austin
62200
Austin TX 78712
512 837-7137

Christian Wilkening
FGB, TU Munich
Arcisstr. 27
8000 München 2 GERMANY

James V. Tompkins (325)
Center for Materials Science & Engineering
The University of Texas at Austin
62201
Austin TX 78712

P.R. Winans
Rocketdyne, Div. of Rockwell Int.
6633 Canoga Ave IB17
P. O. Box 7922
Canoga Park CA 93109-7922
818 718-3798 fax 818 718-4840

N.K. Vail (204, 333, 350,
360)
Department of Chemical Engineering
The University of Texas at Austin
60400
Austin TX 78712
512 471-5838

Wayne Winkelman
Digibotics
2800 Longhorn Blvd. Suite 102
Austin TX 78758
512 832-9040 fax: 832-1163

Ralph Wachter
Office of Naval Research
Computer Science Division, Code 1133
800 N. Quincy Street
Arlington VA 22217-5660
703-696-4304/ fax 703-696-0934

John Wooten
Rockwell International Corp.
Rocketdyne Division
6633 Canoga Ave., MS IB15
P. O. Box 7922
818 718-4897/ fax: 718-4600

Craig T. Wadham
DTM Corporation
1611 Headway Circle, Bldg. 2
Austin TX 78754
512 339-2922 / fax: 512 339-0634

Benny Wu (193)
Department of Mechanical Engineering
The University of Texas at Austin
MC 62200
Austin TX 78712

Gary Waite
Vertical Dimensions
630 So. 4th St. Suite 100
Las Vegas NV 89101
702 387-6453 fax: 702 382-0365

Rick Yeager
DTM Corporation
1611 Headway Circle, Building 2
Austin TX 78754
512 339-2922/ fax: 512 339-0634